

University of Windsor

Scholarship at UWindor

Electronic Theses and Dissertations

Theses, Dissertations, and Major Papers

2010

Solid-State NMR Spectroscopy of Unreceptive Nuclei in Inorganic and Organic Systems

Hiyam Hamaed
University of Windsor

Follow this and additional works at: <https://scholar.uwindsor.ca/etd>

Recommended Citation

Hamaed, Hiyam, "Solid-State NMR Spectroscopy of Unreceptive Nuclei in Inorganic and Organic Systems" (2010). *Electronic Theses and Dissertations*. 391.
<https://scholar.uwindsor.ca/etd/391>

This online database contains the full-text of PhD dissertations and Masters' theses of University of Windsor students from 1954 forward. These documents are made available for personal study and research purposes only, in accordance with the Canadian Copyright Act and the Creative Commons license—CC BY-NC-ND (Attribution, Non-Commercial, No Derivative Works). Under this license, works must always be attributed to the copyright holder (original author), cannot be used for any commercial purposes, and may not be altered. Any other use would require the permission of the copyright holder. Students may inquire about withdrawing their dissertation and/or thesis from this database. For additional inquiries, please contact the repository administrator via email (scholarship@uwindsor.ca) or by telephone at 519-253-3000ext. 3208.

Solid-State NMR Spectroscopy of Unreceptive Nuclei in Inorganic and Organic Systems

By

Hiyam Hamaed

A Dissertation

Submitted to the Faculty of Graduate Studies
through the Department of Chemistry and Biochemistry
in Partial Fulfilment of the Requirements for
the Degree of Doctor of Philosophy
at the University of Windsor.

Windsor, Ontario, Canada

2010

© 2010 Hiyam Hamaed

Declaration of Co-Authorship / Previous Publications

I. Co-Authorship Declaration

Following the rules set by the Faculty of Graduate Studies, this thesis is presented in manuscript format. Most of the work discussed in this dissertation has been published in peer-reviewed journals. I was the principal investigator for all publications and I played a major role in preparing the manuscripts. I acknowledge my advisor, Professor Robert W. Schurko, as a co-author who made a key role in writing/editing of manuscripts. I hereby declare that this thesis incorporates material that is result of joint research, as follows:

The ^{209}Bi NMR study presented in Chapter 3 is a collaboration with Dr. Victor V. Terskikh, a manger of the National Ultrahigh-Field NMR Facility for Solids in Ottawa, who acquired the high field spectra and performed the CASTEP calculations. Mike W. Laschuk was an undergraduate student in our group who helped in synthesizing and packing some of the samples.

The ^{137}Ba NMR investigation discussed in Chapter 4 is collaboration with Eric Ye, a research scientist at the National Ultrahigh-Field NMR Facility for Solids in Ottawa, who acquired the high field spectra and performed the CASTEP calculations. Dr. K. Udachin at the National Research Council in Ottawa acquired the powder X-ray diffraction patterns using Mo X-ray sources which is not available at the University of Windsor.

The ^{115}In NMR study presented in Chapter 5 is a collaboration with Dr. Charles L. B. Macdonald and his students Ben F.T. Cooper at the University of Windsor who

synthesized the samples. Drs. Victor V. Terskikh and Eric Ye helped me in acquiring the high field NMR spectra and running the CASTEP calculations. Tatjana Milovic, an undergraduate student in my group helped in sample packing.

The ^{109}Ag NMR investigation discussed in Chapter 6 is a collaboration with Dr. G.H. Shimizu and his students L.J. May and J.M. Taylor at the University of Calgary who provided us with most of the samples and some of their powder X-ray diffraction data.

The ^{35}Cl NMR study presented in Chapter 7 is a collaboration with Dr. Riqiang Fu. at the National High Magnetic Field Laboratory in Tallahassee Florida, who acquired the high field ^{35}Cl NMR spectra. Jenna Pawlowski was an undergraduate student in my group who helped in synthesizing and crystallizing the different polymorphs as well as obtaining their powder XRD patterns. Benjamin F.T. Cooper obtained the X-ray single crystal structures of some of these drugs and Prof. Holger Eichhorn at the University of Windsor helped me with the thermal gravimetric analysis (TGA) experiments.

The ^{35}Cl NMR investigation discussed in Chapter 8 is a collaboration with Dr. Riqiang Fu at the National High Magnetic Field Laboratory in Tallahassee Florida, who acquired the high field ^{35}Cl NMR spectra. Mike W. Laschuk was an undergraduate student in our group who helped in literature research, synthesizing and packing samples and obtaining their powder XRD patterns. Dr. Luke A. O'Dell was a postdoctoral fellow in my group who helped with the Simpson simulations.

I am aware of the University of Windsor Senate Policy on Authorship and I certify that I have properly acknowledged the contribution of other researchers to my thesis, and have obtained written permission from each of the co-authors to include the above

material(s) in my thesis. I certify that, with the above qualification, this thesis, and the research to which it refers, is the product of my own work.

II. Declaration of Previous Publications

This thesis includes 4 original papers that have been previously published or submitted for publication in peer reviewed journals, as follows:

- Chapter 3: H. Hamaed, M.W. Laschuk, V.V. Terskikh and R.W. Schurko. Application of Solid-State ^{209}Bi NMR to the Structural Characterization of Bismuth-Containing Materials. *J. Amer. Chem. Soc.*, **2009**, 131, 8271–8279.
- Chapter 4: H. Hamaed, E. Ye, K. Udachin and R.W. Schurko. Solid-State ^{137}Ba NMR Spectroscopy: An Experimental and Theoretical Investigation of ^{137}Ba Electric Field Gradient Tensors and Their Relation to Structure and Symmetry. *J. Phys. Chem. B*, **2010**, 114, 6014–6022.
- Chapter 6: H. Hamaed, A.Y.H. Lo, L.J. May, J.M. Taylor, G.H. Shimizu and R.W. Schurko. Investigation of Silver-Containing Layered Materials and Their Interactions with Primary Amines using Solid-State ^{109}Ag and ^{15}N NMR Spectroscopy and First Principles Calculations. *Inorg. Chem*, **2008**, 47, 11245–11256.
- Chapter 7: H. Hamaed, J.M. Pawlowski, B.F.T. Cooper, R. Fu, S.H. Eichhorn and R.W. Schurko. Application of Solid-State ^{35}Cl NMR to the Structural Characterization of Hydrochloride Pharmaceuticals and their Polymorphs. *J. Am. Chem. Soc.*, **2008**, 130, 11056-11065.

I certify that I have obtained a written permission from the copyright owner(s) to include the above published material(s) in my thesis. I certify that the above material describes work completed during my registration as graduate student at the University of

Windsor.

I declare that, to the best of my knowledge, my thesis does not infringe upon anyone's copyright nor violate any proprietary rights and that any ideas, techniques, quotations, or any other material from the work of other people included in my thesis, published or otherwise, are fully acknowledged in accordance with the standard referencing practices. Furthermore, to the extent that I have included copyrighted material that surpasses the bounds of fair dealing within the meaning of the Canada Copyright Act, I certify that I have obtained a written permission from the copyright owner(s) to include such material(s) in my thesis.

Abstract

Nuclei are termed unreceptive if they are not amenable to solid-state NMR (SSNMR) experimentation at standard magnetic field strengths due to (i) low natural abundances or dilution; (ii) low gyromagnetic ratios; (iii) inefficient longitudinal relaxation; (iv) large quadrupole moments; or (v) combinations of these factors. This thesis focuses on applying a variety of SSNMR methods to study unreceptive nuclei in a variety of systems.

The first portion of this thesis focuses upon ultra-wideline (UW) SSNMR of three main group nuclei: ^{209}Bi , ^{137}Ba and ^{115}In . ^{209}Bi and ^{137}Ba SSNMR were applied to a series of systems with important structural motifs, while ^{115}In SSNMR was applied to systems with In in the +1 oxidation state. Extremely broad SSNMR spectra were acquired at field strengths of 9.4 and 21.1 T using frequency-stepped techniques. In all cases, the electric field gradient (EFG) and the chemical shift (CS) tensor parameters obtained from these spectra are used to probe the metal coordination environments. These data are complemented by first principles calculations of the NMR tensors using molecular orbital (MO) and plane wave density functional theory (DFT) methods.

The second portion of this thesis examines applications of SSNMR of unreceptive nuclei to some practical problems. First, ^{109}Ag and ^{15}N SSNMR experiments were performed to study silver supramolecular frameworks, and structural changes which occur upon their reactions with primary amines. ^1H - ^{109}Ag cross polarization/magic-angle spinning (CP/MAS) NMR spectra were used to differentiate Ag sites, and ^1H - ^{15}N CP/MAS NMR spectra provided measurements of $^1J(^{109}\text{Ag}, ^{15}\text{N})$ coupling constants, which are used to probe bonding Ag-N bonding. First principles calculations of silver and nitrogen CS tensors and

$^1J(^{109}\text{Ag}, ^{15}\text{N})$ constants aided in formulating the structural models for the new materials.

Second, ^{35}Cl SSNMR spectra, single-crystal and powder X-ray diffraction data, and ab initio calculations were utilized to study HCl pharmaceuticals and some of their polymorphs. The sensitivity of the ^{35}Cl EFG tensor parameters to subtle changes in the chlorine environments is reflected in the powder patterns, which can be used for structural interpretation, identifying and distinguishing polymorphs, and rapidly providing a spectral fingerprint of each pure pharmaceutical and its polymorphs.

كل وعاء يضيق بما فيه الا وعاء العلم فانه يتسع

Dedicated to my family

Acknowledgment

I wish to extend my appreciation to the many people, without whose help this thesis would not be possible. I would like to express my utmost gratitude to my advisor Prof. Robert W. Schurko for giving me this great opportunity to work in his group and for introducing me to the exciting field of NMR. I am forever grateful to him for making my graduate studies a growing experience from both the scientific and personal perspectives. His enthusiasm and dedication to research have motivated and will always inspire me. I must thank him for giving me the opportunity to work on diverse and exciting projects, and for allowing me to choose and design my projects the way I desire. I am very thankful for his invaluable guidance in teaching me about NMR and his patience in thoroughly editing my manuscripts and thesis. I appreciate him in giving me the chance to present my work at several conferences and in financially supporting my visits to the ultrahigh NMR facilities in Tallahassee and in Ottawa.

I am indebted to my present and past colleagues including Dr. Kris Harris, Aaron Rossini, Alan MacGregor, Bryan Lucier, Tatjana Milovic, Chris Mireault, Alex Reidel, Dr. Luke O'Dell, Dr. Joel Tang, Dr. Andy Lo, Jenna Pawlowski, Mike Laschuk, and Dr. Ivan Hung for their helpful insights and stimulating discussions about NMR, proof reading my manuscripts and providing a cheerful working environment. I am particularly grateful to Dr. Joel Tang for always being willing to help me when needed, even during his busiest time writing his PhD thesis. I am also thankful to Dr. Andy Lo for training me in using the NMR spectrometer and in taking me through the first steps in the NMR journey. I also thank the undergraduate students, including Tatjana Milovic, Jenna

Pawlowski, and Mike Laschuk for collaborating with me on some of the projects presented in this thesis and Bryan Lucier in putting up with my jokes about him.

I extend my appreciation to Prof. Charles L. B. Macdonald and his student Ben Cooper for collaborating with us on a couple of projects and for their helpful insights and discussions. I also thank them and other group members including Erin Norton, Rajoshree Bandyopadhyay, Christopher Allan, Gregory Farrar, and Chris Andrews for great comments regarding crystallization and synthesis of different samples and for their courtesy in allowing me to work in their lab and use their glassware. I am thankful to Dr. Holger Eichhorn for helping me with TGA and DSC experiments and for troubleshooting the X-ray diffractometer.

I am very appreciative to Dr. Riqiang Fu at the National High Magnetic Field Laboratory in Tallahassee, Florida and Drs. Victor Terskikh and Eric Ye at the National Ultrahigh-field NMR Facility for Solids in Ottawa, for making my trip to their facilities extremely comfortable and worthwhile, and for collaborating with us on different projects and providing great insights and comments regarding our collaborative research. I also thank Dr. George K.H. Shimizu and his students Leslie May and Jared Taylor at the University of Calgary for collaborating with us and providing us with interesting materials and Dr. David L. Bryce at the University of Ottawa for making his EFGSHIELD program available for us to use.

I am grateful to Dr. Stephen Loeb and Dr. Tricia Breen Carmichael for serving on my committee during my graduate years, and Dr. Wladyslaw Kedzierski and Dr. Tatyana Polenova for reading and correcting my thesis and attending my defense.

I am very appreciative to Joe Lichaa for fixing my computer problems and to Matthew Revington, Mike Fuerth and Sinisa Jezdic for their help regarding the NMR spectrometers and electronic problems. I also would like to thank Beth Kickham and Kimberly Lefebvre for mailing out my samples to our collaborators and Marlene Bezaire for organizing my defense.

I wish to thank the government of Ontario for an Ontario Graduate Scholarships and the University of Windsor for tuition scholarships throughout my graduate years and the National High Magnetic Field Laboratory in Tallahassee, Florida and the National Ultrahigh-field NMR Facility for Solids in Ottawa, for travel support.

Last but not least, I like express my sincere gratitude to my parents and siblings for their endless and unconditional encouragement, love and support. This accomplishment would not be possible without you.

Table of Contents

Declaration of Co-Authorship/Previous publications.....	iii
Abstract	vii
Dedication.....	ix
Acknowledgements.....	x
List of Tables.....	xvii
List of Figures and Schemes.....	xix
List of Abbreviations.....	xxvi
List of Symbols.....	xxix

Chapter 1

Introduction	1
Bibliography	10

Chapter 2

Concepts and Techniques in Solid-State NMR

2.1 Principles of NMR	16
2.2 NMR Interactions	17
2.2.1 External Interactions	18
2.2.1.1 Zeeman Interaction.....	18
2.2.1.2 Radiofrequency Interaction.....	20
2.2.2 Internal Interactions	22
2.2.2.1 Chemical Shielding Interaction.....	22
2.2.2.2 Direct Dipolar Interaction.....	29
2.2.2.3 Indirect Spin-Spin Interaction or <i>J</i> -coupling.....	30
2.2.2.4 Quadrupolar Interaction.....	31
2.2.2.5 Euler Angles.....	36
2.3 Solid State NMR Techniques	37
2.3.1 Magic Angle Spinning.....	37
2.3.2 Cross Polarization.....	40
2.3.4 Hahn-Echo and Quadrupolar Carr-Purcell Meiboom-Gill sequences..	44
2.3.5 Frequency Stepped Techniques and WURST-QCPMG.....	46
2.3.6 Ab Initio NMR Calculations.....	48
2.4 Bibliography	50

Chapter 3

Application of Solid-State ²⁰⁹Bi NMR to the Structural Characterization of Bismuth-Containing Materials

3.1 Introduction.....	56
3.2 Experimental.....	59
3.2.1 Sample Preparation	59
3.2.2 Solid-State NMR	59

3.2.3 Ab Initio Calculations	61
3.3 Results and Discussion	63
3.3.1 Solid-State ^{209}Bi NMR.....	63
3.3.2 Theoretical Calculations of ^{209}Bi EFG and CS Tensors	73
3.4 Conclusions	79
3.5 Bibliography.....	81

Chapter 4

Solid-State ^{137}Ba NMR Spectroscopy: An Experimental and Theoretical Investigation of ^{137}Ba Electric Field Gradient Tensors and Their Relation to Structure and Symmetry

4.1 Introduction.....	86
4.2 Experimental.....	89
4.2.1 Solid-State NMR	90
4.2.2 Computational Methods	92
4.3 Results and Discussion	93
4.3.1 Solid-State ^{137}Ba NMR	93
4.3.2 Theoretical Calculations of ^{137}Ba EFG and CS Tensors	104
4.4 Conclusions	110
4.5 Bibliography.....	112

Chapter 5

Solid-State ^{115}In NMR Study of Low-Oxidation State Indium Complexes

5.1 Introduction.....	116
5.2 Experimental.....	119
5.2.1 Sample Preparation	119
5.2.2 Solid-State NMR	120
5.2.3 Computational Methods	122
5.3 Results and Discussion	122
5.3.1 Solid-State ^{115}In NMR	122
5.3.2 Theoretical Calculations of ^{115}In EFG and NS Tensors	134
5.4 Conclusions	141
5.5 Bibliography.....	142

Chapter 6

Investigation of Silver-Containing Layered Materials and Their Interactions with Primary Amines Using Solid-State ^{109}Ag and ^{15}N NMR Spectroscopy and First Principles Calculations

6.1 Introduction.....	146
6.2 Experimental.....	150
6.2.1 Sample Preparation	150
6.2.2 Solid-State NMR	152
6.2.3 Ab Initio Calculations	154
6.3 Results and Discussion	154

6.3.1 Solid-State NMR.....	154
6.3.2 Ab Initio Calculations.....	171
6.4 Conclusions.....	178
6.5 Bibliography.....	179

Chapter 7

Application of Solid-State ³⁵Cl NMR to the Structural Characterization of Hydrochloride Pharmaceuticals and their Polymorphs

7.1 Introduction.....	184
7.2 Experimental.....	188
7.2.1 Sample Preparation and XRD.....	188
7.2.2 Solid-State NMR.....	189
7.2.3 Ab Initio Calculations.....	191
7.3 Results and Discussion.....	192
7.3.1 Crystal structures.....	192
7.3.2 Solid-State ³⁵ Cl NMR.....	195
7.3.3 Theoretically calculated NMR interaction tensors.....	203
7.4 Conclusions.....	207
7.5 Bibliography.....	208

Chapter 8

Solid-State ³⁵Cl NMR Spectroscopy of Hydrochloride Pharmaceuticals

8.1 Introduction.....	212
8.2 Experimental.....	216
8.2.1 Powder XRD.....	216
8.2.2 Solid-State NMR.....	217
8.2.3 Ab Initio Calculations.....	218
8.3 Results and Discussion.....	220
8.3.1 Solid-State ³⁵ Cl NMR.....	220
8.3.2 Theoretically calculated NMR interaction tensors.....	235
8.4 Conclusions.....	246
8.5 Bibliography.....	248

Chapter 9

General Conclusions and Future Outlook.....	252
Bibliography.....	261

Appendices

1. Appendix A: Supplementary Information for Chapter 3.....	268
2. Appendix B: Supplementary Information for Chapter 4.....	276
3. Appendix C: Supplementary Information for Chapter 5.....	289
4. Appendix D: Supplementary Information for Chapter 6.....	298

5. Appendix E: Supplementary Information for Chapter 7.....	308
6. Appendix F: Supplementary Information for Chapter 8	318
7. Copyright Release Forms	321
8. Vita Auctoris	322

List of Tables

3.1.	Summary of the experimental ^{209}Bi NMR parameters.....	63
3.2.	Comparison of the experimental and CASTEP ^{209}Bi EFG tensor parameters of the BiOX series.....	75
3.3.	Comparison of the experimental and CASTEP ^{209}Bi CS tensor parameters of the BiOX series	75
3.4.	Comparison of the experimental and Gaussian ^{209}Bi EFG tensor parameters.....	78
4.1.	Summary of the experimental ^{137}Ba NMR parameters	95
4.2.	Comparison of the experimental and CASTEP-calculated ^{137}Ba EFG tensor parameters.....	105
5.1.	Summary of the experimental ^{115}In NMR parameters.....	123
5.2.	Comparison of the experimental and theoretical ^{115}In EFG and CS tensor parameters	135
6.1.	Experimental ^{109}Ag chemical shift parameters.....	157
6.2.	Experimental indirect spin-spin couplings.....	157
6.3.	Experimental ^{15}N chemical shifts.....	160
6.4.	Experimental and theoretical ^{109}Ag chemical shift parameters and $^1J(^{109}\text{Ag}, ^{14}\text{N})$ coupling values.....	173
6.5.	Calculated ^{15}N isotropic chemical shielding values and associated coordination shifts relative to free propylamine in the structural models for 1e	177
7.1.	Crystal structure data for the HCl local anaesthetics.....	193
7.2.	Summary of the experimental ^{35}Cl NMR parameters.....	195
7.3.	Comparison of the experimental and theoretical ^{35}Cl EFG and CS tensor parameters	204
8.1	A comparison of short Cl...H contacts and NMR parameters from experiment and theory.....	221

8.2.	Summary of the experimental ^{35}Cl NMR parameters.	222
8.3.	Comparison of the experimental and theoretical ^{35}Cl EFG and CS tensor parameters	237

List of Figures and Schemes

Figures:

- 2.1. The splitting of the energy levels of a spin-1/2 nucleus in the presence of a static applied magnetic field, B_019
- 2.2. The two vector components of the \mathbf{B}_1 field in the xy-plane. Adapted from Prof. Schurko's NMR notes. (<http://mutuslab.cs.uwindsor.ca/schurko/nmrcourse/notes.html>).....20
- 2.3. The magnetic fields present in the rotating frame. In the case of an on-resonance pulse ($\omega_0 = \omega_{rf}$), only B_1 remains22
- 2.4. An ellipsoid portraying the three principal components of the NS tensor.....24
- 2.5. Representation of the nitrogen CSA in pyridine. Different crystallite orientations with respect to the external static magnetic field, B_0 , lead to different chemical shielding. (R.W. Schurko, NMR Course Notes, 2009. Used with permission)....26
- 2.6. The shielding tensor components determine the shape of the powder pattern.....28
- 2.7. The energy levels of spin-3/2 nuclei under Zeeman, first- and second-order quadrupolar interaction (QI).....34
- 2.8. Analytical simulation of ^{209}Bi SSNMR spectra at 9.4 T as an example of a high half integer spin nucleus to show the effects of the STs on the powder pattern. $C_Q = 180$ MHz and $\eta_Q = 0.6$35
- 2.9. The effects of C_Q and η_Q values on static SSNMR patterns36
- 2.10. Rotation of the CS tensor from the fixed EFG tensor frame of reference (x, y, z) into the CS PAS (X, Y, Z). Courtesy of Dr. Joel A. Tang37
- 2.11. The position of the NMR rotor with respect to B_0 during the MAS experiment...38
- 2.12. The cross polarization pulse sequence.....42
- 2.13. Explanation of the Hartmann-Hahn condition. **A** shows the difference between the ^1H and ^{13}C frequencies in the lab frame. **B** shows that the ^{13}C and ^1H frequencies are matched so that the spin transitions can occur.....43
- 2.14. The echo and QCPMG pulse sequences45

- 2.15.** Individual sub-spectra are acquired at even increments and co-added to produce the whole pattern. The arrows indicate the transmitter frequencies47
- 2.16.** The excitation profile for different offset frequencies. The offset producing a rectangular excitation (middle) provides non-distorted powder pattern.....47
- 3.1.** ^{209}Bi SSNMR spectra (blue - experimental, red - simulated) of BiOI, BiOBr and BiOCl at a) 21.1 T and b) 9.4 T. For BiOCl, simulations with and without satellite transitions are shown. The rolling baselines in some of these spectra arise from underlying satellite transitions which have been partially excited.....64
- 3.2.** ^{209}Bi SSNMR spectra of bismuth nitrate pentahydrate at a) 21.1 T and b) 9.4 T. Not all of the satellite transitions were acquired in order to shorten experimental time, more ST subspectra were acquired in the WURST spectrum due to the shorter experimental time.....68
- 3.3.** ^{209}Bi SSNMR spectra of nonaqua bismuth triflate at a) 21.1 T and b) 9.4 T. The rolling baselines in these spectra arise from underlying satellite transitions which have been partially excited.....70
- 3.4.** ^{209}Bi SSNMR spectra of bismuth acetate at a) 21.1 T and b) 9.4 T. † indicate satellite transitions.....72
- 3.5.** a) ^{209}Bi EFG tensor orientations in a) BiOX series, b) $\text{Bi}(\text{NO}_3)_3 \cdot 5\text{H}_2\text{O}$ c) $[\text{Bi}(\text{H}_2\text{O})_9](\text{OTf})_3$ and d) $\text{Bi}(\text{CH}_3\text{CO}_2)_3$76
- 4.1.** ^{137}Ba static SSNMR spectra of barium nitrate at two different magnetic field strengths94
- 4.2.** ^{137}Ba static SSNMR spectra of barium carbonate at two different magnetic field strengths97
- 4.3.** ^{137}Ba static SSNMR spectra of barium chlorate monohydrate at two different magnetic field strengths. Overlap between the ^{35}Cl CT and ^{37}Cl satellite transition (ST) with the ^{137}Ba spectrum is observed at 9.4 T. #: denote portions of the ^{137}Ba STs. The small distortions in the right-most “shoulders” of each simulated spectrum are artefacts arising from a limited number of angles in the total powder average.....99
- 4.4.** ^{137}Ba static SSNMR spectra of barium chloride dihydrate (left) and anhydrous barium chloride (right) at two different magnetic field strengths. *: indicates interferences from an FM radio frequency.....102

4.5.	¹³⁷ Ba static SSNMR spectrum of barium hydrogen phosphate and its simulation at 21.1 T. *: indicates interferences from an FM radio frequency.....	104
4.6.	Correlations between the experimental and calculated ¹³⁷ Ba a) C_Q and b) η_Q values	106
4.7.	Theoretically calculated ¹³⁷ Ba EFG tensor orientations in a) barium nitrate, b) barium carbonate, c) barium chlorate monohydrate, d) barium chloride dihydrate and e) anhydrous barium chloride.....	107
4.8.	Theoretically calculated ¹³⁷ Ba EFG tensor orientations in BaHPO ₄	110
5.1.	¹¹⁵ In SSNMR patterns of a) [In][GaCl ₄] and b) InCl ₂ . The MAS spectra were acquired with $\nu_{rot} = 18$ kHz, and this spinning speed is fast enough to separate the spinning sidebands from the isotropic powder patterns. The spectra of InCl ₂ reveal two indium sites with different oxidation states. *: impurity at -1020(20) ppm.....	124
5.2.	¹¹⁵ In SSNMR patterns of [In([15]crown-5) ₂][OTf]. The MAS spectrum was acquired with $\nu_{rot} = 12.5$ kHz.....	128
5.3.	¹¹⁵ In SSNMR patterns of a) [In([18]crown-6)]GaCl ₄ and b) [In([18]crown-6)]AlCl ₄ . The MAS spectra were acquired with $\nu_{rot} = 50$ kHz, and this spinning speed is fast enough to separate the spinning sidebands from the isotropic powder patterns. *: impurity at 1130(100) ppm	130
5.4.	¹¹⁵ In NMR spectra of a) InI and b) InBr. The MAS spectra were acquired at $\nu_{rot} = 62.5$ kHz.....	132
5.5.	¹¹⁵ In NMR spectra of a) [In][OTf]. The MAS spectra were acquired at $\nu_{rot} = 62.5$ kHz. *: Impurity	133
5.6.	Correlations between the experimental and calculated ¹¹⁵ In a) C_Q and b) η_Q values	136
5.7.	Correlations between the experimental and calculated ¹¹⁵ In a) chemical shift (CS), b) span (Ω) and c) skew (κ) values.....	137
5.8.	The ¹¹⁵ In EFG tensor orientations in a) [In][GaCl ₄], b) [In([15]crown-5) ₂][OTf], c) InI d) InBr, and f) [In][OTf]. The blue bonds in f are those within 3 Å from the indium, the solid black bonds are within 3.5 Å and the dashed ones are within 4 Å	

.....	138
6.1. Solid-state ^{109}Ag CP/MAS NMR spectra of 1a at two different spinning speeds, (a) $\nu_{\text{rot}} = 2.9$ kHz and (b) $\nu_{\text{rot}} = 2.0$ kHz. Isotropic peaks for the two distinct silver sites are designated as 1 and 2. \clubsuit designates spinning sidebands for site 2; all other peaks are sidebands of site 1.....	155
6.2. Solid-state ^{109}Ag CP/MAS NMR spectra of 1a - 1e . Isotropic peaks are designated with asterisks (*). Spectra of 1a , 1b and 1c were acquired at $\nu_{\text{rot}} = 2.9$ kHz and spectra of 1d and 1e were acquired at $\nu_{\text{rot}} = 2.0$ kHz.....	158
6.3. Solid-state ^{109}Ag CP/MAS NMR spectra of 1e at three different spinning speeds: (a) $\nu_{\text{rot}} = 2.0$ kHz. (b) $\nu_{\text{rot}} = 2.9$ kHz. (c) $\nu_{\text{rot}} = 8.0$ kHz. Isotropic peaks are designated with asterisks (*)......	159
6.4. ^{15}N CP/MAS NMR spectra of 1c (1:1) and 1e (1:2) acquired at two different fields. The doublets around 36 ppm (shown in the inset) correspond to different nitrogen sites of free amines. The doublets at 17 and 22 ppm correspond to nitrogen sites coupled to silver atoms. The insets are expansions taken from 1e	161
6.5. Solid-state ^{109}Ag MAS NMR spectrum of 1e at 9.4 T, $\nu_{\text{rot}} = 8.0$ kHz.....	164
6.6. Solid-state ^1H - ^{109}Ag CP/MAS NMR spectra of (a) 2a , (b) 2b , (c) 2c and (d) 3 at $\nu_{\text{rot}} = 2.0$ kHz. Isotropic peaks are denoted with asterisks (*), remaining peaks are spinning sidebands. $\#$: denotes impurity from the starting materials, 2a	166
6.7. High resolution solid-state ^{109}Ag CP/MAS NMR spectra of (a) 2b and (b) 3 (both processed with two zero-fills). Isotropic peaks are denoted by asterisks (*), and insets are expansions of areas indicated by rectangles. $\#$: denotes impurity from the starting materials, 2a	168
6.8. ^1H - ^{15}N CP/MAS NMR spectrum of 2b . The doublets at 14 and 19 ppm corresponds to nitrogen sites coupled to silver atoms. The peak at 36 ppm correspond to a small amount of unreacted dodecylamine. The low intensity peaks at 27 and 90 ppm correspond to some impurity from the ^{15}N labeled dodecylamine sample. Low intensity peaks in the region of 20 to 30 ppm underlie the main resonances, and can be attributed to either dodecylamines in differing environments or perhaps impurity phases. The asterisks denote an artifact resulting from Fourier transforming a truncated FID, which was necessary to minimize the high-power decoupling and acquisition times.....	169
6.9. Theoretically calculated silver chemical shielding tensor orientations in structural	

	models for 1a at sites (a) Ag(1) (model structure II) and structural models for (c) 2b ($[\text{Ag}(\text{NH}_2\text{C}_3\text{H}_7)_2]^+$, IV) and (d) 1e ($[\text{Ag}(\text{NH}_2\text{C}_3\text{H}_7)_2]^+ \cdot 2(\text{NH}_2\text{C}_3\text{H}_7)$, VI).....	172
6.10.	$^1J(^{109}\text{Ag}, ^{14}\text{N})$ coupling (■) and span (▲) as a function of Ag-N bond length in $[\text{Ag}(\text{NH}_2\text{C}_3\text{H}_7)]^+$	175
7.1.	Partial crystal structures of a) PH, b) TH, c) LH, and d) BH, which focus on the chlorine atom positions. The short chlorine-hydrogen contacts are indicated in red, and longer contacts are marked with dashed lines. For TH and LH, some atoms are deleted for clarity.....	194
7.2.	^{35}Cl SSNMR spectra of a) PH, b) TH, c) LH and d) polymorph LH1.....	197
7.3.	^{35}Cl SSNMR spectra of monohydrated bupivacaine HCl (BH) and its polymorphs: a) commercial BH, b) BH1 is a polymorph obtained from BH by heating it to 120 °C, c) BH2 is a polymorph obtained from BH by heating it to 170 °C.....	199
7.4.	^{13}C NMR of the monohydrated lidocaine hydrochloride (LH) samples acquired at $B_0 = 9.4$ T, $\nu_{\text{rot}} = 9.9$ kHz: a) polymorph LH1, b) commercial LH. LH has one molecule per asymmetric unit, while LH1 has two molecules per asymmetric unit, as clearly seen in the splitting of the chemical shift of the carbonyl group (165 ppm). *: denote spinning sidebands.....	201
7.5.	Powder XRD (left) and ^{13}C NMR spectra (right) acquired at 9.4 T, $\nu_{\text{rot}} = 9.0$ kHz: a) commercial BH. b) polymorph BH1 (heated to 120 °C), c) polymorph BH2 (heated to 170 °C). *: denote spinning sidebands	202
7.6	^{35}Cl EFG tensor orientations in a) PH, b) TH, c) LH and d) BH. The diagrams above are magnifications of the chlorine sites pictured in Figure 7.1.....	205
8.1.	Partial crystal structures of a) AD, b) BU and c) TR which focus on the chlorine atom positions. The short chlorine-hydrogen contacts are indicated in red, and longer contacts are marked with dashed lines. Hydrogens attached to carbon atoms and away (>3.0 Å) from the chlorine ion are deleted for clarity.....	223
8.2.	^{35}Cl SSNMR spectra of a) AD, b) BU, and c) TR. The top patterns are simulations and bottom ones are experimental. *: indicates spinning sidebands.....	224
8.3.	Partial crystal structures of a) RA, b) AM, c) CM, and d) GA which focus on the chlorine atom positions. The short chlorine-hydrogen contacts are indicated in red, and longer contacts are marked with dashed lines. Hydrogens attached to carbon atoms and away (>3.0 Å) from the chlorine ion are deleted for clarity.....	227

8.4.	³⁵ Cl SSNMR spectra of a) RA and b) AM. The top patterns are simulations and bottom ones are experimental. *: indicates spinning sidebands.....	228
8.5.	Partial crystal structures of a) AC, b) HM c) IS and d) TE, which focus on the chlorine atom positions. The short chlorine-hydrogen contacts are indicated in red, and longer contacts are marked with dashed lines. Hydrogens attached to carbon atoms and away (>3.0 Å) from the chlorine ion are deleted for clarity.....	230
8.6.	³⁵ Cl SSNMR spectra of a) AC and b) IS The top patterns are simulations and bottom ones are experimental. *: indicates spinning sidebands.....	231
8.7.	Partial crystal structures of a) DI (chlorine site 1), b) DI (chlorine site 2), c) ME (chlorine site 1) and d) ME (chlorine site 2) monohydrate which focus on the chlorine atom positions. The short chlorine-hydrogen contacts are indicated in red, and longer contacts are marked with dashed lines. Hydrogens attached to carbon atoms and away (>3.0 Å) from the chlorine ion are deleted for clarity.....	233
8.8.	³⁵ Cl SSNMR spectra of a) DI and b) ME. The top patterns are simulations and bottom ones are experimental. *: indicates spinning sidebands.....	234
8.9.	Correlations between the experimental and calculated a) C_Q values and b) η_Q values.....	238
8.10.	Correlations between the experimental and calculated a) δ_{iso} , b) Ω and c) κ values	239
8.11.	³⁵ Cl EFG tensor orientations in a) AD, b) BU and c) TR. The diagrams above are magnifications of the chlorine sites pictured in Figure 8.1.....	241
8.12.	³⁵ Cl EFG tensor orientations in a) RA, b) AM c) AC and d) IS. The diagrams above are magnifications of the chlorine sites pictured in Figures 8.3 and 8.5.....	243
8.13.	³⁵ Cl EFG tensor orientations in a) DI (chlorine site 1), b) DI (chlorine site 2), c) ME (chlorine site 1) and d) ME (chlorine site 2). The diagrams above are magnifications of the chlorine sites pictured in Figure 8.7.....	245

Schemes:

- 3.1.** a) A schematic representation of the crystal structure of BiOCl. The species in the

- BiOX series (X = Br, Cl or I) are isostructural. b) The coordination environment of the Bi atoms consists of a staggered arrangement of four halides and four oxygen atoms (left, side view; right, top view).....65
- 4.1.** The coordination environments of the barium atoms in a) barium nitrate, b) barium carbonate, c) barium chlorate monohydrate, d) barium chloride dihydrate, e) anhydrous barium chloride, f) barium hydrogen phosphate, site 1 and g) barium hydrogen phosphate, site295
- 5.1.** The coordination environments of the indium atom in a) [In][GaCl₄], b) [In([15]crown-5)₂][OTf], c) the structural model of [In([18]crown-6)]AlCl₄ and [In([18]crown-6)]GaCl₄, d) InI, e) InBr, and f) [In][OTf]. The blue bonds in f are those within 3 Å from the indium, the solid black bonds are within 3.5 Å and the dashed ones are within 4 Å126
- 6.1.** Schematic representation of the crystal structures of [Ag(4-pyridinesulfonate)]₄ (**1a**, top) and [Ag(*p*-toluenesulfonate)] (**2a**, bottom). There are two silver sites in **1a** and only one site in **2a**.....147
- 6.2.** A schematic representation showing possible layered arrangements (interdigitated, non-interdigitated, and angled interdigitated) of the U-shaped silver-dodecylamine cations in the structures of **1e** and **2b**. Uncoordinated silver cations, amines and pyridinesulfonate groups are omitted. Three-dimensional extension of these structures back into the page are omitted for clarity.....170
- 7.1** The structures of a) procaine HCl (PH), b) tetracaine HCl (TH), c) lidocaine HCl monohydrate (LH) and d) bupivacaine HCl monohydrate (BH).....187
- 8.1.** The structures of a) adifenine HCl (AD), b) buflomedil HCl (BU), c) trigonelline HCl (TR), d) ranitidine HCl (RA), e) amantadine HCl (AM), f) acebutolol HCl (AC), g) isoxsuprine HCl (IS) h) dibucaine HCl (DI) and i) mexiletine HCl (ME).....215

List of Abbreviations

AC	acebutolol
AD	adiphenine
AM	amantadine
APIs	active pharmaceutical ingredients
BH	monohydrated bupivacaine hydrochloride
B3LYP	Becke's three parameter hybrid functional using the correlation functional of Lee, Yang and Parr
BU	buflomedil
CM	L-cysteine methyl ester
CP	cross-polarization
CPMG	Carr-Purcell Meiboom-Gill
CRAMPS	Combined Rotation and Multiple-Pulse Spectroscopy
CS	chemical shielding
CSA	chemical shielding anisotropy
CT	central transition
DAS	dynamic angle spinning
DFT	Density Functional Theory
DI	dibucaine
DOR	double rotation
CRAZED	COSY Revamped with Asymmetric Z-gradient Echo Detection
EFG	electric field gradient
FID	free induction decay
FT	Fourier transform
FTIR	Fourier-transformed infrared
GA	L-glutamic acid
GADDS	general area detector diffraction system
GGA	generalized gradient approximation
GIAO	gauge-including atomic orbitals
GIPAW	gauge-including projector augmented waves

HF	Hartree Fock
HM	L-histidine HCl monohydrate
IS	isoxsuprine
LA	local anaesthetic
LH	lidocaine hydrochloride
MAS	magic angle spinning
ME	mexiletine
MQMAS	multiple quantum magic angle spinning
MS	mass spectrometric
NMR	nuclear magnetic resonance
NS	nuclear shielding
NQR	nuclear quadrupole resonance
o.d.	outer diameter
PAS	principal axis system
PBE	Perdew, Burke and Ernzerhof
PH	procaine hydrochloride
ppm	part per million
pXRD	powder X-ray diffraction
QCPMG	quadrupolar Carr-Purcell Meiboom-Gill
RA	ranitidine
RAMP/CP	ramped-amplitude cross polarization
rf	radiofrequency
RHF	restricted Hartree-Fock
S/N	signal to noise ratio
SPICP	simultaneous phase-inversion cross polarization
ST	satellite transition
STA	simultaneous thermal analysis
SSNMR	solid state nuclear magnetic resonance
TE	threonine HCl
TGA	thermal gravimetric analysis
TH	tetracaine hydrochloride

TMS	tetramethylsilane
TPPM	two-pulse phase modulation
TR	trigonelline
UW	ultra-wideline nuclear magnetic resonance
UWNMR	ultra-wideline
VACP	variable amplitude cross polarization
VOCS	variable-offset cumulative spectra
WURST	wideband uniform-rate smooth truncation pulse sequence
XRD	X-ray diffraction
ZCW	Zaremba Conroy Wolfsberg
ZORA	zeroth order regular approximation

List of Symbols

α, β, γ	Euler angles
α, β	energy state labels
γ	gyromagnetic ratio
$\delta_{11}, \delta_{22}, \delta_{33}$	principal components of the chemical shift tensor
δ_{iso}	isotropic chemical shift
η_{Q}	asymmetry of the electric field gradient tensor
κ	skew of the nuclear shielding tensor
$\sigma_{11}, \sigma_{22}, \sigma_{33}$	principal components of the nuclear shielding tensor
θ	angle describing the orientation of spin magnetization from the external magnetic field
τ_{p}	length of applied pulse
$\tau_1, \tau_2, \tau_3, \tau_4$	inter-pulse delays
μ	nuclear spin magnetic moment
ω_0	Larmor frequency (rad s^{-1})
ω_1	nutation frequency (rad s^{-1})
ω_{Q}	quadrupolar frequency (rad s^{-1})
ν_0	Larmor frequency (MHz)
ν_1	nutation frequency (Hz)
ν_{rf}	frequency of a radiofrequency pulse (Hz)
ν_{Q}	quadrupolar frequency (MHz)
Ω	span of the nuclear shielding tensor
B_0	magnitude of the applied external magnetic field
B_1	magnitude of the applied radio frequency field
C_{Q}	quadrupolar coupling constant
D^{C}	receptivity with respect to carbon
h	Planck's constant
\hbar	Planck's constant, divided by 2π
\mathcal{H}_{Q}	Quadrupolar Hamiltonian
\mathcal{H}_{Z}	Zeeman Hamiltonian

I	nuclear spin
\mathbf{j}	spin-spin coupling tensor
\mathbf{M}_0	vector describing net magnetization
Q	nuclear electric quadrupole moment
R_{DD}	dipolar coupling constant
T_1	spin-lattice relaxation time constant
T_2	transverse relaxation time constant
V_{11}, V_{22}, V_{33}	principal components of the electric field gradient tensor
Z	indicates the number of molecules in the asymmetric unit

Chapter 1

Introduction

Over the last few decades, solid-state nuclear magnetic resonance (SSNMR) has emerged as a very important technique in the characterization of a variety of materials including, but not limited to, polymers,¹ organic molecules,²⁻⁴ inorganic coordination compounds,^{3,5,6} organometallics,⁷ pharmaceuticals^{8,9} and biological systems,¹⁰⁻¹⁴ etc. SSNMR is often used independently for characterization of systems such as glasses and other amorphous solids,⁵ or as a complementary technique to single crystal and/or powder X-ray diffraction (XRD). It is also an excellent companion technique to solution NMR, especially for cases where certain synthetic products are insoluble, or assume different solution and solid state structures.

In solution, fast molecular tumbling generally leads to the observation of inherently narrow NMR lineshapes. However, in solids, this isotropic molecular motion is absent, causing the NMR lineshapes to be orders of magnitude broader due to the contributions from different anisotropic NMR interactions. Despite the reduction in resolution and signal-to-noise ratio (S/N) in SSNMR spectra, these broad NMR patterns carry a wealth of information about structural and dynamic properties of the sample which cannot be obtained from solution NMR. However, acquisition of SSNMR spectra can be very challenging, and requires specialized hardware and pulse sequences.

SSNMR spectroscopy continues to undergo rapid technological and methodological developments, and novel approaches for efficient spectral acquisition

continue to appear in the literature. For instance, the availability of ultra-high magnetic field spectrometers and the sensitivity¹⁵⁻¹⁷ enhancement techniques enable the acquisition of extremely broad NMR patterns, and have expanded the ability of SSNMR to meet the unique challenges in characterizing a broad array of new solid state materials. Wideline NMR spectroscopy is a terminology that has traditionally been used to refer to the acquisition of wide spectra with powder patterns of breadths ranging from tens of kHz up to ca. 300 kHz.¹⁸⁻²⁰ Many of these wideline SSNMR experiments have focussed on studying molecular-level dynamics using nuclei such as ¹H, ²H, ¹³C and ³¹P.^{18,21-39} Over the last few decades, wideline NMR has extended to include the acquisition of very broad NMR spectra with breadths larger than 300 kHz. Such patterns cannot be acquired in their entirety in a single experiment, and therefore, require special techniques and/or hardware. We designate such spectra as ultra-wideline (UW) NMR spectra, in order to differentiate them from conventional wideline spectra.^{40,41} Acquisition of UW NMR patterns is very challenging due to (i) limitations of the spectral excitation bandwidth which can be attainable using standard 90° pulses, (ii) limitations on the probe detection bandwidths and (iii) the inherently low S/N resulting from the spread of the signal over wide frequency ranges. Efficient acquisition of UW NMR patterns becomes even more difficult for nuclei with low gyromagnetic ratios (γ) and/or low natural abundances, often requiring specialized hardware and/or ultra-high magnetic fields.

Aside from the use of high-power rectangular pulses, a number of techniques have been developed to acquire wideline and UW NMR patterns, including the *variable-frequency pulse* (or stepped-frequency) technique, *point-by-point* techniques (including

frequency-stepped and field-stepped), the *piecewise* technique (or variable-offset cumulative spectra, VOCS) and *adiabatic pulse* techniques (vide infra). We use the four designations in italics above to avoid confusion among some of the techniques which are similarly or redundantly named in the older literature.

The variable-frequency pulse technique uses a train of low-power fixed-frequency selective rf pulses.^{42,43} After the pulse is applied, a single data point is acquired, and the transmitter frequency is changed. The entire pattern is collected using a train of low power pulses without waiting for the spin magnetization to go back to equilibrium after each pulse. There is a reduction in S/N in spectra acquired using this method compared to conventional high-power spin echo techniques, due to the low B_1 fields that are applied. This method has only been applied to acquire wideline NMR spectra (i.e., like ^2H NMR spectra) up to ca. 300 kHz in breadth.

The point-by-point method involves stepping the transmitter frequency in even increments across the desired spectral region at a fixed magnetic field, acquiring a spin echo at each frequency utilizing high-power pulses, and plotting the intensity of the spin echoes as a function of transmitter frequency to form the overall pattern (this is known as a frequency-stepped acquisition).^{44,45} Alternatively, if the proper hardware is available, one may fix the transmitter frequency and step the magnetic field strength (i.e., field-stepped acquisition) in even increments to achieve the same effect (though this is less common in practice).^{46,47} The field-stepped method has found more attention than the variable-frequency pulse techniques and has been applied to study a number of nuclei (i.e., ^{27}Al , $^{63/65}\text{Cu}$, ^{119}Sn , etc) in different systems.^{45,48-51} The frequency-stepped technique has

been used much more widely, since such experiments can be conducted on standard NMR spectrometers.⁵²⁻⁷⁰ However, as in the case of variable-frequency pulse technique, the point-by-point acquisition process (frequency- or field-stepped) can make UW NMR experiment times impractically long, rendering acquisition of such spectra inefficient and costly. For example, Bastow reported a ¹³⁷Ba frequency-stepped NMR spectrum of BaCO₃ which took more than 21 days to acquire.⁴⁴

In 1995, Massiot et al. introduced the *piecewise acquisition* (VOCS) technique⁷¹ which, at first sight, appears to be similar to the frequency-stepped point-by-point technique, in that the transmitter frequency is stepped in even increments, and FIDs are acquired at each point. The major difference is that the FIDs are Fourier transformed to produce sub-spectra, which are subsequently coadded^{71,72} or skyline projected⁷³ to form the full UW NMR pattern. This technique has been proven to be the most efficient for the acquisition of UW NMR spectra of a number of nuclei (i.e., ⁹¹Zr, ⁹³Nb, ^{69/71}Ga, ⁵⁹Co, ¹³⁹La, ²⁰⁹Bi, ⁷⁹Br, ⁶⁷Zn, ¹⁴N, ⁵³Cr, etc.) in a variety of different systems.^{55,60,65-67,70,72,74-77} In addition, the piecewise acquisition technique can be used in combination with a variety of signal enhancing pulse sequences such as the quadrupolar Carr-Purcell-Meiboom-Gill (QCPMG, see Chapter 2),^{57,60,65,67,78-88} and cross polarization (CP) pulse sequences,⁸⁹⁻⁹¹ to further reduce experimental times and obtain high S/N SSNMR spectra.

Recently, more sophisticated methods have been shown to have a great potential for improving the efficiency of UW NMR spectroscopy. One of these methods involves the use of microcoils, which typically have an inner diameter smaller than 1.5 mm.^{40,92,93} Microcoils are capable of generating large B_1 rf fields from very modest power inputs; as

such, the excitation bandwidths associated with microcoils are very large, and broad spectral regions can be probed using conventional echo experiments. The reduced sample sizes, of course, lead to a reduction in sensitivity, but this is partially compensated for by the extremely large, homogenous rf fields. Further, microcoil experiments are very useful when sample sizes are limited.

Another new methodology involves the use of WURST (Wideband Uniform Rate Smooth Truncation) adiabatic pulses,⁹⁴ which are able to achieve uniform excitation bandwidths which are much larger than those achieved with standard rf pulses. Bhattacharyya and Frydman have demonstrated that WURST pulses can be utilized to acquire UW NMR spectra of half-integer quadrupolar nuclei. WURST-80 pulses can be used in Hahn-echo or quadrupolar-echo type sequences to obtain undistorted, high S/N central transition patterns, or to obtain frequency-encoded time domain patterns, which when magnitude processed, resemble the Fourier transformed powder pattern.⁹⁵ Our group has extended this work by optimizing the power and sweep settings of the WURST pulses, and implementing the WURST pulses in a QCPMG-like scheme.⁹⁶ This WURST-QCPMG pulse sequence is very beneficial for the acquisition of UW NMR patterns,^{52,66,97,98} since the broadband excitation of adiabatic pulses is complemented by the signal enhancement from QCPMG. The development of these techniques plays a significant role in expanding the applications of SSNMR spectroscopy to explore nuclei with broad NMR lineshapes which once thought to be difficult to study by NMR.

The first part of this thesis deals with exploring the application of UW SSNMR to a variety of unreceptive nuclei (i.e., ²⁰⁹Bi, ¹¹⁵In, ¹³⁷Ba), which have received little attention

in the history of NMR. Nuclei are designated as unreceptive if they are not amenable to NMR experimentation at standard magnetic field strengths due to (i) low natural abundances or nuclear dilution; (ii) low gyromagnetic ratios (γ); (iii) large longitudinal relaxation time constants (T_1); (iv) large anisotropic NMR interactions or (v) combinations of these factors.

The second part of this thesis focusses upon SSNMR spectroscopy of unreceptive nuclei such ^{109}Ag , ^{15}N and ^{35}Cl . While the powder patterns are not particularly broad for these nuclei, they still present challenges for routine NMR experimentation due to their low gyromagnetic ratios. ^{109}Ag and ^{15}N SSNMR are applied to the study of silver-containing layered supramolecular frameworks and their interactions with primary amines to form coordination complexes. ^{35}Cl SSNMR is applied to examine a series of HCl pharmaceuticals, and some of their solid polymorphs. In order to understand the context of this research, and to appreciate the challenges faced by a SSNMR spectroscopist when acquiring NMR spectra of unreceptive nuclei, a brief discussion about NMR interactions and methods of spectral acquisition is presented in Chapter 2.

The results of the first systematic ^{209}Bi SSNMR study reported in the literature are discussed in Chapter 3.⁶⁶ Extremely broad ^{209}Bi SSNMR spectra were acquired and analysed to obtain structural information about a variety of bismuth-containing systems. This work had multiple aims: First, we demonstrated that the combination of frequency-stepped NMR techniques, specialized pulse sequences and ultra-high magnetic fields render ^{209}Bi SSNMR spectroscopy a powerful method for structural characterization. Second, we established simple correlations between the molecular

structure, symmetries of the bismuth coordination environments, and the ^{209}Bi NMR tensor parameters in periodic and molecular solids. Finally, we demonstrated that the combination of ^{209}Bi SSNMR, ^{209}Bi NQR experiments, first principles calculations and X-ray crystallography is essential for this type of structural characterization, and that this will provide future means for probing a variety of Bi materials.

The application of ^{137}Ba SSNMR to study a variety of barium-containing materials is presented in Chapter 4. ^{137}Ba UW SSNMR spectra of several barium-containing systems were acquired at two different magnetic field strengths (9.4 and 21.1 T) using frequency-stepped techniques. It is demonstrated that the use of the WURST-QCPMG pulse sequence⁹⁶ is very beneficial for rapidly acquiring high S/N ^{137}Ba SSNMR spectra. Analytical simulations of the ^{137}Ba SSNMR spectra at both fields yield the quadrupolar parameters, and in select cases, the barium chemical shift anisotropies (CSAs). Quadrupolar interactions dominate the ^{137}Ba powder patterns, with quadrupolar coupling constants, $C_Q(^{137}\text{Ba})$, ranging from 7.0 to 28.8 MHz. The ^{137}Ba electric field gradient (EFG) parameters extracted from these spectra are correlated to the local environments at the barium sites, via consideration of molecular symmetry and structure, and first principles calculations of ^{137}Ba EFG tensors performed using CASTEP software.

Chapter 5 discusses the application of ^{115}In SSNMR to study a variety of low-oxidation state indium complexes. Recently, interest in synthesising low oxidation state complexes of main group elements has increased due to the potential use of such complexes as new catalysts and materials precursors.⁹⁹⁻¹⁰³ Many of the low-valence indium compounds are insoluble in most organic solvents, which limits their

characterization by routine methods such as solution NMR and single crystal X-ray diffraction; this renders SSNMR as the perfect technique for studying the structures and dynamics of indium low-valence complexes. In this chapter, we demonstrate the usefulness of ^{115}In NMR in characterizing a number of In(I) complexes, some of which do not have known crystal structures. ^{115}In static wide-line and UW SSNMR spectra of several In(I) complexes were acquired with moderate and ultra-high magnetic field strength spectrometers (9.4 and 21.1 T, respectively). ^{115}In magic angle spinning (MAS) spectra were obtained with moderate and ultra-fast (> 60 kHz) spinning rates at 21.1 T. The ^{115}In EFG and CS tensor parameters extracted from both the static and MAS spectra are correlated to the electronic environments of the indium sites and provide key information about the electronic environment and geometry around the indium. In addition, first principles calculations of ^{115}In EFG and CS tensors were performed, in order to investigate the relationships between the NMR tensors, their orientations, and molecular structures.

Multinuclear SSNMR spectroscopy, in combination with powder XRD experiments and ab initio calculations, were utilized to probe the structures of the materials formed after the reactions between primary amines and layered silver supramolecular frameworks (Chapter 6). The layered compounds are selective in their reactions with amines, and may find future applications in separation technology. However, little was known about the intermolecular interactions involved in their specific chemical selectivity. ^{109}Ag , ^{15}N and ^{13}C CP/MAS SSNMR experiments and first principles calculations were very helpful in characterizing these materials and their

interactions with amines. Experimental NMR data are combined with theoretical calculations in order to propose structural models for these materials. This study demonstrates the importance of combining complementary physical characterization methods for obtaining a comprehensive understanding of the molecular structures underlying new materials.

The first application of ^{35}Cl SSNMR experiments to study polymorphism in hydrochloride (HCl) pharmaceuticals is discussed in Chapter 7. ^{35}Cl NMR spectra are presented for a series of HCl local anaesthetic (LA) pharmaceuticals and some of their polymorphs. The ^{35}Cl NMR tensor parameters are extremely sensitive to the chlorine anion environments, providing a fast count of the number of crystallographically distinct chlorine sites, a probe of the hydrogen-bonding environments at the chlorine anions, and a "fingerprint" spectrum for each polymorph. ^{35}Cl NMR data acquired at both standard (9.4 T) and ultra-high (21.1 T) magnetic field strengths were utilized for accurate extraction of NMR parameters. These data were supported by X-ray crystallography, ^{13}C SSNMR and ab initio modelling of the ^{35}Cl NMR tensors. The methodology for experimental acquisition and structural interpretation laid out in this work is of great importance, providing a powerful means of screening for pharmaceutical polymorphs. Due to the success of this work and to the fact that HCl pharmaceuticals constitute more than 50% of pharmaceutical salts and chlorine is present in ca. 25% of drugs, this research was extended to include a variety of HCl pharmaceuticals (Chapter 8).

Bibliography

- (1) Diehl, B. *NMR Spectrosc. Pharm. Anal.* **2008**, 157-180.
- (2) Widdifield, C. M.; Chapman, R. P.; Bryce, D. L. *Annu. Rep. NMR Spectrosc.* **2009**, *66*, 195-326.
- (3) Geppi, M.; Borsacchi, S.; Mollica, G.; Veracini, C. A. *Appl. Spectrosc. Rev.* **2009**, *44*, 1-89.
- (4) Naito, A. *Solid State Nucl. Magn. Reson.* **2009**, *36*, 67-76.
- (5) Singhal, A. *Mater. Sci. Found.* **2009**, *49-51*, 149-192.
- (6) Chierotti, M. R.; Gobetto, R. *Eur. J. Inorg. Chem.* **2009**, 2581-2597.
- (7) Wasylishen, R. E.; Bernard, G. M. In *Comprehensive Organometallic Chemistry III*; Crabtree, R. H., Mingos, D. M. P., Parkin, G., Eds.; Elsevier: Oxford, 2007; Vol. 1, pp 451-482.
- (8) Tishmack, P. A. *Drugs Pharm. Sci.* **2009**, *192*, 381-435.
- (9) Wawer, I. *NMR Spectrosc. Pharm. Anal.* **2008**, 201-231.
- (10) Ghahghaei, A.; Faridi, N. *J. Biomed. Sci. Eng.* **2009**, *2*, 345-358.
- (11) Mulder, F. A. A.; Filatov, M. *Chem. Soc. Rev.* **2010**, *39*, 578-590.
- (12) Fu, R.-q. *Bopuxue Zazhi* **2009**, *26*, 437-456.
- (13) Ramamoorthy, A. *Solid State Nucl. Magn. Reson.* **2009**, *35*, 201-207.
- (14) Matsuoka, S.; Inoue, M. *Chem. Commun.* **2009**, 5664-5675.
- (15) Aliev, A. E.; Law, R. V. *Nucl. Magn. Reson.* **2009**, *38*, 271-321.
- (16) Opella, S. J. *Nat. Methods* **2009**, *6*, 197-198.
- (17) Edgar, M. *Annu. Rep. Prog. Chem., Sect. B, Org. Chem.* **2009**, *105*, 340-362.
- (18) Anderson, S. E. *J. Organometal. Chem.* **1974**, *71*, 263-269.
- (19) Levy, H., II; Grizzle, W. E. *J. Chem. Phys.* **1966**, *45*, 1954-1960.
- (20) Zeigler, R. C.; Maciel, G. E. *J. Am. Chem. Soc.* **1991**, *113*, 6349-6358.
- (21) Fortier-McGill, B.; Reven, L. *Polym. Prepr.* **2008**, *49*, 676-677.
- (22) Leal, C.; Sandstroem, D.; Nevsten, P.; Topgaard, D. *Biochim. Biophys. Acta, Biomembr.* **2008**, *1778*, 214-228.

- (23) Silva, C. L.; Topgaard, D.; Kocherbitov, V.; Sousa, J. J. S.; Pais, A. A. C. C.; Sparr, E. *Biochim. Biophys. Acta, Biomembr.* **2007**, *1768*, 2647-2659.
- (24) Aliev, A. E. *Biopolymers* **2005**, *77*, 230-245.
- (25) Lequeieu, W.; Van De Velde, P.; Du Prez, F. E.; Adriaensens, P.; Storme, L.; Gelan, J. *Polymer* **2004**, *45*, 7943-7951.
- (26) Asano, A.; Kurotu, T. *Polym. Degrad. Stab.* **2002**, *78*, 137-141.
- (27) Ricardo, N. M. P. S.; Lahtinen, M.; Price, C.; Heatley, F. *Polym. Int.* **2002**, *51*, 627-634.
- (28) Mao, J.; Ding, G.; Xing, B. *Commun. Soil Sci. Plant Anal.* **2002**, *33*, 1679-1688.
- (29) Mizuno, M.; Hirai, A.; Matsuzawa, H.; Endo, K.; Suhara, M.; Kenmotsu, M.; Han, C. D. *Macromolecules* **2002**, *35*, 2595-2601.
- (30) Gelfer, M. Y.; Waddon, A.; Schmidt-Rohr, K.; Gale, R.; Kleiner, L.; Berggren, R. *J. Polym. Sci., Part B: Polym. Phys.* **2001**, *39*, 2774-2780.
- (31) Mirau, P. A.; Heffner, S. A.; Schilling, M. *Solid State Nucl. Magn. Reson.* **2000**, *16*, 47-53.
- (32) Geppi, M.; Kenwright, A. M.; Say, B. J. *Solid State Nucl. Magn. Reson.* **2000**, *15*, 195-199.
- (33) Bonev, B. B.; Morrow, M. R. *Can. J. Chem.* **1998**, *76*, 1512-1519.
- (34) Aliev, A. E.; Harris, K. D. M. *Magn. Reson. Chem.* **1998**, *36*, 855-868.
- (35) Quijada-Garrido, I.; Wilhelm, M.; Spiess, H. W.; Barrales-Rienda, J. M. *Macromol. Chem. Phys.* **1998**, *199*, 985-995.
- (36) Mirau, P. A.; Heffner, S. A. *Polym. Prepr.* **1997**, *38*, 876-877.
- (37) Spiess, H. W. *Polym. Spectrosc.* **1996**, 135-150.
- (38) Wilhelm, M.; Lehmann, S.; Jaeger, C.; Spiess, H. W.; Jerome, R. *Magn. Reson. Chem.* **1994**, *32*, S3-S7.
- (39) McMahan, P. E. *J. Polym. Sci., Polym. Phys. Ed.* **1966**, *4*, 639-647.
- (40) Tang, J. A.; O'Dell, L. A.; Aguiar, P. M.; Lucier, B. E. G.; Sakellariou, D.; Schurko, R. W. *Chem. Phys. Lett.* **2008**, *466*, 227-234.
- (41) Tang Joel, A.; Masuda Jason, D.; Boyle Timothy, J.; Schurko Robert, W.

ChemPhysChem **2006**, *7*, 117-130.

- (42) Sindorf, D. W.; Bartuska, V. J. *J. Magn. Reson.* **1989**, *85*, 581-585.
- (43) Kennedy, M. A.; Vold, R. L.; Vold, R. R. *J. Magn. Reson.* **1991**, *92*, 320-331.
- (44) Bastow, T. J. *Chem. Phys. Lett.* **2002**, *354*, 156-159.
- (45) Bryant, P. L.; Harwell, C. R.; Mrse, A. A.; Emery, E. F.; Gan, Z.; Caldwell, T.; Reyes, A. P.; Kuhns, P.; Hoyt, D. W.; Simeral, L. S.; Hall, R. W.; Butler, L. G. *J. Am. Chem. Soc.* **2001**, *123*, 12009-12017.
- (46) Wu, X.; Juban, E. A.; Butler, L. G. *Chem. Phys. Lett.* **1994**, *221*, 65-67.
- (47) Clark, W. G.; Hanson, M. E.; Lefloch, F.; Segransan, P. *Rev. Sci. Instrum.* **1995**, *66*, 2453-2464.
- (48) Poplett, I. J. F.; Smith, M. E. *Solid State Nucl. Magn. Reson.* **1998**, *11*, 211-214.
- (49) Bruening, E. M.; Baenitz, M.; Gippius, A. A.; Strydom, A. M.; Steglich, F.; Walstedt, R. E. *J. Magn. Magn. Mater.* **2007**, *310*, 393-395.
- (50) Baenitz, M.; Gippius, A. A.; Rajarajan, A. K.; Morozova, E. N.; Hossain, Z.; Geibel, C.; Steglich, F. *Phys. B* **2006**, *378-380*, 683-685.
- (51) Bryant, P. L.; Butler, L. G.; Reyes, A. P.; Kuhns, P. *Solid State Nucl. Magn. Reson.* **2000**, *16*, 63-67.
- (52) Hamaed, H.; Ye, E.; Udachin, K.; Schurko, R. W. *J. Phys. Chem. B* **2010**, *114*, 6014-6022.
- (53) Moudrakovski, I.; Lang, S.; Patchkovskii, S.; Ripmeester, J. *J. Phys. Chem. A* **2010**, *114*, 309-316.
- (54) Ooms, K. J.; Terskikh, V. V.; Wasylishen, R. E. *J. Am. Chem. Soc.* **2007**, *129*, 6704-6705.
- (55) O'Dell, L. A.; Schurko, R. W. *Phys. Chem. Chem. Phys.* **2009**, *11*, 7069-7077.
- (56) Sutrisno, A.; Terskikh, V. V.; Huang, Y. *Chem. Commun.* **2009**, 186-188.
- (57) Sutrisno, A.; Lu, C.; Lipson, R. H.; Huang, Y. *J. Phys. Chem. C* **2009**, *113*, 21196-21201.
- (58) Tang, J. A.; Masuda, J. D.; Boyle, T. J.; Schurko, R. W. *ChemPhysChem* **2006**, *7*, 117-130.

- (59) Widdifield, C. M.; Schurko, R. W. *J. Phys. Chem. A* **2005**, *109*, 6865-6876.
- (60) Widdifield, C. M.; Bryce, D. L. *J. Phys. Chem. A* **2010**, *114*, 2102-2116.
- (61) Bowers, G. M.; Lipton, A. S.; Mueller, K. T. *Solid State Nucl. Magn. Reson.* **2006**, *29*, 95-103.
- (62) Chen, F.; Ma, G.; Cavell, G.; Terskikh, V. V.; Wasylishen, R. E. *Chem. Commun.* **2008**, 5933-5935.
- (63) Chen, F.; Ma, G.; Bernard, G. M.; Cavell, R. G.; McDonald, R.; Ferguson, M. J.; Wasylishen, R. E. *J. Am. Chem. Soc.* **2010**, *132*, 5479-5493.
- (64) Lucier, B. E. G.; Tang, J. A.; Schurko, R. W.; Bowmaker, G. A.; Healy, P. C.; Hanna, J. V. *J. Phys. Chem. C* **2010**, 7949-7962.
- (65) Mroue, K. H.; Power, W. P. *J. Phys. Chem. A* **2010**, *114*, 324-335.
- (66) Hamaed, H.; Laschuk, M. W.; Terskikh, V. V.; Schurko, R. W. *J. Am. Chem. Soc.* **2009**, *131*, 8271-8279.
- (67) Hamaed, H.; Lo Andy, Y. H.; Lee David, S.; Evans William, J.; Schurko Robert, W. *J. Am. Chem. Soc.* **2006**, *128*, 12638-12639.
- (68) Hung, I.; Schurko, R. W. *Solid State Nucl. Magn. Reson.* **2003**, *24*, 78-93.
- (69) Bowers, G. M.; Kirkpatrick, R. J. *J. Magn. Reson.* **2007**, *188*, 311-321.
- (70) Forgeron, M. A. M.; Wasylishen, R. E. *Magn. Reson. Chem.* **2008**, *46*, 206-214.
- (71) Massiot, D.; Farnan, I.; Gautier, N.; Trumeau, D.; Trokiner, A.; Coutures, J. P. *Solid State Nucl. Magn. Reson.* **1995**, *4*, 241-248.
- (72) Medek, A.; Frydman, V.; Frydman, L. *J. Phys. Chem. A* **1999**, *103*, 4830-4835.
- (73) Lipton, A. S.; Wright, T. A.; Bowman, M. K.; Reger, D. L.; Ellis, P. D. *J. Am. Chem. Soc.* **2002**, *124*, 5850-5860.
- (74) Bureau, B.; Silly, G.; Buzare, J. Y.; Legein, C.; Massiot, D. *Solid State Nucl. Magn. Reson.* **1999**, *14*, 181-190.
- (75) Hanna, J. V.; Pike, K. J.; Charpentier, T.; Kemp, T. F.; Smith, M. E.; Lucier, B. E. G.; Schurko, R. W.; Cahill, L. S. *Chem.-Eur. J.* **2010**, *16*, 3222-3239.
- (76) Pauvert, O.; Fayon, F.; Rakhmatullin, A.; Kramer, S.; Horvatic, M.; Avignant, D.; Berthier, C.; Deschamps, M.; Massiot, D.; Bessada, C. *Inorg. Chem.* **2009**, *48*, 8709-

8717.

- (77) Smith, L. J.; Wang, X. *Mater. Res. Soc. Symp. Proc.* **2007**, *984E*, 21-26.
- (78) Tang, J. A.; Ellis, B. D.; Warren, T. H.; Hanna, J. V.; Macdonald, C. L. B.; Schurko, R. W. *J. Am. Chem. Soc.* **2007**, *129*, 13049-13065.
- (79) Rossini, A. J.; Mills, R. W.; Briscoe, G. A.; Norton, E. L.; Geier, S. J.; Hung, I.; Zheng, S.; Autschbach, J.; Schurko, R. W. *J. Am. Chem. Soc.* **2009**, *131*, 3317-3330.
- (80) Hung, I.; Schurko, R. W. *J. Phys. Chem. B* **2004**, *108*, 9060-9069.
- (81) Chapman, R. P.; Bryce, D. L. *PCCP* **2009**, 6987-6998.
- (82) Carr, H. Y.; Purcell, E. M. *Phys. Rev.* **1954**, *94*, 630-638.
- (83) Meiboom, S.; Gill, D. *Rev. Sci. Instrum.* **1958**, *29*, 688-691.
- (84) Larsen, F. H.; Lipton, A. S.; Jakobsen, H. J.; Nielsen, N. C.; Ellis, P. D. *J. Am. Chem. Soc.* **1999**, *121*, 3783-3784.
- (85) Larsen, F. H.; Jakobsen, H. J.; Ellis, P. D.; Nielsen, N. C. *J. Magn. Reson.* **1998**, *131*, 144-147.
- (86) Larsen, F. H.; Jakobsen, H. J.; Ellis, P. D.; Nielsen, N. C. *Chem. Phys. Lett.* **1998**, *292*, 467-473.
- (87) Larsen, F. H.; Jakobsen, H. J.; Ellis, P. D.; Nielsen, N. C. *Mol. Phys.* **1998**, *95*, 1185-1195.
- (88) Larsen, F. H.; Jakobsen, H. J.; Ellis, P. D.; Nielsen, N. C. *J. Phys. Chem. A* **1997**, *101*, 8597-8606.
- (89) Pines, A.; Waugh, J. S.; Gibby, M. G. *Chem. Phys. Lett.* **1972**, *15*, 373-376.
- (90) Hung, I.; Rossini, A. J.; Schurko, R. W. *J. Phys. Chem. A* **2004**, *108*, 7112-7120.
- (91) Davis, M. C.; Brouwer, W. J.; Wesolowski, D. J.; Anovitz, L. M.; Lipton, A. S.; Mueller, K. T. *Phys. Chem. Chem. Phys.* **2009**, *11*, 7013-7021.
- (92) Yamauchi, K.; Janssen, J. W. G.; Kentgens, A. P. M. *J. Magn. Reson.* **2004**, *167*, 87-96.
- (93) Kentgens, A. P. M.; Bart, J.; van Bentum, P. J. M.; Brinkmann, A.; Van Eck, E. R. H.; Gardeniers, J. G. E.; Janssen, J. W. G.; Knijn, P.; Vasa, S.; Verkuijlen, M. H. W. *J. Chem. Phys.* **2008**, *128*, 052202-052201 - 052202-052217.

- (94) Kupce, E.; Freeman, R. *J. Magn. Reson. Ser. A* **1995**, *115*, 273-276.
- (95) Bhattacharyya, R.; Frydman, L. *J. Chem. Phys.* **2007**, *127*, 194503/194501-194503/194508.
- (96) O'Dell, L. A.; Schurko, R. W. *Chem. Phys. Lett.* **2008**, *464*, 97-102.
- (97) O'Dell, L. A.; Schurko, R. W. *J. Am. Chem. Soc.* **2009**, *131*, 6658-6659.
- (98) O'Dell, L. A.; Rossini, A. J.; Schurko, R. W. *Chem. Phys. Lett.* **2009**, *468*, 330-335.
- (99) Ellis, B. D.; Macdonald, C. L. B. *Coord. Chem. Rev.* **2007**, *251*, 936-973.
- (100) Dyson, P. J. *Coord. Chem. Rev.* **2004**, *248*, 2443-2458.
- (101) Roesky, P. W. *Dalton Trans.* **2009**, 1887-1893.
- (102) Mindiola, D. J. *Acc. Chem. Res.* **2006**, *39*, 813-821.
- (103) Housecroft, C. E. *Compr. Coord. Chem. II* **2004**, *5*, 555-731.

Chapter 2

Concepts and Techniques in Solid-State NMR

2.1. Principles of NMR

Nuclei which possess a spin-angular momentum, as defined by the nuclear spin number, I , are observable by NMR and are referred to as “NMR active nuclei”. The nuclear spin is an intrinsic property of the nucleus. Three general rules are used to determine whether the nucleus of a particular isotope is NMR active. First if the atomic mass and the number of neutrons are even, the nucleus has a nuclear spin of zero ($I = 0$) and cannot be observed by NMR. Second, if the atomic mass is even and the number of neutrons is odd, the nucleus possesses an integer spin. Lastly, the nucleus has a half integer spin if the atomic mass is odd.¹ The nuclear spin angular momentum, defined by the vector \mathbf{I} , gives rise to the nuclear magnetic dipole moment $\boldsymbol{\mu}$, which is aligned in the direction of the spin axis:

$$\boldsymbol{\mu} = \gamma \hbar \mathbf{I} \quad (2.1)$$

where γ is the gyromagnetic ratio and \hbar is Planck's constant. γ is related to the ratio of the proton's charge and its mass and is expressed as:

$$\gamma = \frac{e}{2m} g \quad (2.2)$$

g is the nuclear g -factor and is unique for each isotope of each element. The gyromagnetic ratio is a very important quantity in NMR, since NMR spectroscopy

depends on the precession of the nuclear spins in a magnetic field, B_0 , and the rate of this precession, known as the Larmor frequency, ω_0 :

$$\omega_0 = -\gamma B_0 \quad (2.3)$$

where B_0 is the external applied magnetic field.

2.2 NMR Interactions

NMR interactions are generally classified into two different types: internal and external interactions. The external interactions are those which depend on B_0 , and the smaller oscillating field, B_1 , which is induced by an applied radiofrequency (rf) pulse and solenoidal coil. The internal interactions are those which arise from the magnetic and/or electronic chemical environment of the nucleus, and include the chemical shielding, direct spin-spin coupling, indirect spin-spin coupling and quadrupolar coupling. Herein, we focus on the interactions which are relevant to the work discussed in this thesis.

Detailed discussions of these interactions are available from other sources.²⁻⁸

In terms of quantum mechanics, NMR interactions are described by the following Hamiltonians:^{2,5,9,10}

$$\hat{\mathcal{H}}_{\text{NMR}} = \hat{\mathcal{H}}_{\text{Z}} + \hat{\mathcal{H}}_{\text{rf}} + \hat{\mathcal{H}}_{\text{CS}} + \hat{\mathcal{H}}_{\text{D}} + \hat{\mathcal{H}}_{\text{J}} + \hat{\mathcal{H}}_{\text{Q}} \quad (2.4)$$

where $\hat{\mathcal{H}}_{\text{Z}}$, $\hat{\mathcal{H}}_{\text{rf}}$, $\hat{\mathcal{H}}_{\text{CS}}$, $\hat{\mathcal{H}}_{\text{D}}$, $\hat{\mathcal{H}}_{\text{J}}$, $\hat{\mathcal{H}}_{\text{Q}}$ describe the Zeeman, radiofrequency, chemical shielding, dipolar, J -coupling and quadrupolar interactions, respectively.

2.2.1. External Interactions

2.2.1.1 Zeeman Interaction

The interaction of the nuclear spin with the applied external magnetic field, B_0 , is known as the Zeeman interaction. It is the basis of the NMR phenomenon, and is represented in its Hamiltonian form as:^{9,11}

$$\hat{\mathcal{H}}_Z = -\hbar\gamma B_0 \mathbf{I}_Z \quad (2.5)$$

where \mathbf{I}_Z is the projection of the nuclear spin angular momentum, \mathbf{I} , along the z -axis, which is the direction of B_0 . When an active NMR nucleus with a nuclear spin quantum number, I , is placed in an external magnetic field, the spin will precess about the quantization axis, z (or B_0), in one of the $2I + 1$ possible orientations. These orientations or energy levels are described by different values of the nuclear spin magnetic quantum number m_I , where $m_I = I, I-1, \dots, -I$.

$$E_m = -m_I \hbar\gamma B_0 \quad (2.6)$$

For the spin-1/2 case, the spin precesses about the field, with one of the two energy levels, $m_I = +1/2$ (α -state), or $m_I = -1/2$ (β -state) (Figure 2.1). The difference in energy between these levels (i.e., from α to β) depends on both B_0 and γ .^{9,6}

$$\Delta E = \gamma \hbar B_0 = \hbar\omega_0 \quad (2.7)$$

If ΔE increases as the result of increasing in B_0 or γ , the population difference between the energy levels increase.

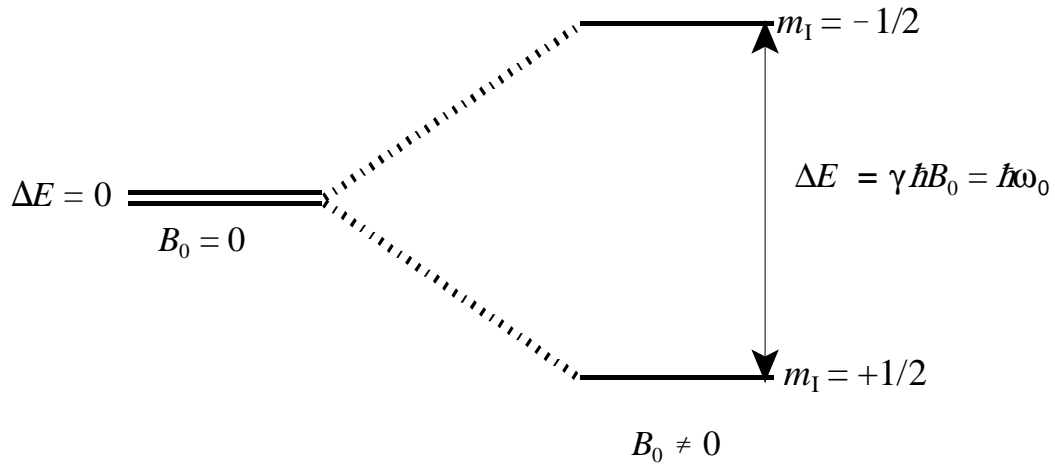


Figure 2.1. The splitting of the energy levels of a spin-1/2 nucleus in the presence of a static applied magnetic field, B_0 .

At thermodynamic equilibrium, the non-degenerate energy states are not equally populated, and the ratio of the population between adjacent energy levels is described by the Maxwell-Boltzmann distribution as:^{6,12}

$$\frac{N_\beta}{N_\alpha} = e^{-\Delta E/kT} \quad (2.8)$$

where N_β and N_α represent the populations of higher (β) and lower (α) energy levels (when $\gamma > 0$), respectively, and k is the Boltzmann constant. As a consequence of longitudinal relaxation, at equilibrium, there are slightly more spins in the α state than in the β state, and as a consequence, there is a bulk magnetization, \mathbf{M}_0 , directed along the direction of B_0 .¹ The difference between spin state populations is relatively small, compared to other forms of spectroscopy, because of the small energy spacings between the different levels. As a result, NMR is an insensitive technique in terms of the

attainable signal-to-noise ratio (S/N).

2.2.1.2. Radiofrequency Interaction

In NMR, a spin transition (i.e., the change of spin state from α to β or vice versa) is induced by applying an rf field, B_1 , in the direction perpendicular to the static external magnetic field, B_0 . The rf Hamiltonian describes the interaction between the nuclear spin and B_1 :

$$\hat{\mathcal{H}}_{\text{rf}} = -B_1(t) \cos[\omega_{\text{rf}}t + \varphi(t)] \sum_i \gamma_n^i I_x^i \quad (2.9)$$

where ω_{rf} is the applied rf and φ is its phase. The nuclear spins interact with \mathbf{B}_1 in a similar fashion as they do with \mathbf{B}_0 ,

excepting that \mathbf{B}_0 is static and \mathbf{B}_1 oscillates

in time in the lab frame. This oscillating

field, \mathbf{B}_1 , can be visualized as vector with

two components rotating about \mathbf{B}_0 in

opposite directions (Figure 2.2). The

effect of the \mathbf{B}_1 field can be easily

understood by transforming this system

into a rotating frame of reference which

rotates at the rf transmitter frequency, ω_{rf} .

In this rotating frame, the effect of the \mathbf{B}_0

field is depleted and the oscillating magnetic field, \mathbf{B}_1 , appears stationary and has a

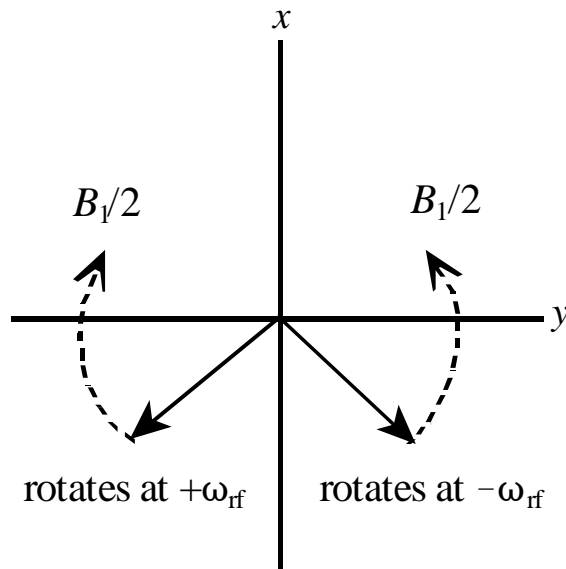


Figure 2.2. The two vector components of the \mathbf{B}_1 field in the xy -plane. Adapted from Prof. Schurko's NMR notes.

(<http://mutuslab.cs.uwindsor.ca/schurko/nmrcourse/notes.html>).

similar effect on the bulk magnetization as \mathbf{B}_0 does in the lab frame (i.e., the magnetization precesses about \mathbf{B}_1 for an on-resonance pulse). In the absence of an rf pulse, the bulk magnetization, \mathbf{M}_0 , precesses along \mathbf{B}_0 at a ω_0 . When an rf pulse is applied along the x -axis of the rotating frame, the bulk magnetization, \mathbf{M}_0 , rotates counterclockwise by an angle θ about the x -axis. The angle θ is called the tip angle and it is defined by:

$$\theta = \tau_p \gamma B_1 = \omega_1 \tau_p \quad (2.10)$$

where ω_1 is called the nutation frequency. If the applied pulse is on resonance (i.e., $\omega_0 = \omega_{rf}$), then the bulk magnetization, \mathbf{M}_0 , appears stationary in the rotating frame and \mathbf{B}_0 appears to be absent. The only remaining field is \mathbf{B}_1 , around which the magnetization precesses. In most NMR experiments, pulses are not applied on resonance. In such cases, the Larmor frequency is then reduced from ω_0 to $(\omega_0 - \omega_{rf})$ and the field along B_0 does not vanish (as it is the case for an on resonance pulse). Thus, in this case there exist two fields, one along the z -axis with magnitude equal to $B_0(1 - \omega_{rf}/\omega_0)/\gamma$ and the second of magnitude B_1 along the x -axis. The resultant effective field is the vectorial sum of the two components and is denoted as \mathbf{B}_{eff} (Figure 2.3) around which the nuclear spin magnetization precesses. In NMR, the allowed spin transitions are defined by the selection rule $\Delta m = \pm 1$. After an rf pulse is applied, absorption of energy occurs causing spin transitions between two different energy levels, and the populations of the two levels become equal, this phenomenon is called saturation. Once the pulse is turned off, the magnetization returns to thermal equilibrium. The system reaches the equilibrium state

by releasing the acquired energy to the surroundings via a phenomenon called relaxation. There are two fundamental spin relaxation processes. Longitudinal or spin-lattice relaxation, whose time constant is denoted by T_1 , is the process by which the magnetization returns back to the initial state of thermal equilibrium (along the z -axis), and transverse or spin-spin relaxation, denoted by T_2 , is the magnetization dephasing or loss of phase coherence in the xy -plane.

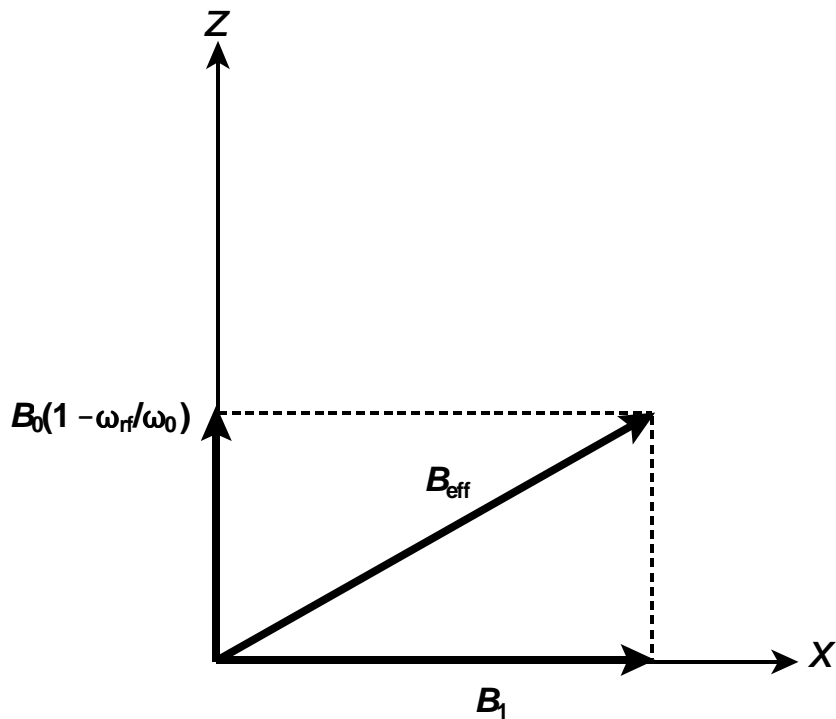


Figure 2.3. The magnetic fields present in the rotating frame. In the case of an on-resonance pulse ($\omega_0 = \omega_{\text{rf}}$), only B_1 remains.⁷

2.2.2. Internal Interactions

2.2.2.1 Chemical Shielding Interaction

Chemical shielding is the interaction between the nuclear spins and the small local

magnetic fields, B_{ind} , which are generated by circulation of the surrounding electrons induced by the static external magnetic field. Chemical shielding is also referred to as nuclear magnetic shielding or just nuclear shielding (NS). We shall use the latter term to differentiate its abbreviation from “chemical shift” (CS) which is discussed below. These local fields change the net magnetic field at the nucleus, leading to changes in its Larmor frequency. The degree of change of the precession frequency reflects the value of the chemical shielding which depends on the total effective magnetic field, B_{eff} , experienced by the nucleus:

$$\vec{B}_{\text{eff}} = \vec{B}_0 + \vec{B}_{\text{ind}} = \vec{B}_0 - \sigma\vec{B}_0 = (1-\sigma)\vec{B}_0 \quad (2.11)$$

The magnitudes of these local magnetic fields depend on the strength of the external applied magnetic field B_0 , but more importantly, upon the nature of the orbitals within the atom or molecule. The latter is what makes nuclear shielding a sensitive probe of subtle changes in molecular structure. The nuclear shielding Hamiltonian is expressed as¹⁰

$$\hat{\mathcal{H}}_{\text{CS}} = -\gamma\hbar\mathbf{I}_z\ddot{\sigma}B_0 \quad (2.12)$$

where $\ddot{\sigma}$ is the nuclear shielding tensor, which is a 3×3 non-symmetric second-rank tensor.

$$\ddot{\sigma} = \begin{pmatrix} \sigma_{xx} & \sigma_{xy} & \sigma_{xz} \\ \sigma_{yx} & \sigma_{yy} & \sigma_{yz} \\ \sigma_{zx} & \sigma_{zy} & \sigma_{zz} \end{pmatrix} \quad (2.13)$$

Here, we only consider the symmetric portion of the NS tensor, which contributes to frequency shifts in NMR spectra to first order. The anti-symmetric components contribute only to relaxation processes, and are discussed elsewhere.¹³ This tensor can be diagonalized by transforming it to its own principal axis system (PAS)

$$\ddot{\sigma} = \begin{pmatrix} \sigma_{11} & 0 & 0 \\ 0 & \sigma_{22} & 0 \\ 0 & 0 & \sigma_{33} \end{pmatrix} \quad (2.14)$$

where σ_{11} , σ_{22} and σ_{33} are the principal components of the NS tensor (Figure 2.4) and are defined such $\sigma_{11} \leq \sigma_{22} \leq \sigma_{33}$.

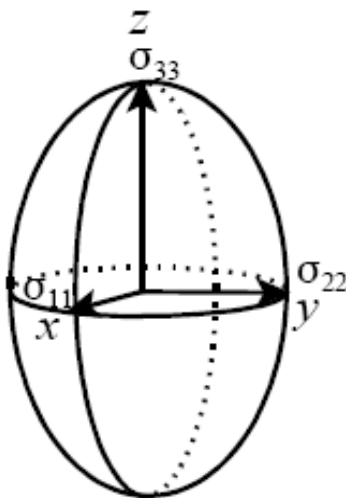


Figure 2.4. An ellipsoid portraying the three principal components of the NS tensor.

The trace of the NS tensor (i.e., the sum of the diagonal components), which is non-zero, defines the isotropic nuclear shielding which is expressed by:^{9,11,14}

$$\sigma_{\text{iso}} = \frac{(\sigma_{11} + \sigma_{22} + \sigma_{33})}{3} \quad (2.15)$$

The nuclear shielding for a given orientation of the NS tensor in an external magnetic field is described by the tip and azimuthal angles, θ and φ and it is expressed as:

$$\omega_{\text{cs}}(\theta, \varphi) = \omega_0(1 - (\sigma_{11}^{\text{PAS}} \sin^2\theta \cos^2\varphi + \sigma_{22}^{\text{PAS}} \sin^2\theta \sin^2\varphi + \sigma_{33}^{\text{PAS}} \cos^2\theta)) \quad (2.16)$$

where θ and φ are the polar angles defining the orientation of B_0 in the PAS of the NS tensor. This equation indicates that the nuclear shielding depends on the orientation of the NS tensor with respect to the magnetic field, and hence upon the orientation of the molecules. The orientation dependence of the symmetric part of the NS is referred to as “anisotropy” or chemical shielding anisotropy (CSA). In a microcrystalline sample, all possible orientations of the crystallites, and hence the molecules, are present with respect to B_0 , therefore all angles θ and φ are possible. However, in solution, a small molecule reorients through one radian at a rate on the order of 10^{-12} s^{-1} . Hence, if reorientation is isotropic, over the course of a second, the NS tensor reorients with respect to B_0 such that all θ and φ are “visited”; hence, sharp peaks representing the average nuclear shielding are observed, as opposed to a distribution of frequencies. In contrast, in the solid state, these different molecular orientations result in a distribution of local magnetic fields, and thus, a range of NMR frequencies, yielding NMR powder patterns.^{3,11} The intensity of the powder pattern at a given frequency is proportional to the number of molecular orientations which have a particular nuclear shielding corresponding to this frequency.

The principal components of the CSA tensor are readily obtained from discontinuities and shoulders of the solid-state NMR patterns influenced only by CSA, which in turn gives us information on the local electronic structure.

To further understand CSA, we consider the nitrogen CSA in pyridine. Three different orientations of the pyridine molecule with respect to B_0 are depicted in Figure 2.5. Each of these orientations is associated with a different nuclear shielding. The combination of all possible orientations lead to the formation of the ^{15}N powder pattern.

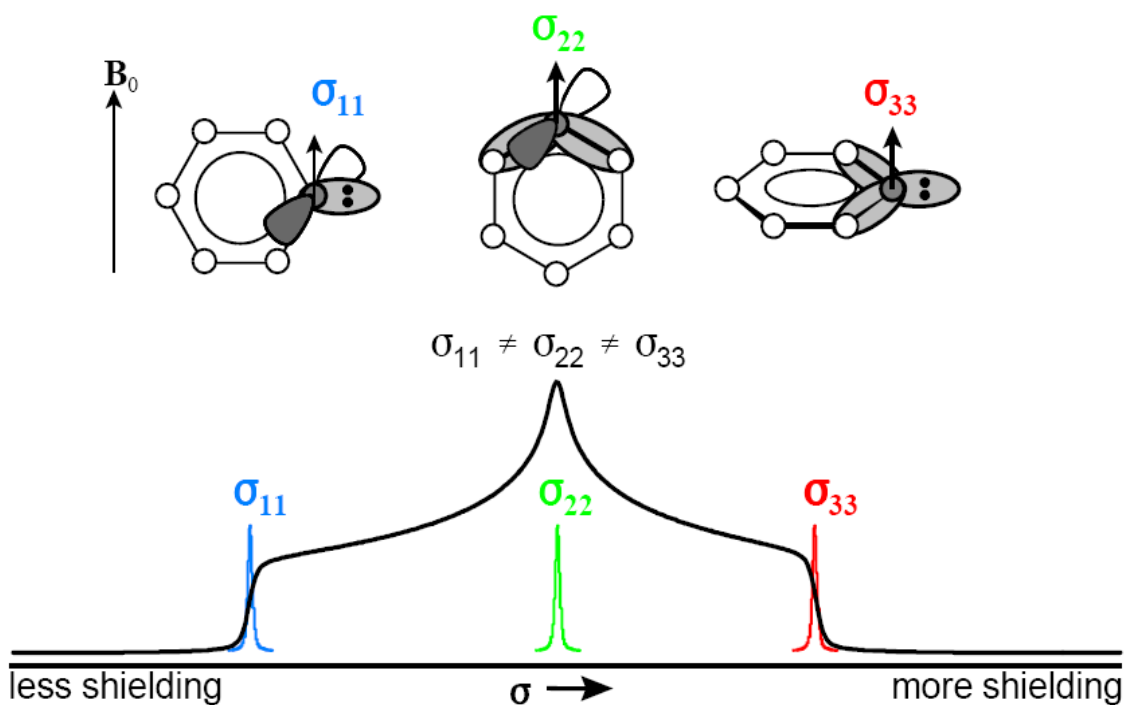


Figure 2.5. Representation of the nitrogen CSA in pyridine. Different crystallite orientations with respect to the external static magnetic field, B_0 , lead to different nuclear shielding. (R.W. Schurko, NMR Course Notes, 2009. Used with permission).

Due the anisotropic nature of the NS tensor, more information regarding the

electronic environment around a nucleus can be obtained. Such information can be extracted from the powder pattern from the values of the span (Ω) and the skew (κ) which are defined, following the Herzfeld and Berger convention, as:^{11,14,15}

$$\Omega = (\sigma_{33} - \sigma_{11}) \quad (2.17)$$

$$\kappa = \frac{3(\sigma_{\text{iso}} - \sigma_{22})}{\Omega} \quad (2.18)$$

The span describes the breadth of the powder pattern, determines the range of the CSA (i.e., a larger span corresponds to a wider powder pattern breadth) and is reported in parts per million (ppm). The skew, which ranges from -1 to 1, defines the degree of axial symmetry of the CSA tensor. The tensor is said to be axially symmetric when the value of the skew is 1 or -1 (Figure 2.6).¹⁶ For an axially symmetric CSA tensor, two of the tensor components are equal and the third is distinct. In the case where all of the components are equal, only the isotropic chemical shift is observed.

In practice, chemical shielding or nuclear shielding is not measured directly in an NMR experiment; rather, the chemical shift is measured, which is defined as the nuclear magnetic shielding of the nucleus in the sample of interest with respect to that of some reference compound. The chemical shift is reported in ppm as:¹²

$$\delta(\text{ppm}) = \frac{\nu_{\text{sample}} - \nu_{\text{ref}}}{\nu_{\text{ref}}} \times 10^6 \quad (2.19)$$

where ν_{sample} is the frequency of the signal for the nucleus in the sample of interest and ν_{ref}

is the frequency of the same nucleus in the standard compound. The relation between the chemical shift and the nuclear shielding is given by:¹²

$$\delta = \frac{\sigma_{\text{ref}} - \sigma_{\text{sample}}}{1 - \sigma_{\text{ref}}} \approx \sigma_{\text{ref}} - \sigma_{\text{sample}} \quad (2.20)$$

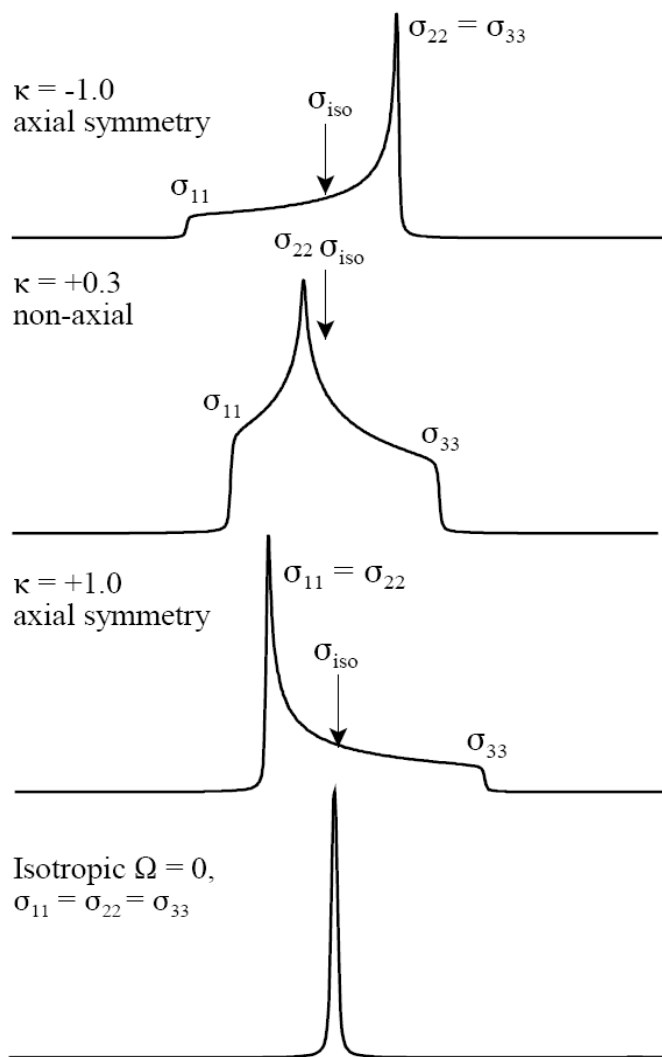


Figure 2.6. The shielding tensor components determine the shape of the powder pattern.

2.2.2.2. Direct Dipolar Interaction

The direct dipolar interaction, also known as the dipole-dipole interaction or direct dipole spin-spin interaction, is the interaction between the magnetic moments of two nuclear spins separated by a distance r_{ij} . It arises from the through-space mutual interactions of small local magnetic fields and is independent of the applied magnetic field B_0 . The dipolar coupling Hamiltonian is given by:^{9,11}

$$\begin{aligned}\hat{\mathcal{H}}_{\text{D}} &= -\sum_{i<j} \frac{1}{2} (\gamma_i \gamma_j \hbar^2 r_{ij}^{-3} (3 \cos^2 \theta_{ij} - 1) [3 I_{iz} I_{jz} - \mathbf{I}_i \cdot \mathbf{I}_j]) \\ &= R_{\text{DD}} [\mathbf{I} \cdot \mathbf{S} - 3 \frac{(\mathbf{I} \cdot \mathbf{r})(\mathbf{S} \cdot \mathbf{r})}{r^2}]\end{aligned}\quad (2.21)$$

$$R_{\text{DD}} = \left(\frac{\mu_0}{4\pi}\right) \frac{\gamma_I \gamma_S \hbar}{r^3} \quad (2.22)$$

where θ_{ij} is the angle between the vector r_{ij} and B_0 . R_{DD} is called the dipolar coupling constant and it is expressed in units of rad s^{-1} . Equation 2.21 indicates that the dipolar interaction is inversely proportional to the cube of the distance between the two nuclei; therefore, only nuclei which are relatively close in space experience a significant dipolar interaction (i.e., for $^1\text{H}-^{13}\text{C} = 1.0 \text{ \AA}$, $R_{\text{DD}} = 30.2 \text{ kHz}$). Also, the dipolar Hamiltonian depends on the gyromagnetic ratios of the nuclei, so this interaction is more important for nuclei with larger magnetic moments (i.e., ^1H , ^{19}F). The dipole-dipole tensor is symmetric and traceless. In liquids the dipolar interaction vanishes, with the exception of long range dipolar effects which are used for signal enhancement in the COSY Revamped

with Asymmetric Z-gradient Echo Detection (CRAZED) magnetic resonance imaging experiments,¹⁷ because of the molecular tumbling which averages out the $(3\cos^2\theta_{ij} - 1)$ term to zero.

2.2.2.3. Indirect Spin-Spin Interaction Or *J*-Coupling

J-coupling or indirect spin-spin coupling describes the mutual interaction between nuclear spins mediated via bonding electrons within a molecule. This interaction is independent of B_0 and its Hamiltonian is expressed by:^{10,11}

$$\hat{\mathcal{H}}_J = \mathbf{I} \cdot \ddot{\mathbf{J}} \cdot \mathbf{S} \quad (2.23)$$

where $\ddot{\mathbf{J}}$ is the spin-spin coupling tensor.

The magnitude of the *J*-coupling is independent of the magnitude of B_0 , and it is described by a second rank tensor. In contrast to the dipolar tensor, the $\ddot{\mathbf{J}}$ tensor is not symmetric and its trace does not vanish, so the *J*-coupling interaction does not average to zero in solution NMR spectra. Indirect spin-spin coupling between two spins, *I* and *S*, causes a splitting of the peaks in the *I* and *S* spectra into $2S + 1$ and $2I + 1$ evenly spaced peaks, respectively. *J*-coupling is a very important probe of molecular structure, and is useful for determining the connectivities between different nuclei. The $|J|$ is proportional to the product of $\gamma_I\gamma_S$, but it is also strongly dependent upon the electronic structure of intervening bonds between the nuclei (unlike R_{DD} , which is through space). *J*-coupling is reported in Hz. Therefore, to compare coupling constants of different nuclei, it is convenient to use the reduced coupling constant, expressed by:¹⁸

$$K_{XY} = 4\pi^2 \frac{J_{XY}}{h\gamma_X\gamma_Y} \quad (2.24)$$

2.2.2.4. Quadrupolar Interaction

Quadrupolar nuclei are nuclei with spins $I > 1/2$. They have a non-spherical positive charge distribution which gives rise to a nuclear electric quadrupole moment. The electric quadrupole moment is unique for each nucleus, and is defined by a scalar value, Q , which is measured in m^2 or barn (10^{-28}m^2). The quadrupolar interaction is the interaction between the nuclear electric quadrupolar moment and the local electric field gradient (EFG) around the nucleus. The EFG at the nucleus is caused by the surrounding electronic charge distribution (i.e, electrons, atoms bonds, etc.); thus, the EFG is very sensitive to small structural changes. The EFG is described by a second-rank tensor as:

$$\ddot{\mathbf{V}} = \begin{pmatrix} V_{xx} & V_{xy} & V_{xz} \\ V_{yx} & V_{yy} & V_{yz} \\ V_{zx} & V_{zy} & V_{zz} \end{pmatrix} \quad (2.25)$$

where V_{xx} , V_{xy} , V_{zy} , etc. represent the gradient of the electric field vector components in a arbitrary reference frame. The EFG tensor can be diagonalized by transforming the matrix into its PAS:¹¹

$$\ddot{\mathbf{V}} = \begin{pmatrix} V_{11} & 0 & 0 \\ 0 & V_{22} & 0 \\ 0 & 0 & V_{33} \end{pmatrix} \quad (2.26)$$

These components are defined such that $|V_{33}| \geq |V_{22}| \geq |V_{11}|$ and this tensor is symmetric and traceless ($V_{11} + V_{22} + V_{33} = 0$).¹⁴ These principal components provide useful information about the spherical and axial symmetry of the EFG tensor through the measurement of the nuclear quadrupolar coupling constant, C_Q , and the asymmetry parameter, η_Q , respectively. The C_Q is defined as:

$$C_Q = \frac{eqeQ}{\hbar} = \frac{eQV_{33}}{\hbar} \quad (2.27)$$

and can also be expressed in terms of the quadrupolar frequency, ν_Q as:

$$\nu_Q = \frac{3C_Q}{2I(2I - 1)} \quad (2.28)$$

The asymmetry parameter, η_Q , is expressed as.^{14,19}

$$\eta_Q = \frac{V_{11} - V_{22}}{V_{33}} \quad (2.29)$$

where η_Q varies from 0 to 1; when $\eta_Q = 0$, the EFG tensor is axially symmetric and $V_{11} = V_{22}$, while if $V_{11} = V_{22} = V_{33} = 0$, the nucleus is located in a site of perfect spherical symmetry, and the C_Q is equal to zero. The C_Q is normally reported in MHz and η_Q is dimensionless. The terminology *distinct* is used throughout this document to denote the principal component of an NMR interaction tensor which is furthest in absolute magnitude from the other two components (i.e., if $\eta_Q = 0.1$, then V_{33} is distinct, and V_{11}

and V_{22} are similar in absolute magnitude). In the cases of perfect axial symmetry, the terminology *unique* is utilized (i.e., if $\eta_Q = 0$, then V_{33} is unique and $V_{11} = V_{22}$; if $\eta_Q = 1$, then V_{11} is unique, and $|V_{33}| = |V_{22}|$).

The quadrupolar Hamiltonian in angular frequency units is expressed by:¹¹

$$\hat{\mathcal{H}}_Q = \frac{eQ}{2I(2I - 1)\hbar} \mathbf{I} \cdot \ddot{\mathbf{V}} \cdot \mathbf{I} \quad (2.30)$$

where \mathbf{I} is the nuclear spin operator, and $\ddot{\mathbf{V}}$ is the EFG tensor. In the case where the Larmor frequency is much larger than the quadrupolar frequency ($\nu_0 \gg \nu_Q$), the quadrupolar Hamiltonian can be treated as a perturbation on the Zeeman Hamiltonian, which is known as the high field approximation. The quadrupolar Hamiltonian can be written as: ¹

$$\hat{\mathcal{H}}_Q = \hat{\mathcal{H}}_Q^{(1)} + \hat{\mathcal{H}}_Q^{(2)} + \dots \quad (2.31)$$

$\hat{\mathcal{H}}_Q^{(1)}$, $\hat{\mathcal{H}}_Q^{(2)}$ represent the first- and second-order quadrupolar Hamiltonians, respectively. In most cases, both the first- and second-order quadrupolar interactions have effects on the spectra of quadrupolar nuclei, and in some cases third-order terms can also contribute to the NMR spectral lineshapes (we will neglect terms higher than second-order in this thesis).¹ The first- and second-order quadrupolar interactions cause large energy shifts in all of the $(2I + 1)$ pure Zeeman levels.

Consider the case of a quadrupolar nucleus with spin-3/2; there are four $(2I + 1)$ quantized energy levels (-3/2, -1/2, +1/2, and +3/2, Figure 2.7). The transition from

-1/2 to +1/2 is called the central transition (CT) and all others are known as satellite transitions (ST).

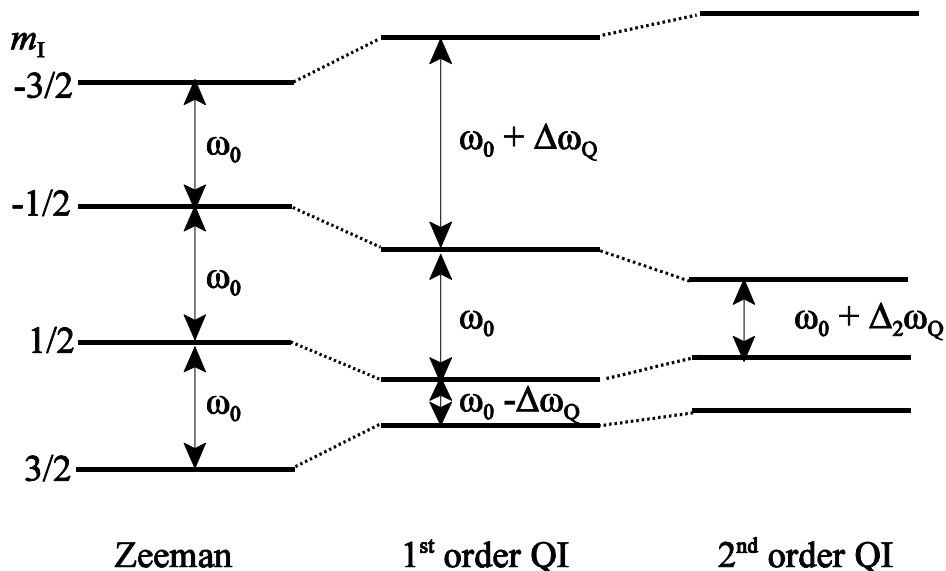


Figure 2.7. The energy levels of spin-3/2 nuclei under Zeeman, first- and second-order quadrupolar interaction (QI).

The CT is only affected by the second-order quadrupolar interaction while the STs are affected by both the first- and second-order quadrupolar interactions. The size of the first-order effect is much larger than the second-order effect, and the STs span much wider frequency ranges than the CT. For this reason, the majority of NMR studies of quadrupolar nuclei focus on observing the CT by applying selective 90° pulses (i.e., these are pulses with lengths determined by the length of the non-selective solution pulse widths scaled by a factor of $(I + 1/2)^{-1}$).²⁰ However, for higher half-integer spin nuclei (i.e., spin-9/2), the ST powder patterns can overlap with the CT (Figure 2.8).

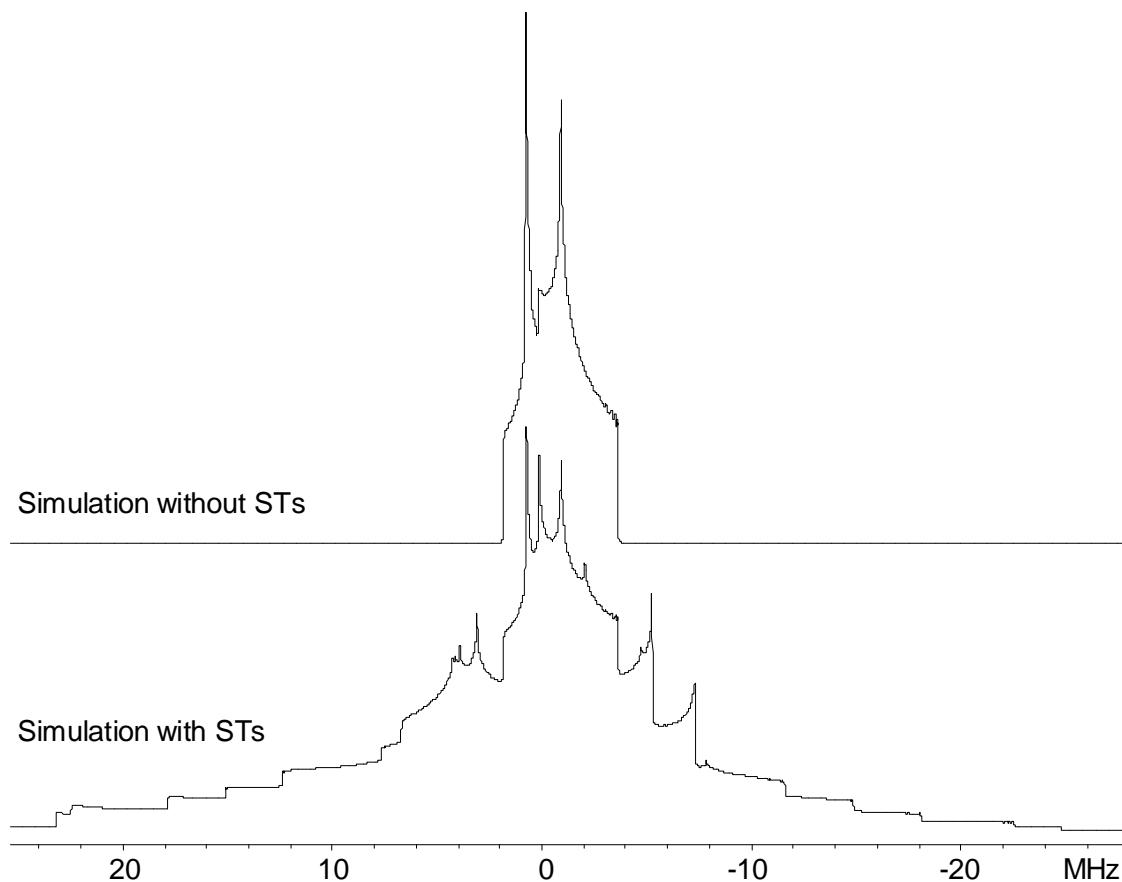


Figure 2.8. Analytical simulation of ^{209}Bi SSNMR spectra at 9.4 T as an example of a high half integer spin nucleus to show the effects of the STs on the powder pattern. $C_Q = 180$ MHz and $\eta_Q = 0.6$.

In solution, the first-order quadrupolar interaction averages to zero, and thus has no influence on the frequency of the observed resonances. However, it has an effect on the quadrupole nuclear spin relaxation, which can lead to some degree of line broadening. However, in the solid state, the effects of the quadrupolar interaction dominate the NMR spectra, and can lead to broad powder patterns with breadths of several MHz. The magnitude of C_Q describes the magnitude of the quadrupolar interaction and determines the breadth of the NMR pattern. Increasing the C_Q , while keeping η_Q constant, will increase the breadth of the pattern; however, changing η_Q while keeping C_Q constant will

change the shape of the powder pattern (Figure 2.9).

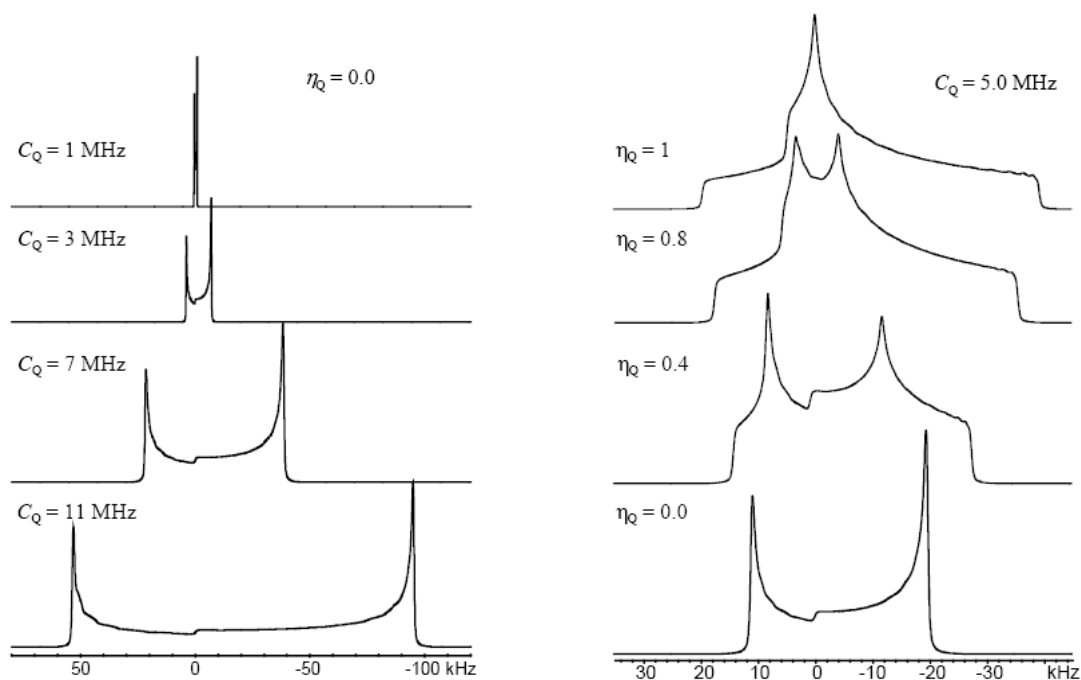


Figure 2.9. The effects of C_Q and η_Q values on static SSNMR patterns

2.2.2.5. Euler Angles

The Euler angles (α , β , γ) define the relative orientation of the CS and EFG tensors, and along with the CS and quadrupolar parameters, all influence the appearance of the SSNMR patterns. All spectral analytical simulations of static spectra reported in this work have been performed using WSolids,²¹ which uses counterclockwise rotation as the positive direction. In this dissertation, the rotation of the CS tensor from a fixed EFG tensor frame into its own PAS is depicted in Figure 2.10.

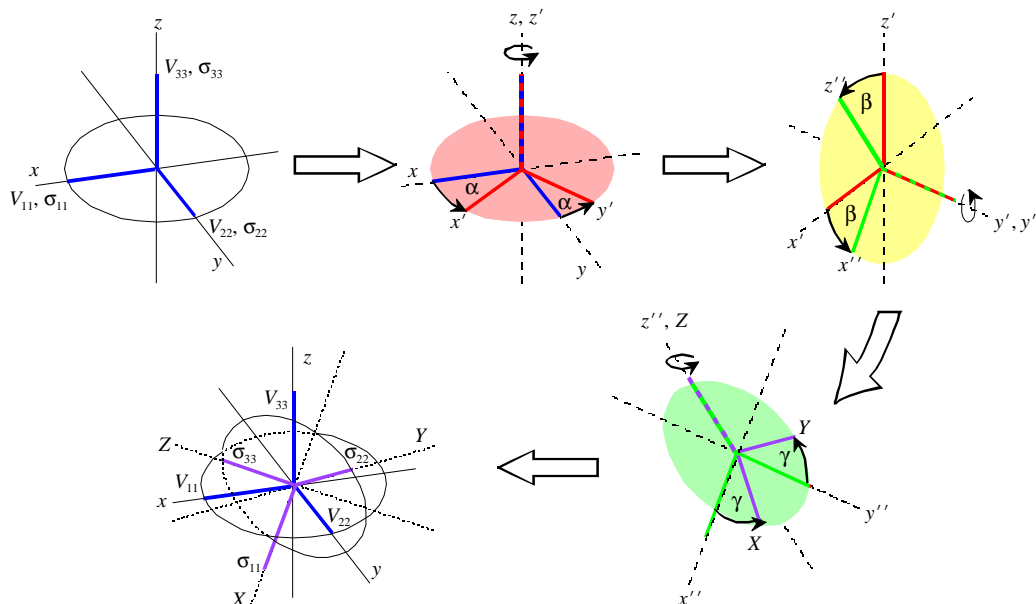


Figure 2.10. Rotation of the CS tensor from the fixed EFG tensor frame of reference (x, y, z) into the CS PAS (X, Y, Z). Courtesy of Dr. Joel A. Tang

2.3 Solid-State NMR Techniques

2.3.1 Magic Angle Spinning (MAS)

Rapid, isotropic, molecular tumbling averages the anisotropic NMR interactions to zero in the solution state resulting in the observation of sharp resonances. In microcrystalline or disordered solids, anisotropic interactions broaden the NMR spectra, and these powder patterns can provide very useful information on chemical systems. However, in the case where there are multiple resonance frequencies observed in a spectrum, it becomes difficult to resolve individual NMR patterns and to extract any useful chemical data. Therefore, it is necessary to use techniques such as MAS to obtain high resolution solid-state NMR spectra.^{22,23} In MAS, the sample is spun about an axis oriented at the magic angle, $\beta = 54.74^\circ$, with respect to B_0 (Figure 2.11). This technique

averages all first-order interactions (CS, dipolar and quadrupolar). Rapid sample rotation at the magic angle was used for the first time by Andrew, Bradbury and Eades in 1958 to average dipolar-broadened lines.²² The basis of the MAS experiments is that most of the first-order interactions have a geometrical spatial dependence of the form $(3\cos^2\theta - 1)$, where θ is the angle between the z -axis of NMR interaction tensor and the static magnetic field, B_0 .⁸ When spinning the sample at the magic angle, the orientation of the tensor with respect to the magnetic field varies with time and the average orientation becomes:^{24,25}

$$\langle 3\cos^2\theta - 1 \rangle = \frac{1}{2}(3\cos^2\beta - 1)(3\cos^2\chi - 1) \quad (2.32)$$

where χ describes the angle of the principal z -axis of the NMR tensor with respect to the spinning axis, which is fixed for each individual spin. Therefore, setting β to 54.74° makes $(3\cos^2\beta - 1) = 0$, so $\langle 3\cos^2\theta - 1 \rangle$ will vanish, and the anisotropy first-order NMR interactions are averaged to zero.

CSA is one of the main sources of inhomogeneous line broadening for spin-1/2 nuclei and can be averaged out completely by MAS provided that the spinning speed is

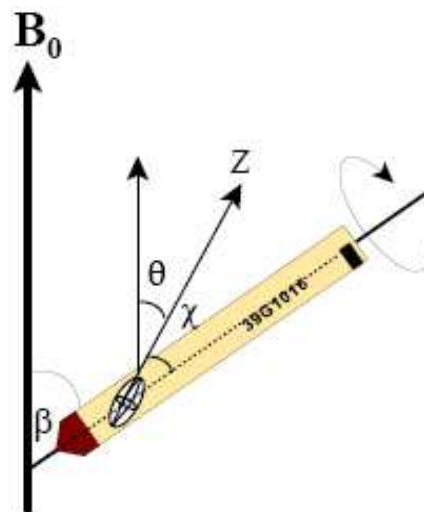


Figure 2.11. The position of the NMR rotor with respect to B_0 during the MAS experiment.

larger than the CSA as measured in Hz; in this case, the isotropic peak will be the only observable peak. However, when the spinning speed is less than the CSA, the NMR pattern will be divided into spikelets under which the intensities are localized. These spikelets are known as spinning sidebands and they flank the isotropic peaks at distances equal to the spinning frequency. Spinning sidebands arise because of the refocusing of the magnetization after each rotor period. After the dephasing of the magnetization, the spins go back to their original positions after each rotor cycle leading to the formation of what are called “rotational echoes” in the frequency spectrum. Spectroscopists often acquire SSNMR spectra of spin-1/2 at low to moderate spinning speeds to get as many spinning sidebands as possible; the intensities of these sidebands are related to the anisotropy of the chemical shift and are used to extract the CSA parameters.¹⁵

Homonuclear and heteronuclear dipolar interactions also contain the angular term $(3\cos^2\theta - 1)$. The dipolar interaction can be averaged out in solids if the sample is spun at the magic angle, β . Unlike the CS tensor, the dipolar tensor is traceless; thus, MAS can completely average dipolar interactions to zero provided that the spinning frequency is larger than the strength of the dipolar coupling.

MAS only averages the first-order quadrupolar interaction. Since the CT is only affected to second-order by the quadrupolar interaction, it is only partially averaged by MAS, owing to the distinct geometrical dependence of second-order NMR interactions. The frequency of the CT to second-order under MAS is given by:⁸

$$\omega_{\frac{1}{2}, -\frac{1}{2}} = - \left(\frac{e^2 q Q}{4I(2I-1)} \right)^2 \frac{1}{\omega_0} (3-4I(I+1)) \left\{ \frac{1}{2} V_{00}^Q + 4V_{20}^Q + 9V_{40}^Q \right\} \quad (2.33)$$

where V_{00}^Q , V_{20}^Q , V_{40}^Q are the zeroth, second and fourth rank tensors, which contain the following Legendre polynomials, respectively.²⁶

$$P_0(\cos\chi)=1 \quad (2.34)$$

$$P_2(\cos\chi)=\frac{1}{2}(3\cos^2\chi-1) \quad (2.35)$$

$$P_4(\cos\chi)=\frac{1}{8}(35\cos^4\chi-30\cos^2\chi+3) \quad (2.36)$$

where χ represents the angle between the rotor axis and B_0 . Spinning at the magic angle causes the $P_2(\cos\chi)$ term to vanish but not the $P_4(\cos\chi)$ term which can only be zero either at 30.56° or at 70.12° . Thus, there is not a single value of χ which makes the $P_2(\cos\chi)$ and $P_4(\cos\chi)$ terms go to zero simultaneously, and as a result, the linewidth of quadrupolar powder pattern gets reduced under MAS, but an anisotropic powder pattern remains, even at very high spinning speeds. However, different techniques have been developed such as multiple quantum MAS (MQMAS),²⁷ double rotation (DOR),²⁸ and dynamic angle spinning (DAS),^{29,30} which provide high resolution spectra of half-integer quadrupoles but such techniques are beyond the scope of this thesis.

2.3.2. Cross Polarization.

The cross-polarization (CP) technique was first introduced by Pines, Gibby and

Waugh.^{31,32} It is a double-resonance experiment which is used to enhance the signal for dilute (low natural abundant) spins in solid samples. CP relies on the transfer of magnetization from the abundant spins (i.e., ^1H , ^{19}F) to the dilute spins (i.e., ^{13}C , ^{15}N , ^{109}Ag) which are dipolar coupled to one another. CP can lead to a maximum theoretical enhancement of the signal by a factor of γ_I/γ_S , where γ_I and γ_S are the gyromagnetic ratios of the abundant and dilute spins, respectively (this is especially attractive for nuclei with low gyromagnetic ratios). Furthermore, CP helps in reducing the experimental time significantly compared to single pulse experiments, since the spin lattice relaxation T_1 of the dilute spin plays no role in determining the recycle delay between acquisitions. Instead, the T_1 of the abundant spins, which is usually much shorter than the T_1 of the dilute spins, is used to determine the delays between scans.

The CP pulse sequence (Figure 2.12) begins with a 90° pulse applied on resonance along the x -axis on the I -spin (i.e. ^1H) channel, which rotates the I -spin magnetization along the negative y -axis in the doubly rotating frame (i.e, a frame that rotates according to the employed rf frequencies). Then, simultaneous on-resonance pulses are applied to the dilute and abundant spins on both channels. The effect of these long (normally in ms) low power pulses is to fix the I magnetization along the y -axis of the rotating frame and allow for the build up of S magnetization, this is known as “spin locking”.

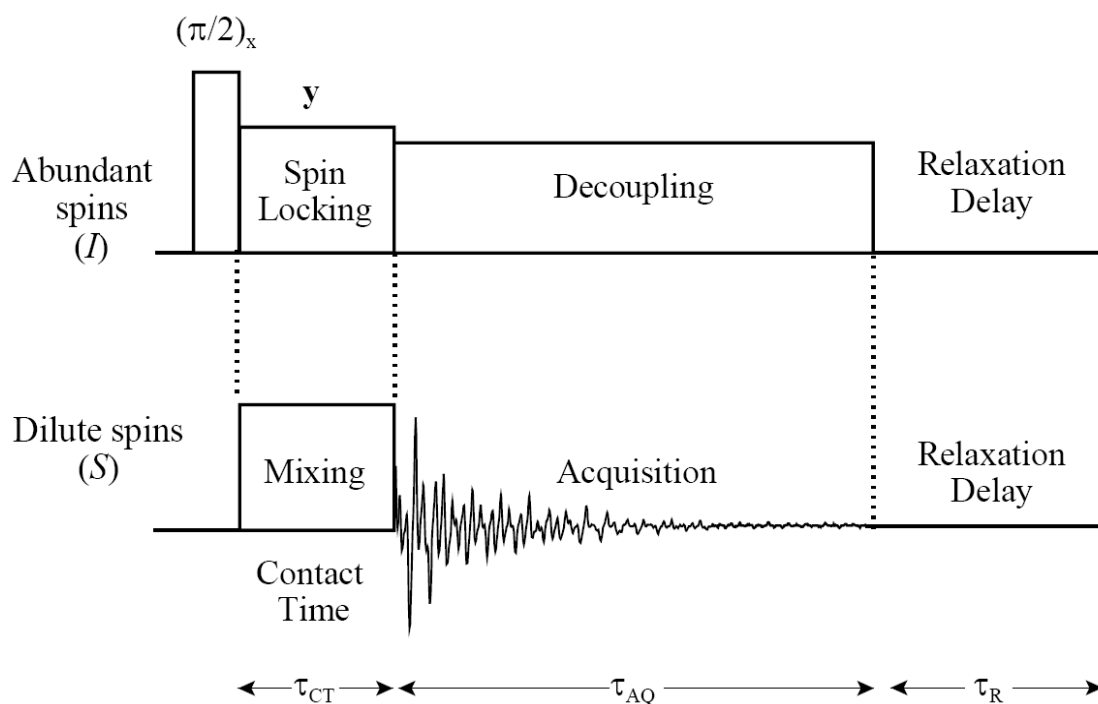


Figure 2.12. The cross polarization pulse sequence.

The amplitude of these pulses are set such that the Hartman-Hahn condition ($\gamma_I B_I = \gamma_S B_S$, or $\omega_I = \omega_S$, under non-spinning conditions) is satisfied (Figure 2.13).^{33,34} Then the *S*-spin magnetization is observed by turning off the lock field on the *S* channel and keeping the decoupling on the *I* channel to get rid of the *I*-*S* dipolar interaction during acquisition.

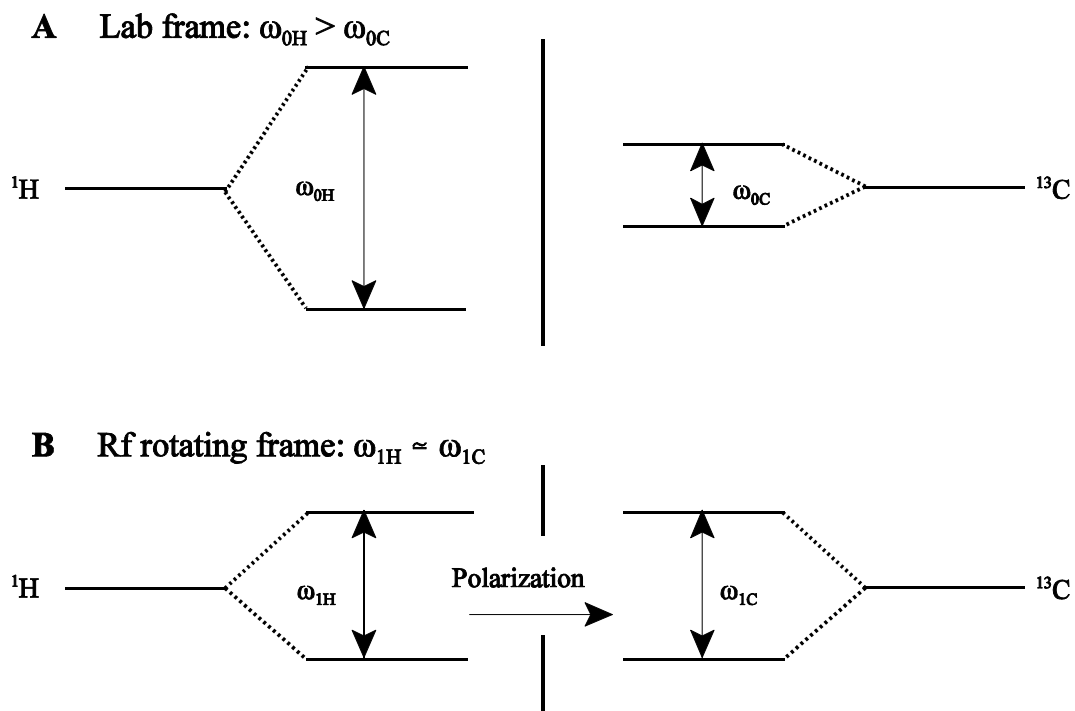


Figure 2.13. Explanation of the Hartmann-Hahn condition. **A** shows the difference between the ^1H and ^{13}C frequencies in the lab frame. **B** shows that the ^{13}C and ^1H frequencies are matched so that the spin transitions can occur.

Magic-angle spinning at high rotational frequencies can greatly decrease the rate of magnetization transfer from the abundant to the dilute spins because of the decoupling of the dipolar interaction. The Hartman-Hahn condition for a static sample is usually Gaussian in shape and fairly broad. However, under MAS, the Hartman-Hahn match splits into a series of sidebands with maximal polarization transfer appearing at the integer multiples of the rotor frequency, $\omega_{1H} - \omega_{1C} = \pm n\omega_R$ ($n = 1, 2$ for the most efficient magnetization transfer). This Hartman-Hahn condition holds reasonably well under moderate MAS speeds.³⁵

Since the CP experiment depends on the dipolar interaction between the dilute and abundant nuclei, and because this interaction is partially averaged when spinning at higher

speeds, the efficiency of the CP experiment decreases. Various CP modified pulse sequences, such as the simultaneous phase-inversion CP (SPICP),³⁶ ramped-amplitude CP (RAMP/CP)³⁷ and variable amplitude CP (VACP),^{38,39} were developed to decrease the sensitivity of the matching condition to high MAS. In this thesis, only the VACP was used and will be discussed in more detail.

In VACP, the ¹H contact pulse consists of a series of pulses with the same phase but different amplitudes.³⁸⁻⁴⁰ The amplitude of the step size between pulses is the same, and the total amplitude variation is about $2\omega_R$. Using variable-amplitude pulses creates a series of Hartman-Hahn conditions, which reduces mismatches between the two spin-locking fields and decreases the loss of signal intensity in comparison to CP.

2.3.4. Hahn-Echo and Quadrupolar Carr-Purcell Meiboom-Gill sequences

The Hahn-echo sequence (Figure 2.14) is the most widely used NMR pulse sequence for the acquisition of NMR spectra of half-integer quadrupolar nuclei.⁴¹⁻⁴³ This technique is very useful for observing the quickly decaying signal of these nuclei by applying a π -pulse after the $\pi/2$ -pulse, which refocuses the magnetization in the *xy* plane. However, this sequence can be time consuming when acquiring UW NMR spectra, particularly in case of unreceptive quadrupolar nuclei.

The quadrupolar Carr-Purcell Meiboom-Gill (QCPMG) sequence (Figure 2.14) was reintroduced in 1997 for the acquisition of broad NMR patterns of half-integer quadrupolar nuclei under MAS or static conditions.⁴⁴⁻⁵⁶

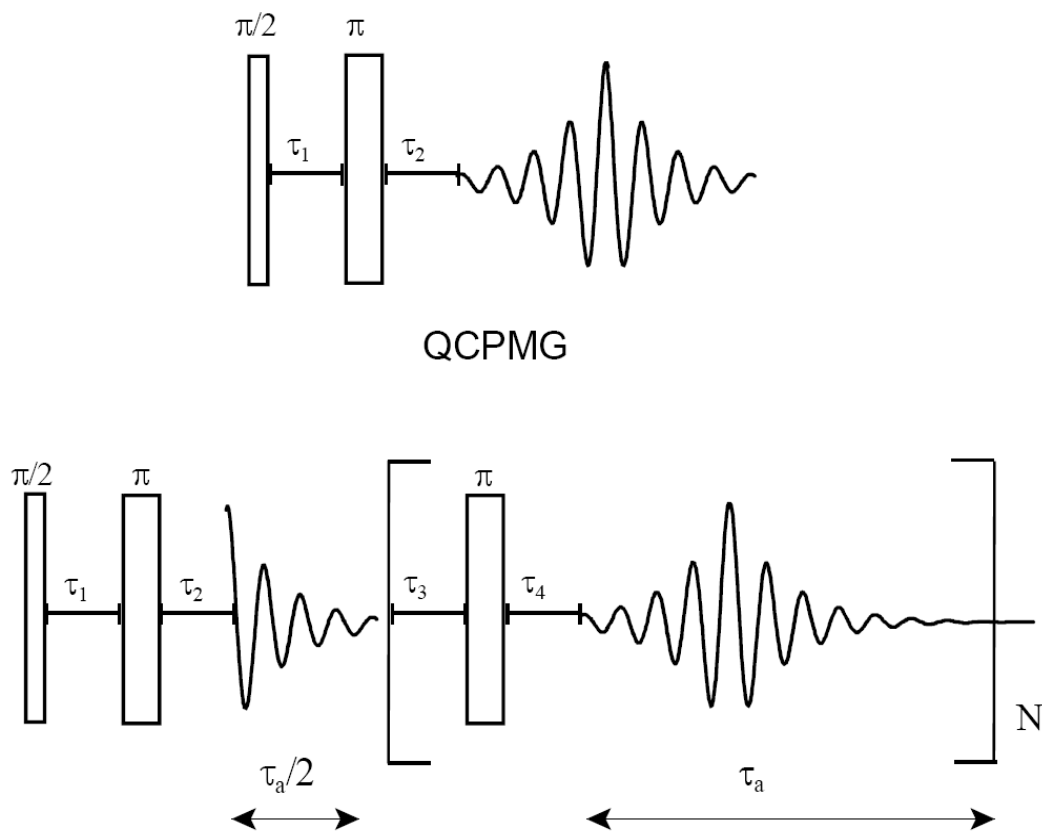


Figure 2.14. The echo and QCPMG pulse sequences.

In comparison to the Hahn-echo sequence, the QCPMG sequence is composed of the first $\pi/2$ and π pulses which produce the first echo, and then a train of π pulses and acquisition periods which are used to detect the signal. Fourier transforming the FID obtained using the QCPMG sequence produces a powder pattern which is composed of “spikelets”. The outer manifold of this pattern matches the manifold of the pure Hahn-echo spectrum. However, since all of the signal is localized beneath the sharp spikelets, the S/N is greatly enhanced.⁵⁷ In certain cases, sensitivity can be enhanced by an order of magnitude or more. The degree of signal enhancement depends on the experimental acquisition time, τ_a , and the transverse relaxation time, T_2 (a longer T_2 results in a longer

echo train, which in turn yields a higher S/N).

2.3.5. Frequency Stepped Techniques and WURST-QCPMG

The breadths of the NMR powder patterns can extend up to several MHz, exceeding the excitation bandwidth achievable with a standard high power rectangular pulse; hence, it is necessary to acquire such patterns using “stepwise” or “piecewise” techniques. Such techniques involve stepping the transmitter frequency across the entire CT powder pattern in even increments, collecting the individual sub-spectra, and then co-adding them to produce the total pattern (Figure 2.15). Determining the correct offset frequency is crucial for obtaining NMR patterns free of distortions. Thus, it is necessary to have a rectangular excitation profile in order to excite the whole pattern evenly. The following equation is used to calculate the excitation profile for a square pulse of amplitude $\omega_1 = \gamma B_1$:⁷

$$E(\omega) = \omega_1 \tau_p \left(\frac{\sin(\omega \tau_p)}{\omega \tau_p} + i \frac{\cos(\omega \tau_p) - 1}{\omega \tau_p} \right) \quad (2.37)$$

where ω_1 is the strength of the B_1 field and τ_p is the pulse length.

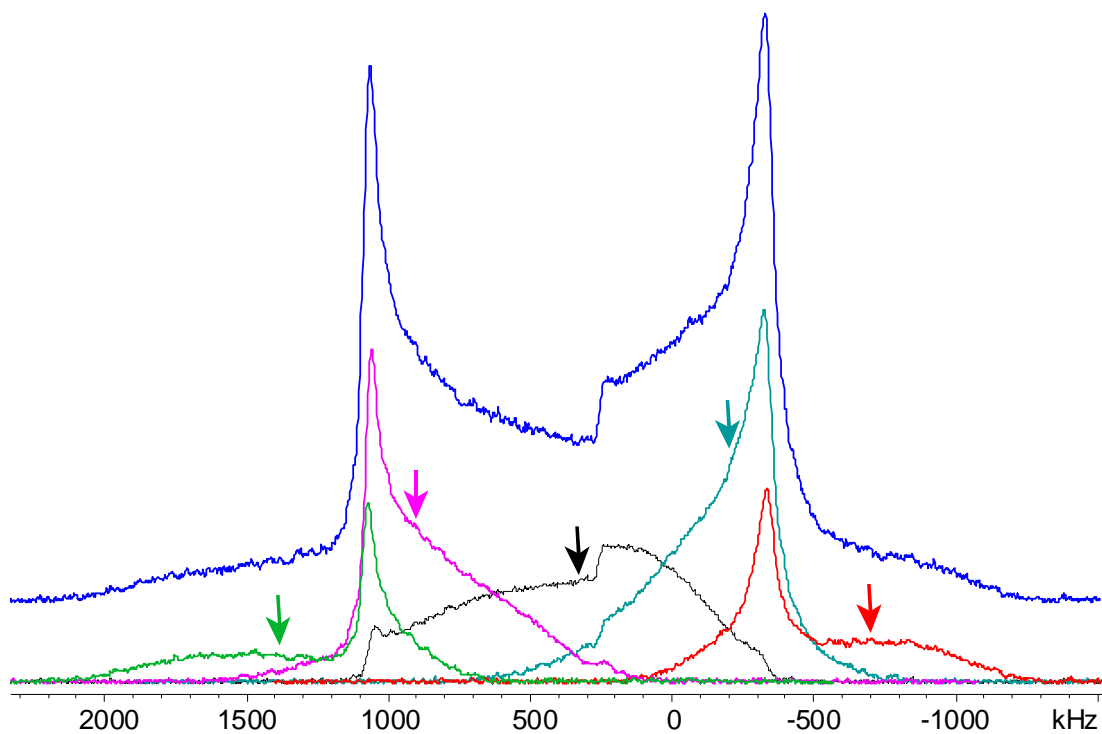


Figure 2.15. Individual sub-spectra are acquired at even increments and co-added to produce the whole pattern. The arrows indicate the transmitter frequencies.

Using this equation, it is possible to determine the optimum offset which leads to an evenly excited NMR pattern. An offset which produces a rectangular excitation profile is the best choice (Figure 2.16). A small offset provides a uniformly excited pattern but unnecessarily increases experimental time; on the other hand, a large offset leads to

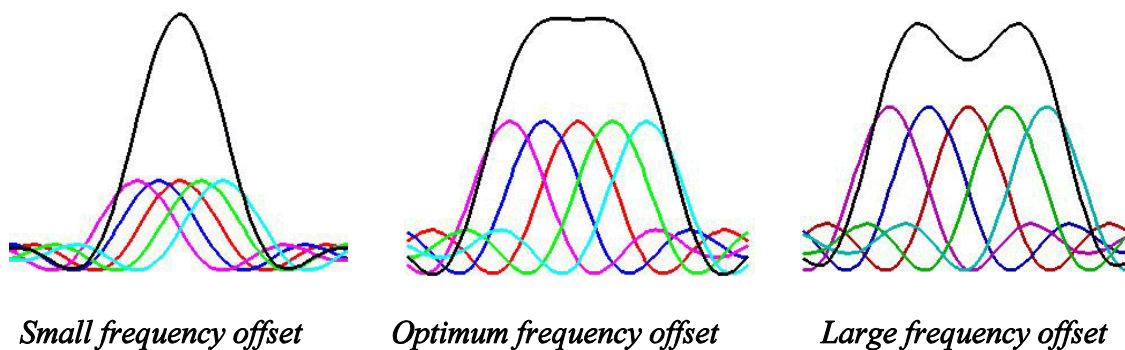


Figure 2.16. The excitation profile for different offset frequencies. The offset producing a rectangular excitation (middle) provides non-distorted powder pattern.

distorted NMR pattern. This frequency-stepped technique has been used in combination with the Hahn-echo and QCPMG pulse sequences.

Adiabatic pulses^{58,59} are becoming increasingly popular in NMR due to their efficacy in achieving broadband excitation. Adiabatic pulses are amplitude- and frequency-modulated pulses which generate a net magnetic field B_{eff} that sweeps slowly through all directions with respect to the external magnetic field, B_0 , and results in a much wider excitation region in comparison to regular rf pulses. Adiabatic WURST (wideband uniform-rate smooth truncation) pulses were developed for excitation of wide frequency ranges by Freeman and co-workers.⁶⁰ Recently, Bhattacharyya and Frydman utilized WURST pulses in echo sequences to acquire wide-line NMR spectra of quadrupolar nuclei, and have shown that this sequence yields uniformly excited powder patterns and significant gains in S/N in comparison to standard Hahn-echo sequences.⁶¹ Our group has extended this work by implementing the WURST pulses in a QCPMG-type pulse sequence.⁶² This WURST-QCPMG sequence is very beneficial for the acquisition of UW NMR patterns,^{55,63-65} since the broadband excitation of adiabatic pulses is complemented with the signal enhancement from the QCPMG echo trains. Due to the larger excitation bandwidth of the WURST pulses, experimental time can be significantly reduced by decreasing the number of individual subspectra which are needed to be acquired in order to obtain broad powder patterns.

2.3.6. Ab Initio NMR Calculations.

Experimental NMR powder patterns yield the NMR tensor components;

however, they don't provide information about the orientation of these components with respect to molecular structures or atomic coordinates (other than via inferences from molecular symmetry). Tensor orientations can be obtained either from single-crystal NMR spectroscopy or first principles calculations. Single-crystal NMR experiments are difficult to perform, requiring specialized probes and large suitable crystals, which are often unobtainable.⁶⁶⁻⁶⁸ Ab initio calculations are very useful for determining the orientations of these tensors and how they are correlated to structure. A large number of publications involving calculations of the NMR tensors have been reported and proven that such calculations are very useful in correlating the NMR parameters to molecular structure and symmetry.⁶⁹⁻⁷⁹ A variety of methods, such as Hartree Fock (HF), density functional theory (DFT) and the gauge-including projector augmented-wave (GIPAW) have been used to predict the NMR tensor parameters.⁸⁰⁻⁸² A detailed description of these methods as applied to the calculations of NMR parameters are described elsewhere.⁸³⁻⁸⁸

In this thesis, HF and B3LYP methods have been used to calculate the NMR parameters using Gaussian03 and Gaussian09 software packages.^{89,90} Also, GIPAW CASTEP calculations have been performed for systems whose structures are periodic in nature.⁸² The accuracy of such calculations (i.e., agreement between experimental and theoretical tensor parameters) depends on the methods and basis sets used, as well as the correctness of the structural models applied.

2.4 Bibliography

- (1) Levitt, M. *Spin Dynamics: Basic Principles of NMR Spectroscopy*, 2001.
- (2) Abragam, A. *The Principles of Nuclear Magnetism*; Oxford University Press: Ely House, London W. 1, 1961.
- (3) Harris, R. K. *Nuclear Magnetic Resonance Spectroscopy*; Longman Scientific and Technical: Essex, 1986.
- (4) Slichter, C. P. *Principles of Magnetic Resonance*; Springer-Verlag: New York, 1990.
- (5) Mehring, M. *Principles of High Resolution NMR in Solids*; 2nd ed.; Springer-Verlag: Berlin, 1983.
- (6) Nelson, J. H. *Nuclear Magnetic Resonance Spectroscopy*; Prentice Hall: Upper Saddle River, 2003.
- (7) Schmidt-Rohr, K.; Spiess, H. W. *Multidimensional solid-state NMR and polymers*; Academic Press: San Diego, 1999.
- (8) Duer, M. J. *Introduction to Solid-State NMR Spectroscopy*; Blackwell Science: Oxford, 2004.
- (9) Cowan, B. *Nuclear Magnetic Resonance and Relaxation*; Cambridge University Press: Cambridge, 1997.
- (10) Haeberlen, U. *High Resolution NMR in Solids: Selective Averaging*; Academic Press: New York, 1976.
- (11) Duer, M. J.; Editor *Solid State NMR Spectroscopy: Principles and Applications* Oxford, 2002.
- (12) Emsley, J. W.; Feeney, J.; Sutcliffe, L. H. *High Resolution Nuclear Magnetic Resonance Spectroscopy*; Pergamon Press: London, 1965; Vol. 1.
- (13) Anet, F. A. L.; O'Leary, D. J. *Concepts Magn. Reson.* **1991**, 3, 193-214.
- (14) Dye, J. L.; Ellaboudy, A. S.; Kim, J. *Pract. Spectrosc.* **1991**, 11, 217-322.
- (15) Herzfeld, J.; Berger, A. E. *J. Chem. Phys.* **1980**, 73, 6021-6030.
- (16) Mason, J. *Solid State Nucl. Magn. Reson.* **1993**, 2, 285-288.
- (17) Branca, R. T.; Galiana, G.; Warren, W. S. *J. Magn. Reson.* **2007**, 187, 38-43.

- (18) Jameson, C. J. In *Multinuclear NMR*; Mason, J., Ed.; Plenum Press: New York, 1987.
- (19) Vega, A. J. *Quadrupolar Nuclei in Solids*; Wiley: New York, 1996.
- (20) Bodart, P. R.; Amoureux, J.-P.; Dumazy, Y.; Lefort, R. *Mol. Phys.* **2000**, *98*, 1545-1551.
- (21) Eichele, K.; Wasylishen, R. E.; WSolids NMR Simulation Package, 1.17.30 ed.; Dalhousie University: Halifax, CA, 2001.
- (22) Andrew, E. R.; Bradbury, A.; Eades, R. G. *Nature (London, United Kingdom)* **1959**, *183*, 1802-1803.
- (23) Lowe, I. J. *Phys. Rev. Lett.* **1959**, *2*, 285-287.
- (24) Klinowski, J.; Editor *New Techniques in Solid-State NMR.*; Springer: New York, 2005.
- (25) Stejskal, E. O.; Memory, J. D. *High Resolution NMR in the Solid State : Fundamentals of CP/MAS*; Oxford University Press: Oxford, 1994.
- (26) Rocha, J.; Morais, C. M.; Fernandez, C. *Top. Curr. Chem.* **2005**, *246*, 141-194.
- (27) Medek, A.; Harwood, J. S.; Frydman, L. *J. Am. Chem. Soc.* **1995**, *117*, 12779-12787.
- (28) Samoson, A.; Lippmaa, E.; Pines, A. *Mol. Phys.* **1988**, *65*, 1013-1018.
- (29) Chmelka, B. F.; Mueller, K. T.; Pines, A.; Stebbins, J.; Wu, Y.; Zwanziger, J. W. *Nature (London)* **1989**, *339*, 42-43.
- (30) Llor, A.; Virlet, J. *Chem. Phys. Lett.* **1988**, *152*, 248-253.
- (31) Pines, A.; Waugh, J. S.; Gibby, M. G. *Chem. Phys. Lett.* **1972**, *15*, 373-376.
- (32) Pines, A.; Gibby, M. G.; Waugh, J. S. *J. Chem. Phys.* **1973**, *59*, 569-590.
- (33) Levitt, M. H.; Suter, D.; Ernst, R. R. *J. Chem. Phys.* **1986**, *84*, 4243-4255.
- (34) Hartmann, S. R.; Hahn, E. L. *Phys. Rev.* **1962**, *128*, 2042-2053.
- (35) Engelke, F. In *Encyclopedia of Nuclear Magnetic Resonance*; John Wiley & sons: Chichester, U.K., 1996, pp 1529-1534.
- (36) Wu, X.; Zilm, K. W. *J. Magn. Reson. Ser. A* **1993**, *104*, 154-165.
- (37) Metz, G.; Wu, X.; Smith, S. O. *J. Magn. Reson. Ser. A* **1994**, *110*, 219-227.
- (38) Peersen, O. B.; Wu, X.; Kustanovich, I.; Smith, S. O. *J. Magn. Reson. Ser. A* **1993**,

104, 334-339.

- (39) Peersen, O. B.; Wu, X.; Smith, S. O. *J. Magn. Reson. Ser. A* **1994**, *106*, 127-131.
- (40) Han, M.; Peersen, O. B.; Bryson, J. W.; O'Halloran, T. V.; Smith, S. O. *Inorg. Chem.* **1995**, *34*, 1187-1192.
- (41) Solomon, I. *Phys. Rev.* **1958**, *110*, 61-65.
- (42) Weisman, I. D.; Bennett, L. H. *Phys. Rev.* **1969**, *181*, 1341-1350.
- (43) Davis, J. H.; Jeffrey, K. R.; Bloom, M.; Valic, M. I.; Higgs, T. P. *Chem. Phys. Lett.* **1976**, *42*, 390-394.
- (44) Srikanth, K.; Schurko, R. W.; Hung, I.; Ramamoorthy, A. *Mater. Sci. Technol.* **2003**, *19*, 1191-1196.
- (45) Jakobsen, H. J.; Bildsoe, H.; Skibsted, J.; Brorson, M.; Gor'kov, P.; Gan, Z. *J. Magn. Reson.* **2010**, *202*, 173-179.
- (46) Mroue, K. H.; Power, W. P. *J. Phys. Chem. A* **2010**, *114*, 324-335.
- (47) Moudrakovski, I.; Lang, S.; Patchkovskii, S.; Ripmeester, J. *J. Phys. Chem. A* **2010**, *114*, 309-316.
- (48) Davis, M. C.; Brouwer, W. J.; Wesolowski, D. J.; Anovitz, L. M.; Lipton, A. S.; Mueller, K. T. *Phys. Chem. Chem. Phys.* **2009**, *11*, 7013-7021.
- (49) Tang, J. A.; Ellis, B. D.; Warren, T. H.; Hanna, J. V.; Macdonald, C. L. B.; Schurko, R. W. *J. Am. Chem. Soc.* **2007**, *129*, 13049-13065.
- (50) Larsen, F. H.; Farnan, I.; Lipton, A. S. *J. Magn. Reson.* **2006**, *178*, 228-236.
- (51) Larsen, F. H. *J. Magn. Reson.* **2004**, *171*, 293-304.
- (52) Larsen, F. H.; Jakobsen, H. J.; Ellis, P. D.; Nielsen, N. C. *Mol. Phys.* **1998**, *95*, 1185-1195.
- (53) Larsen, F. H.; Jakobsen, H. J.; Ellis, P. D.; Nielsen, N. C. *Chem. Phys. Lett.* **1998**, *292*, 467-473.
- (54) Larsen, F. H.; Jakobsen, H. J.; Ellis, P. D.; Nielsen, N. C. *J. Magn. Reson.* **1998**, *131*, 144-147.
- (55) Hamaed, H.; Laschuk, M. W.; Terskikh, V. V.; Schurko, R. W. *J. Am. Chem. Soc.* **2009**, *131*, 8271-8279.

- (56) Hamaed, H.; Lo Andy, Y. H.; Lee David, S.; Evans William, J.; Schurko Robert, W. *J. Am. Chem. Soc.* **2006**, *128*, 12638-12639.
- (57) Hung, I.; Rossini, A. J.; Schurko, R. W. *J. Phys. Chem. A* **2004**, *108*, 7112-7120.
- (58) Garwood, M.; DelaBarre, L. *J. Magn. Reson.* **2001**, *153*, 155-177.
- (59) Tannus, A.; Garwood, M. *NMR Biomed.* **1997**, *10*, 423-434.
- (60) Kupce, E.; Freeman, R. *J. Magn. Reson. Ser. A* **1995**, *115*, 273-276.
- (61) Bhattacharyya, R.; Frydman, L. *J. Chem. Phys.* **2007**, *127*, 194503/194501-194503/194508.
- (62) O'Dell, L. A.; Schurko, R. W. *Chem. Phys. Lett.* **2008**, *464*, 97-102.
- (63) O'Dell, L. A.; Schurko, R. W. *J. Am. Chem. Soc.* **2009**, *131*, 6658-6659.
- (64) O'Dell, L. A.; Rossini, A. J.; Schurko, R. W. *Chem. Phys. Lett.* **2009**, *468*, 330-335.
- (65) Hamaed, H.; Ye, E.; Udachin, K.; Schurko, R. W. *J. Phys. Chem. B* **2010**, *114*, 6014-6022.
- (66) Kovacs, G.; Rohonczy, J. *Solid State Nucl. Magn. Reson.* **2006**, *30*, 55-59.
- (67) Vosegaard, T.; Hald, E.; Dugaard, P.; Jakobsen, H. J. *Rev. Sci. Instrum.* **1999**, *70*, 1771-1779.
- (68) Vosegaard, T.; Langer, V.; Dugaard, P.; Hald, E.; Bildsoe, H.; Jakobsen, H. J. *Rev. Sci. Instrum.* **1996**, *67*, 2130-2133.
- (69) Helgaker, T.; Jaszunski, M.; Pecul, M. *Prog. Nucl. Magn. Reson. Spectrosc.* **2008**, *53*, 249-268.
- (70) Edgar, M. *Annu. Rep. Prog. Chem., Sect. B, Org. Chem.* **2008**, *104*, 312-330.
- (71) Casabianca, L. B.; de Dios, A. C. *J. Chem. Phys.* **2008**, *128*, 052201/052201-052201/052210.
- (72) Bagno, A.; Saielli, G. *Theor. Chem. Acc.* **2007**, *117*, 603-619.
- (73) Bonhomme, C.; Coelho, C.; Baccile, N.; Gervais, C.; Azais, T.; Babonneau, F. *Acc. Chem. Res.* **2007**, *40*, 738-746.
- (74) Facelli, J. C. *Mod. Magn. Reson.* **2006**, *1*, 49-58.
- (75) Stueber, D. *Concept Magn. Reson. A* **2006**, *28A*, 347-368.
- (76) Autschbach, J. *Struct. Bonding (Berlin, Ger.)* **2004**, *112*, 1-48.

- (77) Weber, J.; Schmedt auf der Guenne, J. *Phys. Chem. Chem. Phys.* **2010**, *12*, 583-603.
- (78) Oldfield, E. *Annu. Rev. Phys. Chem.* **2002**, *53*, 349-378.
- (79) Charpentier, T.; Ispas, S.; Profeta, M.; Mauri, F.; Pickard, C. J. *J. Phys. Chem. B* **2004**, *108*, 4147-4161.
- (80) Becke, A. D. *Phys. Rev. A* **1988**, *38*, 3098-3100.
- (81) Lee, C.; Yang, W.; Parr, R. G. *Phys. Rev. B* **1988**, *37*, 785-789.
- (82) Clark, S. J.; Segall, M. D.; Pickard, C. J.; Hasnip, P. J.; Probert, M. I. J.; Refson, K.; Payne, M. C. *Z. Kristallogr.* **2005**, *220*, 567-570.
- (83) Young, D. *Computational Chemistry: A Practical Guide for Applying Techniques to Real World Problems*; John Wiley & Sons: Toronto, 2001.
- (84) Cramer, C. J. *Essentials of Computational Chemistry*; 2nd ed.; John Wiley & Sons: West Sussex, 2004.
- (85) Gao, S.-P.; Pickard, C. J.; Perlov, A.; Milman, V. *J. Phys.: Condens. Matter* **2009**, *21*, 104203/104201-104203/104212.
- (86) Harris, R. K.; Hodgkinson, P.; Pickard, C. J.; Yates, J. R.; Zorin, V. *Magn. Reson. Chem.* **2007**, *45*, S174-S186.
- (87) Hasnip, P. J.; Pickard, C. J. *Comput. Phys. Commun.* **2006**, *174*, 24-29.
- (88) Segall, M. D.; Lindan, P. J. D.; Probert, M. J.; Pickard, C. J.; Hasnip, P. J.; Clark, S. J.; Payne, M. C. *J. Phys.: Condens. Matter* **2002**, *14*, 2717-2744.
- (89) Frisch, M. J.; Trucks, G. W.; Schlegel, H. B.; Scuseria, G. E.; Robb, M. A.; Cheeseman, J. R.; Montgomery, J., J. A.; Vreven, T.; Kudin, K. N.; Burant, J. C.; Millam, J. M.; Iyengar, S. S.; Tomasi, J.; Barone, V.; Mennucci, B.; Cossi, M.; Scalmani, G.; Rega, N.; Petersson, G. A.; Nakatsuji, H.; Hada, M.; Ehara, M.; Toyota, K.; Fukuda, R.; Hasegawa, J.; Ishida, M.; Nakajima, T.; Honda, Y.; Kitao, O.; Nakai, H.; Klene, M.; Li, X.; Knox, J. E.; Hratchian, H. P.; Cross, J. B.; Adamo, C.; Jaramillo, J.; Gomperts, R.; Stratmann, R. E.; Yazyev, O.; Austin, A. J.; Cammi, R.; Pomelli, C.; Ochterski, J. W.; Ayala, P. Y.; Morokuma, K.; Voth, G. A.; Salvador, P.; Dannenberg, J. J.; Zakrzewski, V. G.; Dapprich, S.; Daniels, A. D.; Strain, M. C.; Farkas, O.; Malick, D. K.; Rabuck, A. D.; Raghavachari, K.; Foresman, J. B.; Ortiz, J. V.; Cui, Q.; Baboul, A. G.; Clifford, S.;

Cioslowski, J.; Stefanov, B. B.; Liu, G.; Liashenko, A.; Piskorz, P.; Komaromi, I.; Martin, R. L.; Fox, D. J.; Keith, T.; Al-Laham, M. A.; Peng, C. Y.; Nanayakkara, A.; Challacombe, M.; Gill, P. M. W.; Johnson, B.; Chen, H.; Wong, M. W.; Gonzalez, C.; Pople, J. A.; Rev. B.03 ed.; Gaussian, Inc.: Pittsburgh, 2003.

(90) Frisch, M. J.; Trucks, G. W.; Schlegel, H. B.; Scuseria, G. E.; Robb, M. A.; Cheeseman, J. R.; Scalmani, G.; Barone, V.; Mennucci, B.; Petersson, G. A.; Nakatsuji, H.; Caricato, M.; Li, X.; Hratchian, H. P.; Izmaylov, A. F.; Bloino, J.; Zheng, G.; Sonnenberg, J. L.; Hada, M.; Ehara, M.; Toyota, K.; Fukuda, R.; Hasegawa, J.; Ishida, M.; Nakajima, T.; Honda, Y.; Kitao, O.; Nakai, H.; Vreven, T.; Montgomery, J. A.; Peralta, J., J.E.; Ogliaro, F.; Bearpark, M.; Heyd, J. J.; Brothers, E.; Kudin, K. N.; Staroverov, V. N.; Kobayashi, R.; Normand, J.; Raghavachari, K.; Rendell, A.; Burant, J. C.; Iyengar, S. S.; Tomasi, J.; Cossi, M.; Rega, N.; Millam, J. M.; Klene, M.; Knox, J. E.; Cross, J. B.; Bakken, V.; Adamo, C.; Jaramillo, J.; Gomperts, R.; Stratmann, R. E.; Yazyev, O.; Austin, A. J.; Cammi, R.; Pomelli, C.; Ochterski, J. W.; Martin, R. L.; Morokuma, K.; Zakrzewski, V. G.; Voth, G. A.; Salvador, P.; Dannenberg, J. J.; Dapprich, S.; Daniels, A. D.; Farkas, O.; Foresman, J. B.; Ortiz, J. V.; Cioslowski, J.; Fox, D. J.; Revision A.02 ed.; Gaussian, Inc.: Wallingford CT, 2009.

Chapter 3

Application of Solid-State ^{209}Bi NMR to the Structural Characterization of Bismuth-Containing Materials

3.1. Introduction

Bismuth is an element rarely found naturally in its pure form; however, it is acquired as a byproduct of lead ore mining and is commonly encountered in bismuth oxides^{1,2} and man-made coordination complexes.^{3,4} Recently, bismuth-containing compounds have become important in a number of research areas, including synthesis of pharmaceuticals,⁵⁻⁸ design of superconductors,² and catalytic processes.⁹ With the increased occurrence in the literature of bismuth-containing systems and associated chemistry and materials science implications, methods of characterizing the structure and bonding at the Bi sites are becoming increasingly important.

While X-ray crystallography is useful for structural determinations in highly crystalline systems, and ^1H and ^{13}C NMR experiments are routinely applied for identification of bismuth coordination complexes in solution, characterization of bismuth sites in solid materials has largely been limited to ^{209}Bi nuclear quadrupole resonance (NQR, *vide infra*).¹⁰⁻¹⁹ ^{209}Bi is the only naturally occurring isotope of bismuth and has a nuclear spin of 9/2. Despite its 100% natural abundance, moderate gyromagnetic ratio and high receptivity with respect to ^{13}C , i.e., $D^{\text{C}}(^{209}\text{Bi}) = 848$),²⁰ ^{209}Bi NMR spectroscopy is very limited because of its large nuclear quadrupole moment (Q).²¹ In all but the most spherically symmetric Bi environments, the combination of the large Q and moderate electric field gradients (EFGs) at the Bi site results in sizeable quadrupolar interactions.

These serve to severely broaden ^{209}Bi NMR patterns, and drastically reduce both the T_1 and T_2 relaxation time constants, making routine NMR experimentation very challenging. To date, there are very few ^{209}Bi NMR studies in the literature and no systematic SSNMR study of ^{209}Bi quadrupolar and chemical shift parameters. Reports of ^{209}Bi SSNMR have largely focused on measurement of relaxation time constants and Knight shifts for ^{209}Bi in super- and semiconducting materials²²⁻²⁹ and on spectra of BiVO_4 single crystals.^{30,31}

Despite the aforementioned difficulties, there are reasons why ^{209}Bi SSNMR spectroscopy is an attractive technique for structural characterization. ^{209}Bi SSNMR experiments can be very useful for probing the local Bi environments, as well as for increasing the understanding of structures and dynamics at the molecular/atomic level. Notably, ^{209}Bi SSNMR may be especially valuable for characterization of disordered solids or for microcrystalline solids for which crystal structures are unavailable. The ^{209}Bi quadrupolar interaction is important in this regard: the EFGs at the ^{209}Bi nucleus, which arise from the surrounding atoms and bonds, are described by an EFG tensor, which is a symmetric, traceless, second-rank (3×3) matrix with three principal components defined as $|V_{33}| \geq |V_{22}| \geq |V_{11}|$. The quadrupolar parameters derived from this tensor are the nuclear quadrupolar coupling constant, $C_Q = eQV_{33}/h$, and the asymmetry parameter, $\eta_Q = (V_{11} - V_{22})/V_{33}$. These parameters are sensitive to both major and minor structural changes, with accurate measurements of C_Q and η_Q providing information on the spherical and axial symmetry, respectively, of the ground-state electronic environments at Bi sites.

Numerous bismuth-containing materials have been studied by ^{209}Bi NQR, often referred to as “zero-field NMR”, via measurement of C_Q and η_Q .¹⁰⁻¹⁹ However, ^{209}Bi NQR

is very time-consuming, since extremely wide frequency ranges must be swept to detect the frequencies of interest. This could be alleviated somewhat by theoretical computation of ^{209}Bi quadrupolar parameters; unfortunately, reliable computational methods do not currently exist for universally predicting ^{209}Bi EFG tensor parameters with accuracy.

Frequency-stepped NMR techniques have been shown to be very useful for the acquisition of the ultrawideline (UW) NMR spectra for various nuclei in a variety of materials.³²⁻³⁹ These techniques generally involve stepping the transmitter frequency (at a constant field strength) in even increments, and acquiring individual sub-spectra with limited excitation bandwidths, which are then coadded or projected to generate the final UWNMR spectrum. The S/N of these spectra can be very low due to their extreme breadths. Timely acquisition of high quality spectra is further exacerbated for nuclei with low natural abundances and/or low gyromagnetic ratios. This has been partially addressed by the application of the quadrupolar Carr-Purcell Meiboom-Gill NMR (QCPMG) sequence⁴⁰ for acquisition of frequency-stepped UWNMR spectra.^{39,41} More recently, wideband uniform rate smooth truncation (WURST) and WURST QCPMG sequences have been shown to be very effective for rapid spectral acquisition,⁴²⁻⁴⁴ and should be advantageous for the acquisition of high S/N ^{209}Bi UWNMR spectra.

Herein, we demonstrate the effectiveness of ^{209}Bi frequency-stepped UWNMR techniques for the study of a variety of bismuth-containing materials. To the best of our knowledge, there is no methodical ^{209}Bi SSNMR study of this sort reported in the literature to date. A set of well characterized bismuth complexes (i.e., either by NQR and/or single-crystal XRD) with disparate bismuth environments is examined in order to

start building a database of ^{209}Bi NMR data, which may have use in future structural studies of bismuth-containing systems. First, the ^{209}Bi SSNMR data for solid BiOX systems ($X = \text{Cl}, \text{Br}, \text{and I}$), which have well-known quadrupolar parameters obtained from NQR,¹³ are presented. Then, ^{209}Bi SSNMR data are shown for some Bi coordination compounds for which ^{209}Bi quadrupolar parameters have not been reported, including bismuth nitrate pentahydrate, nonaaquabismuth triflate, and bismuth acetate. Finally, we discuss a preliminary investigation of theoretical ^{209}Bi quadrupolar and chemical shielding parameters obtained from both plane wave (CASTEP) and ab initio (Gaussian 03) methods.

3.2. Experimental

3.2.1 Sample Preparation.

Samples of BiOI, BiOCl, $\text{Bi}(\text{NO}_3)_3 \cdot 5\text{H}_2\text{O}$, and $\text{Bi}(\text{OTf})_3$ were purchased from Sigma-Aldrich Canada, Ltd., and used without further modifications. $\text{Bi}(\text{CH}_3\text{CO}_2)_3$ was purchased from Strem Chemicals Inc. BiOBr was synthesized in our laboratory following slightly modified literature procedures⁴⁵ (our sample was heated at 160 °C in an oven for eight hours). Nonaaquabismuth triflate, $[\text{Bi}(\text{H}_2\text{O})_9](\text{OTf})_3$, was obtained by rehydrating $\text{Bi}(\text{OTf})_3$ in air at room temperature (Figure A.3.1, Appendix A).⁴⁶

3.2.2 Solid-State NMR.

^{209}Bi SSNMR experiments were carried out on a Varian Infinity Plus spectrometer equipped with a 9.4 T ($\nu_0(^1\text{H}) = 399.73 \text{ MHz}$) Oxford wide-bore magnet at

the University of Windsor with $\nu_0(^{209}\text{Bi}) = 65.455$ MHz, and a 21.1 T ($\nu_0(^1\text{H}) = 900.08$ MHz) Bruker Avance II spectrometer ($\nu_0(^{209}\text{Bi}) = 144.64$ MHz) at the National Ultrahigh-field NMR Facility for Solids in Ottawa, Canada. In all cases, NMR powder patterns were too broad to be uniformly excited with a single high-power pulse; hence, spectra were acquired by stepping the transmitter frequency across the entire central transition powder pattern in even increments, collecting the individual sub-spectra, and coadding them to form the total pattern (see Tables A.3.1, A.3.2 for full experimental details).^{34,35} In most instances, spectra were acquired using either the Hahn-echo or solid-echo pulse sequences of the forms $(\pi/2)_x-\tau_1-(\pi)_y-\tau_2\text{-acq}$ and $(\pi/2)_x-\tau_1-(\pi/2)_y-\tau_2\text{-acq}$, respectively, where τ represents the interpulse delays. In cases where the T_2 is long enough, experiments at 9.4 T were performed using either the QCPMG^{40,47,48} or WURST-QCPMG^{43,44} pulse sequences. Bismuth chemical shifts were referenced to a saturated solution of $\text{Bi}(\text{NO}_3)_3 \cdot 5\text{H}_2\text{O}$ in concentrated HNO_3 ($\delta_{\text{iso}} = 0.0$ ppm).²⁰ Analytical simulations of ^{209}Bi NMR spectra were performed using WSolids.⁴⁹

Experiments at 9.4 T. Samples were finely ground and packed into either 5 mm o.d. zirconium oxide rotors or 5 mm glass NMR tubes. ^{209}Bi NMR spectra were collected using a Varian 5 mm double-resonance (HX) static probe. For Hahn-echo and QCPMG experiments, a central-transition selective $\pi/2$ pulse width of $0.75 \mu\text{s}$ ($\nu_1 = 66.7$ kHz) was applied, with an optimized recycle delay of 0.025 s, and spectral widths ranging from 2 to 4 MHz. In the QCPMG experiments, the number of Meiboom-Gill (MG) loops was set to 40. For WURST-QCPMG experiments, a $50 \mu\text{s}$ WURST pulse length, swept with an offset of 2000 kHz at a rate of 40 MHz/ms, was used. The number of echoes was set to

20, the spectral width to 2 MHz, and recycle delay to 0.1 s. In all experiments, the transmitter frequency offset was set between 100 to 150 kHz, in order to ensure uniform excitation. Experimental times ranged from 1 to 14 hours, depending upon the pattern breadth, the number of sub-spectra collected, and the desired S/N. In addition, NQR experiments were performed using the same experimental parameters mentioned above with the NMR probe positioned about 1 m away from the magnet.

Experiments at 21.1 T. Samples were ground and packed into 4 mm o.d. zirconium oxide rotors. ^{209}Bi NMR spectra of all samples were acquired with a 4 mm HX MAS probe, using the frequency-stepped Hahn-echo technique described above. All experiments were conducted with a selective $\pi/2$ pulse width of 1 μs ($\nu_1 = 50.0$ kHz), spectral widths of either 2 or 4 MHz, and optimized recycle delays of 0.2 s. Transmitter frequency offsets of 500 kHz were used, and total experimental times ranged from 1 to 14 hours. In samples with short T_2^* values, the full echo acquisition was often employed to improve the S/N.

3.2.3 Ab Initio Calculations.

^{209}Bi EFG tensor parameters were calculated using both CASTEP software⁵⁰ and Gaussian 03.⁵¹ Ab initio plane-wave density functional theory (DFT) calculations for the BiOX (X = Cl, Br, I) series were performed using the CASTEP NMR program^{50,52} in the Materials Studio 4.3 environment on an HP xw4400 Workstation with a single Intel Dual-Core 2.67 GHz processor and 8 GB DDR RAM. Ultrasoft pseudopotentials⁵² were used for ^{209}Bi EFG calculations with a plane wave basis set cutoff of 610 eV in an

ultrafine accuracy basis set with the Monkhorst-Pack k -space grid size of (6×6×3). The Perdew, Burke, and Ernzerhof (PBE) functionals were used in the generalized gradient approximation (GGA) for the exchange-correlation energy.^{53,54} The magnetic shielding tensors for ²⁰⁹Bi were calculated in ultrafine accuracy basis set using the projector-augmented wave method (GIPAW) implemented in the CASTEP code.^{55,56} The CIF crystal structure files used in the calculations are from the Crystallography Open Database (COD)⁵⁷ and built based on previously published results.^{58,59} CASTEP geometry optimization of the BiOX structures did not show any significant changes in the calculated NMR parameters; therefore, only results for nonoptimized structures are presented for clarity (Table A.3.3, Appendix A).

Ab initio calculations using Gaussian 03 were performed on bismuth nitrate pentahydrate, nonaquaabismuth triflate, and bismuth acetate on Dell Precision workstations. Atomic coordinates were input from the crystal structures reported in the literature.⁶⁰⁻⁶² For the first two compounds, calculations were carried out on clusters composed of a central bismuth atom and coordinating organic moieties. However, for bismuth acetate, a larger structural unit was utilized (vide infra). In some cases, hydrogen atom positions were geometry optimized using the restricted Hartree-Fock (RHF) method with the 18s15p9d3f (333333/33333/333/3) basis set⁶³ on the bismuth atom and 3-21G* basis set on lighter atoms (i.e., C, H, O). Calculations of the EFG tensors were performed using both the RHF and B3LYP methods with the 18s15p9d3f (333333/33333/333/3) and 15s12p8d4f (432222/42222/422/4)⁶³ basis sets on the bismuth atoms and 6-31G* or 6-311G** on the lighter atoms.

3.3 Results and Discussion

3.3.1 Solid-State ^{209}Bi NMR.

Bismuth Oxyhalides, BiOX (X = I, Br, Cl). The bismuth oxyhalides were chosen for preliminary ^{209}Bi SSNMR experiments since they have high Bi contents and moderate quadrupolar coupling constants (previously determined by NQR to be 91.26, 119.58, and 152.46 MHz for X = I, Br, and Cl, respectively).¹³ The ^{209}Bi SSNMR spectra of the BiOX samples and associated simulations are shown in Figure 3.1, with corresponding NMR parameters summarized in Table 3.1. The experimental times required to acquire these spectra were relatively short (see Tables A.3.1 and A.3.2 for details). The spectra reveal that each of these samples has a single chemically distinct bismuth site, in agreement with the crystal structures (Scheme 3.1). The experimental values of C_Q and η_Q are very close to those determined with NQR,¹³ with the values of $C_Q(^{209}\text{Bi})$ increasing with increasing Bi–X interatomic distance. There are larger uncertainties associated with the parameters obtained from NMR experiments than those from NQR due to the wide pattern breadths.

Table 3.1. Summary of the experimental ^{209}Bi NMR parameters.

	$ C_Q(^{209}\text{Bi}) $ /MHz ^a	η_Q^b	$\delta_{\text{iso}}/\text{ppm}^c$	Ω/ppm^d	κ^e	α/deg^f	β/deg	γ/deg
BiOI	91(3)	0.01(1)	3200(100)	1100(200)	0.8(2)	0	0	0
BiOBr	122(3)	0.03(3)	3500(200)	2000(300)	0.9(1)	0	2(2)	0
BiOCl	153(3)	0.01(1)	3500(400)	3000(500)	0.9(1)	0	3(3)	0
$\text{Bi}(\text{NO}_3)_3 \cdot 5\text{H}_2\text{O}$	78.6(8)	0.66(2)	0(100)	1500(300)	0.7(2)	50(10)	35(5)	95(20)
$\text{Bi}(\text{OTf})_3 \cdot 9\text{H}_2\text{O}$	90(1)	0.01(1)	-750(20)	240(40)	0.6(3)	0	0	0
$\text{Bi}(\text{CH}_3\text{CO}_2)_3$	256(10)	0.30(6)	3200(500)	3400(1000)	0.9(1)	0	2(2)	0

^a $C_Q = eQV_{33}/h$; ^b $\eta_Q = (V_{11} - V_{22})/V_{33}$; ^c $\delta_{\text{iso}} = (\delta_{11} + \delta_{22} + \delta_{33})/3$; ^d $\Omega = \delta_{11} - \delta_{33}$; ^e $\kappa = 3(\delta_{22} - \delta_{\text{iso}})/\Omega$.

^f Conventions for the Euler angles are described in the WSolids software package.

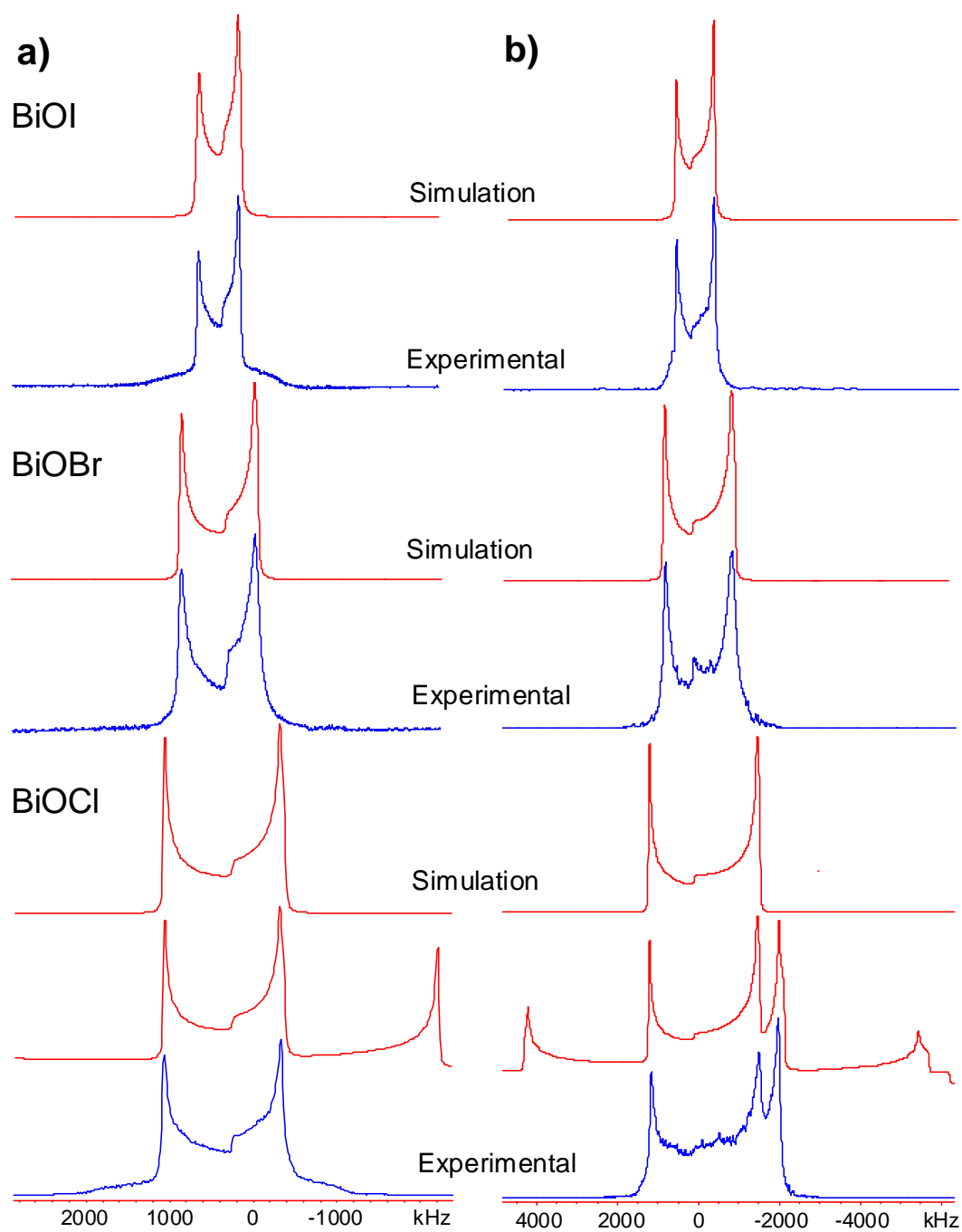
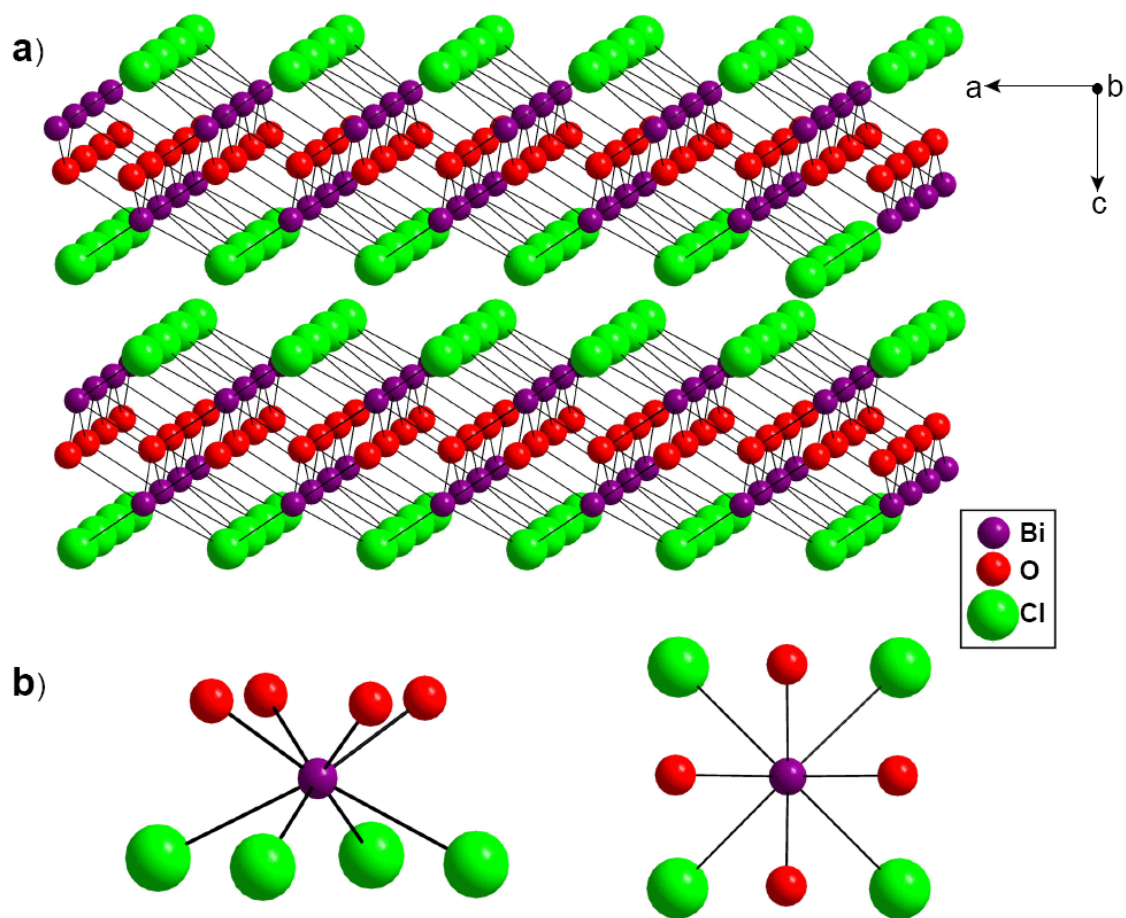


Figure 3.1. ^{209}Bi SSNMR spectra of BiOI, BiOBr and BiOCl at a) 21.1 T and b) 9.4 T. For BiOCl, simulations with and without satellite transitions are shown. The rolling baselines in some of these spectra arise from underlying satellite transitions which have been partially excited.



Scheme 3.1. a) A schematic representation of the crystal structure of BiOCl. The species in the BiOX series (X = Br, Cl or I) are isostructural. b) The coordination environment of the Bi atoms consists of a staggered arrangement of four halides and four oxygen atoms (left, side view; right, top view).

BiOI has the smallest C_Q (91 MHz), and an axially symmetric ($\eta_Q = 0$) central transition (CT) pattern with a breadth of ca. 1.1 MHz at 9.4 T. The experimental time for the spectrum acquired at 21.1 T is significantly reduced compared to that at 9.4 T due to both increased sensitivity ($S_+ \propto B_0^2$) and the reduced spectral breadth of ca. 685 kHz. The contributions of the second-order quadrupolar interaction to the CT breadth scale as the inverse of the applied magnetic field, whereas contributions of bismuth chemical shift

anisotropy (CSA) are directly proportional to the magnetic field strength; hence, it is possible to make relatively accurate determinations of bismuth CS tensor parameters with NMR data at both fields. The span and skew are found to be $\Omega = 1100$ ppm and $\kappa = 0.8$ (see Table 3.1 for definitions of these parameters), and the Euler angles indicate that the largest component of the EFG tensor, V_{33} , is coincident with the most shielded component of the CS tensor, δ_{33} . The CS tensor is almost axially symmetric, meaning that δ_{33} is distinct, and $\delta_{11} \approx \delta_{22}$, consistent with both the relative orientation of the CS and EFG tensors and $\eta_Q = 0$. The contribution of the CSA represents only ca. 165 kHz or 24% of the breadth of the total powder pattern (Figure A.3.2); thus, accurate measurement of CS tensors is more challenging for the remainder of the complexes discussed herein, all of which have markedly large values of C_Q and CT patterns dominated by second-order quadrupolar contributions (Figures A.3.3 & A.3.4).

BiOBr and BiOCl have C_Q 's of 122 and 153 MHz, respectively, and both possess axially symmetric EFG tensors. In addition, the 21.1 T data permits the measurements of effectively axially symmetric CS tensors with significantly larger spans than that of BiOI. Interestingly, in the spectrum of BiOCl, the overlap of the CT and one of the satellite transitions (ST) is observed in the 9.4 T spectrum. The STs for spin-9/2 nuclei are generally "packed" quite tightly about the CT; this foreshadows the increasingly complicated spectra resulting from CT/ST overlaps that are observed for increasing values of C_Q . Traces of the ST patterns are seen on the edges of the CT patterns in all three cases.

It should be mentioned that the Hahn-echo sequence, and not QCPMG, was used

for the acquisitions of these spectra due to the extremely short transverse relaxation time constants, T_2 , of the ^{209}Bi nuclei. Fitting of CPMG echo intensities as a function of time yielded T_2 values of 97(6) μs , 59(7) μs , and 139(10) μs for BiOI, BiOBr, and BiOCl (Figure A.3.5), respectively. The transverse relaxation is likely to be dominated by the quadrupolar relaxation mechanism; however, unlike in the extreme narrowing limit, there is no clear correlation between the magnitude of C_Q and the value of T_2 . It is possible that dipolar relaxation mechanisms may have some influence on the ^{209}Bi T_2 values, since the magnitudes of the ^{209}Bi -X dipolar couplings vary as $R_{\text{DD}}(^{209}\text{Bi}, ^{79/81}\text{Br}) > R_{\text{DD}}(^{209}\text{Bi}, ^{127}\text{I}) > R_{\text{DD}}(^{209}\text{Bi}, ^{35/37}\text{Cl})$, and $T_2(\text{BiOBr}) < T_2(\text{BiOI}) < T_2(\text{BiOCl})$, and the NMR active isotopes are 100% naturally abundant in each case. ^1H MAS NMR spectra acquired for each system (not shown) do not reveal significant amounts of proton-containing impurities that could influence the transverse relaxation rates.

Finally, a comment on the bismuth isotropic chemical shifts should be made. While the C_Q is extremely effective at differentiating the Bi environments in these samples, the δ_{iso} is very similar in all three cases (within the large uncertainties), reinforcing the notion that for samples with similar Bi environments, the quadrupolar parameters are crucial for accurate structural characterization. Bismuth chemical shift differences will mainly be useful for differentiating very distinct Bi environments, as noted from previous solution ^{209}Bi NMR studies,⁶⁴ and as discussed below.

Bismuth Nitrate Pentahydrate, $\text{Bi}(\text{NO}_3)_3 \cdot 5\text{H}_2\text{O}$. Previous attempts to obtain a ^{209}Bi NQR signal for $\text{Bi}(\text{NO}_3)_3 \cdot 5\text{H}_2\text{O}$ were unsuccessful.¹² However, we were able to obtain the ^{209}Bi NMR spectra with relative ease using both the Hahn echo and the WURST-

QCPMG⁴³ pulse sequences (Figure 3.2). It is possible to use the QCPMG-type experiments since the T_2 is much longer (1547(35) μs , Figure A.3.6) than those of the BiOX series. The spectrum reveals a powder pattern corresponding to a single bismuth site, in agreement with the crystal structure.⁶¹

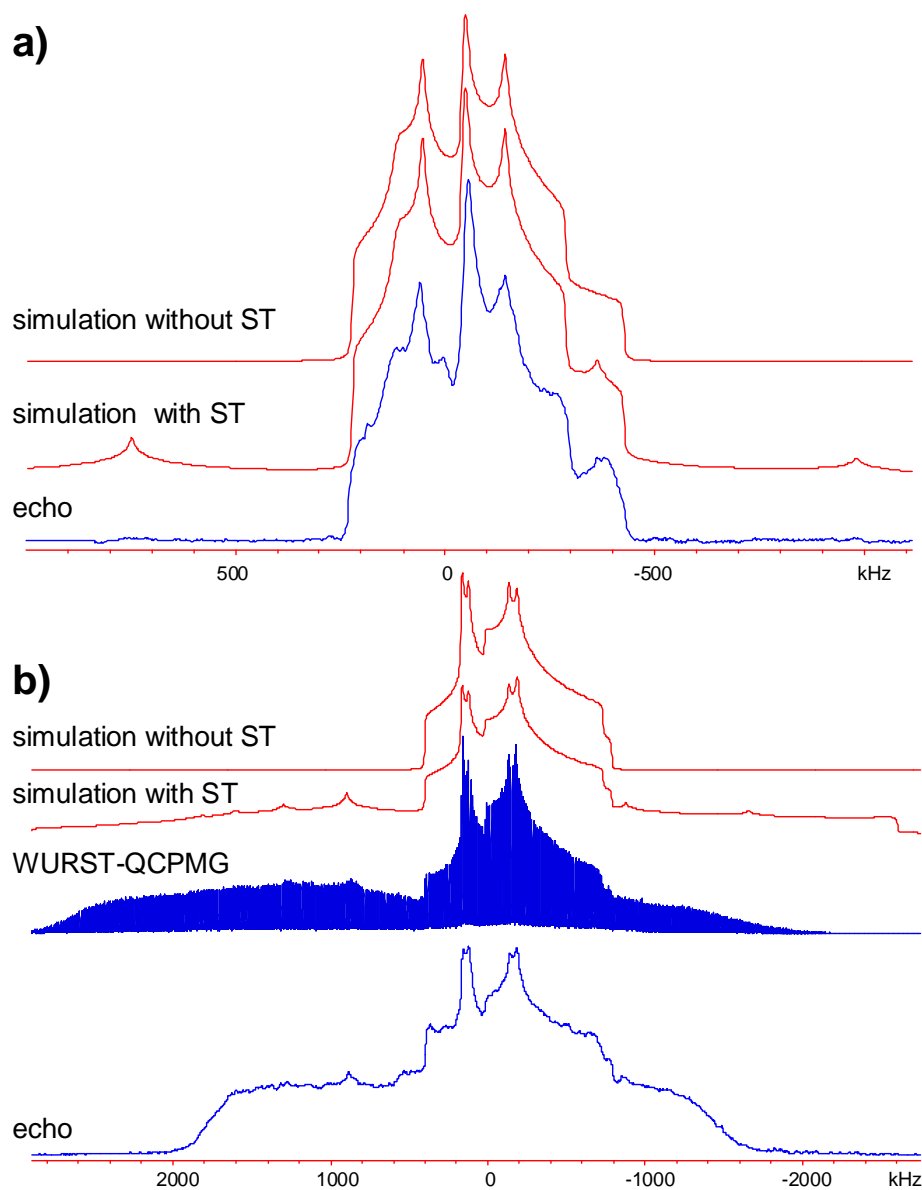


Figure 3.2. ^{209}Bi SSNMR spectra of bismuth nitrate pentahydrate at a) 21.1 T and b) 9.4 T. Not all of the satellite transitions were acquired in order to shorten experimental time, more ST subspectra were acquired in the WURST spectrum due to the shorter experimental time.

The bismuth atom is coordinated by ten oxygen atoms which form an irregular polyhedron comprised of four H₂O molecules, two nearly symmetrically bidentate NO₃⁻ ions (i.e., the Bi-O bond lengths are similar) and one asymmetrically bidentate NO₃⁻.⁶¹ Nine of the Bi-O distances range from 2.32 to 2.67 Å and the tenth is 2.99 Å. The smaller C_Q reflects the higher spherical symmetry of the electronic charge distribution about the bismuth atom compared to those in the BiOX systems. In addition, the value of η_Q indicates that the EFG tensor is nonaxially symmetric, which is consistent with the Bi atoms not being positioned on symmetry elements. Since η_Q is nonzero, some minor interference between ST and CT can be seen by comparison of simulations with and without STs (Figure 3.2).

Nonaaquabismuth Triflate, [Bi(H₂O)₉](OTf)₃. Quadrupolar parameters have not previously been obtained for [Bi(H₂O)₉](OTf)₃. The ²⁰⁹Bi NMR spectrum (Figure 3.3) was obtained in a very short time (i.e., about 1 h at 9.4 T) and reveals a powder pattern corresponding to a single bismuth site, again in agreement with the crystal structure.⁶² The Bi atom in the nonaaquabismuth cation is coordinated by nine H₂O molecules, with Bi-O distances of 2.448 or 2.577 Å. The slightly larger value of C_Q compared to that of Bi(NO₃)₃·5H₂O arises from a slightly less spherically symmetric environment and may be due to the smaller bismuth coordination number; however, this is difficult to definitively ascertain without a larger database of quadrupolar parameters and structures for comparison. The cation has a C_{3h} symmetry, which is reflected by the axially symmetric EFG tensor, with V₃₃ as its unique component. Bi(NO₃)₃·5H₂O and [Bi(H₂O)₉](OTf)₃ have similar values of δ_{iso}; however, these values are distinct from those of the BiOX

series, suggesting that ^{209}Bi nuclei in substantially different environments can be differentiated by chemical shifts extracted from the broad ^{209}Bi SSNMR spectra.

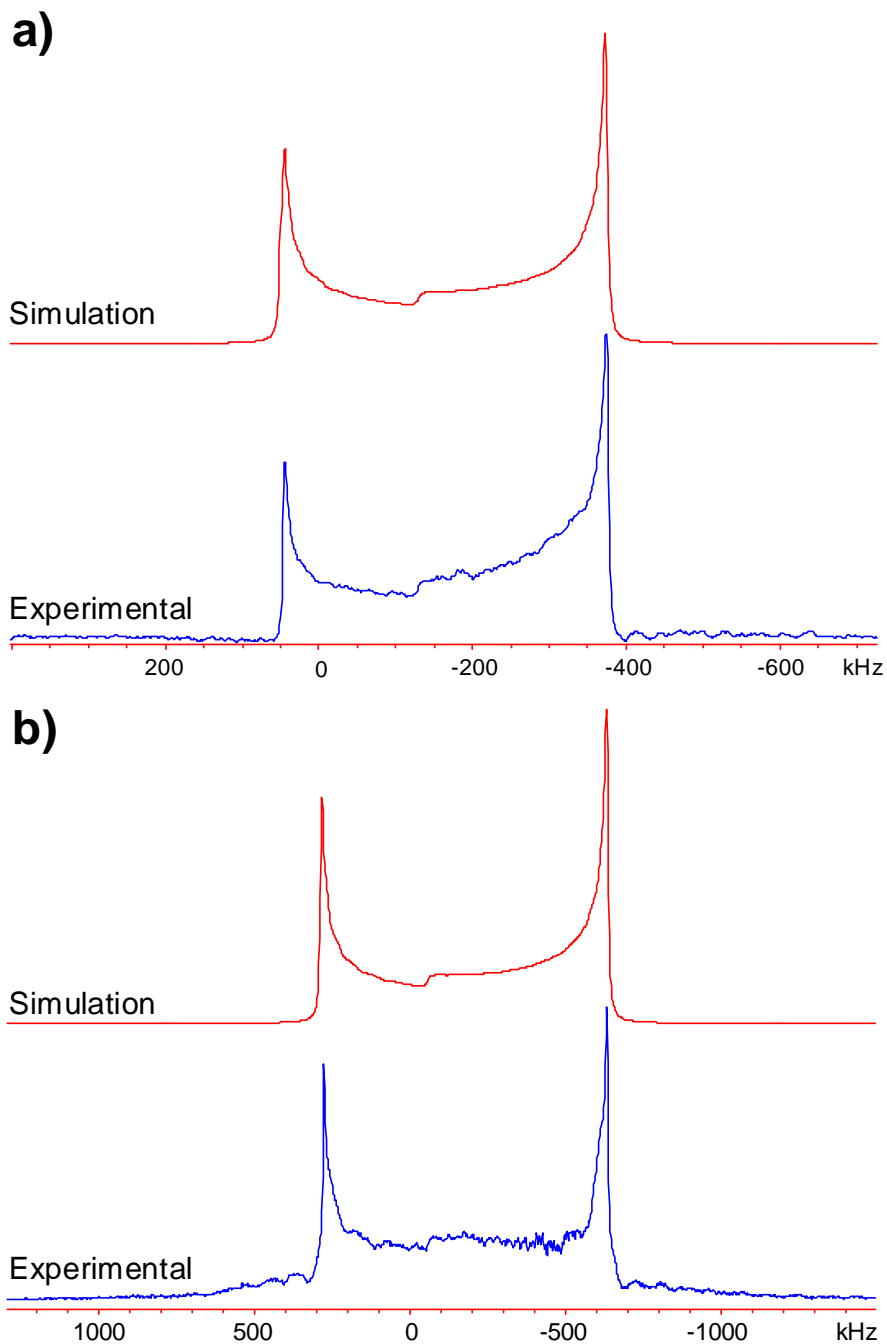


Figure 3.3. ^{209}Bi SSNMR spectra of nonaquaabismuth triflate at a) 21.1 T and b) 9.4 T. The rolling baselines in these spectra arise from underlying satellite transitions which have been partially excited.

Bismuth Acetate, Bi(O₂CCH₃)₃. Bismuth acetate has only one bismuth site in the asymmetric unit, with a coordination environment described as an irregular, nine-vertex polyhedron. The lone electron pair of the bismuth atom occupies a considerable amount of space (i.e., displays stereochemical activity), forcing the bidentate acetato ligands into positions on one side of the Bi atom.⁶⁰ As a result, the spherically asymmetric distribution of atoms results in a large quadrupolar interaction, as reflected in the expansive ²⁰⁹Bi NMR pattern (Figure 3.4).

The spectrum acquired at 9.4 T is extremely broad, requiring the acquisition of 143 QCPMG-subspectra to roughly span the CT and several closely spaced discontinuities from some of the STs. Some of the intensities are inconsistent with the simulation, which could arise from variation in the transverse (T_2) relaxation parameters of the CT and STs, or more likely, differential excitation of the CT and STs (i.e., CTs and STs have distinct nutation rates which can potentially give rise to different relative intensities).^{65,66} It is also possible that these discrepancies may arise from the failure of the high field approximation (i.e., $\nu_0 \gg \nu_Q$), since the C_Q of 256 MHz corresponds to a ν_Q of ca. 10.7 MHz; however, the dominant quantization axis is still the Zeeman axis ($\nu_0(^{209}\text{Bi}) = 65.455$ MHz at 9.4 T). In contrast, the spectrum at 21.1 T ($\nu_0(^{209}\text{Bi}) = 146.927$ MHz) is constructed from 13 subspectra, and the CT and ST discontinuities match well with simulations, suggesting that the high field approximation holds in this case. The C_Q is much larger than those of the previous samples, due to the influence of the stereochemically active lone pairs of the Bi atom.⁶⁰ To further confirm the EFG parameters, NQR experiments were performed and two of the transitions were found

($\nu_{(7/2 \text{ to } 5/2)} = 32.086 \text{ MHz}$ and $\nu_{(9/2 \text{ to } 7/2)} = 43.366 \text{ MHz}$). From these transitions the C_Q was calculated to be $262.61(7) \text{ MHz}$ and $\eta_Q = 0.336(2)$, confirming our NMR results.

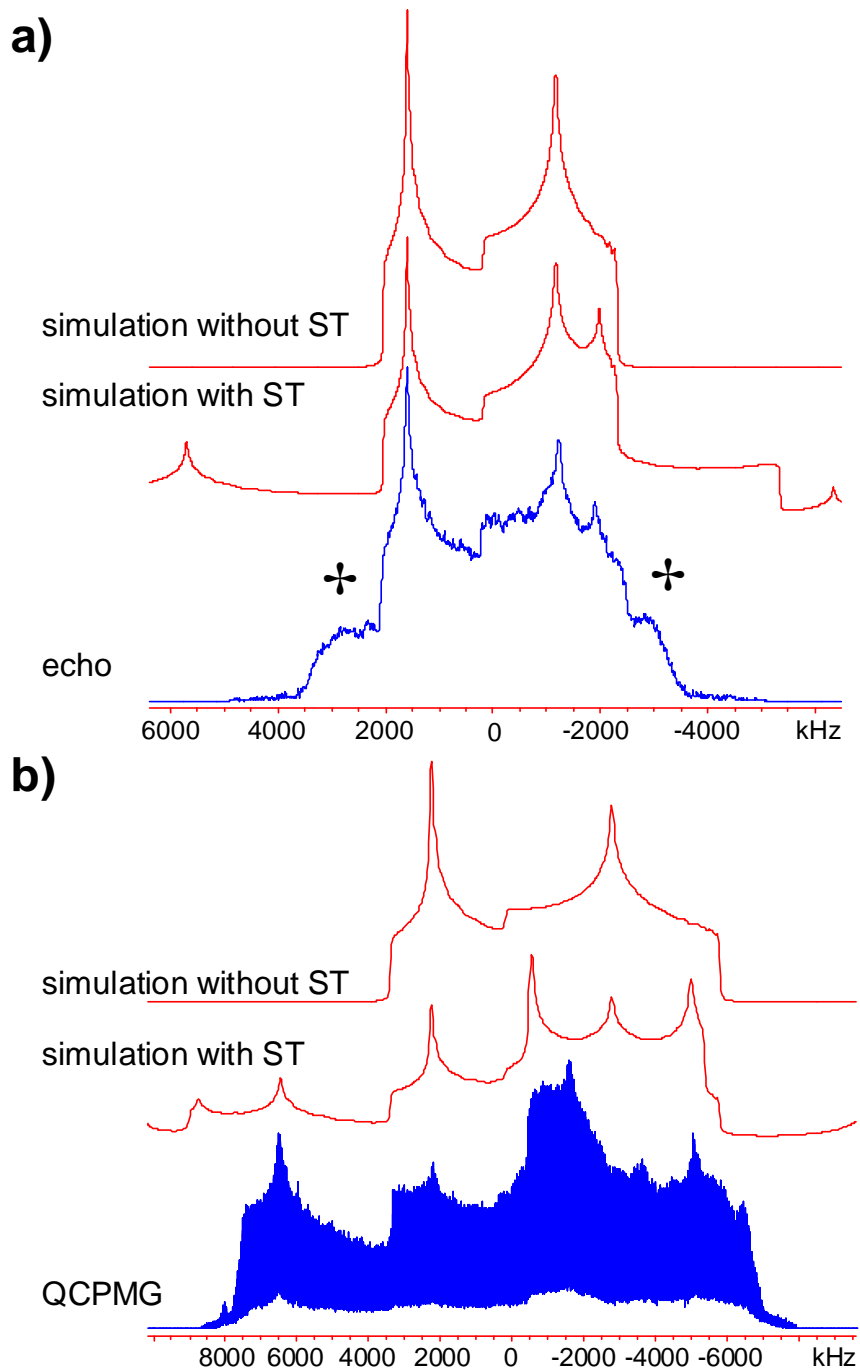


Figure 3.4. ^{209}Bi SSNMR spectra of bismuth acetate at a) 21.1 T and b) 9.4 T. \oplus indicate satellite transitions.

We note that the δ_{iso} is similar to that of the BiOX series, despite the distinct Bi chemistry; this can be attributed, in part, to the large errors associated with the measurement of δ_{iso} . There are very few reports of bismuth chemical shifts in the literature available for comparison to our data. Aside from several studies of ^{209}Bi Knight shifts,^{22,24-27,29} ^{209}Bi chemical shifts have only been reported for species such as the highly symmetric BiF_6^- anion in acetone,²⁹ aqueous solutions of bismuth salts, and the $[\text{Bi}(\text{H}_2\text{O})_6]^{3+}$ cation formed in solutions of $\text{Bi}(\text{NO}_3)_3$ in concentrated nitric acid.⁶⁷ Since the chemical shifts presented herein represent the majority of bismuth chemical shifts reported in the literature, it is difficult to comment further at this time. It is possible that Bi may have a chemical shift range similar to that of antimony, which has been estimated at ca. 3500 ppm.⁶⁸

3.3.2 Theoretical Calculations of ^{209}Bi EFG and CS Tensors.

An appreciation of the relationships between solid-state structures and bismuth NMR interaction tensors will be crucial for making future structural interpretations for the multitude of Bi-containing materials. To develop a basis for understanding these relationships, we have conducted ab initio calculations of the ^{209}Bi EFG tensors for all of the systems discussed above, as well as ^{209}Bi CS tensors for the BiOX series. In this section, we present an examination of the principal components and tensor orientations with respect to the molecular coordinates.

CASTEP Calculations for the BiOX Series. Compounds in the BiOX series crystallize in a tetragonal unit cell with the $P4/nmm$ space group.^{58,59} Their structures

consist of metal-oxygen layers separated by two halide sheets (Scheme 3.1). The bismuth atoms are located on special positions, i.e., $4mm$, and are coordinated by four oxygen atoms and four halide atoms. Due to the periodicity of these structures, CASTEP software⁵⁰ was used to calculate the ^{209}Bi EFG parameters. The calculated C_Q 's (Table 3.2) are consistently lower than the experimental values, and values of η_Q are axially symmetric in all cases. The disagreement between experimental and theoretical C_Q 's may arise from either the nature of the Bi pseudopotential (a full investigation of which is beyond the scope of this thesis) or the degree of uncertainty in the experimentally measured and theoretically calculated ^{209}Bi nuclear quadrupole moments. Bieroń and Pyykkö have pointed out that values of $Q(^{209}\text{Bi})$ have been put forward that range from -370 to -710 mb,²¹ with the most likely candidates being $-370(26)$ mb^{69,70} and $-500(80)$ mb.⁷¹ It is clear from the results for the BiOX species (Table 3.2), and also for the molecular Bi species (vide infra), that arbitrary variation in the magnitude of $Q(^{209}\text{Bi})$ could certainly lead to better agreement in some cases, while simultaneously diminishing agreement in others. In this work, we have elected to utilize $Q(^{209}\text{Bi}) = -370$ mb (0.37×10^{-28} m²) for all of our conversions from a.u. to MHz, since there are numerous reports of $Q(^{209}\text{Bi})$ close to this value, and since this provides uniformity in our comparisons of experimental and theoretical data. Nonetheless, the experimental trend of increasing values of C_Q in the series $X = \text{I, Br, Cl}$ is replicated.

The CS tensor parameters have also been calculated for the BiOX series (Table 3.3). We do not report the theoretical isotropic chemical shifts, as a reliable computational reference standard has yet to be established.

Table 3.2. Comparison of the experimental and CASTEP ^{209}Bi EFG tensor parameters of the BiOX series.

	V_{11} /a.u.	V_{22} /a.u.	V_{33} /a.u.	$C_Q(^{209}\text{Bi})/\text{MHz}^a$	η_Q
BiOI Exp.	-----	-----	-----	91(3)	0
BiOI Cal.	0.3381	0.3381	-0.6763	58.8	0
BiOBr Exp.	-----	-----	-----	122(3)	0
BiOBr Cal.	0.6067	0.6067	-1.2133	105.5	0
BiOCl Exp.	-----	-----	-----	153(3)	0
BiOCl Cal.	0.7402	0.7402	-1.4805	128.7	0

^aTheoretical values of C_Q ($C_Q = eQV_{33}/h$) are calculated by converting from atomic units to Hz by multiplying V_{33} by $(eQ/h)(9.7177 \times 10^{21} \text{ V m}^{-2})$, where $Q(^{209}\text{Bi}) = -0.37 \times 10^{-28} \text{ m}^2$. The absolute values of the experimental C_Q 's are reported, while theoretical values are reported with the calculated signs.

Table 3.3. Comparison of the experimental and CASTEP ^{209}Bi CS tensor parameters of the BiOX series.

	σ_{11}/ppm	σ_{22}/ppm	σ_{33}/ppm	$\sigma_{\text{iso}}/\text{ppm}^a$	Ω/ppm^b	κ^c	α/deg	β/deg	γ/deg
BiOI Exp.	-----	-----	-----	-----	1100(200)	0.8(2)	0	0	0
BiOI Cal.	6279.21	6279.21	7430.62	6663	1151	1	0	0	0
BiOBr Exp.	-----	-----	-----	-----	2000(300)	0.9(1)	0	2(2)	0
BiOBr Cal.	5689.54	5689.54	6766.67	6049	1077	1	0	0	0
BiOCl Exp.	-----	-----	-----	-----	3000(500)	0.9(1)	0	3(3)	0
BiOCl Cal.	5699.3	5699.3	6799.32	6066	1100	1	0	0	0

^a $\sigma_{\text{iso}} = (\sigma_{11} + \sigma_{22} + \sigma_{33})/3$; ^b Span: $\Omega = \sigma_{33} - \sigma_{11}$; ^c Skew: $\kappa = 3$

The theoretical span for BiOI matches very well with experimental data, while those for BiOBr and BiOCl are overestimated. In all cases, the bismuth CS tensors are predicted to be axially symmetric, in good agreement with experiment. The largest component of the EFG tensor, V_{33} , is aligned along the c axis of the unit cell, as expected (Figure 3.5a), and the V_{11} and V_{22} are consistently oriented along the Bi–O bonds; however, given that the $\eta_Q = 0$, the precise orientations of V_{11} and V_{22} are not terribly relevant in this case.

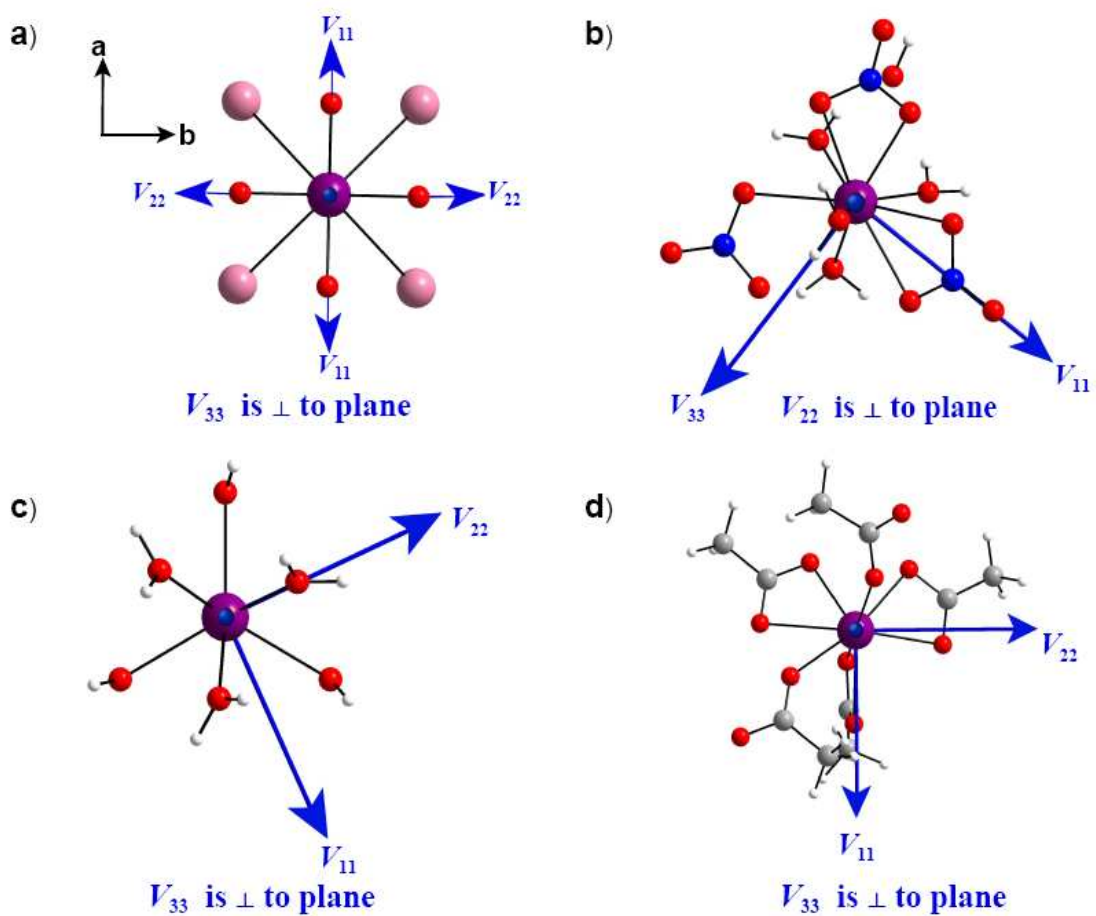


Figure 3.5. a) ^{209}Bi EFG tensor orientations in a) BiOX series, b) $\text{Bi}(\text{NO}_3)_3 \cdot 5\text{H}_2\text{O}$ c) $[\text{Bi}(\text{H}_2\text{O})_9](\text{OTf})_3$ and d) $\text{Bi}(\text{CH}_3\text{CO}_2)_3$.

Furthermore, the most shielded component of the CS tensor, δ_{33} , is found to be collinear

with V_{33} , and the associated Euler angles are in excellent agreement with experiment.

Gaussian 03 Calculations for the Molecular Species. Calculations of the ^{209}Bi EFG tensors on the nonperiodic, molecular systems were performed using Gaussian 03⁵¹ software. The basis sets and methods which are in best agreement with the experiment are discussed separately for each system. Little success was achieved with calculations of ^{209}Bi CS tensors on these species, and hence these results are not discussed at this time.

Both the RHF and B3LYP methods overestimate the values of C_Q for $\text{Bi}(\text{NO}_3)_3 \cdot 5\text{H}_2\text{O}$ (Table 3.4); however, the B3LYP method predicts a nonaxially symmetric tensor, in agreement with experiment. The discrepancy between the experimental and theoretically calculated C_Q may be due to longer range interactions which were not accounted for in the calculations, or possibly deficiencies in the Bi basis sets. The EFG tensor has an unusual orientation, with V_{22} oriented near the molecular pseudo-threefold axis, and the distinct component, V_{11} , pointing approximately in the direction of one of the bidentate ligands ($\angle(\text{N}-\text{Bi}-V_{11}) = 18.4^\circ$, Figure 3.5b).

As for $\text{Bi}(\text{NO}_3)_3 \cdot 5\text{H}_2\text{O}$, the calculations on $[\text{Bi}(\text{H}_2\text{O})_9](\text{OTf})_3$ using the B3LYP method with (333333/33333/333/3) and 6-31G* basis sets yield C_Q and η_Q values in good agreement with the experimental values, suggesting that the Bi basis set may indeed be suitable for such calculations, and/or that longer-range influences on the ^{209}Bi EFG tensor are less significant in this molecule.

Table 3.4. Comparison of the experimental and Gaussian ^{209}Bi EFG tensor parameters.^a

Method	Basis sets (Bi, other atoms) ^b	V_{11} /a.u.	V_{22} /a.u.	V_{33} /a.u.	$C_Q(^{209}\text{Bi})/\text{MHz}^c$	η_Q
$\text{Bi}(\text{NO}_3)_3 \cdot 5\text{H}_2\text{O}$						
Experimental	----	----	----	----	78.6(8)	0.66(2)
RHF	A, 6-31G*	-0.5317	-0.5654	1.0972	-95.4	0.03
RHF	B, 6-31G*	-0.5362	-0.5815	1.1178	-97.2	0.04
RHF	A, 6-311G**	-0.561	-0.5933	1.1544	-100.4	0.03
B3LYP	A, 6-31G*	-0.172	-0.9953	1.1674	-101.5	0.7
B3LYP	A, 6-311G**	-0.2088	-1.03	1.2388	-107.7	0.66
$[\text{Bi}(\text{H}_2\text{O})_9](\text{OTf})_3$						
Experimental	----	----	----	----	90(1)	0.01(1)
RHF	A, 6-31G*	0.3997	0.403	-0.8027	69.8	0
RHF	A, 6-311G**	0.3925	0.3955	-0.7881	68.5	0
B3LYP	A, 6-31G*	0.4692	0.4782	-0.9474	82.4	0
B3LYP	A, 6-311G**	0.4584	0.4664	-0.9248	80.4	0
$\text{Bi}(\text{CH}_3\text{CO}_2)_3$						
Experimental	----	----	----	----	256(10)	0.30(6)
RHF ^d	A, 6-31G*	-0.3146	-0.9511	1.2658	-110.0	0.5
RHF ^d	A, 6-311G**	-0.3959	-0.968	1.3639	-118.6	0.42
RHF ^e	A, 6-31G*	-1.269	-1.8692	3.1383	-272.8	0.19
RHF ^e	A, 6-311G**	-1.3431	-1.8929	3.2361	-281.3	0.17
B3LYP ^e	A, 6-31G*	-0.9307	-1.1102	2.041	-177.4	0.09
B3LYP ^e	A, 6-311G**	-0.992	-1.1195	2.1115	-183.6	0.06
RHF ^f	A, 6-31G*	-1.1677	-1.7945	2.9622	-257.5	0.21
RHF ^f	A, 6-311G**	-1.2365	-1.7755	3.012	-261.9	0.18
B3LYP ^f	A, 6-31G*	-0.8791	-1.1977	2.0768	-180.6	0.15
B3LYP ^f	A, 6-311G**	-0.9341	-1.1875	2.1217	-184.4	0.12

^aDefinitions of parameters are given in Table 3.2. ^bA and B denote the basis sets (333333/333333/333/3) and (432222/42222/422/4), respectively. ^cThe absolute values of the experimental C_Q 's are reported while the theoretical values are reported with the calculated signs. ^dCalculations conducted on a cluster consisting of a single bismuth atom and coordinated acetate ligands (Figure A.3.7a). ^eCalculations conducted on a cluster consisting of three bismuth atoms and nine acetate ligands (Figure A.3.7b). ^fCalculations conducted on a cluster consisting of seven bismuth atoms with eighteen acetate ligands (Figure A.3.7c).

V_{33} is the unique component of the EFG tensor and is oriented along the C_3 axis (Figure 3.5c), akin to the orientations of metal EFG tensors in $\text{Co}(\text{acac})_3$ and $\text{Al}(\text{acac})_3$.^{72,73} V_{11} and V_{22} are identical, as indicated by $\eta_Q = 0$.

For $\text{Bi}(\text{CH}_3\text{CO}_2)_3$, calculations performed on small clusters (i.e., structural units with one bismuth atom and coordinated acetate ligands, see Figure A.3.7) yield values of C_Q and η_Q that are in poor agreement with experiment. Since bismuth acetate has a polymeric structure,⁶⁰ a larger cluster consisting of three bismuth atoms and nine acetate ligands was used. For this larger cluster, the RHF calculations predict C_Q and η_Q values in good agreement with experiment, and further increasing the size of the structural unit to include seven bismuth atoms and eighteen acetate ligand produces even better agreement. These data are much better than those from similar B3LYP calculations; however, it is unclear why the RHF calculations are superior in this instance. The RHF calculation, performed on the largest structural unit with the RHF method and the (333333/333333/333/3) and 6-31G* basis sets (Table 3.4), predicts a nearly axially symmetric tensor, with the distinct V_{33} component oriented close to the shortest Bi–O bond ($\angle(V_{33}\text{-Bi-O}) = 159^\circ$) (Figure 3.5d).

3.4 Conclusions

This is the first detailed account of solid-state ^{209}Bi NMR spectroscopy of broad central and satellite transition powder patterns. Frequency-stepped techniques have been shown to be very useful for the acquisition of extremely broad ^{209}Bi NMR patterns. Acquisition of ^{209}Bi NMR spectra at 9.4 T is possible, but is predicted to become

increasingly inconvenient for the many systems with larger values of $C_Q(^{209}\text{Bi})$. However, acquisition of ^{209}Bi NMR spectra at 21.1 T is much more rapid and should enable the investigation of an enormous array of Bi-containing materials and compounds, providing both quadrupolar and chemical shift data. For extremely large C_Q 's, it is possible that ^{209}Bi SSNMR at 21.1 T or higher may be utilized to acquire UW "histogram" spectra⁷⁴ to provide rough estimates of quadrupolar parameters, thereby improving the efficiency of complementary ^{209}Bi NQR experiments, which can then be conducted to refine these parameters in very short time frames as we showed for the bismuth acetate sample.

The ^{209}Bi quadrupolar interaction dominates the shapes and breadths of the NMR patterns; however, extraction of the quadrupolar parameters is relatively straightforward, even in cases where there is overlap between the CT and STs. The quadrupolar parameters and (to a lesser degree) isotropic chemical shifts reflect the geometry, symmetry, and coordination environment of the bismuth atom. Theoretical calculations of the ^{209}Bi EFG and CS tensor parameters are in reasonably good agreement with the experimental values and will help in structural predictions for which crystallographic data are not available. Clearly, our work suggests that some further effort is required on the development of suitable basis sets for bismuth, as well as on the refinement of the value of $Q(^{209}\text{Bi})$. Finally, the ^{209}Bi EFG and CS tensor orientations within the atomic coordinate systems/molecular frames provide us with a starting point for the rationalization of the origin of these tensors and their correlations to molecular structure and symmetry. We hope that this work encourages future ^{209}Bi NMR and NQR studies on the ever expanding catalog of Bi-containing systems.

3.5 Bibliography

- (1) Mehring, M. *Coord. Chem. Rev.* **2007**, *251*, 974-1006.
- (2) Breunig, H. J. *Kirk-Othmer Ency. Chem. Tech. (5th Edition)* **2004**, *4*, 16-43.
- (3) Briand, G. G.; Burford, N. *Adv. Inorg. Chem.* **2000**, *50*, 285-357.
- (4) Stavila, V.; Davidovich, R. L.; Gulea, A.; Whitmire, K. H. *Coord. Chem. Rev.* **2006**, *250*, 2782-2810.
- (5) Briand, G. G.; Burford, N. *Chem. Rev.* **1999**, *99*, 2601-2657.
- (6) Sadler, P. J.; Li, H.; Sun, H. *Coord. Chem. Rev.* **1999**, *185-186*, 689-709.
- (7) Yang, N.; Sun, H. *Coord. Chem. Rev.* **2007**, *251*, 2354-2366.
- (8) Sun, H.; Sadler, P. J. *Top. Biol. Inorg. Chem.* **1999**, *2*, 159-185.
- (9) Hua, R. *Curr. Org. Synth.* **2008**, *5*, 1-27.
- (10) Kravchenko, E. A.; Orlov, V. G.; Shlykov, M. P. *Russ. Chem. Rev.* **2006**, *75*, 77-93.
- (11) Van der Kelen, G. P.; De Ketelaere, R. F. *J. Mol. Struct.* **1974**, *23*, 329-335.
- (12) Zemnukhova, L. A.; Kuznetsov, S. I.; Davidovich, R. L. *Russ. Chem. Bull.* **1998**, *47*, 2169-2172.
- (13) Bastow, T. J.; Whitfield, H. J. *J. Magn. Reson.* **1977**, *26*, 461-468.
- (14) Kravchenko, E. A.; Kargin, Y. F.; Egorysheva, A. V.; Buslaev, Y. A. *Russ. J. Coord. Chem.* **2001**, *27*, 542-547.
- (15) Swiger, E. D.; Green, P. J.; McKown, G. L.; Graybeal, J. D. *J. Phys. Chem.* **1965**, *69*, 949-952.
- (16) Buslaev, Y. A.; Kravchenko, E. A.; Pakhomov, V. I.; Skorikov, V. M.; Semin, G. K. *Chem. Phys. Lett.* **1969**, *3*, 455-456.
- (17) Kravchenko, E. A.; Morgunov, V. G.; Kargin, Y. F.; Egorysheva, A. V.; Orlov, V. G.; Shlikov, M. P. *Appl. Magn. Reson.* **2004**, *27*, 65-75.
- (18) Gopalakrishnan, K. V.; Gupta, L. C.; Vijayaraghavan, R. *Pramana* **1976**, *6*, 343-348.
- (19) Brill, T. B.; Long, G. G. *Inorg. Chem.* **1970**, *9*, 1980-1985.
- (20) Harris, R. K.; Becker, E. D.; Cabral De Menezes, S. M.; Goodfellow, R.; Granger,

- P. Pure Appl. Chem.* **2001**, *73*, 1795-1818.
- (21) Bieron, J.; Pyykko, P. *Phys. Rev. Lett.* **2001**, *87*, 133003/133001-133003/133004.
- (22) Dudnik, E. F.; Gene, V. V.; Mnushkina, I. E. *Izv Akad Nauk SSSR, Ser. Fizich* **1979**, *43*, 1723-1725.
- (23) Dupree, R.; Walstedt, R. E. *AIP Conf. Proc.* **1976**, *29*, 350-351.
- (24) Dupree, R.; Gardner, J. A. *J. Phys., Colloque* **1980**, 20-23.
- (25) Reyes, A. P.; Heffner, R. H.; Canfield, P. C.; Thompson, J. D.; Fisk, Z. *Phys. Rev. B* **1994**, *49*, 16321-16330.
- (26) Reyes, A. P.; Le, L. P.; Heffner, R. H.; Ahrens, E. T.; Fisk, Z.; Canfield, P. C. *Physica B* **1995**, *206 & 207*, 332-335.
- (27) Fukushima, E. *J. Chem. Phys.* **1971**, *55*, 2463-2466.
- (28) Flynn, C. P.; Seymour, E. F. W. *Proc. Phys. Soc. London* **1959**, *73*, 945-947.
- (29) Morgan, K.; Sayer, B. G.; Schrobilgen, G. J. *J. Magn. Reson.* **1983**, *52*, 139-142.
- (30) Lim, A. R.; Choh, S. H.; Jang, M. S. *J. Phys.: Condens. Matter* **1992**, *4*, 1607-1613.
- (31) Lim, A. R.; Choh, S. H.; Jang, M. S. *Solid State Commun.* **1996**, *97*, 699-702.
- (32) Lipton, A. S.; Wright, T. A.; Bowman, M. K.; Reger, D. L.; Ellis, P. D. *J. Am. Chem. Soc.* **2002**, *124*, 5850-5860.
- (33) Sparks, S. W.; Ellis, P. D. *J. Am. Chem. Soc.* **1986**, *108*, 3215-3218.
- (34) Medek, A.; Frydman, V.; Frydman, L. *J. Phys. Chem. A* **1999**, *103*, 4830-4835.
- (35) Massiot, D.; Farnan, I.; Gautier, N.; Trumeau, D.; Trokiner, A.; Coutures, J. P. *Solid State Nucl. Magn. Reson.* **1995**, *4*, 241-248.
- (36) Kennedy, M. A.; Vold, R. L.; Vold, R. R. *J. Magn. Reson.* **1991**, *92*, 320-331.
- (37) Bastow, T. J. *Z. Naturforsch., A: Phys. Sci.* **1994**, *49*, 320-328.
- (38) Bastow, T. J.; Smith, M. E. *Solid State Nucl. Magn. Reson.* **1992**, *1*, 165-174.
- (39) Tang, J. A.; Ellis, B. D.; Warren, T. H.; Hanna, J. V.; Macdonald, C. L. B.; Schurko, R. W. *J. Am. Chem. Soc.* **2007**, *129*, 13049-13065.
- (40) Larsen, F. H.; Jakobsen, H. J.; Ellis, P. D.; Nielsen, N. C. *J. Phys. Chem. A* **1997**, *101*, 8597-8606.
- (41) Tang, J. A.; Masuda, J. D.; Boyle, T. J.; Schurko, R. W. *ChemPhysChem* **2006**, *7*,

117-130.

- (42) Bhattacharyya, R.; Frydman, L. *J. Chem. Phys.* **2007**, *127*, 194503/194501-194503/194508.
- (43) O'Dell, L. A.; Schurko, R. W. *Chem. Phys. Lett.* **2008**, *464*, 97-102.
- (44) O'Dell, L. A.; Rossini, A. J.; Schurko, R. W. *Chem. Phys. Lett.* **2009**, *468*, 330-335.
- (45) Zhang, X.; Ai, Z.; Jia, F.; Zhang, L. *J. Phys. Chem. C* **2008**, *112*, 747-753.
- (46) Louer, M.; Le Roux, C.; Dubac, J. *Chem. Mat.* **1997**, *9*, 3012-3016.
- (47) Lipton, A. S.; Bergquist, C.; Parkin, G.; Ellis, P. D. *J. Am. Chem. Soc.* **2003**, *125*, 3768-3772.
- (48) Lipton, A. S.; Heck, R. W.; Sears, J. A.; Ellis, P. D. *J. Magn. Reson.* **2004**, *168*, 66-74.
- (49) Eichele, K.; Wasylishen, R. E.; WSolids NMR Simulation Package, 1.17.30 ed.; Dalhousie University: Halifax, CA, 2001.
- (50) Clark, S. J.; Segall, M. D.; Pickard, C. J.; Hasnip, P. J.; Probert, M. I. J.; Refson, K.; Payne, M. C. *Z. Kristallogr.* **2005**, *220*, 567-570.
- (51) Frisch, M. J.; Trucks, G. W.; Schlegel, H. B.; Scuseria, G. E.; Robb, M. A.; Cheeseman, J. R.; Montgomery, J. J. A.; Vreven, T.; Kudin, K. N.; Burant, J. C.; Millam, J. M.; Iyengar, S. S.; Tomasi, J.; Barone, V.; Mennucci, B.; Cossi, M.; Scalmani, G.; Rega, N.; Petersson, G. A.; Nakatsuji, H.; Hada, M.; Ehara, M.; Toyota, K.; Fukuda, R.; Hasegawa, J.; Ishida, M.; Nakajima, T.; Honda, Y.; Kitao, O.; Nakai, H.; Klene, M.; Li, X.; Knox, J. E.; Hratchian, H. P.; Cross, J. B.; Adamo, C.; Jaramillo, J.; Gomperts, R.; Stratmann, R. E.; Yazyev, O.; Austin, A. J.; Cammi, R.; Pomelli, C.; Ochterski, J. W.; Ayala, P. Y.; Morokuma, K.; Voth, G. A.; Salvador, P.; Dannenberg, J. J.; Zakrzewski, V. G.; Dapprich, S.; Daniels, A. D.; Strain, M. C.; Farkas, O.; Malick, D. K.; Rabuck, A. D.; Raghavachari, K.; Foresman, J. B.; Ortiz, J. V.; Cui, Q.; Baboul, A. G.; Clifford, S.; Cioslowski, J.; Stefanov, B. B.; Liu, G.; Liashenko, A.; Piskorz, P.; Komaromi, I.; Martin, R. L.; Fox, D. J.; Keith, T.; Al-Laham, M. A.; Peng, C. Y.; Nanayakkara, A.; Challacombe, M.; Gill, P. M. W.; Johnson, B.; Chen, H.; Wong, M. W.; Gonzalez, C.; Pople, J. A.; Rev. B.03 ed.; Gaussian, Inc.: Pittsburgh, 2003.

- (52) Profeta, M.; Mauri, F.; Pickard, C. J. *J. Am. Chem. Soc.* **2003**, *125*, 541-548.
- (53) Perdew, J. P.; Burke, K.; Ernzerhof, M. *Phys. Rev. Lett.* **1996**, *77*, 3865-3868.
- (54) Perdew, J. P.; Burke, K.; Ernzerhof, M. *Phys. Rev. Lett.* **1998**, *80*, 891.
- (55) Pickard, C. J.; Mauri, F. *Phys. Rev. B* **2001**, *63*, 245101/245101-245101/245113.
- (56) Yates, J. R.; Pickard, C. J.; Mauri, F. *Phys. Rev. B* **2007**, *76*, 024401/024401-024401/024411.
- (57) *Crystallography Open Database* (<http://www.crystallography.net/>).
- (58) Bannister, F. A. *Mineral. Mag. and J. Mineral. Soc.* **1935**, *24*, 49-58.
- (59) Bannister, F. A. *Nature* **1934**, *134*, 856-857.
- (60) Troyanov, S. I.; Pisarevskii, A. P. *Koord. Khim.* **1991**, *17*, 909-913.
- (61) Lazarini, F. *Acta Crystallogr., Sect. C: Cryst. Struct. Commun.* **1985**, *C41*, 1144-1145.
- (62) Frank, W.; Reiss, G. J.; Schneider, J. *Angew. Chem., Int. Ed. Engl.* **1995**, *34*, 2416-2417.
- (63) Huzinaga, S., Ed. *Gaussian Basis Sets for Molecular Calculations*; Elsevier: New York, 1984.
- (64) Dixon, K. R. In *Multinuclear NMR*; Mason, J., Ed.; Plenum Press: New York, 1987, p 369.
- (65) Man, P. P. In *Encyclopedia of Analytical Chemistry*; A., M. R., Ed.; J. Wiley: Chichester, 2000, pp 12224-12265.
- (66) Man, P. P. *J. Chem. Phys.* **1997**, *106*, 3908-3919.
- (67) Fedotov, M. A.; Yukhin, Y. M.; Shubin, A. A.; Udalova, T. A. *Zh. Neorg. Khim.* **1998**, *43*, 307-310.
- (68) Dixon, K. R. In *Multinuclear NMR*; Mason, J., Ed.; Plenum Press: New York, 1987, pp 60-61 & 369.
- (69) Raghavan, P. *At. Data Nucl. Data Tables* **1989**, *42*, 189-291.
- (70) Lee, W.; Chen, M. Y.; Cheng, S. C.; Macagno, E. R.; Rushton, A. M.; Wu, C. S. *Nucl. Phys. A* **1972**, *181*, 14-24.
- (71) Beetz, R.; De Boer, F. W. N.; Panman, J. K.; Konijn, J.; Pavlopoulos, P.; Tibell, G.;

Zioutas, K.; Bergstrom, I.; Fransson, K.; et al. *Z. Phys. A* **1978**, 286, 215-232.

(72) Schurko, R. W.; Wasylshen, R. E.; Foerster, H. *J. Phys. Chem. A* **1998**, 102, 9750-9760.

(73) Eichele, K.; Chan, J. C. C.; Wasylshen, R. E.; Britten, J. F. *J. Phys. Chem. A* **1997**, 101, 5423-5430.

(74) Bowers, G. M.; Kirkpatrick, R. J. *J. Magn. Reson.* **2007**, 188, 311-321.

Chapter 4

Solid-State ^{137}Ba NMR Spectroscopy: An Experimental and Theoretical Investigation of ^{137}Ba Electric Field Gradient Tensors and Their Relation to Structure and Symmetry

4.1 Introduction

The number of solid-state NMR (SSNMR) studies on quadrupolar nuclei continues to grow due to the development of new pulse sequences, improvements in NMR hardware and the ever-increasing availability of NMR spectrometers with ultrahigh magnetic fields. There is burgeoning interest in the characterization of structure and dynamics at the molecular/atomic level from the perspective of quadrupolar nuclei, since they account for approximately 73% of the NMR-active nuclei in the periodic table, and are present in innumerable materials. Many quadrupolar nuclei are difficult to study by routine NMR methods, since they may have large quadrupolar interactions which result in immense spectral breadths, presenting challenges for both uniform excitation and detection and acquisition of high signal-to-noise (S/N) NMR spectra. A variety of techniques have been developed for the rapid and efficient acquisition of quadrupolar-dominated powder patterns.¹⁻⁴ Recently, much work has been dedicated to the SSNMR spectroscopy of unreceptive quadrupolar nuclei (e.g., ^{79}Br , ^{127}I , ^{209}Bi , ^{115}In , ^{73}Ge , ^{14}N , ^{33}S , ^{87}Sr , ^{25}Mg , ^{43}Ca etc.),⁵⁻¹⁹ which are defined as nuclei which may have low gyromagnetic ratios, low natural abundances, broad anisotropic patterns, long relaxation times, or combinations of these characteristics. These studies have shown that such SSNMR spectra can provide rich structural information for a variety of materials; however,

numerous challenges exist in acquiring broad powder patterns of high quality for inherently unreceptive nuclei.

Barium has two NMR-active isotopes, ^{137}Ba and ^{135}Ba , both of which are classified as unreceptive. Both have nuclear spins of $3/2$, large nuclear electric quadrupole moments ($Q = 24.5$ and 16.0 fm^2 , respectively),²⁰ small gyromagnetic ratios (2.9930×10^7 and $2.6755 \times 10^7 \text{ rad T}^{-1} \text{ s}^{-1}$, respectively) and low natural abundances (11.3% and 6.6%, respectively).²⁰ The combination of these properties renders the routine acquisition of barium NMR spectra very difficult. Despite the fact that ^{135}Ba has a smaller quadrupole moment, ^{137}Ba NMR is more commonly applied due to its higher receptivity (i.e., with respect to carbon, $D^{\text{C}}(^{137}\text{Ba}) = 4.62$ and $D^{\text{C}}(^{135}\text{Ba}) = 1.93$). In spite of the inherent difficulties encountered in ^{137}Ba NMR experiments, the resulting spectra can be very useful for probing the chemical environments of different barium sites, and a significant amount of information on structure and dynamics at the molecular level can be obtained. In particular, the quadrupolar interaction which is manifested in the central transition ($+1/2 \leftrightarrow -1/2$) of ^{137}Ba SSNMR spectra is very diagnostic. The quadrupolar interaction results from coupling of the nuclear quadrupole moment to the electric field gradient (EFG) at the nuclear origin. The EFGs are described by a symmetric, traceless, second-rank (3×3) tensor with three principal components defined such that $|V_{33}| \geq |V_{22}| \geq |V_{11}|$. The nuclear quadrupolar coupling constant, $C_{\text{Q}} = eQV_{33}/h$, and the asymmetry parameter, $\eta_{\text{Q}} = (V_{11} - V_{22})/V_{33}$, are sensitive to both major and minor structural changes, providing information on the spherical and axial symmetry, respectively, of the ground state electronic environments at the Ba sites.

^{137}Ba SSNMR experiments could increase our understanding of the numerous barium-containing systems important in different applications such as glass manufacturing, well-drilling fluids, emulsification of liquids, NO storage and the development of ultrasonic and electronic devices.²¹⁻²⁴ Notably, ^{137}Ba SSNMR may be especially valuable for characterization of materials for which crystal structures are unavailable or unobtainable (i.e., disordered solids, sub-microcrystalline powders, etc.). However, of the relatively few ^{137}Ba SSNMR studies reported to date, most have focused on systems in which the barium sites exist in spherically symmetric environments, such as in BaO ,²⁵ BaTiO_3 ,²⁵⁻²⁸ BaZrO_3 ,²⁵ $\text{YBa}_2\text{Cu}_3\text{O}_y$ ^{29,30} and $\text{Ba}_x\text{Sr}_{1-x}\text{TiO}_3$ ($0 \leq x \leq 1$),³¹ which have small quadrupolar interactions and correspondingly narrow patterns.²⁵⁻²⁷ MacKenzie et al. reported the ^{137}Ba NMR spectra of several barium-containing systems acquired under conditions of magic-angle spinning (MAS),³² which were challenging to acquire due to the wide powder pattern breadths. Recently, Sutrisno et al. demonstrated the utility of $^{137/135}\text{Ba}$ SSNMR experiments in probing the barium environment in β -barium borate.³³

The problems associated with acquiring high S/N ^{137}Ba SSNMR spectra can be solved in part by the use of ultrahigh magnetic field strength spectrometers (i.e., 21.1 T) and/or the use of specialized SSNMR techniques such as the quadrupolar Carr-Purcell Meiboom-Gill (QCPMG) pulse sequence,³⁴ and the recently reported Wideband Uniform Rate Smooth Truncation (WURST)-QCPMG sequence.³⁵⁻³⁷ In addition, high S/N ultra-wideline (UW) NMR spectra (i.e., ranging from 300 kHz to several MHz in breadth) can be rapidly acquired using stepwise (or piecewise) methods.^{34,35,37-39} Individual sub-spectra

with limited excitation bandwidths are acquired by stepping the transmitter frequency in even increments at a constant field strength, and then co-added or projected to obtain the total UWNMR pattern. The acquisition of such spectra can be very time consuming, and this is further exacerbated for nuclei like ^{137}Ba , which has both a low natural abundance and low gyromagnetic ratio. However, the combination of the WURST-QCPMG pulse sequence and piecewise acquisitions at ultrahigh magnetic fields should enable the acquisition of high quality spectra.

In this work, we present the first systematic ^{137}Ba SSNMR study of a series of barium-containing species using a combination of frequency-stepped NMR techniques and the WURST-QCPMG pulse sequence. The ^{137}Ba NMR spectra of six barium-containing compounds, including barium nitrate, barium carbonate, barium chlorate monohydrate, barium chloride, barium chloride dihydrate and barium hydrogen phosphate, have been acquired at two different field strengths (9.4 T and 21.1 T), and anisotropic quadrupolar and chemical shift tensor parameters obtained via spectral analysis are presented. In addition, experimental data are complemented by a series of theoretical ^{137}Ba EFG tensors, calculated using plane-wave CASTEP methods,⁴⁰ in order to draw correlations between the experimental NMR parameters, the calculated NMR tensors and the local Ba environments.

4.2 Experimental Details

Samples of barium nitrate ($\text{Ba}(\text{NO}_3)_2$), barium carbonate (BaCO_3), barium chlorate monohydrate ($\text{Ba}(\text{ClO}_3)_2 \cdot \text{H}_2\text{O}$), barium chloride dihydrate ($\text{BaCl}_2 \cdot 2\text{H}_2\text{O}$), anhydrous

barium chloride (BaCl_2) and barium hydrogen phosphate (BaHPO_4), were purchased from Sigma-Aldrich and their identities were confirmed using powder X-ray diffraction (XRD) (Figures B.4.1- B.4.6, Appendix B). Powder X-ray diffraction data were collected on a Bruker Apex 2 Kappa diffractometer at room temperature, using graphite monochromatized Mo $K\alpha$ radiation ($\lambda = 0.71073 \text{ \AA}$).

4.2.1 Solid-State NMR.

^{137}Ba SSNMR experiments were performed on a Varian Infinity Plus spectrometer at the University of Windsor equipped with a 9.4 T ($\nu_0(^1\text{H}) = 399.73 \text{ MHz}$) Oxford wide-bore magnet ($\nu_0(^{137}\text{Ba}) = 44.422 \text{ MHz}$) and a 21.1 T ($\nu_0(^1\text{H}) = 900.08 \text{ MHz}$) Bruker Avance II spectrometer ($\nu_0(^{137}\text{Ba}) = 100.02 \text{ MHz}$) at the National Ultrahigh-Field NMR Facility for Solids in Ottawa, Canada. In most cases, the NMR powder patterns were much wider than the excitation bandwidth achievable with a standard high power rectangular pulse; hence, spectra were acquired by stepping the transmitter frequency across the entire central transition (CT) powder pattern in even increments, collecting the individual sub-spectra, and co-adding them to form the total pattern^{41,42} (see Tables B.4.1, B.4.2 in Appendix B for full experimental details). Barium chemical shifts were referenced to a 1 M aqueous solution of BaCl_2 ($\delta_{\text{iso}} = 0.0 \text{ ppm}$).³² Analytical simulations of ^{137}Ba NMR spectra were performed using WSolids.⁴³ The uncertainties in the NMR tensor parameters were determined by visual comparison of the experimental and simulated spectra, and bidirectional variation of single parameters from their values corresponding to the best fit.

Experiments at 9.4 T. Samples were finely ground and packed into either 5 mm o.d. zirconium oxide MAS rotors or 5 mm glass NMR tubes. ^{137}Ba NMR spectra were acquired using either a Varian 5 mm double-resonance (HX) static probe or a Varian 5 mm triple-resonance (HXY) MAS probe. All spectra were collected using the WURST-QCPMG pulse sequence.^{35,37} WURST-80 pulse shapes⁴⁴ were used with a 50 μs WURST pulse length, and swept at a rate of 10 or 40 MHz/ms with an offset of either 250 or 1000 kHz and an rf power of 28 kHz. The number of echoes ranged between 40 and 160, depending on the transverse relaxation characteristics of ^{137}Ba in each sample. A spectral width of either 500 or 800 kHz and an optimized recycle delay of 0.1 s were used. The frequency step size was set between 100 and 200 kHz, in order to ensure uniform excitation. Further experimental details are given in Table B.4.1. High-power proton decoupling was tested for all proton-containing samples ($\nu(^1\text{H}) = 35$ kHz); the only differences were observed for barium chloride dihydrate (vide infra).

Experiments at 21.1 T. Samples were ground and packed into 7 mm o.d. zirconium oxide rotors. ^{137}Ba NMR spectra were acquired with a 7 mm static probe using the frequency-stepped techniques outlined above, with a solid-echo pulse sequence of the form $(\pi/2)_x-\tau_1-(\pi/2)_y-\tau_2\text{-acq}$, where the τ_1 and τ_2 represent interpulse delays. Experiments were conducted with a selective $\pi/2$ pulse width of 4 μs ($\nu_1 = 31$ kHz), spectral widths between 250 kHz and 1 MHz, calibrated recycle delays between 0.2 s and 0.5 s and transmitter frequency offsets of 100 kHz. Further experimental details are given in Table B.4.2. In the case of the barium hydrogen phosphate sample, the ^{137}Ba NMR spectrum was collected using the WURST-QCPMG pulse sequence.^{35,37} WURST-80

pulse shapes⁴⁴ with a 50 μ s WURST pulse length, swept at a rate of 20 MHz/ms, a sweep width of 1000 kHz and rf power of 6 kHz were used. The number of echoes was set to 96. A spectral width of 1000 kHz and recycle delay of 0.2 s were used.

4.2.2 Computational methods.

¹³⁷Ba EFG and CS tensor parameters were calculated for all structures. Ab initio plane-wave density functional theory (DFT) calculations were performed using the CASTEP NMR program^{40,45} in the Materials Studio 4.3 environment on a HP xw4400 workstation with a single Intel Dual-Core 2.67 GHz processor and 8 GB DDR RAM. Ultrasoft pseudopotentials were used for ¹³⁷Ba EFG calculations with a plane wave basis set cut-off of 550 eV in a fine accuracy basis set with the Monkhorst-Pack *k*-space grid sizes of 4×4×4, 5×3×4, 3×3×3, 4×2×4, 3×3×5, 4×1×1 for barium nitrate, barium carbonate, barium chlorate monohydrate, barium chloride dihydrate, anhydrous barium chloride and barium hydrogen phosphate, respectively. The Perdew, Burke and Ernzerhof (PBE) functionals were used in the generalized gradient approximation (GGA) for the exchange-correlation energy.^{46,47} The magnetic shielding tensors for ¹³⁷Ba were calculated in a fine accuracy basis set using the projector augmented-wave method (GIPAW) implemented in the CASTEP code.^{48,49} Relativistic effects are included in CASTEP calculations at the level of the scalar-relativistic zeroth-order regular approximation (ZORA).⁵⁰ The chemical shifts were calculated using $\delta_{\text{iso}}(\text{sample}) - \delta_{\text{iso}}(\text{ref}) = \sigma_{\text{iso}}(\text{ref}) - \sigma_{\text{iso}}(\text{sample})$ where $\delta_{\text{iso}}(\text{ref})$ and $\sigma_{\text{iso}}(\text{ref})$ are the ¹³⁷Ba experimental chemical shift (279 ppm)³² and the calculated chemical shielding (5262.28 ppm) of

BaZrO₃, respectively. The CIF crystal structure files used in the calculations were obtained from the literature.⁵¹⁻⁵⁸ Proton positions were geometry optimized only in the case of barium hydrogen phosphate, since the structures utilized in the calculations for barium chloride dihydrate and barium chlorate monohydrate were determined from neutron diffraction experiments.⁵⁶

4.3 Results and Discussion

4.3.1 Solid-State ¹³⁷Ba NMR. In this section, we discuss the ¹³⁷Ba SSNMR data for a series of systems in which the Ba atoms are in distinct coordination environments. The NMR spectra were acquired at two different magnetic field strengths to enable accurate deconvolution of the contributions of the second-order quadrupolar interaction and the barium chemical shift anisotropy (CSA). The experimentally measured C_Q 's range from 7.0 to 28.8 MHz (Table 4.1), with central transition powder pattern breadths ranging from 145 kHz to 4.0 MHz at 9.4 T.

Barium Nitrate. Using the WURST-QCPMG pulse sequence,³⁷ the NMR pattern of barium nitrate was acquired very rapidly in a single experiment (11 minutes at 9.4 T with a breadth of 145 kHz, Figure 4.1). Analytical simulation of the spectrum reveals a single barium site, which is consistent with the known crystal structures.^{51,52,58} The C_Q is 7.0 MHz, in agreement with that measured by Weiden and Weiss from a ¹³⁷Ba single-crystal NMR experiment.⁵⁹ This value is the smallest among the samples discussed herein (Table 4.1), likely due to the high spherical symmetry around the barium atom resulting from coordination to the twelve oxygen atoms of the nitrate groups arranged in a

distorted cuboctahedron (Scheme 4.1a).^{52,58} The η_Q is 0, indicating the axially symmetric electronic environment at the barium site (the V_{33} component of the EFG tensor is the unique component and is therefore positioned along the threefold rotational axis of the molecule).

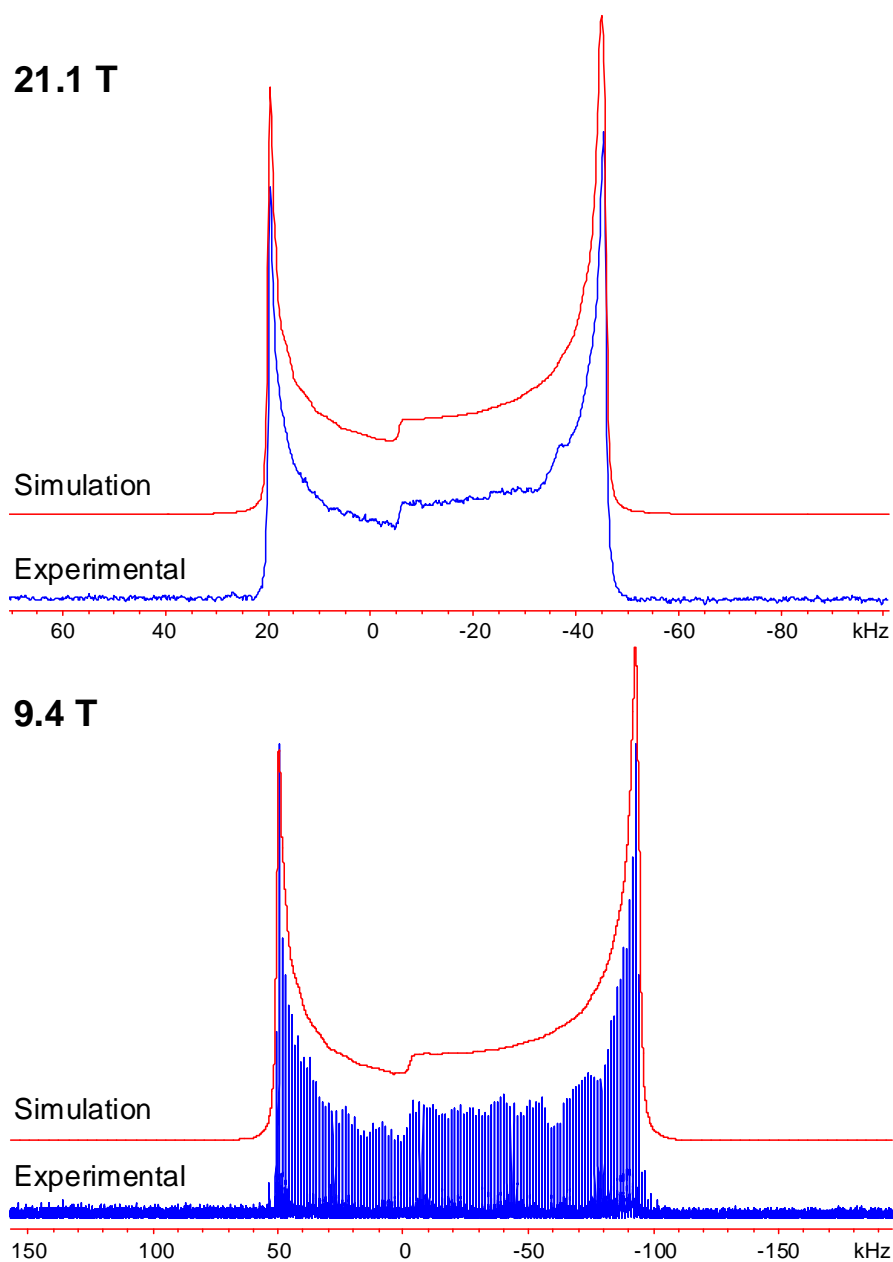


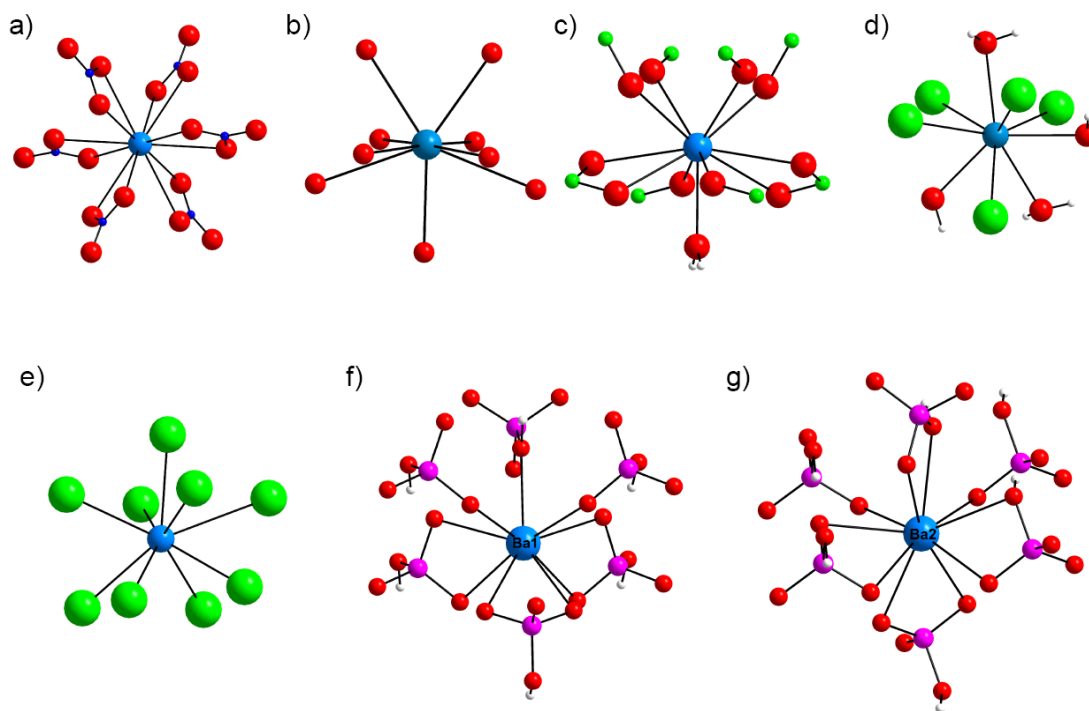
Figure 4.1 ^{137}Ba static SSNMR spectra of barium nitrate at two different magnetic field strengths.

Table 4.1. Summary of the experimental ^{137}Ba NMR parameters.

	$ C_Q(^{137}\text{Ba}) $ /MHz ^a	η_Q^b	$\delta_{\text{iso}}/\text{ppm}^c$	Ω/ppm^d	κ^e	α/deg^f	β/deg	γ/deg
Ba(NO ₃) ₂	7.0(1)	0.01(1)	-42(8)	25(20)	0.8(2)	40(20)	10(25)	----
BaCO ₃	17.4(6)	0.33(4)	50(200)	150(150)	0.5(5)	----	----	----
Ba(ClO ₃) ₂ ·H ₂ O	25.4(6)	0.48(4)	0(200)	200(100)	-0.8(2)	----	----	----
BaCl ₂ ·2H ₂ O	28.8(3)	0.94(2)	150(100)	150(150)	-0.5(5)	----	----	----
BaCl ₂	28.7(3)	0.81(2)	200(200)	400(300)	0.5(5)	----	----	----
BaHPO ₄ site1	15.5(1.0)	0.85(4)	-120(60)	----	----	----	----	----
BaHPO ₄ site 2	22.5(1.0)	0.82(4)	0(200)	----	----	----	----	----

^a $C_Q = eQV_{33}/h$; ^b $\eta_Q = (V_{11} - V_{22})/V_{33}$; ^c $\delta_{\text{iso}} = (\delta_{11} + \delta_{22} + \delta_{33})/3$; ^d $\Omega = \delta_{11} - \delta_{33}$; ^e $\kappa = 3(\delta_{22} - \delta_{\text{iso}})/\Omega$.

^f Conventions for the Euler angles are described in the WSolids software package



Scheme 4.1. The coordination environments of the barium atoms in a) barium nitrate, b) barium carbonate, c) barium chlorate monohydrate, d) barium chloride dihydrate, e) anhydrous barium chloride, f) barium hydrogen phosphate, site 1 and g) barium hydrogen phosphate, site2

This agrees with the earlier assumptions of Weiden and Weiss, who assigned (but did not measure) an η_Q of 0 due to the molecular symmetry. The high field spectrum allows for the measurement of the barium CSA parameters (Figures 4.1 & B.4.7); however, the span

(Ω) of the CS tensor is rather small, and represents a contribution of only 4 % of the total breadth of the CT pattern. This indicates that accurate measurement of barium CS tensor parameters will be more challenging for complexes with larger values of C_Q , where the CT patterns are dominated by second-order quadrupolar contributions.

Barium Carbonate. A static ^{137}Ba SSNMR spectrum of barium carbonate was previously obtained by Bastow, who reported an extremely long acquisition time (21 days at 9.4 T using the stepwise echo technique),⁶⁰ in spite of the large sample size that was used (i.e., in a 10 mm transverse coil). Our spectrum was obtained by collecting fifteen and seven sub-spectra at 9.4 T and 21.1 T, respectively (total experimental times were only 6.8 hours and 2.4 hours for the whole patterns at 9.4 T and 21.1 T, Figure 4.2). Simulations of both high- and low-field spectra reveal NMR parameters identical to those obtained by Bastow. The C_Q is much larger than that of the nitrate sample, since the nine coordinating oxygen atoms (Scheme 4.1b) are positioned such that there is great variation in the Ba-O distances, and give rise to a non-spherically symmetric environment about the Ba centre.⁵³ In addition, the Ba-O distances are shorter in the carbonate than in the nitrate, which may also augment the magnitude of C_Q . The value of η_Q indicates that V_{33} is the distinct component of the EFG tensor and should be oriented either along/within or perpendicular to a molecular symmetry element (there is a single mirror plane in this unit, which must also contain one of V_{11} or V_{22}). The slightly different values of V_{11} and V_{22} (and non-zero η_Q) correspond to the absence of a threefold (or higher) rotational symmetry axis. The barium CSA contribution is very small and its effect on the NMR spectra at both fields is negligible. This is confirmed by the ratio of the CT pattern

breadths at 9.4 T and 21.1 T, which is ca. 2.1:1.0; since the CT pattern breadths scale as the inverse of the external magnetic field, it is clear that the second order quadrupolar interaction is dominant.

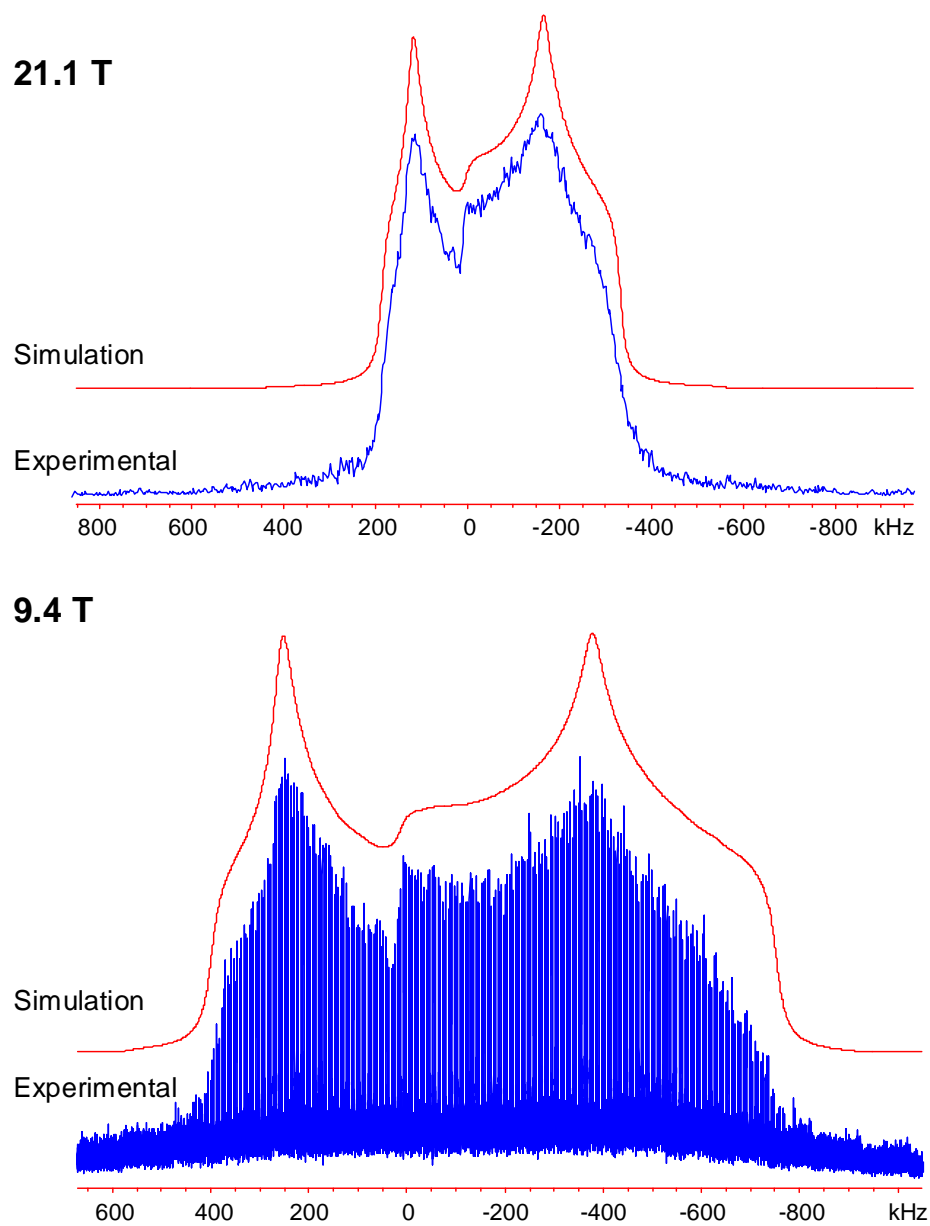


Figure 4.2. ^{137}Ba static SSNMR spectra of barium carbonate at two different magnetic field strengths.

It is also interesting to note that the shapes of the CT powder patterns indicate some degree of disorder in the sample (the same phenomenon is observed in the spectrum reported by Bastow), since they do not have the typical sharp discontinuities associated with highly crystalline samples. This is not surprising, since carbonates are known to readily absorb water from the air. The presence of water in the sample was confirmed via ^1H MAS NMR experiments (Figures B.4.8, B.4.9).

Barium Chlorate Monohydrate. The ^{137}Ba quadrupolar parameters of barium chlorate monohydrate were obtained by Nakamura and Enokiya from the Zeeman splittings of ^{135}Ba and ^{137}Ba nuclei in a single crystal by using the proton signal enhancement caused by the frequency crossing of $\nu_{\text{NQR}}(^{135}\text{Ba}$ or $^{137}\text{Ba})$ with $\nu_0(^1\text{H})$; a directly excited NQR signal was not observed.⁶¹ The low natural abundances of $^{135/137}\text{Ba}$ make these types of NQR experiments challenging, and as a result, large sample sizes (i.e., on the order of 5 to 30 g) are traditionally utilized,^{61,62} rendering these experiments impractical for cases in which sample sizes are limited.

We were able to obtain the ^{137}Ba SSNMR spectra at two different magnetic fields. The spectrum acquired at 9.4 T shows overlap between ^{137}Ba and $^{35}\text{Cl}/^{37}\text{Cl}$ powder patterns ($\nu_0(^{35/37}\text{Cl}) = 39.260$ and 32.680 MHz, Figure 4.3). The ^{35}Cl EFG parameters were previously measured by NQR spectroscopy ($C_Q = 58.687$ MHz and $\eta_Q = 0.027$).⁶³⁻⁶⁵ Using these parameters, analytical simulations reveal that the ^{35}Cl and ^{37}Cl NMR pattern breadths exceed 30 MHz, and result in the observed overlap; unfortunately, it is very difficult to obtain a precise fit of the overlapping patterns (Figure B.4.10). Due to the much higher natural abundance of chlorine (n.a. = 75.5% and 24.5% for ^{35}Cl and ^{37}Cl ,

respectively), as well as the difference in T_2 characteristics between ^{137}Ba and $^{35/37}\text{Cl}$, the ^{137}Ba signal in the low frequency side of the pattern is obstructed by the $^{35/37}\text{Cl}$ signals.

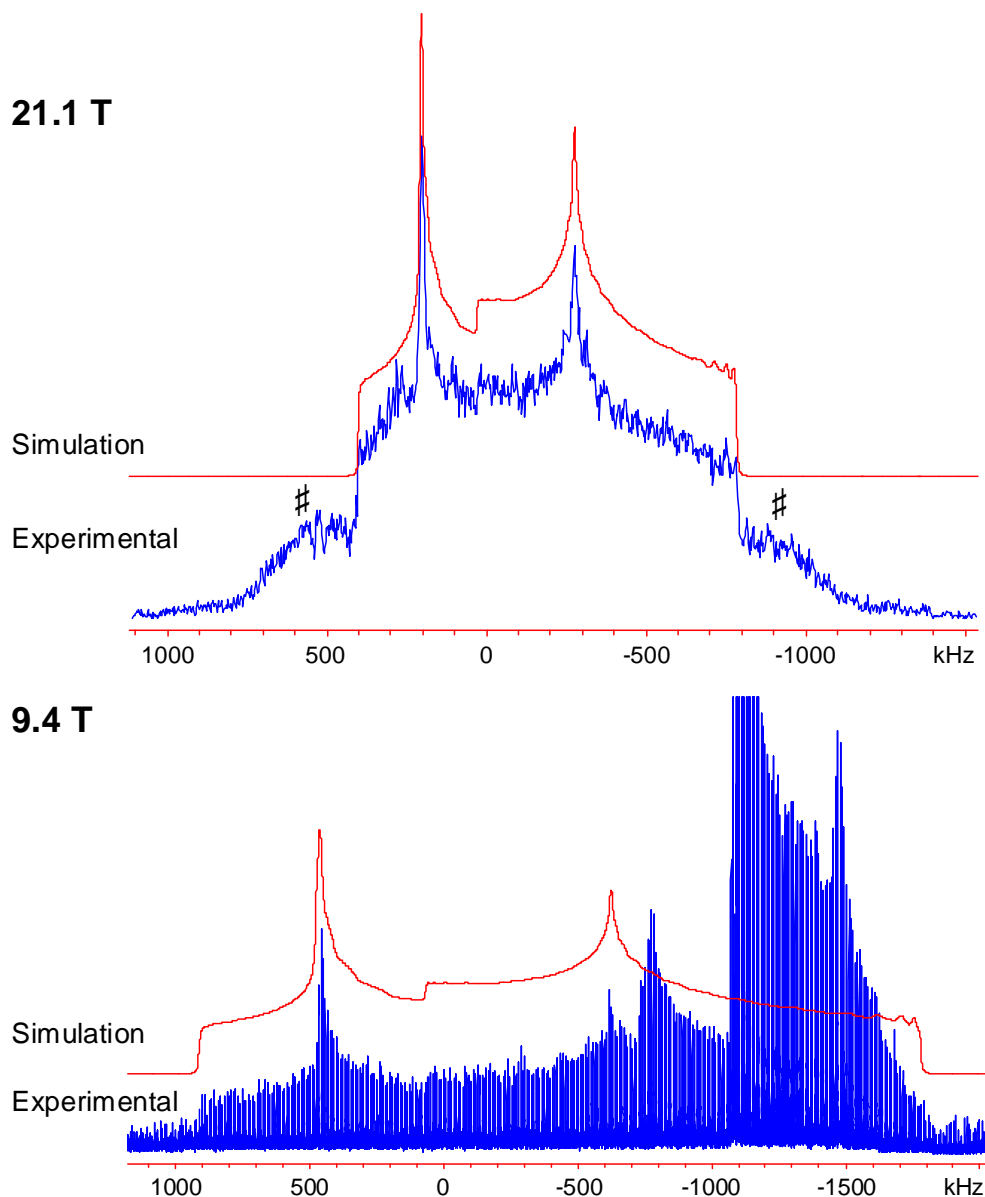


Figure 4.3. ^{137}Ba static SSNMR spectra of barium chlorate monohydrate at two different magnetic field strengths. Overlap between the ^{35}Cl CT and ^{37}Cl satellite transition (ST) with the ^{137}Ba spectrum is observed at 9.4 T. #: denote portions of the ^{137}Ba STs. The small distortions in the right-most “shoulders” of each simulated spectrum are artefacts arising from a limited number of angles in the total powder average.

However, the ^{137}Ba NMR spectrum acquired at 21.1 T displays no such overlap, since the ^{137}Ba and ^{35}Cl Larmor frequencies are further apart $\nu_0(^{35/37}\text{Cl}) = 88.125$ and 73.356 MHz, and the CT pattern breadths scale as the inverse of B_0 (though traces of interference from the ^{137}Ba satellite transitions are observed). The barium ion in this site is surrounded by one water oxygen and ten other oxygen atoms from different chlorate groups.⁵⁴ The larger C_Q compared to that of the previous two samples is due to further reduction of spherical symmetry at the barium site. The shortest Ba-O bond of 2.731 \AA is to the lone water molecule in the arrangement of eleven oxygen atoms (the other ten Ba-O distances range from 2.790 to 3.004 \AA). The $\eta_Q = 0.48$ indicates that V_{33} is the distinct component of the EFG tensor, which is likely oriented along the twofold rotational axis of molecule, which includes the lone Ba-OH₂ bond (Scheme 1c).⁵⁴

Dihydrate and Anhydrous Forms of Barium Chloride. The ^{137}Ba quadrupolar parameters of barium chloride dihydrate were previously obtained from NQR experiments on single crystal⁶⁶ and polycrystalline samples.⁶⁷ In the former case, the extraction of the quadrupolar parameters was complicated by crystal twinning, while in the latter case, a very large amount of crystalline sample was used (i.e., 25 g) in order to obtain the signal (again, this can be inconvenient and impractical in many situations where sample sizes are limited). In contrast, our ^{137}Ba SSNMR spectra were obtained at 9.4 T and 21.1 T using a small amount of a powdered sample (i.e., 0.2 g). Simulations of the spectra (Figure 4.4) reveal a single barium site, in agreement with the crystal structure.⁵⁶ The C_Q value is similar to that obtained from NQR; however, the η_Q value of $0.78(14)$ is different.^{66,67} The η_Q value obtained from our NMR experiments is likely

more accurate, since the previously reported η_Q value was estimated from calculations and quadrupolar parameters of analogous systems, and not directly measured in the NQR experiments (NQR experiments on spin-3/2 nuclei do not readily permit determination of η_Q ,⁶⁸ unless special techniques are applied).^{69,70} The barium atom is coordinated to four oxygen and five chlorine atoms (Scheme 4.1d), with Ba-O bond distances varying from 2.844 to 2.887 Å, and Ba-Cl distances varying from 3.131 to 3.340 Å.⁵⁶ The chlorine and oxygen atoms are arranged such that no simple geometrical assignments of shape can be made; in fact, the arrangement of atoms has been described “approximately as a square antiprism with one square face enlarged to accommodate the fifth Cl⁻ ion.”⁵⁶ The complete absence of spherical/platonic symmetry, coupled with the different Ba-O and Ba-Cl distances and distinct electronic characteristics of the Cl and O atoms give rise to the largest C_Q observed in this series. Since the η_Q is close to 1.0, it is known that V_{11} is the distinct component, and V_{22} and V_{33} are very similar in magnitude. However, due to the absence of any symmetry elements, it is difficult to make any postulations regarding the orientation of the EFG tensor components.

The ¹³⁷Ba SSNMR spectra of the anhydrous form at both fields (Figure 4.4) indicate a single barium site, consistent with the crystal structure.⁵⁵ Simulations of these spectra reveal NMR parameters similar to those of the dihydrate sample. The barium atom in this case has a ninefold coordination to chlorine atoms forming a three-face centred trigonal prism (Scheme 1e), and the Ba-Cl bond distances vary from 3.063 to 3.544 Å.⁵⁵ Due to the difference between the barium chemical environments in the anhydrous and dihydrate samples and the much larger Ba-Cl distances in the former, it is

difficult to qualitatively rationalize the similarity of the C_Q values (though certainly, the aspherical environment yields a large C_Q). Again, the η_Q value of the anhydrous form indicates that V_{11} is the distinct component; however, in this case, the V_{11} must be oriented perpendicular to the mirror plane since $V_{22} \approx V_{33}$.

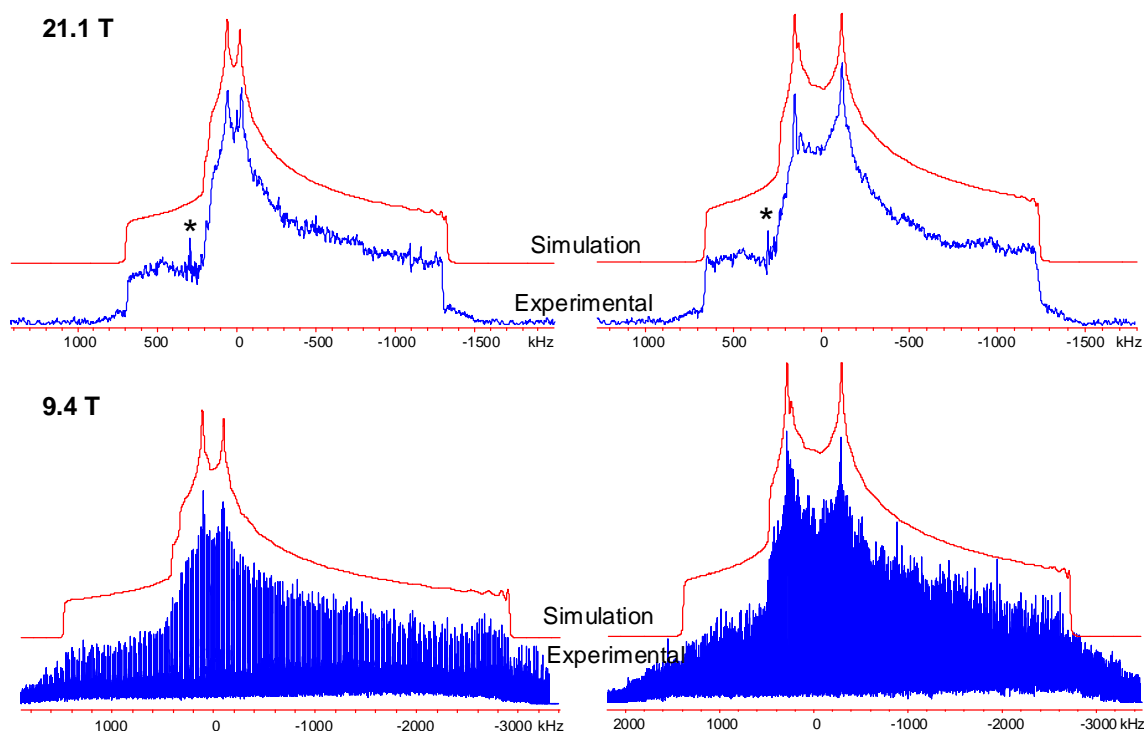


Figure 4.4. ^{137}Ba static SSNMR spectra of barium chloride dihydrate (left) and anhydrous barium chloride (right) at two different magnetic field strengths. *: indicates interferences from an FM radio frequency.

It would be very difficult to differentiate the Ba sites in the anhydrous and dihydrate forms based on the values of C_Q and η_Q alone. However, there is a large difference in their transverse relaxation times, $T_2(^{137}\text{Ba})$, which are measured from the QCPMG echo trains. The T_2 is much longer in the anhydrous form (13.2 ± 5.2 ms) than in the dihydrate (3.1 ± 2.0 ms). This difference arises from the presence of dipolar

couplings between water protons and ^{137}Ba nuclei in the dihydrate sample, which serve to increase the efficiency of transverse relaxation; this was confirmed by applying ^1H decoupling during acquisition, which helps to reduce the dipolar contribution to the overall transverse relaxation ($T_2 = 9.6 \pm 5.7$ ms). In principle, one could differentiate these sites in a mixed sample by acquiring QCPMG echo trains of varying lengths.

Barium Hydrogen Phosphate. The acquisitions of the ^{137}Ba SSNMR spectra of barium hydrogen phosphate were more challenging than those of the previous systems, due to the presence of two overlapping powder patterns (Figure 4.5) resulting from two crystallographically distinct barium sites, as well as substantially reduced transverse relaxation times (and correspondingly shorter CPMG trains). We were unable to obtain a full, high S/N powder pattern at 9.4 T; however, a high quality spectrum was acquired at 21.1 T using the WURST-QCPMG pulse sequence. The two sites have very different NMR parameters which reflect the difference in their coordination environments⁵⁷ and demonstrate the sensitivity of the ^{137}Ba NMR to the structural differences. The two barium sites are ninefold (Ba1) and tenfold (Ba2) (Scheme 4.1f, g) coordinated by oxygen atoms, and are assigned to the smaller and larger C_Q values, respectively, on the basis of the higher spherical symmetry of the former (see computational section below for further discussion). The high η_Q values indicate the V_{11} is the distinct component of the EFG tensor in both cases (vide infra).

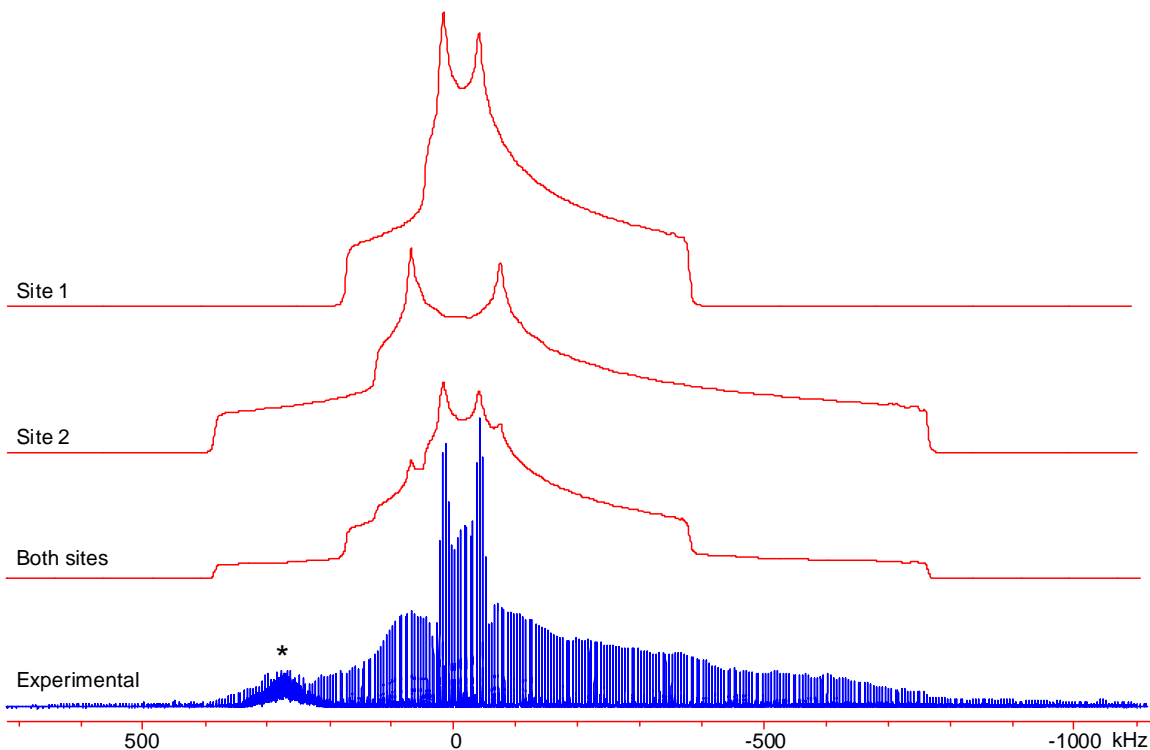


Figure 4.5. ^{137}Ba static SSNMR spectrum of barium hydrogen phosphate and its simulation at 21.1 T. *: indicates interferences from an FM radio frequency.

4.3.2 Theoretical calculations of ^{137}Ba EFG and CS tensors.

Ab initio calculations were performed in order to correlate the ^{137}Ba EFG tensors to the solid-state structure at the barium sites. The development of such correlations is crucial for future applications of ^{137}Ba SSNMR spectroscopy and associated structural interpretations for many barium-containing systems which are disordered or do not have known crystal structures. Due the periodic nature of the systems herein, CASTEP software was used for the calculations of the NMR parameters (see computational methods for details). The results of all of these calculations are compared to the experimental values in Tables 4.2 and B.4.3.

Table 4.2. Comparison of the experimental and CASTEP-calculated ^{137}Ba EFG tensor parameters

	V_{11} (au)	V_{22} (au)	V_{33} (au)	$C_Q(^{137}\text{Ba})/\text{MHz}^a$	η_Q
Ba(NO ₃) ₂ Exp.	----	----	----	7.0(1)	0.01(1)
Ba(NO ₃) ₂ Cal.	0.0464	0.0464	-0.0927	-5.3	0.00
BaCO ₃ Exp.	----	----	----	17.4(6)	0.33(4)
BaCO ₃ Cal.	-0.1241	-0.1385	0.2626	15.1	0.06
Ba(ClO ₃) ₂ ·H ₂ O Exp.	----	----	----	25.4(6)	0.48(4)
Ba(ClO ₃) ₂ ·H ₂ O Cal.	0.0629	0.3868	-0.4497	-25.9	0.72
BaCl ₂ ·2H ₂ O Exp.	----	----	----	28.8(3)	0.94(2)
BaCl ₂ ·2H ₂ O Cal.	0.0077	0.5490	-0.5567	-32.0	0.97
BaCl ₂ Exp.	----	----	----	28.7(3)	0.81(2)
BaCl ₂ Cal.	0.0301	0.4688	-0.4989	-28.7	0.88
BaHPO ₄ , site 1 Exp.	----	----	----	15.5(1.0)	0.85(4)
BaHPO ₄ , site1 Cal.	0.0123	0.2625	-0.2748	-15.8	0.91
BaHPO ₄ , site 2 Exp.	----	----	----	22.5(1.0)	0.82(4)
BaHPO ₄ , site 2 Cal.	0.0882	0.3411	-0.4293	-24.7	0.59

^a The signs of experimental C_Q values are unknown; signs of theoretically calculated values of C_Q are determined from calculations.

Plotting the experimental C_Q 's versus the calculated values provides an excellent linear correlation (Figure 4.6a); however, this correlation is only satisfactory for the η_Q values (see Figure 4.6b and discussion below). Since the anisotropic chemical shift parameters have a minimal influence on the ^{137}Ba CT NMR spectra, it is difficult to make accurate comparisons of these data and the theoretically calculated magnetic shielding tensors; hence, the barium CS tensor parameters is not discussed in detail herein (some preliminary data is summarized in Table B.4.3).

CASTEP calculations were performed on the three different structures of barium nitrate reported in the literature.^{51,52,58} The best agreement with experiment is obtained from calculations utilizing coordinates based on the most recently reported structure by Trounov et al. (Tables 4.2 and B.4.4). While all calculations predict axially symmetric EFG tensors ($\eta_Q = 0$), theoretically calculated values of C_Q vary with subtle changes in

molecular structure, demonstrating that even small displacements in O positions can lead to significant changes in the magnitude of V_{33} .

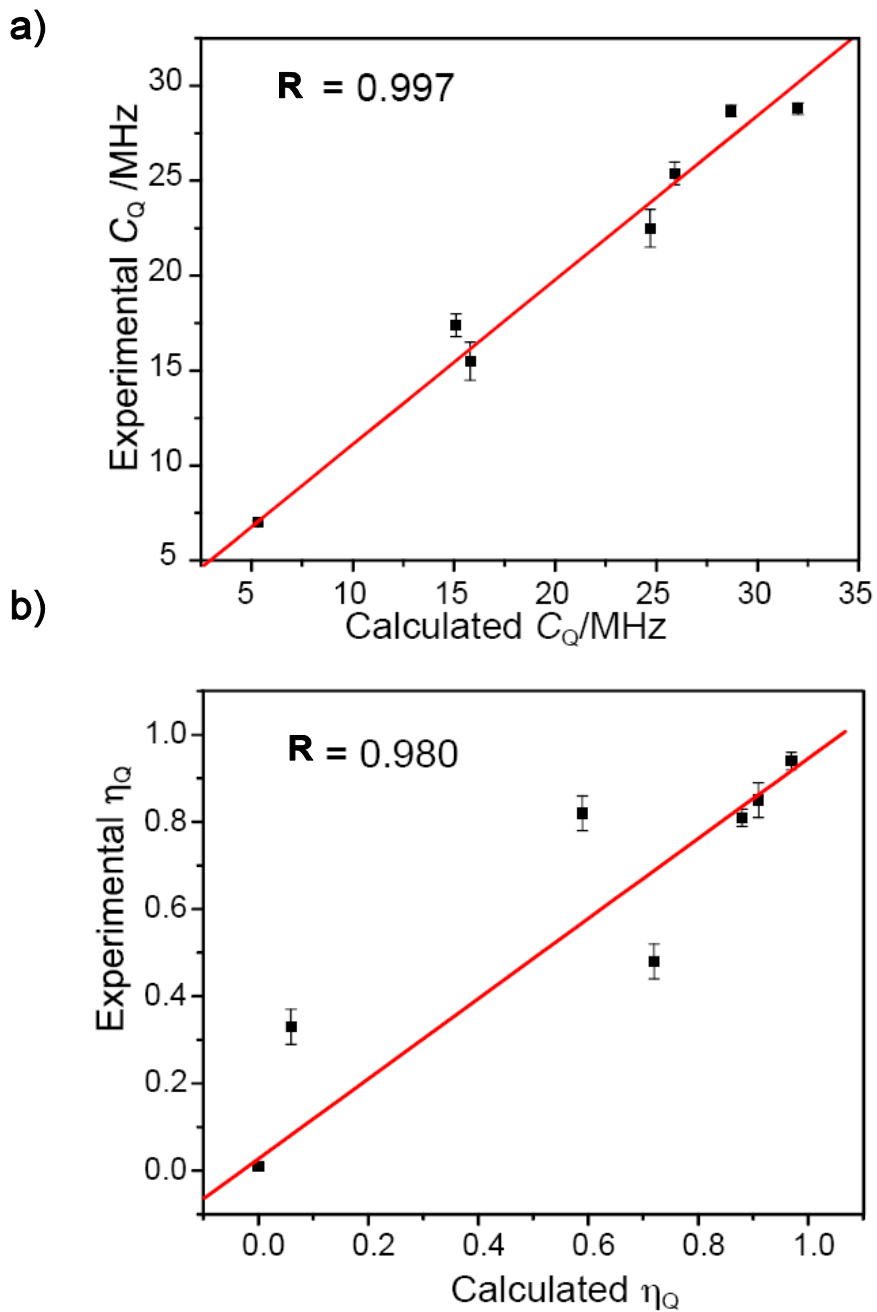


Figure 4.6. Correlations between the experimental and calculated ^{137}Ba a) C_Q and b) η_Q values.

Furthermore, geometry optimization of the structure and the use of varying degrees of basis set flexibility in the EFG calculations did not result in significant variation in the calculated values of C_Q (Table B.4.4). It is likely that limitations in the basis set or density functional may account for discrepancies between experimental and calculated C_Q values, and not long range electrostatic interactions, since these are inherently taken into account in the CASTEP calculations. The largest component of the EFG tensor, V_{33} , is aligned along the threefold rotational axis of the molecule, in accordance with the axial symmetry of the EFG tensor (Figure 4.7a), and consistent with our predictions based on symmetry.

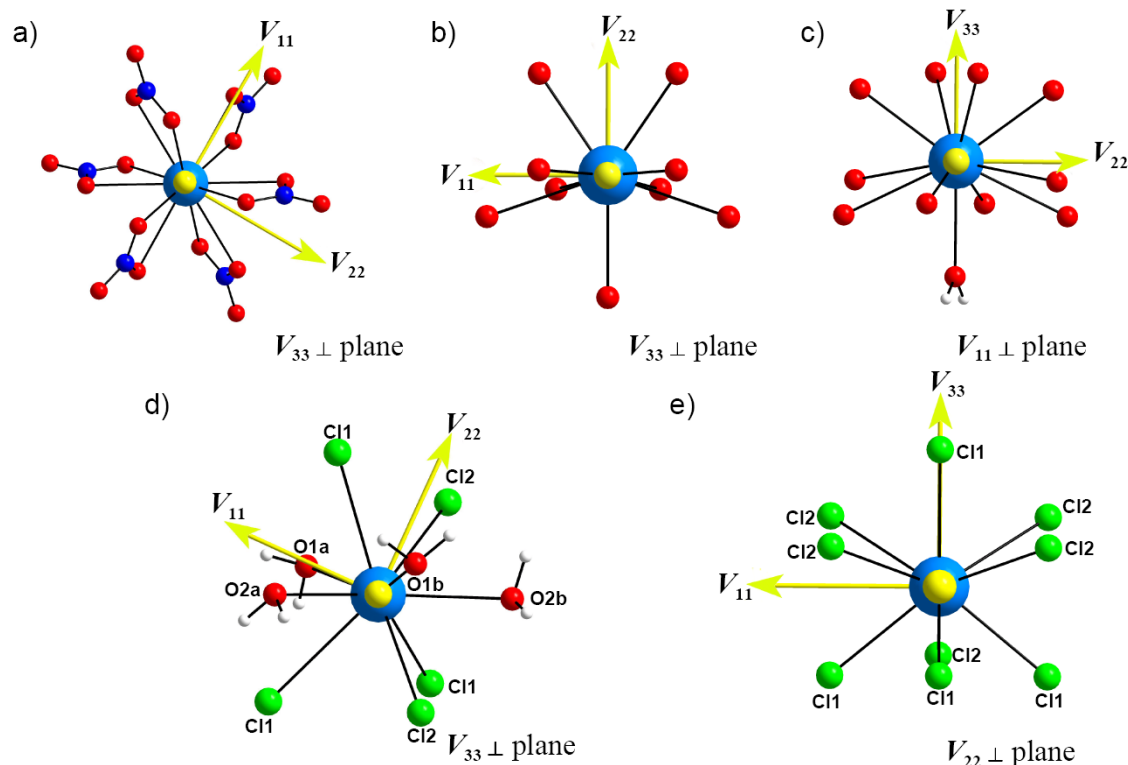


Figure 4.7. Theoretically calculated ^{137}Ba EFG tensor orientations in a) barium nitrate, b) barium carbonate, c) barium chlorate monohydrate, d) barium chloride dihydrate and e) anhydrous barium chloride.

The calculated C_Q for barium carbonate is in good agreement with the experimental value. V_{33} , the distinct component of the EFG tensor, is positioned within the crystallographic mirror plane (Figure 4.7b), and lies close to an approximate plane formed by four O atoms. The theoretical value of η_Q is 0.06, which indicates that the EFG tensor is essentially axially symmetric ($V_{11} \approx V_{22}$), and that V_{11} and V_{22} are directed into similar chemical environments. This is surprisingly different from the experimentally measured tensor, in which V_{11} and V_{22} are not similar. We are uncertain of the origin of this discrepancy; however, given the mirror plane symmetry of the BaO_6 coordination environment, and the distinct V_{11} and V_{22} environments indicated by symmetry and by calculated tensor orientations, we believe that the experimental value is far more reliable.

The calculated C_Q value in the barium chlorate monohydrate case is in excellent agreement with experiment; however, the calculated η_Q is slightly higher. In this case, the discrepancy between the experimental and theoretical η_Q values may result from the observation of an “average” or “effective” η_Q , which results from librational motion of the water molecules⁵⁴ which may alter the magnitude(s) of V_{11} and/or V_{22} . As expected, the largest component of the EFG, V_{33} , is oriented along the Ba-O_{water} bond ($\angle V_{33} - Ba - O = 180^\circ$), which lies along the C_2 rotational axis, with V_{11} and V_{22} oriented in different environments (Figure 4.7c).

Both the C_Q and η_Q values for barium chloride dihydrate are in good agreement with experiment. As discussed above, these large values of C_Q result from the absence of any sort of spherical/platonic symmetry about the barium centre. In this case, V_{11} is the

distinct component of the EFG tensor, and is oriented almost in the center of a distorted pyramid formed by two Cl1, O1a and O2a atoms, and V_{22} is oriented at an angle with the plane formed by O1a, O2a, and O2b ($\angle V_{22}\text{-Ba-O2b} = 67.36^\circ$, Figure 4.7d). For the anhydrous system, both the C_Q and η_Q values are in excellent agreement with experimental data. Again, V_{11} is the distinct component, and as predicted, is oriented perpendicular to a crystallographic mirror plane formed by one Cl2 and two Cl1 atoms, and bisects two separate planes formed by one Cl1 and two Cl2 atoms (Figure 4.7e). V_{22} and V_{33} are contained within the former plane, with the latter oriented very close (ca. 14°) to the shorter in-plane Ba-Cl2 bond. These two systems have very similar local barium geometries in terms of atom positions, as evidenced by the similar values of C_Q and tensor orientations; however, the disparate η_Q values reflect the changing atom identities (O vs. Cl) and bond lengths.

The calculated values of C_Q and η_Q for barium hydrogen phosphate are in very good agreement with experiment and confirm the assignment of the two sites based on the NMR data. The nine-coordinate Ba1 site has a crystallographic mirror plane which contains the lone Ba-O-H arrangement of atoms; the O atoms are arranged in a distorted monocapped square prismatic environment. V_{11} is the distinct component, and is directed perpendicular to this plane; V_{22} and V_{33} are positioned within the plane, oriented at ca. 11° and 101° , respectively, from the unique Ba-O(H) bond (Figure 4.8a). The Ba2 site is in a general position with no symmetry elements, and much lower spherical symmetry than Ba1. V_{11} is again the distinct component, and is oriented along the direction of the two bidentate-bound phosphate groups, Figure 4.8b (i.e., $V_{11}\text{-Ba-P}_{\text{bident}}$ of 1.4° and 7.9°). V_{22}

and V_{33} are directed into similar environments comprised of a shallow pyramid of O atoms from four monodentate phosphate ligands (one of them is nominally bidentate with a much lengthier Ba-O bond, V_{22} lies ca. 6.7° from this bond).

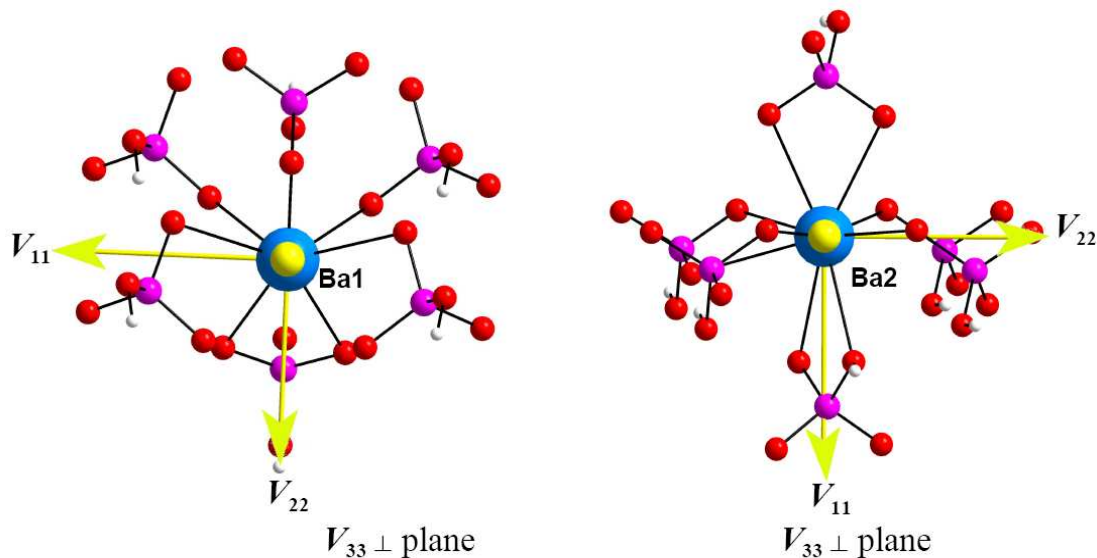


Figure 4.8. Theoretically calculated ^{137}Ba EFG tensor orientations in BaHPO_4 .

4.4 Conclusions

Herein, we have shown that acquisition of ^{137}Ba ultra-wideline SSNMR spectra of barium-containing materials is feasible at moderate and ultrahigh magnetic field strengths. Using the WURST-QCPMG pulse sequence, along with frequency-stepped acquisitions, the ^{137}Ba NMR spectra can be rapidly acquired with high resolution and reasonably good S/N. Furthermore, using ultrahigh magnetic field strengths, experimental times can be significantly decreased (or S/N enhanced) due to the reduction

in the second-order quadrupolar pattern breadths resulting from their inverse dependence on the external magnetic field strength.

The shapes and breadths of the ^{137}Ba NMR patterns are dominated by the quadrupolar interaction. The quadrupolar parameters, C_Q and η_Q , which are extracted from these spectra are extremely sensitive to the nature of the barium site geometries, symmetries and coordination environments. The values of C_Q increase in magnitude as the Ba environments become less spherically symmetric. Theoretical calculations of the ^{137}Ba EFG tensor parameters are generally in good agreement with the experimental values, and will undoubtedly be helpful in future structural predictions for which crystallographic data are not available. Further to this, the ^{137}Ba EFG tensor orientations provide insight into the origin of these tensors and their correlations to molecular structure and symmetry. From this work, we hope that ^{137}Ba SSNMR spectroscopy will continue to be applied to characterize molecular structure (and potentially dynamics) in a wide variety of barium-containing systems, aiding chemists and material scientists in understanding these systems at the molecular level.

4.5 Bibliography

- (1) Siegel, R.; Nakashima, T. T.; Wasylishen, R. E. *Concept Magn. Reson. A* **2005**, *26A*, 47-61.
- (2) Ashbrook, S. E.; Duer, M. J. *Concepts Magn. Reson., Part A* **2006**, *28A*, 183-248.
- (3) Smith, M. E.; Van Eck, E. R. H. *Prog. Nucl. Magn. Reson. Spectrosc.* **1999**, *34*, 159-201.
- (4) Ashbrook, S. E. *Phys. Chem. Chem. Phys.* **2009**, *11*, 6892-6905.
- (5) Chapman, R. P.; Widdifield, C. M.; Bryce, D. L. *Prog. Nucl. Magn. Reson. Spectrosc.* **2009**, *55*, 215-237.
- (6) Hamaed, H.; Laschuk, M. W.; Terskikh, V. V.; Schurko, R. W. *J. Am. Chem. Soc.* **2009**, *131*, 8271-8279.
- (7) Chen, F.; Ma, G.; Cavell, R. G.; Terskikh, V. V.; Wasylishen, R. E. *Chem. Commun.* **2008**, 5933-5935.
- (8) Lipton, A. S.; Wright, T. A.; Bowman, M. K.; Reger, D. L.; Ellis, P. D. *J. Am. Chem. Soc.* **2002**, *124*, 5850-5860.
- (9) Michaelis, V. K.; Aguiar, P. M.; Terskikh, V. V.; Kroeker, S. *Chem. Commun.* **2009**, 4660-4662.
- (10) O'Dell, L. A.; Schurko, R. W. *Phys. Chem. Chem. Phys.* **2009**, *11*, 7069-7077.
- (11) Jakobsen, H. J.; Bildsoe, H.; Skibsted, J.; Brorson, M.; Gor'kov, P.; Gan, Z. *J. Magn. Reson.* **2010**, *202*, 173-179.
- (12) Moudrakovski, I.; Lang, S.; Patchkovskii, S.; Ripmeester, J. *J. Phys. Chem. A* **2010**, *114*, 309-316.
- (13) Sutrisno, A.; Terskikh, V. V.; Huang, Y. *Chem. Commun.* **2009**, 186-188.
- (14) Bowers, G. M.; Lipton, A. S.; Mueller, K. T. *Solid State Nucl. Magn. Reson.* **2006**, *29*, 95-103.
- (15) Cahill, L. S.; Hanna, J. V.; Wong, A.; Freitas, J. C. C.; Yates, J. R.; Harris, R. K.; Smith, M. E. *Chem.-Eur. J.* **2009**, *15*, 9785-9798, S9785/9781-S9785/9783.
- (16) Pallister, P. J.; Moudrakovski, I. L.; Ripmeester, J. A. *Phys. Chem. Chem. Phys.*

2009, *11*, 11487-11500.

(17) Laurencin, D.; Wong, A.; Chrzanowski, W.; Knowles, J. C.; Qiu, D.; Pickup, D. M.; Newport, R. J.; Gan, Z.; Duer, M. J.; Smith, M. E. *Phys. Chem. Chem. Phys.* **2010**, *12*, 1081-1091.

(18) Laurencin, D.; Gervais, C.; Wong, A.; Coelho, C.; Mauri, F.; Massiot, D.; Smith, M. E.; Bonhomme, C. *J. Am. Chem. Soc.* **2009**, *131*, 13430-13440.

(19) Bryce, D. L.; Bultz, E. B.; Aebi, D. *J. Am. Chem. Soc.* **2008**, *130*, 9282-9292.

(20) Harris, R. K.; Becker, E. D.; Cabral De Menezes, S. M.; Goodfellow, R.; Granger, P. *Pure Appl. Chem.* **2001**, *73*, 1795-1818.

(21) Dibello, P. M.; Manganaro, J. L.; Aguinaldo, E. R.; Mahmood, T.; Lindahl, C. B. *Kirk-Othmer Encycl. Chem. Technol. (5th Ed.)* **2004**, *3*, 351-375.

(22) Vijatovic, M. M.; Bobic, J. D.; Stojanovic, B. D. *Sci. Sintering* **2008**, *40*, 235-244.

(23) Symalla, M. O.; Drochner, A.; Vogel, H.; Buechel, R.; Pratsinis, S. E.; Baiker, A. *Appl. Catal., B* **2009**, *89*, 41-48.

(24) Taye, A.; Klotzsche, G.; Michel, D.; Mulla-Osman, S.; Bottcher, R. *J. Phys.: Condens. Matter* **1999**, *11*, 871-879.

(25) Dec, S. F.; Davis, M. F.; Maciel, G. E.; Bronnimann, C. E.; Fitzgerald, J. J.; Han, S. *S. Inorg. Chem.* **1993**, *32*, 955-959.

(26) Bastow, T. J. *J. Phys.: Condens. Matter* **1989**, *1*, 4985-4991.

(27) Forbes, C. E.; Hammond, W. B.; Cipollini, N. E.; Lynch, J. F. *J. Chem. Soc., Chem. Commun.* **1987**, 433-436.

(28) Bastow, T. J.; Whitfield, H. J. *Solid State Commun.* **2001**, *117*, 483-488.

(29) Shore, J.; Yang, S.; Haase, J.; Schwartz, D.; Oldfield, E. *Phys. Rev. B: Condens. Matter* **1992**, *46*, 595-598.

(30) Yakubowskii, A.; Egorov, A.; Lutgemeier, H. *Appl. Magn. Reson.* **1992**, *3*, 665-676.

(31) Gervais, C.; Veautier, D.; Smith, M. E.; Babonneau, F.; Belleville, P.; Sanchez, C. *Solid State Nucl. Magn. Reson.* **2004**, *26*, 147-152.

(32) MacKenzie, K. J. D.; Meinhold, R. H. *Ceram. Int.* **2000**, *26*, 87-92.

(33) Sutrisno, A.; Lu, C.; Lipson, R. H.; Huang, Y. *J. Phys. Chem. C* **2009**, *113*,

21196–21201.

- (34) Larsen, F. H.; Lipton, A. S.; Jakobsen, H. J.; Nielsen, N. C.; Ellis, P. D. *J. Am. Chem. Soc.* **1999**, *121*, 3783-3784.
- (35) O'Dell, L. A.; Rossini, A. J.; Schurko, R. W. *Chem. Phys. Lett.* **2009**, *468*, 330-335.
- (36) O'Dell, L. A.; Schurko, R. W. *J. Am. Chem. Soc.* **2009**, *131*, 6658-6659.
- (37) O'Dell, L. A.; Schurko, R. W. *Chem. Phys. Lett.* **2008**, *464*, 97-102.
- (38) Bowers, G. M.; Kirkpatrick, R. J. *J. Magn. Reson.* **2007**, *188*, 311-321.
- (39) Bhattacharyya, R.; Frydman, L. *J. Chem. Phys.* **2007**, *127*, 194503/194501-194503/194508.
- (40) Clark, S. J.; Segall, M. D.; Pickard, C. J.; Hasnip, P. J.; Probert, M. I. J.; Refson, K.; Payne, M. C. *Z. Kristallogr.* **2005**, *220*, 567-570.
- (41) Medek, A.; Frydman, V.; Frydman, L. *J. Phys. Chem. A* **1999**, *103*, 4830-4835.
- (42) Massiot, D.; Farnan, I.; Gautier, N.; Trumeau, D.; Trokiner, A.; Coutures, J. P. *Solid State Nucl. Magn. Reson.* **1995**, *4*, 241-248.
- (43) Eichele, K.; Wasylishen, R. E.; WSolids NMR Simulation Package, 1.17.30 ed.; Dalhousie University: Halifax, CA, 2001.
- (44) Kupce, E.; Freeman, R. *J. Magn. Reson. Ser. A* **1995**, *115*, 273-276.
- (45) Profeta, M.; Mauri, F.; Pickard, C. J. *J. Am. Chem. Soc.* **2003**, *125*, 541-548.
- (46) Perdew, J. P.; Burke, K.; Ernzerhof, M. *Phys. Rev. Lett.* **1996**, *77*, 3865-3868.
- (47) Perdew, J. P.; Burke, K.; Ernzerhof, M. *Phys. Rev. Lett.* **1998**, *80*, 891.
- (48) Pickard, C. J.; Mauri, F. *Phys. Rev. B* **2001**, *63*, 245101/245101-245101/245113.
- (49) Yates, J. R.; Pickard, C. J.; Mauri, F. *Phys. Rev. B* **2007**, *76*, 024401/024401-024401/024411.
- (50) Yates, J. R.; Pickard, C. J.; Payne, M. C.; Mauri, F. *J. Chem. Phys.* **2003**, *118*, 5746-5753.
- (51) Birnstock, R. *Z. Kristallogr. Kristallgeom. Kristallphys. Kristallchem.* **1967**, *124*, 310-334.
- (52) Nowotny, H.; Heger, G. *Acta Crystallogr., Sect. C: Cryst. Struct. Commun.* **1983**, *C39*, 952-956.

- (53) Antao, S. M.; Hassan, I. *Phys. Chem. Miner.* **2007**, *34*, 573-580.
- (54) Sikka, S. K.; Momin, S. N.; Rajagopal, H.; Chidambaram, R. *J. Chem. Phys.* **1968**, *48*, 1883-1890.
- (55) Busing, W. R. *Trans. Amer. Crystallogr. Ass.* **1970**, *6*, 57-72.
- (56) Padmanabhan, V. M.; Busing, W. R.; Levy, H. A. *Acta Crystallogr., Sect. B: Struct. Sci.* **1978**, *B34*, 2290-2292.
- (57) BenChaabane, T.; Smiri, L.; Bulou, A. *Solid State Sci.* **2004**, *6*, 197-204.
- (58) Trounov, V. A.; Tserkovnaya, E. A.; Gurin, V. N.; Korsukova, M. M.; Derkachenko, L. I.; Nikanorov, S. P. *Tech. Phys. Lett.* **2002**, *28*, 351-353.
- (59) Weiden, N.; Weiss, A. *Magn. Reson. Relat. Phenom., Proc. Congr. AMPERE, 18th* **1975**, *1*, 257-258.
- (60) Bastow, T. J. *Chem. Phys. Lett.* **2002**, *354*, 156-159.
- (61) Nakamura, S.; Enokiya, H. *J. Phys. Soc. Jpn.* **1963**, *18*, 183-188.
- (62) Volkov, A. F. *J. Magn. Reson.* **1973**, *11*, 73-76.
- (63) Krishnan, V.; Moorthy, T. V. K.; Ramakrishna, J. Z. *Naturforsch., A: Phys. Sci.* **1986**, *41A*, 338-340.
- (64) Vargas, H.; Pelzl, J.; Dimitropoulos, C. *J. Magn. Reson.* **1978**, *30*, 423-429.
- (65) Chihara, H.; Nakamura, N. *Landolt-Bornstein Group III: Condensed Matter; Volume 39: Nuclear Quadrupole Resonance Spectroscopy Data. Supplement to Volumes III/20 and III/31*, Springer: Berlin, Germany, 1998.
- (66) Graybeal, J. D.; Pathania, M.; Ing, S. D. *J. Magn. Reson.* **1973**, *9*, 27-34.
- (67) Graybeal, J. D.; McKown, R. J. *J. Phys. Chem.* **1969**, *73*, 3156-3157.
- (68) Korneva, I.; Ostafin, M.; Sinyavsky, N.; Nogaj, B.; Mackowiak, M. *Solid State Nucl. Magn. Reson.* **2007**, *31*, 119-123.
- (69) Harbison, G. S.; Slokenbergs, A. Z. *Naturforsch., A: Phys. Sci.* **1990**, *45*, 575-580.
- (70) Harbison, G. S.; Slokenbergs, A.; Barbara, T. M. *J. Chem. Phys.* **1989**, *90*, 5292-5298.

Chapter 5

Solid-State ^{115}In NMR Study of Low-Oxidation State Indium Complexes

5.1 Introduction

There is increasing interest in exploring new compounds with metal elements in low oxidation states for the synthesis of new catalysts or materials precursors.¹⁻⁶ Compounds with metal elements in lower oxidation states have significantly different structural features and reactivities than corresponding higher oxidation state compounds.^{7,8} For group 13 elements, the +3 oxidation state is usually the most stable, and is commonly involved in complexes behaving as Lewis acids. In contrast, compounds containing group 13 elements in the +1 oxidation state are relatively rare, and can behave either as Lewis bases or Lewis acids.^{9,10} In particular, In(I) compounds exhibit unique behavior and redox properties which make them useful as either reagents or catalysts used to affect several types of organic transformations.^{6,11-14} The majority of In(I) salts are insoluble in most common organic solvents,⁷ which limits their structural characterization by routine methods (i.e., single crystal X-ray diffraction and solution NMR).

Indium has two NMR-active isotopes, ^{113}In and ^{115}In , which are quadrupolar nuclei (both have nuclear spins of 9/2). They both have large nuclear electric quadrupole moments ($Q = 79.9$ and 81.0 fm^2 , respectively),¹⁵ moderate gyromagnetic ratios (5.8845×10^7 and $5.8972 \times 10^7 \text{ rad T}^{-1} \text{ s}^{-1}$, respectively) and natural abundances of 4.3%

and 95.7%, respectively.¹⁵ Of the two isotopes, ¹¹⁵In is preferred for NMR due to its much higher receptivity (i.e., with respect to carbon, $D^C(^{113}\text{In}) = 88.5$ and $D^C(^{115}\text{In}) = 1.98 \times 10^3$); however, its quadrupole moment is the largest among all NMR-active isotopes of the main group elements.¹⁵ The large Q can lead to sizeable quadrupolar interactions, resulting in very broad NMR patterns which are challenging to acquire.¹⁶ The quadrupolar interaction is the interaction of the nuclear quadrupole moment with the electric field gradient (EFG) at the nucleus. The EFG is described by a symmetric, traceless, second-rank (3×3) tensor with three principal components defined such that $|V_{33}| \geq |V_{22}| \geq |V_{11}|$. These components provide information about the spherical and axial symmetry of the ground state electronic environment at the nuclear site through measurements of the quadrupolar coupling constant, $C_Q = eQV_{33}/h$, and the asymmetry parameter, $\eta_Q = (V_{11} - V_{22})/V_{33}$, respectively. Measurements of the ¹¹⁵In EFG tensor components, along with the indium chemical shift tensor parameters (which describe the indium chemical shift anisotropy, CSA) provide useful information about the chemical environments of the indium atoms.

Solution-state ¹¹⁵In NMR spectroscopy has been used to identify different indium sites in a variety of In(III)-containing systems through measurements of the isotropic chemical shifts, δ_{iso} .¹⁷⁻²⁶ However, in cases where indium sites are not in a highly spherically symmetric environments, it is often difficult to observe the ¹¹⁵In NMR signal, due to fast quadrupolar relaxation in solution.²⁰ Many In(I) compounds are insoluble in commonly used solvents, limiting the application of solution-state NMR spectroscopy for their study. ¹¹⁵In solid-state NMR (SSNMR) is an excellent alternative for

characterization of such systems, since the anisotropic NMR interaction tensors obtained from these spectra provide rich structural information. Most of the ^{115}In SSNMR studies reported to date have largely focused on indium materials which are used (or have the potential to be used) as semi-conductors or conductors.²⁷⁻³⁴ Many of these studies report indium Knight shifts, sometimes the quadrupolar parameters, and rarely, the chemical shift (CS) tensor parameters. In addition, most of these studies deal with indium materials in which In is in the +3 oxidation state and/or exists in highly symmetric environments. Recently, Chen et. al have shown the utility of ^{115}In SSNMR for studying indium coordination complexes in which the indium is in the +3 oxidation state.^{16,35}

Herein, we describe the first detailed ^{115}In SSNMR study of low-oxidation state indium compounds. ^{115}In SSNMR data are obtained for eight samples with a variety of structural motifs, including $[\text{In}][\text{GaCl}_4]$, InCl_2 , $[\text{In}(15\text{-crown-5})_2][\text{OTf}]$, $[\text{In}([18]\text{crown-6})][\text{GaCl}_4]$, $[\text{In}([18]\text{crown-6})][\text{AlCl}_4]$, $[\text{In}][\text{OTf}]$, InBr and InI . Static (i.e., stationary sample) NMR spectra were acquired at both moderate and ultra-high magnetic field strengths (9.4 and 21.1 T) in order to accurately measure the EFG and the CS tensor parameters. In addition, magic-angle spinning (MAS) spectra were obtained at 21.1 T in order to average the contribution of indium CSA to the central transition (CT) pattern, and to separate the central isotropic powder pattern from the spinning sidebands, thereby allowing for accurate measurements of C_Q , η_Q and δ_{iso} . In most cases, the use of ultra-fast ($\nu_{\text{rot}} \geq 50$ kHz) MAS was necessary, due to the sizeable anisotropic NMR interactions. There are very few reports of ^{115}In MAS NMR in the literature,^{29,32,36,37} to the best of our knowledge, this is the first report of ^{115}In ultra-fast MAS NMR spectra. Analytical

simulations of the ^{115}In static NMR spectra are used to determine the quadrupolar and CS parameters, which are correlated to the local structure and symmetry. Finally, first principles calculations of the ^{115}In EFG and nuclear magnetic shielding (NS) tensor parameters are presented for systems for which structures are available, using the plane-wave CASTEP methods.³⁸

5.2 Experimental Details

5.2.1 Sample Preparations.

Samples of $[\text{In}][\text{GaCl}_4]$, InCl_2 , InBr , and InI were purchased from Sigma-Aldrich. $[\text{In}([\text{15}]\text{crown-5})_2][\text{OTf}]$ and $[\text{In}][\text{OTf}]$ were synthesized as described in the literature.^{12,39}

Synthesis of $[\text{In}([\text{18}]\text{crown-6})][\text{AlCl}_4]$. Toluene (30 mL) was added to AlCl_3 (0.251 g, 1.89 mmol) and InCl (0.284 g, 1.89 mmol) in a 100 mL Schlenk flask and refluxed overnight, or until no traces of InCl were visible. The solution was then brought to room temperature and a toluene (10 mL) $[\text{18}]\text{crown-6}$ (0.500 g, 1.89 mmol) solution was added to the reaction mixture. Immediately upon addition of $[\text{18}]\text{crown-6}$, a colour change was observed followed by the formation of a colourless product. All volatile components were removed under reduced pressure and the product was obtained as a colourless powder after washing with pentane (84.5% yield).

Synthesis of $[\text{In}([\text{18}]\text{crown-6})][\text{GaCl}_4]$. Toluene (30 mL) was added to GaCl_3 (0.333 g, 1.89 mmol) and InCl (0.284 g, 1.89 mmol) in a 100 mL Schlenk flask and refluxed overnight, or until no traces of InCl were visible. The solution was then brought to room temperature and a toluene (10 mL) $[\text{18}]\text{crown-6}$ (0.500 g, 1.89 mmol) solution

was added to the reaction mixture. All volatile components were removed under reduced pressure, and the product was obtained as a colourless powder after washing with pentane (89% yield).

5.2.2 Solid-State NMR.

^{115}In SSNMR experiments were performed on a Varian Infinity Plus spectrometer equipped with a 9.4 T ($\nu_0(^1\text{H}) = 399.73$ MHz) Oxford wide-bore magnet ($\nu_0(^{115}\text{In}) = 87.59$ MHz) at the University of Windsor and a 21.1 T ($\nu_0(^1\text{H}) = 900.08$ MHz) Bruker Avance II spectrometer ($\nu_0(^{115}\text{In}) = 197.23$ MHz) at the National Ultrahigh-field NMR Facility for Solids in Ottawa, Canada. In some cases, the NMR patterns were much wider than the excitation bandwidth achievable with an ideal high power rectangular pulse; thus, spectra were collected by stepping the transmitter frequency across the entire CT powder pattern in even increments, acquiring the individual sub-spectra, and co-adding them to form the total pattern^{40,41} (see Appendix C, Tables C.5.1-C.5.3 for full experimental details). Indium chemical shifts were referenced to a 0.1 M solution of $\text{In}(\text{NO}_3)_3$ in 0.5 M HNO_3 ($\delta_{\text{iso}} = 0.0$ ppm).¹⁶ Analytical simulations of ^{115}In NMR spectra were performed using WSolids,⁴² and MAS NMR spectra with spinning sidebands were simulated using DMFIT.⁴³

Experiments at 9.4 T. Samples were finely ground and packed into either 5 mm o.d. zirconium oxide rotors or 5 mm glass NMR tubes. ^{115}In static NMR spectra were acquired using a Varian 5 mm triple-resonance MAS probe (HXY). Spectra were collected using either the Hahn-echo sequence of the form $(\pi/2)_x-\tau_1-(\pi)_y-\tau_2$ -acq (where the

τ_1 and τ_2 represent interpulse delays), or the WURST-echo pulse sequence.⁴⁴ For the Hahn-echo experiments, CT selective $\pi/2$ pulse widths between 0.45 and 1.1 μs , an optimized recycle delay of 0.1 s and a spectrum width of 1 or 2 MHz were used. The transmitter offset frequency was set between 35 and 150 kHz. For the WURST-echo experiments, WURST-80 pulse shapes⁴⁵ were used with a 50 μs WURST pulse length, and swept at a rate of 40 MHz/ms with an offset of 1000 kHz and rf power of 17 kHz. A spectral width of 2 MHz and recycle delay of 0.1 s were used. The frequency step size was set to 250 kHz, in order to ensure uniform excitation. Further experimental details are given in Table C.5.1.

Experiments at 21.1 T. For the static ^{115}In NMR experiments, samples were ground and packed into 4 mm o.d. NMR glass tubes and spectra were acquired on a 4 mm home-built static (HX) probe using a solid-echo pulse sequence of the form $(\pi/2)_x-\tau_1-(\pi/2)_y-\tau_2\text{-acq}$. Experiments were conducted with a selective $\pi/2$ pulse width of 1 μs ($\nu_1 = 50$ kHz), spectral widths between 200 and 1000 kHz, a recycle delay of 1 s. In cases where piecewise acquisition was necessary, the transmitter frequency offsets were set between 60 and 150 kHz. A ^1H decoupling power of 55 kHz was applied for the spectral acquisitions of proton-containing samples; however, decoupling did not seem to alter the shape of the powder patterns compared to spectra acquired without decoupling. Further experimental details are given in Table C.5.2.

MAS NMR spectra were acquired using either 4 mm or 1.3 mm Bruker double-resonance probes, using the solid-echo pulse sequence with rotor-synchronized echo delays. Selective $\pi/2$ pulse widths of 0.5 (100 kHz) or 1 μs ($\nu_1 = 50$ kHz), spectral widths

between 200 and 1000 kHz, a recycle delay of either 0.5 or 1 s were used, with spinning speeds from 12.5 to 62.5 kHz (Table C.5.3).

5.2.3 Computational methods.

^{115}In EFG and CS tensor parameters were calculated for all systems with available crystal structures.^{12,39,46-48} Ab initio plane-wave density functional theory (DFT) calculations were performed using the CASTEP NMR program^{38,49} in the Materials Studio 4.3 environment on a HP xw4400 Workstation with a single Intel Dual-Core 2.67 GHz processor and 8 GB DDR RAM. Ultrasoft pseudopotentials were used for ^{115}In EFG calculations with a plane wave basis set cut-off of 550 eV in a fine accuracy basis set with the Monkhorst-Pack k -space grid sizes of (2×4×3), (3×3×3), (5×2×5), (6×2×5) and (5×4×1) for $[\text{In}][\text{GaCl}_4]$, $[\text{In}(15\text{-crown-5})_2][\text{OTf}]$, InI , InBr and $[\text{In}][\text{OTf}]$, respectively. The Perdew, Burke and Ernzerhof (PBE) functionals were used in the generalized gradient approximation (GGA) for the exchange-correlation energy.^{50,51} The magnetic shielding tensors for ^{115}In were calculated in a fine accuracy basis set using the projector augmented-wave method (GIPAW) implemented in the CASTEP code.^{52,53} Relativistic effects are included in CASTEP calculations at the level of the scalar-relativistic zeroth-order regular approximation (ZORA).⁵⁴

5.3 Results and Discussion

5.3.1 Solid-state ^{115}In NMR.

In this section, the ^{115}In SSNMR data are discussed for the eight samples. The

EFG and CS tensor parameters are summarized in Table 5.1. We note that the MAS NMR spectra were only obtained at 21.1 T; because the breadth of the CT NMR spectra is inversely proportional to the applied magnetic field strength, it is possible to separate the spinning sidebands from the isotropic powder pattern, and accurately determine C_Q , η_Q , and δ_{iso} . In all cases (with the exception of the In(III) site in InCl_2), the isotropic chemical shifts are consistent with the indium sites being in the +1 oxidation state, since the measured chemical shifts indicate that nuclei of the In(I) sites are much more shielded than those reported of In(III) complexes in solution and in the solid state,^{16,24} and consistent with chemical shifts of In(I) sites measured with solution ^{115}In NMR spectroscopy.²²

Table 5.1. Summary of the experimental ^{115}In NMR parameters.

	$ C_Q(^{115}\text{In}) /$ MHz ^a	η_Q^b	$\delta_{\text{iso}}/\text{ppm}^c$	Ω/ppm^d	κ^e	α/deg^f	β/deg	γ/deg
$[\text{In}^+][\text{GaCl}_4]$	22.0(6)	0.2(1)	-1115(10)	60(20)	0.7(3)	65(20)	8(6)	5(5)
InCl ₂ Site 1	10.0(15)	0.75(20)	-1080(5)	30(10)	-0.5(3)	40(20)	30(10)	5(5)
InCl ₂ Site 2	29.5(15)	0.16(8)	80(10)	60(10)	-0.6(3)	55(20)	90(5)	10(5)
$[\text{In}([15]\text{crown-5})_2][\text{OTf}]$	28.4(10)	0.18(10)	-1192(15)	75(15)	0.2(4)	50(30)	90(10)	5(5)
$[\text{In}([18]\text{crown-6})][\text{GaCl}_4]$	57.0(15)	0.10(5)	-1110(20)	50(30)	0.2(6)	10(10)	20(10)	10(10)
$[\text{In}([18]\text{crown-6})]\text{AlCl}_4$	60.2(10)	0.07(6)	-1115(10)	45(30)	0.0(6)	30(20)	35(20)	20(10)
InI	44(1)	0.7(1)	-480(20)	110(50)	0.8(2)	45(40)	5(5)	0
InBr	67(2)	0.58(8)	-580(40)	140(40)	0.4(3)	30(20)	5(5)	30(20)
InOTf	80.5(15)	0.07(3)	-1045(15)	260(60)	0.3(2)	50(30)	3(3)	30(20)

^a $C_Q = eQV_{33}/h$; ^b $\eta_Q = (V_{11} - V_{22})/V_{33}$; ^c $\delta_{\text{iso}} = (\delta_{11} + \delta_{22} + \delta_{33})/3$; ^d $\Omega = \delta_{11} - \delta_{33}$; ^e $\kappa = 3(\delta_{22} - \delta_{\text{iso}})/\Omega$.

^f Conventions for the Euler angles are described in the WSolids software package

Indium Gallium Chloride, [In][GaCl₄]. The ^{115}In SSNMR spectra of $[\text{In}][\text{GaCl}_4]$

(Figure 5.1a) reveal a single indium site in agreement with the crystal structure.⁴⁶

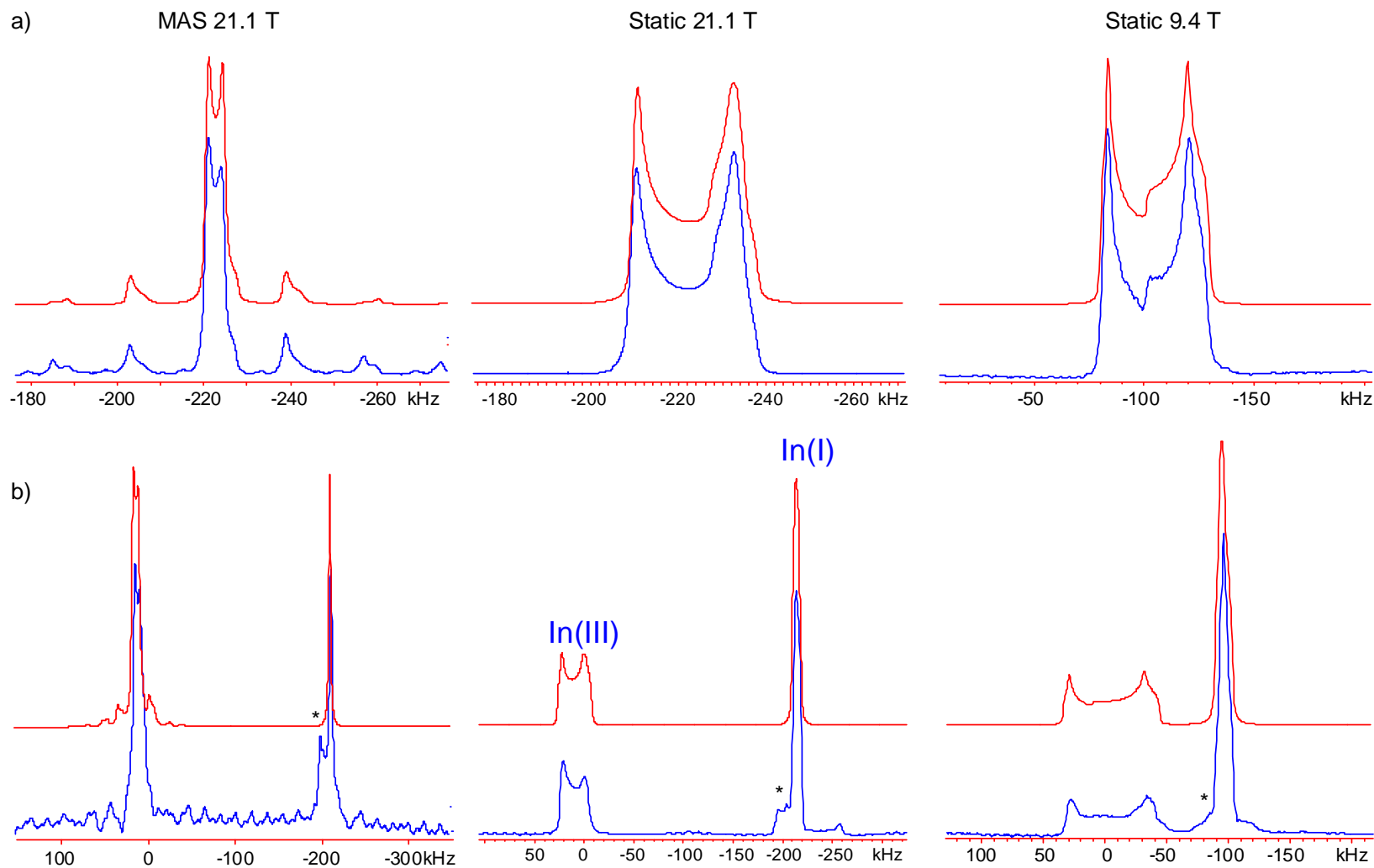
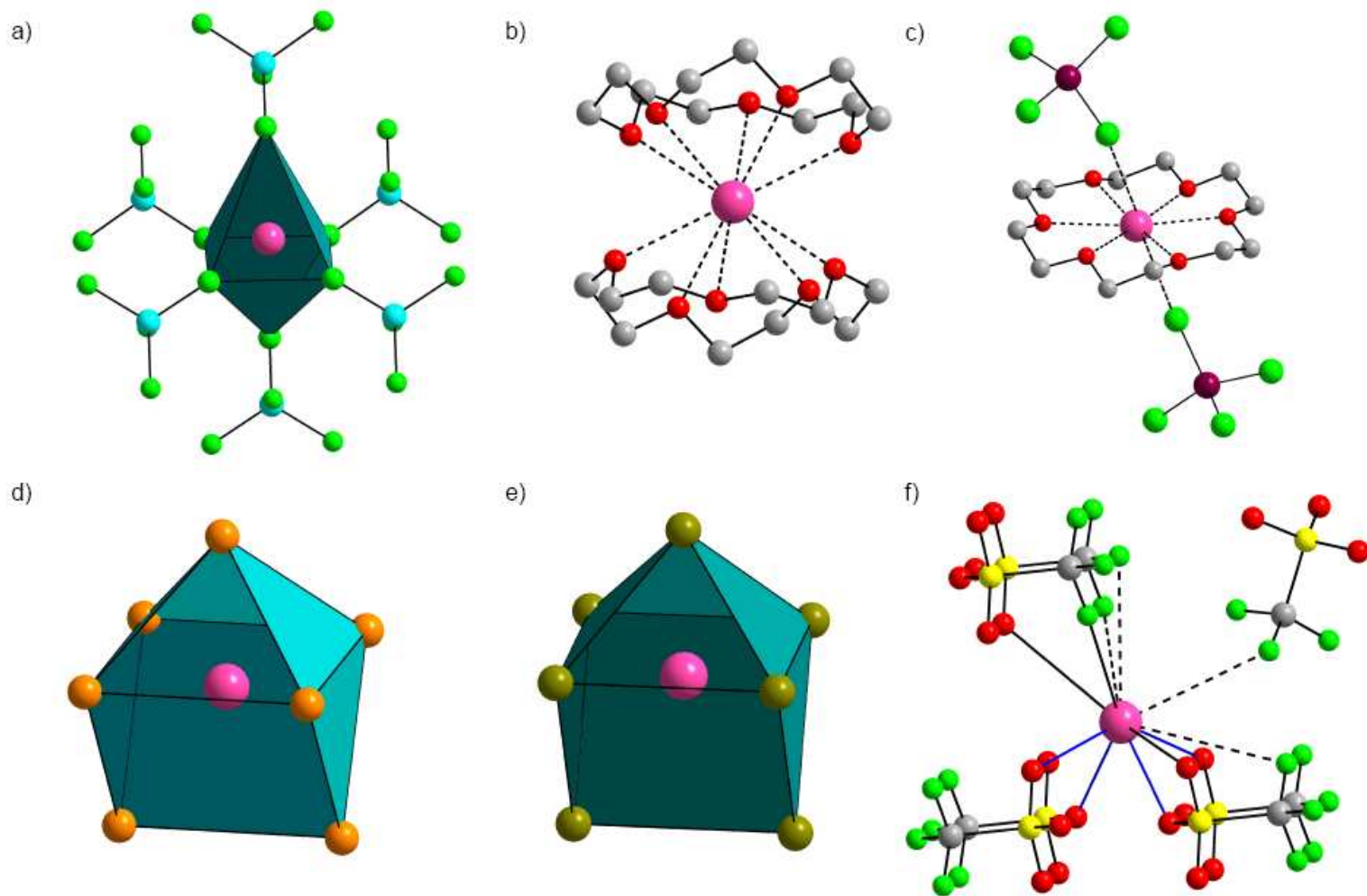


Figure 5.1. ^{115}In SSNMR patterns of a) $[\text{In}][\text{GaCl}_4]$ and b) InCl_2 . The MAS spectra were acquired with $\nu_{\text{rot}} = 18$ kHz, and this spinning speed is fast enough to separate the spinning sidebands from the isotropic powder patterns. The spectra of InCl_2 reveal two indium sites with different oxidation states. *: impurity at -1020(20) ppm, top and bottom traces are simulated and experimental spectra, respectively.

The indium site in this structure is coordinated by six chlorine atoms in a distorted octahedral environment (Scheme 5.1a). The C_Q value (Table 5.1) is small, given the large nuclear electric quadrupole moment of ^{115}In , and in comparison to the large C_Q values of the six-coordinate indium(III) complexes reported by Chen et al.^{16,35} This small C_Q is similar to that of $\text{Na}_3\text{In(III)Cl}_6$ ($C_Q = 20.11$ MHz), in which the indium atom is also in a distorted octahedral environment.³⁰ The non-zero η_Q value indicates the absence of a threefold (or higher) rotational symmetry axis, and that the largest component of the EFG tensor, V_{33} , is distinct and is likely oriented along/within or perpendicular to the mirror plane containing the four equatorial chlorine atoms. Despite the fact that the NMR pattern of $[\text{In}][\text{GaCl}_4]$ is dominated by the quadrupolar interaction, the CSA contribution has a major effect on its shape, as clearly seen from the static spectrum acquired at 21.1 T (Figure C.5.1, Appendix C). The nearly null value of the Euler angle β indicates that V_{33} and the principal component of the CS tensor corresponding to the direction of the highest shielding, σ_{33} , are almost coincident.

Indium dichloride, InCl_2 . The empirical formula of InCl_2 is deceiving since it suggests that In is in the +2 oxidation state and the sample is paramagnetic. However, it has been suggested that this sample has monovalent and trivalent indium sites in 1:1 ratio and the formula is better described as $[\text{In(I)}]^+[\text{In(III)Cl}_4]^-$;^{7,48,55} to date, the crystal structure is still unknown. Currently, there is still a debate in the literature concerning the environment of the two indium sites, particularly the In(III) site. In some reports, it is believed that the In(III) is coordinated to four chlorine atoms in a slightly distorted tetrahedral environment, as is the case for the Ga(III) in GaCl_2 structure.^{56,57}



Scheme 5.1. The coordination environments of the indium atom in a) $[\text{In}][\text{GaCl}_4]$, b) $[\text{In}([\text{15}]\text{crown-5})_2][\text{OTf}]$, c) the structural model of $[\text{In}([\text{18}]\text{crown-6})]\text{AlCl}_4$ and $[\text{In}([\text{18}]\text{crown-6})]\text{GaCl}_4$, d) InI , e) InBr , and f) $[\text{In}][\text{OTf}]$. The blue bonds in f are those within 3 Å from the indium, the solid black bonds are within 3.5 Å and the dashed ones are within 4 Å.

However, other reports predict that the In(III) is coordinated to six chlorine atoms, which is believed to be the most stable coordination state of In(III) with chlorine ligands.^{7,48,58} Our ¹¹⁵In SSNMR spectra reveal two distinct powder patterns separated by more than 1000 ppm (Figure 5.1b); confirming the divalent nature of InCl₂. The powder patterns have isotropic shifts of -1080 and + 80 ppm, and are assigned to the In(I) and In(III) sites, respectively. The In(III) site has an isotropic chemical shift and quadrupolar parameters similar to those of In(III)Cl₃ ($\delta_{\text{iso}} = 74(10)$ ppm, $C_Q = 28.8(5)$ MHz and $\eta_Q = 0.11(10)$), measured by Bryce and co-workers,⁵⁹ indicating that the In(III) site in InCl₂ is very likely to be coordinated to six chlorine ligands in a distorted octahedral environment (as is the case for In(III)Cl₃). The near-zero η_Q value indicates that the EFG tensor is close to being axially symmetric, consistent with a distorted octahedral environment. The In(I) site in InCl₂ has a very small C_Q , indicating that it is in an environment of higher spherical symmetry than In(III). It is possible that this indium site is in a less distorted octahedral environment, or even more likely, it maybe coordinated to 10 or more chlorine atoms, due to the tendency of In(I) to acquire a larger coordination number.⁴⁸ The high η_Q value of this site reveals the absence of a rotational symmetry axis and that the EFG tensor is not axially symmetric. This η_Q value is similar to that of Ga(I) site in GaCl₂ ($\eta_Q \approx 1$),⁵⁹ in which the Ga is coordinated to eight Cl atoms with an irregular dodecahedral geometry.⁶⁰

Indium(I)-15-Crown-5-Sandwich Trifluoromethanesulfonate, [In(15-crown-5)₂][OTf]. This is the first reported compound with bonds between indium metal and [15]crown-5; in addition, it is unusually soluble in toluene.¹² The structure exhibits a single indium site residing on an inversion center (Scheme 5.1b). The ¹¹⁵In NMR spectra

reveal the presence of a single indium site with a relatively small C_Q (Figure 5.2), which is consistent with its highly spherically symmetric environment. The small non-zero η_Q confirms the absence of a threefold (or higher) rotational axis and consistent with the presence of an inversion center. The indium CSA also makes a significant contribution to the powder pattern (Figure C.5.2), with the Euler angle of $\beta = 90^\circ$ revealing that σ_{33} is oriented in a direction perpendicular to V_{33} . However, the skew and other Euler angles do not indicate the co-alignment of σ_{11} or σ_{22} with V_{33} .

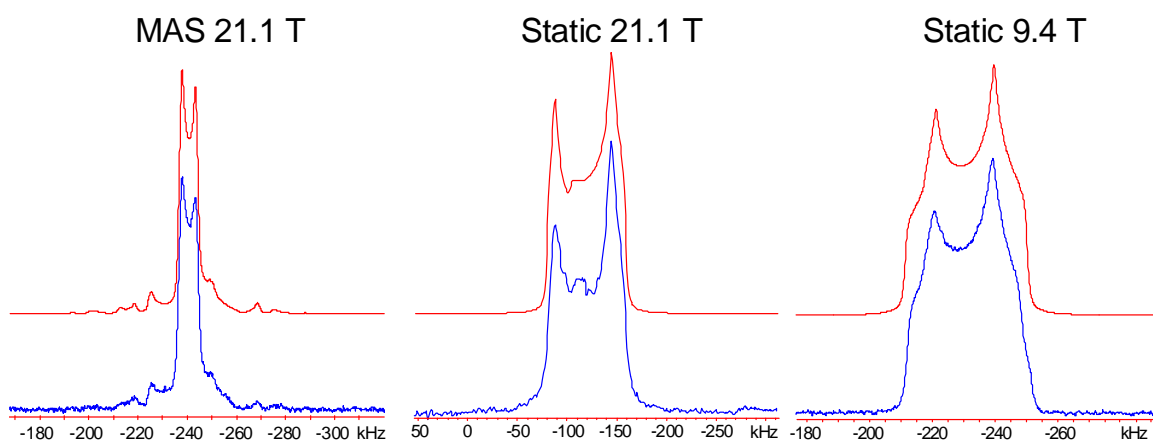


Figure 5.2. ^{115}In SSNMR patterns of $[\text{In}([\text{15}]\text{crown-5})_2][\text{OTf}]$. The MAS spectrum was acquired with $\nu_{\text{rot}} = 12.5$ kHz. Top and bottom traces are simulated and experimental spectra, respectively.

Indium(I)[18]Crown-6-Gallium Tetrachloride and Indium(I)[18]Crown-Aluminum Tetrachloride, $[\text{In}([\text{18}]\text{crown-6})][\text{GaCl}_4]$ and $[\text{In}([\text{18}]\text{crown-6})][\text{AlCl}_4]$. The structures of these samples have not been obtained due to the difficulties in growing crystals suitable for single-crystal XRD experiments. Therefore, ^{115}In SSNMR is an ideal tool for providing insights into the electronic and bonding environments of the indium sites, and the arrangement of the different ligands in these structures. The NMR patterns

of both samples (Figure 5.3) are much broader than those discussed above, due to the larger quadrupolar interactions in these systems. The large quadrupolar interactions yield static CT patterns which must be acquired in a piecewise manner (three subspectra) at 9.4 T; in addition, the MAS NMR spectrum acquired at 9.4 T would be very convoluted, since there is overlap between the isotropic powder pattern and spinning sidebands (data not shown). Due to the inverse dependence of the CT pattern breadth on B_0 , it was possible to acquire an MAS spectrum at 21.1 T using an ultra-fast MAS NMR probe ($\nu_{\text{rot}} = 50$ kHz). Further, the static ^{115}In NMR spectrum could have been acquired at 21.1 T in a single experiment, but the spectrum was obtained in three pieces to ensure uniform excitation. The combination of the static NMR spectra at two fields, and the simulation of the full MAS spinning sidebands manifold, allow for refinement of the NMR tensor parameters.

Simulations of the spectra reveal a single indium site in each of $[\text{In}([18]\text{crown-6})][\text{GaCl}_4]$ and $[\text{In}([18]\text{crown-6})][\text{AlCl}_4]$ with similar NMR parameters, indicating that these sites exist in similar chemical environments. The large C_Q , in comparison to that of the [15]crown-5 complex, indicates a reduction in spherical symmetry at the indium sites, and η_Q values indicate nearly axially symmetric EFG tensors. The CSA contribution is less important in these patterns due to the dominant quadrupolar interactions; however, the static CT powder patterns could not be accurately simulated without the inclusion of the CS tensor parameters (Figure C.5.3). The stoichiometries for these systems are different from that of the [15]crown-5 complex (i.e., there is only one crown per indium site), suggesting that they may have very different structures and indium environments.

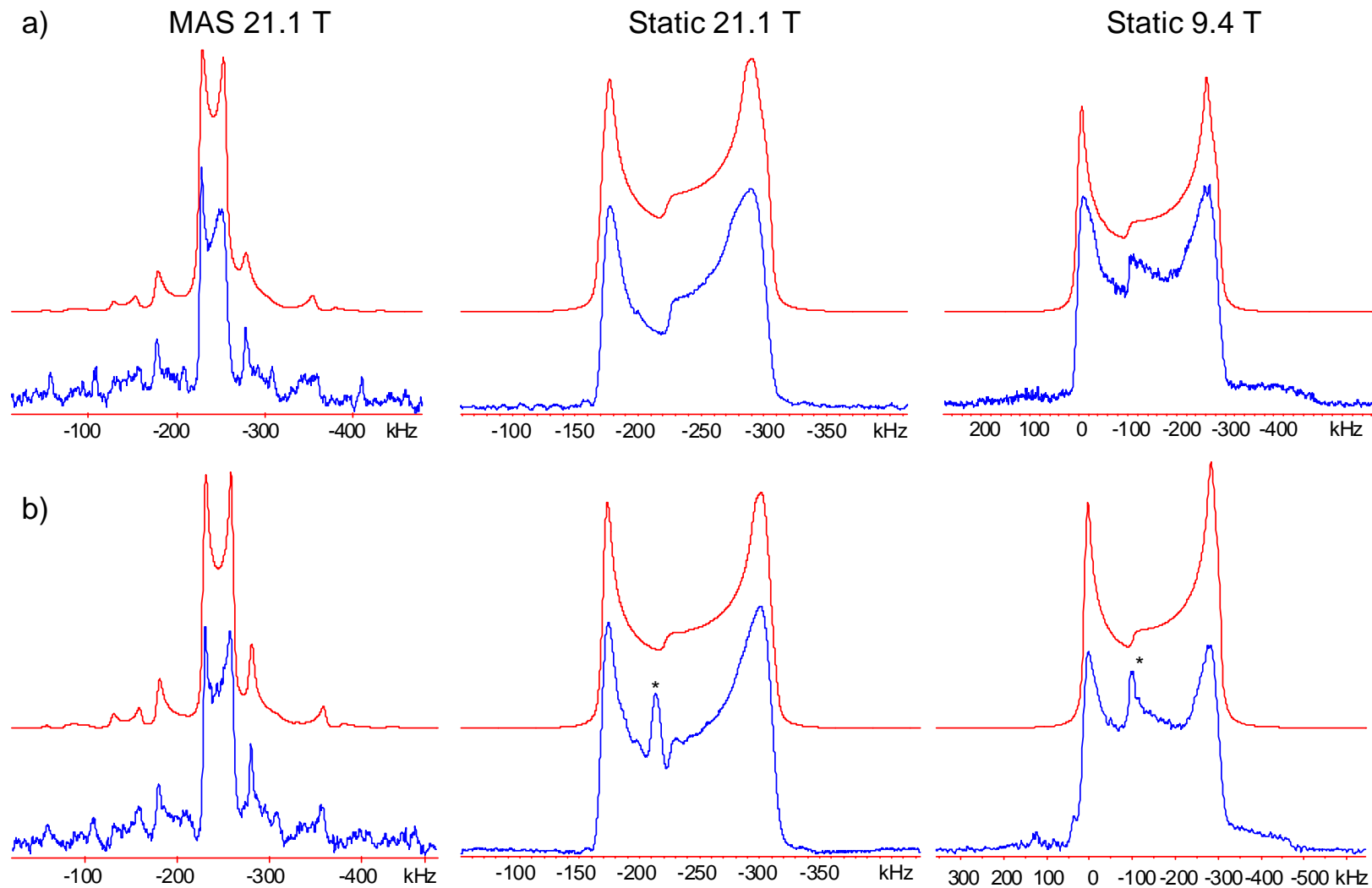


Figure 5.3. ^{115}In SSNMR patterns of a) $[\text{In}([18]\text{crown-6})]\text{GaCl}_4$ and b) $[\text{In}([18]\text{crown-6})]\text{AlCl}_4$. The MAS spectra were acquired with $\nu_{\text{rot}} = 50$ kHz, and this spinning speed is fast enough to separate the spinning sidebands from the isotropic powder patterns. *: impurity at 1130(100) ppm, top and bottom traces are simulated and experimental spectra, respectively.

Given that the [18]crown-6 cavity is large enough to accommodate the In(I) ion,⁶¹ and given the large C_Q 's and near-zero η_Q 's, we propose a structural model pictured in Figure 5.1c. The presence of GaCl₄ and AlCl₄ are confirmed by ⁷¹Ga and ²⁷Al SSNMR spectra (Figure C.5.4), based on their solution chemical shifts.²⁴ However, further ¹¹⁵In NMR experiments should be performed on similar well-characterized systems, which in combination with first principles calculations, can be utilized to confirm the proposed structures.

Indium(I) Iodide and Indium(I) Bromide, InI and InBr. The structures of InI and InBr are isomorphous, each having seven halogen atoms in the first coordination sphere of In.⁶² The coordination geometry around the indium is described as a “7-octahedron”⁴⁸ or as capped trigonal prismatic (Scheme 5.1d, 5.1e). Simulations of the NMR spectra (Figure 5.4) reveal a single indium site each case, in agreement with the structures.^{47,48} The relatively large C_Q values result in broad NMR patterns which necessitate the use of ultra-fast spinning speeds (62.5 kHz) in order to obtain the MAS NMR spectra. The C_Q of InBr is higher than that of InI, possibly due to the longer In-X distances in the latter. This trend was also observed for ²⁰⁹Bi C_Q 's in the isostructural BiOX (X = Cl, Br, I) systems,⁶³ ⁶⁹Ga C_Q 's in GaX systems, ⁷⁵As C_Q 's in AsX₃, ^{121/123}Sb C_Q 's in SbX₃ and ⁹³Nb in (NbX₅)_y (y = 2 or 4) systems.⁶⁴ In all of these cases, the C_Q values increase with increasing electronegativity of the halide atoms. The CSA contributions are small in both cases; however, the inclusion of the CS tensor parameters is again necessary in order to achieve the best fits (Figures C.5.5 and C.5.6). Finally, the nearly zero values of β indicate that V_{33} and σ_{33} are almost coincident in both systems.

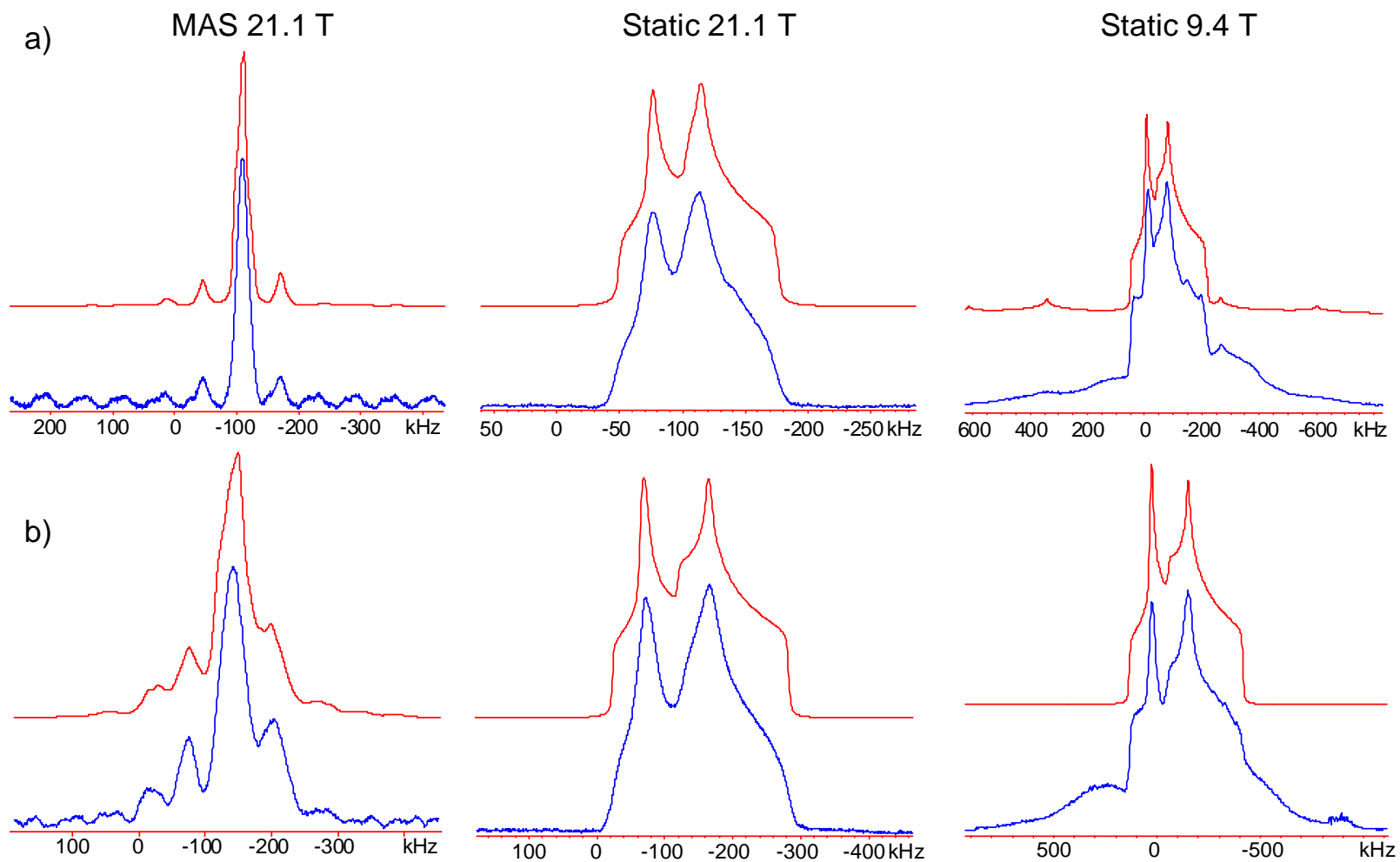


Figure 5.4. ^{115}In NMR spectra of a) InI and b) InBr. The MAS spectra were acquired at $\nu_{\text{rot}} = 62.5$ kHz. Top and bottom traces are simulated and experimental spectra, respectively.

Indium(I) Trifluoromethanesulfonate, [In][OTf]. The structure of [In][OTf] has two indium sites with very similar geometry.³⁴ The coordination environment of the indium atoms consist of four short contacts (less than 3 Å) with oxygen atoms of different triflate anions, and eight other oxygen and fluorine contacts within 4 Å. The four short contacts are arranged in an approximately “see-saw” geometry³⁴ and are oriented to one side of the indium atom (Scheme 5.1f). The ¹¹⁵In NMR patterns (Figure 5.5) are the broadest (i.e. 575 kHz at 9.4 T and 290 kHz at 21.1 T) of all of the spectra discussed so far.

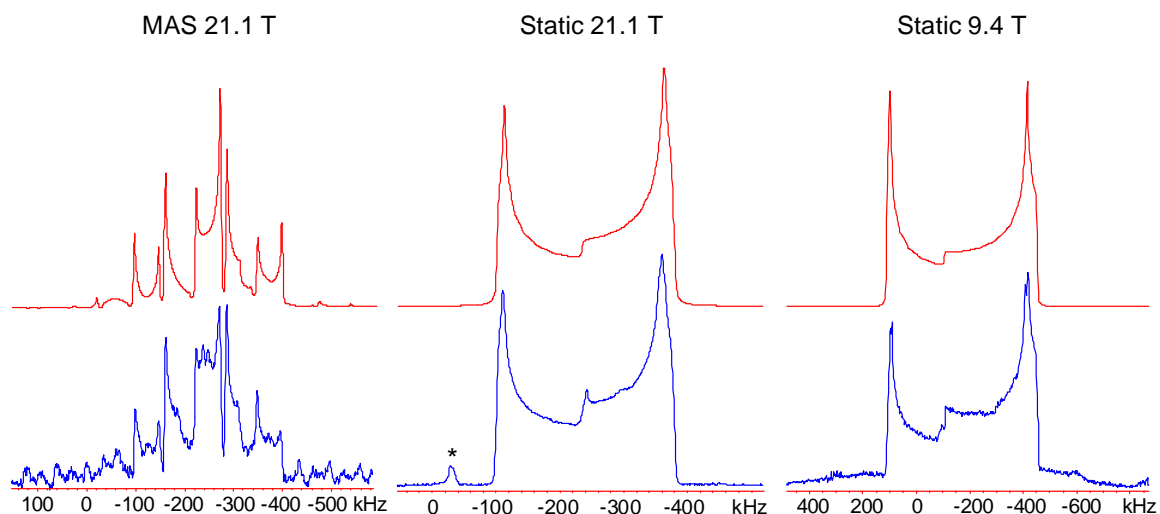


Figure 5.5. ¹¹⁵In NMR spectra of a) [In][OTf]. The MAS spectra were acquired at $\nu_{\text{rot}} = 62.5$ kHz. *: Impurity, top and bottom traces are simulated and experimental spectra, respectively.

Due to the structural similarities of the two sites, the NMR parameters are very similar, and differing sets of parameters cannot be obtained from the spectra acquired at 21.1 T. Surprisingly, there is some evidence of the two separate sites in the static ¹¹⁵In NMR spectrum acquired at 9.4 T. Structurally similar sites are most often distinguished via

slight differences in values of δ_{iso} , which are more easily differentiated at higher magnetic fields due to the higher frequency dispersion of chemical shifts. In this case, it is very likely that the values of δ_{iso} for the two In(I) sites are identical, and therefore not resolved at either field. However, the C_Q (and possibly η_Q) values are different enough that two patterns can be partially resolved at 9.4 T, since the effect of the second-order quadrupolar interaction on the CT pattern breadth scales as the inverse of B_0 . Unfortunately, we were not able to obtain reliable parameters from a two site fit, and therefore only report one set of parameters with larger uncertainties (a two site fit of the 9.4 T spectrum is possible, but the parameters for each site are within the other site's experimental uncertainties, Figure C.5.7). The C_Q value of [In][OTf] is the largest among those of all of the systems studied herein. The almost zero η_Q value indicates that the EFG tensor is axially symmetric and that V_{33} is the distinct component. The span is also the largest of the systems herein, but contributes only to ca. 9% of the total breadth of the NMR pattern (Figure C.5.8).

5.3.2 Theoretical calculations of ^{115}In EFG and NS tensors.

First principles calculations of the ^{115}In NMR tensor parameters were performed in order to correlate the tensor orientations and parameters with molecular structure and symmetry, and to provide a deeper insight into the physical origins of the NMR interactions. The development of such correlations will be helpful in modeling the structures of indium containing systems for which single crystals suitable for XRD experiments are unobtainable (i.e., amorphous and nano- or microcrystalline systems).

Due to the periodic nature of the most of the systems herein, CASTEP software was used for the calculations of the NMR parameters. The results of these calculations are compared to the experimental values in Tables 5.2. The calculated C_Q values are consistently overestimated; however, certain experimental trends are replicated (*vide infra*).

Table 5.2. Comparison of the experimental and theoretical ^{115}In EFG and CS tensor parameters.

	V_{11} (au)	V_{22} (au)	V_{33} (au)	$C_Q(^{115}\text{In})/\text{MHz}^a$	η_Q	$\delta_{\text{iso}}/\text{ppm}$	Ω/ppm	κ	α/deg	β/deg	γ/deg
$[\text{In}^+][\text{GaCl}_4]$ Exp.	----	----	----	22.0(6)	0.2(1)	-1115(10)	60(20)	0.7(3)	65(20)	8(6)	5(5)
$[\text{In}^+][\text{GaCl}_4]$ Cal.	0.1074	0.1127	-0.2201	-41.9	0.02	-1115	112	0.83	90	5	90
$[\text{In}([15]\text{Crown-5})_2][\text{OTf}]$ Exp.	----	----	----	28.4(10)	0.18(10)	-1192(15)	75(15)	0.2(4)	50(30)	90(10)	5(5)
$[\text{In}([15]\text{Crown-5})_2][\text{OTf}]$ Cal.	-0.0959	-0.1466	0.2425	46.2	0.21	-1153	109	0.30	19	76	13
InI Exp.	----	----	----	44(1)	0.7(1)	-480(20)	110(50)	0.8(2)	0	0	0
InI Cal.	0.0622	0.2443	-0.3065	-58.3	0.59	-545	29	-0.29	45(40)	5(5)	0
InBr Exp.	----	----	----	67(2)	0.58(8)	-580(40)	140(40)	0.4(3)	0	0	0
InBr Cal.	0.0924	0.3525	-0.4449	-84.7	0.58	-583	120	0.94	30(20)	5(5)	30(20)
InOTf Exp.	----	----	----	80.5(15)	0.07(3)	-1045(15)	260(60)	0.3(2)	50(30)	3(3)	30(20)
$[\text{In}][\text{OTf}]$ Cal. Site 1	0.2066	0.3309	-0.5375	-102.3	0.23	-1083	236	0.44	51	2	22
$[\text{In}][\text{OTf}]$ Cal. Site 2	0.2442	0.3292	-0.5734	-109.1	0.15	-1075	248	0.56	44	10	28

^a Values of C_Q ($C_Q = eQV_{33}/h$) are calculated by converting from atomic units to Hz by multiplying V_{33} by $(eQ/h)(9.7177 \times 10^{21} \text{ Vm}^{-2})$, where $Q(^{115}\text{In}) = 0.81 \times 10^{-28} \text{ m}^2$. The signs of experimental C_Q values are unknown; signs of theoretically calculated values of C_Q are determined from calculations. ^b The calculated CS are reported with respect to $[\text{In}][\text{GaCl}_4]$ using the equation: $\delta_{\text{iso}(\text{sample})}/\text{ppm} = \sigma_{\text{iso}}([\text{In}][\text{GaCl}_4])/\text{ppm} - \sigma_{\text{iso}}(\text{sample})/\text{ppm} - 1115 \text{ ppm}$

This could arise from either the limitations of the basis set or density functional, and/or the degree of uncertainty in the experimentally measured and theoretically calculated ^{115}In nuclear quadrupole moments;^{65,66} however, plotting the experimental values of C_Q versus calculated values yields excellent linear correlation ($R = 0.990$, Figure 5.6a). In tests of several of the systems, the use of different basis sets did not result in significant variation in the calculated values of C_Q . The correlation for the experimental and calculated η_Q values is reasonable ($R = 0.808$, Figure 5.6b). There are excellent correlations between the experimental and calculated isotropic chemical shifts and spans ($R(\delta_{\text{iso}}) = 0.999$ and $R(\Omega) = 0.944$, respectively); however, the correlation is only fair for the skew values ($R = 0.718$, when the κ of InI is excluded, Figure 5.7).

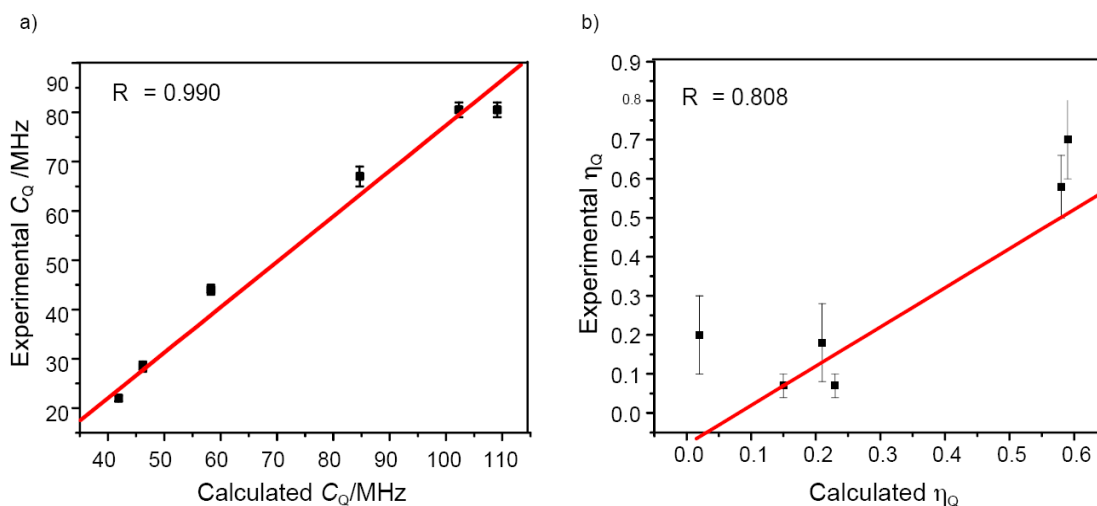


Figure 5.6. Correlations between the experimental and calculated ^{115}In a) C_Q and b) η_Q values.

Investigating the orientations of the indium EFG and nuclear shielding (NS) tensors with respect to the periodic (or molecular) solid-state structures is important for understanding the origins of these tensors. Some specific cases are discussed below.

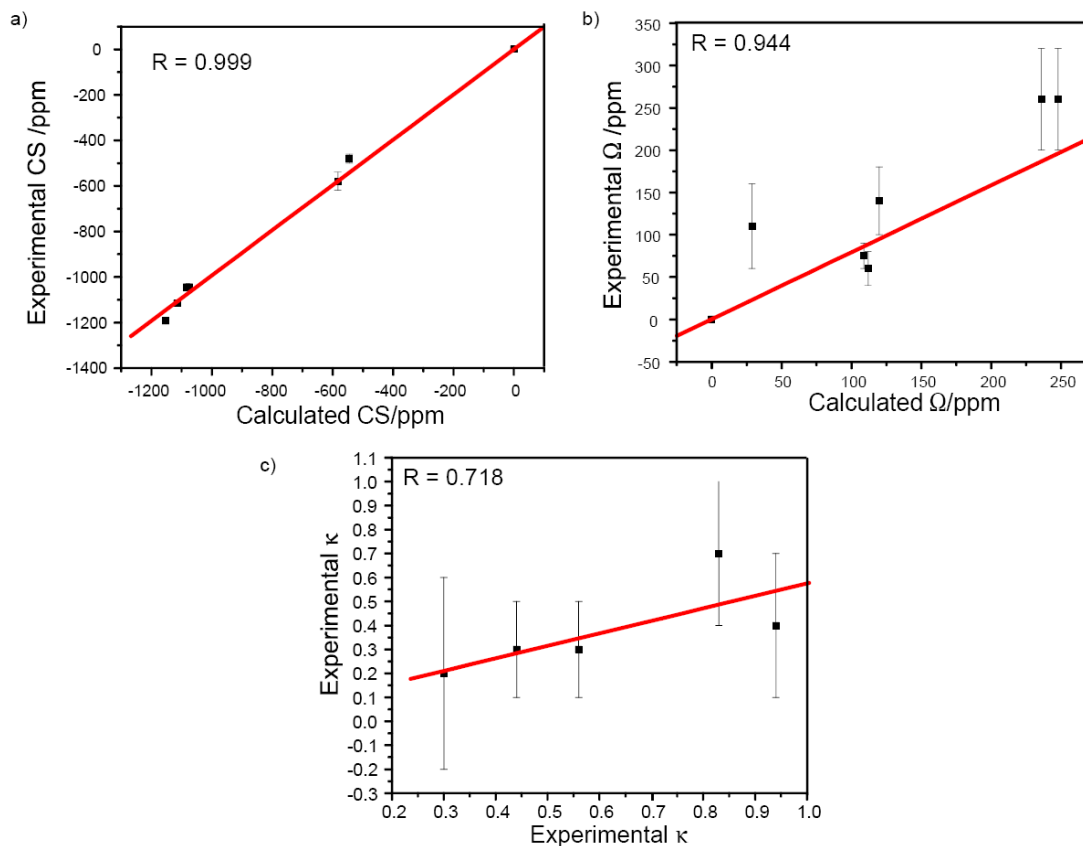


Figure 5.7. Correlations between the experimental and calculated ^{115}In a) chemical shift (CS), b) span (Ω) and c) skew (κ) values.

For $[\text{In}][\text{GaCl}_4]$, the largest component of the EFG tensor, V_{33} , is the distinct component and is positioned in the mirror plane containing the four equatorial chlorine atoms, perfectly bisecting the angles $\angle(\text{Cl1-In-Cl2})$ and $\angle(\text{Cl3-In-Cl4})$ (Figure 5.8a), and V_{11} bisects the angles $\angle(\text{Cl1-In-Cl3})$ and $\angle(\text{Cl2-In-Cl4})$. In addition, the NS tensor is nearly coincident with the EFG tensor ($\angle(V_{11}\text{-In-}\sigma_{11}) = 0^\circ$, $\angle(V_{22}\text{-In-}\sigma_{22}) = 5.02^\circ$, $\angle(V_{33}\text{-In-}\sigma_{33}) = 5.02^\circ$), in agreement with experimental predictions.

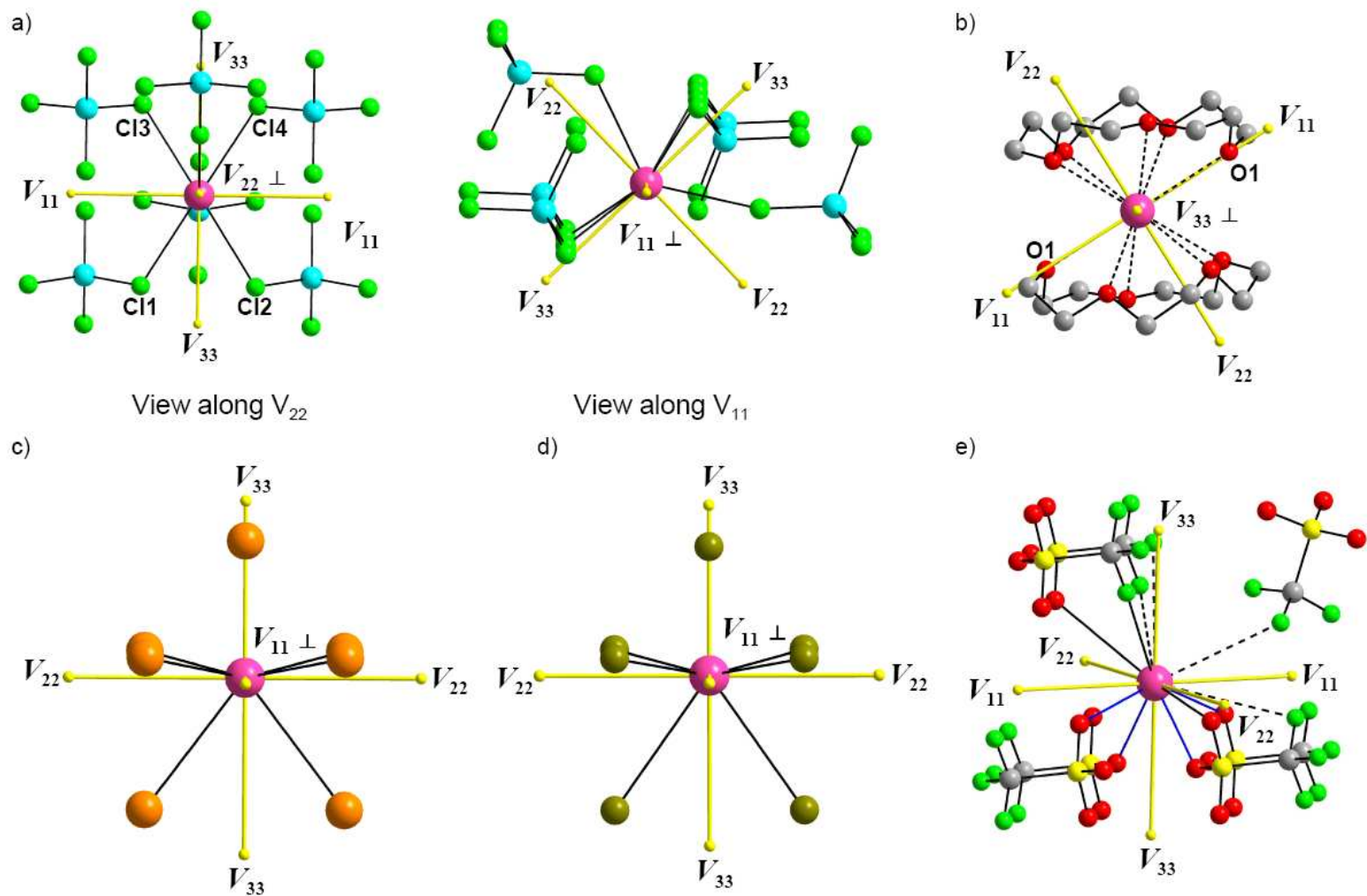


Figure 5.8. The ^{115}In EFG tensor orientations in a) $[\text{In}][\text{GaCl}_4]$, b) $[\text{In}([15]\text{crown-5})_2][\text{OTf}]$, c) InI d) InBr , and f) $[\text{In}][\text{OTf}]$. The blue bonds in f are those within 3 \AA from the indium, the solid black bonds are within 3.5 \AA and the dashed ones are within 4 \AA .

For calculations conducted upon $[\text{In}(\text{15-crown-5})_2][\text{OTf}]$, the triflate anions were replaced by fluorine atoms (i.e. fluorine atoms were positioned at the xyz coordinate of the triflate sulfur atoms), due to the disorder in the triflate groups. V_{33} , the distinct component, is oriented in the direction perpendicular to the fivefold pseudo-rotational axis, indicating that the largest change in the EFG is in this direction (Figure 5.8b). V_{11} and V_{22} are similar in magnitude, with V_{11} aligned close to two of the In-O contacts ($\angle V_{11}\text{-In-O1} = 5.95^\circ$). The NS tensor is oriented such that σ_{33} is in the direction of the pseudo-fivefold rotational axis and thus nearly perpendicular to V_{33} ($\angle(V_{33}\text{-In-}\sigma_{33}) = 76.06^\circ$), in agreement with experimental findings.

The orientations of the EFG tensors in InBr and InI are similar, which is unsurprising, since they are isostructural (Figure 5.8c, d). In both cases, the η_Q values indicate that all three components of the EFG tensor are different. V_{33} is oriented exactly along the shortest InX (X = I, Br) bonds. V_{11} and V_{22} bisect the X-In-X angles, with V_{11} oriented at 90° from the longest equatorial In-X bonds, and V_{22} in the plane of these bonds. In the case of InI, the NS tensor components are oriented such that σ_{22} is aligned with V_{22} , and V_{33} is aligned with σ_{33} , as expected from the experiment. In the case of InBr, V_{33} and σ_{33} are also coincident, in agreement with the experiment. V_{22} and V_{11} are aligned with σ_{11} and σ_{22} , respectively.

In the case of $[\text{In}][\text{OTf}]$, the NMR parameters of both indium sites are very similar; therefore, we only discuss the tensor orientation of site 2. Each indium site has four short In-O contacts from the four different OTf groups. The four short contacts are about a pseudo-twofold rotational axis (though there is no twofold rotational axis at the In

site or in the overall cluster model). V_{33} is oriented close to this pseudo-twofold axis (Figure 5.8e), and V_{11} and V_{22} are oriented into similar environments, resulting in a near zero η_Q value. V_{33} is almost coincident with σ_{33} , as predicted experimentally.

Finally, a comment should be made on the signs of the quadrupolar coupling constants, and the importance of these signs in thinking about the relationships between the tensor parameters, tensor orientations and local In environments. C_Q signs are not available from SSNMR spectra of quadrupolar nuclei, though they are available indirectly from SSNMR spectra of spin-1/2 nuclei which are J - and dipolar-coupled to quadrupolar nuclei.⁶⁷ However, the signs of C_Q are available from first principles calculations, and do provide some insight into the nature of the environment into which V_{33} is directed. In all of the complexes discussed herein, excepting $[\text{In}([\text{15}]\text{crown-5})_2][\text{OTf}]$, the C_Q values are negative and the V_{33} components of the EFG tensor are oriented along short In-X (X = Cl, O, I, Br) contacts. Interestingly, in $[\text{In}([\text{15}]\text{crown-5})_2][\text{OTf}]$, which has a positive value of C_Q , the V_{33} component is not aligned near any atoms, bonds or other sources of electron density. This is consistent with recent predictions from a detailed theoretical study of the relationships between EFG tensor components, orientation, signs and local structure, in which it is shown that negative electronic charge distributions that are stretched in a particular direction generally produce negative EFGs along this direction, while the absence of such charge distributions results in positive EFGs.⁶⁸

5.4 Conclusions

This work represents the first systematic study of low-oxidation state indium complexes using ^{115}In SSNMR. ^{115}In SSNMR is proven to be a valuable tool for characterization of a variety of low-oxidation state indium complexes, including microcrystalline and/or multi-valence systems. The NMR parameters extracted from the ^{115}In SSNMR spectra provide information about the electronic environment, geometry, symmetry and oxidation states of the indium sites. Such information is particularly useful for systems which are insoluble in most organic solvents (as is the case for most In(I) complexes), and/or systems with unknown structures.

Theoretical calculations of the ^{115}In EFG and CS tensor parameters are, for the most part, in good correlation with the experimental values. The orientations of the EFG and CS tensor components provide insight into the origin of these tensors and their correlations to molecular structure and symmetry. These calculations will also be helpful, in combination with experimental NMR, for proposing structural models in cases where crystallographic data are not available. We hope that this work will encourage the use of ^{115}In SSNMR spectroscopy as a primary technique for probing the indium chemical environments in a wide variety of indium-containing systems.

5.5 Bibliography

- (1) Ellis, B. D.; Macdonald, C. L. B. *Coord. Chem. Rev.* **2007**, *251*, 936-973.
- (2) Dyson, P. J. *Coord. Chem. Rev.* **2004**, *248*, 2443-2458.
- (3) Roesky, P. W. *Dalton Trans.* **2009**, 1887-1893.
- (4) Mindiola, D. J. *Acc. Chem. Res.* **2006**, *39*, 813-821.
- (5) Housecroft, C. E. *Compr. Coord. Chem. II* **2004**, *5*, 555-731.
- (6) Linti, G.; Schnockel, H. *Coord. Chem. Rev.* **2000**, *206-207*, 285-319.
- (7) Tuck, D. G. *Chem. Soc. Rev.* **1993**, *22*, 269-276.
- (8) Macdonald C.L.B.; B.D., E. In *Encyclopedia of Inorganic Chemistry*; R.B., K., Ed.; John Wiley & Sons Ltd, 2005.
- (9) Andrews, C. G.; Macdonald, C. L. B. *Angew. Chem., Int. Edit.* **2005**, *44*, 7453-7456.
- (10) Andrews, C. G.; MacDonald, C. L. B. *J. Organomet. Chem.* **2005**, *690*, 5090-5097.
- (11) Aldridge, S. *Angew. Chem., Int. Edit.* **2006**, *45*, 8097-8099.
- (12) Cooper, B. F. T.; Macdonald, C. L. B. *J. Organomet. Chem.* **2008**, *693*, 1707-1711.
- (13) Baker, R. J.; Jones, C. *Coord. Chem. Rev.* **2005**, *249*, 1857-1869.
- (14) Gemel, C.; Steinke, T.; Cokoja, M.; Kempter, A.; Fischer, R. A. *Eur. J. Inorg. Chem.* **2004**, 4161-4176.
- (15) Harris, R. K.; Becker, E. D.; Cabral De Menezes, S. M.; Goodfellow, R.; Granger, P. *Pure Appl. Chem.* **2001**, *73*, 1795-1818.
- (16) Chen, F.; Ma, G.; Cavell, G.; Terskikh, V. V.; Wasylishen, R. E. *Chem. Commun.* **2008**, 5933-5935.
- (17) McGarvey, B. R.; Trudell, C. O.; Tuck, D. G.; Victoriano, L. *Inorg. Chem.* **1980**, *19*, 3432-3436.
- (18) Colton, R.; Dakternieks, D.; Hauenstein, J. *Aust. J. Chem.* **1981**, *34*, 949-955.
- (19) Malyarick, M. A.; Ilyuhin, A. B.; Petrosyants, S. P. *Polyhedron* **1993**, *12*, 2403-2409.
- (20) Cheng, F.; Friend, S. I.; Hector, A. L.; Levason, W.; Reid, G.; Webster, M.; Zhang, W. *Inorg. Chem.* **2008**, *47*, 9691-9700.

- (21) Caravan, P.; Orvig, C. *Inorg. Chem.* **1997**, *36*, 236-248.
- (22) Kuznetsov, A. N.; Popovkin, B. A.; Henderson, W.; Taylor, M. J.; Bengtsson-Kloo, L. *Dalton* **2000**, 1777-1781.
- (23) Alcock, N. W.; Degnan, I. A.; Howarth, O. W.; Wallbridge, M. G. H. *J. Chem. Soc., Dalton Trans.* **1992**, 2775-2780.
- (24) Hinton, J. F.; Briggs, R. W. *NMR Period. Table* **1978**, 279-308.
- (25) Malyarick, M. A.; Petrosyants, S. P. *Inorg. Chem.* **1993**, *32*, 2265-2268.
- (26) Kodweiss, J.; Koehnlein, D.; Koessler, G.; Lutz, O.; Messner, W.; Mohn, K. R.; Nolle, A.; Nothaft, G.; Ruppert, P.; et al. *Z. Naturforsch., A: Phys. Sci.* **1986**, *41A*, 471-477.
- (27) Tomita, Y.; Yamada, K.; Ohki, H.; Okuda, T. *Z. Naturforsch., A: Phys. Sci.* **1998**, *53*, 466-472.
- (28) Schmidt, E. V.; Ermakov, V. L.; Gnezdilov, O. I.; Matukhin, V. L.; Korzun, B. V.; Fadeeva, A. A.; Khabibullina, I. K. *J. Appl. Spectrosc.* **2009**, *76*, 667-671.
- (29) Jung, W.-S.; Han, O. H.; Chae, S.-A. *Mater. Lett.* **2007**, *61*, 3413-3415.
- (30) Yamada, K.; Kumano, K.; Okuda, T. *Solid State Ionics* **2005**, *176*, 823-829.
- (31) Yamada, K.; Kumano, K.; Okuda, T. *Solid State Ionics* **2006**, *177*, 1691-1695.
- (32) Han, O. H.; Timken, H. K. C.; Oldfield, E. *J. Chem. Phys.* **1988**, *89*, 6046-6052.
- (33) Khabibullin, I. K.; Matukhin, V. L.; Ermakov, V. L.; Gnezdilov, O. I.; Korzun, B. V.; Schmidt, E. V. *Semiconductors* **2009**, *43*, 1-3.
- (34) Tomita, Y.; Yonekura, H.; Yamauchi, Y.; Yamada, K.; Kobayashi, K. *Z. Naturforsch., A: Phys. Sci.* **2002**, *57*, 447-450.
- (35) Chen, F.; Ma, G.; Bernard, G. M.; Cavell, R. G.; McDonald, R.; Ferguson, M. J.; Wasylshen, R. E. *J. Am. Chem. Soc.* **2010**, *132*, 5479-5493.
- (36) Boehlmann, W.; Klepel, O.; Michel, D.; Papp, H. *Stud. Surf. Sci. Catal.* **2002**, *142B*, 1355-1362.
- (37) Iijima, T.; Hashi, K.; Goto, A.; Shimizu, T.; Ohki, S. *Jpn. J. Appl. Phys., Part 1* **2006**, *45*, 651-655.
- (38) Clark, S. J.; Segall, M. D.; Pickard, C. J.; Hasnip, P. J.; Probert, M. I. J.; Refson, K.;

- Payne, M. C. *Z. Kristallogr.* **2005**, *220*, 567-570.
- (39) MacDonald, C. L. B.; Corrente, A. M.; Andrews, C. G.; Taylor, A.; Ellis, B. D. *Chem. Commun.* **2004**, 250-251.
- (40) Medek, A.; Frydman, V.; Frydman, L. *J. Phys. Chem. A* **1999**, *103*, 4830-4835.
- (41) Massiot, D.; Farnan, I.; Gautier, N.; Trumeau, D.; Trokiner, A.; Coutures, J. P. *Solid State Nucl. Magn. Reson.* **1995**, *4*, 241-248.
- (42) Eichele, K.; Wasylishen, R. E.; WSolids NMR Simulation Package, 1.17.30 ed.; Dalhousie University: Halifax, CA, 2001.
- (43) Massiot, D.; Fayon, F.; Capron, M.; King, I.; Le Calve, S.; Alonso, B.; Durand, J.-O.; Bujoli, B.; Gan, Z.; Hoatson, G. *Magn. Reson. Chem.* **2002**, *40*, 70-76.
- (44) O'Dell, L. A.; Schurko, R. W. *Chem. Phys. Lett.* **2008**, *464*, 97-102.
- (45) Kupce, E.; Freeman, R. *J. Magn. Reson. Ser. A* **1995**, *115*, 273-276.
- (46) Meyer, G.; Staffel, T.; Irmeler, M. *Thermochim. Acta* **1990**, *160*, 63-70.
- (47) Meyer, G.; Staffel, T. *Z. Anorg. Allg. Chem.* **1989**, *574*, 114-118.
- (48) Staffel, T.; Meyer, G. *Z. Anorg. Allg. Chem.* **1987**, *552*, 113-122.
- (49) Profeta, M.; Mauri, F.; Pickard, C. J. *J. Am. Chem. Soc.* **2003**, *125*, 541-548.
- (50) Perdew, J. P.; Burke, K.; Ernzerhof, M. *Phys. Rev. Lett.* **1996**, *77*, 3865-3868.
- (51) Perdew, J. P.; Burke, K.; Ernzerhof, M. *Phys. Rev. Lett.* **1998**, *80*, 891.
- (52) Pickard, C. J.; Mauri, F. *Phys. Rev. B* **2001**, *63*, 245101/245101-245101/245113.
- (53) Yates, J. R.; Pickard, C. J.; Mauri, F. *Phys. Rev. B* **2007**, *76*, 024401/024401-024401/024411.
- (54) Yates, J. R.; Pickard, C. J.; Payne, M. C.; Mauri, F. *J. Chem. Phys.* **2003**, *118*, 5746-5753.
- (55) Warren, W. W., Jr.; Schoenherr, G.; Hensel, F. *Chem. Phys. Lett.* **1983**, *96*, 505-508.
- (56) Aiken, J. K.; Haley, J. B.; Terrey, H. *Trans. Faraday Soc.* **1936**, *32*, 1617-1622.
- (57) Okuda, T.; Shimoe, H.; Monta, M.; Nakata, A.; Terao, H.; Yamada, K. *J. Mol. Struct.* **1994**, *319*, 197-201.
- (58) Khan, M. A.; Tuck, D. G. *Inorg. Chim. Acta* **1985**, *97*, 73-76.

- (59) Chapman, R. P.; Bryce, D. L. *Phys. Chem. Chem. Phys.* **2009**, *11*, 6987-6998.
- (60) Garton, G.; Powell, H. M. *J. Inorg. Nucl. Chem.* **1957**, *4*, 84-89.
- (61) Kloo, L. A.; Taylor, M. J. *J. Chem. Soc., Dalton Trans.* **1997**, 2693-2696.
- (62) Levy, F.; Mooser, E. *Helv. Phys. Acta* **1972**, *45*, 69-73.
- (63) Hamaed, H.; Laschuk, M. W.; Terskikh, V. V.; Schurko, R. W. *J. Am. Chem. Soc.* **2009**, *131*, 8271-8279.
- (64) Semin, G. K.; Babushkina, T. A.; Yohobson, G. G. *Nuclear Quadrupole Resonance in Chemistry*; John Wiley & Sons: New York, 1975.
- (65) Errico, L. A.; Weissmann, M.; Renteria, M. *Los Alamos National Laboratory, Preprint Archive, Nuclear Experiment* **2004**, 1-6, arXiv:nucl-ex/0408005.
- (66) Errico, L. A.; Renteria, M. *Phys. Rev. B* **2006**, *73*, 115125/115121-115125/115126.
- (67) Harris, R. K.; Olivieri, A. C. *Prog. Nucl. Magn. Reson. Spectrosc.* **1992**, *24*, 435-456.
- (68) Autschbach, J.; Zheng, S.; Schurko, R. W. *Conc. Magn. Reson.* **2010**, *36A*, 84 - 126.

Chapter 6

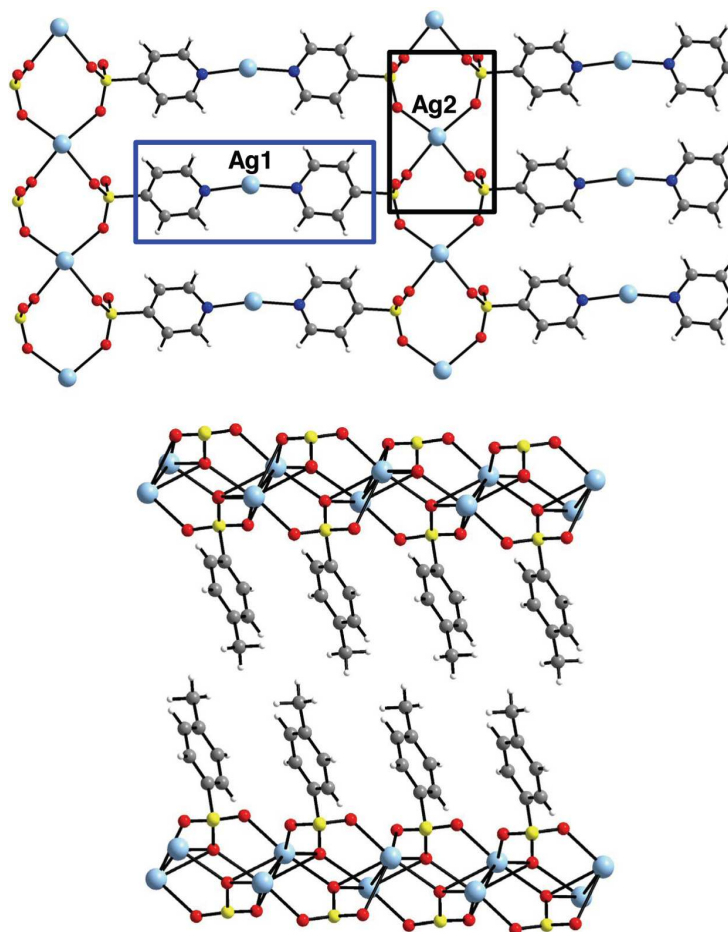
Investigation of Silver-Containing Layered Materials and Their Interactions with Primary Amines Using Solid-State ^{109}Ag and ^{15}N NMR Spectroscopy and First Principles Calculations

6.1 Introduction

Coordination network materials, also referred to as metal-organic frameworks (MOFs), represent a compromise between wholly inorganic or organic solids, often having the chemical and physical properties of the individual building blocks, as well as new properties that result from their connectivity.¹⁻⁶ Solid silver sulfonates are representative of this subtle balance, as they are able to form stable layered networks composed of sulfonate bridges between silver ions.⁷⁻¹² The flexibility of their coordination chemistry and the adaptability of their lamellar structures enable the possibilities of selective reactivity or absorption of guest molecules.¹³⁻¹⁵

Shimizu and co-workers recently reported the synthesis and characterization of several new layered materials formed by the reaction of silver sulfonates with primary amines;^{13,15} interestingly, layered solids were not produced in reactions of silver sulfonates with any other class of organic reactants. It was proposed that the new layered materials were likely formed from the intercalation of primary amines, on the basis of interlayer distances determined by powder X-ray diffraction (XRD). After publication of this study, several questions arose regarding the nature of these materials and the mechanism behind their synthesis. First, does the formation of these new materials actually result from the intercalation of primary amines? Second, are there selective

interactions between the silver atoms and amine nitrogen atoms? Finally, can a combination of XRD methods and solid-state NMR of silver and nitrogen sites in these materials lend insight into their structures and the nature of their formation? While detailed crystal structures are available for the silver sulfonate starting materials (Scheme 6.1), they are not available for many intercalation or layered solids, since most often, the samples have long-range disorder and suitably sized single crystals cannot be isolated.



Scheme 6.1 Schematic representation of the crystal structures of $[\text{Ag}(4\text{-pyridinesulfonate})]_4$ (**1a**, top) and $[\text{Ag}(p\text{-toluenesulfonate})]$ (**2a**, bottom). There are two silver sites in **1a** and only one site in **2a**.

Solid-state NMR (SSNMR) represents a powerful complementary tool for the characterization of structure, connectivity and dynamics in such systems; most notably, the understanding of metal-ligand bonding interactions is crucial for the future rational design of such materials.

While ^{15}N NMR experiments on solid materials have become increasingly routine, solid-state silver NMR spectroscopy is infrequently applied despite the regular occurrence and significance of silver sites in a variety of technologically important materials.¹⁶⁻²² This is partly due to the fact that ^{107}Ag and ^{109}Ag (both spin-1/2) have low gyromagnetic ratios (γ) and correspondingly low receptivities (0.198 and 0.28, respectively, compared to ^{13}C). In addition, $^{107/109}\text{Ag}$ nuclei in solids often have exceedingly large longitudinal relaxation time constants (T_1) which may be on the order of minutes to hours, making acquisition of high-quality ^{109}Ag NMR spectra very challenging.^{22,23} Further, NMR experiments on low- γ nuclei (e.g., $\nu_0 = 18.67$ MHz at 9.4 T) are plagued by acoustic probe ringing, resulting in interference in the NMR free induction decay (FID) which partially or wholly obliterates the signal.

The cross-polarization magic-angle spinning (CP/MAS) experiment can address the sensitivity problems stemming from poor receptivity and long relaxation times; however, there must be spatially proximate, dipolar-coupled, abundant nuclei present (e.g., ^1H , ^{19}F , etc.).^{24,25} The experimental time can be reduced due to the signal enhancement from CP (e.g., the maximum theoretical signal-to-noise ratio (S/N) enhancement factor for ^1H - ^{109}Ag CP/MAS NMR experiments is proportional to $\gamma(^1\text{H})/\gamma(^{109}\text{Ag}) = 21.7$) and the use of shorter recycle delays, since the CP/MAS NMR experiment depends on the T_1 of the abundant spin (which is typically much smaller than

that of ^{109}Ag). If higher spinning speeds are required or weaker dipolar couplings are present, the variable-amplitude CP (VACP) or RAMP-CP experiments can be used to obtain optimal CP signal.²⁶⁻³⁰ However, all of the CP experiments place a significant amount of stress on the solid-state NMR probes, since long contact times of 30 ms or more are often needed to obtain reasonable CP to the low-gamma silver nuclides. The use of silver NMR is continuing to increase, due to the availability of new hardware for low- γ nuclei,^{31,32} the development of pulse sequences for S/N enhancement,³³⁻³⁵ and the recent proliferation of ultra-high field NMR spectrometers.³⁶⁻⁴⁰

Herein, we report upon the application of solid-state ^{109}Ag , ^{15}N and ^{13}C NMR experiments to the study of the molecular structure of silver-containing layered materials. The silver-containing systems include $[\text{Ag}(4\text{-pyridinesulfonate})]_4$ (**1a**), four samples of **1a** reacted with $\text{C}_{12}\text{H}_{25}\text{NH}_2$ in different ratios, 1:0.5, 1:1, 1:1.5 and 1:2, (**1b**, **1c**, **1d** and **1e**, respectively, where **1c** and **1e** were synthesized with 98% isotopically enriched $\text{C}_{12}\text{H}_{25}^{15}\text{NH}_2$),¹⁵ $[\text{Ag}(p\text{-toluenesulfonate})]$ (**2a**),¹³ **2a** reacted with $\text{C}_{12}\text{H}_{25}\text{NH}_2$ and $\text{C}_9\text{H}_{19}\text{NH}_2$ in a 1:2 ratio (**2b** and **2c**, respectively),¹³ and $[\text{Ag}(\text{C}_{12}\text{H}_{25}\text{NH}_2)_2]^+[\text{NO}_3]^-$ (**3**).⁴¹ Due to the extreme sensitivity of silver chemical shift (CS) tensors to structural changes,⁴² ^{109}Ag NMR experiments can be used to probe structural differences between starting materials and amine-containing samples. ^{109}Ag and ^{15}N NMR experiments on systems synthesized with ^{15}N -enriched dodecylamine are used to identify the nature of the silver-nitrogen interactions, since they are crucial in the formation of these materials.⁴³ Finally, *ab initio* calculations of silver and nitrogen chemical shielding tensors, as well as one-bond ^{109}Ag - $^{14/15}\text{N}$ J -couplings, are presented to aid in proposing a tentative structural model for these new materials.

6.2 Experimental

6.2.1 Sample Preparation

All chemicals were purchased from Sigma Aldrich Chemical Co. and used as received. The 98% enriched ^{15}N -dodecylamine was purchased from Cambridge Isotope Laboratories. C, N and H chemical analyses were obtained on a Control Equipment Corporation Model 440 system, with samples weighed in ambient laboratory atmosphere. FT-IR data were obtained from KBr pellets on a Nicolet Nexus 470 Fourier transform spectrometer. DSC/TGA experiments were carried out on a Netzsch 449C Simultaneous Thermal Analyzer in a nitrogen atmosphere. Samples (ca. 5 mg) were placed in aluminum pans and referenced against an empty pan for the DSC measurements. Typical heating programs involved data collection between 25 and 450 °C with heating rates of 5 °C/min.

Synthesis of alkylamine materials. *Synthesis of **1b -1e**.* An appropriate stoichiometric amount of dodecylamine (unlabelled or 98% ^{15}N -enriched) was dissolved in diethyl ether and added to **1a** suspended in diethyl ether (e.g., for **1c**, 1.0 mmol of dodecylamine was added per silver center to produce the 1:1 complex). The heterogeneous mixture was stirred for 6 hours, after which time the ether was removed by filtration. No uptake of diethyl ether by the host was observed in either the presence or absence of amine molecules (as determined by powder XRD and simultaneous thermal analysis (STA)). Samples of **1a**, **2b**, **2c** and **3** were synthesized as described in the literature.^{13,15,41}

[Ag(4-pyridinesulfonate)]₄ reacted with C₁₂H₂₅NH₂ in 1:0.5, 1b. Yield: 95%.
Anal.Cald for AgC₁₁H_{17.5}N_{1.5}SO₃ (357.51 g/mol): C, 36.83; H, 4.92; N, 5.86. Found: C,

36.12; H, 4.66; N, 5.68. DSC/TGA: 97 °C (11.8 J g⁻¹, endo), 132 °C (28.5 J g⁻¹, endo), 145 °C to 215 °C (68.5 J g⁻¹, exo), 210 °C to 280 °C (112.5 J g⁻¹, endo), -8.5 % obsd and -25.6% calcd for loss of 0.5 eq C₁₂H₂₅NH₂ in the first two mass loss combined, 290 °C to 410 °C (114.2 J g⁻¹, endo, 5.5 J g⁻¹, endo), loss of remaining amine molecules and decomposition of the material.

[Ag(4-pyridinesulfonate)]₄ reacted with C₁₂H₂₅NH₂ in 1:1, 1c. Yield: 93%.

Anal. Calcd for AgC₁₇H₂₉N₂SO₃ (451.37 g/mol): C, 45.24; H, 6.92; N, 6.21. Found: C, 44.65; H, 6.73; N, 6.01. DSC/TGA: 95 °C (12.0 J g⁻¹, endo), 103 °C (4.7 J g⁻¹, endo), 128 °C (39.9 J g⁻¹, endo), 145 °C to 215 °C (70.5 J g⁻¹, exo), 215 °C to 280 °C (116.5 J g⁻¹, endo), -22.0% obsd and -41.1% calcd for loss of 1.0 eq C₁₂H₂₅NH₂ in the first two mass loss combined, 280 °C to 406 °C (111.2 J g⁻¹, endo; 9.2 J g⁻¹, endo), loss of remaining amine molecules and decomposition of the material.

[Ag(4-pyridinesulfonate)]₄ reacted with C₁₂H₂₅NH₂ in 1:1.5, 1d. Yield: 97%.

Anal. Calcd for AgC₂₃H_{44.5}N_{2.5}SO₃ (544.05 g/mol): Calcd: C, 50.78; H, 8.24; N, 6.44. Found: C, 50.69; H, 8.28; N, 6.40. DSC/TGA: 96 °C (15.6 J g⁻¹, endo), 108 °C (66.7 J g⁻¹, endo), 115 °C to 250 °C (77.9 J g⁻¹, exo), -32.4% obsd and -51.1% calcd for loss of 1.5 C₁₂H₂₅NH₂, 255 °C to 415 °C (139.2 J g⁻¹, endo; 50.9 J g⁻¹, endo), loss of remaining amine and decomposition of the material.

[Ag(4-pyridinesulfonate)]₄ reacted with C₁₂H₂₅NH₂ in 1:2, 1e. Yield: 95%.

Anal. Calcd for AgC₂₉H₅₄N₃SO₃ (632.69 g/mol): C, 55.05; H, 8.60; N, 6.64. Found: C, 55.12; H, 8.77; N, 6.45. DSC/TGA: 95 °C (16.6 J g⁻¹, endo), 114 °C (66.7 J g⁻¹, endo), 115 °C to 254 °C (94.2 J g⁻¹, exo), -37.9% obsd and -58.3% calcd for loss of 2.0 C₁₂H₂₅NH₂, 254 °C to 416 °C (152.2 J g⁻¹, endo; 96.9 J g⁻¹, endo), loss of the remaining

amine and decomposition of the material.^{13,15,41}

6.2.2 Solid-State NMR.

All samples were finely powdered and packed into 5 mm outer diameter zirconium oxide rotors. Solid-state ^{109}Ag , ^{15}N and ^{13}C CP/MAS and VACP/MAS NMR spectra were acquired using a Varian Infinity Plus NMR spectrometer with an Oxford 9.4 T ($\nu_0(^1\text{H}) = 400$ MHz) wide bore magnet, operating at resonance frequencies of $\nu_0(^{109}\text{Ag}) = 18.61$ MHz, $\nu_0(^{15}\text{N}) = 40.50$ MHz and $\nu_0(^{13}\text{C}) = 100.52$ MHz. A Varian-Chemometrics 5 mm triple resonance (HXY) MAS probe was used for all experiments. Probe tuning and matching for low-frequency ^{109}Ag NMR experiments, and acquisition of spectra with reduced acoustic ringing, were accomplished using a Varian low-gamma tuning box and low-gamma pre-amplifier. In addition, ^{15}N CP/MAS NMR spectra of **1c** and **1e** were acquired on a Bruker 900 MHz spectrometer using a 3.2 mm HX MAS probe at the National Ultra-high Field NMR Facility for Solids in Ottawa, Ontario, Canada. The two-pulse phase modulation (TPPM) decoupling sequence⁴⁴ was used for all of the CP/MAS experiments.

^1H - ^{109}Ag CP/MAS NMR. Silver chemical shifts were referenced to a 9 M aqueous solution of AgNO_3 ($\delta_{\text{iso}} = 0.0$ ppm) by using solid silver methane-sulfonate, AgSO_3CH_3 , as a secondary reference ($\delta_{\text{iso}} = 87.2$ ppm).²⁰ Proton-decoupled ^{109}Ag VACP/MAS NMR spectra were acquired with spinning rates (ν_{rot}) ranging from 2.0 to 8.0 kHz, and calibrated recycle times between 6 and 20 s. Proton $\pi/2$ pulse widths ranged between 3.75 and 5.5 μs . Hartmann-Hahn matching²⁴ fields of $\nu_1(^1\text{H}) = 16.8$ and 27.8 kHz were applied with optimized contact times of 30 or 35 ms. In one special case,

proton-decoupled $^{109}\text{Ag}\{^1\text{H}\}$ Bloch decay (single-pulse) experiments were acquired, using a 60° pulse widths of $8\ \mu\text{s}$ and a recycle delay of 300 s. Additional experimental parameters and details are summarised in Table D.6.1, Appendix D).

^1H - ^{15}N CP/MAS NMR. Nitrogen chemical shifts were referenced to liquid NH_3 ($20\ ^\circ\text{C}$), $\delta_{\text{iso}} = 0\ \text{ppm}$, by setting the chemical shift of the ammonium peak of a doubly-labeled solid $^{15}\text{NH}_4^{15}\text{NO}_3$ (98% ^{15}N) sample to 23.8 ppm.⁴⁵ The ^1H - ^{15}N CP/MAS NMR spectra at 9.4 T were acquired at $\nu_{\text{rot}} = 5$ or 6 kHz with an optimized recycle delay of 4 s. A proton $\pi/2$ pulse width of $3.75\ \mu\text{s}$, and a contact time of 2 ms were used, with the collection of between 64 to 152 transients. The ^1H - ^{15}N CP/MAS NMR spectra at 21.1 T were acquired with $\nu_{\text{rot}} = 10$ kHz and a recycle delay of 20 s. A proton $\pi/2$ pulse width of $2.5\ \mu\text{s}$, and contact time of 2 ms were utilized, with 1024 transients collected in each experiment. Additional experimental parameters are summarised in Table D.6.2.

^1H - ^{13}C CP/MAS NMR. ^1H - ^{13}C CP/MAS NMR spectra have been acquired for most of the systems for purposes of probing sample identity and purity; relevant spectra are included in Appendix D (Figures D.6.1-D.6.3). Carbon chemical shifts were referenced to the high frequency chemical shift of solid adamantane ($\delta_{\text{iso}} = 38.57\ \text{ppm}$ with respect to tetramethylsilane, TMS). Spectra with two different spinning speeds were acquired for each sample, and optimized recycle delays of 6 to 12 s were applied. Additional experimental details are summarised in Table D.6.3.

Silver chemical shift parameters were obtained via simulations of experimental spectra using the WSolids software package.⁴⁶

6.2.3 Ab initio calculations.

Ab initio calculations of chemical shielding and J -coupling tensors were performed using Gaussian 03⁴⁷ on Dell precision workstations running Red Hat Linux as well as on Alpha and Opteron workstations on SHARCNET.⁴⁸ All of the calculations were performed using the Restricted Hartree Fock (RHF) method with the valence double-zeta plus polarization (DZVP) basis set⁴⁹ on both the silver and nitrogen atoms⁵⁰ and 6-311G** on all of the other atoms. Molecular coordinates used in the calculations on **1a**¹⁵ and on $[\text{Ag}(\text{NH}_3)_2]_2\text{SO}_4$ (**4**),⁵¹ were taken from the crystal structure data, and those used in the calculations on **1e** and **2b** are based on a structure similar to that reported by Smith et al.⁴³ In all cases, hydrogen atom positions were geometry optimized, using the 6-311G** basis set on all H atoms. The nuclear magnetic shielding tensors were calculated using the gauge-including atomic orbitals method (GIAO).^{52,53}

6.3 Results & Discussion

6.3.1. Solid-state NMR.

In this section, we will first discuss the ^1H - ^{109}Ag CP/MAS NMR spectra of the parent compound **1a**, along with similar spectra of samples **1b** to **1e**, which are obtained from the reaction of **1a** with stoichiometric amounts of amine. Then, ^{15}N CP/MAS NMR data are discussed for **1c** (1:1) and **1e** (1:2), in an effort to further refine our understanding of the layered solids. Third, ^{109}Ag and ^{15}N NMR data are presented for a different series of layered materials, **2a** to **2c**, and compared to the first series of materials, as well as to $[\text{Ag}(\text{C}_{12}\text{H}_{25}\text{NH}_2)_2]^+[\text{NO}_3]^-$ (**3**). Finally, a thorough discussion of ab initio calculations of silver and nitrogen chemical shift tensors, silver-nitrogen

J-couplings, and their use in defining and proposing a structural model for the layered solids, is presented.

[Ag(4-pyridinesulfonate)]₄ (**1a**). ¹H-¹⁰⁹Ag CP/MAS NMR spectra of **1a** acquired at two MAS speeds (Figure 6.1) reveal two peaks with isotropic chemical shifts of 283 and 25 ppm (silver CS parameters are summarized in Table 6.1).

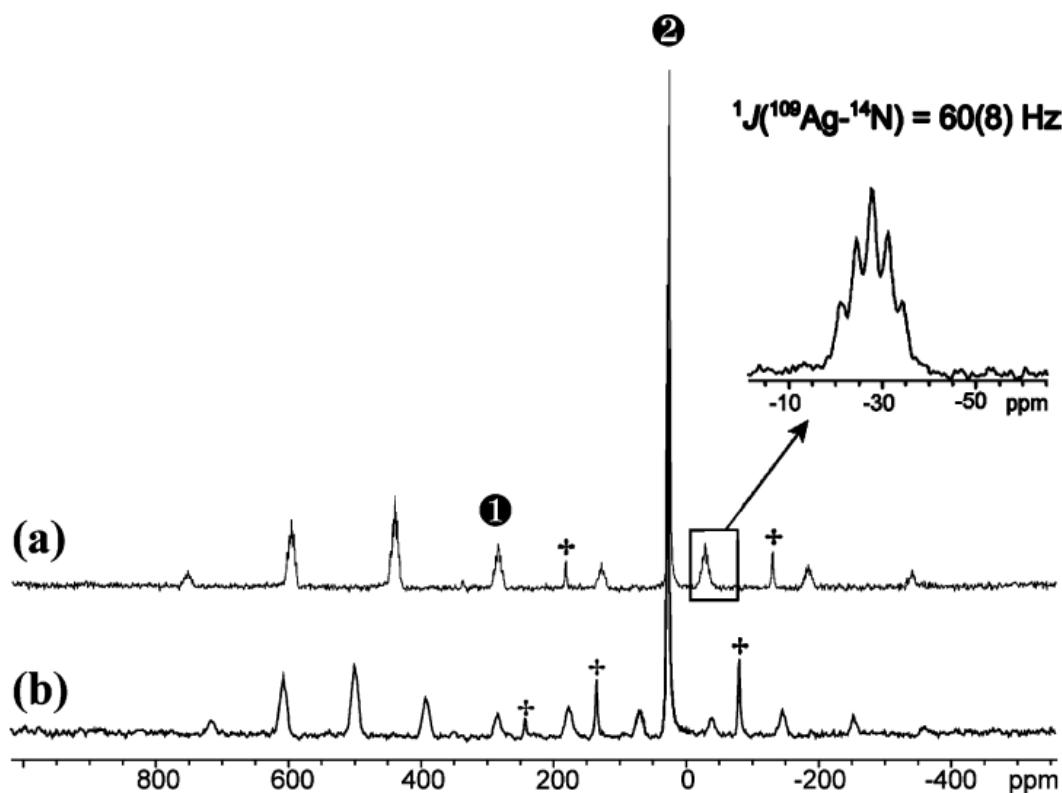


Figure 6.1 Solid-state ¹⁰⁹Ag CP/MAS NMR spectra of **1a** at two different spinning speeds, (a) $\nu_{\text{rot}} = 2.9$ kHz and (b) $\nu_{\text{rot}} = 2.0$ kHz. Isotropic peaks for the two distinct silver sites are designated as 1 and 2. † designates spinning sidebands for site 2; all other peaks are sidebands of site 1.

The two shifts indicate the presence of two crystallographically distinct silver sites, in agreement with the known crystal structure of **1a**.¹⁵ Since the Ag(1) nucleus, the pyridine ligated center, is in a nearly linear environment (N-Ag-N = 168.62°) and the Ag(2)

nucleus, the sulfonate ligated center, is in a distorted tetrahedral environment (Scheme 6.1), the assignment of the resonances is straightforward. Ag(1) should have a significantly larger CSA than Ag(2), since the magnetic shielding is distinct in directions parallel and perpendicular to the N-Ag-N bonding arrangement. On the other hand, Ag(2) is in a relatively spherically symmetric environment by comparison, and the CSA is reduced. Therefore, Ag(1) and Ag(2) are assigned to the peaks at 283 ppm and 25 ppm, respectively. Herzfeld-Berger analysis⁵⁴ was used to extract the silver CS tensor parameters for site 1 using the slow-spinning spectrum (2.0 kHz), yielding a span and skew of $\Omega = 1163$ ppm and $\kappa = 0.74$, respectively. The skew indicates that the shielding tensor is nearly axially symmetric, from which it may be inferred that the distinct component, δ_{33} , is directed along or near the direction of the N-Ag-N bonding arrangement. An accurate CS tensor cannot be obtained from the small manifold of sidebands for Ag(2), but an upper limit of $\Omega = 250$ ppm can be estimated from ab initio calculations (*vide infra*), which is comparable to experimentally measured silver CS tensors for Ag nuclei in five- and six-coordinate silver atoms in AgSO_3CH_3 (183.4(5) ppm) and [Ag(*p*-toluenesulfonate)] (163(4) ppm), respectively.²¹

The ^{109}Ag NMR spectrum acquired at $\nu_{\text{rot}} = 2.9$ kHz (Figure 6.1a) was processed with less line broadening than the slow-spinning spectrum, and fine structure is clearly visible. Closer examination of the pattern with $\delta_{\text{iso}} = 283$ ppm reveals a quintet of 1:2:3:2:1 intensity (Figure 6.1, inset) which arises from indirect spin-spin coupling between ^{109}Ag and two ^{14}N nuclei, $^1J(^{109}\text{Ag}, ^{14}\text{N})$, where ^{14}N is a spin $I = 1$ nucleus (n.a. = 99.63%). The magnitude of $^1J(^{109}\text{Ag}, ^{14}\text{N})$, 60(8) Hz (Table 6.2), is typical for a silver atom bound to an sp^2 nitrogen.²¹

Table 6.1. Experimental ^{109}Ag chemical shift parameters.^a

Compounds	δ_{iso} (ppm) ^b	Ω (ppm) ^c	κ ^d
1a (site 1)	283(2)	1163(50)	0.74(5)
(site 2)	25(2)	-----	-----
1b (site 1)	283(2)	-----	-----
(site 2)	25(2)	-----	-----
(site 3)	508(2)	991(50)	0.95(5)
1c (site 1)	283(2)	1128(50)	0.90(5)
(site 2)	25(2)	-----	-----
(site 3)	508(2)	991(50)	0.95(5)
1d (site 1)	283(2)	1106(50)	0.99(1)
(site 2)	25(2)	-----	-----
(site 3)	507(2)	1031(50)	0.99(1)
1e	507(2)	1031(50)	0.96(4)
2a	46(1)	-----	-----
2b	457(2)	1497(50)	0.96(4)
2c	474(2)	1530(50)	0.99(1)
3	454(2)	1322(50)	0.99(1)

^a The CS tensor is described by three principle components ordered such that $\delta_{11} \geq \delta_{22} \geq \delta_{33}$.

^b $\delta_{\text{iso}} = (\delta_{11} + \delta_{22} + \delta_{33})/3$, ^c $\Omega = \delta_{11} - \delta_{33}$, ^d $\kappa = 3(\delta_{22} - \delta_{\text{iso}})/\Omega$

Table 6.2. Experimental indirect spin-spin couplings.

Compounds	$^1J(^{109}\text{Ag}, ^{14}\text{N})$ (Hz)	$^1J(^{109}\text{Ag}, ^{15}\text{N})$ (Hz) ^a	$^1K(\text{Ag}, \text{N})$ ^b ($\text{N A}^{-2} \text{m}^{-3}$)
1a (site 1)	60(8)	-----	$-1.47663 \cdot 10^{22}$
1e	-----	61(8)	$1.07023 \cdot 10^{22}$
2b	50(8)	70(5)	$-1.23053 \cdot 10^{22}$
2c	50(8)	-----	$-1.23053 \cdot 10^{22}$
3	50(8)	-----	$-1.23053 \cdot 10^{22}$

^a Values of $^1J(^{109}\text{Ag}, ^{15}\text{N})$ were measured from ^{109}Ag and ^{15}N NMR spectra of labeled complexes. ^b Reduced coupling were calculated using (ref. 58) $K_{XY} = 4\pi^2 \frac{J_{XY}}{h\gamma_X\gamma_Y}$

Complex **1a** reacted with $C_{12}H_{25}NH_2$ in ratios of 1:0.5, 1:1 1:1.5 and 1:2, (**1b**, **1c**, **1d** and **1e**). The 1H - ^{109}Ag CP/MAS NMR spectra of **1b**, **1c**, **1d** and **1e** are compared to the parent sample, **1a**, in Figure 6.2.

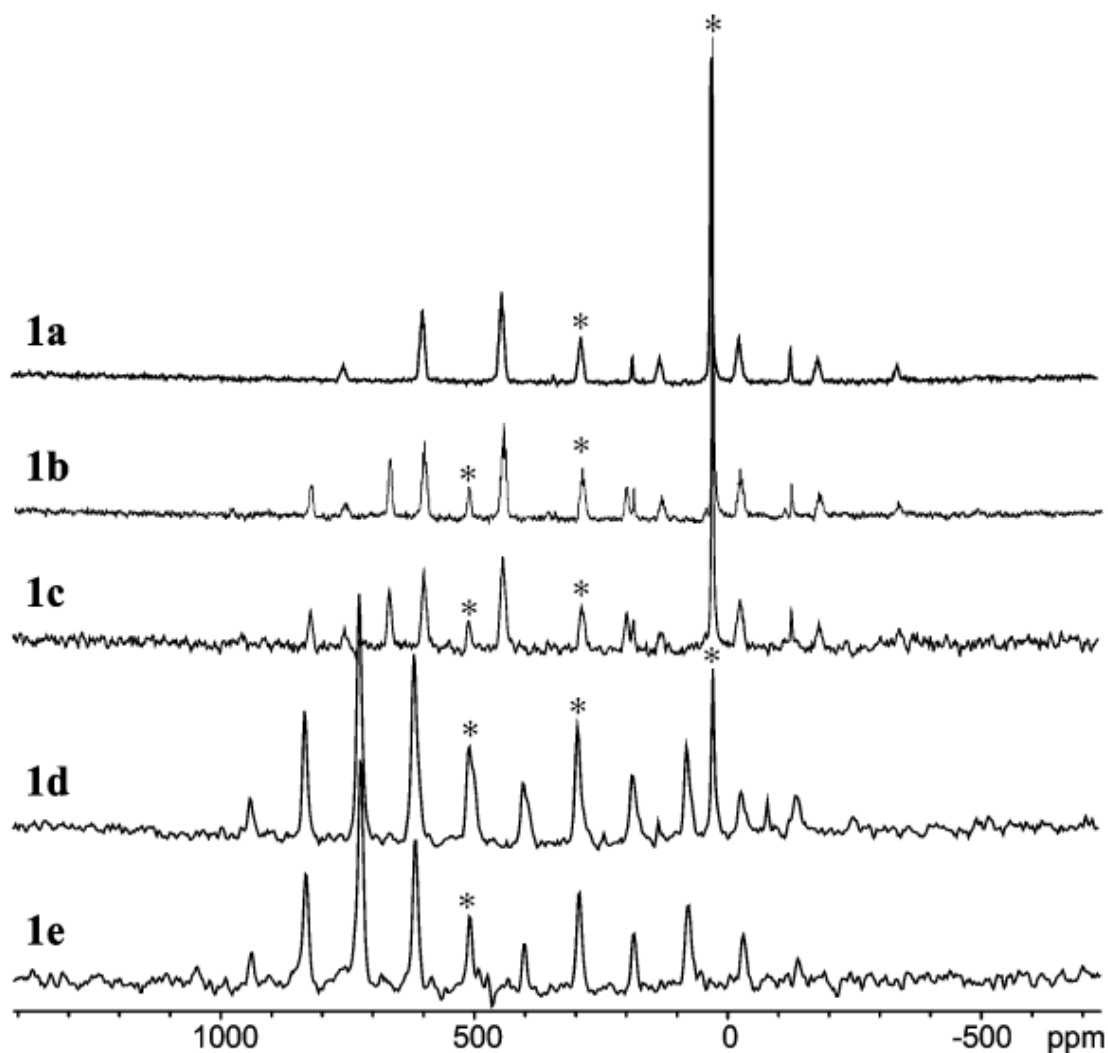


Figure 6.2. Solid-state ^{109}Ag CP/MAS NMR spectra of **1a** - **1e**. Isotropic peaks are designated with asterisks (*). Spectra of **1a**, **1b** and **1c** were acquired at $\nu_{rot} = 2.9$ kHz and spectra of **1d** and **1e** were acquired at $\nu_{rot} = 2.0$ kHz.

As the loading level of the dodecylamine is increased, a new spinning sideband manifold emerges with a distinct isotropic shift (ca. 507 ppm). The intensity of this pattern

increases with increasing amine loading level until only this pattern remains (**1e**). Silver CS tensor parameters extracted from the lower-spinning speed powder patterns of **1e** are $\delta_{\text{iso}} = 507$ ppm, $\Omega = 1031$ ppm and $\kappa = 0.96$ (Figure 6.3a, 6.3b). The higher frequency shift (i.e., the ^{109}Ag nucleus is deshielded relative to those in the parent compound), in combination with the span and skew, suggest the existence of a distinct silver environment from those of **1a**.

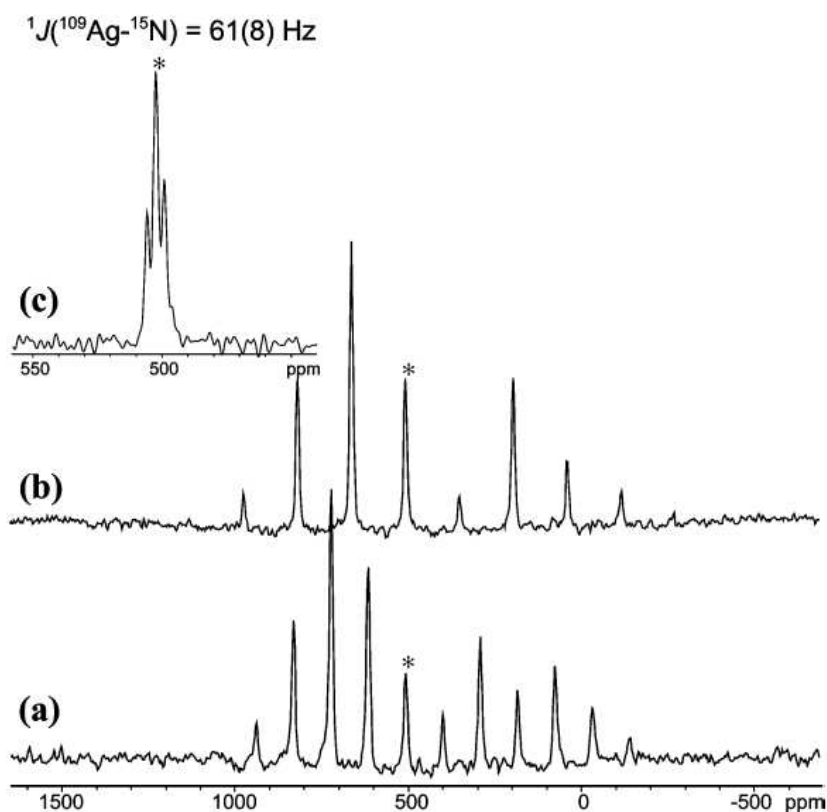


Figure 6.3. Solid-state ^{109}Ag CP/MAS NMR spectra of **1e** at three different spinning speeds: **(a)** $v_{\text{rot}} = 2.0$ kHz. **(b)** $v_{\text{rot}} = 2.9$ kHz. **(c)** $v_{\text{rot}} = 8.0$ kHz. Isotropic peaks are designated with asterisks (*).

^1H - ^{109}Ag CP/MAS NMR spectra of **1e** were also acquired at a higher spinning speed ($v_{\text{rot}} = 8.0$ kHz), revealing triplets of 1:2:1 intensity (Figure 6.3c). The size of the splitting is ca. 61(8) Hz, indicating that the ^{109}Ag nucleus is J -coupled to two ^{15}N nuclei in

the sp^3 environments of the dodecylamines. The distinct multiplets arising from J -coupling to ^{14}N nuclei of the pyridine rings are not observed, indicating that silver-pyridine nitrogen bonds are absent. The data indicate that, at loadings above one equivalent of amine, the primary species present involves a major reconstruction of the coordination polymer backbone. The higher loadings of amine may enable a requisite degree of swelling to allow the transformation, may displace the pyridine ligands directly, or may likely lead to some combination of the two factors. Clearly, simple intercalation of the primary amine is not the only process occurring; rather, what is being witnessed is the gradual formation of **1e**, which has new silver coordination sites.

^1H - ^{15}N CP/MAS NMR experiments were conducted on **1c** and **1e** at 9.4 T and 21.1 T (Figure 6.4, Table 6.3). The spectra are essentially identical, unlike their distinct ^{109}Ag NMR spectra. In the ^{15}N NMR spectra acquired at 9.4 T, there are two higher frequency peaks at 36.9 and 36.4 ppm, and two lower frequency peaks centered at 22.0 and 17.2 ppm, the latter of which are split due to $^1J(^{109}\text{Ag}, ^{15}\text{N}) = 61(8)$ Hz, in agreement with splittings measured in the corresponding ^{109}Ag NMR spectra of **1e**.

Table 6.3. Experimental ^{15}N chemical shifts.

Compounds	δ_{iso} (ppm) of coordinated nitrogen	δ_{iso} (ppm) of uncoordinated nitrogen
1c	21.9(5), 17.2(5)	36.9(5), 36.5(5)
1e	21.9(5), 17.2(5)	36.9(5), 36.4(5)
2b	19.4(5), 14.0(5)	minor species, 36.6(5) ppm

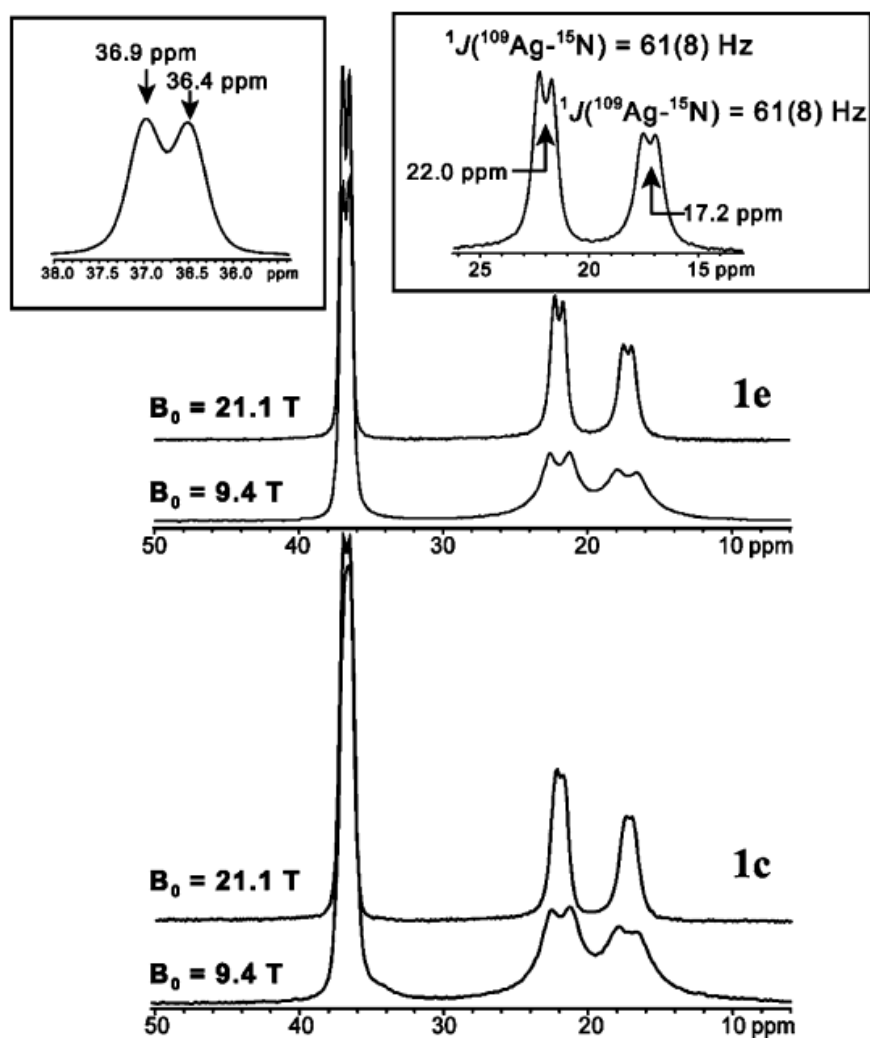


Figure 6.4. ^{15}N CP/MAS NMR spectra of **1c** (1:1) and **1e** (1:2) acquired at two different fields. The doublets around 36 ppm (shown in the inset) correspond to different nitrogen sites of free amines. The doublets at 17 and 22 ppm correspond to nitrogen sites coupled to silver atoms. The insets are expansions taken from **1e**.

Due to the similarity of gyromagnetic ratios of ^{107}Ag and ^{109}Ag , the $^1J(^{107}\text{Ag}, ^{15}\text{N})$ and $^1J(^{109}\text{Ag}, ^{15}\text{N})$ could not be differentiated. Integration of the ^{15}N CP/MAS NMR spectra of both samples reveals intensity ratios of 1:1 between these two regions (this was assessed under multiple contact times). The shifts and integrated intensities of all of the peaks, as

well as the J -coupling observed for the low-frequency resonances, were confirmed by experiments conducted at 21.1 T, since the difference in Hz for the peaks split by J -coupling is constant regardless of the field strength, and easily differentiated from peaks with different chemical shifts, which are constant in ppm. The high frequency peaks have similar isotropic shifts to “free” dodecylamine (*vide infra*),⁵⁵ and indicate the presence of a non-coordinated amine species. The low-frequency, J -split peaks are assigned to nitrogen atoms of the dodecylamine which are interacting with silver atoms in the newly formed material.^{22,41,56} Coordinative displacement of sulfonate ligands by high loadings of amines has been observed.⁵⁷ This assignment is consistent with the numerous negative coordination shifts, $\Delta\delta = \delta_{\text{iso}}^{\text{coord}} - \delta_{\text{iso}}^{\text{free}}$, reported for coordination of amine ligands to transition metals.^{45,58,59}

These data confirm the notion that **1e** is gradually being formed from **1a** and dodecylamine. Previous XRD experiments¹⁵ conducted at room and higher temperatures for **1c** and **1e** were proposed to reveal the “reversible” release of amine and the regeneration of **1a** for the former, while such behaviour was not observed for the latter. It is possible that the combination of “free” dodecylamine released upon heating **1c**, along with the remaining unreacted **1a**, gave the impression that a reversible intercalation of the amine was occurring. In fact, the disparate set of ¹⁰⁹Ag NMR spectra and identical set of ¹⁵N NMR spectra for these samples demonstrate that samples **1b**, **1c** and **1d** are likely simple mixtures of **1a** and **1e**.

However, this does raise some questions regarding the formation of **1e** from **1a**. Aside from the highly selective reaction at the silver site, which requires cleavage of two

sub-2.0 Å Ag-pyridyl bonds in **1a** and replacement by two amine molecules, it is likely that the amine is playing a role in exfoliating the layers of **1a** and “bowing” the layers such that the silver sites are exposed to reaction with the primary amines. Such layer bending has been observed for more rigid molecular sheets such as those in graphite.⁶⁰ Unfortunately, the formation of a layered solid phase consisting of **1a** and intercalated amine would be very difficult to distinguish by NMR from **1a** and free amine, and may only exist transiently during the formation of **1e**. While the formation of a transitory layered solid en route to the formation of **1e** is plausible, and is somewhat consistent with the ¹⁰⁹Ag NMR data, the ¹⁵N NMR spectra strongly suggest the constant presence of **1a** and **1e**.

Complex **1e** is clearly not an intercalation solid, and its structure must now be considered. Since **1e** is known to have a layered structure from powder XRD patterns,¹⁵ and based on known structures of analogous silver systems, it is possible that the silver-diamine cations form bilayers.^{41,61} However, since sample **1e** has a 1:2 ratio of silver atoms to dodecylamines, it seems that half of the silver sites are unaccounted for in this model. It is possible that the ¹H-¹⁰⁹Ag CP/MAS NMR experiments are unable to detect silver sites which are not proximate to an abundant proton source. Hence, lengthy ¹⁰⁹Ag{¹H} Bloch-decay MAS NMR experiments, run with a recycle time of 300 s, reveal a sharp peak at 425 ppm (Figure 6.5) with no fine structure ($\Delta\nu_{1/2} = 78$ Hz) which was not observed in previously discussed ¹H-¹⁰⁹Ag CP/MAS NMR spectra. The silver resonance at 507 ppm in this spectrum, corresponding to the amine-coordinated silver, is broad and more difficult to observe. The new peak has a shift similar to those observed for silver

sites in Ag_2SO_3 (between 409 and 466 ppm),²¹ likely corresponding to an isolated, uncoordinated silver ion.

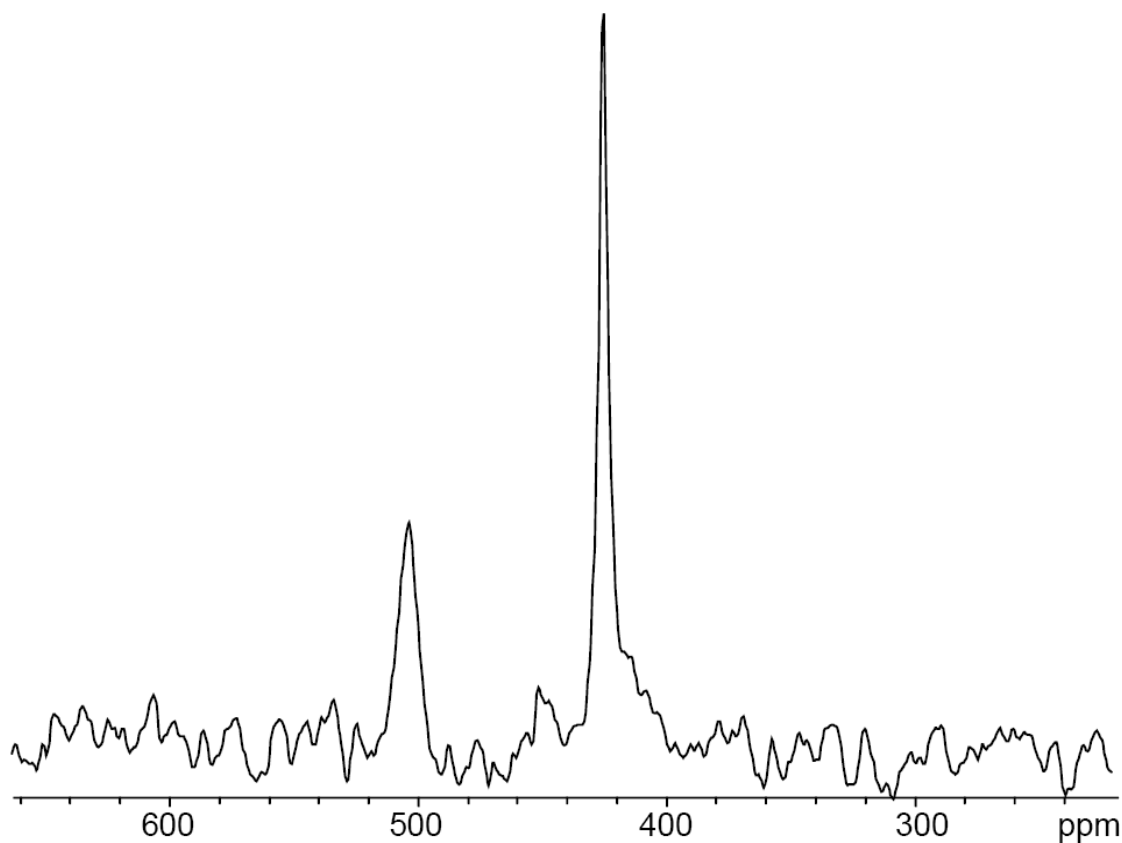


Figure 6.5. Solid-state ^{109}Ag MAS NMR spectrum of **1e** at 9.4 T, $\nu_{\text{rot}} = 8.0$ kHz

We are cautious in our definition of “isolated” in this case: by *isolated*, we refer to a Ag site which is not strongly coordinated by oxygen atoms (as in **1a**), and there are no coordination shifts indicating hydrogen bonding, nor fine structure to indicate the presence of nearby NMR active nuclides. Unfortunately, the integrated intensities of these peaks (isolated:coordinated, 1.5:1.0) are not quantitatively representative of the amount of silver, since the ^{109}Ag relaxation time constants are different for each site, and part of the broader, high frequency signal is lost due to the rapidly decaying FID. In fact,

the T_2 associated with the broad resonance is so short that this resonance is not observed in Hahn-echo experiments with interecho delays of $\tau = 125 \mu\text{s}$; hence, only Bloch decay experiments could be applied.

If the silver-diamine cations form bilayers, then the “free” dodecylamine molecules, silver ions and pyridinesulfonate counteranions are likely positioned between the layers, or perhaps among the alkyl chains of the dodecylamines;^{41,43,61} however, no interactions of these species with the diamine cations are detected, and the precise arrangement of these species is unknown at this time. The structural positioning of the uncoordinated dodecylamines could potentially be very interesting, as they could be located among the layers in a variety of scenarios. In addition, they may play a role in the gradual conversion of **1a** to **1e** with addition of amine, since the 1:1 reaction does not completely form a new layered solid.

Solid-state NMR spectra indicate that the structure of **1e** is very different from that of **1a**: in the former, the silver atom is strongly coordinated to two dodecylamine nitrogen atoms, as opposed to the nitrogen atoms in the pyridine-sulfonate moieties in the latter. The increased axial symmetry of the silver CS tensor also indicates that the N-Ag-N arrangement of atoms is increasingly linear in **1e** in comparison to that in **1a**. A reaction has occurred in which half of the dodecylamine molecules coordinate to silver atoms to form silver diamine cations, while the remaining dodecylamine molecules do not have strong bonding interactions with silver atoms. A structural model is further developed below, via comparison to data for other samples, as well as through theoretical calculations on model systems.

Ag(*p*-toluenesulfonate) (**2a**), and **2a** reacted with C₁₂H₂₅NH₂ and C₉H₁₉NH₂ in 1:2 ratios (**2b** and **2c**). The ¹H-¹⁰⁹Ag CP/MAS NMR spectrum of **2a** has one sharp (FWHH of 100 Hz), isotropic peak at 46 ppm (Figure 6.6a).

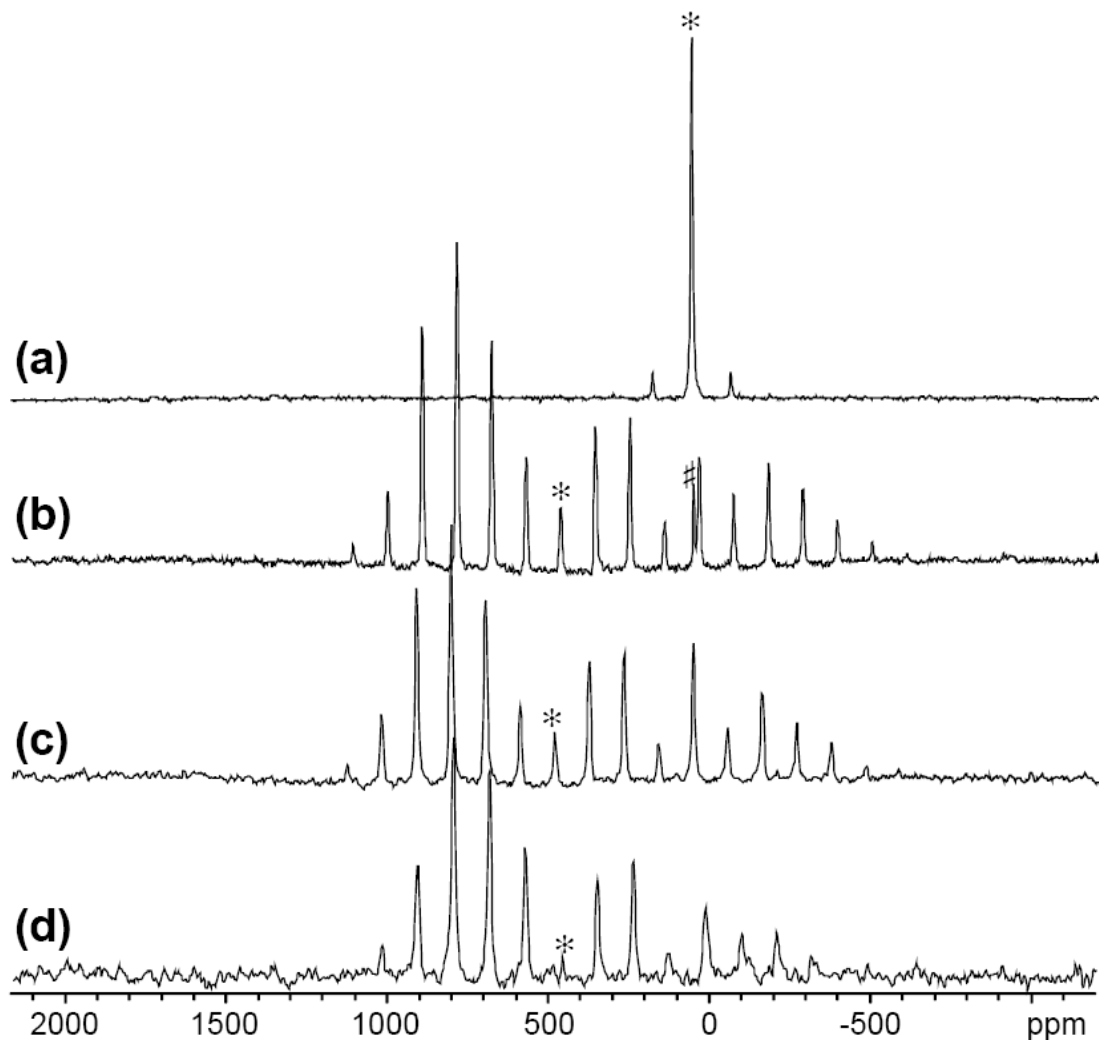


Figure 6.6. Solid-state ¹H-¹⁰⁹Ag CP/MAS NMR spectra of (a) **2a**, (b) **2b**, (c) **2c** and (d) **3** at $\nu_{\text{rot}} = 2.0$ kHz. Isotropic peaks are denoted with asterisks (*), remaining peaks are spinning sidebands. #: denotes impurity from the starting materials, **2a**.

This isotropic shift is the same as per Penner and Li, who also reported silver CS tensor parameters of $\Omega = 163$ ppm and $\kappa = 0.15$.²¹ The observation of one peak for this sample is consistent with the crystal structure, since the four silver atoms in the unit cell are

related by an inversion centre, and are therefore chemically and magnetically equivalent. The arrangement of atoms around the silver site is described as trigonal prismatic, featuring five oxygen atoms and two other silver atoms as nearest neighbours.¹³ The structure of **2a** is distinct from that of **1a** in that the inorganic and organic moieties are not contained within the same layer (Scheme 6.1); thus, **2a** is classified as a hybrid inorganic-organic solid, with the toluene moieties “pendant” into the interlayer region.¹³

Sample **2a** was reacted with two equivalents of unlabeled dodecylamine and nonylamine to produce **2b** and **2c**, respectively.¹³ The ¹⁰⁹Ag CP/MAS NMR spectrum of **2b** has a single isotropic peak at 457 ppm, flanked by a large set of spinning sidebands (Figure 6.6b). The span is very large, $\Omega = 1497$ ppm, and the CS tensor is axially symmetric, $\kappa = 0.96$. Once again, the high-frequency shift and CS tensor characteristics indicate that the silver is in a linear or near-linear environment, suggesting the formation of a diamine cation. The ¹⁰⁹Ag CP/MAS NMR spectrum of **2b** acquired at $\nu_{\text{rot}} = 2.9$ kHz, and processed with no additional line broadening and two zero fills, provides enough resolution to identify 1:2:3:2:1 multiplets with $^1J(^{109}\text{Ag}, ^{14}\text{N}) = 50(8)$ Hz (Figure 6.7a) confirming the proposed cation formation. Similar results are observed for **2c** (Figure 6.6c), demonstrating that the alkyl chain lengths do not have much influence on the ¹⁰⁹Ag NMR parameters. Prior work indexing the powder XRD patterns of a nonylamine intercalate was consistent with a layered AgRSO₃ network where the amine defined the interlayer region; however, as for the first series of compounds, it was not possible to determine the nature of the amine's interaction with the layers.¹³

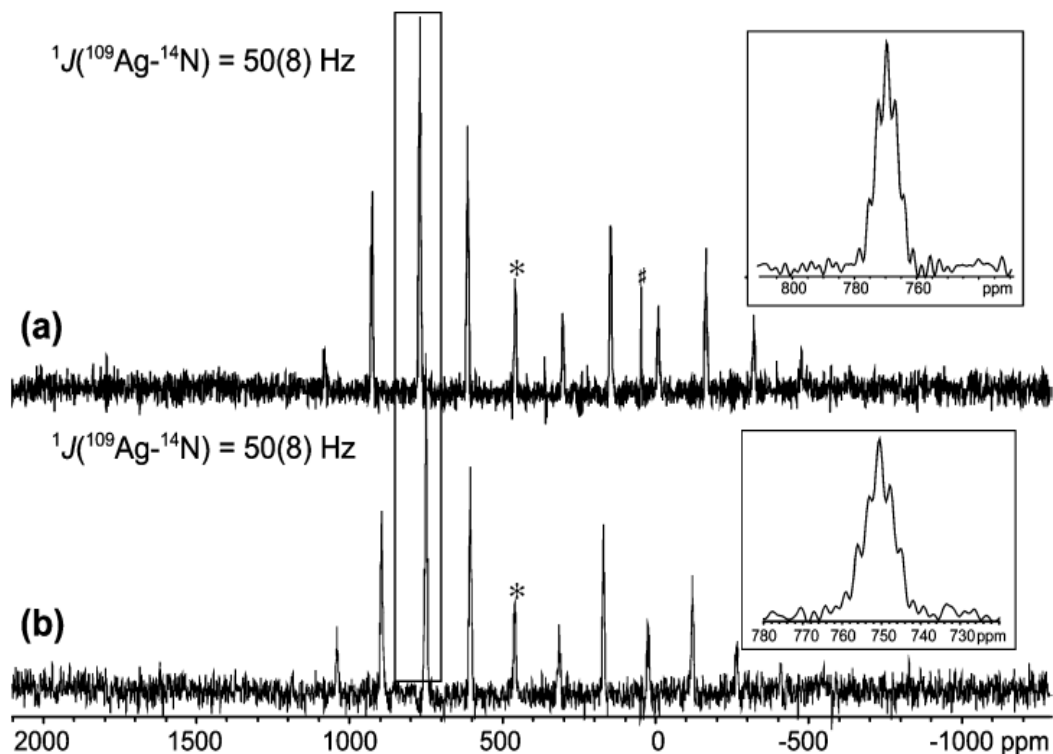


Figure 6.7. High resolution solid-state ^{109}Ag CP/MAS NMR spectra of (a) **2b** and (b) **3** (both processed with two zero-fills). Isotropic peaks are denoted by asterisks (*), and insets are expansions of areas indicated by rectangles. #: denotes impurity from the starting materials, **2a**.

A sample of **2b** was made with ^{15}N -labeled dodecylamine to confirm the binding of the dodecylamine to the silver sites. The ^1H - ^{109}Ag CP/MAS NMR spectrum of the labeled **2b** reveals a single silver site with a spinning sideband pattern identical to that of the unlabeled sample, with the exception of the presence of 1:2:1 triplets and $^1J(^{109}\text{Ag}, ^{15}\text{N}) = 70(5)$ Hz (Figure D.6.4). The ^1H - ^{15}N CP/MAS spectrum of the labeled **2b** (Figure 6.8) indicates that most of the dodecylamine is involved in direct coordination to silver sites, with δ_{iso} of 19.4(5) and 14.0(5) ppm, and $^1J(^{109}\text{Ag}, ^{15}\text{N})$ matching the corresponding ^{109}Ag NMR spectrum. However, unlike in the case of **1e**, there is not a 1:1

ratio of coordinated and uncoordinated amine. The peak at 36.6 ppm corresponding to "free" amine is of very low integrated intensity, and now corresponds to a mere impurity, along with several other peaks which are separate from or underlying the main resonances at 19 and 14 ppm.

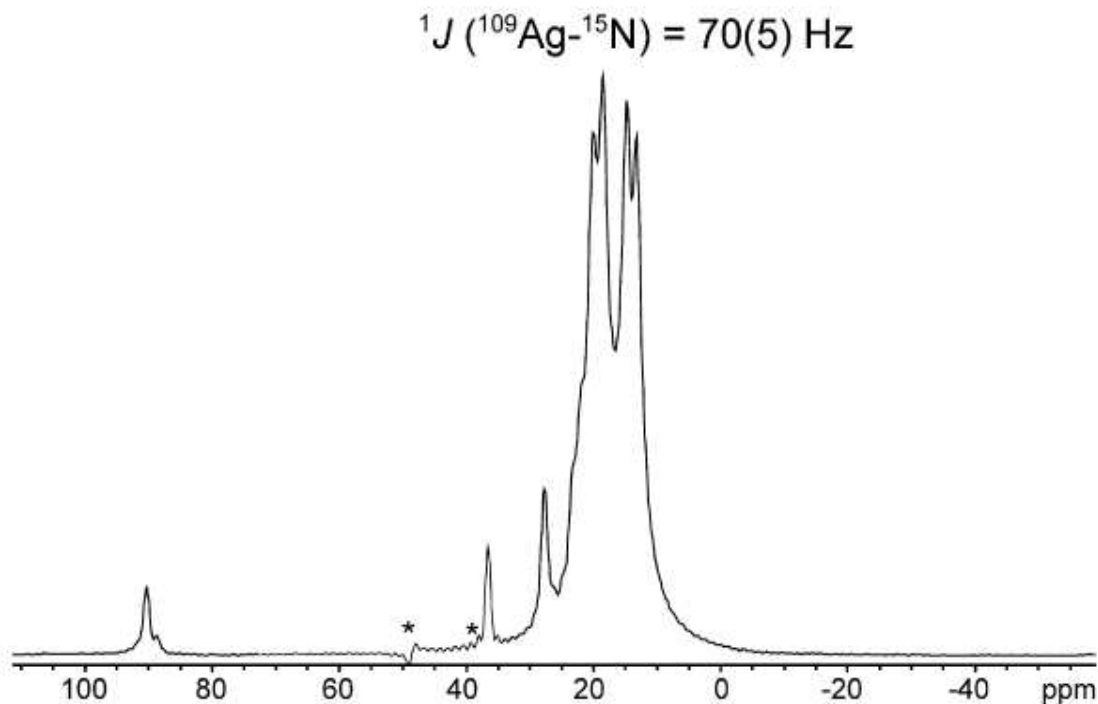
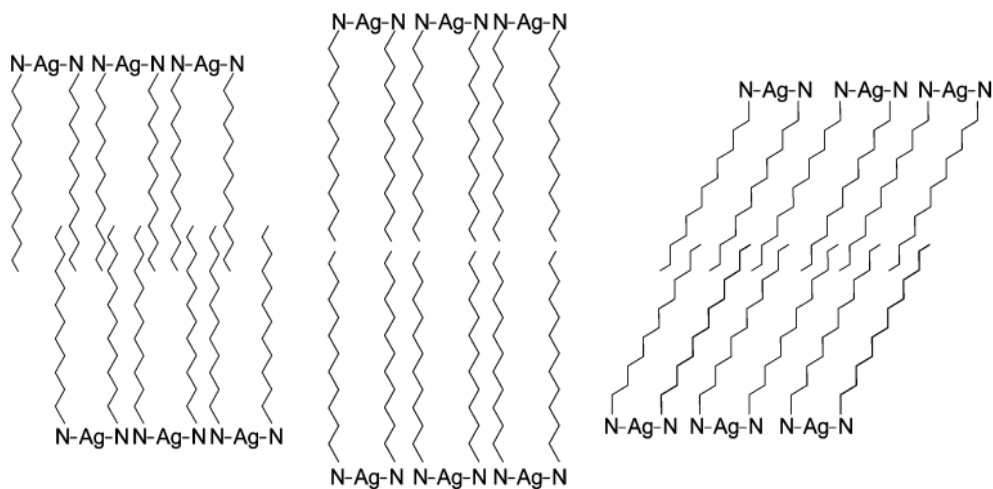


Figure 6.8. ^1H - ^{15}N CP/MAS NMR spectrum of **2b**. The doublets at 14 and 19 ppm correspond to nitrogen sites coupled to silver atoms. The peak at 36 ppm corresponds to a small amount of unreacted dodecylamine. The low intensity peaks at 27 and 90 ppm correspond to some impurity from the ^{15}N labeled dodecylamine sample. Low intensity peaks in the region of 20 to 30 ppm underlie the main resonances, and can be attributed to either dodecylamines in differing environments or perhaps impurity phases. The asterisks denote an artifact resulting from Fourier transforming a truncated FID, which was necessary to minimize the high-power decoupling and acquisition times.

$[\text{Ag}(\text{C}_{12}\text{H}_{25}\text{NH}_2)_2]^+[\text{NO}_3]^-$ (**3**). Further understanding of the structures of **2b** and **2c** can be made by considering the $[\text{Ag}(\text{C}_{12}\text{H}_{25}\text{NH}_2)_2]^+[\text{NO}_3]^-$ (**3**) coordination compound. It has been proposed that the silver diamine cations of **3** consist of N-Ag-N in a near-linear arrangement, and alkyl chains which adopt a "U-shape," resulting in self-assembly

into a bilayered structure.^{41,61} The ^1H - ^{109}Ag CP/MAS NMR spectrum of **3** (Figure 6.6d) looks remarkably like those of **2b** and **2c**, with $\delta_{\text{iso}} = 454$ ppm, $\Omega = 1322$ ppm and $\kappa = 0.99(1)$. ^1H - ^{109}Ag CP/MAS NMR experiments on unlabeled **3** at $\nu_{\text{rot}} = 2.7$ kHz and processed with two zero fills and minimal line broadening (Figure 6.7b) reveal 1:2:3:2:1 multiplets with $^1J(^{109}\text{Ag}, ^{14}\text{N}) = 50(8)$ Hz, confirming that each silver is bonded to two dodecylamine molecules.

The similarity of the silver chemical shift tensors and J -coupling parameters of **2b**, **2c** and **3** suggests that they have comparable structures, with silver atoms in linear N-Ag-N arrangements. The ^{109}Ag and ^{15}N NMR data, along with powder XRD data on **1e** and **2b**, suggest that the structures of **1e**, **2b**, **2c** and **3** all consist of silver-diamine cations which adopt the proposed “U-shaped” structures and form bilayers (Scheme 6.2).



Scheme 6.2. A schematic representation showing possible layered arrangements (interdigitated, non-interdigitated, and angled interdigitated) of the U-shaped silver-dodecylamine cations in the structures of **1e** and **2b**. Uncoordinated silver cations, amines and pyridinesulfonate groups are omitted. Three-dimensional extension of these structures back into the page are omitted for clarity.

The “free” dodecylamines do not seem to be necessary for the stabilization and/or formation of the layered structures, except in the case of **1e**. The positions of additional species (including anions for all species and “free” dodecylamines for **1e**) cannot be directly probed with the ^{109}Ag or ^{15}N NMR experiments, though theoretical structural modeling may be utilized to shed further light on these structural aspects.

6.3.2. Ab initio calculations.

First principles calculations of silver and nitrogen chemical shielding tensors, as well as $^1J(^{109}\text{Ag}, ^{14}\text{N})$ coupling constants, can be readily performed with modern computational chemistry suites such as Gaussian 03. In this section, we first present calculations of silver CS tensor parameters and J -coupling constants on a model compound for a well-characterized structure, $[\text{Ag}(\text{NH}_3)_2]_2\text{SO}_4$, in order to determine which method and basis sets yield the best agreement between experiment and theory, as well as to establish an approximate chemical shift scale (no absolute chemical shielding standard has been reported for silver to date). Second, calculations of NMR interactions of structural models for **1a** are presented (Figure 6.9a, 6.9b), since it has two well-characterized, distinct silver sites. Third, we discuss the computation of NMR parameters for $[\text{Ag}(\text{NH}_2\text{R})_2]^+$ units (Table D.6.4), which are used as structural models for **1e** and **2b** (Figure 6.9c, 6.9d). A preliminary exploration into the potential environments of additional species, including “free” or non-coordinated amine and organic sulfonate anions, is also presented.

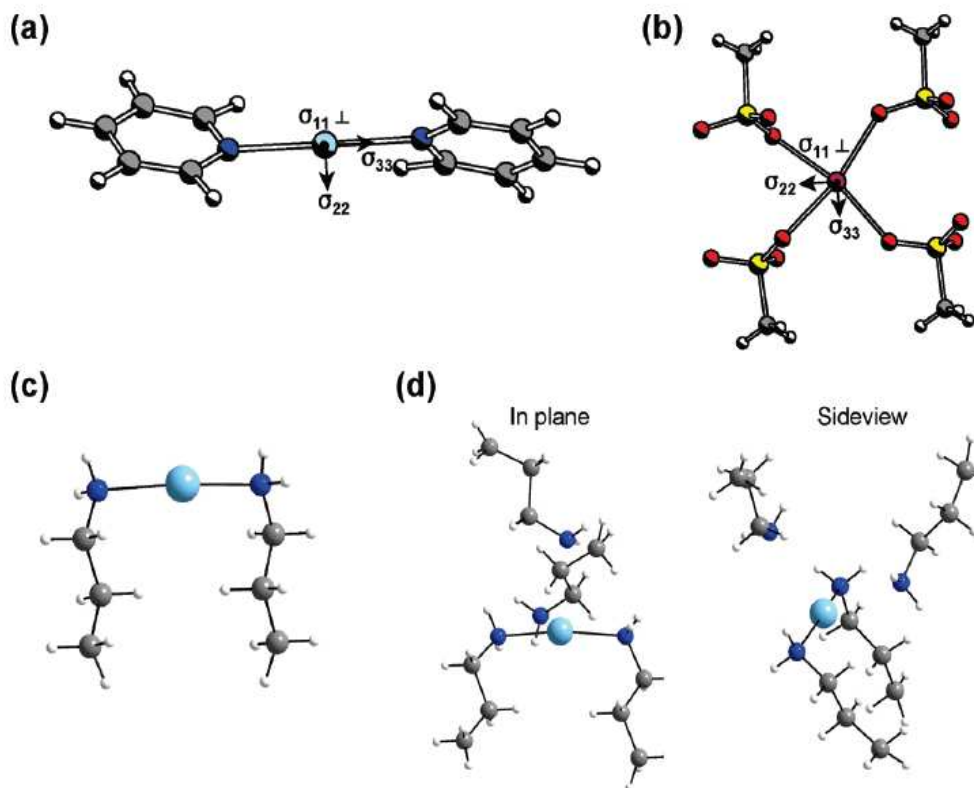


Figure 6.9. Theoretically calculated silver chemical shielding tensor orientations in structural models for **1a** at sites (a) Ag(1) (model structure **II**) and (b) Ag(2) (**III**) and structural models for (c) **2b** ($[\text{Ag}(\text{NH}_2\text{C}_3\text{H}_7)_2]^+$, **IV**) and (d) **1e** ($[\text{Ag}(\text{NH}_2\text{C}_3\text{H}_7)_2]^+ \cdot 2(\text{NH}_2\text{C}_3\text{H}_7)$, **VI**).

$[\text{Ag}(\text{NH}_3)_2]_2\text{SO}_4$ is a reasonable starting model compound for choosing an appropriate method and basis sets, since it has a known crystal structure⁵¹ and silver CS tensor parameters and $^1J(^{109}\text{Ag}, ^{14}\text{N})$ coupling constants have been measured.²² Following Bowmaker et al., the model cluster $[(\text{Ag}(\text{NH}_3)_2)_3(\text{HSO}_4)_2]^+$ (**I**) is investigated, using geometry optimized protons on the sulfonate groups. The silver atom is coordinated to two sp^3 -nitrogen atoms, similar to that in **1e** and **2b**. The RHF method, with DZVP basis sets⁴⁹ on silver and nitrogen atoms^{49,50} and 6-311G** on all other atoms, yields the best agreement with experimentally measured silver CS tensors and $^1J(^{109}\text{Ag}, ^{14}\text{N})$ (Table 6.4, Table D.6.5), producing results similar to those of Bowmaker and co-workers,²² who used

DFT calculations with the ADF suite, including zeroth-order relativistic approximation (ZORA).²²

Table 6.4. Experimental and theoretical ¹⁰⁹Ag chemical shift parameters and ¹J(¹⁰⁹Ag, ¹⁴N) coupling values.

Structural Unit *	$r(\text{Ag-N})$ (Å)	σ_{iso} (ppm)	δ_{iso} (ppm) ^{a,b}	Ω (ppm)	κ	¹ J(¹⁰⁹ Ag, ¹⁴ N) (Hz)
[Ag(NH ₃) ₂] ₂ SO ₄ (sample 4)						
Experimental	2.11	-----	657(2)	1708(50)	0.62(5)	47(8)
[(Ag(NH ₃) ₂) ₃ (HSO ₄) ₂] ⁺ (I)	2.11	3546	657	1652	0.84	41
Ag(PS) (sample 1a)						
Experimental (site 1)	2.16	-----	283(2)	1163(50)	0.74(5)	60(8)
[Ag(py) ₂] ⁺ (II)	2.16	3988	215	1100	0.87	38
Experimental (site 2)	-----	-----	25(2)	-----	-----	-----
[Ag(SO ₃ Me) ₄] ³⁻ (III)	-----	4174	29	257	-0.53	-----
(sample 2b)						
Experimental	-----	-----	457(2)	1395(50)	0.92(5)	50(8)
[Ag(NH ₂ C ₃ H ₇) ₂] ⁺ (IV)	2.10	3729	474	1366	0.93	42
[Ag(NH ₂ C ₆ H ₁₃) ₂] ⁺ (V)	2.10	3728	475	1370	0.93	42
(sample 1e)						
Experimental	-----	-----	507(2)	1031(50)	0.96(4)	43(8)
[Ag(NH ₂ C ₃ H ₇) ₄] ⁺ (VI)	2.10	3652	526	1231	0.83	38
[Ag ₇ (NH ₂ C ₃ H ₇) ₄] ⁺ (VI)	2.15	3741	452	1096	0.83	35

* The model structure formulae and reference numbers (in boldface Roman numerals) are listed below.

^a The chemical shifts were calculated using $\delta_{\text{iso}}(\text{sample}) - \delta_{\text{iso}}(\text{ref}) = \sigma_{\text{iso}}(\text{ref}) - \sigma_{\text{iso}}(\text{sample})$ where $\delta_{\text{iso}}(\text{ref})$ and $\sigma_{\text{iso}}(\text{ref})$ are the ¹⁰⁹Ag experimental chemical shift and the calculated chemical shielding, respectively.

^b The δ_{iso} of the Ag(2) site of **1a** was set to 25 ppm as an approximate chemical shift reference. See text for details. ^c This unit is taken from the reported crystal structure with adding two hydrogen atoms to avoid the negative charge. ^d The positions of the uncoordinated amines were optimized.

To further test the consistency of the choice of method and basis sets, similar calculations were conducted on model systems for **1a**. The structural unit used to model site Ag(1) in **1a** consists of a silver atom bonded to two pyridine rings, {Ag[py]₂}⁺ (**II**, Figure 6.9a), in which the sulfonate groups are replaced by hydrogen atoms to reduce computational expense. The calculated values of Ω and κ are in good agreement with experimental data, and the CS tensor is oriented such that σ_{33} (the most shielded

component) is near the Ag-N bonds ($\angle\sigma_{33}\text{-Ag-N1} = 5.75^\circ$ and $\angle\sigma_{33}\text{-Ag-N2} = 5.64^\circ$). The skew is not axially symmetric, since the N-Ag-N angle is not exactly 180° , and σ_{11} and σ_{22} are oriented in different environments, as predicted from experiment. However, the theoretical value of $^1J(^{109}\text{Ag}, ^{14}\text{N})$ is less than the experimental value, and the isotropic shift is not accurately reproduced. The structural model for site Ag(2), $[\text{Ag}(\text{SO}_3\text{Me})_4]^{3-}$ (**III**, Figure 6.9b) is also based on the crystal structure; however, to reduce computational expense, the pyridine moieties on the sulfur atoms were replaced by methyl groups. There are no experimental silver CS tensor data for this site; however, we found that by setting $\delta_{\text{iso}} = 25$ ppm (the experimental value) for the Ag(2) site, the relative chemical shift values of all of the other model compounds scaled well with experimental values. This is by no means an endorsement of this particular model as an absolute chemical shielding standard; a detailed experimental and theoretical determination of such a standard is beyond the scope of this paper.

The ^{109}Ag and ^{15}N NMR spectra of **1e** and **2b** indicate that the silver sites are coordinated to two dodecylamines; hence, one of the structural models used for these species is $[\text{Ag}(\text{NH}_2\text{C}_3\text{H}_7)_2]^+$ (**IV**, Figure 6.9c). The starting model for **IV** was constructed from a crystal structure reported by Smith et al.,⁴³ with optimized proton positions. In order to reduce computational expense, the alkyl chains only have three carbons; this feature of our model is justified by aforementioned ^{109}Ag NMR data for **2b** and **2c**, as well as calculations on $[\text{Ag}(\text{NH}_2\text{C}_6\text{H}_{13})_2]^+$ (**V**, not pictured), both of which reveal that CS and J -coupling parameters are not influenced to any great degree by chain length differences.

Different structural parameters were varied in order to observe corresponding changes in NMR parameters. The variation of the silver CS span and $^1J(^{109}\text{Ag}, ^{14}\text{N})$ as a function of internuclear distance (Figure 6.10, Table D.6.4) reveals that both the Ω and

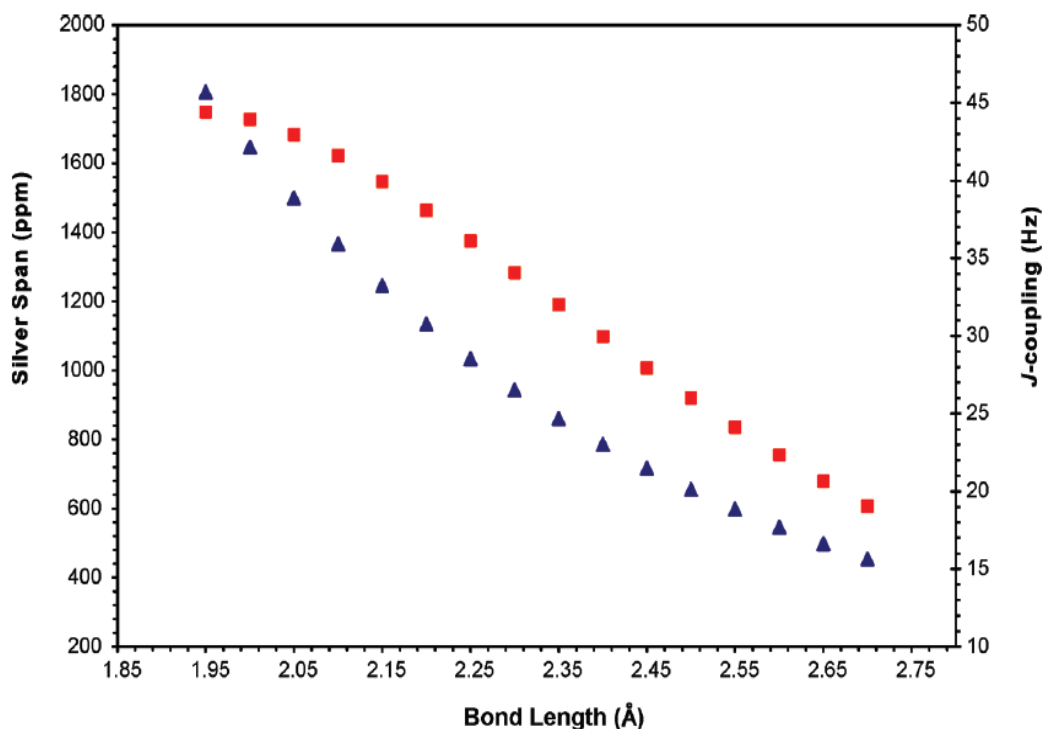


Figure 6.10. $^1J(^{109}\text{Ag}, ^{14}\text{N})$ coupling (■) and span (▲) as a function of Ag-N bond length in $[\text{Ag}(\text{NH}_2\text{C}_3\text{H}_7)]^+$.

$^1J(^{109}\text{Ag}, ^{14}\text{N})$ increase with decreasing Ag-N bond length; this behaviour is expected for the latter, since its magnitude is dominated by the Fermi-contact mechanism and increasing s -character in the Ag-N bond.⁶² The best agreement between the theoretical silver CS tensor parameters and those of **2b** is observed at $r(\text{Ag-N}) = 2.10 \text{ \AA}$ (Table D.6.4), while $^1J(^{109}\text{Ag}, ^{14}\text{N})$ is slightly underestimated. This value of $r(\text{Ag-N})$ is a reasonable equilibrium bond length for this structure, since there are a number of analogous molecules having Ag-N(sp^3) bond distances of ca. 2.1 \AA ^{22,51,63-65} and similar values of $^1J(^{109}\text{Ag}, ^{14}\text{N})$.²²

While model structure **IV** may be adequate for describing **2b**, the parameters are clearly distinct from **1e**, and simple geometrical adjustments to the $[\text{Ag}(\text{NH}_2\text{C}_3\text{H}_7)_2]^+$ coordinates (Ag-N bonds, as well as $\angle(\text{N-Ag-N})$ and $\angle(\text{C-N-N-C})$, Tables D.6.6 and D.6.7) are insufficient for modeling this system. Hence, calculations were conducted on numerous structural models which include additional non-coordinated amine units and pyridine sulfonate ions, all of which exert considerable influence on the CS tensors and *J*-couplings. Interestingly, fairly good agreement was found in structural models incorporating two additional propylamine units which are weakly coordinated (through geometry optimization) to the silver atom, $[\text{Ag}(\text{NH}_2\text{C}_3\text{H}_7)_2]^+ \cdot 2(\text{NH}_2\text{C}_3\text{H}_7)$ (Figure 6.9d, **VI**). Specifically, calculations involving Ag-N bonds of 2.10 and 2.15 Å, and weakly coordinated amines with Ag-N distances of 2.9 and 3.1 Å, yield reasonably good agreement with experimental data for **1e**, suggesting that weaker, long-range interactions are key in determining the silver tensor characteristics, and hence, influencing its overall structure.

Theoretical nitrogen chemical shifts are also of use in modeling the structure of **2b** (Table 6.5). Our experimental results indicate a coordination shift, $\Delta\delta = \delta_{\text{iso}}^{\text{coord}} - \delta_{\text{iso}}^{\text{free}}$, of between ca. -15 and -20 ppm in **1e** and between ca. -14 and -22 ppm in **2b**. Calculations are in excellent agreement, predicting coordination shifts of $\Delta\delta = -16$ to -22 ppm for coordination of two propylamine molecules to silver to form the cationic diamine complex. As expected, calculations predict that additional long-range interactions between silver and propylamines will yield no noticeable change in isotropic chemical shift, with $\Delta\delta$ ranging from -0.2 to +1.0 ppm.

Table 6.5. Calculated ^{15}N isotropic chemical shielding values and associated coordination shifts relative to free propylamine in the structural models for **1e**.

Structural Unit	Ag-N (Å)	σ_{iso} (ppm)	$\Delta\delta^a$	
[Ag(NH ₂ C ₃ H ₇) ₂] ⁺	2.10	273.7	-22.0	
	2.15	271.0	-19.3	
	2.20	268.5	-16.8	
[Ag(NH ₂ C ₃ H ₇) ₄] ⁺ ^b (site 1)	2.10	272.2	-20.8	
	(site 2)	2.10	268.5	-17.1
	(site 3)	2.90	251.6	0.2
	(site 4)	3.02	250.4	1.1
[Ag(NH ₂ C ₃ H ₇) ₄] ⁺ ^b (site 1)	2.15	269.8	-18.2	
	(site 2)	2.15	266.2	-14.7
	(site 3)	2.90	252.0	-0.1
	(site 4)	3.02	250.7	0.9

^a $\Delta\delta = \delta_{\text{iso}}^{\text{coord}} - \delta_{\text{iso}}^{\text{free}}$, where $\delta_{\text{iso}}^{\text{coord}}$ is the ^{15}N chemical shift of the nitrogen site coordinated to the silver atom and $\delta_{\text{iso}}^{\text{free}}$ is the ^{15}N chemical shift of free propylamine. The RHF/6-311G** nitrogen σ_{iso} for propylamine is 251.7 ppm. The coordination shift is defined as $\Delta\delta \approx -\Delta\sigma$. ^b The position of the third amine was geometry optimized in this calculation.

Ab initio calculations of silver CS tensors, silver-nitrogen J -couplings and nitrogen coordination shifts are all useful in the elucidation of the local structure of the silver-dodecylamine cations in layered systems like **2b**. However, for systems like **1e**, in which there may be additional long-range interactions, the structures are more difficult to model on the basis of NMR data; further investigations and structural refinement are required. It is possible that molecular dynamics/annealing simulations combined with first principles calculations of silver and nitrogen NMR tensors may be useful for future elucidation of the structures of these complex materials; notably, the nature of the long-

range layered structure and counteranion positions.

6.4 Conclusions

Layered silver supramolecular frameworks reacted with primary amines have been characterized using SSNMR, powder XRD and ab initio calculations. ^{109}Ag and ^{15}N NMR spectroscopy have been utilized to demonstrate that new materials (**1e** and **2b**) are formed which consist of silver diamine cations, counteranions and, in the case of **1e**, “free” amine molecules and uncoordinated silver sites. Amines are crucial in the formation of these materials as both non-coordinative guests and highly selective reactants at the silver sites. ^{109}Ag and ^{15}N NMR data, along with complementary NMR parameters obtained from ab initio calculations, unequivocally demonstrate the formation of silver diamine cations and the disappearance of the original metal-organic frameworks. The combined powder XRD and NMR data suggest that the silver diamine cations are responsible for forming a bilayered structure. Though the positions of the counteranions are somewhat ambiguous, ab initio calculations demonstrate that additional amines that are weakly coordinated to the silver sites may influence the silver CS tensors while not producing an observable J -coupling, and suggest that these amines may be crucial in stabilizing the layered structure of **1e**. In a broader view, this study demonstrates the importance of combining complementary physical characterization methods for obtaining a more comprehensive understanding of molecular structure underlying new materials.

6.5 Bibliography

- (1) Kitagawa, S.; Kitaura, R.; Noro, S.-I. *Angew. Chem., Int. Ed.* **2004**, *43*, 2334-2375.
- (2) Bradshaw, D.; Claridge, J. B.; Cussen, E. J.; Prior, T. J.; Rosseinsky, M. J. *Acc. Chem. Res.* **2005**, *38*, 273-282.
- (3) Janiak, C. *Dalton Trans.* **2003**, 2781-2804.
- (4) Eddaoudi, M.; Kim, J.; Rosi, N.; Vodak, D.; Wachter, J.; O'Keeffe, M.; Yaghi Omar, M. *Science* **2002**, *295*, 469-472.
- (5) Yaghi, O. M.; O'Keeffe, M.; Ockwig, N. W.; Chae, H. K.; Eddaoudi, M.; Kim, J. *Nature* **2003**, *423*, 705-714.
- (6) Maspoch, D.; Ruiz-Molina, D.; Wurst, K.; Domingo, N.; Cavallini, M.; Biscarini, F.; Tejada, J.; Rovira, C.; Veciana, J. *Nat. Mater.* **2003**, *2*, 190-195.
- (7) Hoffart, D. J.; Dalrymple, S. A.; Shimizu, G. K. H. *Inorg. Chem.* **2005**, *44*, 8868-8875.
- (8) Cote, A. P.; Shimizu, G. K. H. *Inorg. Chem.* **2004**, *43*, 6663-6673.
- (9) Melcer, N. J.; Enright, G. D.; Ripmeester, J. A.; Shimizu, G. K. H. *Inorg. Chem.* **2001**, *40*, 4641-4648.
- (10) Shimizu, G. K. H.; Enright, G. D.; Ratcliffe, C. I.; Preston, K. F.; Reid, J. L.; Ripmeester, J. A. *Chem. Commun.* **1999**, 1485-1486.
- (11) Shimizu, G. K. H.; Enright, G. D.; Ratcliffe, C. I.; Ripmeester, J. A. *Chem. Commun.* **1999**, 461-462.
- (12) Shimizu, G. K. H.; Enright, G. D.; Ratcliffe, C. I.; Ripmeester, J. A.; Wayner, D. D. M. *Angew. Chem., Int. Ed.* **1998**, *37*, 1407-1409.
- (13) Shimizu, G. K. H.; Enright, G. D.; Ratcliffe, C. I.; Rego, G. S.; Reid, J. L.; Ripmeester, J. A. *Chem. Mat.* **1998**, *10*, 3282-3283.
- (14) Cote, A. P.; Ferguson, M. J.; Khan, K. A.; Enright, G. D.; Kulynych, A. D.; Dalrymple, S. A.; Shimizu, G. K. H. *Inorg. Chem.* **2002**, *41*, 287-292.
- (15) May, L. J.; Shimizu, G. K. H. *Chem. Mat.* **2005**, *17*, 217-220.
- (16) Fijolek, H. G.; Oriskovich, T. A.; Benesi, A. J.; Gonzalez-Duarte, P.; Natan, M. J.

Inorg. Chem. **1996**, *35*, 797-799.

- (17) Fijolek, H. G.; Gonzalez-Duarte, P.; Park, S. H.; Suib, S. L.; Natan, M. J. *Inorg. Chem.* **1997**, *36*, 5299-5305.
- (18) Mustarelli, P.; Tomasi, C.; Quartarone, E.; Magistris, A.; Cutroni, M.; Mandanici, A. *Phys. Rev. B* **1998**, *58*, 9054-9061.
- (19) Ramnial, T.; Abernethy, C. D.; Spicer, M. D.; McKenzie, I. D.; Gay, I. D.; Clyburne, J. A. C. *Inorg. Chem.* **2003**, *42*, 1391-1393.
- (20) Penner, G. H.; Li, W. *Solid State Nucl. Magn. Reson.* **2003**, *23*, 168-173.
- (21) Penner, G. H.; Li, W. *Inorg. Chem.* **2004**, *43*, 5588-5597.
- (22) Bowmaker, G. A.; Harris, R. K.; Assadollahzadeh, B.; Apperley, D. C.; Hodgkinson, P.; Amornsakchai, P. *Magn. Reson. Chem.* **2004**, *42*, 819-826.
- (23) Smith, M. E. *Annu. Rep. NMR Spectrosc.* **2001**, *43*, 121-175.
- (24) Hartmann, S. R.; Hahn, E. L. *Phys. Rev.* **1962**, *128*, 2042-2053.
- (25) Levitt, M. H.; Suter, D.; Ernst, R. R. *J. Chem. Phys.* **1986**, *84*, 4243-4255.
- (26) Peersen, O. B.; Wu, X.; Kustanovich, I.; Smith, S. O. *J. Magn. Reson. Ser. A* **1993**, *104*, 334-339.
- (27) Peersen, O. B.; Wu, X.; Smith, S. O. *J. Magn. Reson. Ser. A* **1994**, *106*, 127-131.
- (28) Metz, G.; Wu, X.; Smith, S. O. *J. Magn. Reson. Ser. A* **1994**, *110*, 219-227.
- (29) Metz, G.; Ziliox, M.; Smith, S. O. *Solid State Nucl. Magn. Reson.* **1996**, *7*, 155-160.
- (30) Cook, R. L.; Langford, C. H. *Polymer News* **1999**, *24*, 6-15.
- (31) Lipton, A. S.; Sears, J. A.; Ellis, P. D. *J. Magn. Reson.* **2001**, *151*, 48-59.
- (32) Fujiwara, T.; Ramamoorthy, A. *Annu. Rep. NMR Spectrosc.* **2006**, *58*, 155-175.
- (33) Hung, I.; Rossini, A. J.; Schurko, R. W. *J. Phys. Chem. A* **2004**, *108*, 7112-7120.
- (34) Siegel, R.; Nakashima, T. T.; Wasylishen, R. E. *J. Phys. Chem. B* **2004**, *108*, 2218-2226.
- (35) Zhao, X.; Hoffbauer, W.; Schmedt auf der Gunne, J.; Levitt, M. H. *Solid State Nucl. Magn. Reson.* **2004**, *26*, 57-64.
- (36) Fu, R.; Gunaydin-Sen, O.; Dalal, N. S. *J. Am. Chem. Soc.* **2007**, *129*, 470-471.
- (37) Samoson, A.; Tuherm, T.; Gan, Z. *Solid State Nucl. Magn. Reson.* **2001**, *20*, 130-

136.

- (38) Stebbins, J. F.; Du, L.-S.; Kroeker, S.; Neuhoff, P.; Rice, D.; Frye, J.; Jakobsen, H. J. *Solid State Nucl. Magn. Reson.* **2002**, *21*, 105-115.
- (39) Fu, R.; Brey, W. W.; Shetty, K.; Gor'kov, P.; Saha, S.; Long, J. R.; Grant, S. C.; Chekmenev, E. Y.; Hu, J.; Gan, Z.; Sharma, M.; Zhang, F.; Logan, T. M.; Brueschweller, R.; Edison, A.; Blue, A.; Dixon, I. R.; Markiewicz, W. D.; Cross, T. A. *J. Magn. Reson.* **2005**, *177*, 1-8.
- (40) Gan, Z.; Gor'kov, P.; Cross, T. A.; Samoson, A.; Massiot, D. *J. Am. Chem. Soc.* **2002**, *124*, 5634-5635.
- (41) Albeniz, A. C.; Barbera, J.; Espinet, P.; Lequerica, M. C.; Levelut, A. M.; Lopez-Marcos, F. J.; Serrano, J. L. *Eur. J. Inorg. Chem.* **2000**, 133-138.
- (42) Penner, G. H.; Liu, X. L. *Prog. Nucl. Magn. Reson. Spectrosc.* **2006**, *49*, 151-167.
- (43) Smith, G.; Thomasson, J. H.; White, J. M. *Aust. J. Chem.* **1999**, *52*, 317-324.
- (44) Bennett, A. E.; Rienstra, C. M.; Auger, M.; Lakshmi, K. V.; Griffin, R. G. *J. Chem. Phys.* **1995**, *103*, 6951-6958.
- (45) Schurko, R. W.; Wasylishen, R. E. *J. Phys. Chem. A* **2000**, *104*, 3410-3420.
- (46) Eichele, K.; Wasylishen, R. E.; v. 1.17.30 ed.: WSolids1: Solid-State NMR Spectrum Simulation, 2001.
- (47) Frisch, M. J.; Trucks, G. W.; Schlegel, H. B.; Scuseria, G. E.; Robb, M. A.; Cheeseman, J. R.; Montgomery, J. J. A.; Vreven, T.; Kudin, K. N.; Burant, J. C.; Millam, J. M.; Iyengar, S. S.; Tomasi, J.; Barone, V.; Mennucci, B.; Cossi, M.; Scalmani, G.; Rega, N.; Petersson, G. A.; Nakatsuji, H.; Hada, M.; Ehara, M.; Toyota, K.; Fukuda, R.; Hasegawa, J.; Ishida, M.; Nakajima, T.; Honda, Y.; Kitao, O.; Nakai, H.; Klene, M.; Li, X.; Knox, J. E.; Hratchian, H. P.; Cross, J. B.; Adamo, C.; Jaramillo, J.; Gomperts, R.; Stratmann, R. E.; Yazyev, O.; Austin, A. J.; Cammi, R.; Pomelli, C.; Ochterski, J. W.; Ayala, P. Y.; Morokuma, K.; Voth, G. A.; Salvador, P.; Dannenberg, J. J.; Zakrzewski, V. G.; Dapprich, S.; Daniels, A. D.; Strain, M. C.; Farkas, O.; Malick, D. K.; Rabuck, A. D.; Raghavachari, K.; Foresman, J. B.; Ortiz, J. V.; Cui, Q.; Baboul, A. G.; Clifford, S.; Cioslowski, J.; Stefanov, B. B.; Liu, G.; Liashenko, A.; Piskorz, P.; Komaromi, I.; Martin, R. L.; Fox, D. J.; Keith, T.; Al-Laham, M. A.; Peng, C. Y.; Nanayakkara, A.;

Challacombe, M.; Gill, P. M. W.; Johnson, B.; Chen, H.; Wong, M. W.; Gonzalez, C.; Pople, J. A.; Rev. B.03 ed.; Gaussian, Inc.: Pittsburgh, 2003..

(48) This work was made possible by the facilities of the Shared Hierarchical Academic Research Computing Network (SHARCNET:www.sharcnet.ca).

(49) Basis sets were obtained from the Extensible Computational Chemistry Environment Basis Set Database, V., as developed and distributed by the Molecular Science Computing Facility, Environmental and Molecular Sciences Laboratory which is part of the Pacific Northwest Laboratory, P.O. Box 999, Richland, Washington 99352, USA, and funded by the U.S. Department of Energy. The Pacific Northwest Laboratory is a multi-program laboratory operated by Battelle Memorial Institute for the U.S. Department of Energy under contract DE-AC06-76RLO 1830. Contact Karen Schuchardt for further information.

(50) Godbout, N.; Salahub, D. R.; Andzelm, J.; Wimmer, E. *Can. J. Chem.* **1992**, *70*, 560-571.

(51) Zachwieja, U.; Jacobs, H. *Z. Kristallogr.* **1992**, *201*, 207-212.

(52) Ditchfield, R. *Mol. Phys.* **1974**, *27*, 789-807.

(53) Wolinski, K.; Hinton, J. F.; Pulay, P. *J. Am. Chem. Soc.* **1990**, *112*, 8251-8260.

(54) Herzfeld, J.; Berger, A. E. *J. Chem. Phys.* **1980**, *73*, 6021-6030.

(55) Antonelli, D. M. *Microporous Mesoporous Mat.* **1999**, *30*, 315-319.

(56) Drew, M. G. B.; Farrell, D.; Morgan, G. G.; McKee, V.; Nelson, J. *Dalton* **2000**, 1513-1519.

(57) Liu, P.; Lian, Z.-X.; Cai, J. *Polyhedron* **2006**, *25*, 3045-3052.

(58) Mason, J. *Chem. Rev.* **1981**, *81*, 205-227.

(59) Witanowski, M.; Stefaniak, L.; Webb, G. A. *Annu. Rep. NMR Spectrosc.* **1986**, *18*, 1-761.

(60) Zabel, H.; Kamitakahara, W. A.; Nicklow, R. M. *Phys. Rev. B* **1982**, *26*, 5919-5926.

(61) Neve, F.; Ghedini, M.; Demunno, G.; Levelut, A. M. *Chem. Mat.* **1995**, *7*, 688-693.

(62) Jameson, C. J. In *Multinuclear NMR*; Mason, J., Ed., 1987, p 639.

- (63) You, Z. L.; Zhu, H. L.; Liu, W. S. *Acta Crystallogr. Sect. E: Struct. Rep. Online* **2004**, *E60*, m1903-m1905.
- (64) You, Z. L.; Yang, L.; Zou, Y.; Zeng, W. J.; Liu, W. S.; Zhu, H. L. *Acta Crystallogr., Sect. C: Cryst. Struct.* **2004**, *C60*, m117-m118.
- (65) You, Z. L.; Zhu, H. L.; Liu, W. S. *Acta Crystallogr., Sect. C: Cryst. Struct.* **2004**, *C60*, m231-m232.

Chapter 7

Application of Solid-State ^{35}Cl NMR to the Structural Characterization of Hydrochloride Pharmaceuticals and their Polymorphs

7.1 Introduction

Polymorphs, which are distinct, stable phases of a pure substance resulting from a minimum of two different arrangements of the molecules or atoms in the solid state, are of great interest in many areas of chemistry.^{1,2} Most active pharmaceutical ingredients (APIs) can adopt more than one polymorphic phase, and can also crystallize as pseudo-polymorphs, in which the molecules are in distinct hydration or solvation environments. Identification of different polymorphs, or polymorph screening, is of great importance in the pharmaceutical industry and associated laboratories,³⁻⁷ since (i) ca. 80% of solid pharmaceuticals possess more than one polymorphic form,⁸ and (ii) different polymorphs can have distinct physicochemical properties such as solubility, melting point, dissolution rate, density, hardness and/or crystal morphology, all of which can affect the bioavailability, handling, packing, shelf-life and/or patenting of a drug.⁹⁻¹¹

Traditionally, single-crystal and powder X-ray diffraction (XRD) have been the primary methods for solid-state characterization of pharmaceuticals.^{12,13} In many cases, isolation of crystals suitable for single-crystal XRD studies is very difficult for standard pharmaceuticals. Powder XRD is useful for distinguishing polymorphs, but is often limited for detection of slight structural/conformational changes,^{14,15} and for providing specific information on the intra- and intermolecular origins of polymorphism.

Solid-state nuclear magnetic resonance (SSNMR) experiments are an excellent complement to XRD methods,^{16,17} since they are sensitive to changes in the local electronic environments of nuclei resulting from alterations in molecular structure such as bond length and angle variation, hydrogen bonds and other intra- and intermolecular interactions.¹⁸⁻²⁰ SSNMR spectroscopy also provides the added benefit of being able to examine disordered or non-crystalline phases of solid pharmaceuticals. In general, ¹³C SSNMR experiments have been key in probing pharmaceutical polymorphism, allowing for the study of site-specific chemical changes, non-stoichiometric hydration and solid-state dynamics in heterogeneous and disordered samples, as well as quantification of mixtures of crystalline and/or amorphous forms.²¹ In numerous cases where ¹³C NMR spectra are ambiguous, SSNMR of other nuclides in pharmaceuticals have proven useful, including ¹H, ²H, ¹⁵N, ³¹P and ¹⁹F, and even ²³Na, all of which seem very promising for probing polymorphism.²²⁻²⁸

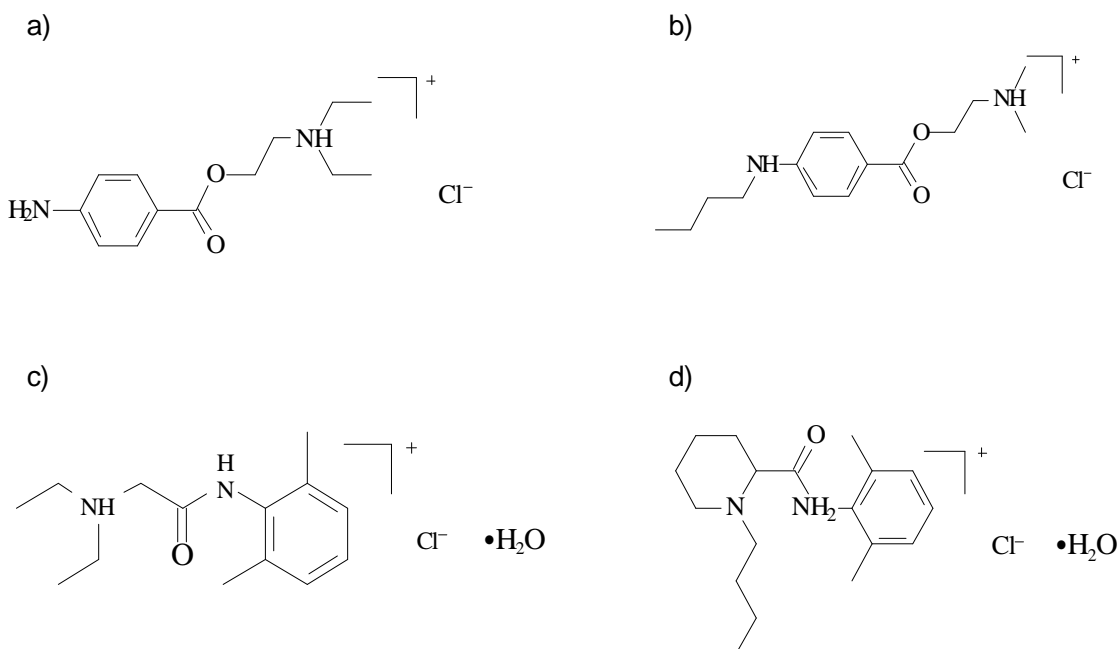
Chlorine SSNMR, to the best of our knowledge, has not been applied for the investigation of pharmaceutical polymorphism, despite the plenitude of hydrochloride (HCl) pharmaceuticals. It is estimated that 50% of all pharmaceutical salts, which are more soluble than non-ionic species and extremely useful in solid dosage forms, are HCl pharmaceuticals, and that chlorine is present in final formulations of ca. 25% of drugs.²⁹ It has recently been demonstrated that chlorine NMR is an excellent probe of the Cl⁻ ion binding environment in HCl amino acids,^{30,31} and is very useful for distinguishing pseudo-polymorphs of chlorine-containing coordination compounds.³² ³⁵Cl NQR has been applied to study the temperature and phase dependence of ³⁵Cl quadrupolar

frequencies in numerous species;³³⁻³⁵ however, this technique is restricted to systems with larger C_Q 's, and not generally applicable for $C_Q < \text{ca. } 10 \text{ MHz}$. Chlorine has two naturally-occurring NMR-active nuclides, ^{35}Cl and ^{37}Cl , both of which are half-integer quadrupoles (both spin $3/2$, $Q(^{35}\text{Cl}) = -0.082 \times 10^{-28} \text{ m}^2$, $Q(^{37}\text{Cl}) = -0.065 \times 10^{-28} \text{ m}^2$)^{36,37} with low gyromagnetic ratios, and are regarded as unreceptive low-gamma nuclei, despite their relatively high natural abundances (75.53% and 24.47%, respectively). The recent increase in the availability of ultra-high magnetic fields and signal-enhancing pulse sequences has made routine $^{35/37}\text{Cl}$ SSNMR experimentation a viable option for investigating such systems. Given the sensitivity of the $^{35/37}\text{Cl}$ quadrupolar interaction to site geometry and chemistry,³⁰ and the relatively wide chlorine chemical shift range,³⁸ $^{35/37}\text{Cl}$ SSNMR should be an excellent probe of structure and polymorphism in HCl pharmaceuticals.

One class of drugs prone to polymorphism is HCl local anaesthetics (LAs). LA molecules generally have common structural features which determine their pharmaceutical activities, including a hydrophilic end group, which is normally a tertiary or secondary amine, and a hydrophobic end group, which is usually aromatic.³⁹ These groups are linked by ester or amide bridges and possess one or more aliphatic chains as substituents.⁴⁰ While these structural features allow for conformational flexibility, which undoubtedly influences the drug activity, they also account for the high possibility of polymorph formation.^{39,40} The anionic chlorine sites, which adopt unique positions in the unit cell, are expected to have distinct quadrupolar and chemical shift parameters. This suggests that ^{35}Cl NMR spectra can serve as indicators and/or identifiers of different solid

phases, providing rapid, unambiguous differentiation of structural polymorphs. Notably, ^{35}Cl SSNMR should find much utility in cases where ^{13}C NMR data are indeterminate or there is a disordered phase(s) unamenable to XRD characterization.

Herein, we report a preliminary study of the application of solid-state ^{35}Cl NMR spectroscopy for the structural characterization of HCl salts of procaine (PH), tetracaine (TH), monohydrated lidocaine (LH) and monohydrated bupivacaine (BH) (Scheme 7.1) as well as some polymorphs of LH and BH.



Scheme 7.1. The structures of a) procaine HCl (PH), b) tetracaine HCl (TH), c) lidocaine HCl monohydrate (LH) and d) bupivacaine HCl monohydrate (BH).

Quadrupolar and chemical shift parameters extracted from ^{35}Cl SSNMR spectra can be used to distinguish different chlorine environments in these samples; of particular interest is the relationship between the quadrupolar parameters and number of short $\text{Cl}\cdots\text{H}$ hydrogen bonds. These data are complemented by single-crystal structures, powder XRD

patterns and ^1H - ^{13}C CP/MAS NMR spectra. We hope to demonstrate that the combination of these methods will give us insight into relationships between the structures of the solid pharmaceuticals and the NMR parameters, and that ^{35}Cl SSNMR spectroscopy is much needed as a routine screen for polymorphism in pharmaceutical HCl species.

7.2 Experimental

7.2.1 Sample preparation and XRD.

Samples were purchased from Sigma-Aldrich Canada, Ltd. Crystals of PH were obtained directly from the bottle, whereas crystals of LH, TH and BH were grown by slow evaporation from acetone, isopropanol and a solution of water/acetone,⁴¹ respectively. Commercial BH was heated in an oven at 120°C for one day to form polymorph BH1, and was also heated at 170°C for 12 hours using a silicon oil bath to form BH2. Monohydrated lidocaine HCl polymorph (LH1) was synthesized by dissolving approximately 1 g of the commercial lidocaine HCl (LH) monohydrate in acetonitrile (30 mL) and a small amount of MgSO_4 was added. The mixture was left to stir under nitrogen overnight. The sample was filtered and acetonitrile was then removed under reduced pressure. Elemental analysis on LH1 was performed by Atlantic Microlabs, Inc. (Anal. Calcd. for LH1: Cl, 12.27%; C, 58.22%; H, 8.72%; N, 9.69%; O, 11.08%. Found: Cl, 12.22%, C, 58.16%; H, 8.85%; N, 9.61%; O, 11.10%).

Single crystal and powder X-ray diffraction. Single crystals were covered in Nujol and placed into the cold N_2 stream of a Kryoflex low-temperature device. The

experiments were performed using the SMART⁴² data collection software on a Bruker APEX CCD diffractometer using a graphite monochromator with Mo-K α radiation ($\lambda = 0.71073 \text{ \AA}$) source at a temperature of -100 °C. A hemisphere of data was collected using a counting time of 30 s per frame. The data reductions were performed using SAINT⁴³ and absorption corrections were applied using SADABS.⁴⁴ The structures were solved by direct methods and refined by full-matrix least-squares on F^2 with anisotropic displacement parameters for all non-H atoms using the SHELXL software package.⁴⁵ Powder XRD patterns were collected using a D8 DISCOVER X-ray diffractometer equipped with an Oxford Cryosystems 700 Cryostream Plus Cooler. This diffractometer uses a Cu-K α ($\lambda = 1.54056 \text{ \AA}$) radiation source with a Bruker AXS HI-STAR area detector running under the General Area Detector Diffraction System (GADDS).

TGA and MS. Thermal gravimetric analysis with mass spectrometric detection of evolved gases was conducted on a Mettler Toledo TGA SDTA 851e that was attached to a Pfeiffer Vacuum ThermoStar mass spectrometer (1-300 amu) via a thin glass capillary. Helium (99.99%) was used to purge the system with a flow rate of 30 mL/min. Samples were held at 25 °C for 30 min before being heated to 125 °C at a rate of 2 °C/min. A mass range between 15 m/z and 100 m/z was constantly scanned at a frequency of about 1.6 scans per second.

7.2.2 Solid-State NMR.

³⁵Cl SSNMR experiments were carried out on a Varian Infinity Plus spectrometer equipped with an Oxford 9.4 T ($\nu_0(^1\text{H}) = 400 \text{ MHz}$) wide-bore magnet with

$\nu_0(^{35}\text{Cl}) = 39.26$ MHz. The ^{35}Cl isotope was chosen instead of ^{37}Cl because of its higher receptivity. High-field ^{35}Cl NMR data were collected on an ultra-wide bore 900 MHz (21.1 T) built-in-house superconducting NMR magnet ($\nu_0(^{35}\text{Cl}) = 88.125$ MHz) at the NHMFL in Tallahassee, Florida, as well as on a 900 MHz Bruker Avance II spectrometer at the National Ultrahigh-field NMR Facility for Solids in Ottawa, Canada. All spectra were acquired using the Hahn-echo pulse sequence, and chlorine chemical shifts were referenced to NaCl(s) ($\delta_{\text{iso}} = 0.0$ ppm), following Bryce and co-workers.^{31,38}

Experiments at 9.4 T. Samples were finely ground and packed into 5 mm o.d. zirconium oxide rotors. ^{35}Cl NMR spectra were collected on a double resonance (HX) static probe. Central-transition selective $\pi/2$ pulse widths between 1.0 and 2.3 μs were applied with an optimized recycle delay of 0.5 s. In cases where NMR powder patterns were too broad to be uniformly excited with a single pulse, spectra were acquired by stepping the transmitter frequency across the entire central transition powder pattern in even increments, collecting individual sub-spectra, and co-adding them.^{46,47} Experimental times at 9.4 T ranged from 5 to 80 hours, depending upon the desired S/N, pattern breadth and the number of sub-spectra collected. Further experimental NMR details can be found in the supporting information (Table E.7.1-E.7.3, Appendix E).

^1H - ^{13}C CP/MAS NMR spectra of BH and LH were acquired at $\nu_{\text{rot}} = 9.0$ and 9.9 kHz, respectively, on a 5 mm HXY probe at 9.4 T. A ^1H $\pi/2$ pulse width of 3.25 μs , optimized contact time of 4 ms, recycle delay of 4 s and ^1H decoupling fields of ca. 62 kHz, using the TPPM sequence,⁴⁸ were applied. Carbon chemical shifts were referenced with respect to TMS using the high frequency chemical shift of solid

adamantane ($\delta_{\text{iso}} = 38.57$ ppm) as a secondary reference.

Experiments at 21.1 T. ^{35}Cl NMR spectra of BH obtained in Ottawa were acquired on a Bruker HX 3.2 mm MAS probe. The ^{35}Cl MAS NMR experiment on BH was performed with a spinning frequency of $\nu_{\text{rot}} = 15$ kHz. MAS and static spectra were acquired using selective $\pi/2$ pulse widths of 3.6 and 6.0 μs , respectively, and optimized recycle delays of 1.0 s. The ^{35}Cl MAS NMR experiments conducted at the NHMFL were performed with $\nu_{\text{rot}} \approx 22$ kHz on a built-in-house HX 3.2 mm MAS probe. Selective $\pi/2$ pulse widths of 2.3 or 3.3 μs with ^1H decoupling fields of ca. 60 kHz and optimized recycle delays of 1.0 or 2.0 s were employed. For static ^{35}Cl NMR experiments, samples were packed in a rectangular glass container ($7.5 \times 5 \times 11$ mm) and spectra were acquired on a low-E rectangular-flat coil HX probe.⁴⁹ Selective $\pi/2$ pulse widths of ca. 2.0 μs with proton decoupling rf fields of ca. 60.0 kHz were used. Analytical simulations of ^{35}Cl NMR spectra were performed using WSolids.⁵⁰

7.2.3 Ab initio calculations.

^{35}Cl EFG and CS tensor parameters were calculated using Gaussian 03⁵¹ on Dell Precision workstations and the SHARCNET grid of high performance clusters.⁵² Atomic coordinates were input from the crystal structures obtained in our laboratory. All calculations were carried out on clusters comprised of a central chlorine atom and surrounding organic moieties. Hydrogen atom positions (within 3.6 Å of Cl atoms) were optimized using the B3LYP method,³⁰ since crystallographic proton positions are estimated during structural refinement. EFG calculations were performed using the

Restricted Hartree Fock (RHF) method with the cc-pVTZ basis set on Cl atoms and cc-pVDZ or 6-31G* basis sets on the other atoms (following Bryce et al.),³⁰ and with the 6-311+G* on all atoms (for comparison). CS tensor parameters were calculated using the B3LYP method with the aug-cc-pVDZ basis set on the chlorine atom and cc-pVDZ basis set on the other atoms.³⁰ The nuclear magnetic shielding tensors were calculated using the gauge-including atomic orbitals method (GIAO).^{53,54} The EFG and CS tensor parameters were extracted from the Gaussian output using EFGShield program.⁵⁵

7.3 Results and Discussion

7.3.1 Crystal structures.

Single-crystal X-ray diffraction (XRD) structures of PH⁵⁶ and LH,⁵⁷ and a structure of TH from synchrotron powder XRD data,⁵⁸ have previously been reported. Newly refined single-crystal XRD structures for PH, TH and LH were determined in our laboratory, and we also report the crystal structure for monohydrated bupivacaine (BH). The crystallographic parameters for these samples are listed in Table 7.1, and partial crystal structures are shown in Figure 7.1. Powder XRD patterns were obtained for all four parent samples, and found to match very well with simulated powder XRD patterns, ensuring the purity of the bulk samples (Figures E.7.1-E.7.4). Structural features of these systems will be addressed in the NMR discussion below.

Table 7.1. Crystal structure data for the HCl local anaesthetics.

	Procaine HCl	Tetracaine HCl	Lidocaine HCl·H₂O	Bupivacaine HCl·H₂O
empirical formula	C ₁₃ H ₂₁ ClN ₂ O ₂	C ₁₅ H ₂₅ ClN ₂ O ₂	C ₁₄ H ₂₅ ClN ₂ O ₂	C ₁₈ H ₃₁ ClN ₂ O ₂
formula weight (g/mol)	272.77	300.82	288.81	342.90
temperature (K)	173(2)	173(2)	173(2)	173(2)
wavelength (Å)	0.71073	0.71073	0.71073	0.71073
crystal system, space group	Orthorhombic, Pbca	Triclinic, P -1	Triclinic, P1 21/n 1	Orthorhombic, Pbca
unit cell dimensions (Å, deg)				
a (Å)	14.009(2)	7.3436(10)	8.391(2),	18.5429(18)
b (Å)	8.2472(12)	8.5082(12)	7.0150(17)	7.2296(7)
c (Å)	24.853(4)	13.6340(19)	26.163(6)	28.476(3)
α (deg)	90.0	105.5420(10)	90.0	90.0
β (deg)	90.0	91.8630(10)	91.414(3)	90.0
γ (deg)	90.0	99.5810(10)	90.0	90.0
volume (Å ³)	2871.4(7)	806.60(19)	1539.5(6)	3817.4(6)
Z	8	2	4	8
calculated density (g cm ⁻³)	1.262	1.239	1.246	1.193
absorption coefficient (mm ⁻¹)	0.263	0.241	0.249	0.211
F(000)	1168	324	624	1488
crystal size (mm)	0.3 × 0.2 × 0.2	0.2 × 0.1 × 0.1	0.2 × 0.1 × 0.1	0.2 × 0.1 × 0.1
θ range for data collection(deg)	1.64 to 28.3	2.53 to 28.20	1.56 to 28.27	1.43 to 28.23
limiting indices	-18 ≤ h ≤ 18, -10 ≤ k ≤ 10, -32 ≤ l ≤ 32	-9 ≤ h ≤ 9, -10 ≤ k ≤ 10, -17 ≤ l ≤ 17	-11 ≤ h ≤ 10, -9 ≤ k ≤ 9, -33 ≤ l ≤ 33	-23 ≤ h ≤ 24, -9 ≤ k ≤ 9, -37 ≤ l ≤ 37
reflections collected/unique	30086/3433 [R _(int) = 0.0447]	8886/3614 [R _(int) = 0.0268]	15806/3503 [R _(int) = 0.1231]	39005/4472 [R _(int) = 0.0986]
refinement method	Full-matrix least-squares on F ²			
data/restraints/parameters	3433/0/175	3614/0/189	3503/0/188	4472/0/224
goodness-of-fit on F ²	1.089	1.239	1.457	1.173
final R indices [I > 2σ (I)] ^a	R ₁ = 0.0428, wR ₂ = 0.1161	R ₁ = 0.0599, wR ₂ = 0.1399	R ₁ = 0.1396, wR ₂ = 0.2690	R ₁ = 0.0808, wR ₂ = 0.1671
R indices all data	R ₁ = 0.0621, wR ₂ = 0.1231	R ₁ = 0.0677, wR ₂ = 0.1462	R ₁ = 0.1897, wR ₂ = 0.2812	R ₁ = 0.1342, wR ₂ = 0.1970
largest diff, peak & hole (e Å ⁻³)	0.323 & -0.229	0.317 & -0.372	0.585 & -0.357	0.413 & -0.280

^a $R_1(F) = \sum(|F_o| - |F_c|) / \sum|F_o|$ for reflections with $F_o > 4(\sigma(F_o))$; $wR_2(F^2) = \{\sum w(|F_o|^2 - |F_c|^2)^2 / \sum w|F_o|^2\}^{1/2}$ where w is the weight given for each reflection.

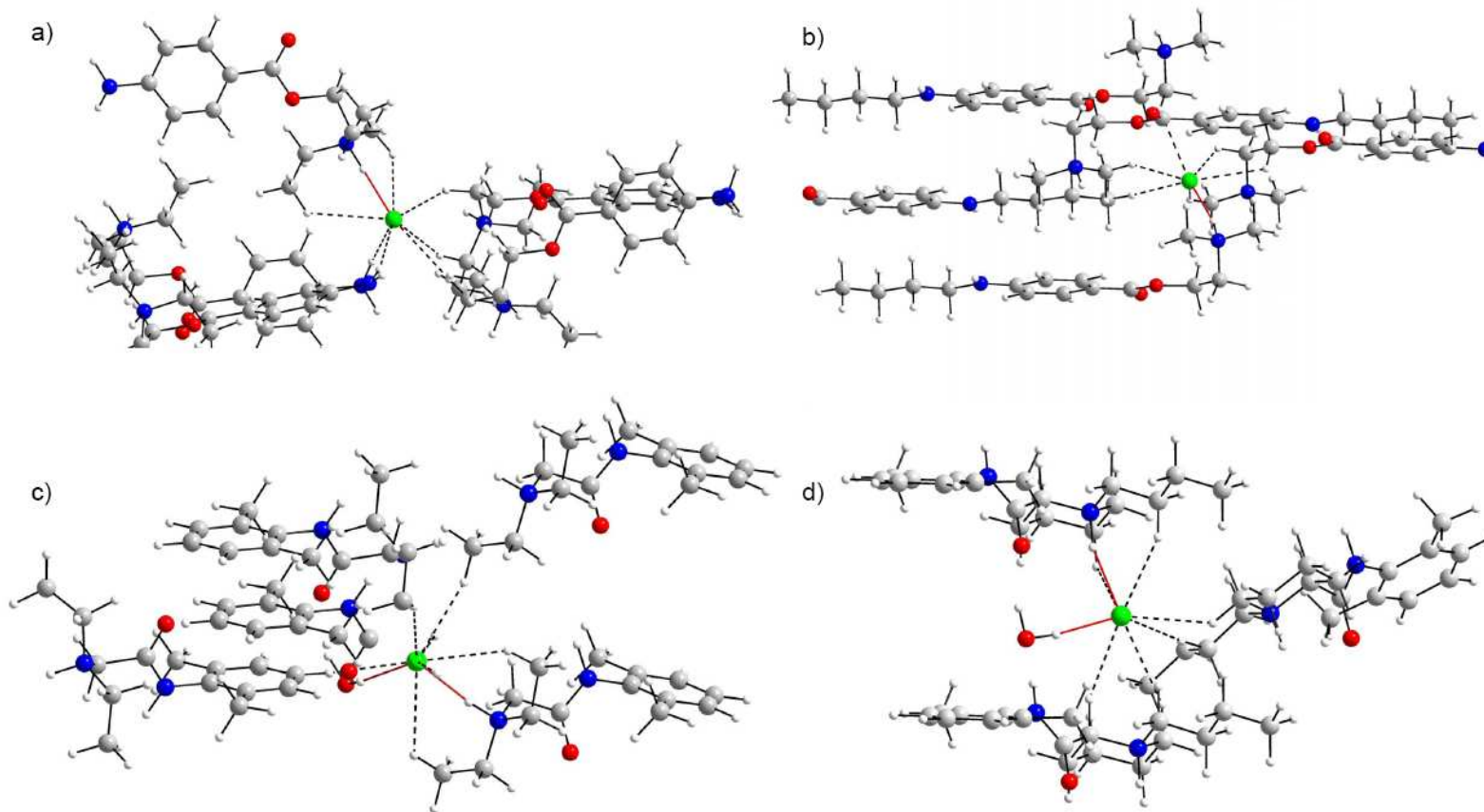


Figure 7.1. Partial crystal structures of a) PH, b) TH, c) LH, and d) BH, which focus on the chlorine atom positions. The short chlorine-hydrogen contacts are indicated in red, and longer contacts are marked with dashed lines. For TH and LH, some atoms are deleted for clarity.

7.3.2 Solid-state ^{35}Cl NMR.

In this section, solid-state ^{35}Cl NMR spectra of the four parent compounds, as well as polymorphs of LH and BH, will be discussed. Magic-angle spinning (MAS) NMR spectra were acquired at 21.1 T, in order to separate the central isotropic powder pattern from the spinning sidebands, thereby allowing for the accurate determination of the quadrupolar coupling constants, C_Q , asymmetry parameters, η_Q , and isotropic chemical shifts, δ_{iso} (see Table 7.2 for definitions and conventions). Static ^{35}Cl NMR spectra were acquired at both 9.4 and 21.1 T, in order to deconvolute spectral contributions from the electric field gradient (EFG) and chemical shielding (CS) tensors, and to extract the anisotropic chlorine CS parameters.

Table 7.2. Summary of the experimental ^{35}Cl NMR parameters.

	C_Q/MHz^a	η_Q^b	$\delta_{\text{iso}}/\text{ppm}^c$	Ω/ppm^d	κ^e	$\alpha/^\circ$	$\beta/^\circ$	$\gamma/^\circ$
PH	4.87 (7)	0.28(4)	96(6)	125(25)	-0.4(3)	95(15)	3(2)	32(8)
TH	6.00(10)	0.27(4)	71(6)	80(15)	0.4(3)	60(8)	8(5)	10(10)
LH	4.67(7)	0.77(3)	100(4)	110(15)	-0.85(3)	12(3)	40(10)	80(3)
LH1 site 1	2.52(12)	0.95(5)	85(10)	20(10)	-0.8(2)	90(40)	50(50)	60(40)
LH1 site 2	5.32 (10)	0.32(10)	110(10)	45(10)	0.8(2)	5(5)	50(15)	40(40)
BH	3.66 (10)	0.72(8)	96(10)	100(25)	0.2(4)	105(20)	90(5)	5(5)
BH1 site 1	4.75(20)	0.65(10)	118(10)	160(40)	0.9(1)	10(10)	3(1)	0(2)
BH1 site 2	5.85(20)	0.26(4)	95(10)	160(40)	-0.2(1)	18(4)	50(5)	80(5)
BH2	4.58 (5)	0.56(6)	118(5)	120(10)	0.8(1)	10(10)	0(2)	50(50)

^a Theoretical values of C_Q ($C_Q = eQV_{33}/h$) are calculated by converting from atomic units to Hz by multiplying V_{33} by $(eQ/h)(9.7177 \times 10^{21} \text{ Vm}^{-2})$, where $Q(^{35}\text{Cl}) = -0.082 \times 10^{-28} \text{ m}^2$; ^b $\eta_Q = (V_{11} - V_{22})/V_{33}$;

^c $\delta_{\text{iso}} = (\delta_{11} + \delta_{22} + \delta_{33})/3$; ^d $\Omega = \delta_{11} - \delta_{33}$; ^e $\kappa = 3(\delta_{22} - \delta_{\text{iso}})/\Omega$.

PH and TH. PH has been recrystallized from a variety of solvents and stored at high humidity, but no polymorphic forms have been observed.⁵⁹ TH, unlike PH, is known to form polymorphs arising either from heating or different recrystallization

processes.⁵⁹ However, for the purpose of this work, PH and TH polymorphism will not be discussed further; rather, these compounds will serve as benchmarks for comparison of ³⁵Cl NMR parameters with structural data for HCl LA salts and other analogous chlorine-containing systems.

According to our single crystal X-ray structure of PH (Figure 7.1a), there is one crystallographic Cl site with a close Cl...HN contact of 2.150 Å and seven longer Cl...H contacts between 2.545 Å and 3.087 Å, similar to the previously reported structure.⁵⁶ ³⁵Cl NMR spectra (Figure 7.2a) show powder patterns corresponding to a single Cl site with parameters similar to those of cocaine HCl ($C_Q = 5.027$ MHz, $\eta_Q = 0.2$)⁶⁰ and quinuclidine HCl ($C_Q = 5.25$ MHz, $\eta_Q = 0.05$).⁶¹ Both have chlorine environments similar to that of PH, with each Cl surrounded by eight H atoms, and single close contacts (Cl...HN = 2.098 and 1.888 Å, respectively).⁶²

A crystal structure of TH was obtained in our laboratory after recrystallization of commercial TH from isopropanol (Figure 7.1b). This new structure is similar to a previously reported one,⁵⁸ and has a single short Cl...HN contact of 2.112 Å and six longer Cl...HC contacts ranging from 2.794 to 3.044 Å. ³⁵Cl NMR spectra of TH (Figure 7.2b) reveal similar NMR parameters to those of PH. The slightly larger C_Q for TH is consistent with its shorter Cl...HN contact; clearly, short, single Cl...H contacts dominate the magnitude of V_{33} , the largest component of the EFG tensor.³¹ For both PH and TH, static NMR spectra acquired at 21.1 T allow for refinement of the quadrupolar parameters, as well as the determination of the principal components of the chlorine CS tensors and the relative orientation of the CS and EFG tensors (Table 7.2).

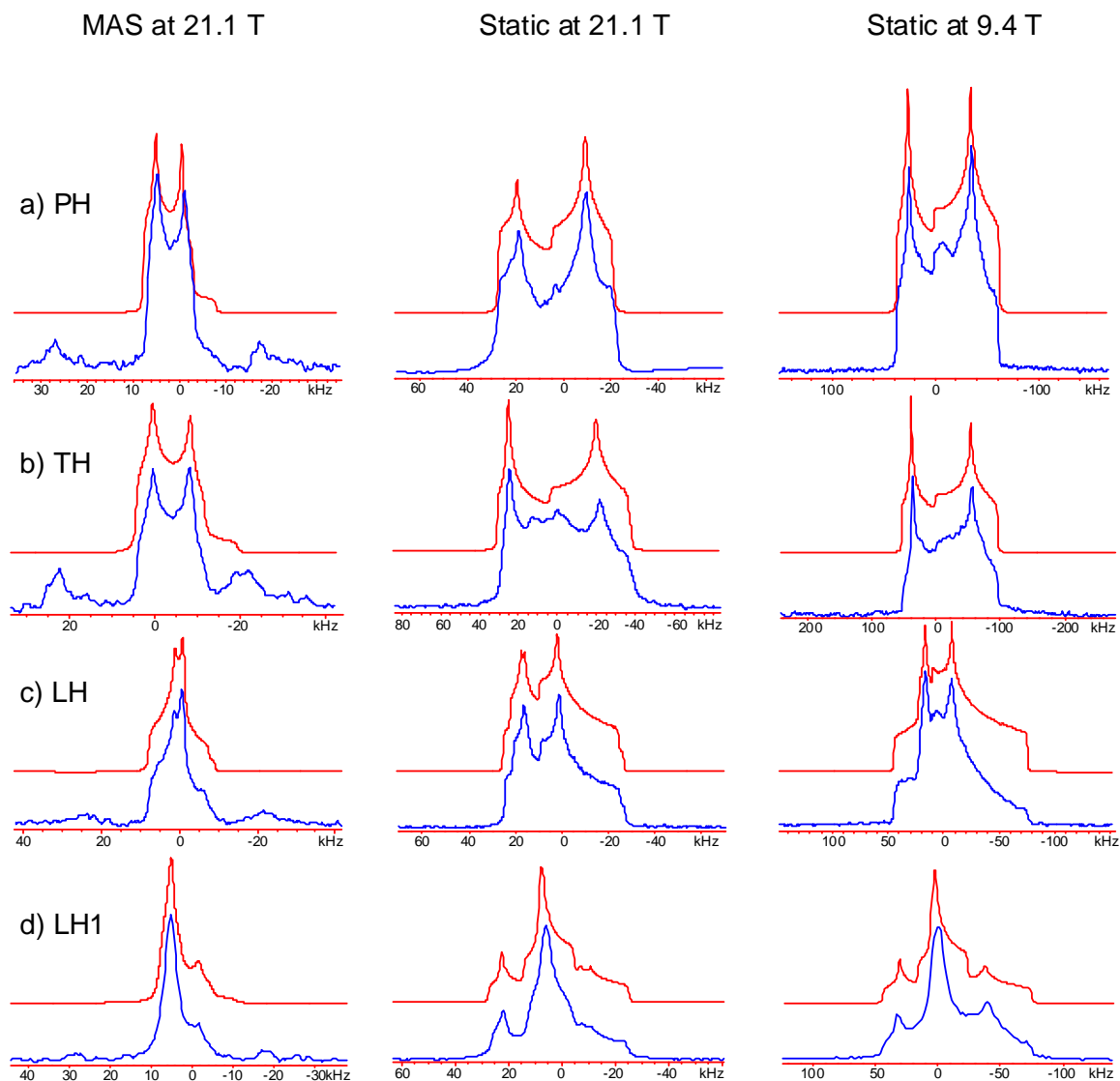


Figure 7.2. ^{35}Cl SSNMR spectra of a) PH, b) TH, c) LH and d) polymorph LH1. Top and bottom traces are simulated and experimental spectra, respectively.

The chlorine chemical shift anisotropy (CSA) parameters are in the range of those reported in the literature for similar systems.³⁸

LH & polymorph LH1. The crystal structure of LH determined in our laboratory (Figure 7.1c) is different from that previously reported;⁵⁷ however, they both have only one chlorine site in the asymmetric unit. The Cl^- ion in our structure has two hydrogen

bonds ($\text{Cl}\cdots\text{H} = 2.206$ and 2.402 \AA) and seven more distant $\text{Cl}\cdots\text{H}$ contacts (ranging from 2.7 to 3.1 \AA). ^{35}Cl NMR spectra (Figure 7.2c) of this sample reveal a value of C_Q close to that of PH; however, the η_Q is distinct from those of PH and TH. The higher η_Q for LH indicates a reduction in the axial symmetry of the ^{35}Cl EFG tensor, which possibly results from the presence of two short $\text{Cl}\cdots\text{H}$ contacts, as opposed to the single contacts in PH and TH.

It is well known that the presence of coordinating or non-coordinating water molecules can influence the solid-state structures of hydrated pharmaceutical solids.^{22,63,64} There have been no other reports of LH polymorphs; nevertheless, a new form (LH1) was made in our laboratory. Thermal gravimetric analysis (TGA) and solution ^1H NMR experiments confirm that both the commercial LH and LH1 samples are monohydrates. TGA curves (Figure E.7.5) show that the water molecules are lost at different temperatures (at $65 \text{ }^\circ\text{C}$ for LH and $50 \text{ }^\circ\text{C}$ for LH1), implying structural differences between these forms. LH1 has a distinct powder XRD pattern from LH, but a crystal suitable for single-crystal XRD could not be obtained. The ^1H - ^{13}C CP/MAS NMR spectra are slightly different, with similar groupings of peaks on a coarse chemical shift scale, but clear distinctions on a finer scale (Figure 7.3). While this data combination is indicative of polymorphism, little insight into the actual differences between LH and LH1 is readily available.

On the other hand, the ^{35}Cl NMR spectra of LH1 reveal two overlapping second-order patterns, which are especially apparent in the static spectra (Figure 7.2d & E.7.6).

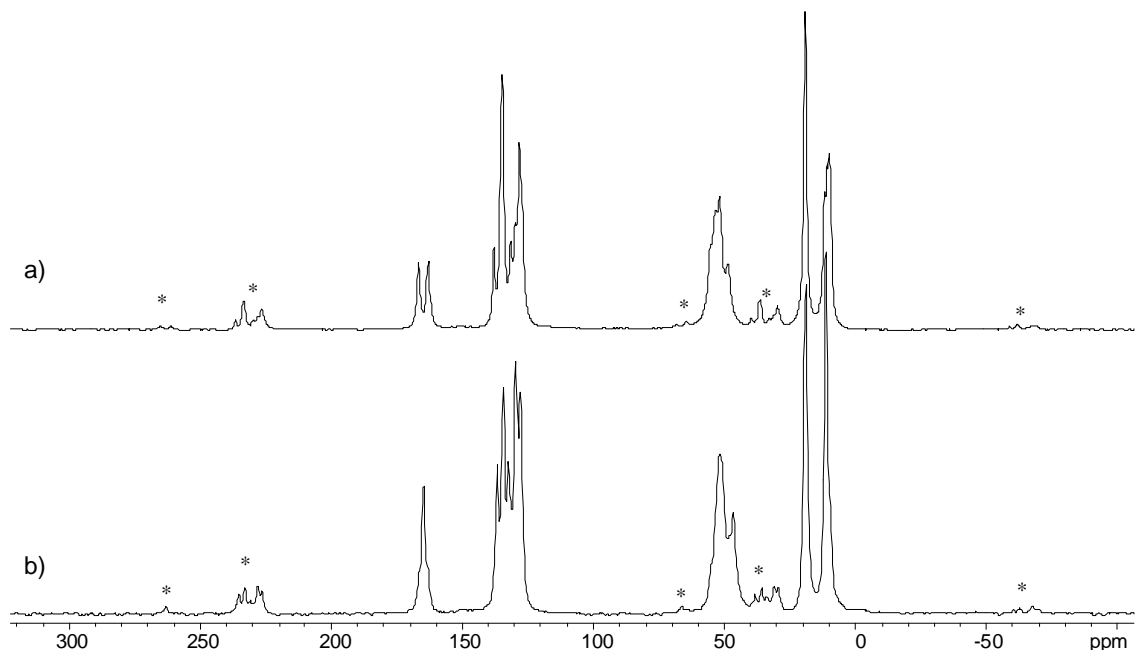


Figure 7.3. ^{13}C NMR of the monohydrated lidocaine hydrochloride (LH) samples acquired at $B_0 = 9.4$ T, $\nu_{\text{rot}} = 9.9$ kHz: a) polymorph LH1, b) commercial LH. LH has one molecule per asymmetric unit, while LH1 has two molecules per asymmetric unit, as clearly seen in the splitting of the chemical shift of the carbonyl group (165 ppm). *: denote spinning sidebands.

These spectra indicate the presence of two chlorine environments with quadrupolar parameters distinct from that of LH. Site 1, which is distinguished by a narrower central pattern, has a small C_Q , a high η_Q and a small span, all of which are similar to analogous parameters reported for L-cysteine methyl ester HCl,⁶¹ which has a Cl^- ion with three short $\text{Cl}\cdots\text{HN}$ contacts (ranging between 2.256 and 2.389 Å).⁶⁵ Site 2 has a broad pattern with two clearly visible discontinuities, arising from a larger C_Q and η_Q closer to zero, and a slightly larger span. These values are similar to those measured for PH, TH and quinuclidine HCl,⁶¹ all of which have a Cl^- ion with only one short $\text{Cl}\cdots\text{H}$ contact, suggesting that site 2 is of a similar nature. The identification of these two structurally

unique Cl sites confirms that LH and LH1 are polymorphs, and intimates two possibilities: (i) LH1 is a single phase with two crystallographically distinct Cl sites; or (ii) LH1 is a mixture of two phases, each with a crystallographically distinct Cl site; the TGA data suggests that the former is highly probable. Information obtained from ^{35}Cl SSNMR in this case is invaluable in considering options for refinement of powder XRD data, additional ^{13}C and ^1H NMR experiments, etc., for further polymorph characterization; of course, full discussion of this complete characterization is beyond the scope of the current work.

BH and polymorphs BH1 and BH2. The crystal structure of anhydrous BH has been reported in the literature;⁴¹ however, the commercial BH is monohydrate. Recrystallization of the commercial BH, and ensuing refinement of single-crystal XRD data, reveals a single chlorine site with two hydrogen bonds ($\text{Cl}\cdots\text{HO} = 2.106 \text{ \AA}$ and $\text{Cl}\cdots\text{HN} = 2.374 \text{ \AA}$) and six other $\text{Cl}\cdots\text{HC}$ contacts ranging between 2.835 and 3.045 \AA . ^{35}Cl SSNMR spectra of BH (Figure 7.4a) reveal a smaller C_Q and a higher η_Q than those of the LAs discussed above. The $\text{Cl}\cdots\text{HN}$ contact in BH is the longest of the four pharmaceuticals, and the $\text{Cl}\cdots\text{HO}$ contact is short by comparison. As a result, the quadrupolar parameters for BH are extremely different from the complexes discussed thus far, with V_{33} no longer dominated by a short $\text{Cl}\cdots\text{HN}$ contact.

BH is known to form polymorphs when heated, or solvates when recrystallized from different solvents.⁶⁶ Heating the BH sample to 120 °C leads to the formation of a polymorph, BH1, whose structure is unknown. The ^{35}Cl NMR spectra indicate the presence of two distinct chlorine sites with environments different than those in the

commercial BH (Figure 7.4b & E.7.7). In addition, the spectral discontinuities are not as sharp as in NMR spectra of highly crystalline samples, indicating some degree of disorder.

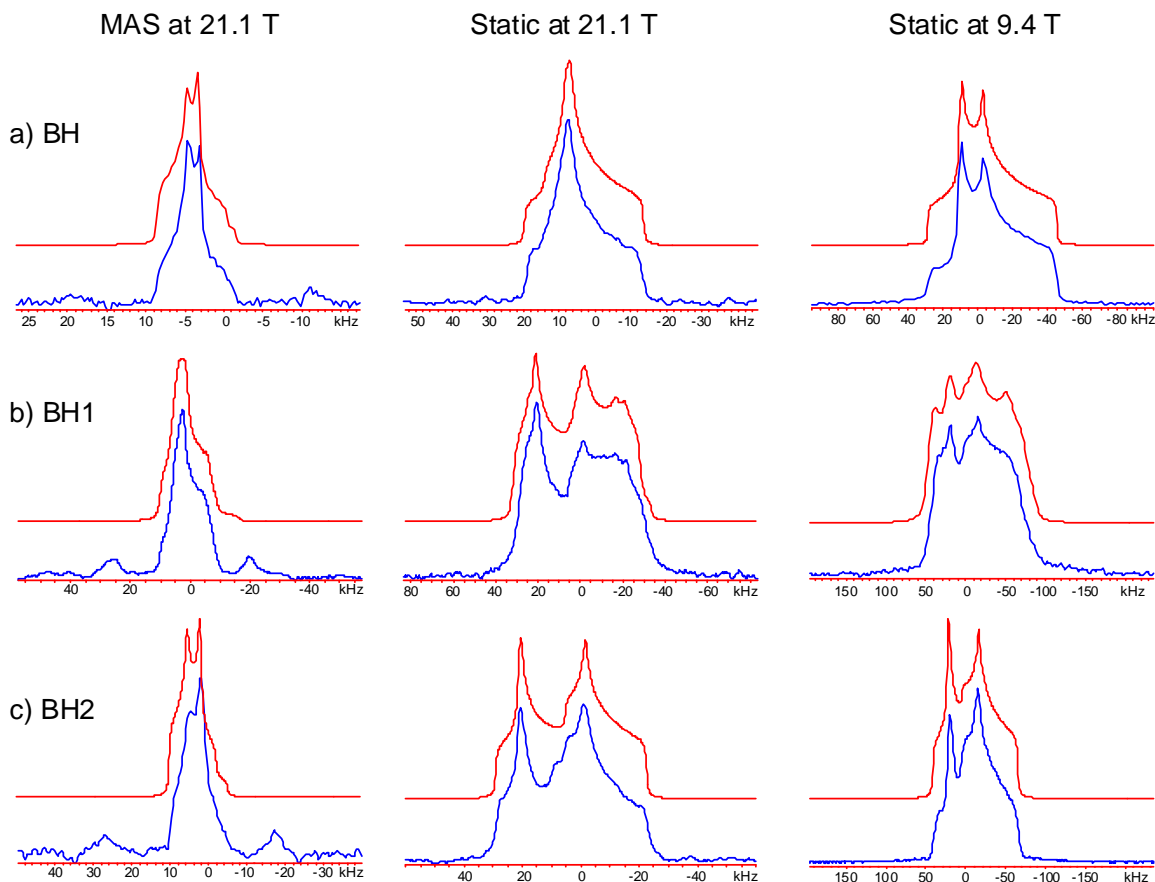


Figure 7.4. ^{35}Cl SSNMR spectra of monohydrated bupivacaine HCl (BH) and its polymorphs: a) commercial BH, b) BH1 is a polymorph obtained from the BH sample by heating it to 120° , c) BH2 is a polymorph obtained from the BH by heating it to 170° . Top and bottom traces are simulated and experimental spectra, respectively.

However, the fact that discontinuities are observed at all is consistent with some crystallinity, as confirmed by the corresponding powder XRD patterns and ^{13}C NMR data acquired by us (Figure 7.5) and others.⁶⁶ Both sites have larger quadrupolar interactions than that of BH: site 1 ($C_Q = 4.75$ MHz) is similar to the chlorine site in LH (two $\text{Cl} \cdots \text{H}$

bonds), whereas site 2 ($C_Q = 5.85$ MHz) indicates a coordination environment similar to that in TH (one Cl \cdots H bond).

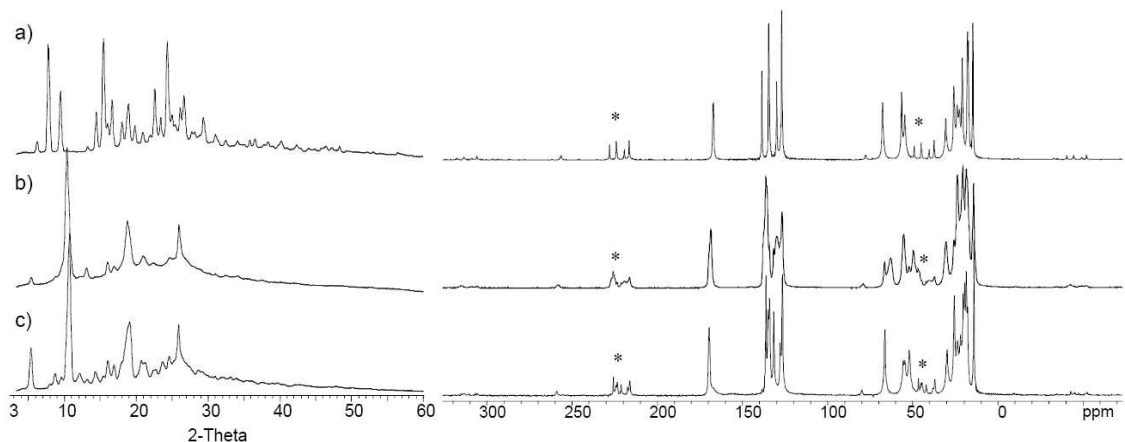


Figure 7.5. Powder XRD (left) and ^{13}C NMR spectra (right) acquired at 9.4 T, $v_{\text{rot}} = 9.0$ kHz: a) commercial BH. b) polymorph BH1 (heated to 120 °C), c) polymorph BH2 (heated to 170 °C). *: denote spinning sidebands.

Heating the BH sample to 170 °C leads to the formation of another crystalline polymorph, BH2.⁶⁶ Comparisons of powder XRD patterns and ^{13}C NMR spectra (Figure 7.5) of BH1 and BH2 indicate subtle differences between the two samples, but are inconclusive with regard to polymorphism, and are not particularly useful for any structural interpretation. However, ^{35}Cl NMR data (Figure 7.4c) indicate that BH2 has only one chlorine site, with quadrupolar parameters that are similar to site 1 of BH1. In addition, the discontinuities in the ^{35}Cl NMR powder patterns of BH2 are sharper than those of BH1, consistent with indications of higher crystallinity of BH2 indicated by both sharper powder XRD peaks and ^{13}C NMR peaks (Figure 7.5). In comparing ^{35}Cl NMR data for BH1 and BH2, it is surmised that (i) BH1 is a mixture of a non-crystalline phase

with one type of chlorine environment and a crystalline phase with a second distinct chlorine environment, and (ii) BH2 is comprised solely of one crystalline phase. Therefore, heating from room temperature to 120 °C produces new crystalline and disordered phases in BH1, the latter of which is detected by ^{35}Cl NMR but not by powder XRD. The disordered phase disappears after heating to 170 °C, leaving only a unique crystalline phase, BH2, which is similar, but not identical to the crystalline phase in BH1. In this instance, the ^{35}Cl NMR data are crucial in demonstrating that BH1 and BH2 are distinct polymorphs, and reveal a phase undetectable by XRD techniques.

7.3.3 Theoretically calculated NMR interaction tensors.

An appreciation of the relationships between solid-state structures and chlorine NMR interaction tensors will be crucial for making future structural interpretations for the many HCl pharmaceuticals for which crystal structures are unavailable. To develop a basis for understanding these relationships, we have conducted ab initio calculations of the ^{35}Cl EFG and CS tensors of the four parent pharmaceuticals, and carefully examined the principal components and tensor orientations with respect to the molecular coordinates. Following the work of Bryce et al.,³⁰ RHF calculations were found to provide the closest agreement with experiment for EFG tensor parameters, and B3LYP calculations were considerably better for CS tensor parameters (full details on the basis sets are given in the Experimental Section and Appendix E, with key results are summarized in Tables 7.3 & E.7.4). In all calculations, the molecular coordinates were taken from single-crystal structures, and only proton positions were geometry optimized.

Table 7.3. Comparison of the experimental and theoretical ^{35}Cl EFG and CS tensor parameters.

	C_Q/MHz	η_Q	$\delta_{\text{iso}}/\text{ppm}$	Ω/ppm	κ	$\alpha/^\circ$	$\beta/^\circ$	$\gamma/^\circ$
PH Exp.	4.87(7)	0.28(4)	96(6)	125(25)	-0.4(3)	95(15)	3(2)	32(8)
PH Cal.	-5.41	0.286	96	114.4	-0.16	21	6	72
TH Exp.	6.0(1)	0.27(4)	71(6)	80(15)	0.4(3)	60(8)	8(5)	10(10)
TH Cal.	-6.11	0.20	105	103.4	0.49	51	31	57
LH Exp.	4.67(7)	0.77(3)	100(4)	110(15)	-0.85(3)	12(3)	40(10)	80(3)
LH Cal.	-4.097	0.437	120	115.05	-0.52	50	78	75
BH Exp.	3.66(10)	0.72(8)	96(10)	100(25)	0.2(4)	105(20)	90(5)	5(5)
BH Cal.	3.91	0.84	108	117.24	-0.1	164	85	4.2

^a Definitions of parameters are given in Table 7.1. ^b All theoretical EFG parameters are obtained from RHF calculations featuring cc-PVTZ on the Cl atoms and 6-31G* on all other atoms. Other calculations producing reasonable agreement with experiment are included in Appendix E, Table E.7.4. Only the signs of the theoretical C_Q 's are reported, since the signs of the experimental values can not be determined from the ^{35}Cl NMR spectra.

In general, the agreement between the experimental and theoretical ^{35}Cl EFG parameters is quite good, with the only significant discrepancy being the values of η_Q for LH (expt. 0.77, theor. 0.44). It is instructive at this point to consider the EFG tensor orientations and local atomic coordinates to understand the origins of the ^{35}Cl quadrupolar parameters. PH and TH, as noted earlier, both feature single, short Cl...HN contacts, with the shorter contact distance corresponding to the larger value of C_Q in TH. Visualization of the tensor orientation aids in understanding these EFG parameters: in each case, V_{33} is found to be oriented close to the Cl...HN bond axis ($\angle(V_{33}\text{-Cl-H}) = 4.6^\circ$ and 24.8° , in PH and TH, respectively), accounting for its dependence on contact length (Figure 7.6a, 7.6b). Since there are no other short contacts, V_{11} and V_{22} are similar to one another, and the value of η_Q is closer to zero than to one.

LH and BH both possess two short hydrogen-bonding contacts: Cl...HN and Cl...HO. These environments are distinct from those of PH and TH, as reflected in the

higher values of η_Q . For LH, V_{33} is again oriented very near to the Cl \cdots HN bond axis (Figure 7.6c, $\angle(V_{33}\text{-Cl-H}) = 11.6^\circ$), and the $r(\text{Cl}\cdots\text{H})$ is very similar to that in PH, accounting for their similar values of C_Q . However, V_{11} and V_{22} are differentiated from one another by the presence of the short Cl \cdots HO contact with an H₂O molecule.

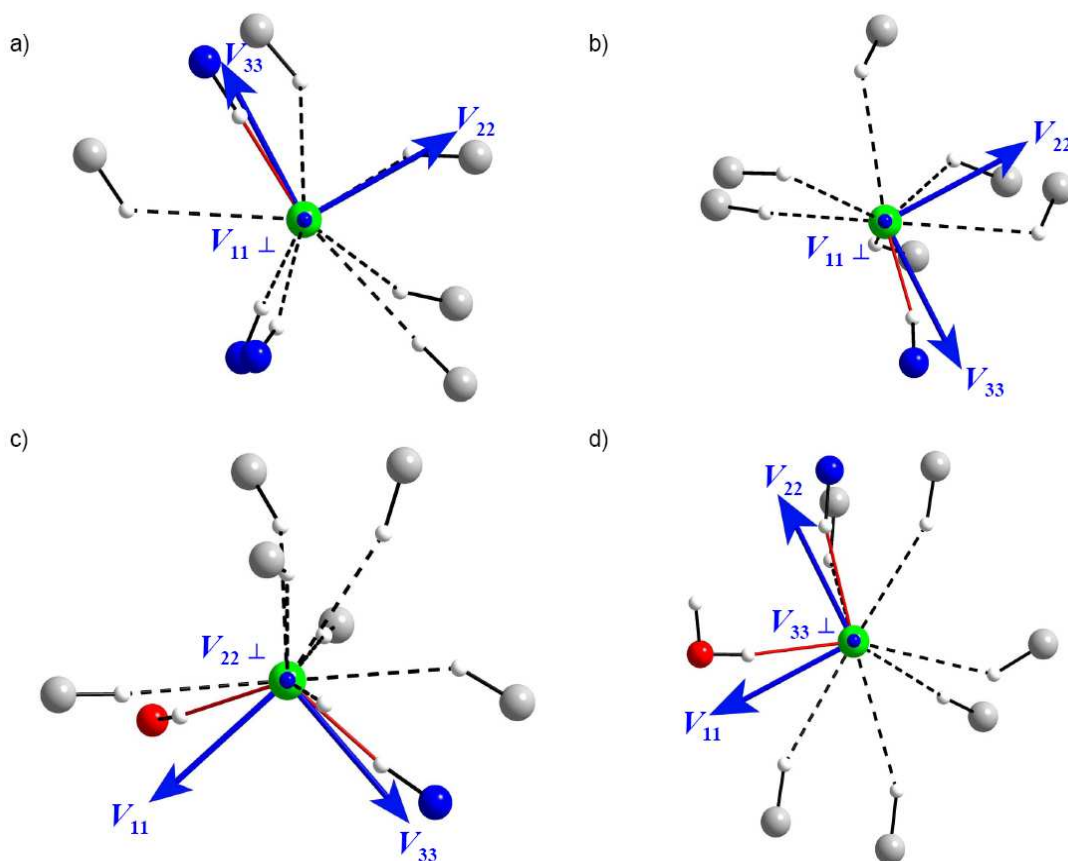


Figure 7.6. ³⁵Cl EFG tensor orientations in a) PH, b) TH, c) LH and d) BH. The diagrams above are magnifications of the chlorine sites pictured in Figure 7.1.

Rapid motion of the H₂O molecule and variation in proton coordinates very likely accounts for the discrepancy between experimental and theoretical values of η_Q . The Cl \cdots HN contact in BH is the longest of the four pharmaceuticals (2.374 Å, geom. opt. 2.182 Å), and the Cl \cdots HO contact is short by comparison (2.106 Å, geom. opt. 2.087 Å).

As a result, the ^{35}Cl EFG tensor is oriented differently from all of the other cases discussed: V_{11} , the most distinct component, is aligned close to the $\text{Cl}\cdots\text{HO}$ bond ($\angle(V_{11}\text{-Cl-H}) = 24.4^\circ$), and V_{22} is near the $\text{Cl}\cdots\text{HN}$ bond ($\angle(V_{22}\text{-Cl-H}) = 13.0^\circ$). Not only is the value of V_{33} reduced in comparison to the other systems, but the theoretically determined sign of V_{33} is observed to be opposite, which is consistent with V_{33} being oriented approximately perpendicular to the $\text{NH}\cdots\text{Cl}\cdots\text{HO}$ plane.⁶⁷ As further experimental and theoretical ^{35}Cl NMR data are accumulated for well-characterized HCl pharmaceuticals, it is anticipated that ab initio calculations will play a major role in structural characterization of polymorphs.

Examination of the theoretical CS tensor parameters also reveals good general agreement with experimental data. There are no simple correlations between basic structural features and CS tensor parameters, with one exception: we note that for PH and TH, the Euler angles indicate that V_{33} and the most shielded component of the CS tensor, σ_{33} , are nearly coincident, while for LH and BH, the higher values of β indicate non-coincidence of these components (Figure E.7.8). This is consistent with one short contact dominating the CS tensor components in the former cases, and two short contacts resulting in a change in tensor orientation in the latter cases. Of course, a wider spread of complexes will have to be examined in a forthcoming study to get a better handle on the relation of chlorine CSA to structure, since the origin of CS tensor parameters are somewhat more complex than those of the EFG tensor; nonetheless, these results show promise for future detailed structural investigations.

7.4 Conclusions

This study represents the first application of ^{35}Cl SSNMR for the structural characterization of and identification of polymorphism in solid pharmaceuticals. ^{35}Cl SSNMR spectroscopy is clearly a powerful complementary technique to XRD and ^{13}C SSNMR experiments, providing clear information on the number of chlorine sites, and showing great utility for identifying sites in non-crystalline, disordered or even impurity phases, especially in cases where the solid-state ^{13}C NMR spectra or powder XRD experiments cannot unambiguously differentiate polymorphs. The use of ultra-high field NMR spectrometers is crucial for the success of such work, for both fast acquisition of high S/N NMR spectra and accurate determination of anisotropic quadrupolar and chemical shift parameters. The sensitivity of the ^{35}Cl EFG and CS tensor parameters to the chlorine chemical environment allows for prediction of the number of short hydrogen bonds around the Cl^- ion. Theoretically calculated chlorine EFG and CS tensors are in good agreement with experimental data, and will help to improve the predictive abilities of the solid-state ^{35}Cl NMR experiments. Consideration of the tensor orientations in the molecular frames provides a deeper understanding of the correlation between NMR parameters and chlorine-hydrogen bonding environments in LAs, and holds strong promise for application to a wide array of HCl pharmaceuticals and related systems.

7.5 Bibliography

- (1) McCrone, W. C. In *Physics and Chemistry of The Organic Solid State*; A, F. D. L. M. W., Ed.; Interscience: New York, 1965; Vol. 2, pp 725-767.
- (2) Nangia, A. *Acc. Chem. Res.* **2008**, *41*, 595-604.
- (3) Reutzel-Edens, S. M. *Curr. Opin. Drug Discov. Devel.* **2006**, *9*, 806-815.
- (4) Threlfall, T. L. *Analyst* **1995**, *120*, 2435-2460.
- (5) Miller, S. P. F.; Raw, A. S.; Yu, L. X. *Polymorphism* **2006**, 385-403.
- (6) Singhal, D.; Curatolo, W. *Adv. Drug Delivery Rev.* **2004**, *56*, 335-347.
- (7) Hilfiker, R.; De Paul, S. M.; Szelagiewicz, M. *Polymorphism* **2006**, 287-308.
- (8) Lohani, S.; Grant, D. J. W. *Polymorphism* **2006**, 21-42.
- (9) Karpinski, P. H. *Chem. Eng. Technol.* **2006**, *29*, 233-238.
- (10) Llinas, A.; Box, K. J.; Burley, J. C.; Glen, R. C.; Goodman, J. M. *J. Appl. Crystallogr.* **2007**, *40*, 379-381.
- (11) Brittain, H. G.; Grant, D. J. W. *Polymorphism in Pharmaceutical Solids*; Marcel Dekker: New York, 1999; Vol. 95 pp 279-330.
- (12) Maiwald, M. *Am. Pharm. Rev.* **2006**, *9*, 95-99.
- (13) Brittain, H. G. *Polymorphism in Pharmaceutical Solids*; Marcel Dekker: New York, 1999; Vol. 95 pp 227-278.
- (14) Zell, M. T.; Padden, B. E.; Grant, D. J. W.; Schroeder, S. A.; Wachholder, K. L.; Prakash, I.; Munson, E. J. *Tetrahedron* **2000**, *56*, 6603-6616.
- (15) Padden, B. E.; Zell, M. T.; Dong, Z.; Schroeder, S. A.; Grant, D. J. W.; Munson, E. *J. Anal. Chem.* **1999**, *71*, 3325-3331.
- (16) Harris, R. K. *Analyst* **2006**, *131*, 351-373.
- (17) Berendt, R. T.; Sperger, D. M.; Munson, E. J.; Isbester, P. K. *Trends Anal. Chem.* **2006**, *25*, 977-984.
- (18) Christopher, E. A.; Harris, R. K.; Fletton, R. A. *Solid State Nucl. Magn. Reson.*

1992, *1*, 93-101.

- (19) Petkova, A. T.; Leapman, R. D.; Guo, Z.; Yau, W.-M.; Mattson, M. P.; Tycko, R. *Science* **2005**, *307*, 262-265.
- (20) Byrn, S. R.; Pfeiffer, R. R.; Stephenson, G.; Grant, D. J. W.; Gleason, W. B. *Chem. Mat.* **1994**, *6*, 1148-1158.
- (21) Harris, R. K. *J. Pharm. Pharmacol.* **2007**, *59*, 225-239.
- (22) Vogt, F. G.; Brum, J.; Katrincic, L. M.; Flach, A.; Socha, J. M.; Goodman, R. M.; Haltiwanger, R. C. *Cryst. Growth Des.* **2006**, *6*, 2333-2354.
- (23) Li, Z. J.; Abramov, Y.; Bordner, J.; Leonard, J.; Medek, A.; Trask, A. V. *J. Am. Chem. Soc.* **2006**, *128*, 8199-8210.
- (24) Wawer, I.; Pisklak, M.; Chilmonczyk, Z. *J. Pharm. Biomed. Anal.* **2005**, *38*, 865-870.
- (25) Chupin, V.; De Kroon, A. I. P. M.; De Kruijff, B. *J. Am. Chem. Soc.* **2004**, *126*, 13816-13821.
- (26) Smith, E. D. L.; Hammond, R. B.; Jones, M. J.; Roberts, K. J.; Mitchell, J. B. O.; Price, S. L.; Harris, R. K.; Apperley, D. C.; Cherryman, J. C.; Docherty, R. *J. Phys. Chem. B* **2001**, *105*, 5818-5826.
- (27) Wenslow, R. M. *Drug Dev. Ind. Pharm.* **2002**, *28*, 555-561.
- (28) Griffin, J. M.; Dave, M. R.; Steven, B. P. *Angew. Chem., Int. Ed. Engl.* **2007**, *46*, 8036-8038.
- (29) Bighley, L. D. B., S. M.; Monkhouse, D. C. In *Encyclopedia of Pharmaceutical Technology*; Swarbrick, J. B., J. C., Ed.; Marcel Dekker, 1995; Vol. 13, pp 453-499.
- (30) Bryce, D. L.; Sward, G. D. *J. Phys. Chem. B* **2006**, *110*, 26461-26470.
- (31) Bryce, D. L.; Sward, G. D.; Adiga, S. *J. Am. Chem. Soc.* **2006**, *128*, 2121-2134.
- (32) Bryce, D. L.; Bultz, E. B. *Chem.-Eur. J.* **2007**, *13*, 4786-4796.
- (33) Lucken, E. A. C. *Nuclear Quadrupole Coupling Constants*; Academic Press: London, 1969.

- (34) Biedenkapp, D.; Weiss, A. *Ber. Bunsen-Ges. Phys. Chem.* **1966**, *70*, 788-796.
- (35) Ramananda, D.; Ramesh, K. P.; Uchil, J. *Magn. Reson. Chem.* **2007**, *45*, 860-864.
- (36) Pyykko, P. *Mol. Phys.* **2001**, *99*, 1617-1629.
- (37) Harris, R. K.; Becker, E. D.; Cabral de Menezes, S. M.; Goodfellow, R.; Granger, P. *Solid State Nucl. Magn. Reson.* **2002**, *22*, 458-483.
- (38) Bryce, D. L.; Sward, G. D. *Magn. Reson. Chem.* **2006**, *44*, 409-450.
- (39) Schmidt, A. C.; Niederwanger, V.; Griesser, U. J. *J. Therm. Anal. Calorim.* **2004**, *77*, 639-652.
- (40) Schmidt, A. C.; Senfter, N.; Griesser, U. J. *J. Therm. Anal. Calorim.* **2003**, *73*, 397-408.
- (41) Csoeregh, I. *Acta Crystallogr., Sect. C: Cryst. Struct. Commun.* **1992**, *C48*, 1794-1798.
- (42) SMART; Bruker AXS Inc.: Madison, WI, 2001.
- (43) SAINTPlus; Bruker AXS Inc.: Madison, WI, 2001.
- (44) SADABS; Bruker AXS Inc.: Madison, WI, 2001.
- (45) Sheldrick, G. M.; v 6.10 ed.; Bruker AXS Inc.: Madison, Wisconsin, 2000.
- (46) Medek, A.; Frydman, V.; Frydman, L. *J. Phys. Chem. A* **1999**, *103*, 4830-4835.
- (47) Massiot, D.; Farnan, I.; Gautier, N.; Trumeau, D.; Trokiner, A.; Coutures, J. P. *Solid State Nucl. Magn. Reson.* **1995**, *4*, 241-248.
- (48) Bennett, A. E.; Rienstra, C. M.; Auger, M.; Lakshmi, K. V.; Griffin, R. G. *J. Chem. Phys.* **1995**, *103*, 6951-6958.
- (49) Gor'kov, P. L.; Chekmenev, E. Y.; Li, C.; Cotten, M.; Buffy, J. J.; Traaseth, N. J.; Veglia, G.; Brey, W. W. *J. Magn. Reson.* **2007**, *185*, 77-93.
- (50) Eichele, K.; Wasylishen, R. E.; WSolids NMR Simulation Package, 1.17.30 ed.; Dalhousie University: Halifax, CA, 2001.
- (51) Frisch, M. J.; et. al. Rev. B.03 ed.; Gaussian, Inc.: Pittsburgh, 2003.
- (52) This work was made possible by the facilities of the Shared Hierarchical Academic

Research Computing Network (SHARCNET:www.sharcnet.ca).

- (53) Ditchfield, R. *Mol. Phys.* **1974**, 27, 789-807.
- (54) Wolinski, K.; Hinton, J. F.; Pulay, P. *J. Am. Chem. Soc.* **1990**, 112, 8251-8260.
- (55) Adiga, S.; Aebi, D.; Bryce, D. L. *Can. J. Chem.* **2007**, 85, 496-505.
- (56) Dexter, D. D. *Acta Crystallogr., Sect. B: Struct. Sci.* **1972**, 28, 77-82.
- (57) Hanson, A. W.; Roehrl, M. *Acta Crystallogr., Sect. B: Struct. Sci.* **1972**, 28, 3567-3571.
- (58) Nowell, H.; Atfield, J. P.; Cole, J. C.; Cox, P. J.; Shankland, K.; Maginn, S. J.; Motherwell, W. D. S. *New J. Chem.* **2002**, 26, 469-472.
- (59) Giron, D.; Draghi, M.; Goldbronn, C.; Pfeffer, S.; Piechon, P. *J. Therm. Anal.* **1997**, 49, 913-927.
- (60) Yesinowski, J. P.; Buess, M. L.; Garroway, A. N.; Ziegeweid, M.; Pines, A. *Anal. Chem.* **1995**, 67, 2256-2263.
- (61) Bryce, D. L.; Gee, M.; Wasylshen, R. E. *J. Phys. Chem. A* **2001**, 105, 10413-10421.
- (62) Zhu, N.; Harrison, A.; Trudell, M. L.; Klein-Stevens, C. L. *Struct. Chem.* **1999**, 10, 91-103.
- (63) Lester, C.; Lubey, G.; Dicks, M.; Andol, G.; Vaughn, D.; Cambron, R. T.; Poiesz, K.; Redman-Furey, N. *J. Pharm. Sci.* **2006**, 95, 2631-2644.
- (64) Vogt, F. G.; Dell'Orco, P. C.; Diederich, A. M.; Su, Q.; Wood, J. L.; Zuber, G. E.; Katrincic, L. M.; Mueller, R. L.; Busby, D. J.; DeBrosse, C. W. *J. Pharm. Biomed. Anal.* **2006**, 40, 1080-1088.
- (65) Gorbitz, C. H. *Acta Chem. Scand.* **1989**, 43, 871-875.
- (66) Lubach, J. W.; Padden, B. E.; Winslow, S. L.; Salsbury, J. S.; Masters, D. B.; Topp, E. M.; Munson, E. J. *Anal. Bioanal. Chem.* **2004**, 378, 1504-1510.
- (67) Tang, J. A.; Ellis, B. D.; Warren, T. H.; Hanna, J. V.; Macdonald, C. L. B.; Schurko, R. W. *J. Am. Chem. Soc.* **2007**, 129, 13049-13065.

Chapter 8

Solid-State ^{35}Cl NMR Spectroscopy of Hydrochloride Pharmaceuticals

8.1 Introduction

Chlorine is present in ca. 25% of known pharmaceuticals, and HCl drugs constitute more than 50% of pharmaceutical salts.^{1,2} The ubiquity of chlorine anions in many classes of pharmaceuticals suggests that they may play important roles as NMR probe sites for structural characterization. An understanding of the structure of pharmaceuticals in the solid state is crucial in the consideration of the molecular origins of a number of their properties, including bioavailability, handling, packing, shelf life, and/or patenting of a drug.³⁻⁸ In addition, the definitive identification of structural polymorphs, solvates and hydrates of various pharmaceuticals is important in all of these respects.

Single-crystal X-ray diffraction (XRD) crystallography and high-resolution NMR spectroscopy both play pivotal roles in the characterization of the molecular structures of pharmaceuticals and their polymorphs;^{9,10} however, these techniques are limited in terms of the types of systems that can be characterized, and/or the level of clear structural information that is available. For instance, isolation of crystals suitable for single-crystal XRD studies is often very difficult or simply impossible for many standard pharmaceutical solids. Further, amorphous/disordered solids are not subject to characterization via XRD. While solution NMR is useful for structural characterization,

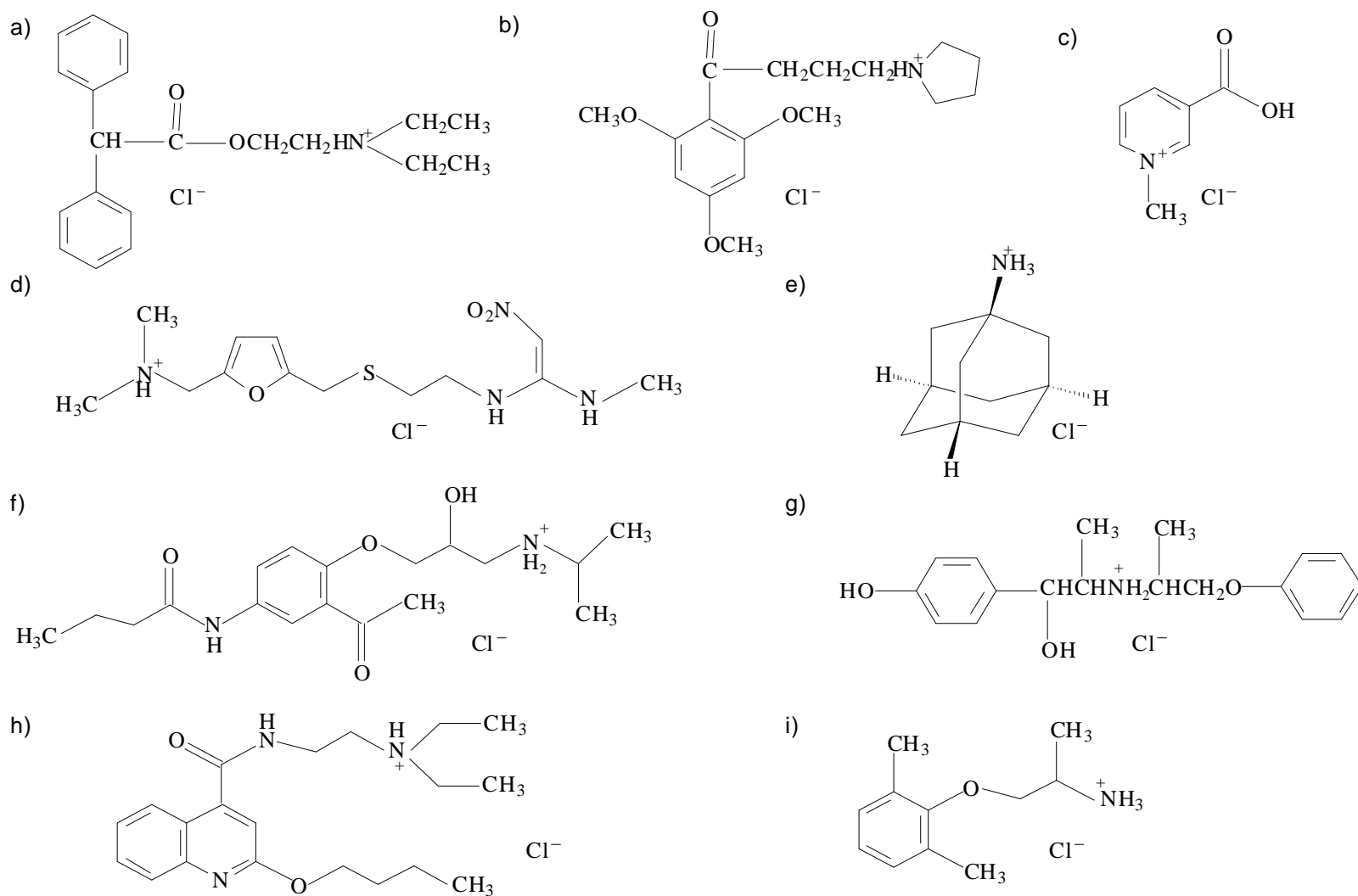
there are many cases in which the molecular structures of pharmaceuticals in solution are different from the solid-state structures (and solution NMR does not address issues surrounding any of the bulk solid properties listed above).^{11,12} Solid-state NMR (SSNMR) spectroscopy is an excellent complementary technique for structural characterization, and can also function as a standalone technique in cases where XRD and solution NMR are not applicable.^{12,13} SSNMR is sensitive to subtle changes in the local electronic environments of nuclei resulting from alterations in molecular structure such as variation in bond lengths and angles, hydrogen bonding and other intra- and intermolecular interactions. SSNMR spectroscopy is able to probe molecular structures of disordered or non-crystalline phases of solid pharmaceuticals, or other samples unsuitable for XRD experiments, and is capable of providing information on differences in molecular structure, reactivity, stability and polymorphism.

Traditionally, ¹³C SSNMR experiments have been key in probing pharmaceutical solids, allowing for the study of site-specific chemical changes, hydration, solid-state dynamics, and quantification of mixtures of crystalline and/or amorphous phases.¹¹ In cases where ¹³C NMR spectra are ambiguous in their meaning, SSNMR of other nuclides has been applied, including ¹H, ²H, ¹⁵N, ³¹P and ¹⁹F, and ²³Na.¹⁴⁻²⁰ In the previous chapter and recent publication,²¹ we demonstrated that ³⁵Cl SSNMR spectroscopy is a very useful probe of the different anionic chlorine sites present in local anesthetic HCl drugs and their polymorphs. ³⁵Cl SSNMR provides clear information on the number of chlorine sites (and potentially their structural environments) and shows great utility for distinguishing sites in microcrystalline, non-crystalline, disordered and/or even impurity phases. The

sensitivity of the chlorine chemical shift (CS) and electric field gradient (EFG) tensors to small changes in the Cl^- environments is reflected in the striking differences between the ^{35}Cl SSNMR powder patterns. ^{35}Cl SSNMR is very useful in cases where solid-state ^{13}C NMR spectra or powder XRD data are indeterminate; of course, it can be used to complement or support results from these techniques as well. We have now extended this research to include a variety of HCl pharmaceuticals.

Chlorine has two NMR-active isotopes, ^{35}Cl and ^{37}Cl , which are both half-integer quadrupoles (both spin = 3/2, $Q(^{35}\text{Cl}) = -0.082 \times 10^{-28} \text{ m}^2$ and $Q(^{37}\text{Cl}) = -0.065 \times 10^{-28} \text{ m}^2$)^{22,23} Due to their low gyromagnetic ratios, they are classified as unresponsive, low-gamma nuclei, despite their relatively high natural abundances (75.53% and 24.47%, respectively). SSNMR experiments on ^{35}Cl are more common due to its higher receptivity. The recent availability of ultra-high magnetic field spectrometers and signal-enhancing pulse sequences (vide infra) has made $^{35/37}\text{Cl}$ SSNMR experimentation a viable option for the routine investigation of a variety of chlorine-containing systems. In part, the work of Bryce et al. on HCl salts of amino acids was the inspiration for our work in this area.²⁴⁻²⁷ A wide range of applications of ^{35}Cl SSNMR has been recently reviewed by Bryce et. al.,^{28,29} and we refer readers to these articles for further details.

Herein, we describe the application of solid-state ^{35}Cl NMR spectroscopy for the structural characterization of HCl salts of adiphenine (AD), buflomedil (BU), trigonelline (TR), ranitidine (RA), amantadine (AM), acebutolol (AC), isoxsuprine (IS), dibucaine (DI), and mexiletine (ME) (Scheme 8.1). These drugs are used in the treatment of a variety of medical conditions or diseases such as hypertension, arrhythmias, vasodilation,



Scheme 8.1. The structures of a) adiphenine HCl (AD), b) buflomedil HCl (BU), c) trigonelline HCl (TR), d) ranitidine HCl (RA), e) amantadine HCl (AM), f) acebutolol HCl (AC), g) isoxsuprine HCl (IS) h) dibucaine HCl (DI) and i) mexiletine HCl (ME).

viral infections, peptic ulcers, etc. ^{35}Cl magic angle spinning (MAS) SSNMR spectra were acquired at 21.1 T, and static spectra were acquired at both 21.1 T and 9.4 T. Our previous work has shown that the use of ultrahigh-field NMR spectrometers is crucial for both the fast acquisition of high S/N NMR spectra and the accurate determination of anisotropic quadrupolar and chemical shift parameters. The WURST-QCPMG pulse sequence^{30,31} is very beneficial for the acquisition of broad, static ^{35}Cl NMR powder patterns, combining the uniform broadband excitation of WURST pulses^{32,33} with dramatic signal enhancement of the QCPMG protocol.³⁴ Quadrupolar and chemical shift (CS) parameters extracted from ^{35}Cl SSNMR spectra are used to distinguish different chlorine environments in these drugs; in particular, the quadrupolar parameters are related to the number of short $\text{Cl}\cdots\text{H}$ hydrogen contacts with the chlorine ions, as well as the local geometry. These data are complemented by first principles calculations of EFG and nuclear shielding (NS) tensors, in order to correlate the local chlorine environments with the local structure and symmetry, and to develop a basic understanding of the origins of the chlorine NMR interaction tensors.

8.2 Experimental

8.2.1 Powder XRD.

All samples were purchased from Sigma-Aldrich Canada, Ltd. and their purities and crystal structures were confirmed using powder XRD. Powder XRD patterns were collected using a D8 DISCOVER X-ray diffractometer equipped with an Oxford Cryosystems 700 Cryostream Plus Cooler. A $\text{Cu-K}\alpha$ ($\lambda = 1.54056 \text{ \AA}$) radiation source

with a Bruker AXS HI-STAR area detector running under the General Area Detector Diffraction System (GADDS) were used.

8.2.2 Solid-State NMR.

Static ^{35}Cl SSNMR spectra were acquired on a Varian Infinity Plus spectrometer equipped with an Oxford 9.4 T ($\nu_0(^1\text{H}) = 400$ MHz) wide-bore magnet at the University of Windsor with $\nu_0(^{35}\text{Cl}) = 39.26$ MHz. Ultra-high field ^{35}Cl NMR experiments were carried out on an ultra-wide bore 900 MHz (21.1 T) home-built superconducting NMR magnet ($\nu_0(^{35}\text{Cl}) = 88.125$ MHz) at the NHMFL in Tallahassee, Florida. Spectra were acquired using either a Hahn-echo or WURST-QCPMG pulse sequence,^{30,31} and chlorine chemical shifts were referenced to NaCl(s) ($\delta_{\text{iso}} = 0.0$ ppm).³¹ Analytical simulations of ^{35}Cl static and some MAS NMR spectra were performed using WSolids.³⁵ Simulations of ^{35}Cl MAS NMR spinning sideband manifolds were generated with SIMPSON,³⁶ using 10 gamma angles and powder averaging over 4180 crystal orientations calculated using the Zaremba Conroy Wolfsberg (ZCW) method.

Experiments at 21.1 T. For the MAS experiments, samples were finely ground and packed into 3.2 mm zirconia rotors. ^{35}Cl MAS NMR experiments were performed with spinning speeds (ν_{rot}) ranging from 20 to 23.4 kHz on a home-built HX 3.2 mm MAS probe. Selective ^{35}Cl $\pi/2$ pulse widths ranged between 2.0 and 2.2 μs . ^1H decoupling fields of ca. 90 kHz and optimized recycle delays between 1.0 and 3.0 s were utilized. For static ^{35}Cl NMR experiments, samples were packed in a rectangular glass container ($7.5 \times 5 \times 11$ mm) and spectra were acquired using a low-E rectangular-flat coil HX probe.³⁷ Selective $\pi/2$ pulse widths of 2.5 μs with proton decoupling rf fields of ca.

62 kHz were employed. Additional experimental NMR details are included in Appendix F (Tables F.8.1 and F.8.2).

Experiments at 9.4 T. Samples were finely ground and packed into either 5 mm o.d. zirconium oxide rotors or glass NMR tubes. ^{35}Cl NMR spectra were collected on either a double resonance (HX) static probe or a triple resonance MAS (HXY) probe. For the Hahn-echo experiments, central-transition selective $\pi/2$ pulse widths between 1.5 and 2.2 μs and an optimized recycle delay of 0.5 s were used. A 50 kHz ^1H decoupling field was applied in most cases. For the WURST-QCPMG³⁰ experiments, spectra were collected using the WURST-80 pulse shape.³² The WURST pulse length was set to 50 μs and swept at a rate of 10 or 12 MHz/ms with an offset of either 250 or 300 kHz and rf power of 14 or 18 kHz. A ^1H decoupling field of 42 kHz was applied in these experiments. The number of echoes ranged between 35 and 120, depending on the transverse relaxation characteristics of ^{35}Cl in each sample. A recycle delay of 0.5 s and a spectral width of either 500 or 800 kHz were used. Further experimental NMR details are included in Appendix F (Table F.8.3).

8.2.3 Ab initio calculations.

^{35}Cl EFG and NS tensor parameters were calculated using Gaussian 09³⁸ on the SHARCNET grid of high performance clusters.³⁹ Atomic coordinates were taken from the crystal structures reported in the literature.⁴⁰⁻⁴⁹ In some cases, calculations were carried out on clusters comprised of a central chlorine atom and surrounding organic moieties which have protons within 3.6 Å from the chlorine anions. In certain cases (BU,

AC, AM, DI and ME), more than one chlorine atom was included in the calculation (vide infra). Hydrogen positions were optimized using the B3LYP method.²⁵ EFG calculations were performed using the Restricted Hartree Fock (RHF) method with the cc-pVTZ basis set on Cl atoms and 6-31G* basis sets on the other atoms.²⁵ NS tensor parameters were calculated using the B3LYP method with the aug-cc-pVDZ basis set on the chlorine atom and cc-pVDZ basis set on the other atoms,²⁵ using the gauge-including atomic orbitals method (GIAO).^{50,51} The EFG and NS tensor parameters were extracted from the Gaussian output using EFGShield program.⁵² Calculated isotropic NS values were converted to isotropic CS values using the following equation: $\delta_{\text{iso(sample)}/\text{ppm}} = \sigma_{\text{iso}}(\text{HCl, g})/\text{ppm} - \sigma_{\text{iso}}(\text{sample})/\text{ppm} + 28 \text{ ppm} + 45.37 \text{ ppm}$, where $\sigma_{\text{iso}}(\text{HCl, g}) = 952.62 \text{ ppm}$ (from a B3LYP/aug-cc-pVDZ(Cl) calculation on HCl), 28 ppm is the chemical shift of HCl⁵³ and 45.37 ppm is the difference between the chemical shift of NaCl (s) and NaCl (l).²⁶

EFG calculations on RA were also performed using CASTEP NMR program^{54,55} in the Materials Studio 4.3 environment on an HP xw4400 workstation with a single Intel Dual-Core 2.67 GHz processor and 8 GB DDR RAM. Ultrasoft pseudopotentials were used for ³⁵Cl EFG calculations with a plane wave basis set cut-off of 450 eV in a coarse accuracy basis set with the Monkhorst-Pack *k*-space with a grid size of 1×2×1. The Perdew, Burke and Ernzerhof (PBE) functionals were used in the generalized gradient approximation (GGA) for the exchange-correlation energy.^{56,57}

8.3 Results and Discussion

In this section, the ^{35}Cl SSNMR data for the HCl pharmaceuticals are presented followed by a discussion of the ab initio calculation results. The discussion is organized such that the samples are grouped based on the number and type of $\text{Cl}\cdots\text{H}$ contacts and/or the number of chlorine sites.

8.3.1 Solid-state ^{35}Cl NMR.

The HCl pharmaceuticals are listed in Table 8.1, along with short hydrogen-bond contacts, quadrupolar coupling constants, C_Q , asymmetry parameters, η_Q , and isotropic chemical shifts, δ_{iso} .

Table 8.1: A comparison of short Cl...H contacts and experimentally determined NMR parameters.

		Key Cl...H Contacts (Experimental) (Å) ^a	Key Cl...H Contacts (Theoretical) (Å) ^b	C _Q /MHz	η _Q	δ _{iso} /ppm
AD	Cl...HN	2.05	2.037	5.94(6)	0.18(3)	128(5)
BU	Cl...HN	2.184	1.951	5.67(13)	0.18(6)	75(10)
TH ^c	Cl...HN	2.112	1.899	6.00(10)	0.27(4)	71(6)
TR	Cl...HO	1.909	1.878	7.50(12)	0.05(3)	70(10)
RA	Cl...HN	2.132	2.017	4.70(10)	0.92(3)	75(5)
	Cl...HN	2.366	2.208			
LH ^c	Cl...HN	2.206	1.995	4.67(7)	0.77(3)	100(4)
	Cl...HOH	2.402	2.246			
AM	Cl...HN	2.076	2.122	2.90(4)	0.68(3)	131(5)
	Cl...HN	2.184	2.117			
	Cl...HN	2.319	2.182			
CM ^c	Cl...HN	2.256	-----	2.37(1)	0.81(3)	94
	Cl...HN	2.269	-----			
	Cl...HN	2.389	-----			
GA ^c	Cl...HO	2.073	-----	3.61(1)	0.65(2)	102(1)
	Cl...HN	2.107	-----			
	Cl...HN	2.137	-----			
AC	Cl...HN	2.162	2.11	4.57(5)	0.50(4)	95(5)
	Cl...HN	2.408	2.267			
	Cl...HO	2.197	2.103			
HM ^c	Cl...HN	2.165	-----	4.59(3)	0.46(2)	93(1)
	Cl...HN	2.265	-----			
	Cl...HO	2.233	-----			
IS	Cl...HO	2.328	2.171	5.50(15)	0.25(5)	120(10)
	Cl...HO	2.36	2.183			
	Cl...HN	2.34	2.146			
	Cl...HN	2.529	2.402	5.4(1)	0.94(2)	99(10)
TE ^c	Cl...HN	2.3	-----			
	Cl...HN	2.351	-----			
	Cl...HO	2.206	-----			
	Cl...HO	2.313	-----			
DI site 1	Cl...HN	-----	2.01	4.65(20)	0.86(7)	105(15)
	Cl...HN	-----	2.361			
DI site 2	Cl...HN	-----	1.928	4.00(20)	0.93 (7)	95(15)
	Cl...HN	-----	2.254			
	Cl...HOH	-----	2.111			
ME site 1	Cl...HN	2.227	2.013	5.45(10)	0.40(8)	90(5)
	Cl...HN	2.288	2.103			
ME site 2	Cl...HN	2.284	2.101	3.10(10)	0.55(10)	130(5)
	Cl...HN	2.323	2.121			
	Cl...HN	2.455	2.307			
	Cl...HN	2.486	2.355			

^a This is a list of the shortest Cl...H contacts in this series of HCl pharmaceuticals. The upper threshold is 2.60 Å. ^b This is a list of the shortest Cl...H contacts as determined via first principles energy minimization and geometry optimization. See the experimental section for details. ^c These systems are included for comparison.

These parameters were obtained for all samples from numerical/analytical simulations of ^{35}Cl MAS SSNMR spectra which were acquired at 21.1 T in order to reduce/remove overlap between the isotropic pattern and its spinning sidebands, and to average the effects of chemical shift anisotropy (CSA). Static ^{35}Cl NMR spectra were acquired at both 9.4 and 21.1 T, in order to deconvolute the effects of the EFG and CS tensors on the powder patterns and accurately measure the CS tensor parameters. A complete listing of all of the EFG and CS tensor parameters extracted from the simulations of the ^{35}Cl NMR spectra are summarized in Table 8.2.

Table 8.2. Summary of the experimental ^{35}Cl NMR parameters.

	C_Q/MHz^a	η_Q^b	$\delta_{\text{iso}}/\text{ppm}^c$	Ω/ppm^d	κ^e	$\alpha/^\circ$	$\beta/^\circ$	$\gamma/^\circ$
AD	5.94(6)	0.18(3)	128(5)	155(20)	0.60(20)	10(10)	13(2)	35(15)
BU	5.67(13)	0.18(6)	75(10)	125(30)	-0.60(20)	5(5)	8(4)	45(10)
TR	7.50(12)	0.05(3)	70(10)	120(30)	0.80(20)	30(20)	12(5)	50(15)
RA	4.70(10)	0.92(3)	75(5)	70(15)	0.30(30)	55(10)	95(10)	10(10)
AM	2.90(4)	0.68(3)	131(5)	50(5)	0.60(20)	80(10)	80(10)	20(20)
AC	4.57(5)	0.50(4)	95(5)	95(10)	-0.30(30)	15(5)	15(5)	60(5)
IS	5.50(15)	0.25(5)	120(10)	50(20)	0.50(40)	40(20)	55(15)	20(20)
DI site 1	4.65(20)	0.86(7)	105(15)	100(20)	-0.26(60)	70(15)	80(50)	90(10)
DI site 2	4.00(20)	0.93(7)	95(15)	80(20)	-0.20(60)	95(15)	100(50)	10(10)
ME site 1	5.45(10)	0.40(8)	90(5)	80(20)	-0.80(20)	40(30)	100(20)	0
ME site 2	3.10(10)	0.55(10)	130(5)	75(20)	0.80(20)	10(10)	5(5)	0

^a C_Q ($C_Q = eQV_{33}/h$) where $Q(^{35}\text{Cl}) = -0.082 \times 10^{-28} \text{ m}^2$; ^b $\eta_Q = (V_{11} - V_{22})/V_{33}$; ^c $\delta_{\text{iso}} = (\delta_{11} + \delta_{22} + \delta_{33})/3$; ^d $\Omega = \delta_{11} - \delta_{33}$; ^e $\kappa = 3(\delta_{22} - \delta_{\text{iso}})/\Omega$.

Systems with single Cl sites with one short Cl...H contact: Adiphenine (AD),

Buflomedil (BU) and Trigonelline (TR) Hydrochlorides. The crystal structures of AD

and BU both have single Cl sites involved in only one short hydrogen contact (Cl...HN),

(Table 8.1 and Figures 8.1a, 8.1b).^{41,42}

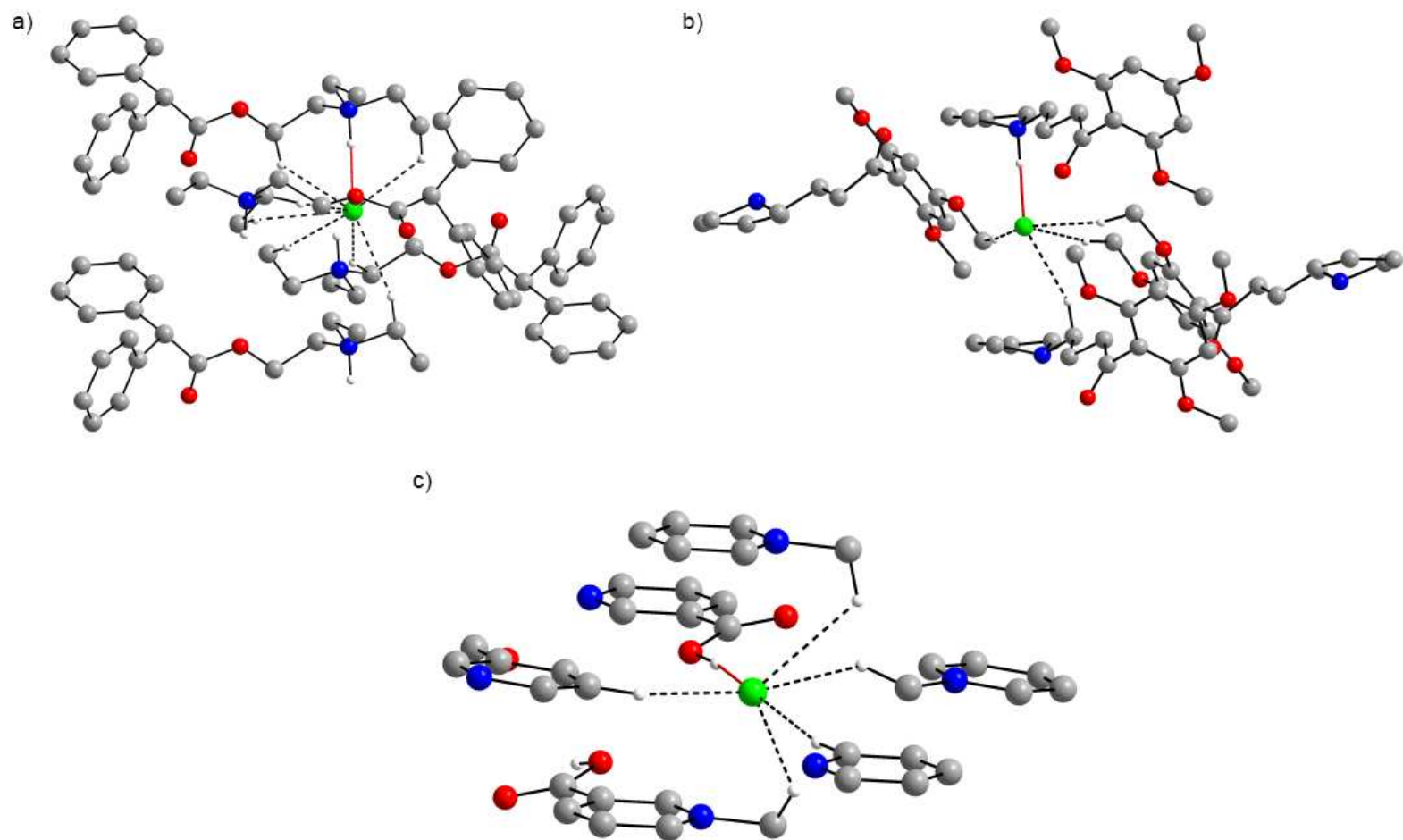


Figure 8.1. Partial crystal structures of a) AD, b) BU and c) TR which focus on the chlorine atom positions. The short chlorine-hydrogen contacts are indicated in red, and longer contacts are marked with dashed lines. Hydrogens attached to carbon atoms and away (>3.0 Å) from the chlorine ion are deleted for clarity.

The ^{35}Cl NMR spectra of each of these pharmaceuticals (Figures 8.2a, 8.2b) indicate a single chlorine site, in agreement with the known structures. Simulation of these spectra reveal EFG and CS tensor parameters which are similar to those of tetracaine hydrochloride (TH), in which the chlorine ion is also engaged in a single hydrogen contact of similar length (Table 8.1).²¹ The η_Q value, which is the same for both AD and BU, indicates a nearly axially symmetric ^{35}Cl EFG tensor, also similar to the case of TH.

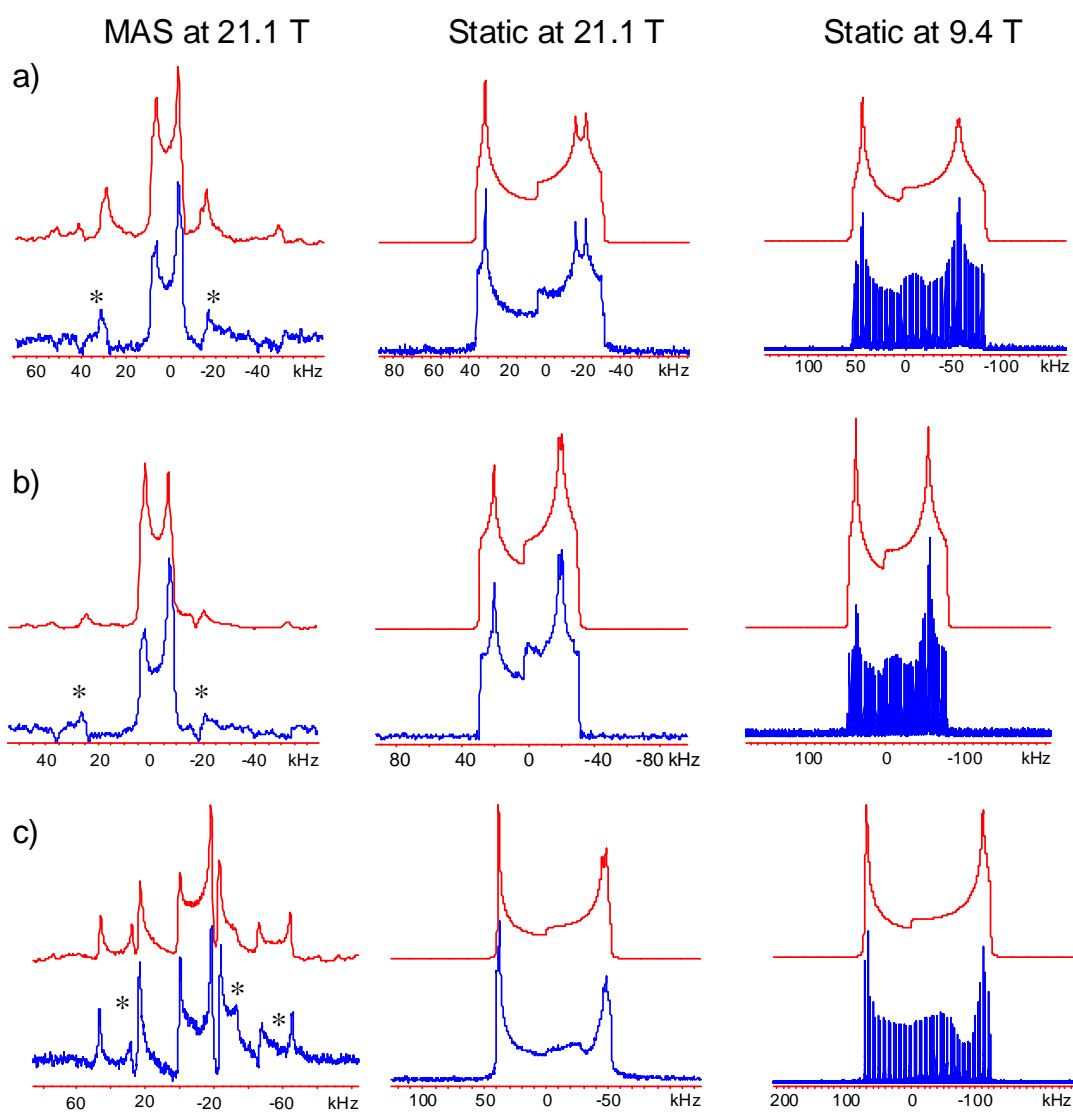


Figure 8.2. ^{35}Cl SSNMR spectra of a) AD, b) BU, and c) TR. The top patterns are simulations and bottom ones are experimental. *: indicates spinning sidebands.

The crystal structure of TR also has a single Cl^- site engaged in only one short hydrogen contact with the COOH group (Table 8.1, Figure 8.1c).⁴⁰ Such distances are in the lower limit of the range of typical $\text{Cl}\cdots\text{H}$ hydrogen bonds in organic HCl salts.²⁵ The ^{35}Cl NMR spectra (Figure 8.2c) indicate the presence of a single chlorine environment, in agreement with the crystal structure. Simulation of these spectra reveal a C_Q (Table 8.2) which is the largest of all of the ^{35}Cl C_Q values of hydrochloride salts reported to date,²⁸ the second largest being that of aspartic acid hydrochloride ($C_Q = 7.1$ MHz).²⁷ The η_Q value near zero indicates an axially symmetric ^{35}Cl EFG tensor; this means that the largest component of the EFG tensor, V_{33} , is unique, and most likely oriented along (or close to) the $\text{Cl}\cdots\text{HO}$ hydrogen bond.

It is obvious from these data that for HCl drugs with single short $\text{Cl}\cdots\text{H}$ contacts, the C_Q values increase with decreasing $\text{Cl}\cdots\text{H}$ distance; this trend is consistent with our previous observations.²¹ Thus, the larger C_Q in TR in comparison to those of AD and BU is likely due to the much shorter $\text{Cl}\cdots\text{HO}$ contact. The chlorine CS tensor parameters in these systems are consistent with those of HCl salts. The Euler angle β , in all three cases, is close to zero, indicating that the largest component of the EFG tensor, V_{33} , is almost coincident with the largest CS tensor component, δ_{33} .

Systems with single Cl^- sites and multiple $\text{Cl}\cdots\text{HN}$ contacts: Ranitidine Hydrochloride (RA) and Amantadine Hydrochloride (AM). There are several crystal structures for RA reported in the literature.^{43,58,59} Based on the powder XRD diffraction pattern (Figure F.8.1, Appendix F), our sample has the same crystal structure as that reported by Hempel et al.,⁴³ which has a single Cl^- engaged in two hydrogen bonds

(Cl···HN, Table 8.1 and Figure 8.3a). The ^{35}Cl NMR spectra reveal a single chlorine site (Figure 8.4a). The values of C_Q and η_Q are similar to those of lidocaine HCl (LH), where the chlorine site is in a similar environment; making two short hydrogen contacts.²¹

The single chlorine site in the AM structure has three short hydrogen contacts with protons of different NH_3 groups (Figure 8.3b).⁴⁴ ^{35}Cl NMR spectra reveal a single chlorine site in agreement with the crystal structure (Figure 8.4b). Simulation of the narrow central transition pattern yields a C_Q value between those of L-cysteine methyl ester (CM) and L-glutamic acid (GA).^{24,26} In the case of CM, the chlorine anion is involved in three hydrogen bonds arranged in a similar manner to the chlorine ion in AM, but with longer Cl···HN distances (Figure 8.3c).⁶⁰ In the structure of GA, the chlorine is also engaged in three hydrogen contacts (one Cl···HO and two Cl···HN, Figure 8.3d) which are shorter than those of AM and CM.⁶¹ The slightly larger C_Q of GA in comparison to those of AM and CM is likely due to the shorter Cl···H distances and/or the drop in spherical symmetry around the chlorine anion (due to fact that one of these distances is associated with an OH group). In comparing the NMR parameters of RA and AM, it seems possible that the C_Q value may decrease with an increasing number of hydrogen bonds, unless these bonds are arranged in a non-spherically symmetric environment around the chlorine. The high η_Q value indicates that V_{11} is the distinct component of the EFG tensor (i.e., $V_{22} \approx V_{33}$). The CS tensor parameters are also in the range of those of HCl salts, and the Euler angle β is close to 90° indicating that the direction of the largest shielding is perpendicular to V_{33} .

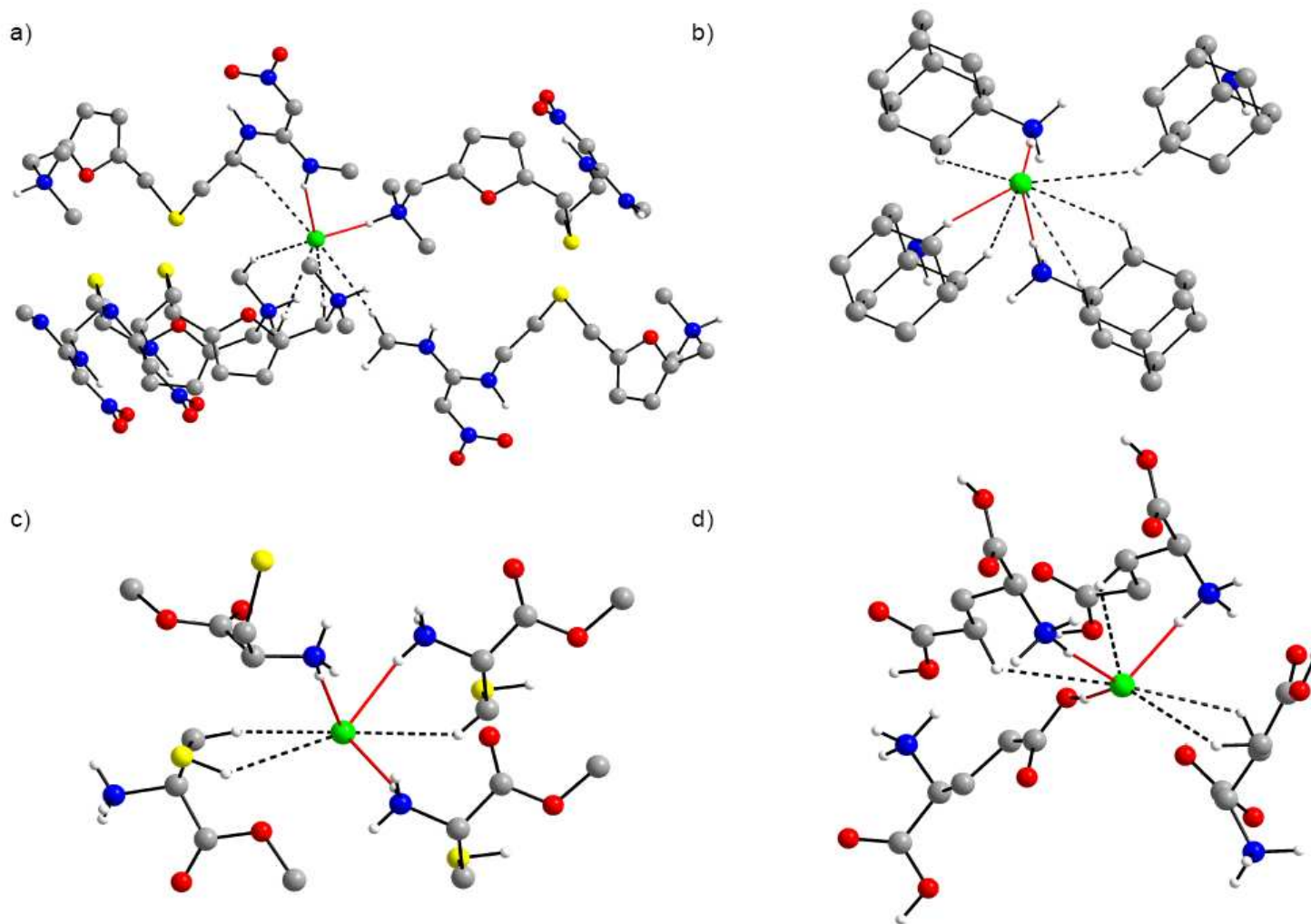


Figure 8.3. Partial crystal structures of a) RA, b) AM, c) CM, and d) GA which focus on the chlorine atom positions. The short chlorine-hydrogen contacts are indicated in red, and longer contacts are marked with dashed lines. Hydrogens attached to carbon atoms and away ($>3.0 \text{ \AA}$) from the chlorine ion are deleted for clarity.

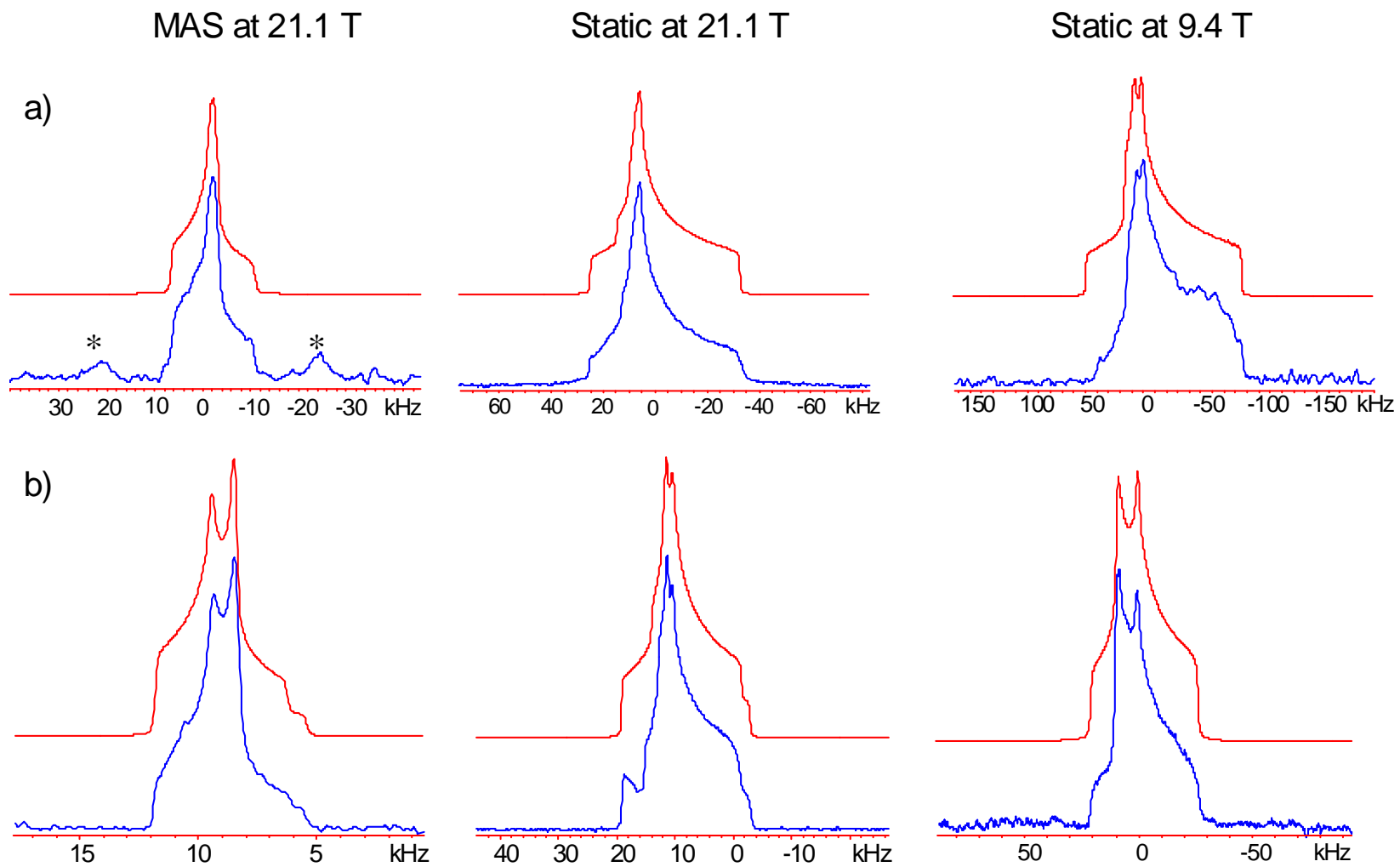


Figure 8.4. ^{35}Cl SSNMR spectra of a) RA and b) AM. The top patterns are simulations and bottom ones are experimental. *: indicates spinning sidebands.

Systems with single Cl⁻ sites with multiple Cl⁻⋯HN and Cl⁻⋯HO contacts: Acebutolol Hydrochloride (AC) and Isoxsuprine Hydrochloride (IS). The chlorine anion in AC is involved in three hydrogen contacts (one Cl⁻⋯HO and two Cl⁻⋯HN, Figure 8.5a). The ³⁵Cl SSNMR spectra of AC (Figure 8.6a) reveal a single chlorine site in agreement with the crystal structure.⁴⁷ Simulation of the NMR spectra reveals EFG and CS tensor parameters similar to those of L-histidine HCl monohydrate (HM),²⁷ which also has a single chlorine site, three short hydrogen contacts (one Cl⁻⋯HO and two Cl⁻⋯HN, Figure 8.5b) and a local geometry similar to that in AC.⁶² AM, AC and HM all have similar local Cl⁻ environments; however, the significantly larger values of C_Q in AC and HM compared to that of AM likely result from the presence of the single short Cl⁻⋯HO contacts in the former two systems which lead to non-spherically symmetric environments around the chlorine sites. This is considered further in the theoretical section below.

The structure of IS has a single chlorine site involved in four short hydrogen contacts (Figure 8.5c).⁴⁸ Simulations of the ³⁵Cl NMR spectra (Figure 8.6b) reveal parameters which are similar to those of threonine HCl (TE),²⁷ indicating comparable chlorine hydrogen environments: the Cl ion is also involved in four hydrogen bonds (two Cl⁻⋯HO and two Cl⁻⋯HN contacts, Figure 8.5d).⁴⁹ The η_Q indicates an EFG tensor approaching axial symmetry, with V₃₃ as the distinct component. The large C_Q in this system may arise from the arrangement of hydrogen bonds to one side of the chlorine anion, which produces a non spherically symmetric electronic distribution and larger EFG

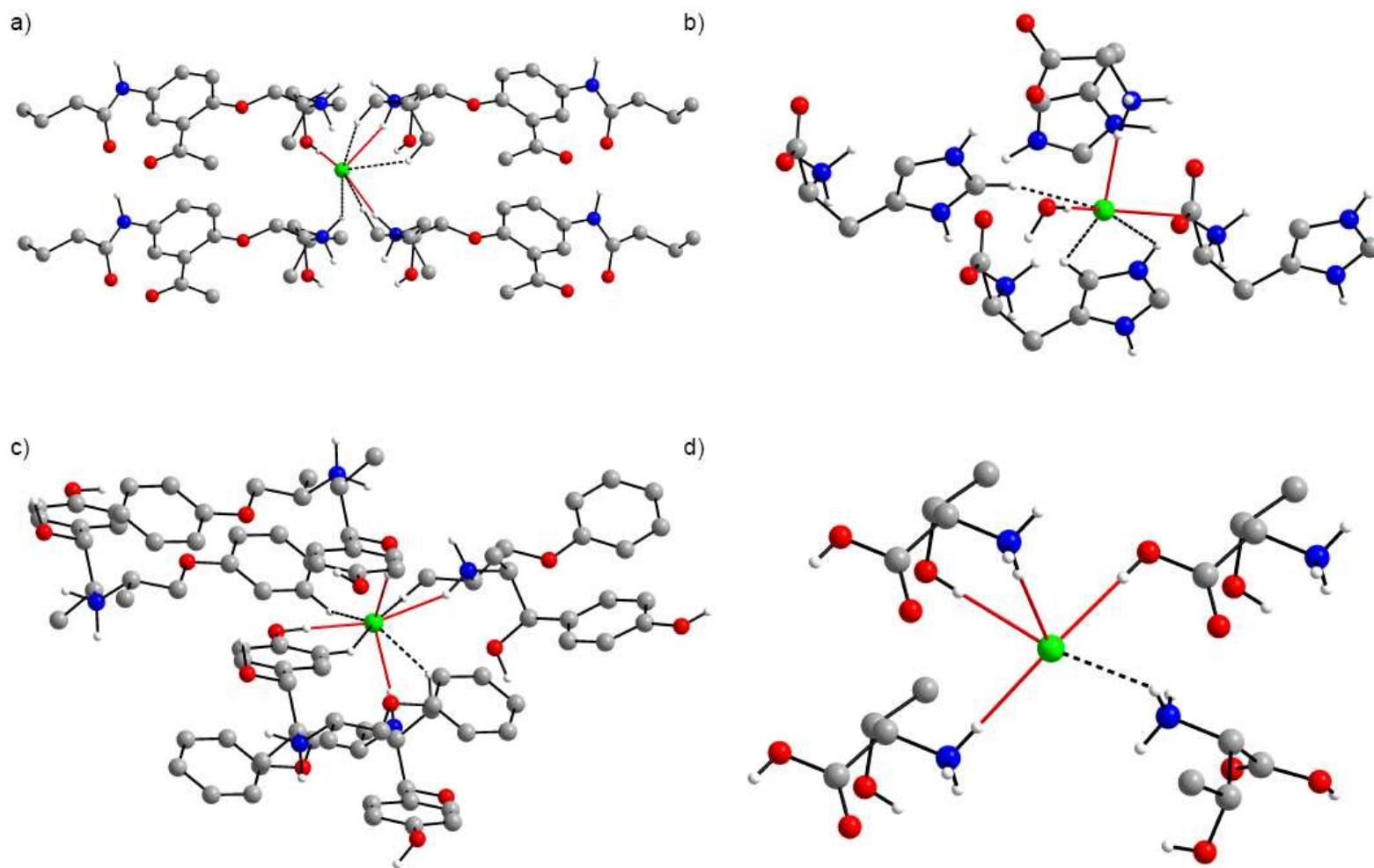


Figure 8.5. Partial crystal structures of a) AC, b) HM c) IS and d) TE, which focus on the chlorine anion positions. The short chlorine-hydrogen contacts are indicated in red, and longer contacts are marked with dashed lines. Hydrogens attached to carbon atoms and greater than 3.0 Å from the chlorine ion are deleted for clarity.

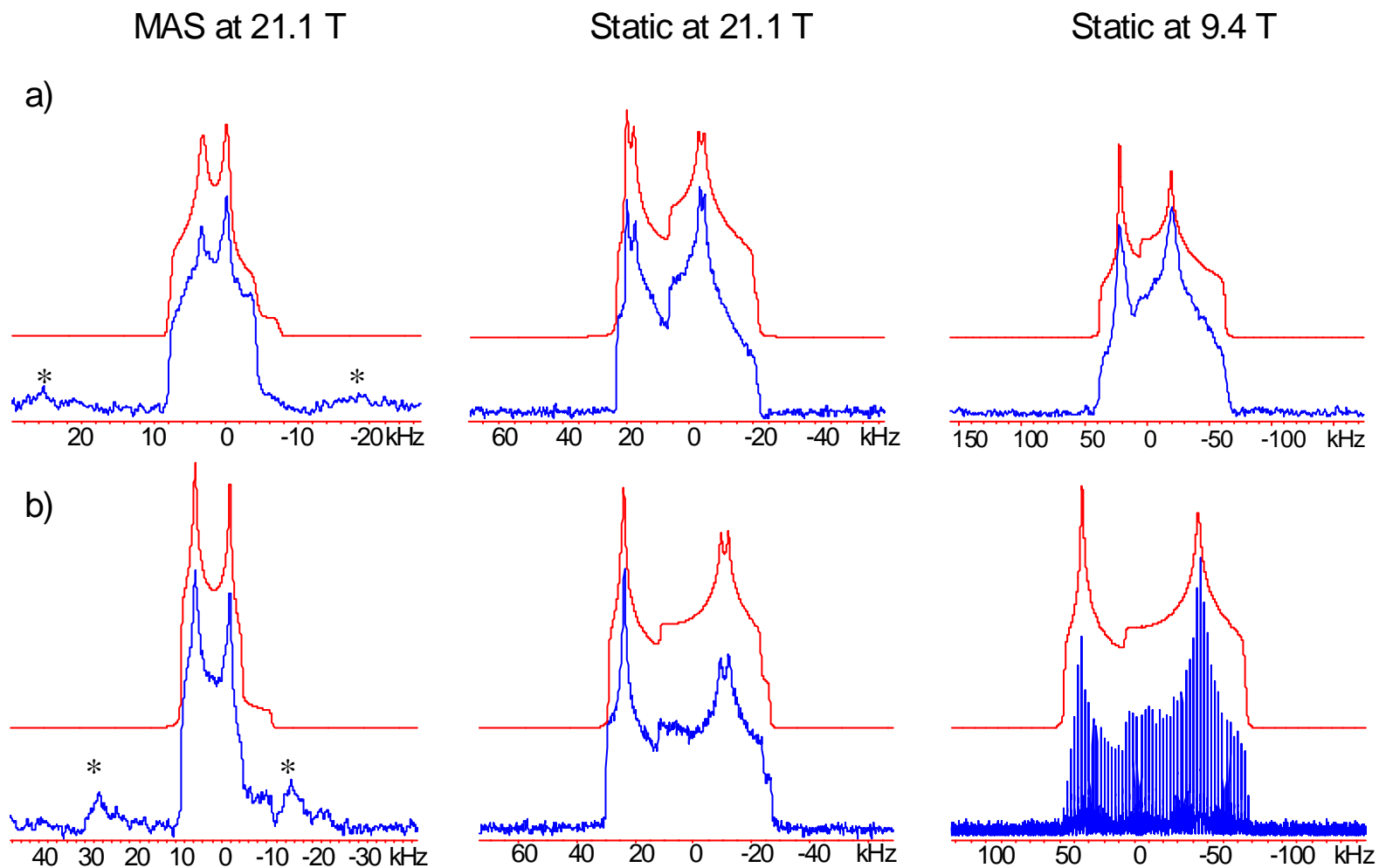


Figure 8.6. ^{35}Cl SSNMR spectra of a) AC and b) IS. The top patterns are simulations and bottom ones are experimental. *: indicates spinning sidebands.

Systems with multiple Cl⁻ sites: Dibucaine Hydrochloride (DI) and Mexiletine Hydrochloride (ME). The crystal structure of DI has two chlorine sites in the asymmetric unit.^{45,46} Cl1 and Cl2 are engaged in two and three hydrogen contacts, respectively. All of the hydrogen positions were not determined in the crystal structure; therefore, computational geometry optimization was utilized to predict their positions (Figure 8.7a, b). While reasonably good simulations of the high-field MAS and low-field static spectra could be obtained with consideration of only a single chlorine site, the high-field static spectrum clearly reveals the presence of two overlapping powder patterns with very similar chemical shifts and η_Q values, but a noticeable difference in C_Q (Figures 8.8a and F.8.2). This illustrates both the importance and advantage of obtaining NMR spectra under different experimental conditions, and exemplifies the improvements in resolution that high magnetic fields can offer when studying quadrupolar nuclei. The pattern with a larger C_Q value is assigned to Cl1 (two H contacts) and that of a smaller C_Q is assigned to Cl2 (three H contacts, vide infra). The NMR parameters of Cl1 are similar to those of RA and LH,²¹ in which the chlorine sites also make two short hydrogen contacts. The C_Q value of Cl2 is close to that of GA, in which the chlorine is also involved in three short hydrogen contacts with a similar local geometry (Figure 8.3d). The Cl2 site has a smaller C_Q value in comparison to Cl1; this corresponds well to the higher spherically symmetric local environment of the former.

The Cl1 and Cl2 sites in ME have two and four hydrogen bonds, respectively (Figure 8.7c, d).⁶³

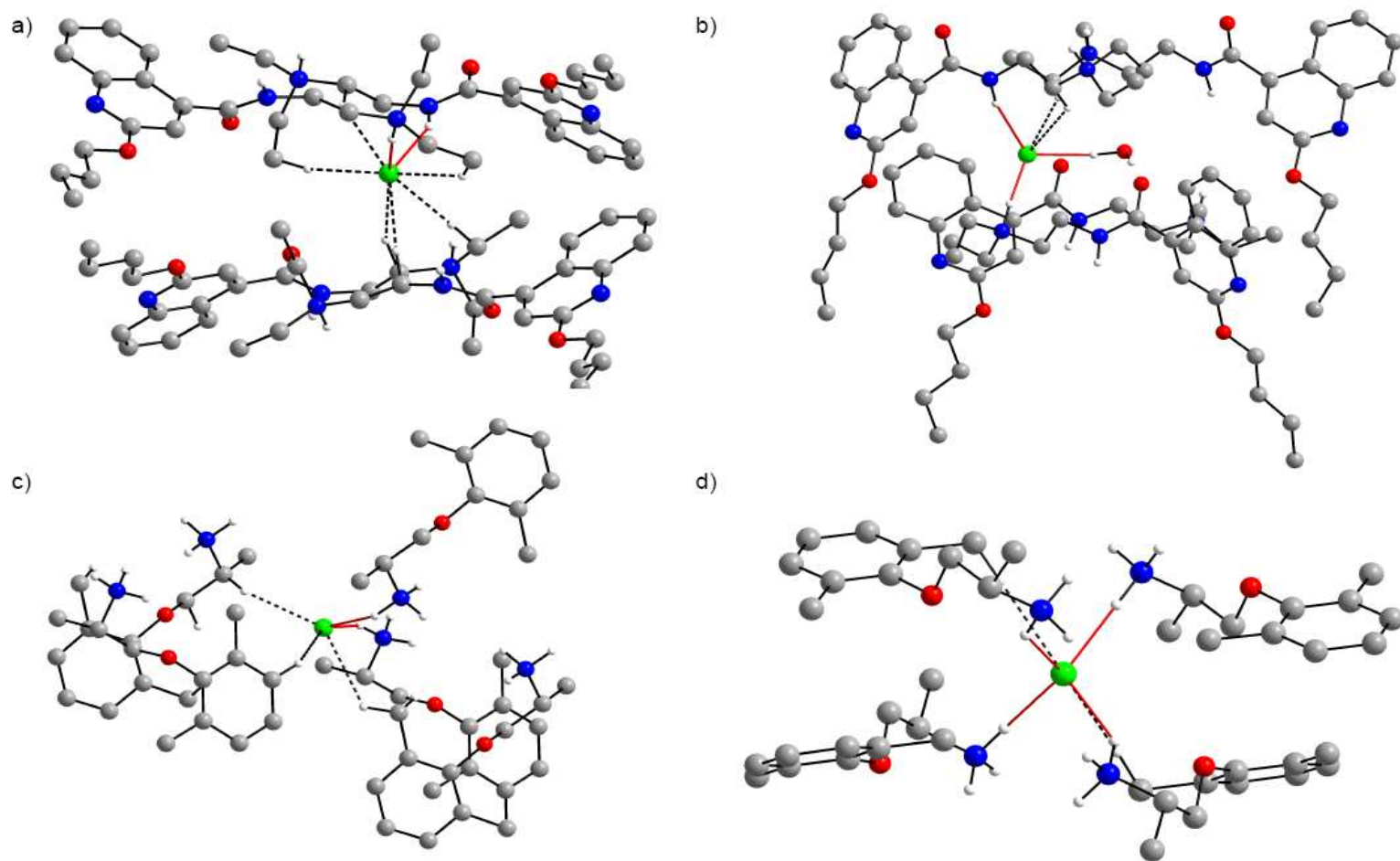


Figure 8.7. Partial crystal structures of a) DI (chlorine site 1), b) DI (chlorine site 2), c) ME (chlorine site 1) and d) ME (chlorine site 2) monohydrate which focus on the chlorine atom positions. The short chlorine-hydrogen contacts are indicated in red, and longer contacts are marked with dashed lines. Hydrogens attached to carbon atoms and away ($>3.0 \text{ \AA}$) from the chlorine ion are deleted for clarity.

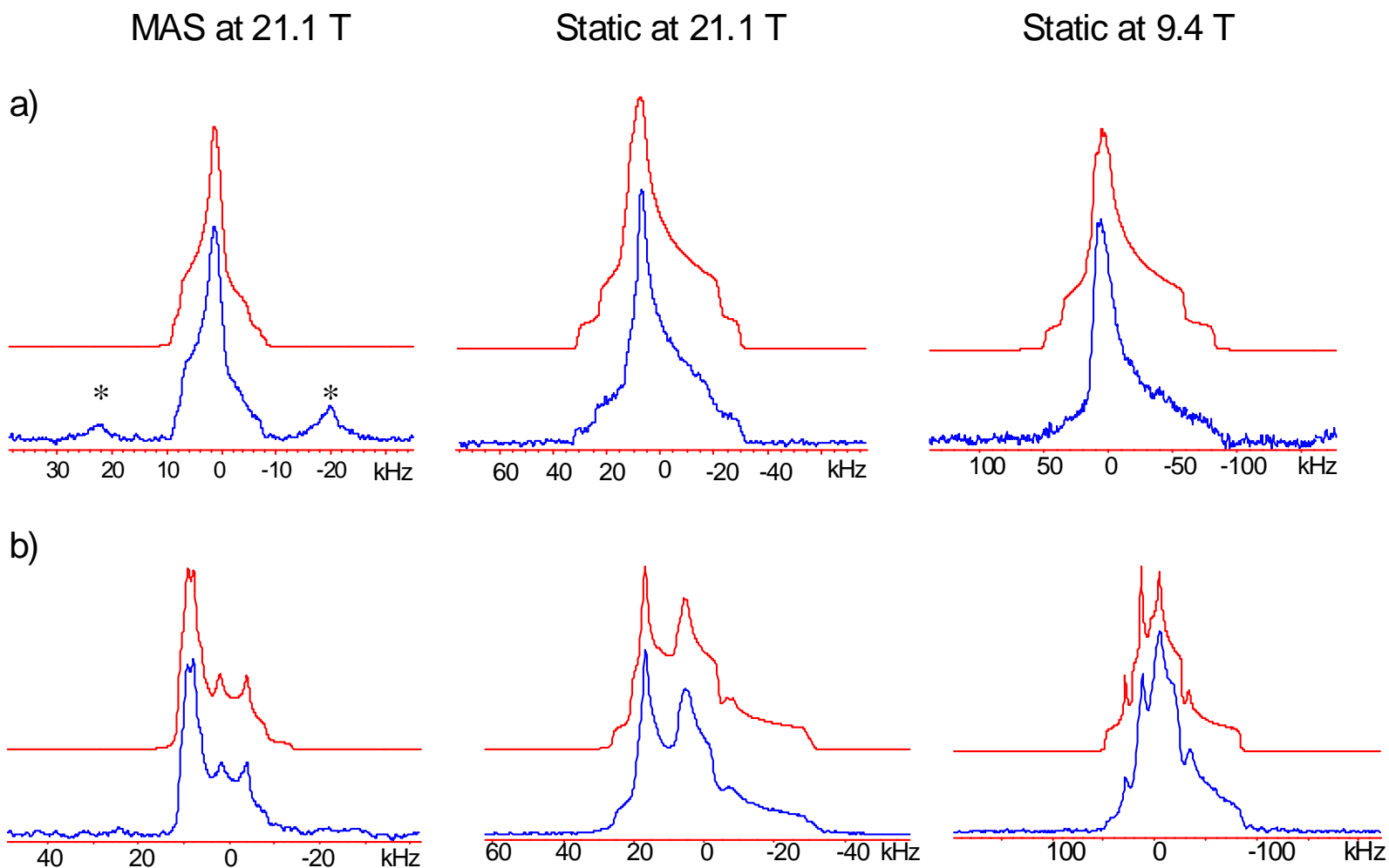


Figure 8.8. ^{35}Cl SSNMR spectra of a) DI and b) ME. The top patterns are simulations and bottom ones are experimental. *: indicates spinning sidebands.

In agreement with the structure, the ^{35}Cl NMR spectra reveal two overlapping chlorine patterns (Figure 8.8b) with distinct NMR parameters which are easily distinguished, unlike in the case of DI. The larger C_Q value is assigned to the Cl1 site which has two hydrogen contacts, and the smaller C_Q is assigned to Cl2 which has four hydrogen contacts, and is in an environment of increased spherical symmetry compared to Cl1. The C_Q for Cl1 is larger than those of RA in which the Cl ions are each also involved in two hydrogen contacts; this is likely due to the shorter average hydrogen contact for Cl1.

In summary, in systems where the chlorine ion is involved in a single hydrogen contact, the C_Q value seems to increase with decreasing the Cl \cdots H distance. This trend still applies for structures with multiple Cl \cdots H contacts, but the arrangement of the short hydrogen contacts around the chlorine ions must also be taken into account. In all cases, increasingly spherically symmetric arrangements of hydrogen atoms result in reduced values of C_Q .

8.3.2 Theoretically calculated NMR interaction tensors.

Ab initio calculations of the ^{35}Cl EFG and nuclear shielding (NS) tensors have been performed to examine the relationships between chlorine NMR tensors and the solid-state structures of the pharmaceutical compounds. Understanding such relationships will be crucial for making future structural interpretations for the many HCl salts for which crystal structures are unavailable or unobtainable. Previous work by our group²¹ and by Bryce et al.²⁵ demonstrated that RHF calculations provide consistent agreement with experiment for EFG tensor parameters, and B3LYP calculations are better

for the NS tensor parameters. In all cases, the molecular coordinates were taken from single-crystal structures.⁴⁰⁻⁴⁹ Proton positions were geometry optimized, since proton positions obtained from X-ray crystal structures are generally unreliable. This is crucial for accurately calculating the NMR tensor parameters; particularly, this is important for the EFG tensors, which are strongly dependent on longer-range electrostatic interactions. Details on all of the clusters and datasets used are in the experimental section.

The calculated ³⁵Cl NMR parameters are generally in agreement with the experimental values (Table 8.3). There is good correlation ($R = 0.976$) between the calculated and experimental C_Q values (Figure 8.9a), with the exception of BU ($R = 0.983$ when excluding BU). For BU, increasing the cluster size for the EFG calculation failed to improve agreement. The η_Q values are also in reasonable agreement with experimental values, though with a lower correlation than for C_Q ($R = 0.455$ or $R = 0.808$ when excluding RA). This is likely due to the proportionality of C_Q to only V_{33} , while η_Q depends on accurate calculation of all three tensor parameters. The theoretical NS tensor parameters are also in reasonable agreement within the experimental values and in most cases are within experimental uncertainty (Figures 8.10a, 8.10b and 8.10c). The slight discrepancies in certain cases could be due to the long range interactions which are not accounted for in the calculations (for EFG tensors) or inadequacies in basis sets (for the CS tensors). Nonetheless, these calculations seem to provide good enough EFG tensor data for meaningful comparison with experiment, and explorations of the relations between NMR interaction tensors and the local structure and symmetry.

Table 8.3. Comparison of the experimental and theoretical ^{35}Cl EFG and CS tensor parameters.^{a, b}

		C_Q/MHz^c	η_Q	$\delta_{\text{iso}}/\text{ppm}$	Ω/ppm	κ
AD	Exp.	5.94(6)	0.18(3)	128(5)	155(20)	0.60(20)
AD	Cal.	-5.88	0.42	126	139	0.94
BU	Exp.	5.67(13)	0.18(6)	75(10)	125(30)	-0.60(20)
BU	Cal.	-6.66	0.13	58	112	-0.39
TR	Exp.	7.50(12)	0.05(3)	70(10)	120(30)	0.80(20)
TR	Cal.	-7.91	0.24	71	173	0.44
RA	Exp.	4.70(10)	0.92(3)	75(5)	70(15)	0.30(30)
RA	Cal.	-4.43	0.35	58	81	0.11
AM	Exp.	2.90(4)	0.68(3)	131(5)	50(5)	0.60(20)
AM	Cal.	2.83	0.98	160	64	0.22
AC	Exp.	4.57(5)	0.50(4)	95(5)	95(10)	-0.30(30)
AC	Cal.	-4.52	0.82	102	83	-0.015
IS	Exp.	5.50(15)	0.25(5)	120(10)	50(20)	0.50(40)
IS	Cal.	5.05	0.05	128	42	0.44
DI site 1	Exp.	4.65(20)	0.86(7)	105(15)	100(20)	-0.26(60)
DI site 2	Exp.	4.00(20)	0.93(7)	95(15)	80(20)	-0.20(60)
DI site 1	Cal.	-4.69	0.61	102	105	-0.26
DI site 2	Cal.	4.11	0.64	106	92	-0.19
ME site 1	Exp.	5.45(10)	0.40(8)	90(5)	80(20)	-0.80(20)
ME site 2	Exp.	3.10(10)	0.55(10)	130(5)	75(20)	0.80(20)
ME site 1	Cal.	-5.4	0.64	104	94	-0.47
ME site 2	Cal.	-3.95	0.75	143	78	0.96

^a Definitions of parameters are given in Table 8.2.

^b All theoretical EFG parameters are obtained from RHF calculations featuring cc-PVTZ on the Cl atoms and 6-31G* on all other atoms. ^cValues of C_Q ($C_Q = eQV_{33}/h$) are calculated by converting from atomic units to Hz by multiplying V_{33} by $(eQ/h)(9.7177 \times 10^{21} \text{ Vm}^2)$ where $Q(^{35}\text{Cl}) = -0.082 \times 10^{-28} \text{ m}^2$. Only the signs of the calculated C_Q values are reported since the experimental signs can not be determined.

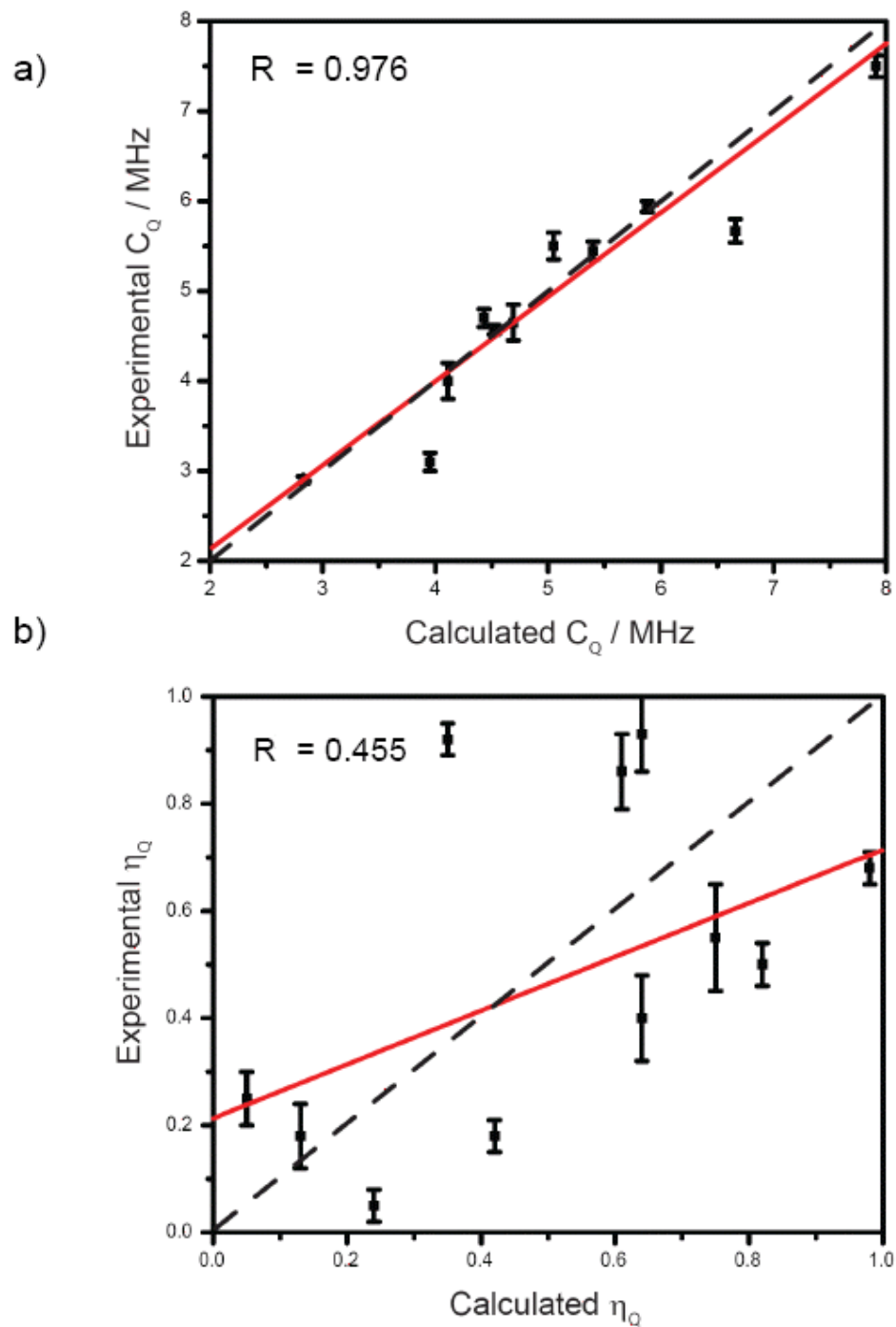


Figure 8.9. Correlations between the experimental and calculated a) C_Q values and b) η_Q values.

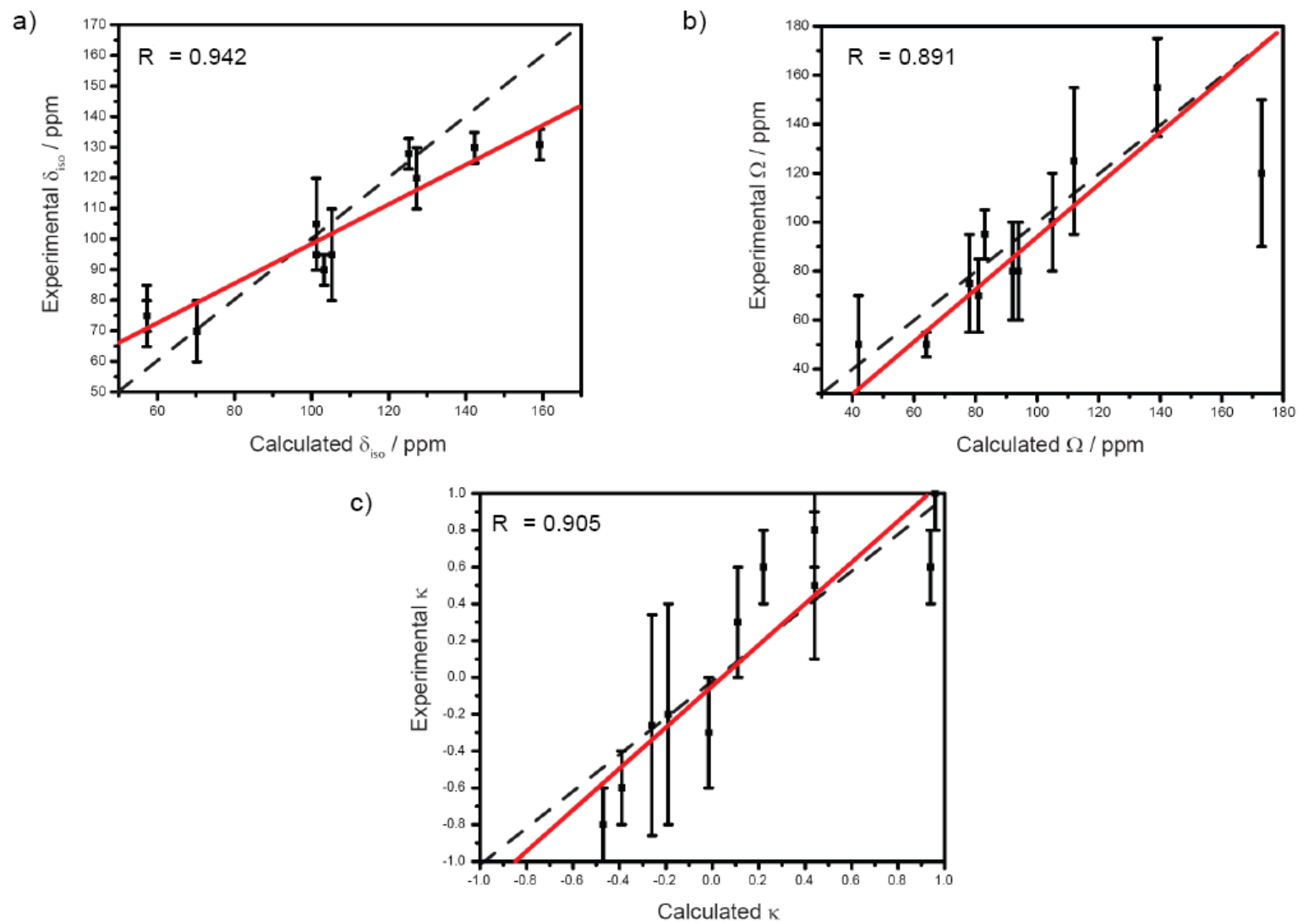


Figure 8.10. Correlations between the experimental and calculated a) δ_{iso} , b) Ω and c) κ values.

In examining all of the NMR tensor data summarized in Tables 8.2 and 8.3, it is clear that there is significantly more variation in the EFG tensor parameters than the NS tensor parameters. It seems that local variation in hydrogen bonding does not produce much variance in the CS tensor parameters; further, no real trends relating structure and NS tensor parameters can be discerned. Therefore, we focus upon examining the EFG tensor orientations with respect to local atomic coordinates, in order to better understand the origins of the ^{35}Cl quadrupolar parameters, and their dependence on the local structure.

The chlorine anions in AD, BU and TR all have single short $\text{Cl}\cdots\text{H}$ contacts. In all of these cases, V_{33} is the distinct component of the EFG tensor and is oriented close to the direction of the hydrogen bond ($\angle(V_{33}\text{-Cl-H}) = 8.7^\circ, 2.6^\circ$ and 3.9° in AD and BU, TR, respectively, Figures 8.11a, 8.11b, and 8.11c). The chlorine ions in RA and AM have two and three short $\text{Cl}\cdots\text{HN}$ contacts, respectively. The C_Q value for RA is in excellent agreement with the experiment, however, the η_Q value is significantly underestimated, which may arise from incomplete treatment of the long range interactions (i.e., insufficient cluster sizes). It is interesting to note that our CASTEP DFT calculation on this system, which takes into account the longer range electrostatic interactions, was successful in predicting η_Q , while overestimating the value of C_Q ($C_Q = 5.72$ MHz and $\eta_Q = 0.86$). All three components are oriented into different environments, with V_{22} approximately bisects the angle formed by the two short hydrogen contacts ($\angle(V_{22}\text{-Cl-H1}) = 125.55^\circ$ and $\angle(V_{22}\text{-Cl-H2}) = 131.83^\circ$, Figure 8.12a). The theoretical C_Q value for AM is also in excellent agreement with the experiment; however, η_Q is overestimated in this case.

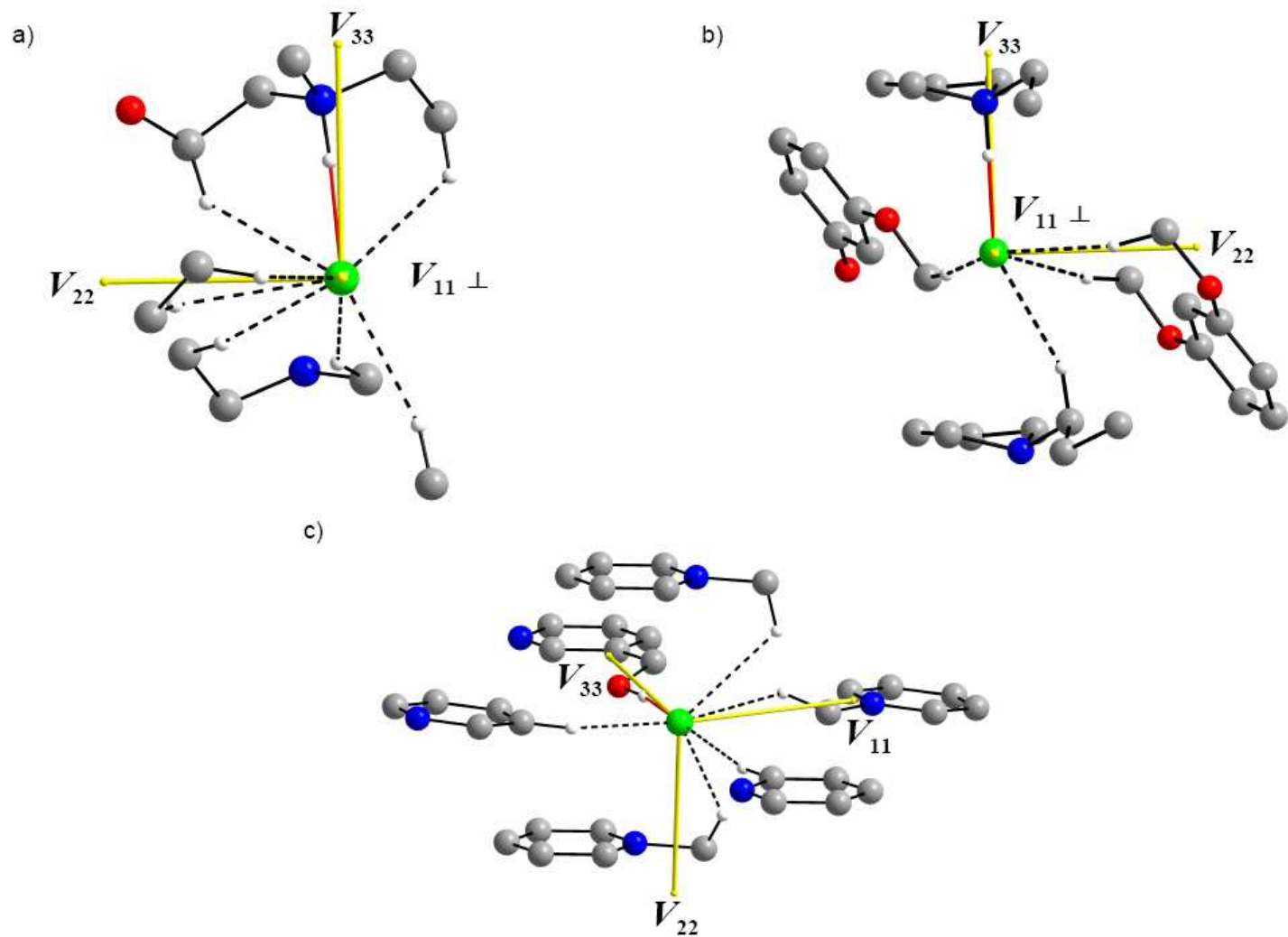


Figure 8.11. ^{35}Cl EFG tensor orientations in a) AD, b) BU and c) TR. The diagrams above are magnifications of the chlorine sites pictured in Figure 8.1.

Each of the three hydrogen atoms on each nitrogen atom make short contacts with different chlorine ions; thus, in order to ensure that the proton positions are in energy minimized positions, and that the EFG tensors are calculated according to the best model, it was necessary to include multiple chlorine sites in the calculation input file. The EFG tensors are oriented such that V_{11} is aligned close to the shortest Cl...HN bond ($\angle(V_{11}\text{-Cl-H}) = 5.6^\circ$, Figure 8.12b), and V_{33} approximately bisects the angle formed between the chlorine and the other two nearby hydrogen atoms.

AC and IS both feature multiple Cl...HN and Cl...HO contacts. The calculated EFG tensor parameters for both are in good agreement with experiment; however, their parameters and tensor orientations are very different due to the distinct arrangements of these short contacts. In AC, which has three short H contacts, each of the EFG tensor components are distinct (in agreement with experiment), with V_{11} positioned near the Cl...H1 bond ($\angle(V_{11}\text{-Cl-H1}) = 26.81^\circ$) and nearly perpendicular to the Cl...H2 bond ($\angle(V_{11}\text{-Cl-H}) = 92.49^\circ$). V_{22} almost bisects the (H1-Cl-H2) angle and V_{33} is oriented near both the Cl...H2 and the Cl...H3 bonds ($\angle(V_{33}\text{-Cl-H2}) = 26.24^\circ$ and $\angle(V_{33}\text{-Cl-H3}) = 33.38^\circ$, Figure 8.12c). In IS, which has four short H contacts (Figure 8.12d), V_{11} and V_{22} point into similar environments: V_{11} is oriented very close to a Cl...HO contact ($\angle(V_{11}\text{-Cl-HO}) = 14.13^\circ$) and a Cl...HN contact ($\angle(V_{11}\text{-Cl-HN}) = 12.55^\circ$), and V_{22} is also close to two different Cl...HO and Cl...HN contacts ($\angle(V_{11}\text{-Cl-HO}) = 26.2^\circ$ and $\angle(V_{11}\text{-Cl-HN}) = 28.8^\circ$). V_{33} is directed into a completely distinct environment, not oriented near any of the short H bonds, which may account for the value of η_Q near zero.

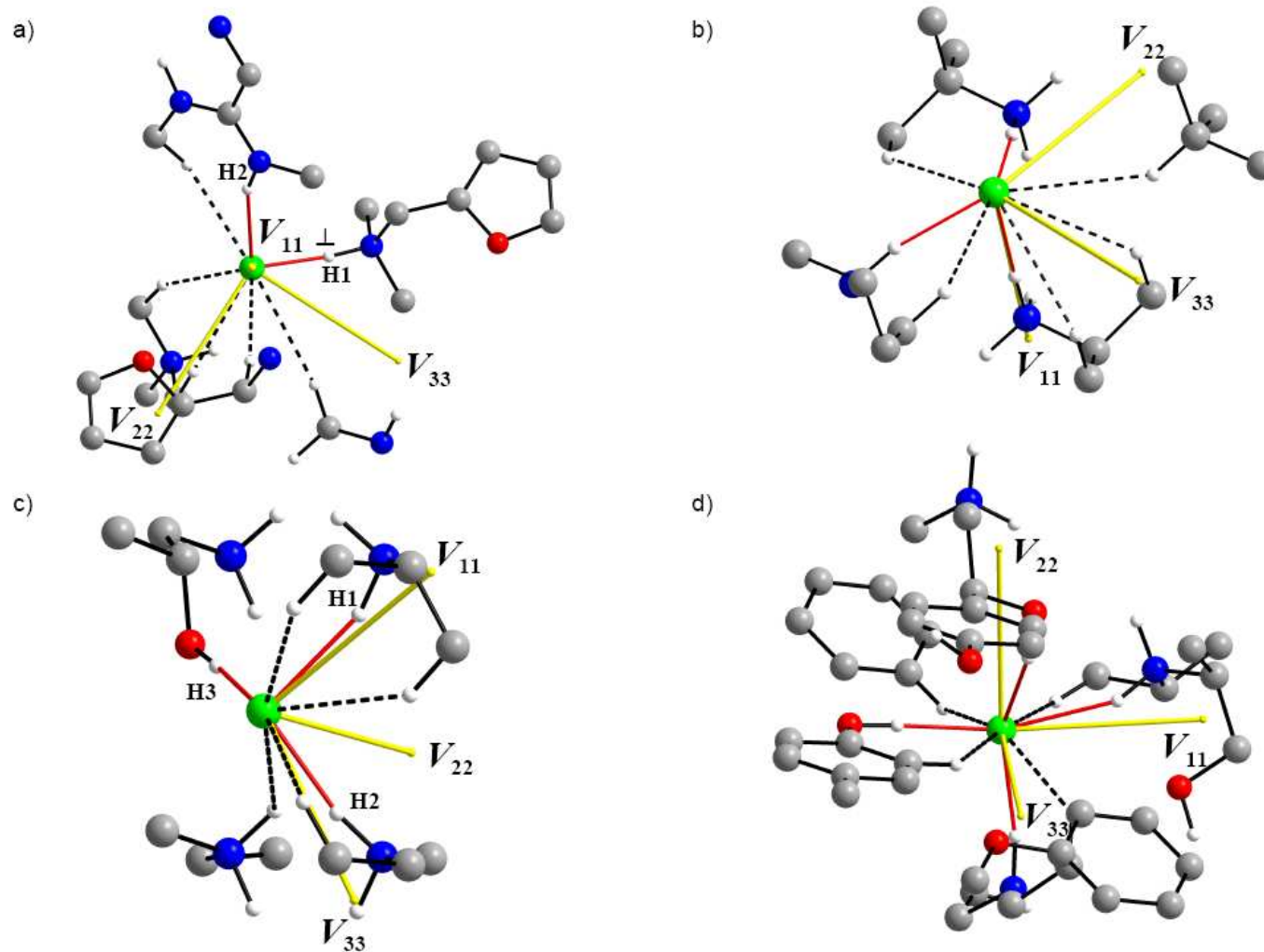


Figure 8.12. ^{35}Cl EFG tensor orientations in a) RA, b) AM c) AC and d) IS. The diagrams above are magnifications of the chlorine sites pictured in Figures 8.3 and 8.5.

Both DI and ME have two crystallographically distinct chlorine sites, both of which have to be included in the input files for the calculation of the EFG tensors. The calculated C_Q and η_Q values for both systems are in good agreement with experimental values. For Cl1 in DI, which is involved in two hydrogen bonds, V_{11} and V_{33} are oriented close to the short hydrogen contacts, ($\angle(V_{33}\text{-Cl-H1}) = 8.61^\circ$ and $\angle(V_{11}\text{-Cl-H2}) = 18.26^\circ$, Figure 8.13a), similar to the Cl⁻ environment in RA. For Cl2, which is engaged in three hydrogen contacts, V_{11} and V_{22} are oriented close to the short hydrogen bonds, with V_{22} near the shortest contact ($\angle(V_{22}\text{-Cl-H1}) = 14.76^\circ$ and $\angle(V_{11}\text{-Cl-H2}) = 21.34^\circ$, Figure 8.13b). For the Cl1 site in ME, V_{11} is oriented such that it nearly bisects the angle formed between the chlorine ion and its closest hydrogen atoms, with V_{22} nearly perpendicular to this plane (Figure 8.13c). In the case of Cl2, V_{33} is oriented near the direction of the two short hydrogen contacts ($\angle(V_{33}\text{-Cl-H1}) = 14.77^\circ$ and $\angle(V_{33}\text{-Cl-H2}) = 27.28^\circ$) and V_{11} is positioned near the longest hydrogen contact ($\angle(V_{11}\text{-Cl-H3}) = 32.82^\circ$, Figure 8.13d).

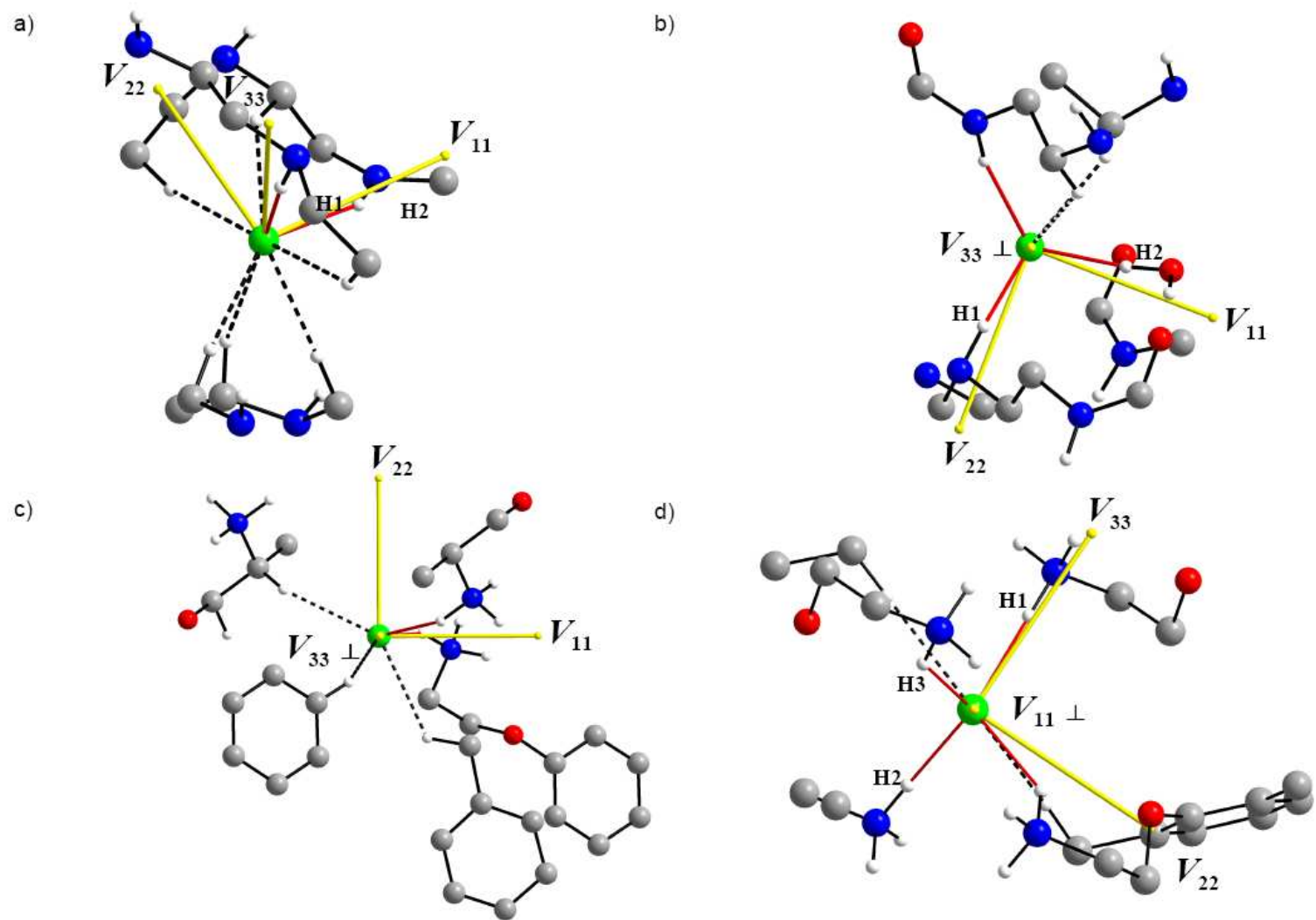


Figure 8.13. ^{35}Cl EFG tensor orientations in a) DI (chlorine site 1), b) DI (chlorine site 2), c) ME (chlorine site 1) and d) ME (chlorine site 2). The diagrams above are magnifications of the chlorine sites pictured in Figure 8.7.

8.4 Conclusions

A series of HCl pharmaceuticals with a variety of chlorine hydrogen-bonding environments have been studied using ^{35}Cl SSNMR spectroscopy. Extraction of the EFG and CS tensor parameters from these spectra aids in the elucidation of correlation between the ^{35}Cl EFG tensor parameters to chlorine anion environments. For Cl environments with single short Cl \cdots H contacts, the magnitude of C_Q is largely governed by the interatomic distance. The EFG-structure relationships for Cl environments with multiple short Cl \cdots H contacts are somewhat more complex. Of course, spherically asymmetric arrangements of H atom positions with short Cl \cdots H distances result in larger C_Q values. Interestingly, the orientations of principal components of the EFG tensor are often constrained in directions near to the short contacts; however, in this limited data set, a general statement for all such complexes cannot be made at this time. Continued work in this area is necessary in order to provide the means to make reliable predictions of structure at the local chlorine sites; nonetheless, each pattern acts as a unique NMR fingerprint for each solid pharmaceutical.

The use of ultra-high field NMR spectrometers was crucial for the success of this work, for both rapid collection of high S/N NMR spectra and accurate determination of anisotropic quadrupolar and chemical shift parameters. Theoretically calculated chlorine EFG and CS tensors are in good agreement with experimental values, and help in analyzing and confirming the data obtained via solid-state ^{35}Cl NMR experiments. Consideration of the tensor orientations in the molecular frames contributes a better understanding of the relationship between NMR parameters and chlorine-hydrogen bonding environments in these pharmaceuticals, and holds strong promise for application

to a wide array of HCl pharmaceuticals and related systems.

8.5 Bibliography

- (1) Council, C. C. "The Benefits of Chlorine Chemistry in Pharmaceuticals," Global Insights, 2006.
- (2) Bighley, L. D. B., S. M.; Monkhouse, D. C. In *Encyclopedia of Pharmaceutical Technology*; Swarbrick, J. B., J. C., Ed.; Marcel Dekker, 1995; Vol. 13, pp 453-499.
- (3) Byrn, S. R.; Pfeiffer, R. R.; Stephenson, G.; Grant, D. J. W.; Gleason, W. B. *Chem. Mat.* **1994**, *6*, 1148-1158.
- (4) Giron, D. *J. Therm. Anal. Calorim.* **2001**, *64*, 37-60.
- (5) Giron, D. *J. Therm. Anal. Calorim.* **2003**, *73*, 441-457.
- (6) Giron, D. *Am. Pharm. Rev.* **2005**, *8*, 32, 34-35, 37.
- (7) Giron, D. *Am. Pharm. Rev.* **2005**, *8*, 72,74,76,78-79.
- (8) Giron, D. *Pharmacokinetic Profiling in Drug Research: Biological, Physicoche* **2006**, 307-329.
- (9) Maiwald, M. *Am. Pharm. Rev.* **2006**, *9*, 95-99.
- (10) Brittain, H. G. *Polymorphism in Pharmaceutical Solids*; Marcel Dekker: New York, 1999; Vol. 95 pp 227-278.
- (11) Harris, R. K. *J. Pharm. Pharmacol.* **2007**, *59*, 225-239.
- (12) Harris, R. K. *Analyst* **2006**, *131*, 351-373.
- (13) Berendt, R. T.; Sperger, D. M.; Munson, E. J.; Isbester, P. K. *Trends Anal. Chem.* **2006**, *25*, 977-984.
- (14) Vogt, F. G.; Brum, J.; Katrincic, L. M.; Flach, A.; Socha, J. M.; Goodman, R. M.; Haltiwanger, R. C. *Cryst. Growth Des.* **2006**, *6*, 2333-2354.
- (15) Li, Z. J.; Abramov, Y.; Bordner, J.; Leonard, J.; Medek, A.; Trask, A. V. *J. Am. Chem. Soc.* **2006**, *128*, 8199-8210.
- (16) Wawer, I.; Pisklak, M.; Chilmonczyk, Z. *J. Pharm. Biomed. Anal.* **2005**, *38*, 865-870.
- (17) Chupin, V.; De Kroon, A. I. P. M.; De Kruijff, B. *J. Am. Chem. Soc.* **2004**, *126*, 13816-13821.

- (18) Smith, E. D. L.; Hammond, R. B.; Jones, M. J.; Roberts, K. J.; Mitchell, J. B. O.; Price, S. L.; Harris, R. K.; Apperley, D. C.; Cherryman, J. C.; Docherty, R. *J. Phys. Chem. B* **2001**, *105*, 5818-5826.
- (19) Wenslow, R. M. *Drug Dev. Ind. Pharm.* **2002**, *28*, 555-561.
- (20) Griffin, J. M.; Dave, M. R.; Steven, B. P. *Angew. Chem., Int. Ed. Engl.* **2007**, *46*, 8036-8038.
- (21) Hamaed, H.; Pawlowski, J. M.; Cooper, B. F. T.; Fu, R.; Eichhorn, S. H.; Schurko, R. W. *J. Am. Chem. Soc.* **2008**, *130*, 11056-11065.
- (22) Pyykko, P. *Mol. Phys.* **2001**, *99*, 1617-1629.
- (23) Harris, R. K.; Becker, E. D.; Cabral de Menezes, S. M.; Goodfellow, R.; Granger, P. *Solid State Nucl. Magn. Reson.* **2002**, *22*, 458-483.
- (24) Bryce, D. L.; Gee, M.; Wasylshen, R. E. *J. Phys. Chem. A* **2001**, *105*, 10413-10421.
- (25) Bryce, D. L.; Sward, G. D. *J. Phys. Chem. B* **2006**, *110*, 26461-26470.
- (26) Bryce, D. L.; Sward, G. D.; Adiga, S. *J. Am. Chem. Soc.* **2006**, *128*, 2121-2134.
- (27) Chapman, R. P.; Bryce, D. L. *Phys. Chem. Chem. Phys.* **2007**, *9*, 6219-6230.
- (28) Widdifield, C. M.; Chapman, R. P.; Bryce, D. L. *Annu. Rep. NMR Spectrosc.* **2009**, *66*, 195-326.
- (29) Chapman, R. P.; Widdifield, C. M.; Bryce, D. L. *Prog. Nucl. Magn. Reson. Spectrosc.* **2009**, *55*, 215-237.
- (30) O'Dell, L. A.; Schurko, R. W. *Chem. Phys. Lett.* **2008**, *464*, 97-102.
- (31) O'Dell, L. A.; Rossini, A. J.; Schurko, R. W. *Chem. Phys. Lett.* **2009**, *468*, 330-335.
- (32) Kupce, E.; Freeman, R. *J. Magn. Reson. Ser. A* **1995**, *115*, 273-276.
- (33) Bhattacharyya, R.; Frydman, L. *J. Chem. Phys.* **2007**, *127*, 194503/194501-194503/194508.
- (34) Larsen, F. H.; Jakobsen, H. J.; Ellis, P. D.; Nielsen, N. C. *J. Phys. Chem. A* **1997**, *101*, 8597-8606.
- (35) Eichele, K.; Wasylshen, R. E.; WSolids NMR Simulation Package, 1.17.30 ed.; Dalhousie University: Halifax, CA, 2001.
- (36) Bak, M.; Rasmussen, J. T.; Nielsen, N. C. *J. Magn. Reson.* **2000**, *147*, 296-330.

- (37) Gor'kov, P. L.; Chekmenev, E. Y.; Li, C.; Cotten, M.; Buffy, J. J.; Traaseth, N. J.; Veglia, G.; Brey, W. W. *J. Magn. Reson.* **2007**, *185*, 77-93.
- (38) Frisch, M. J.; Trucks, G. W.; Schlegel, H. B.; Scuseria, G. E.; Robb, M. A.; Cheeseman, J. R.; Scalmani, G.; Barone, V.; Mennucci, B.; Petersson, G. A.; Nakatsuji, H.; Caricato, M.; Li, X.; Hratchian, H. P.; Izmaylov, A. F.; Bloino, J.; Zheng, G.; Sonnenberg, J. L.; Hada, M.; Ehara, M.; Toyota, K.; Fukuda, R.; Hasegawa, J.; Ishida, M.; Nakajima, T.; Honda, Y.; Kitao, O.; Nakai, H.; Vreven, T.; Montgomery, J. A.; Peralta, J., J.E.; Ogliaro, F.; Bearpark, M.; Heyd, J. J.; Brothers, E.; Kudin, K. N.; Staroverov, V. N.; Kobayashi, R.; Normand, J.; Raghavachari, K.; Rendell, A.; Burant, J. C.; Iyengar, S. S.; Tomasi, J.; Cossi, M.; Rega, N.; Millam, J. M.; Klene, M.; Knox, J. E.; Cross, J. B.; Bakken, V.; Adamo, C.; Jaramillo, J.; Gomperts, R.; Stratmann, R. E.; Yazyev, O.; Austin, A. J.; Cammi, R.; Pomelli, C.; Ochterski, J. W.; Martin, R. L.; Morokuma, K.; Zakrzewski, V. G.; Voth, G. A.; Salvador, P.; Dannenberg, J. J.; Dapprich, S.; Daniels, A. D.; Farkas, O.; Foresman, J. B.; Ortiz, J. V.; Cioslowski, J.; Fox, D. J.; Revision A.02 ed.; Gaussian, Inc.: Wallingford CT, 2009.
- (39) This work was made possible by the facilities of the Shared Hierarchical Academic Research Computing Network (SHARCNET:www.sharcnet.ca) and Compute/Calcul Canada.
- (40) Szafran, M.; Koput, J.; Dega-Szafran, Z.; Katrusiak, A.; Pankowski, M.; Stobiecka, K. *Chem. Phys.* **2003**, *289*, 201-219.
- (41) Guy, J. J.; Hamor, T. A. *J. Chem. Soc., Perkin Trans.* **1973**, 942-947.
- (42) Ravikumar, K.; Sridhar, B. *Acta Crystallogr., Sect. E: Struct. Rep.* **2006**, *E62*, o4832-o4834.
- (43) Hempel, A.; Camerman, N.; Mastropaolo, D.; Camerman, A. *Acta Crystallogr., Sect. C: Cryst. Struct. Commun.* **2000**, *C56*, 1048-1049.
- (44) Belanger-Gariepy, F.; Brisse, F.; Harvey, P. D.; Butler, I. S.; Gilson, D. F. R. *Acta Crystallogr., Sect. C: Cryst. Struct. Commun.* **1987**, *C43*, 756-759.
- (45) Hayward, B. S.; Donohue, J. J. *Cryst. Mol. Struct.* **1978**, *7*, 275-294.
- (46) Donohue, J.; Hayward, B. S. *J. Cryst. Mol. Struct.* **1980**, *10*, 157-161.

- (47) Carpy, A.; Gadret, M.; Hickel, D.; Leger, J. M. *Acta Crystallogr., Sect. B: Struct. Sci.* **1979**, *B35*, 185-188.
- (48) Yathirajan, H. S.; Nagaraj, B.; Narasegowda, R. S.; Nagaraja, P.; Bolte, M. *Acta Crystallogr., Sect. E: Struct. Rep.* **2004**, *E60*, o2228-o2229.
- (49) Sivy, J.; Kettmann, V.; Fresova, E. *Acta Crystallogr., Sect. C: Cryst. Struct. Commun.* **1991**, *C47*, 2695-2696.
- (50) Ditchfield, R. *Mol. Phys.* **1974**, *27*, 789-807.
- (51) Wolinski, K.; Hinton, J. F.; Pulay, P. *J. Am. Chem. Soc.* **1990**, *112*, 8251-8260.
- (52) Adiga, S.; Aebi, D.; Bryce, D. L. *Can. J. Chem.* **2007**, *85*, 496-505.
- (53) Gee, M.; Wasylshen, R. E.; Laaksonen, A. *J. Phys. Chem. A* **1999**, *103*, 10805-10812.
- (54) Clark, S. J.; Segall, M. D.; Pickard, C. J.; Hasnip, P. J.; Probert, M. I. J.; Refson, K.; Payne, M. C. *Z. Kristallogr.* **2005**, *220*, 567-570.
- (55) Profeta, M.; Mauri, F.; Pickard, C. J. *J. Am. Chem. Soc.* **2003**, *125*, 541-548.
- (56) Perdew, J. P.; Burke, K.; Ernzerhof, M. *Phys. Rev. Lett.* **1996**, *77*, 3865-3868.
- (57) Perdew, J. P.; Burke, K.; Ernzerhof, M. *Phys. Rev. Lett.* **1998**, *80*, 891.
- (58) Ishida, T.; In, Y.; Inoue, M. *Acta Crystallogr., Sect. C: Cryst. Struct. Commun.* **1990**, *C46*, 1893-1896.
- (59) Mirmehrabi, M.; Rohani, S.; Murthy, K. S. K.; Radatus, B. *J. Cryst. Growth* **2004**, *260*, 517-526.
- (60) Gorbitz, C. H. *Acta Chem. Scand.* **1989**, *43*, 871-875.
- (61) Sequeira, A.; Rajagopal, H.; Chidambaram, R. *Acta Crystallogr., Sect. B: Struct. Sci.* **1972**, *28*, 2514-2519.
- (62) Fuess, H.; Hohlwein, D.; Mason, S. A. *Acta Crystallogr., Sect. B: Struct. Sci.* **1977**, *B33*, 654-659.
- (63) Kiss, A.; Repasi, J. *Analyst* **1993**, *118*, 661-664.

Chapter 9

General Conclusions and Future Outlook

In this thesis, it has been demonstrated that solid-state NMR (SSNMR) methods such as the WURST-QCPMG pulse sequence and piecewise spectral acquisitions, along with specialized hardware and ultra-high magnetic fields, are extremely important for the study of unreceptive nuclei in a myriad of different materials. Many unreceptive nuclei were once thought to be impossible or impractical to study with SSNMR; however, we have demonstrated that it is possible to acquire high quality spectra, and obtain NMR interaction parameters which can shed light on structure and dynamics at the molecular level. The combination of SSNMR data with powder- and single-crystal X-ray diffraction (XRD) techniques, and first principles calculations of NMR interaction tensors, provides information about the electronic and chemical environment of metal and halogen nuclei, and will be useful in future structural characterizations of a variety of systems for which crystallographic data are not available and/or obtainable (i.e., amorphous/disordered solids, micro- and nanocrystals, nanoparticles, etc.).

In Chapter 3, the development and application of ^{209}Bi SSNMR were discussed, and from this work, a number of future applications become apparent. The sensitivity of the ^{209}Bi NMR parameters to the bismuth chemical environment, and the predictive power of theoretically calculated NMR tensor parameters, strongly imply that ^{209}Bi SSNMR may be useful for the characterization of a variety of Bi-containing materials and compounds. There is increasing interest in synthesizing a variety of bismuth-containing systems which

have applications or potential applications as pharmaceuticals,¹⁻³ catalysts,⁴ nanowires and nanoparticles,⁵ and electronics and solar energy technologies.⁶ Since our work is the first of its kind involving ²⁰⁹Bi SSNMR reported in the literature, there is a paucity of ²⁰⁹Bi NMR data from which structural interpretations can be made. It is of great importance to conduct ²⁰⁹Bi SSNMR experiments on a wide variety of bismuth complexes with known crystal structures, in order to build a database of ²⁰⁹Bi NMR tensor parameters. This database can then be used to study bismuth-containing materials with unknown structures such as bismuth subsalicylate,⁷ which is the active ingredient of Peptobismol; Bi₂S₃ nanomaterials,^{5,8,9} which are important for thermoelectric devices, and bismuth borate glasses,⁶ which are utilized in solar energy technologies. Many of these materials are not amenable to study via single-crystal XRD, and little is known about their molecular-level structures. ²⁰⁹Bi SSNMR can provide useful information regarding the number of bismuth sites, and their coordination environments, local geometries and symmetries.

Based on our ²⁰⁹Bi NMR data and on previous ²⁰⁹Bi NQR studies,¹⁰ the ²⁰⁹Bi quadrupolar coupling constant, C_Q , can be very large leading to extremely broad NMR patterns. In such cases, it is not practical to obtain whole ultra-wideline (UW) SSNMR patterns, since such experiments will be very time consuming, and only the key discontinuities and shoulders are necessary to extract the quadrupolar parameters; therefore, NMR experiments will be performed at ultra-high magnetic field strengths to obtain the key features of the NMR spectra using the histogram-style spikelet method outlined by Kirkpatrick and co-workers.¹¹ These spectra can be simulated to obtain a rough estimate of the quadrupolar tensor parameters, which can then be used to identify

the range of NQR frequencies. Finally, NQR experiments can then be rapidly conducted to refine the parameters (as we demonstrated for bismuth acetate). This combination of UW SSNMR and NQR experiments is the most efficient way to obtain the quadrupolar parameters, since time-consuming scans of large NQR frequencies ranges will be rendered unnecessary.

The ^{137}Ba SSNMR study presented in Chapter 4 shows that ^{137}Ba SSNMR spectra can be efficiently acquired using UW NMR methods. As with the ^{209}Bi SSNMR study, this work is the first of its kind showing the feasibility of acquiring UW ^{137}Ba NMR spectra at moderate and ultra-high magnetic field strengths in reasonable time frames. This study will open up the application of ^{137}Ba SSNMR to study a wide variety of barium-containing systems.

Barium titanate is one of the most prominent of all piezoelectric and ferroelectric materials, and has been extensively studied due to its significance in the electroceramics industry for its potential use in transducers and capacitors.^{12,13} Barium titanate exhibits a variety of different phases and forms (i.e., crystalline, microcrystalline, nano-powders and films).^{14,15} Doping barium titanate and other barium perovskites with a variety of different metals (i.e., indium, yttrium, strontium, iron etc.) has yielded improved electronic properties¹⁶⁻²⁰ which will lead to a number of potential applications, such as pyroelectric sensors, gas detection sensors and microwave voltage tunable devices,²¹ and as such, there is an increasing interest in synthesizing a wide variety of such systems. A number of techniques have been used to characterize barium titanate in its pure and doped forms such as XRD, scanning electron microscope and transmission electron

microscopy.^{14,15,22,18} Several ^{137}Ba SSNMR studies have been reported on barium titanate in its pure forms.²³⁻³¹ In most of these studies, the barium sites exist in highly spherically symmetric environments, leading to sharp ^{137}Ba NMR resonances. However, there are very few ^{137}Ba SSNMR studies involving doped barium perovskites,³²⁻³⁴ in which the barium sites exist in a variety of different environments. Our methodology should aid in expanding the investigations of these systems, since such techniques are not limited to narrow ^{137}Ba lineshapes. The measurements of the NMR tensor parameters will provide information about the different barium environments in these systems, including their coordination environments and local geometries.

In Chapter 5, it was demonstrated that ^{115}In SSNMR spectroscopy is useful for probing In(I) and In(III) sites in solid-state compounds, and is an excellent complementary tool in combination with XRD techniques and ^{115}In solution NMR spectroscopy. Most of the ^{115}In SSNMR studies reported in the literature have primarily focused on indium systems which are used (or have the potential to be used) as semiconductors or conductors and in which the indium atoms are in the In(III) oxidation state.³⁵⁻⁴² Solution-state ^{115}In NMR spectroscopy has been used to identify a wide variety of In(III)-containing systems through measurements of the isotropic chemical shifts.⁴³⁻⁵² However, the majority of In^I salts are insoluble in most common organic solvents,⁵³ which limits their structural characterization by single-crystal XRD and solution NMR. Our work represents the first systematic ^{115}In SSNMR study of low-oxidation state indium complexes, and shows that ^{115}In NMR parameters are very sensitive to the indium coordination environment, symmetry and geometry. Due to the increasing interest in

exploring new low-oxidation state indium compounds,⁵⁴⁻⁵⁸ this work should be a great help in further characterizing newly synthesized indium-containing systems, particularly in case where XRD technique and solution NMR can not be applied. The combination of NMR experiments with first principles calculations should be key in proposing structural models for non-crystalline systems; such work is currently underway in our research group.

In Chapter 6, multinuclear (i.e., ^{109}Ag , ^{15}N , and ^{13}C) SSNMR experiments were utilized to characterize silver-containing layered networks and their interactions with primary amines, and provided valuable information above and beyond that obtained by powder XRD experiments, leading to the development of the correct structural and chemical models for these systems. The structures of the parent supramolecular networks are known from single crystal data; however, their interactions with primary amines lead to the formation of new layered materials for which single-crystal X-ray structures cannot be obtained. Solid-state ^{109}Ag , ^{15}N and ^{13}C CP/MAS NMR experiments, in combination with powder X-ray diffraction experiments and ab initio calculations, provide comprehensive information regarding the structures of these new materials, revealing that they are not intercalation solids as originally supposed, but rather, silver coordination complexes (silver diamine molecules). ^{109}Ag CS tensor parameters aided in identifying the different silver sites in these materials, and measurements of indirect spin-spin coupling constants, $^1J(^{109}\text{Ag}, ^{15}\text{N})$ and $^1J(^{109}\text{Ag}, ^{14}\text{N})$, accurately distinguished the nature of Ag-N bonding in each system. First principles calculations of silver CS tensors and $^1J(^{109}\text{Ag}, ^{14}\text{N})$ coupling constants in model complexes aided in formulating the proposed

structural models for the new materials, which are largely comprised of layers of silver-diamine cations. The methodology outlined in this work should be applicable not only to silver-containing layered materials, but also to silver-containing nanoparticles, nanowires, etc.

There is great interest in nanoparticles, since they exhibit novel characteristics that are different from their bulk materials.⁵⁹ Nanoparticles have many current and potential applications in a wide variety of areas such as biomedical engineering (i.e., bioimaging, drug delivery, and transplants),⁶⁰⁻⁶² information storage,⁶³ catalysis,⁶⁴ optical sensing biosensors,^{65,66} and surface enhanced Raman scattering (SERS).^{67,68} Silver nanoparticles are widely studied due to their biocompatibility (i.e., their use as labeling agents for imaging of cells and organisms) and antibacterial properties.^{69,70} Capping silver nanoparticles with amine functional groups is a common synthetic approach, since amines protect and stabilize the nanoparticles, causing them to be more uniform in size and shape.⁷¹⁻⁸⁰ Based on data from FTIR spectroscopy and thermal gravimetric analysis (TGA), it is proposed that the silver ions are linked to the organic ligands through the amine groups; however, the nature of the interactions of the amine with the silver atoms is not fully understood.

A variety of techniques have been used to characterize nanoparticles;^{81,82} however, ¹⁰⁹Ag SSNMR spectroscopy has been sparingly applied.⁸³⁻⁸⁶ Since the ¹⁰⁹Ag CS tensor parameters are sensitive to the electronic and chemical environments of the silver sites, and the combination of ¹⁰⁹Ag and ¹⁵N SSNMR experiments will be key in understanding the type of interactions between the silver and the nitrogen atoms. It may be possible to

use ^{109}Ag SSNMR to differentiate core and surface silver sites, as well as identifying interactions between surface Ag sites and surrounding ligands. In particular, ^1H - ^{109}Ag CP/MAS NMR experiments will be very useful for transferring polarization from protonated surface ligands to surface sites,⁸⁷ thereby enhancing the signal at these sites, identifying the bonding interactions, and helping to further describe core and surface Ag sites.

Polymorphism is a critical issue in the pharmaceutical industry since (i) ca. 80% of solid pharmaceutical drugs possess more than one polymorphic form,⁸⁸ and (ii) different polymorphs can have distinct physicochemical properties which can affect the performance and characteristics of a drug.⁸⁹⁻⁹¹ Identification and characterization of different polymorphs is crucial for the isolation of new polymorphs with improved physicochemical properties such as solubility, dissolution rate, and/or hardness,⁹²⁻⁹⁶ as well as aiding in securing patents for different active pharmaceutical ingredients. Traditionally, single-crystal and powder X-ray diffraction experiments have been the primary methods for characterization of solid pharmaceuticals and their polymorphs. However, in many cases, isolation of crystals suitable for single-crystal XRD experiments is very difficult. Further, powder XRD is limited in that (i) Rietveld refinements of powder XRD data which provide detailed structural information are usually not possible (or, if they are possible, very time consuming), and (ii) it fails to detect slight structural changes among polymorphs,^{97,98} and (iii) it is not useful for amorphous solids. Earlier SSNMR studies on pharmaceuticals focused on nuclei such as ^1H , ^2H , ^{13}C , ^{15}N , ^{31}P and ^{19}F .⁹⁹⁻¹⁰⁷ In Chapters 7 and 8, we have shown that ^{35}Cl SSNMR experiments can provide

spectra that act as accurate and rapid probes of chlorine ion environments in a variety of HCl pharmaceuticals, and can act as a fingerprinting tool for identifying different hydrochloride polymorphs. We believe that adaptation of these techniques is crucial for the pharmaceutical industry, since HCl drugs constitute more than 50% of pharmaceutical salts and chlorine is present in ca. 25% of known pharmaceuticals.^{108,109}

The sensitivity of the ^{35}Cl quadrupolar NMR parameters to the local chlorine environment allows for the prediction of the number of short $\text{Cl}\cdots\text{H}$ contacts, which is crucial for identifying the structural differences between the polymorphs. Due to the large number of HCl pharmaceuticals, this work will be continued, in order to study a wide range of HCl pharmaceuticals with different chlorine ion environments, and to build a database of NMR tensor parameters from which definitive trends between the NMR parameters and chlorine environments can be established. In addition, to confirm our predictions of the number of short $\text{Cl}\cdots\text{H}$ contacts, newly developed high-resolution ^1H SSNMR techniques¹¹⁰ using the Combined Rotation and Multiple-Pulse Spectroscopy (CRAMPS)^{111,112} pulse sequence, along with ultra-fast MAS (up to 70 kHz) can be used to identify the different hydrogen sites. Furthermore, high-resolution two-dimensional (2D) heteronuclear correlation spectra¹¹³ will be used to estimate the distances between the chlorine atom and its nearby protons. Lastly, our newly developed ^{14}N SSNMR methodology^{114,115} will be applied to these systems; ^{14}N UW SSNMR spectra may play a similar role to ^{35}Cl SSNMR, providing accurate fingerprinting and structural characterization of a wide range of pharmaceuticals. ^{35}Cl and ^{14}N NMR data, along with pXRD patterns, will be used to build structural models on which first principles

calculations can be performed, in order to predict the solid-state structures for the different polymorphs.

In conclusion, the studies reported in this thesis should open up new opportunities for NMR spectroscopists to examine and explore other unreceptive nuclei in the periodic table (i.e. ^{53}Cr , ^{101}Ru , ^{73}Ge , ^{87}Sr , ^{95}Mo etc.), as well as other nuclei that may be of importance in the pharmaceutical industry such as ^{23}Na , ^{39}K , ^{25}Mg and ^{195}Pt . Libraries of NMR tensor data for these nuclei will provide new insights into structure, reactivity and dynamics that will enable chemists and materials scientists to apply new levels of rational design in the synthesis and preparation of new compounds and materials.

Bibliography

- (1) Yang, N.; Sun, H. *Coord. Chem. Rev.* **2007**, *251*, 2354-2366.
- (2) Salvador, J. A. R.; Ppinto, R. M. A.; Silvestre, S. M. *Mini-Rev. Org. Chem.* **2009**, *6*, 241-274.
- (3) Salvador, J. A. R.; Pinto, R. M. A.; Silvestre, S. M. *Curr. Org. Synth.* **2009**, *6*, 426-470.
- (4) Hua, R. *Curr. Org. Synth.* **2008**, *5*, 1-27.
- (5) Kharissova, O. V.; Kharisov, B. I. *Synth. React. Inorg., Met.-Org., Nano-Met. Chem.* **2008**, *38*, 491-502.
- (6) Chen, Y.; Huang, Y.; Liu, Y. *Mater. Sci. Found.* **2008**, *46-47*, 119-148.
- (7) Bierer, D. W. *Rev Infect Dis* **1990**, *12*, S3-S8.
- (8) Cademartiri, L.; Scotognella, F.; O'Brien, P. G.; Lotsch, B. V.; Thomson, J.; Petrov, S.; Kherani, N. P.; Ozin, G. A. *Nano Lett.* **2009**, *9*, 1482-1486.
- (9) Zhu, Y.; Qian, Y. *Sci. China, Ser. G: Phys., Mech. Astron.* **2009**, *52*, 13-20.
- (10) Chihara, H.; Nakamura, N. *Landolt-Bornstein Group III: Condensed Matter; Volume 39: Nuclear Quadrupole Resonance Spectroscopy Data. Supplement to Volumes III/20 and III/31*; Springer: Berlin, Germany, 1998.
- (11) Bowers, G. M.; Kirkpatrick, R. J. *J. Magn. Reson.* **2007**, *188*, 311-321.
- (12) Vijatovic, M. M.; Bobic, J. D.; Stojanovic, B. D. *Sci. Sintering* **2008**, *40*, 235-244.
- (13) Vijatovic, M. M.; Bobic, J. D.; Stojanovic, B. D. *Sci. Sintering* **2008**, *40*, 155-165.
- (14) Schlom, D. G.; Chen, L.-Q.; Eom, C.-B.; Rabe, K. M.; Streiffer, S. K.; Triscone, J.-M. *Annu. Rev. Mater. Res.* **2007**, *37*, 589-626.
- (15) Mitoseriu, L.; Buscaglia, V.; Buscaglia, M. T.; Viviani, M.; Nanni, P. *New Dev. Adv. Funct. Ceram.* **2007**, 119-143.
- (16) Zhao, F.; Liu, Q.; Wang, S.; Brinkman, K.; Chen, F. *Int. J. Hydrogen Energy* **2010**, *35*, 4258-4263.
- (17) Kishiki, T.; Higuchi, M.; Asaka, T.; Azuma, Y. *Key Eng. Mater.* **2010**, *421-422*, 235-238.

- (18) Efimov, K.; Halfer, T.; Kuhn, A.; Heitjans, P.; Caro, J.; Feldhoff, A. *Chem. Mater.* **2010**, *22*, 1540-1544.
- (19) Xing, Z. W.; Wu, N. J.; Ignatiev, A. *J. Appl. Phys.* **2010**, *107*, 023706/023701-023706/023703.
- (20) Zegenhagen, J.; Haage, T.; Jiang, Q. D. *Appl. Phys. A: Mater. Sci. Process.* **1998**, *67*, 711-722.
- (21) Nayak, M.; Ezhilvalavan, S.; Tseng, T. Y. *Handb. Thin Film Mater.* **2002**, *3*, 99-167.
- (22) Himanshu, A. K.; Choudhary, B. K.; Gupta, D. C.; Bandyopadhyay, S. K.; Sinha, T. P. *Phys. B* **2010**, *405*, 1608-1614.
- (23) Bastow, T. J. *J. Phys.: Condens. Matter* **1989**, *1*, 4985-4991.
- (24) Bastow, T. J.; Whitfield, H. J. *Solid State Commun.* **2001**, *117*, 483-488.
- (25) Dec, S. F.; Davis, M. F.; Maciel, G. E.; Bronnimann, C. E.; Fitzgerald, J. J.; Han, S. S. *Inorg. Chem.* **1993**, *32*, 955-959.
- (26) Fitzgerald, J. J.; Han, S. S.; Dec, S. F.; Davis, M. F.; Bronnimann, C. E.; Maciel, G. E. *NIST Spec. Publ.* **1991**, *804*, 173-178.
- (27) Forbes, C. E.; Hammond, W. B.; Cipollini, N. E.; Lynch, J. F. *J. Chem. Soc., Chem. Commun.* **1987**, 433-436.
- (28) MacKenzie, K. J. D.; Meinhold, R. H. *Ceram. Int.* **2000**, *26*, 87-92.
- (29) Taye, A.; Klotzsche, G.; Michel, D.; Mulla-Osman, S.; Bottcher, R. *J. Phys.: Condens. Matter* **1999**, *11*, 871-879.
- (30) Sedykh, P.; Haase, J.; Michel, D.; Charnaya, E. V. *Ferroelectrics* **2008**, *363*, 215-226.
- (31) Sedykh, P.; Michel, D. *Phys. Rev. B: Condens. Matter Mater. Phys.* **2009**, *79*, 134119/134111-134119/134118.
- (32) Gervais, C.; Veautier, D.; Smith, M. E.; Babonneau, F.; Belleville, P.; Sanchez, C. *Solid State Nucl. Magn. Reson.* **2004**, *26*, 147-152.
- (33) Yakubowskii, A.; Egorov, A.; Lutgemeier, H. *Appl. Magn. Reson.* **1992**, *3*, 665-676.
- (34) Brinkmann, D. *Appl. Magn. Reson.* **2004**, *27*, 207-213.

- (35) Tomita, Y.; Yamada, K.; Ohki, H.; Okuda, T. *Z. Naturforsch., A: Phys. Sci.* **1998**, *53*, 466-472.
- (36) Schmidt, E. V.; Ermakov, V. L.; Gnezdilov, O. I.; Matukhin, V. L.; Korzun, B. V.; Fadeeva, A. A.; Khabibullina, I. K. *J. Appl. Spect.* **2009**, *76*, 667-671.
- (37) Jung, W.-S.; Han, O. H.; Chae, S.-A. *Mater. Lett.* **2007**, *61*, 3413-3415.
- (38) Yamada, K.; Kumano, K.; Okuda, T. *Solid State Ionics* **2005**, *176*, 823-829.
- (39) Yamada, K.; Kumano, K.; Okuda, T. *Solid State Ionics* **2006**, *177*, 1691-1695.
- (40) Han, O. H.; Timken, H. K. C.; Oldfield, E. *J. Chem. Phys.* **1988**, *89*, 6046-6052.
- (41) Khabibullin, I. K.; Matukhin, V. L.; Ermakov, V. L.; Gnezdilov, O. I.; Korzun, B. V.; Schmidt, E. V. *Semiconductors* **2009**, *43*, 1-3.
- (42) Tomita, Y.; Yonekura, H.; Yamauchi, Y.; Yamada, K.; Kobayashi, K. *Z. Naturforsch., A: Phys. Sci.* **2002**, *57*, 447-450.
- (43) McGarvey, B. R.; Trudell, C. O.; Tuck, D. G.; Victoriano, L. *Inorg. Chem.* **1980**, *19*, 3432-3436.
- (44) Colton, R.; Dakternieks, D.; Hauenstein, J. *Aust. J. Chem.* **1981**, *34*, 949-955.
- (45) Malyarick, M. A.; Ilyuhin, A. B.; Petrosyants, S. P. *Polyhedron* **1993**, *12*, 2403-2409.
- (46) Cheng, F.; Friend, S. I.; Hector, A. L.; Levason, W.; Reid, G.; Webster, M.; Zhang, W. *Inorg. Chem.* **2008**, *47*, 9691-9700.
- (47) Caravan, P.; Orvig, C. *Inorg. Chem.* **1997**, *36*, 236-248.
- (48) Kuznetsov, A. N.; Popovkin, B. A.; Henderson, W.; Taylor, M. J.; Bengtsson-Kloo, L. *Dalton* **2000**, 1777-1781.
- (49) Alcock, N. W.; Degnan, I. A.; Howarth, O. W.; Wallbridge, M. G. H. *J. Chem. Soc., Dalton Trans.* **1992**, 2775-2780.
- (50) Hinton, J. F.; Briggs, R. W. *NMR Period. Table* **1978**, 279-308.
- (51) Malyarick, M. A.; Petrosyants, S. P. *Inorg. Chem.* **1993**, *32*, 2265-2268.
- (52) Kodweiss, J.; Koehnlein, D.; Koessler, G.; Lutz, O.; Messner, W.; Mohn, K. R.; Nolle, A.; Nothaft, G.; Ruppert, P.; et al. *Z. Naturforsch., A: Phys. Sci.* **1986**, *41A*, 471-477.

- (53) Tuck, D. G. *Chem. Soc. Rev.* **1993**, *22*, 269-276.
- (54) Aldridge, S. *Angew. Chem., Int. Edit.* **2006**, *45*, 8097-8099.
- (55) Cooper, B. F. T.; Macdonald, C. L. B. *J. Organomet. Chem.* **2008**, *693*, 1707-1711.
- (56) Baker, R. J.; Jones, C. *Coord. Chem. Rev.* **2005**, *249*, 1857-1869.
- (57) Gemel, C.; Steinke, T.; Cokoja, M.; Kempter, A.; Fischer, R. A. *Eur. J. Inorg. Chem.* **2004**, 4161-4176.
- (58) Pardoe, J. A. J.; Downs, A. J. *Chem. Rev.* **2007**, *107*, 2-45.
- (59) Bhinder, S. S.; Dadra, P. *Asian J. Chem.* **2009**, *21*, S167-S171.
- (60) Zhang, J. Z. *J. Phys. Chem. Lett.* **2010**, *1*, 686-695.
- (61) Chanana, M.; Mao, Z.; Wang, D. *J. Biomed. Nanotechnol.* **2009**, *5*, 652-668.
- (62) Pankhurst, Q. A.; Thanh, N. K. T.; Jones, S. K.; Dobson, J. *J. Phys. D: Appl. Phys.* **2009**, *42*, 224001/224001-224001/224015.
- (63) Osaka, T.; Iida, H.; Tominaka, S.; Hachisu, T. *Isr. J. Chem.* **2008**, *48*, 333-347.
- (64) Moshfegh, A. Z. *J. Phys. D: Appl. Phys.* **2009**, *42*, 233001/233001-233001/233030.
- (65) Murphy, C. J. *Anal. Chem.* **2002**, *74*, 520A-526A.
- (66) Kang, H.; Wang, L.; O'Donoghue, M.; Cao, Y. C.; Tan, W. *Opt. Biosens. (2nd Ed.)* **2008**, 583-621.
- (67) Kneipp, K.; Kneipp, H.; Kneipp, J. *Acc. Chem. Res.* **2006**, *39*, 443-450.
- (68) Rycenga, M.; Camargo, P. H. C.; Li, W.; Moran, C. H.; Xia, Y. *J. Phys. Chem. Lett.* **2010**, *1*, 696-703.
- (69) Krutyakov, Y. A.; Kudrinskiy, A. A.; Olenin, A. Y.; Lisichkin, G. V. *Russ. Chem. Rev.* **2008**, *77*, 233-257.
- (70) Nair, L. S.; Laurencin, C. T. *J. Biomed. Nanotechnol.* **2007**, *3*, 301-316.
- (71) Kim, K.; Lee, H. B.; Lee, J. W.; Shin, K. S. *J. Colloid Interface Sci.* **2010**, *345*, 103-108.
- (72) Kavitha, M.; Parida, M. R.; Prasad, E.; Vijayan, C.; Deshmukh, P. C. *Macromol. Chem. Phys.* **2009**, *210*, 1310-1318.
- (73) Kim, K.; Lee, H. S. *Can. J. Anal. Sci. Spectrosc.* **2007**, *52*, 121-129.
- (74) Ramajo, L.; Parra, R.; Reboredo, M.; Castro, M. *J. Chem. Sci.* **2009**, *121*, 83-87.

- (75) Mahapatra, S. S.; Karak, N. *Mater. Chem. Phys.* **2008**, *112*, 1114-1119.
- (76) Tobita, M.; Yasuda, Y. *J. Phys. Chem. C* **2008**, *112*, 13851-13855.
- (77) Chen, M.; Feng, Y.-G.; Wang, X.; Li, T.-C.; Zhang, J.-Y.; Qian, D.-J. *Langmuir* **2007**, *23*, 5296-5304.
- (78) Frattini, A.; Pellegrini, N.; Nicastro, D.; de Sanctis, O. *Mater. Chem. Phys.* **2005**, *94*, 148-152.
- (79) Kumar, A.; Joshi, H.; Pasricha, R.; Mandale, A. B.; Sastry, M. *J. Colloid Interface Sci.* **2003**, *264*, 396-401.
- (80) Nakamoto, M.; Yamamoto, M.; Kashiwagi, Y. *Met. Nanoclusters Catal. Mater. Sci.* **2008**, 367-372.
- (81) Baer, D. R.; Gaspar, D. J.; Nachimuthu, P.; Techane, S. D.; Castner, D. G. *Anal. Bioanal. Chem.* **2010**, *396*, 983-1002.
- (82) Chen, Z.; Wu, J.; Pathak, Y. *Drugs Pharm. Sci.* **2009**, *191*, 252-269.
- (83) Bercier, J. J.; Jirousek, M.; Graetzel, M.; van der Klink, J. J. *J. Phys.: Condens. Matter* **1993**, *5*, L571-L576.
- (84) Zartilas, S.; Kourkoumelis, N.; Hadjidakou, S. K.; Hadjiliadis, N.; Zachariadis, P.; Kubicki, M.; Denisov, A. Y.; Butler, I. S. *Eur. J. Inorg. Chem.* **2007**, 1219-1224.
- (85) Nozaki, K.; Itami, T. *J. Phys.: Condens. Matter* **2006**, *18*, 3617-3627.
- (86) Kuwata, N.; Kawamura, J.; Nakamura, Y.; Okuda, K.; Tatsumisago, M.; Minami, T. *Solid State Ionics* **2000**, *136-137*, 1061-1066.
- (87) Lo, A. Y. H.; Sudarsan, V.; Sivakumar, S.; van Veggel, F.; Schurko, R. W. *J. Am. Chem. Soc.* **2007**, *129*, 4687-4700.
- (88) Lohani, S.; Grant, D. J. W. *Polymorphism* **2006**, 21-42.
- (89) Karpinski, P. H. *Chem. Eng. Technol.* **2006**, *29*, 233-238.
- (90) Llinas, A.; Box, K. J.; Burley, J. C.; Glen, R. C.; Goodman, J. M. *J. Appl. Crystallogr.* **2007**, *40*, 379-381.
- (91) Brittain, H. G.; Grant, D. J. W. *Polymorphism in Pharmaceutical Solids*; Marcel Dekker: New York, 1999; Vol. 95 pp 279-330.
- (92) Reutzel-Edens, S. M. *Curr. Opin. Drug Discov. Devel.* **2006**, *9*, 806-815.

- (93) Threlfall, T. L. *Analyst* **1995**, *120*, 2435-2460.
- (94) Miller, S. P. F.; Raw, A. S.; Yu, L. X. *Polymorphism* **2006**, 385-403.
- (95) Singhal, D.; Curatolo, W. *Adv. Drug Delivery Rev.* **2004**, *56*, 335-347.
- (96) Hilfiker, R.; De Paul, S. M.; Szelagiewicz, M. *Polymorphism* **2006**, 287-308.
- (97) Zell, M. T.; Padden, B. E.; Grant, D. J. W.; Schroeder, S. A.; Wachholder, K. L.; Prakash, I.; Munson, E. J. *Tetrahedron* **2000**, *56*, 6603-6616.
- (98) Padden, B. E.; Zell, M. T.; Dong, Z.; Schroeder, S. A.; Grant, D. J. W.; Munson, E. *J. Anal. Chem.* **1999**, *71*, 3325-3331.
- (99) Wawer, I. *NMR Spectrosc. Pharm. Anal.* **2008**, 201-231.
- (100) Harris, R. K. *J. Pharm. Pharmacol.* **2007**, *59*, 225-239.
- (101) Vogt, F. G.; Brum, J.; Katrincic, L. M.; Flach, A.; Socha, J. M.; Goodman, R. M.; Haltiwanger, R. C. *Cryst. Growth Des.* **2006**, *6*, 2333-2354.
- (102) Li, Z. J.; Abramov, Y.; Bordner, J.; Leonard, J.; Medek, A.; Trask, A. V. *J. Am. Chem. Soc.* **2006**, *128*, 8199-8210.
- (103) Wawer, I.; Pisklak, M.; Chilmonczyk, Z. *J. Pharm. Biomed. Anal.* **2005**, *38*, 865-870.
- (104) Chupin, V.; De Kroon, A. I. P. M.; De Kruijff, B. *J. Am. Chem. Soc.* **2004**, *126*, 13816-13821.
- (105) Smith, E. D. L.; Hammond, R. B.; Jones, M. J.; Roberts, K. J.; Mitchell, J. B. O.; Price, S. L.; Harris, R. K.; Apperley, D. C.; Cherryman, J. C.; Docherty, R. *J. Phys. Chem. B* **2001**, *105*, 5818-5826.
- (106) Wenslow, R. M. *Drug Dev. Ind. Pharm.* **2002**, *28*, 555-561.
- (107) Griffin, J. M.; Dave, M. R.; Steven, B. P. *Angew. Chem., Int. Ed. Engl.* **2007**, *46*, 8036-8038.
- (108) Council, C. C. "The Benefits of Chlorine Chemistry in Pharmaceuticals," Global Insights, 2006.
- (109) Bighley, L. D. B., S. M.; Monkhouse, D. C. In *Encyclopedia of Pharmaceutical Technology*; Swarbrick, J. B., J. C., Ed.; Marcel Dekker, 1995; Vol. 13, pp 453-499.
- (110) Mafra, L.; Siegel, R.; Fernandez, C.; Schneider, D.; Aussenac, F.; Rocha, J. J.

Magn. Reson. **2009**, *199*, 111-114.

(111) Ryan, L. M.; Taylor, R. E.; Paff, A. J.; Gerstein, B. C. *J. Chem. Phys.* **1980**, *72*, 508-515.

(112) Taylor, R. E.; Pembleton, R. G.; Ryan, L. M.; Gerstein, B. C. *J. Chem. Phys.* **1979**, *71*, 4541-4545.

(113) Siegel, R.; Rocha, J.; Mafra, L. *Chem. Phys. Lett.* **2009**, *470*, 337-341.

(114) O'Dell, L. A.; Schurko, R. W. *J. Am. Chem. Soc.* **2009**, *131*, 6658-6659.

(115) O'Dell, L. A.; Schurko, R. W. *Phys. Chem. Chem. Phys.* **2009**, *11*, 7069-7077.

Appendices

1. Appendix A: Supplementary Information for Chapter 3

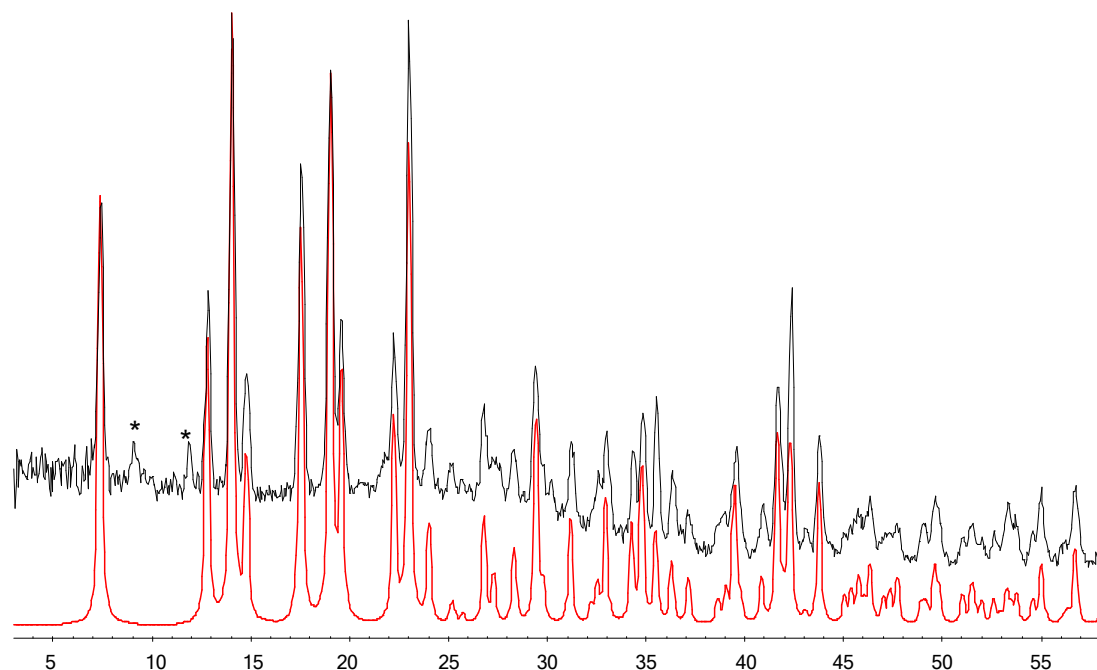


Figure A.3.1. Experimental (top) and simulated (bottom)¹ powder XRD patterns of nonaqua bismuth triflate. *: indicates a small impurity from the anhydrous bismuth triflate sample. Experimental pattern was collected using a D8 DISCOVER X-ray diffractometer equipped with an Oxford Cryosystems 700 Cryostream Plus Cooler. This diffractometer uses a Cu-K α ($\lambda = 1.54056 \text{ \AA}$) radiation source with a Bruker AXS HI-STAR area detector running under the General Area Detector Diffraction System (GADDS).

Table A.3.1. ^{209}Bi NMR Experimental Parameters at 9.4 T

	pw90 (μs)	MG Loops	$\tau_1 - \tau_4$ (μs)	Recycle Delay (s)	Offset Frequency (kHz)	Scans per Piece	Total Number of Pieces
Echo							
BiOI	0.75	--	30-20	0.025	150	87568	15
BiOBr	0.75	--	30-20	0.025	125	106144	19
BiOCl	0.75	--	30-20	0.025	115	35984	30
$\text{Bi}(\text{NO}_3)_3 \cdot 5\text{H}_2\text{O}$	0.75	--	30-20	0.025	100	16656	33
$\text{Bi}(\text{OTf})_3 \cdot 9\text{H}_2\text{O}$	0.75	--	30-20	0.025	100	12048	14
QCPMG							
$\text{Bi}(\text{CH}_3\text{CO}_2)_3$	0.75	40	20	0.025	100	10368	143
WURST QCPMG							
$\text{Bi}(\text{NO}_3)_3 \cdot 5\text{H}_2\text{O}$	50	20	--	0.1	150	7316	34

Table A.3.2. ^{209}Bi NMR Experimental Parameters at 21.1T

	pw90 (μs)	$\tau_1 - \tau_2$ (μs)	Recycle Delay (s)	Offset Frequency (kHz)	Scans per Piece	Total Number of Pieces
Echo						
BiOI	1	30-10	0.2	500	10240	2
BiOBr	1	30-10	0.2	500	20480	3
BiOCl	1	30-10	0.2	500	20480	5
$\text{Bi}(\text{NO}_3)_3 \cdot 5\text{H}_2\text{O}$	1	30-10	0.2	500	40960	3
$\text{Bi}(\text{OTf})_3 \cdot 9\text{H}_2\text{O}$	1	30-10	0.2	500	20480	2
$\text{Bi}(\text{CH}_3\text{CO}_2)_3$	1	30-10	0.2	500	20480	13

Table A.3.3. Comparison of the CASTEP ^{209}Bi NMR parameters of the optimized and non-optimized structure of BiOCl

	$ C_Q(^{209}\text{Bi}) /\text{MHz}$	η_Q	$\delta_{\text{iso}}/\text{ppm}$	Ω/ppm	κ
BiOCl (not optimized)	128.7	0	6066	1100	1
BiOCl (optimized)	133	0	5989	1051	1

For BiOCl, maximum forces observed in the CASTEP calculations were 0.6 eV/Å before and less than 0.02 eV/Å after the geometry optimization. At the same time, all calculated ^{209}Bi NMR parameters were found to be within ca. 5% of one another.

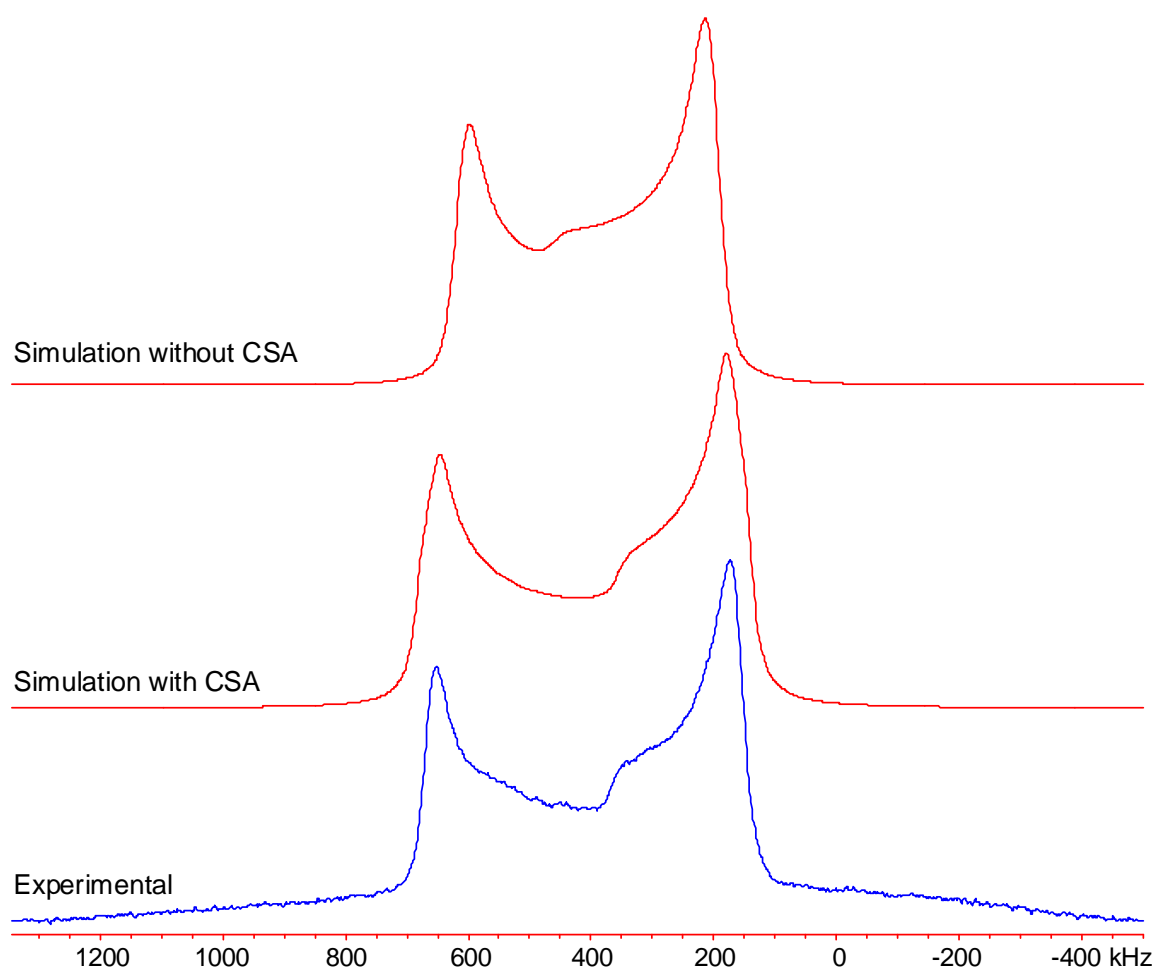


Figure A.3.2. Effects of the ^{209}Bi CSA on the powder pattern of BiOI.

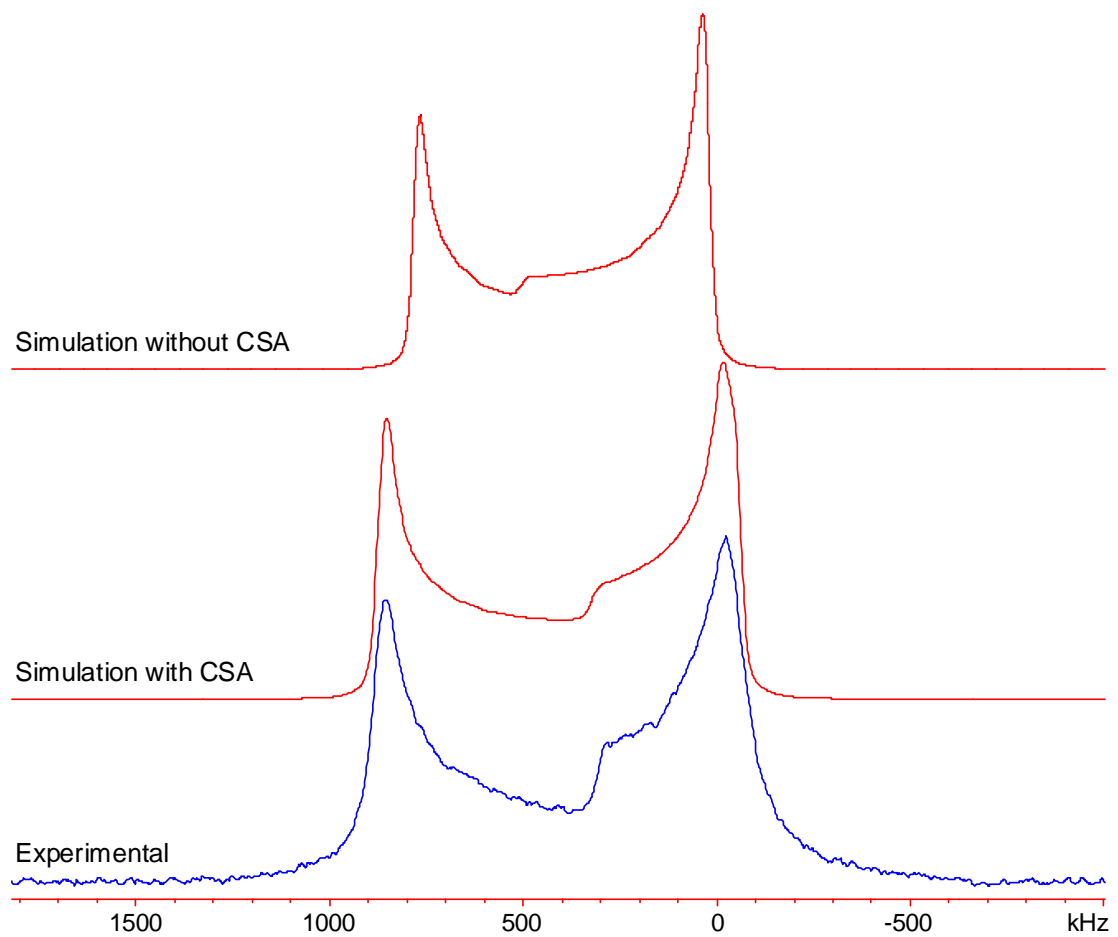


Figure A.3.3. Effects of the ^{209}Bi CSA on the powder pattern of BiOBr.

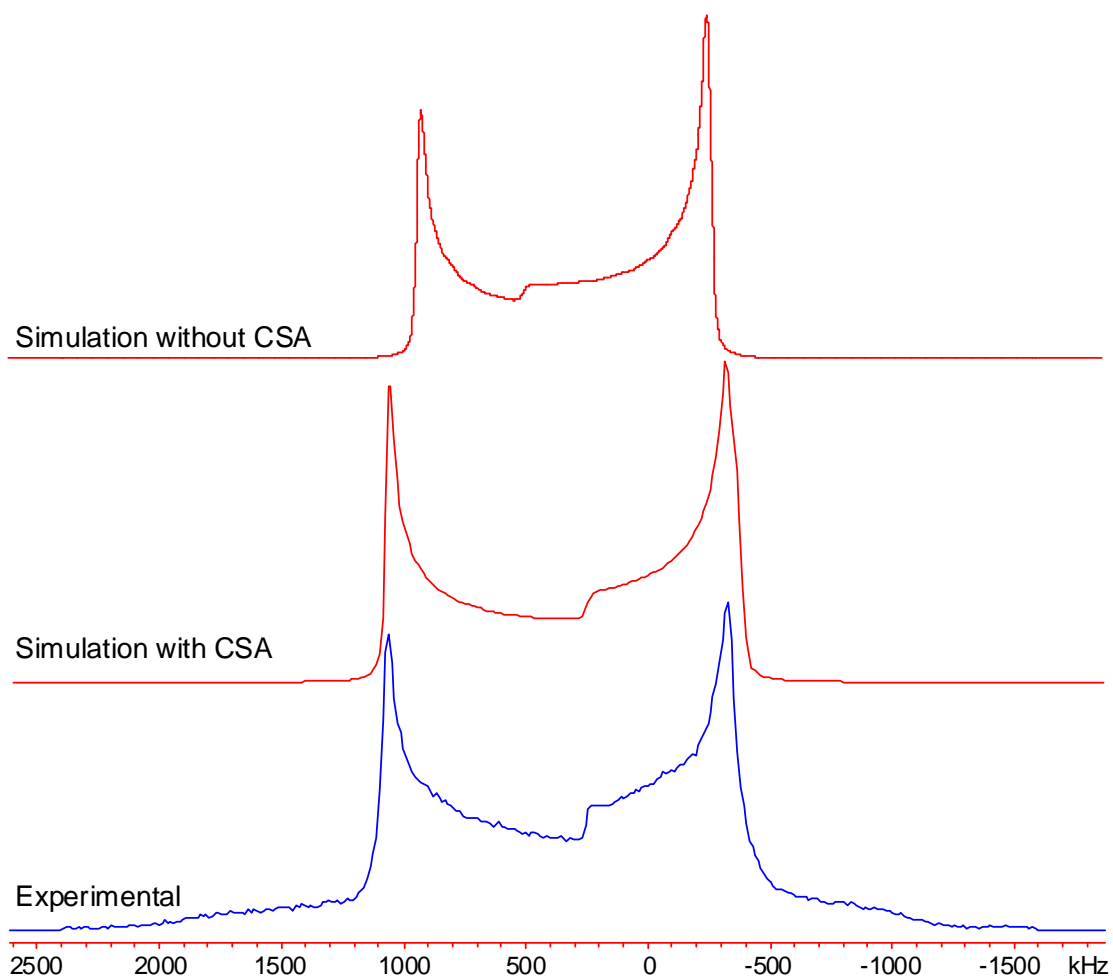


Figure A.3.4. Effects of the ^{209}Bi CSA on the powder pattern of BiOCl.

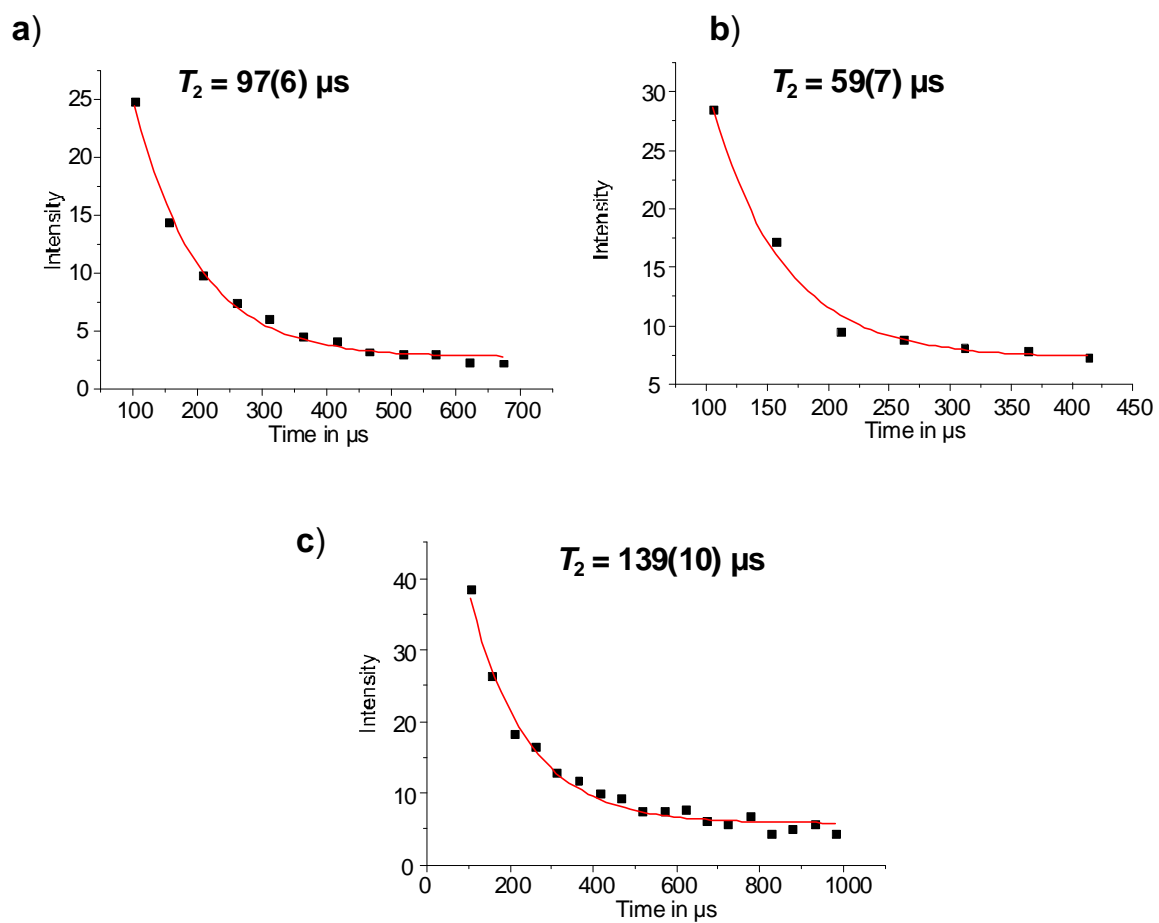
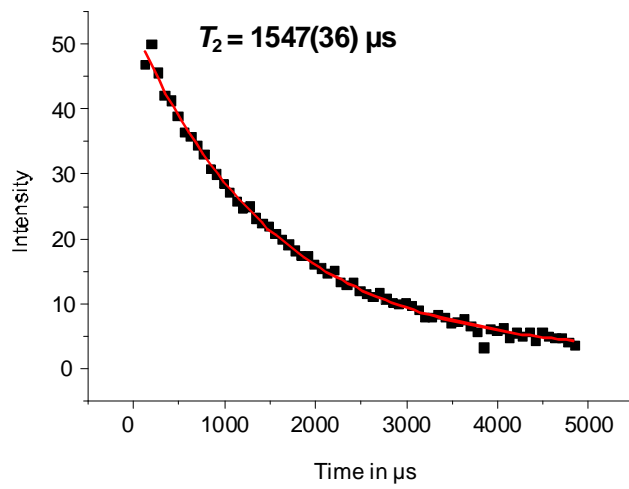


Figure A.3.5. Plots of ^{209}Bi transverse relaxation (T_2) behaviour in a) BiOI, b) BiOBr and c) BiOCl.

a)



b)

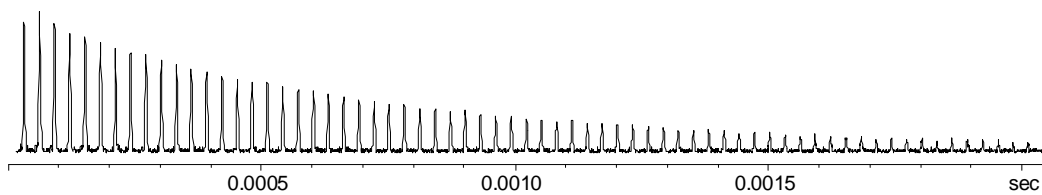


Figure A.3.6. a) ^{209}Bi transverse relaxation (T_2) behaviour in $\text{Bi}(\text{NO}_3)_3 \cdot 5\text{H}_2\text{O}$. b) train of echoes used in the T_2 calculations.

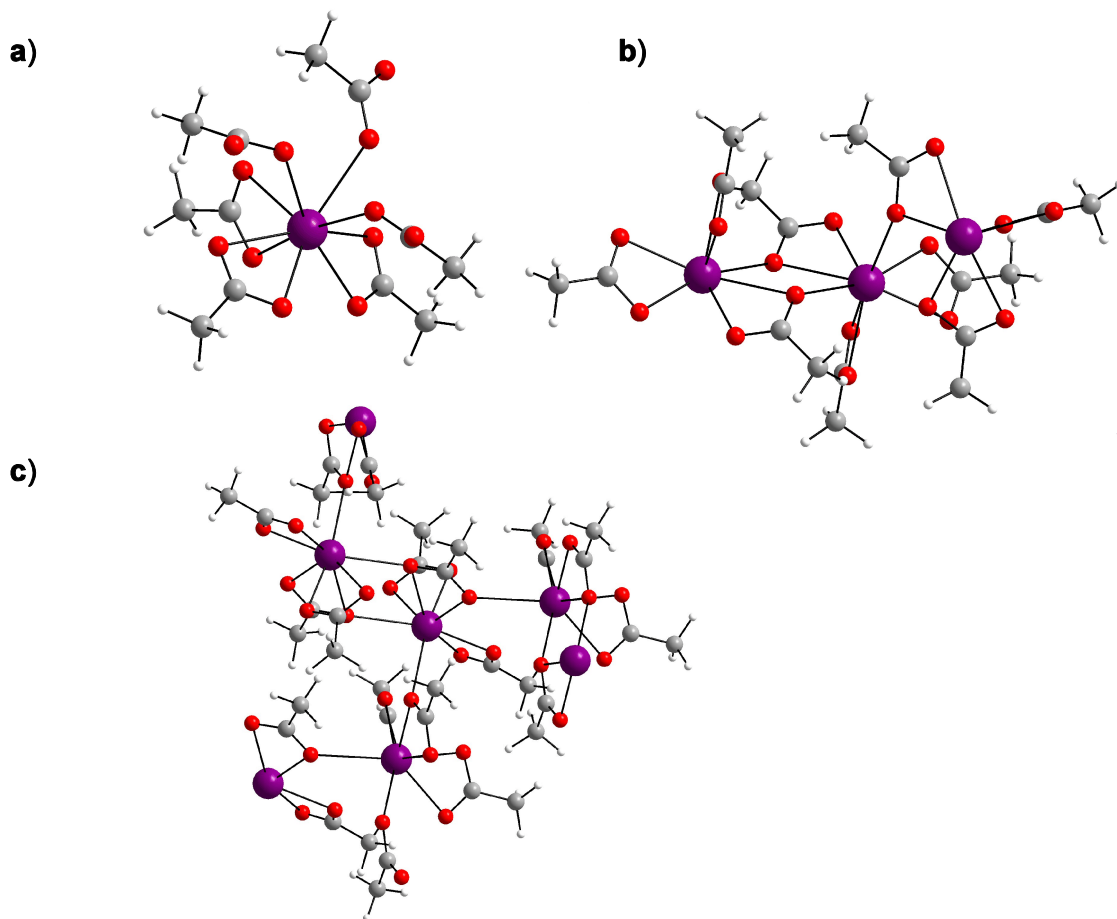


Figure A.3.7. The clusters which were input in the ^{209}Bi EFG calculations of bismuth acetate. The reported EFG parameters are those of the central bismuth atoms.

References For Appendix A

- (1) Frank, W.; Reiss, G. J.; Schneider, J. *Angew. Chem., Int. Ed. Engl.* **1995**, *34*, 2416-2417.

2. Appendix B: Supplementary Information for Chapter 4

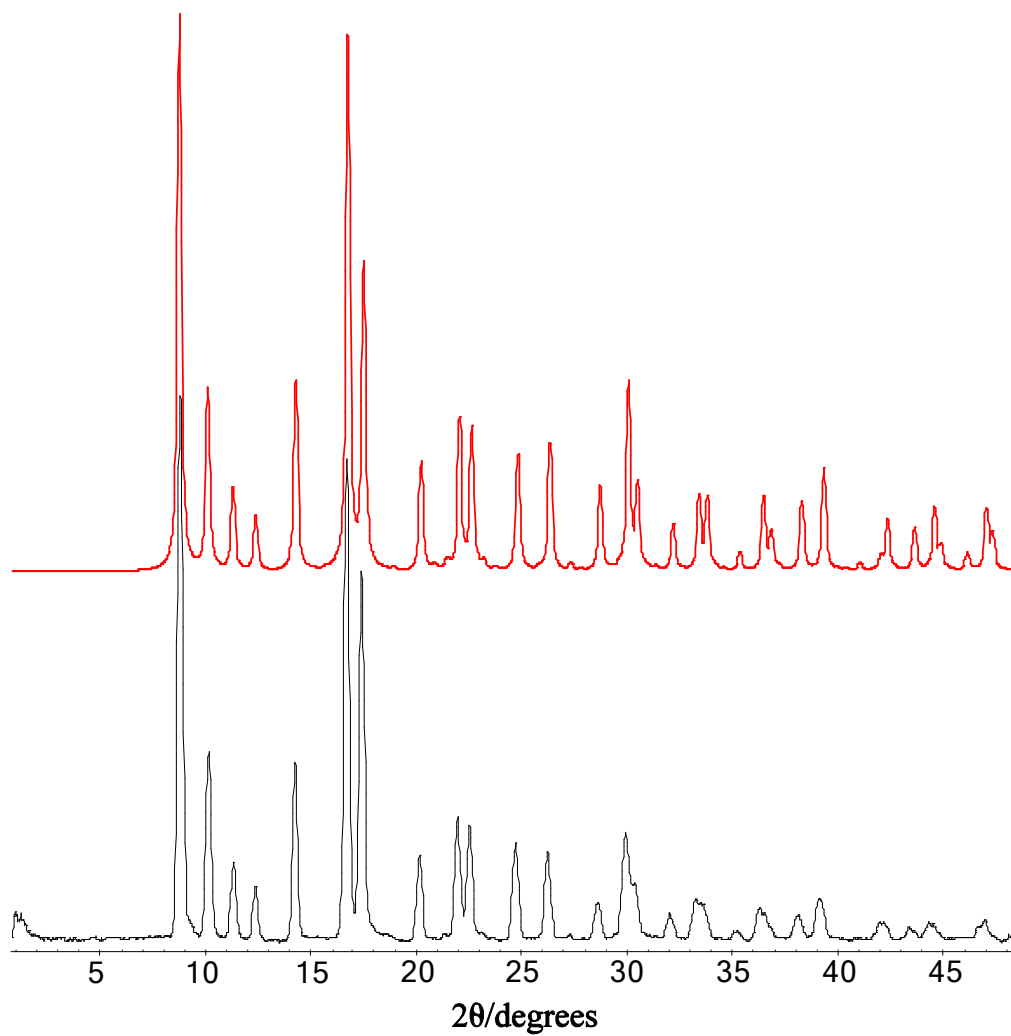


Figure B.4.1. Simulated (top)¹ and experimental (bottom) powder XRD patterns of barium nitrate.

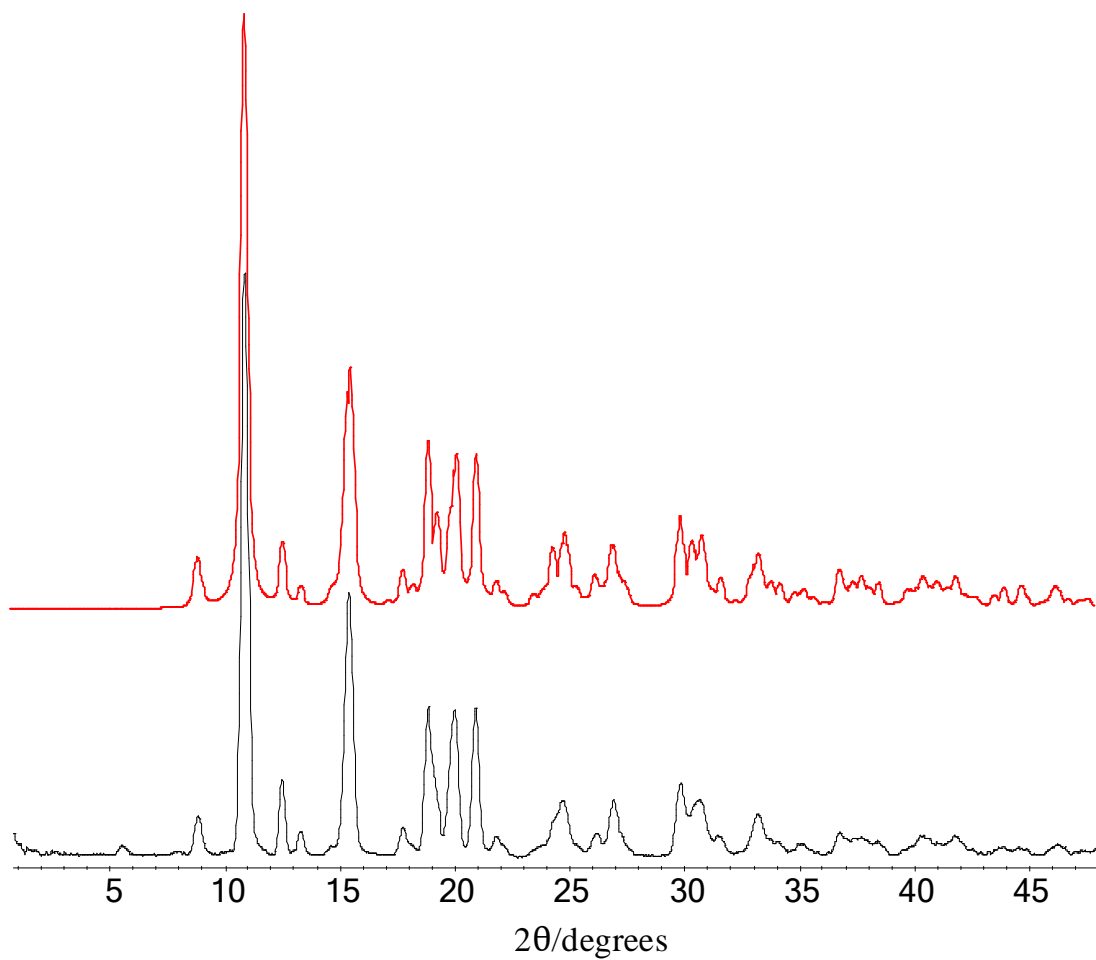


Figure B.4.2. Simulated (top)² and experimental (bottom) powder XRD patterns of barium carbonate.

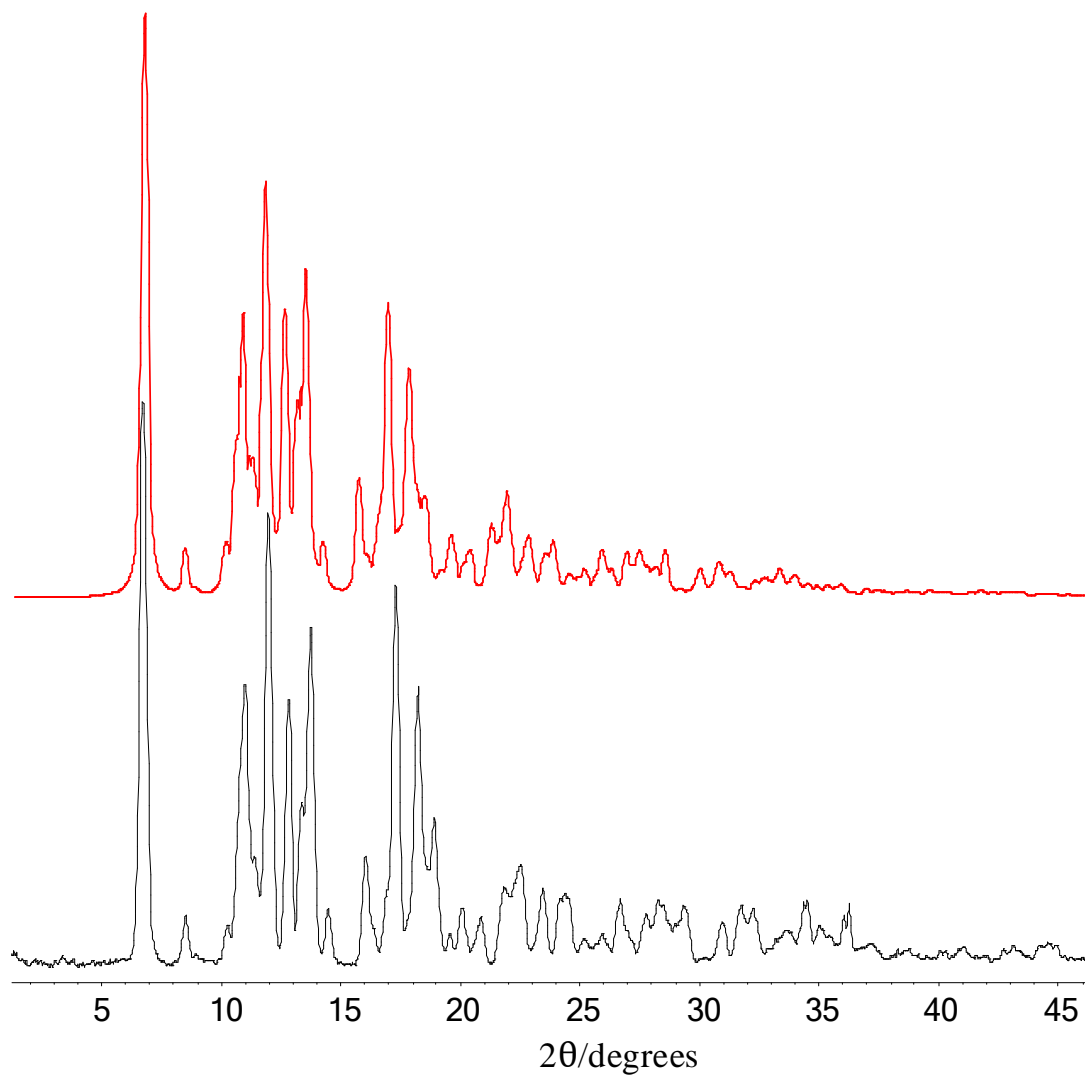


Figure B.4.3. Simulated (top)³ and experimental (bottom) powder XRD patterns of barium chlorate monohydrate.

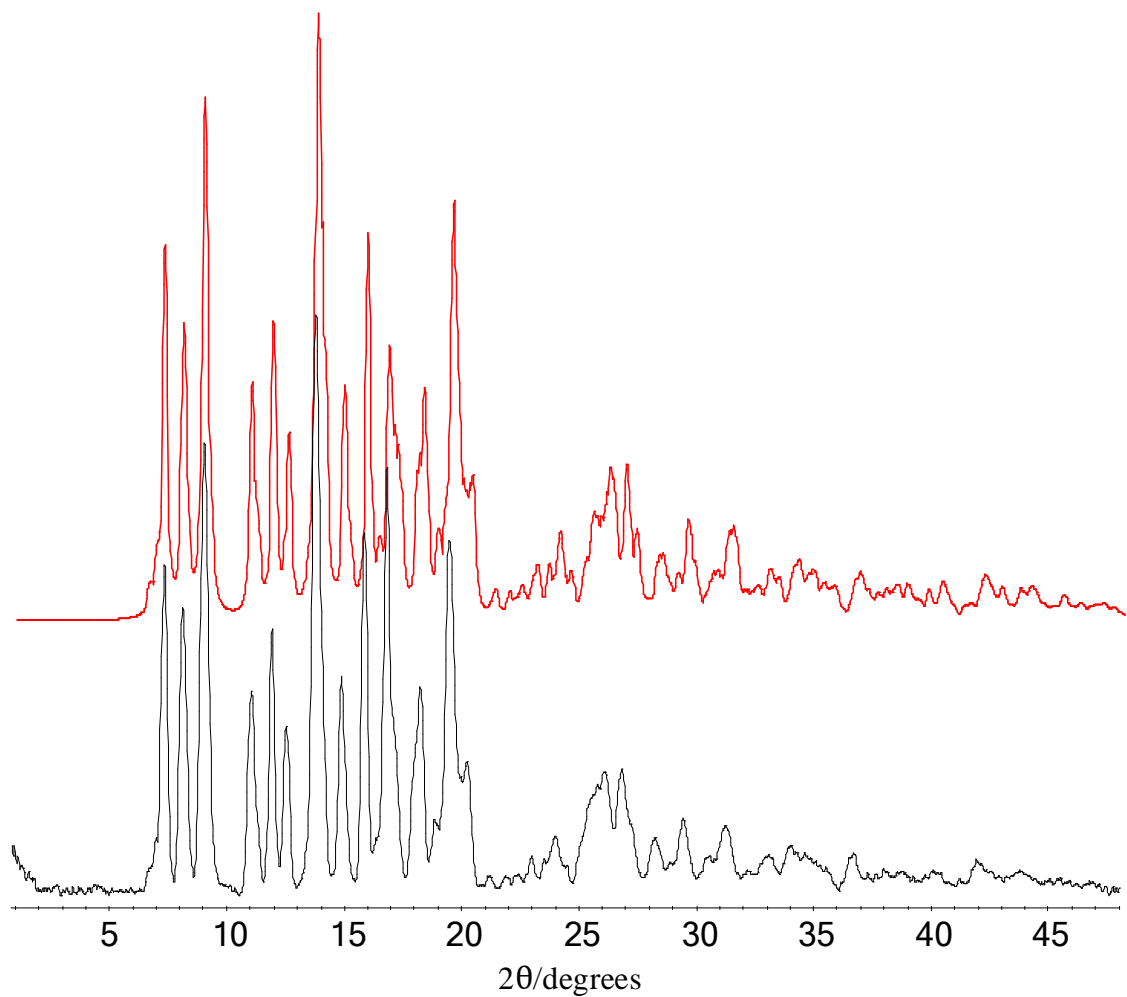


Figure B.4.4. Simulated (top)⁴ and experimental (bottom) powder XRD patterns of barium chloride dihydrate.

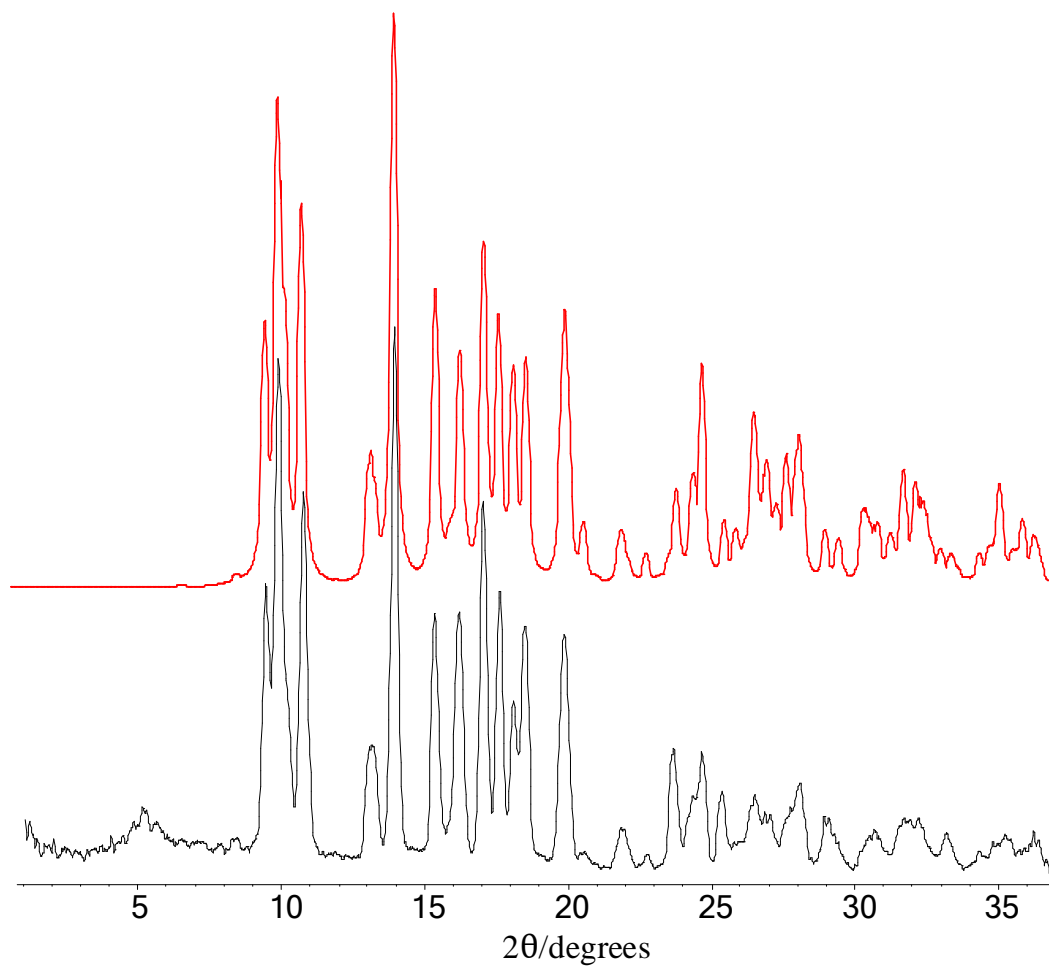


Figure B.4.5. Simulated (top)⁵ and experimental (bottom) powder XRD patterns of anhydrous barium chloride.

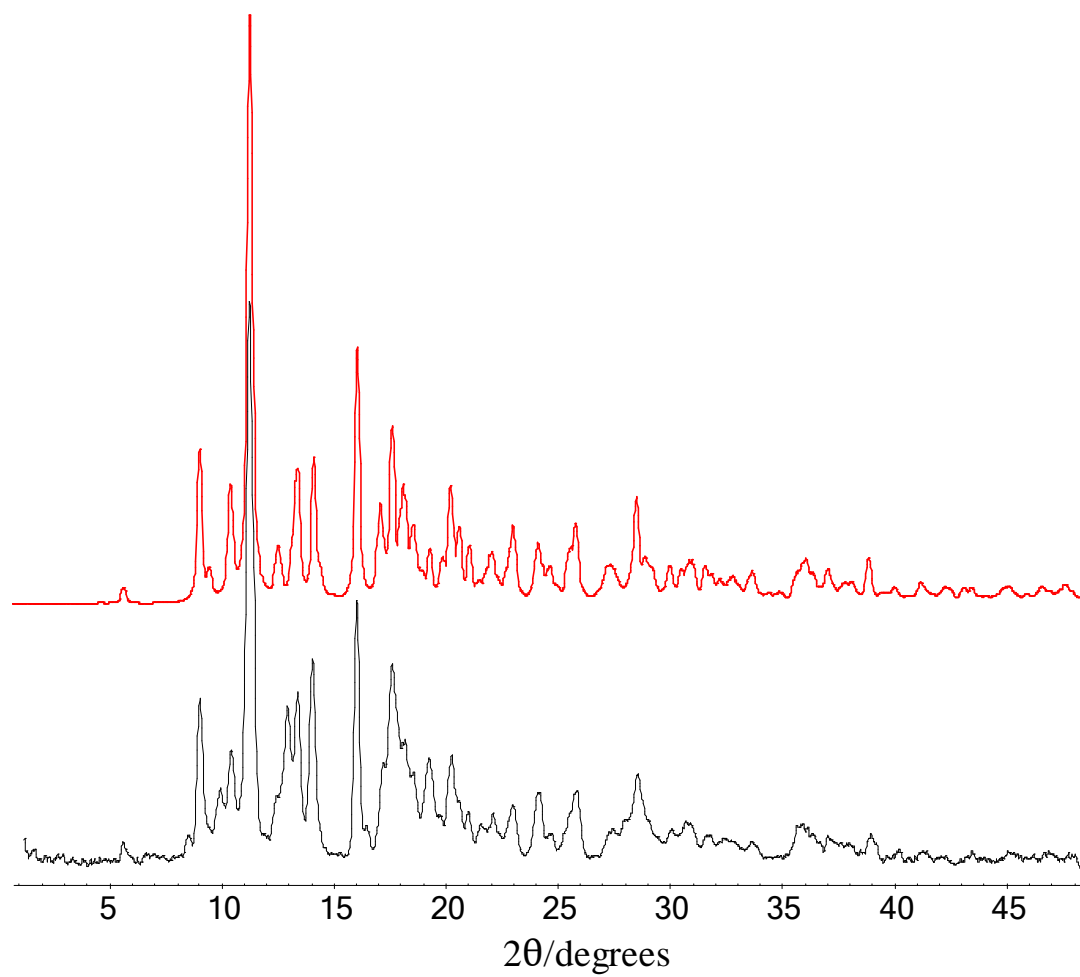


Figure B.4.6. Simulated (top)⁶ and experimental (bottom) powder XRD patterns of barium hydrogen phosphate.

Table B.4.1. ^{137}Ba NMR Experimental Parameters at 9.4 T

	rf power (kHz)	Echo size	# of echoes acquired	Recycle Delay (s)	Frequency step size (kHz)	Scans per Piece	Total Number of Pieces
$\text{Ba}(\text{NO}_3)_2$	25.8	400	50	0.1	-----	6776	1
BaCO_3	29.5	200	80	0.1	100	16404	15
$\text{Ba}(\text{ClO}_3)_2 \cdot \text{H}_2\text{O}$	27.8	100	40	0.1	200	52352	15
$\text{BaCl}_2 \cdot 2\text{H}_2\text{O}$	29.5	50	90	0.1	200	12440	46
BaCl_2	27.8	100	160	0.1	200	16072	25

Table B.4.2. ^{137}Ba NMR Experimental Parameters at 21.1T

	rf power (kHz)	Echo delay (μs)	Recycle Delay (s)	Frequency step size (kHz)	Scans per Piece	Total Number of Pieces
$\text{Ba}(\text{NO}_3)_2$	31	50	0.5	-----	4096	1
BaCO_3	31	50	0.2	100	6144	7
$\text{Ba}(\text{ClO}_3)_2 \cdot \text{H}_2\text{O}$	31	50	0.2	100	6144	17
$\text{BaCl}_2 \cdot 2\text{H}_2\text{O}$	31	50	0.2	100	12288	22
BaCl_2	31	50	0.2	100	12288	21

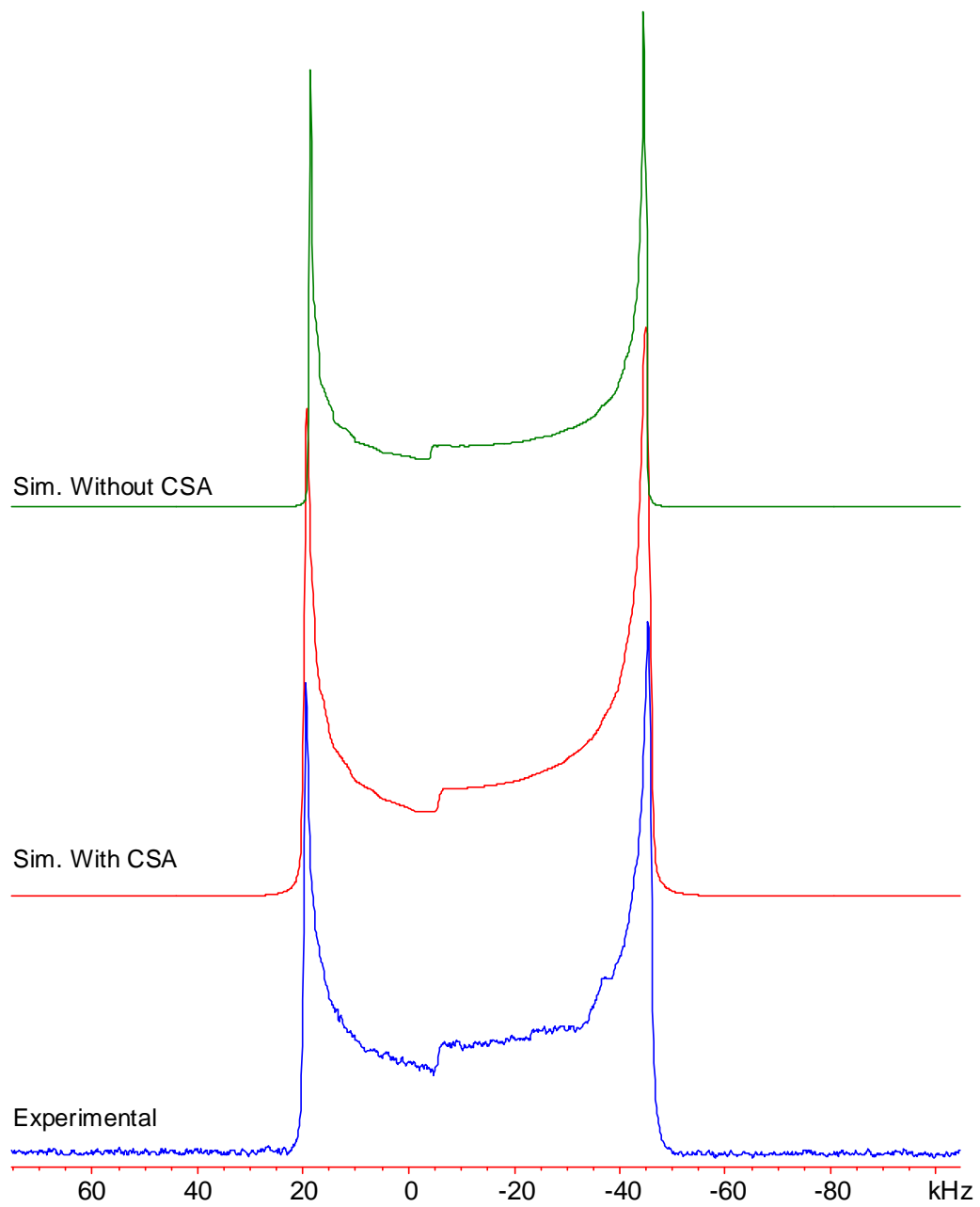


Figure B.4.7. The NMR spectrum of barium nitrate at 21.1 T and its simulations with and without CSA.

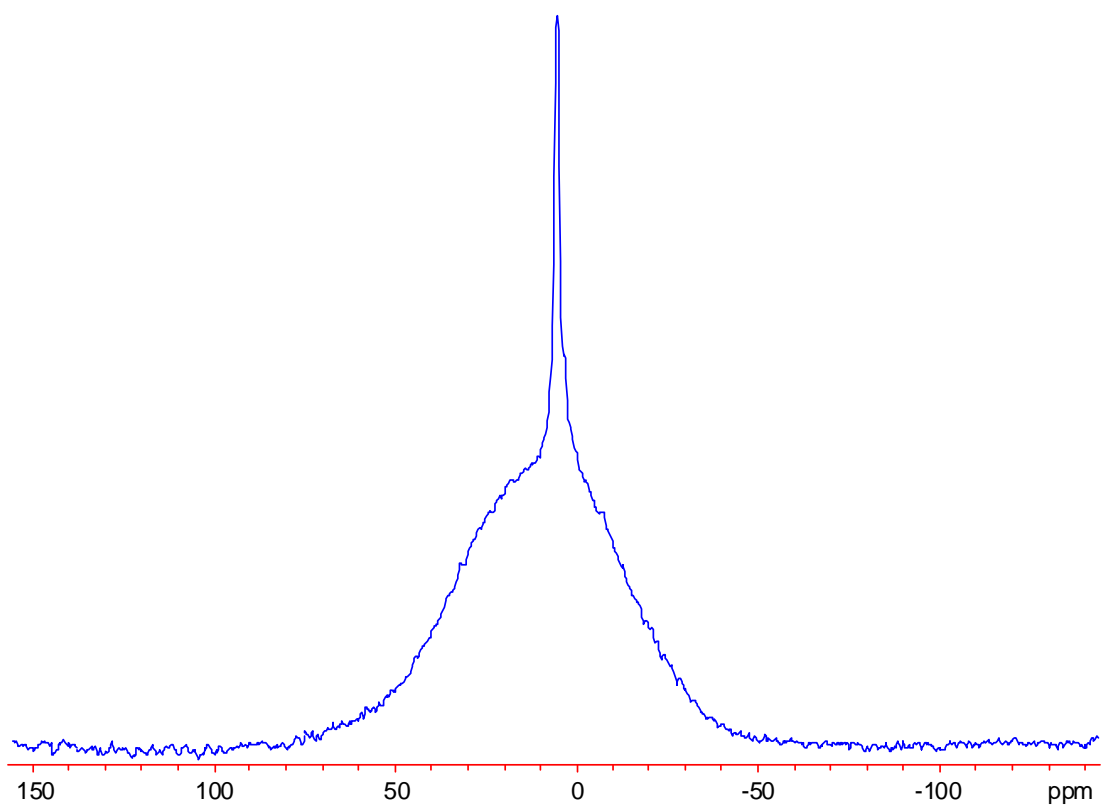


Figure B.4.8. ^1H MAS SSNMR spectrum of barium carbonate.

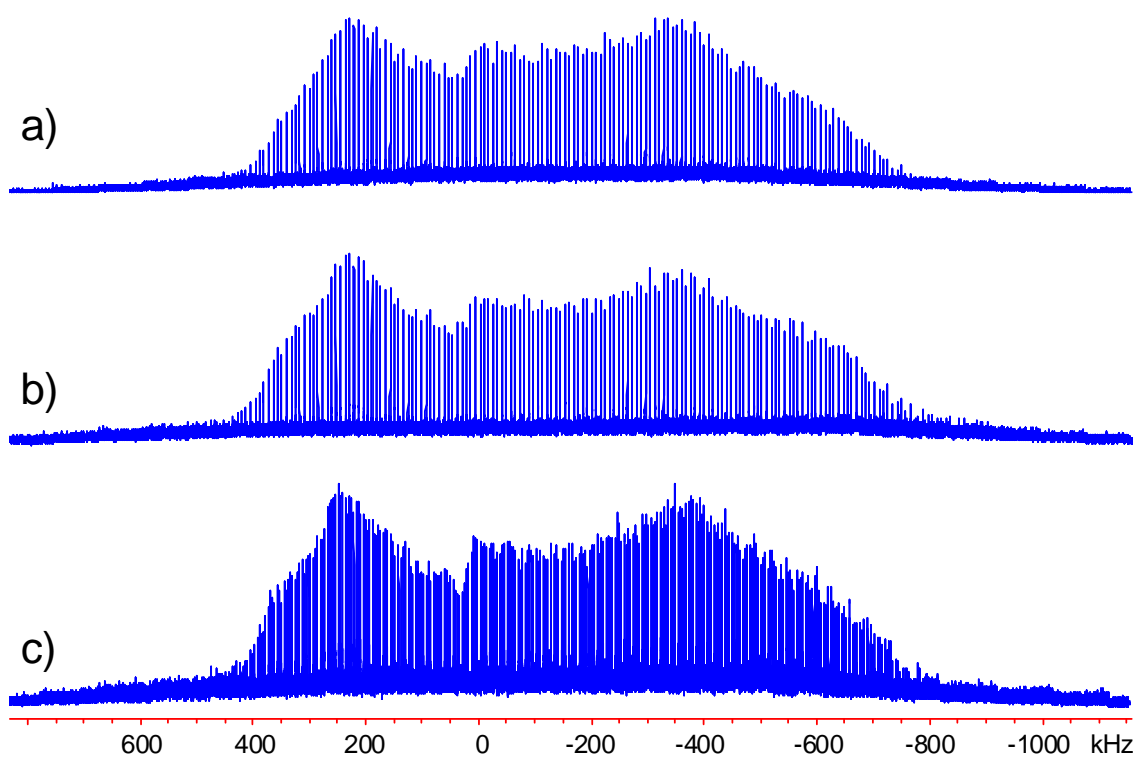


Figure B.4.9. ^{137}Ba NMR spectra of BaCO_3 before and after drying: a) dried in the oven at 200°C , b) dried under vacuum while heated to 100°C and c) commercial sample. Drying the sample helps in getting rid of most of the water but the shape of the ^{137}Ba spectrum basically remains the same; nevertheless, the powder XRD pattern (Figure B.4.2) confirms that our sample has the same crystal structure as the one reported by Antao.² A range of ^1H decoupling powers were utilized; the edges of the pattern did not sharpen even at higher decoupling powers.

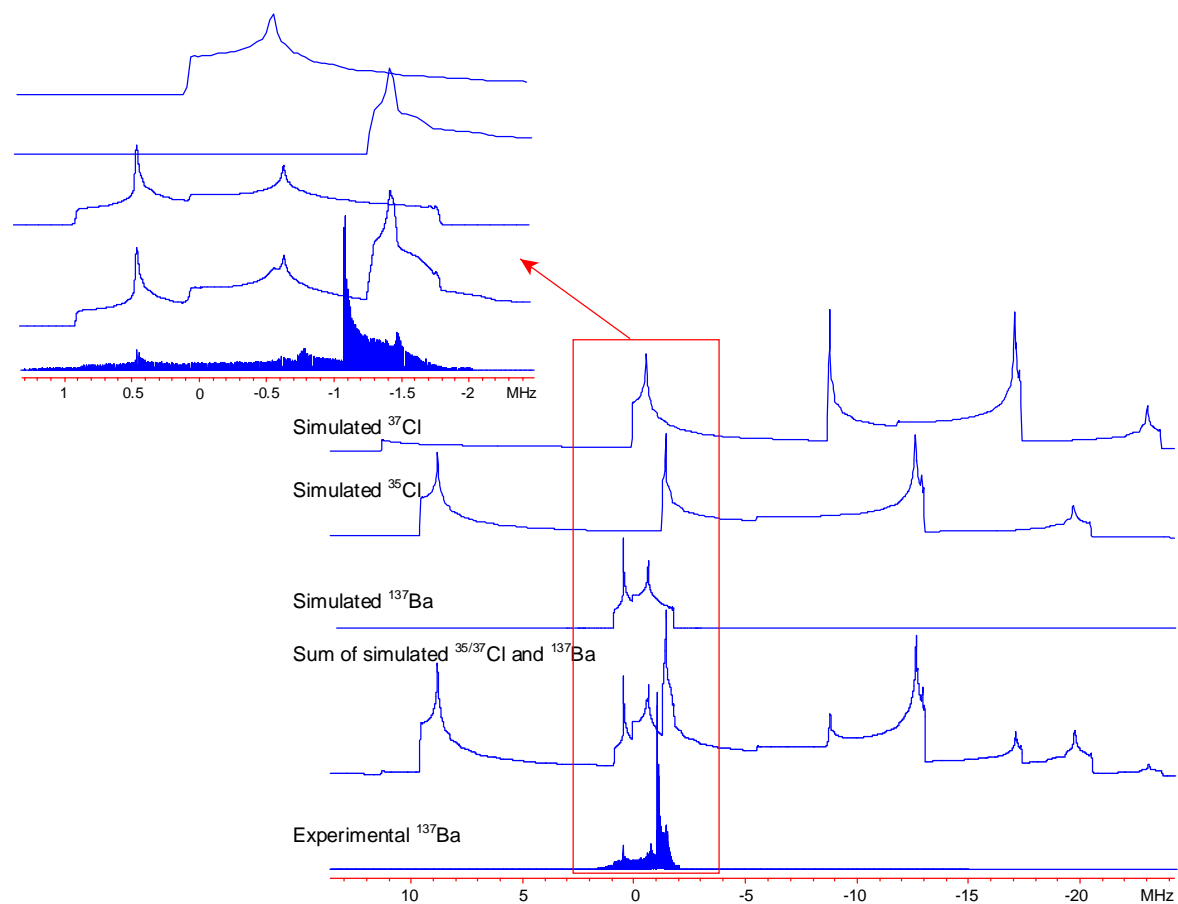


Figure B.4.10. ^{37}Cl and ^{35}Cl NMR spectra of barium chlorate monohydrate are simulated based on the EFG parameters obtained from NQR, these simulated spectra are then added to the ^{137}Ba simulated spectrum and the sum is compared with the experimental pattern to show the overlap of the ^{37}Cl satellite transitions and the ^{35}Cl central transitions with the ^{137}Ba spectrum. These simulations are rough estimate to the positions of the chlorine signals with respect to the barium spectrum and clearly prove the possible overlap between the chlorine and the barium signals.

Table B.4.3. Comparison of the experimental and CASTEP-calculated ^{137}Ba CS tensor parameters.

	σ_{11}/ppm	σ_{22}/ppm	σ_{33}/ppm	$\sigma_{\text{iso}}/\text{ppm}^a$	$\delta_{\text{iso}}/\text{ppm}^b$	Ω/ppm^c	κ^d
Ba(NO ₃) ₂ Exp.	-----	-----	-----	-----	-42(8)	25(20)	0.8(2)
Ba(NO ₃) ₂ Cal.	5484.30	5484.30	5534.38	5501.00	40	50.08	1.0
Ba(CO ₃) ₂ Exp.	-----	-----	-----	-----	50(200)	150(150)	0.5(5)
Ba(CO ₃) ₂ Cal.	5369.02	5370.48	5502.40	5413.96	127	133.38	0.98
Ba(ClO ₃) ₂ ·H ₂ O Exp.	-----	-----	-----	-----	0(200)	200(100)	-0.8(2)
Ba(ClO ₃) ₂ ·H ₂ O Cal.	5524.12	5531.21	5547.55	5534.29	7	23.43	0.4
BaCl ₂ ·2H ₂ O Exp.	-----	-----	-----	-----	150(100)	150(150)	-0.5(5)
BaCl ₂ ·2H ₂ O Cal.	5388.47	5360.98	5302.62	5350.70	190	85	-0.36
BaCl ₂ Exp.	-----	-----	-----	-----	200(200)	400(300)	0.5(5)
BaCl ₂ Cal.	5220.00	5271.16	5389.17	5293.44	248	169.16	0.4
BaHPO ₄ Exp. site1	-----	-----	-----	-----	-120(60)	-----	-----
BaHPO ₄ Exp. site2	-----	-----	-----	-----	0(200)	-----	-----
BaHPO ₄ Cal. site1	5460.08	5449.53	5392.90	5434.17	107	67.18	-0.68
BaHPO ₄ Cal. site 2	5443.18	5496.17	5558.26	5499.20	42	115.08	0.07

^a $\sigma_{\text{iso}} = (\sigma_{11} + \sigma_{22} + \sigma_{33})/3$; ^b The chemical shifts were calculated using $\delta_{\text{iso}}(\text{sample}) - \delta_{\text{iso}}(\text{ref}) = \sigma_{\text{iso}}(\text{ref}) - \sigma_{\text{iso}}(\text{sample})$ where $\delta_{\text{iso}}(\text{ref})$ and $\sigma_{\text{iso}}(\text{ref})$ are the ^{137}Ba experimental chemical shift (279 ppm)⁷ and the calculated chemical shielding (5262.28 ppm) of BaZrO₃, respectively. ^c Span: $\Omega = \sigma_{33} - \sigma_{11}$;

^d Skew: $\kappa = 3(\sigma_{\text{iso}} - \sigma_{22})/\Omega$

Table B.4.4. Comparison of the CASTEP ^{137}Ba EFG tensor parameters for the three published crystal structures of barium nitrate

Reference	Basis set accuracy	C_Q (MHz)	η_Q	k space (MP grid size)	Basis set cut off energy (eV)	Average Ba-O distance (Å)
8	Fine	-14.4	0	4×4×4	550	2.917
9	Fine	-11.2	0	4×4×4	550	2.91
10	Fine	-5.3	0	4×4×4	550	2.905
Exp.		7	0			
9	Coarse	-11.1	0	2×2×2	450	2.91
9	Medium	-11.9	0	2×2×2	500	2.91
9	Fine	-11.2	0	4×4×4	550	2.91
9	Ulrafine	-11.3	0	4×4×4	610	2.91
9	Fine, geom opt	-11.9	0	4×4×4	550	2.91

References For Appendix B

- (1) Trounov, V. A.; Tserkovnaya, E. A.; Gurin, V. N.; Korsukova, M. M.; Derkachenko, L. I.; Nikanorov, S. P. *Tech. Phys. Lett.* **2002**, 28, 351.
- (2) Antao, S. M.; Hassan, I. *Phys. Chem. Miner.* **2007**, 34, 573.
- (3) Sikka, S. K.; Momin, S. N.; Rajagopal, H.; Chidambaram, R. *J. Chem. Phys.* **1968**, 48, 1883.
- (4) Padmanabhan, V. M.; Busing, W. R.; Levy, H. A. *Acta Crystallogr. B* **1978**, B34, 2290.
- (5) Busing, W. R. *Trans. Amer. Crystallogr. Ass.* **1970**, 6, 57.
- (6) BenChaabane, T.; Smiri, L.; Bulou, A. *Solid State Sci.* **2004**, 6, 197.
- (7) MacKenzie, K. J. D.; Meinhold, R. H. *Ceram. Int.* **2000**, 26, 87.
- (8) R. Birnstock, *Z. Kristallogr.* 1967, 124, 310-334.
- (9) H. Nowotny, G. Heger, *Acta Crystallogr. C*, 1983, 39, 952-956.
- (10) V.A. Trounov, E.A. Tserkovnaya, V.N. Gurin, M.M. Korsukova, L.I. Derkachenko, S.P. Nikanorov, *Tech. Phys.*

3. Appendix C: Supplementary Information for Chapter 5

Table C.5.1. ^{115}In Static NMR Experimental Parameters at 9.4 T

	rf power (kHz)	Recycle Delay (s)	Spectral Width (kHz)	Number of Pieces	Offset frequency (kHz)	Number of Scans per Piece
$[\text{In}^+][\text{GaCl}_4]$	67	0.1	1000	1	----	8544
$\text{In}(\text{II})\text{Cl}_2$	45	0.1	2000	5	35	1584
$[\text{In}([15]\text{Crown-5})_2][\text{OTf}]$	77	0.1	1000	1	----	579152
$[\text{In}([18]\text{crown-6})]\text{GaCl}_4$	111	0.1	1000	3	150	18848
$[\text{In}([18]\text{crown-6})]\text{AlCl}_4$	111	0.1	1000	3	150	66288
InI	67	0.1	2000	6	100	17824
InBr	67	0.1	2000	8	125	8544
WURST-Echo						
$\text{In}[\text{OTf}]$	17	0.1	2000	5	250	15736

Table C.5.2. ^{115}In Static NMR Experimental Parameters at 21.1T

	rf power (kHz)	Recycle Delay (s)	Spectral Width (kHz)	Number of Pieces	Offset Frequency (kHz)	Number of Scans per Piece
$[\text{In}^+][\text{GaCl}_4]$	50	1	200	1	----	1024
$\text{In}(\text{II})\text{Cl}_2$	50	1	1000	3	110	1024
$[\text{In}([15]\text{Crown-5})_2][\text{OTf}]$	50	1	200	1	----	2976
$[\text{In}([18]\text{crown-6})]\text{GaCl}_4$	50	1	500	3	60	2048
$[\text{In}([18]\text{crown-6})]\text{AlCl}_4$	50	1	500	3	60	16384
$\text{In}[\text{OTf}]$	50	1	1000	3	120	2048
InI	50	1	500	1	----	1782
InBr	50	1	1000	1	----	5557

Table C.5.3. ^{115}In MAS NMR Experimental Parameters at 21.1T

	ν_{rot} (kHz)	rf power (kHz)	Recycle Delay (s)	Spectral Width (kHz)	Number of Scans
$[\text{In}^+][\text{GaCl}_4]$	18	50	1	200	2200
$\text{In}(\text{II})\text{Cl}_2$	18	50	1	500	5836
$[\text{In}([15]\text{Crown-5})_2][\text{OTf}]$	12.5	50	0.5	200	4096
$[\text{In}([18]\text{crown-6})]\text{GaCl}_4$	50	100	0.5	1000	20480
$[\text{In}([18]\text{crown-6})]\text{AlCl}_4$	50	100	0.5	1000	136000
$\text{In}[\text{OTf}]$	62.5	100	0.5	1000	16000
InI	62.5	100	0.5	1000	10240
InBr	62.5	100	0.5	1000	16400

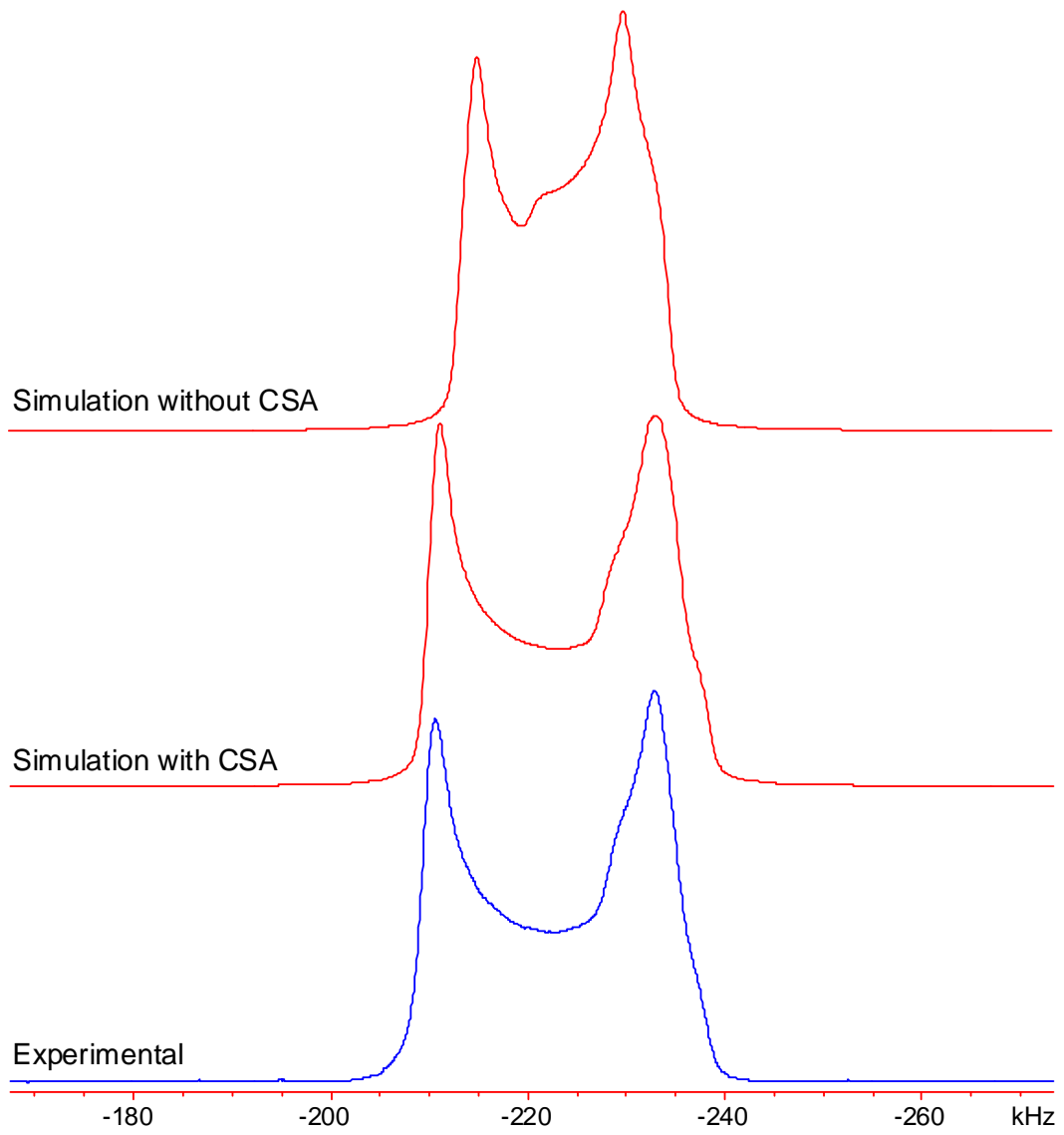


Figure C.5.1. The contribution of ^{115}In CSA on the NMR pattern of $\text{In}[\text{GaCl}_4]$

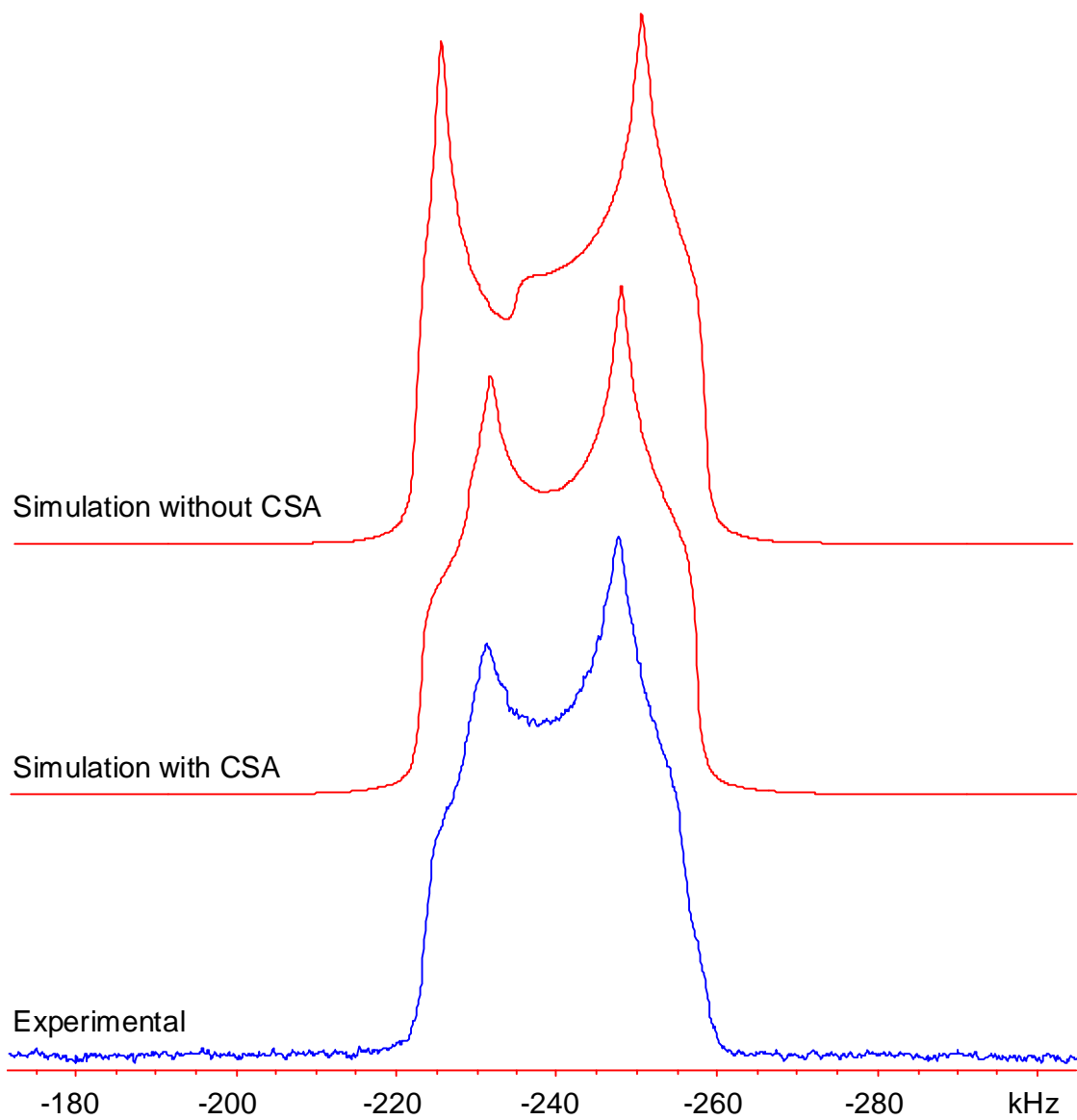


Figure C.5.2. The contribution of ^{115}In CSA on the NMR pattern of $[\text{In}([15]\text{crown-5})_2][\text{OTf}]$.

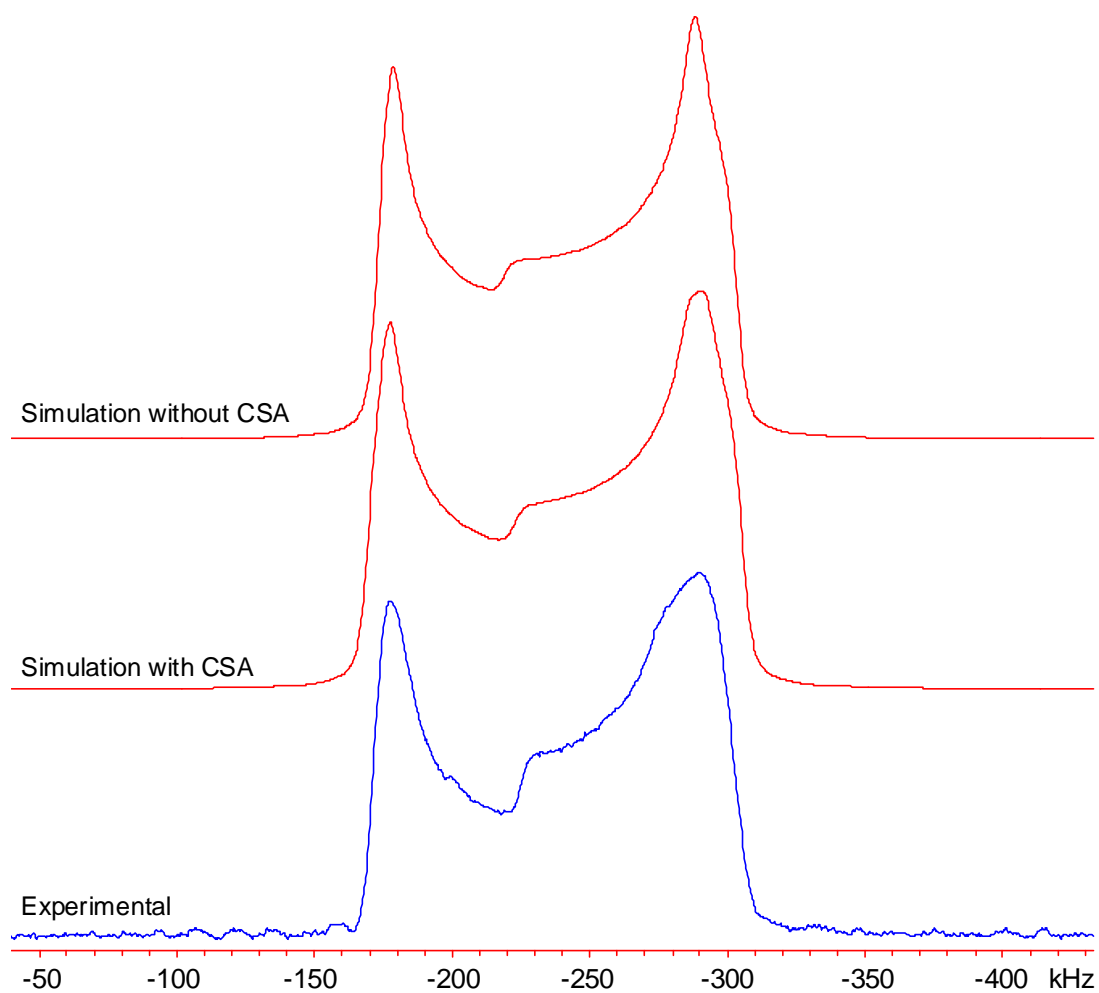


Figure C.5.3. The contribution of ^{115}In CSA on the NMR pattern of $[\text{In}([18]\text{crown-6})]\text{GaCl}_4$

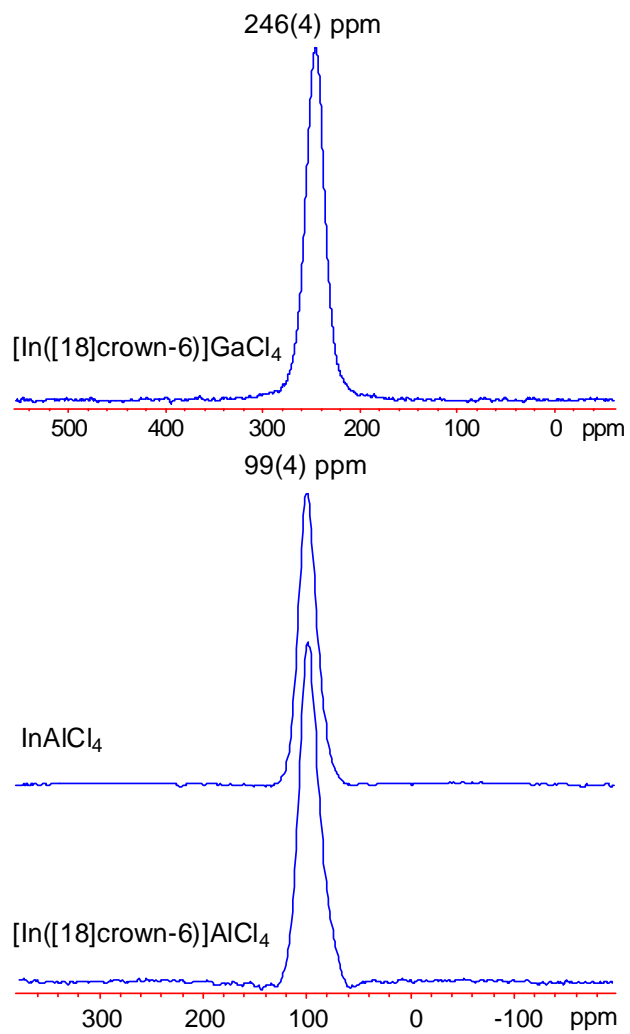


Figure C.5.4. Static ^{71}Ga SSNMR spectrum of $[\text{In}([18]\text{crown-6})]\text{GaCl}_4$ and ^{27}Al SSNMR spectra of AlCl_3 and $[\text{In}([18]\text{crown-6})]\text{AlCl}_4$ at 9.4 T

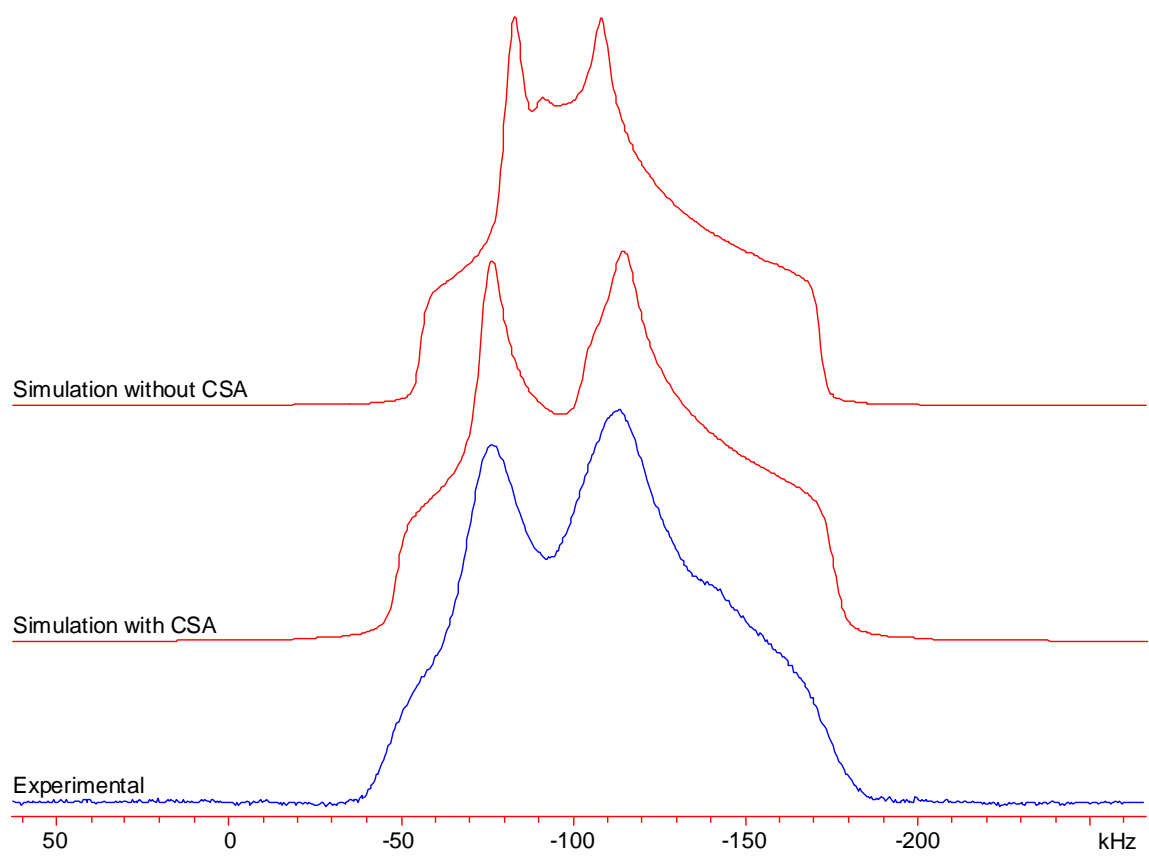


Figure C.5.5. The contribution of ^{115}In CSA on the NMR pattern of InI

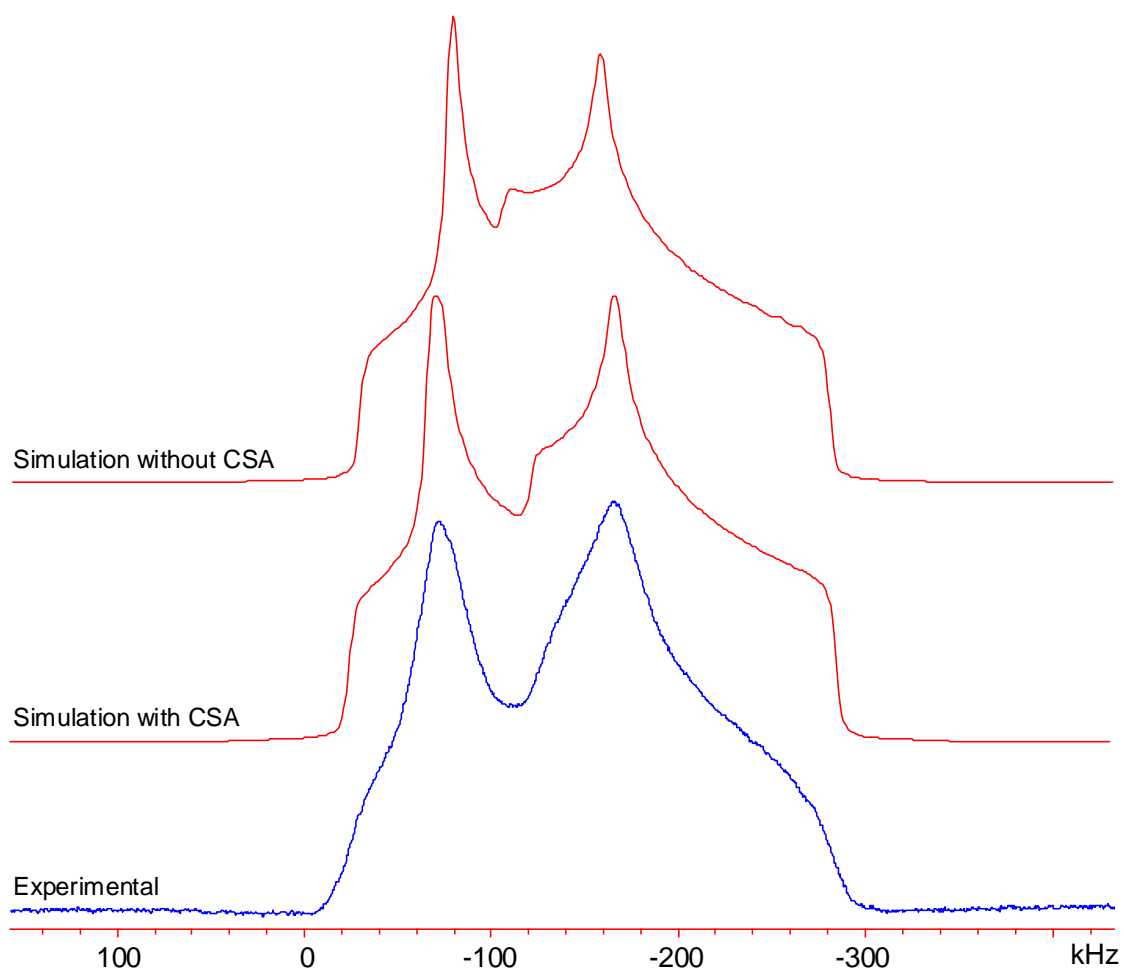


Figure C.5.6. The contribution of ^{115}In CSA on the NMR pattern of InBr

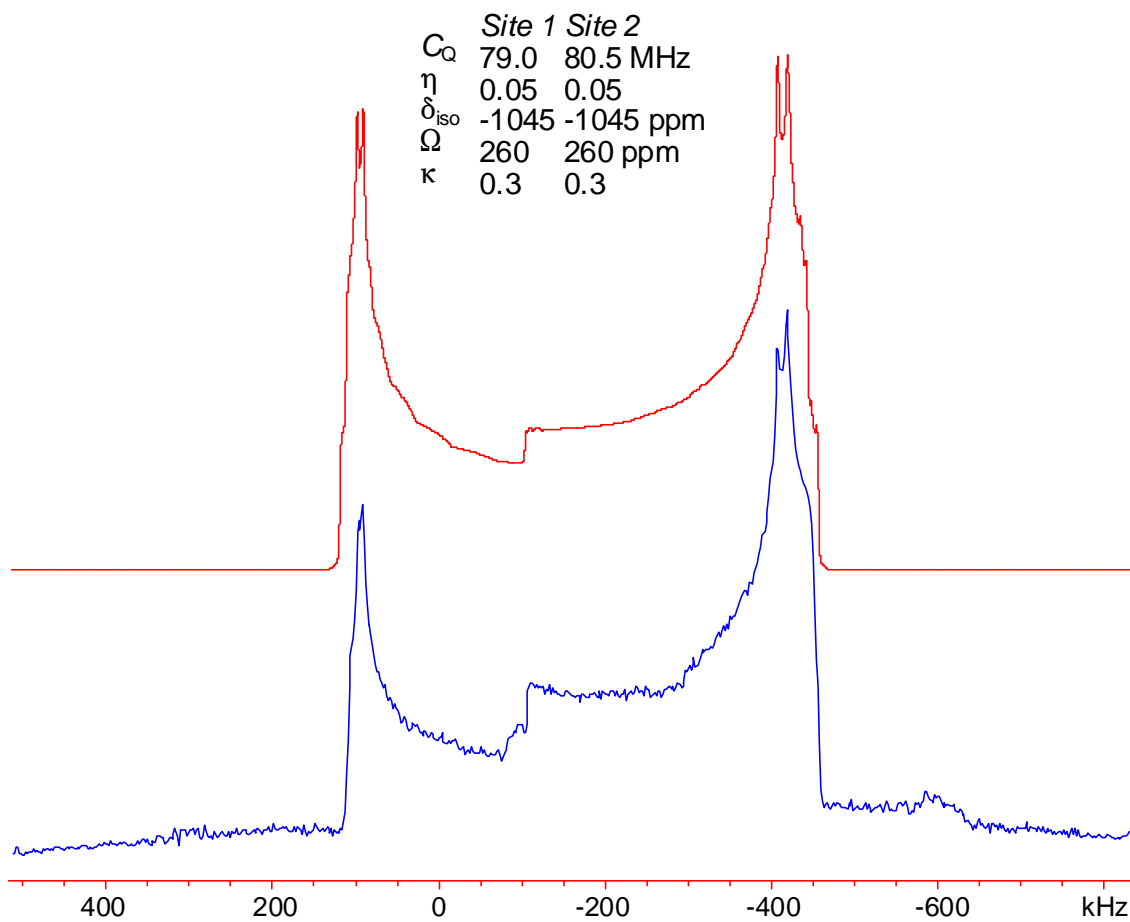


Figure C.5.7. Simulation of ^{115}In NMR pattern of $[\text{In}][\text{OTf}]$ at 9.4 T with parameters of two indium sites

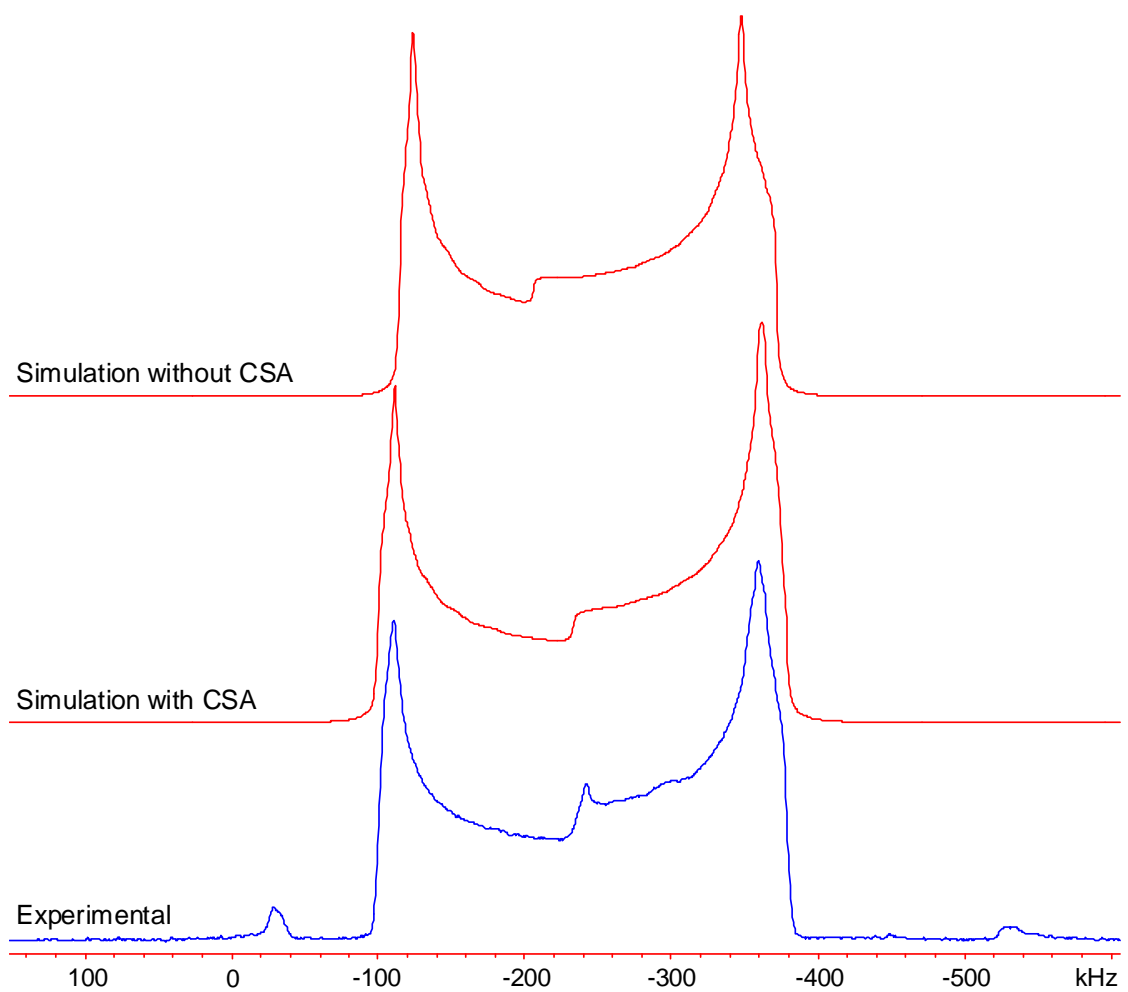


Figure C.5.8. The contribution of ^{115}In CSA on the NMR pattern of $[\text{In}][\text{OTf}]$

4. Appendix D: Supplementary Information for Chapter 6

Table D.6.1. ^{109}Ag NMR Experimental Parameters

Compound	Spectral Frequency (MHz)	Spinning Speed (kHz)	pw90H (μs)	CP Power (kHz)	Contact Time (ms)	Recycle Delay (s)	Spectral Width (kHz)	Number of Scans
1a	18.607141	2.0/2.9	5.5	16.8	35	10	40	2000/1292
1b	18.607141	2.9	5.0	18.6	30	6	40	27732
1c	18.607141	2.9	5.5	16.8	35	10	40	5932
1d	18.609046	2.0/3.1	5.5	16.8	30	10	100	6628/8512
1e	18.609046	2.0/2.9/8.0	5.0	18.6/27.8	35	10	100	4692/15660
1e (MAS)^a	18.609369	8.0	-----	-----	-----	300	40	796
2a	18.602978	2.0	3.75	16.8	30	20	50	2288
2b	18.607661	2.0/3.5	5.0	16.8	35	6	100	13468/25824
3	18.612367	2.0/2.7	5.0	18.6	30	8	100	10644/11468

^a this spectrum was acquired with 1-pulse sequence using a 8 μs pulse on the ^{109}Ag channel.

Table D.6.2. ^{15}N NMR Experimental Parameters

Compound	Spectral Frequency (MHz)	Spinning Speed (kHz)	pw90H (μs)	Decoupling Power (kHz)	Contact Time (ms)	Recycle Delay (s)	Spectral Width (kHz)	Number of Scans
1b	40.506222	5.0	3.75	60	2	4	15	672
1e	40.506222	5.0	3.75	60	2	4	15	744
1b	91.221550	10.0	2.50	100	2	20	30	1024
1e	91.221550	10.0	2.50	100	2	20	30	1024
2b	40.506222	6.0	3.80	70	2	4	100	1872

Table D.6.3. ^{13}C NMR Experimental Parameters

Compound	Spectral Frequency (MHz)	Spinning Speed (kHz)	pw90H (μs)	Decoupling Power (kHz)	Contact Time (ms)	Recycle Delay (s)	Spectral Width (kHz)	Number of Scans
1a	100.52683	5.0/7.0	4.6	40	15	10	50	500/5480
1b	100.52353	5.0/7.0	2.5	42	12	6	50	244/132
1c	100.52683	5.0/7.0	2.5	42	12	10	50	168/156
1d	100.52683	5.0/7.0	2.5	42	12	10	50	144/144
1e	100.52683	5.0/7.0	2.5	42	12	10	50	148/160
2a	100.52683	5.0/7.0	2.5	42	12	10	50	184/128
2b	100.51982	5.0/7.0	2.5	34	12	10	50	44/108
3	100.52683	5.0/7.0	4.0	34	5	12	50	192/176

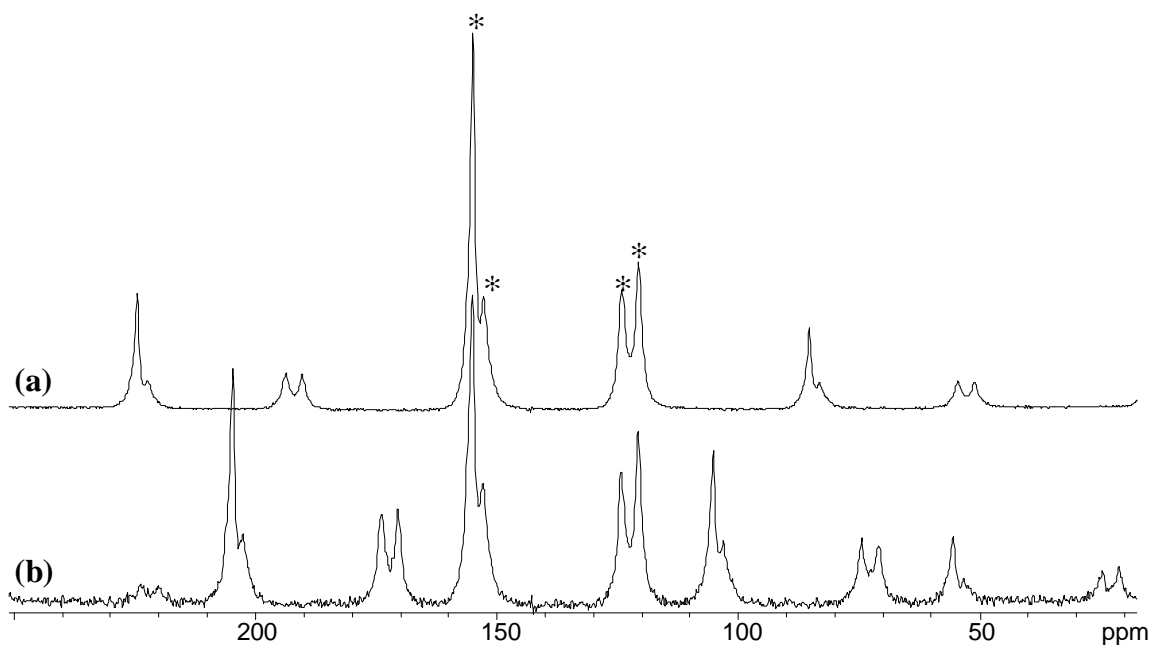


Figure D.6.1. Solid-state ^1H - ^{13}C CP/MAS NMR spectra of **1a** at two different spinning speeds. **(a)** $v_{\text{rot}} = 7.0$ kHz. **(b)** $v_{\text{rot}} = 5.0$ kHz. There are four isotropic peaks in the ^1H - ^{13}C CP/MAS NMR spectrum at 120.5, 123.9, 152.6 and 154.8 ppm which have an intensity ratio of 1:1:1:2 (for different contact times). These resonances are assigned to carbon nuclei which are meta, meta, para and ortho to the nitrogen atom, respectively.¹⁻³
 *: isotropic peaks.

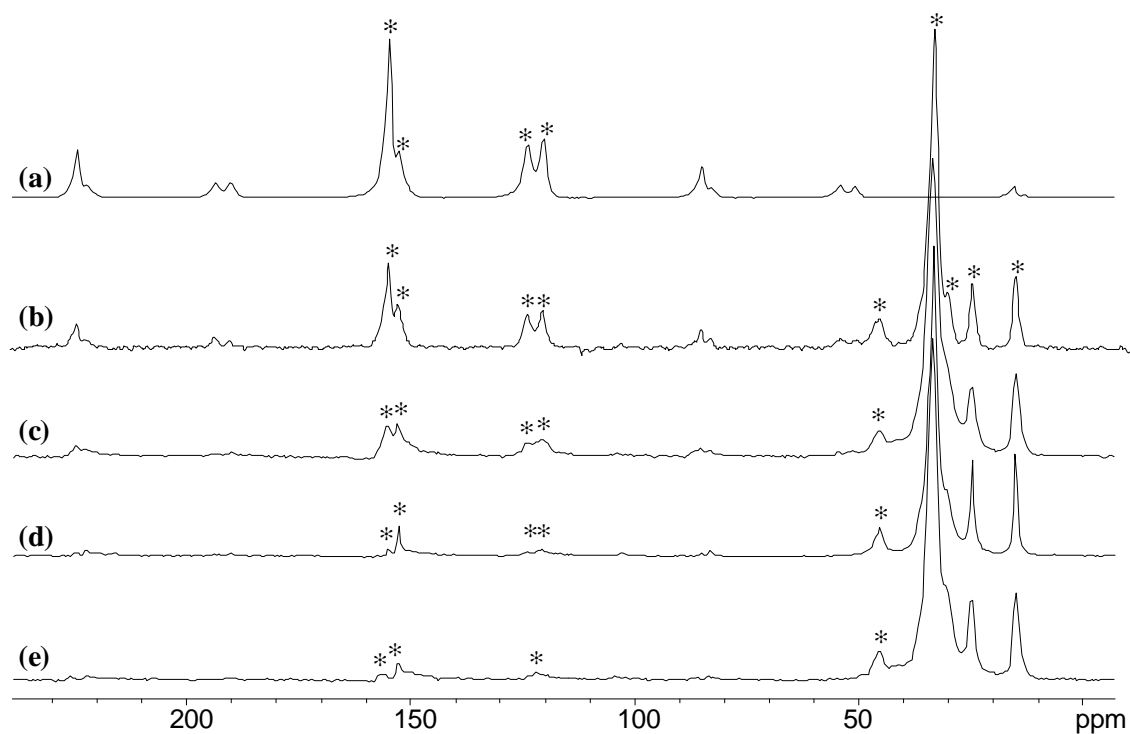


Figure D.6.2. Solid-state ^{13}C CP/MAS NMR spectra of (a) **1a**, (b) **1b**, (c) **1c**, (d) **1d** and (e) **1e** at $\nu_{\text{rot}} = 7.0$ kHz. *: isotropic peaks. There are five peaks corresponding to the carbon atoms of the dodecylamine which are at 45.3, 33.6, 30.6, 25.2 and 15.1, respectively.⁴ These peaks correspond to C1, C2-C9, C10, C11 and C12 in the chain.

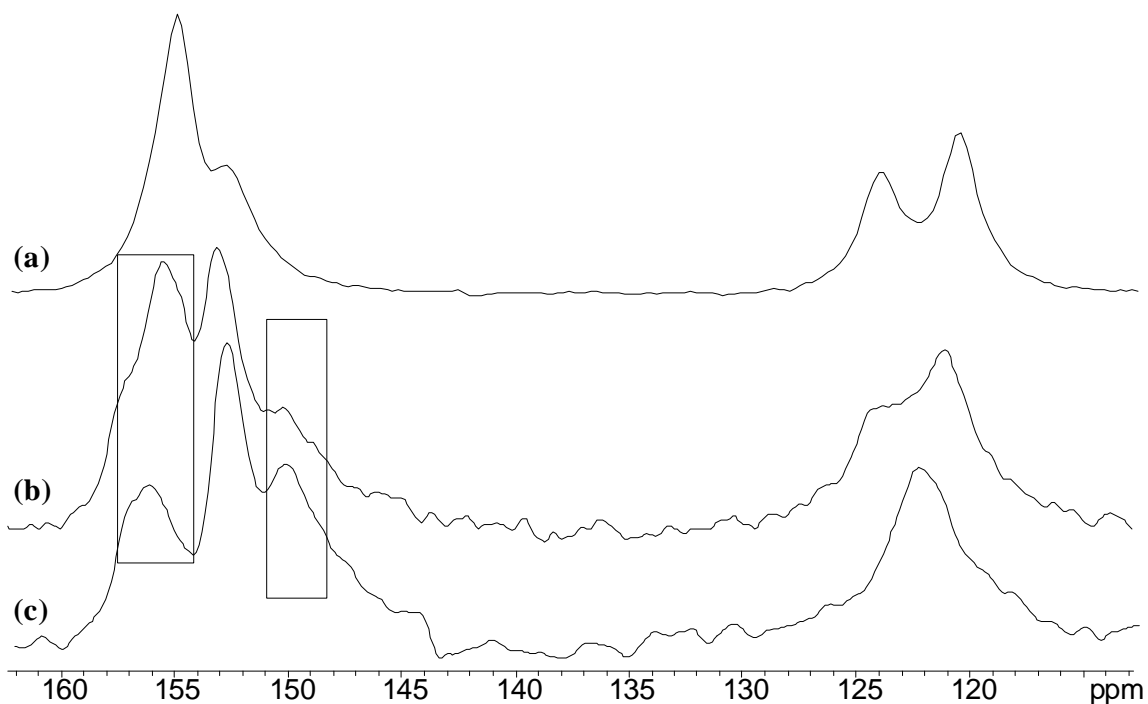


Figure D.6.3. Expanded pyridine region of the ^{13}C CP/MAS NMR spectra of **(a) 1a**, **(b) 1c**, and **(c) 1e** at $\nu_{\text{rot.}} = 7.0$ kHz. Close examination of the region from 115 to 160 ppm reveals subtle differences in carbon chemical shifts between the parent material (**1a**) and the new layered solid (**1e**). The carbon chemical shifts in **1e** are similar to those for 4-pyridine sulfonic acid;⁵ notably, there are only three distinct high-frequency resonances and one low-frequency resonance. This data supports the cleavage of the silver-nitrogen bond and the presence of the pyridinesulfonate anions. Interestingly, the ^{13}C NMR spectrum of the 1:1 sample, **1c**, has resonances present in both the spectra of **1a** and **1e**, confirming that **1c** is comprised of a mixture of materials.

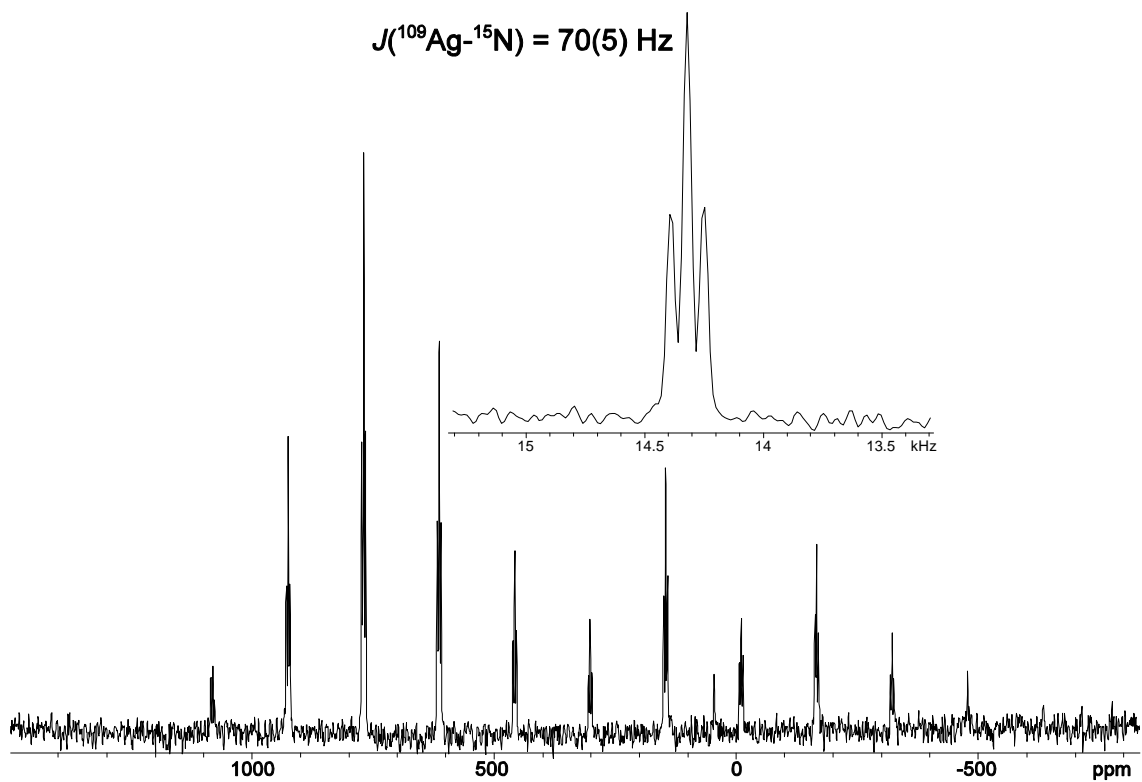


Figure D.6.4. ^1H - ^{109}Ag CP/MAS NMR spectrum of ^{15}N -labeled **2b** at $\nu_{\text{rot}} = 2.9 \text{ kHz}$.

Table D.6.4. Theoretical ^{109}Ag chemical shift parameters and $^1J(^{109}\text{Ag}, ^{14}\text{N})$ coupling values as a function of Ag-N bond length in $[\text{Ag}(\text{NH}_2\text{C}_3\text{H}_7)_2]^+$.

Ag-N (Å)	σ_{iso} (ppm)	δ_{iso} (ppm)	Ω (ppm)	κ	$^1J(^{109}\text{Ag}, ^{14}\text{N})$ (Hz)	SCF Energies (10^7 kJ/mole)
1.95	3414	786	1806	0.91	45	-14553961.0800000
2.00	3528	671	1646	0.92	44	-14554007.7853353
2.05	3633	566	1500	0.92	43	-14554043.5010371
2.10	3729	470	1366	0.93	42	-14554070.3998895
2.15	3817	382	1245	0.94	40	-14554090.2246470
2.20	3897	302	1134	0.94	38	-14554104.3539070
2.25	3970	228	1034	0.94	36	-14554113.9689872
2.30	4038	161	943	0.95	34	-14554119.9091549
2.35	4100	100	860	0.95	32	-14554122.9175055
2.40	4156	43	785	0.95	30	-14554123.5781863
2.45	4207	-8	717	0.95	28	-14554122.3660454
2.50	4254	-55	655	0.95	26	-14554119.6697356
2.55	4297	-98	598	0.95	24	-14554115.8089114
2.60	4336	-137	546	0.94	22	-14554111.0475145
2.65	4372	-173	497	0.94	21	-14554105.6034088
2.70	4405	-206	453	0.94	19	-14554099.6559947

Table D.6.5. Theoretical ^{109}Ag chemical shift parameters and $^1J(^{109}\text{Ag}, ^{14}\text{N})$ coupling values of **4** using different basis sets.

Basis Set ^a	σ_{iso} (ppm)	δ_{iso} (ppm)	Ω (ppm)	κ	$^1J(^{109}\text{Ag}, ^{14}\text{N})$ (Hz)
6-311G** / STO-3G	3747	452	1705	0.67	26
6-311G**/ Ahlrichs Coulomb Fitting	865	3334	1081	0.15	0.1
6-311G**/ DeMon Coulomb Fitting	3759	440	795	0.90	76
6-311G**/ DGauss A1 DFT Exchange Fitting	3617	582	251	0.42	26
6-311G**/ WTBS	3810	389	1244	0.87	32
6-311G**/ Stuttgart RSC 1997 ECP	213	3986	154	0.58	0.06
6-311G**/ cc-pVDZ-PP	209	3990	160	0.60	0.06
6-311G** DZVP ^b	3546	653	1652	0.84	41
6-311G** DZVP ^c	3206	993	1978	0.74	33

^a The first basis set was used on all the atoms except the silver on which the second basis set was used.

^b This calculation was done using the DZVP basis set on both the silver and nitrogen atoms.

^c Calculation was done using the B3LYP method while all of the other ones were done with RHF.

Table D.6.6. CS tensor parameters and J -coupling a span as a function of $\angle\text{N-Ag-N}$ in $[\text{Ag}(\text{NH}_2\text{C}_3\text{H}_7)]^+$

$\angle\text{N-Ag-N}$	Ag-N (Å)	σ_{iso} (ppm)	δ_{iso} (ppm) ^a	Ω (ppm)	κ	$^1J(^{109}\text{Ag}, ^{14}\text{N})$ (Hz)
160°	2.15	3817	382	1223	0.92	39.2
165°	2.15	3817	382	1245	0.94	40
175°	2.15	3817	382	1268	0.95	40.6
180°	2.15	3817	382	1274	0.96	40.6

Table D.6.7. CS tensor parameters and J -coupling a span as a function of $\angle\text{C-N-N-C}$ in $[\text{Ag}(\text{NH}_2\text{C}_3\text{H}_7)]^+$

$\angle\text{C-N-N-C}$	Ag-N (Å)	σ_{iso} (ppm)	δ_{iso} (ppm) ^a	Ω (ppm)	κ	$^1J(^{109}\text{Ag}, ^{14}\text{N})$
62°	2.15	3817	382	1244	0.94	39.9
-180°	2.15	3831	368	1295	0.82	38.4
0°	2.15	3837	362	1260	0.78	38.3
-62°	2.15	3846	353	1265	0.85	38.4

Table D.6.8. Atomic coordinates of the structural unit used to calculate the ^{109}Ag CS tensor parameters of Ag(1) in 1a.

	x	y	z
Ag	0.002715	-0.199543	0.000445
C	-2.678406	1.098652	0.368297
C	-4.051086	1.230409	0.578582
C	-4.871953	0.199546	0.165421
C	-2.956061	-0.975488	-0.612982
C	-4.336514	-0.903115	-0.467958
C	2.680873	1.100008	-0.383903
C	2.963255	-0.960866	0.623617
C	4.343545	-0.887182	0.477674
C	4.876465	0.208571	-0.169669
C	4.053243	1.232225	-0.595859
H	-2.071708	1.824824	0.62323
H	-4.437856	2.02522	1.001767
H	-5.837651	0.248122	0.325012
H	-2.547999	-1.76141	-1.032757
H	-4.904095	-1.622524	-0.815381
H	1.779214	1.457328	-0.524372
H	2.556983	-1.742324	1.053346
H	4.912066	-1.605867	0.825059
H	5.843252	0.262048	-0.320872
H	4.405433	2.030299	-1.042445
N	-2.140445	0.011113	-0.184971
N	2.145385	0.018352	0.183141

Table D.6.9. Atomic coordinates of the structural unit used to calculate the ^{109}Ag CS tensor parameters of Ag(2) in **1a**.

	x	y	z
Ag	-0.134211	-0.000001	-0.000003
C	2.818352	3.836477	-0.554325
C	-2.591248	3.836482	-0.554317
C	-2.591254	-3.83647	0.554318
C	2.818346	-3.836473	0.55432
H	2.04755	4.316113	-0.274478
H	3.497927	4.307355	-0.086402
H	3.188887	3.816049	-1.428846
H	-3.36205	4.316116	-0.274469
H	-1.911673	4.307358	-0.086392
H	-2.220713	3.816059	-1.428838
H	-3.362056	-4.316103	0.274468
H	-1.911679	-4.307347	0.086394
H	-2.22072	-3.816046	1.428839
H	2.047544	-4.316107	0.274471
H	3.497921	-4.30735	0.086396
H	3.18888	-3.816049	1.428842
O	3.478861	1.351925	-0.867848
O	1.30799	1.864211	0.104508
O	3.31982	2.215955	1.39967
O	-1.930739	1.351929	-0.86785
O	-1.930742	-1.351927	0.867853
O	1.307988	-1.864225	-0.104511
O	-4.10161	1.864214	0.104506
O	-2.08978	2.215959	1.399668
O	-4.101612	-1.864219	-0.104504
O	-2.089782	-2.215947	-1.399667
O	3.478858	-1.351932	0.867845
O	3.319818	-2.215951	-1.399665
S	2.725901	2.159873	0.080561
S	-2.683699	2.159877	0.080558
S	-2.683702	-2.159874	-0.080557
S	2.725898	-2.159877	-0.080554

Table D.6.10. Atomic coordinates of $[\text{Ag}(\text{NH}_2\text{C}_3\text{H}_7)_2]^+$ unit used in the calculation

	x	y	z
Ag	-0.01204	-1.12846	-0.09423
C	-2.76663	0.079637	-0.07365
C	2.744011	0.141647	0.314711
C	-2.13403	1.418427	0.244625
C	2.105261	1.391937	-0.20992
C	-2.83508	2.6009	-0.40699
C	2.760513	2.680991	0.256815
H	-2.79719	-0.03917	-1.03593
H	-3.67811	0.069535	0.258609
H	2.68435	0.130204	1.282853
H	3.682913	0.133357	0.07124
H	-2.13719	1.542986	1.205959
H	-1.21001	1.402864	-0.04782
H	-3.76332	2.611174	-0.12146
H	-2.82484	2.480116	-1.36961
H	2.12557	1.36731	-1.17903
H	1.174001	1.401646	0.063075
H	3.703837	2.658057	0.03467
H	2.68155	2.748181	1.221467
H	2.415037	3.419254	-0.26903
H	-2.50097	3.422125	-0.01347
H	-2.45549	-1.89975	0.294608
H	-2.02299	-0.93139	1.530588
H	2.33099	-1.13861	-1.20292
H	2.451496	-1.86309	0.23803
N	-2.01405	-1.03055	0.532148
N	2.082125	-1.05849	-0.23418

References for Appendix D

- (1) Gallego, M. L.; Cano, M.; Campo, J. A.; Heras, J. V.; Pinilla, E.; Torres, M. R.; Cornago, P.; Claramunt, R. M. *Eur. J. Inorg. Chem.* **2005**, 4370.
- (2) Buston, J. E. H.; Claridge, T. D. W.; Heyes, S. J.; Leech, M. A.; Moloney, M. G.; Prout, K.; Stevenson, M. *Dalton Trans.* **2005**, 3195.
- (3) Contakes, S. M.; Klausmeyer, K. K.; Rauchfuss, T. B. *Inorg. Chem.* **2000**, 39, 2069.
- (4) Eggert, H.; Djerassi, C. *J. Am. Chem. Soc.* **1973**, 95, 3710.
- (5) May, L. J.; Shimizu, G. K. H. *Chem. Mat.* **2005**, 17, 217.

5. Appendix E: Supplementary Information for Chapter 7

Table E.7.1. ^{35}Cl MAS NMR Experimental Parameters at 21.1 T.

	v_{rot} (kHz)	pw90 (μs)	Decoupling Power (kHz)	Recycle Delay (s)	Spectral Width (kHz)	# of Scans
PH	22.1	2.3	58.1	1.0	166.67	4400
TH	22.2	2.3	58.1	1.0	166.67	12000
LH	22.1	2.3	58.1	2.0	166.67	5120
LH1	22.1	3.3	62.0	1.0	166.67	10240
BH	15.0	3.6	0.0	1.0	300.00	512
BH1	22.1	2.3	58.1	1.0	166.67	51200
BH2	22.1	3.3	62.0	1.0	166.67	6400

Table E.7.2. ^{35}Cl Static NMR Experimental Parameters at 21.1 T.

	pw90 (μs)	Decoupling Power (kHz)	Recycle Delay (s)	Spectral Width (kHz)	# of Scans
PH	2.1	60.0	1.0	166.67	5200
TH	2.1	60.0	1.0	166.67	3600
LH	2.1	60.0	3.0	166.67	5120
LH1	2.0	62.0	1.0	166.67	9200
BH	6.0	100	1.0	300.00	2696
BH1	2.1	60.0	1.0	166.67	3200
BH2	2.0	62.0	1.0	166.67	3048

Table E.7.3. ^{35}Cl Static NMR Experimental Parameters at 9.4 T.

	pw90 (μs)	Decoupling Power (kHz)	Recycle Delay (s)	Spectral Width (kHz)	Offset Frequency (kHz)	# of Scans	# of pieces acquired
PH	2.3	58.8	0.5	800.00	31	36352	2
TH	1.5	42	0.5	800.00	70	59248	3
LH	2.3	58.8	0.5	800.00	57	137072	2
LH1	2.3	58.8	0.5	800.00	-----	90704	1
BH	1.0	27.4	0.5	800.00	-----	111952	1
BH1	2.3	58.8	0.5	800.00	40	51760	6
BH2	2.3	58.8	0.5	800	36	144352	4

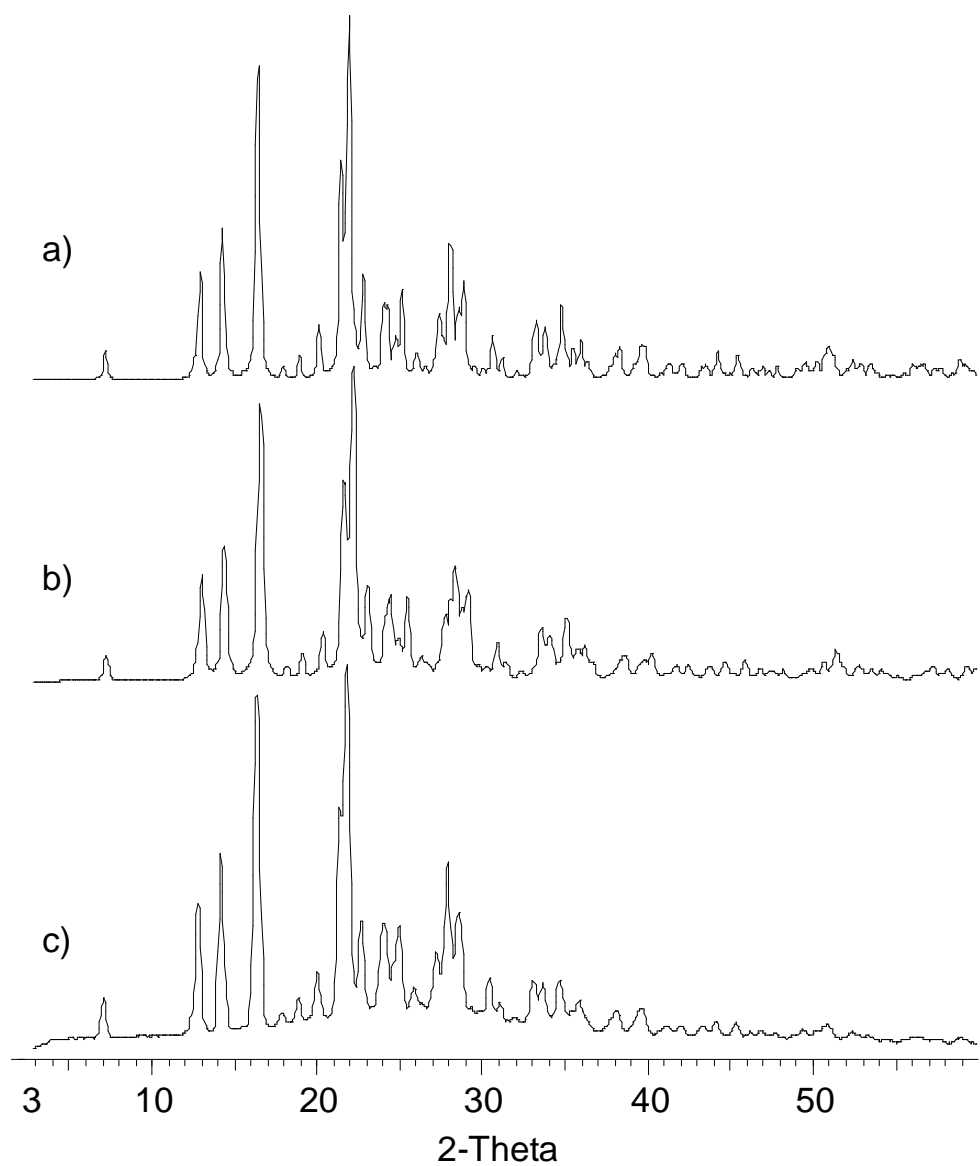


Figure E.7.1. Simulated and experimental powder XRD patterns of procaine HCl (PH). a) Calculated XRD pattern obtained from the reported crystal structure.¹ b) Calculated XRD pattern obtained from the crystal structure acquired in our laboratory. c) Powder XRD pattern of the commercial PH.

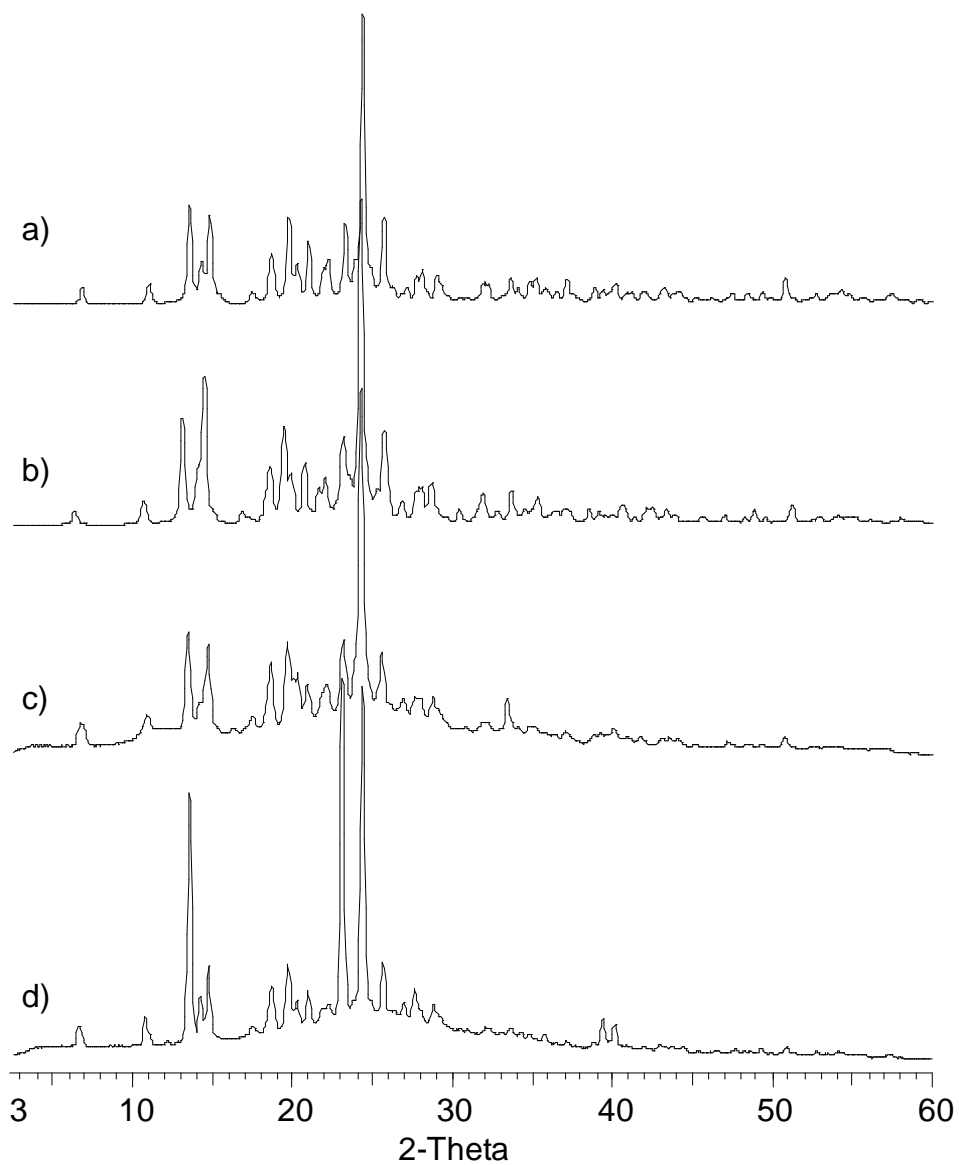


Figure E.7.2. Simulated and experimental powder XRD patterns of tetracaine HCl (TH) samples. a) Calculated XRD pattern obtained from the reported crystal structure.² b) Calculated XRD pattern obtained from the crystal structure acquired in our laboratory after recrystallization from isopropanol. c) Powder XRD pattern of the commercial TH recrystallized from isopropanol. d) Powder XRD pattern of the commercial TH.

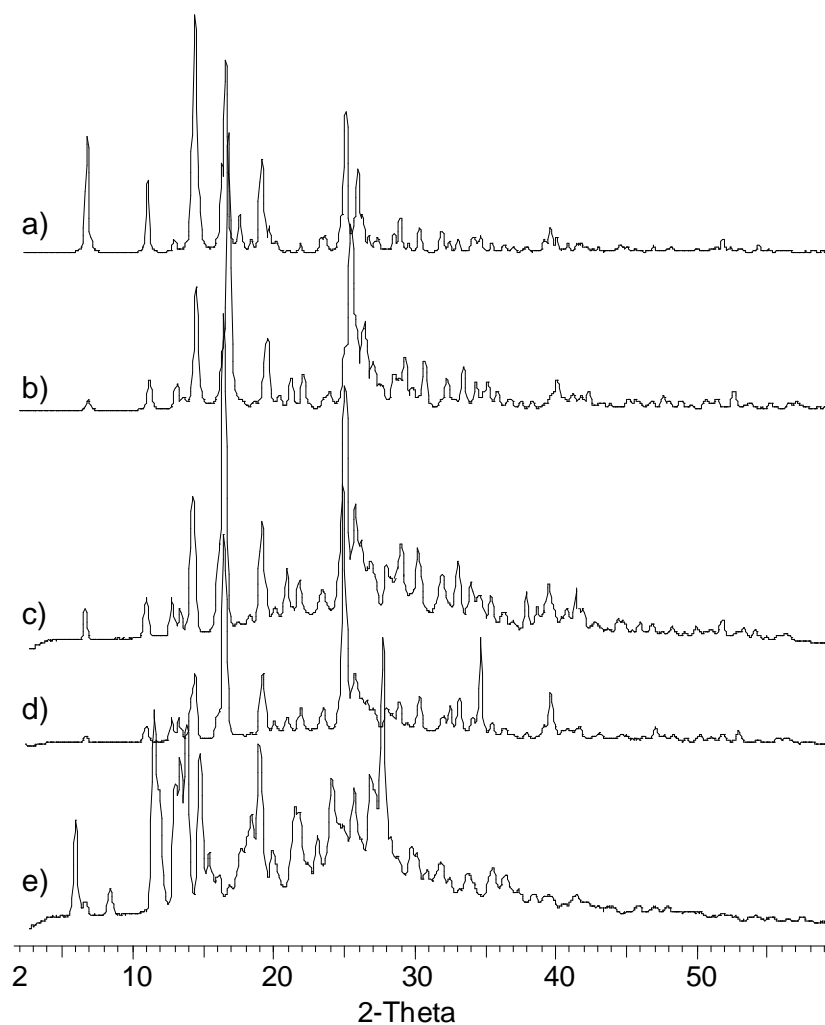


Figure E.7.3. Simulated and experimental powder XRD patterns of the commercial monohydrated lidocaine HCl (LH) and its polymorph. a) Calculated XRD pattern obtained from the reported crystal structure.³ b) Calculated XRD pattern obtained from the crystal structure acquired in our laboratory after recrystallization from acetone. c) Powder XRD pattern of the commercial LH recrystallized from acetone. d) Powder XRD pattern of the commercial LH. e) Powder XRD pattern of the LH polymorph.

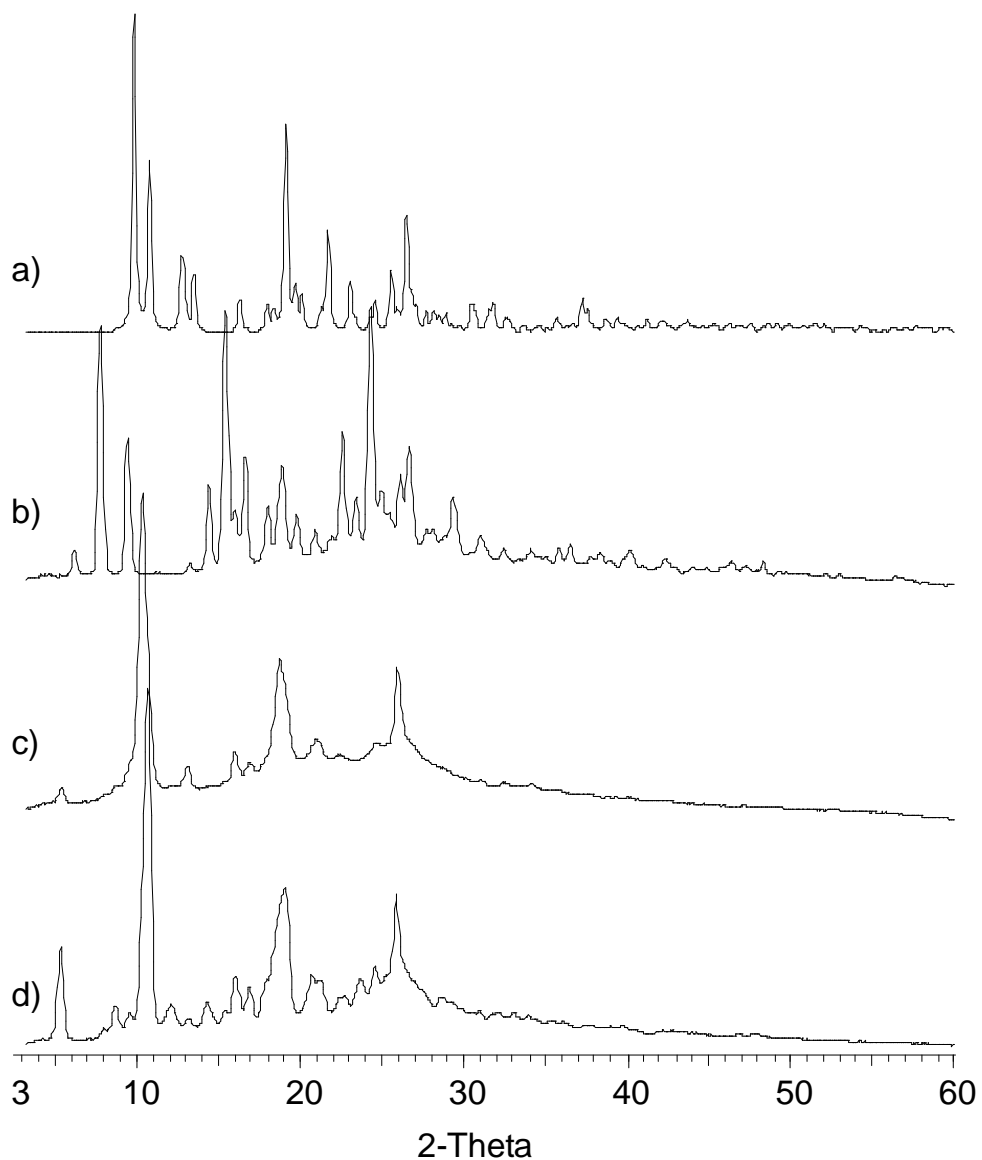


Figure E.7.4. Simulated and experimental powder XRD patterns of bupivacaine HCl (BH) samples. a) Calculated XRD pattern obtained from the reported crystal structure of anhydrous BH.⁴ b) Experimental pattern of the commercial BH. c) Experimental pattern of the commercial BH heated to 120°C. d) Experimental pattern of the commercial BH heated to 170°C.

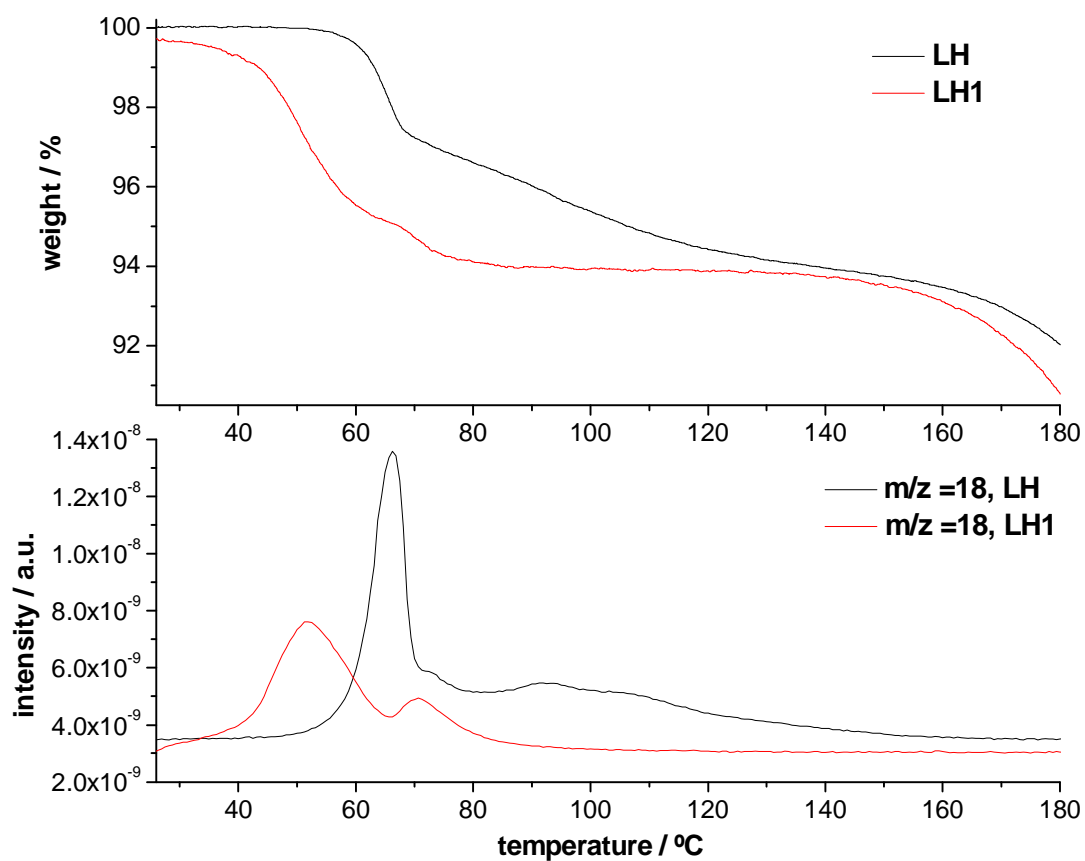


Figure E.7.5. TGA curves of monohydrated lidocaine hydrochloride (LH) and its polymorph (LH1) (top), and simultaneous MS analysis of evolved gases between 15-100 m/z (bottom). Shown are the ion intensity curves at m/z = 18 (H₂O).

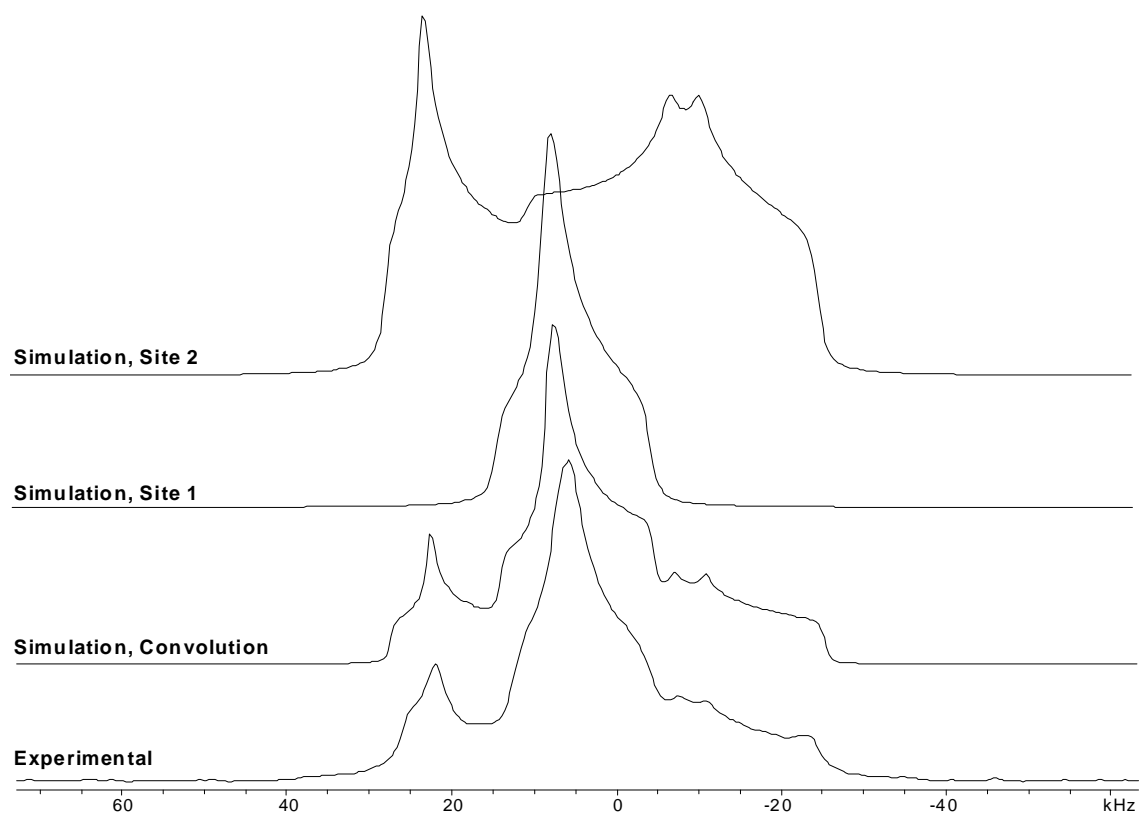


Figure E.7.6. Deconvolution of the two ^{35}Cl NMR patterns in LH1.

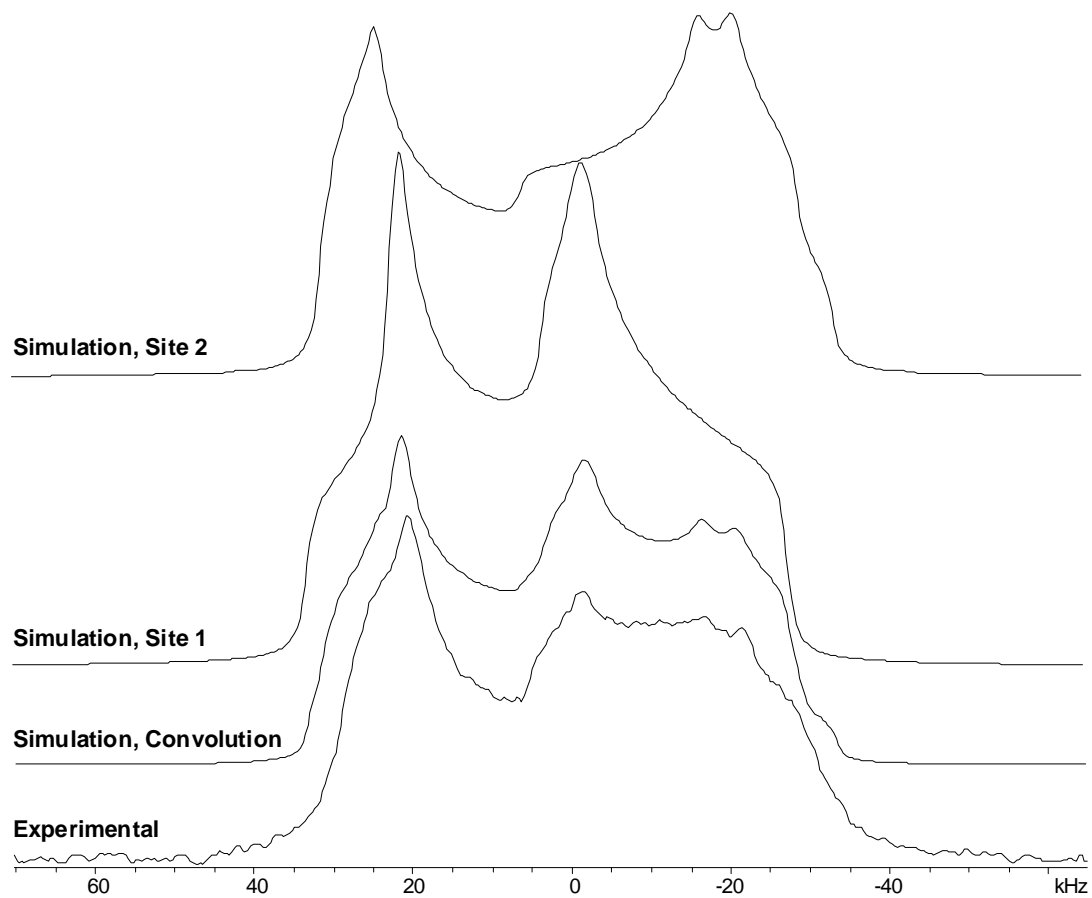


Figure E.7.7. Deconvolution of the two ^{35}Cl NMR patterns in BH1 (heated at 120°C).

Table E.7.4. Summary of theoretical ^{35}Cl EFG tensors (different basis sets).

	Basis Set ^a	$V_{33}(\text{au})$	C_Q/MHz^b	η_Q^c
PH	Experimental	-----	4.87(7)	0.28(4)
	cc-pVTZ/ 6-31G*	-0.281945	-5.409	0.286
	cc-pVTZ /cc-pVDZ	-0.275383	-5.283	0.338
	6-311+G*	-0.238951	-4.584	0.461
TH	Experimental	-----	6.0(1)	0.27(4)
	cc-pVTZ/ 6-31G*	-0.318306	-6.107	0.197
	cc-pVTZ /cc-pVDZ	-0.303549	-5.824	0.199
	6-311+G*	-0.305163	-5.855	0.218
LH	Experimental	-----	4.67(7)	0.77(3)
	cc-pVTZ/ 6-31G*	-0.213556	-4.097	0.437
	cc-pVTZ /cc-pVDZ	-0.213080	-4.088	0.425
	6-311+G*	-0.206542	-3.962	0.557
BH	Experimental	-----	3.66(10)	0.72(8)
	cc-pVTZ/ 6-31G*	0.203813	3.91	0.84
	cc-pVTZ /cc-pVDZ	0.200183	3.84	0.82
	6-311+G*	0.183848	3.53	0.71

^aThe first basis set was used on the chlorine atom while the second was used for all the other atoms;

^bTheoretical values of C_Q are calculated by converting from atomic units to Hz by multiplying V_{33} by $(eQ/h)(9.7177 \times 10^{21} \text{ Vm}^{-2})$, where $Q(^{35}\text{Cl}) = -0.082 \times 10^{-28} \text{ m}^2$; ^c $\eta_Q = (V_{11} - V_{22})/V_{33}$.

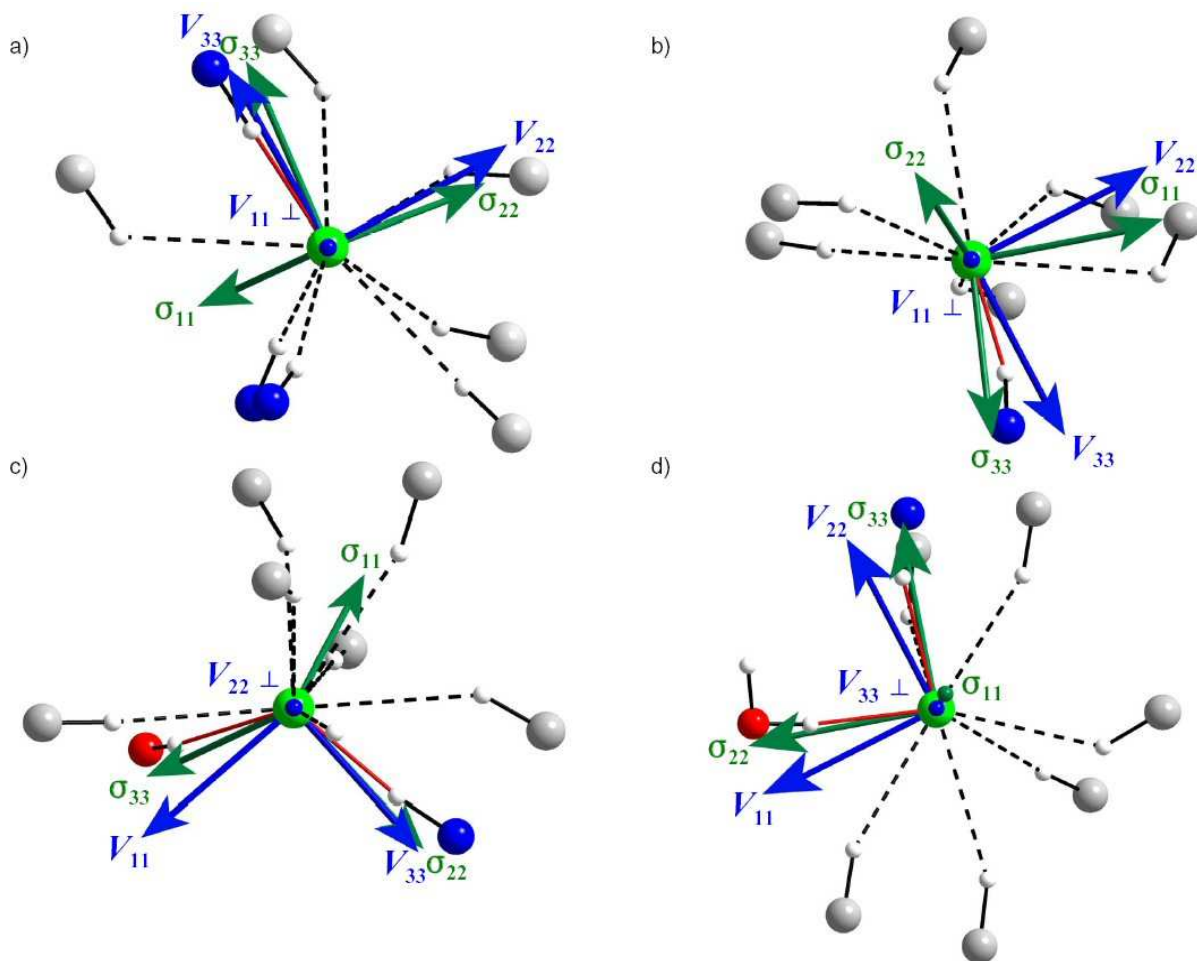


Figure E.7.8. ^{35}Cl EFG and CS tensor orientations in a) PH, b) TH, c) LH and d) BH. The diagrams above are magnifications of the chlorine sites pictured in Figure 7.1.

References for Appendix E

- (1) Dexter, D. D. *Acta Crystallogr., Sect. B: Struct. Sci.* **1972**, 28, 77.
- (2) Nowell, H.; Atfield, J. P.; Cole, J. C.; Cox, P. J.; Shankland, K.; Maginn, S. J.; Motherwell, W. D. S. *New J. Chem.* **2002**, 26, 469.
- (3) Hanson, A. W.; Roehrl, M. *Acta Crystallogr., Sect. B: Struct. Sci.* **1972**, 28, 3567.
- (4) Csoeregh, I. *Acta Crystallogr., Sect. C: Cryst. Struct. Commun.* **1992**, C48, 1794.

6. Appendix F: Supplementary Information for Chapter 8

Table F.8.1. ^{35}Cl MAS NMR Experimental Parameters at 21.1 T.

	ν_{rot} (kHz)	pw90 (μs)	Decoupling Power (kHz)	Recycle Delay (s)	Spectral Width (kHz)	# of Scans
TR	23.33	2.1	90	1.0	250	6144
AD	22.31	2.1	90	1.0	250	6144
BU	22.35	2.1	90	1.5	250	5120
DI	21.00	2.2	90	3.0	125	19008
RA	22.20	2.0	90	1.0	167	10240
ME	22.46	2.0	90	1.0	167	10240
AM	20.06	2.2	90	1.0	125	3200
AC	21.72	2.2	90	2.0	125	6144
IS	21.11	2.2	90	1.0	125	6144

Table F.8.2. ^{35}Cl Static NMR Experimental Parameters at 21.1 T.

	pw90 (μs)	Decoupling Power (kHz)	Recycle Delay (s)	Spectral Width (kHz)	# of Scans
TR	2.5	62	1.5	250	2048
AD	2.5	62	1.5	250	2048
BU	2.5	62	1.5	250	2048
DI	2.5	62	1.5	250	2048
RA	2.5	62	1.0	167	20480
ME	2.5	62	1.0	167	10240
AM	2.5	62	1.0	250	1600
AC	2.5	62	1.5	250	2048
IS	2.5	62	1.0	250	1600

Table F.8.3. ^{35}Cl Static NMR Experimental Parameters at 9.4 T.

	pw90 (μs)	# of echoes	Decoupling Power (kHz)	Recycle Delay (s)	Spectral Width (kHz)	# of Scans
Echo						
ME	2.2	1	50	0.5	800	63424
AM	1.5	1	50	0.5	250	20000
AC	2.0	1	0	0.5	500	23872
DI	1.5	1	50	0.5	400	139120
WURST-QCPMG						
RA	50	1	0	0.5	500	115064
TR	50	120	42	0.5	800	2142
BU	50	35	42	0.5	500	7483
AD	50	35	42	0.5	500	114624
IS	50	35	42	0.5	500	8409

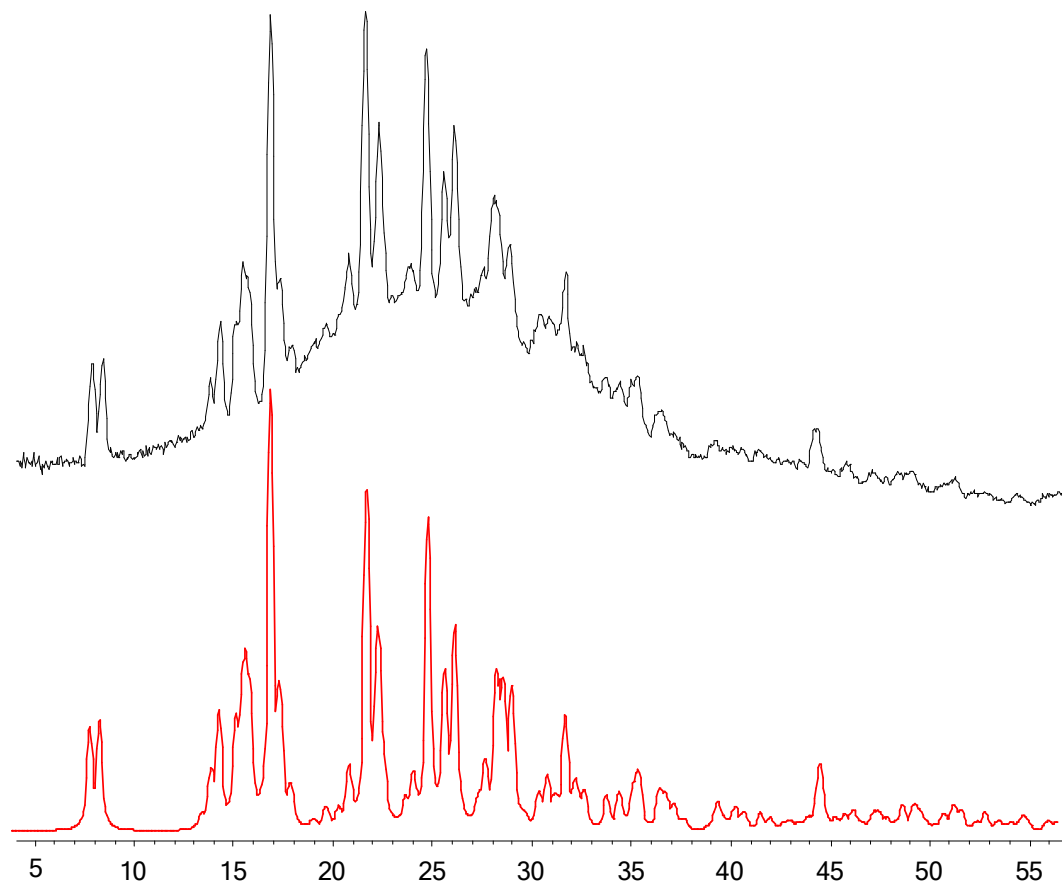


Figure F.8.1. Experimental (top) and simulated (bottom) powder XRD patterns of ranitidine hydrochloride

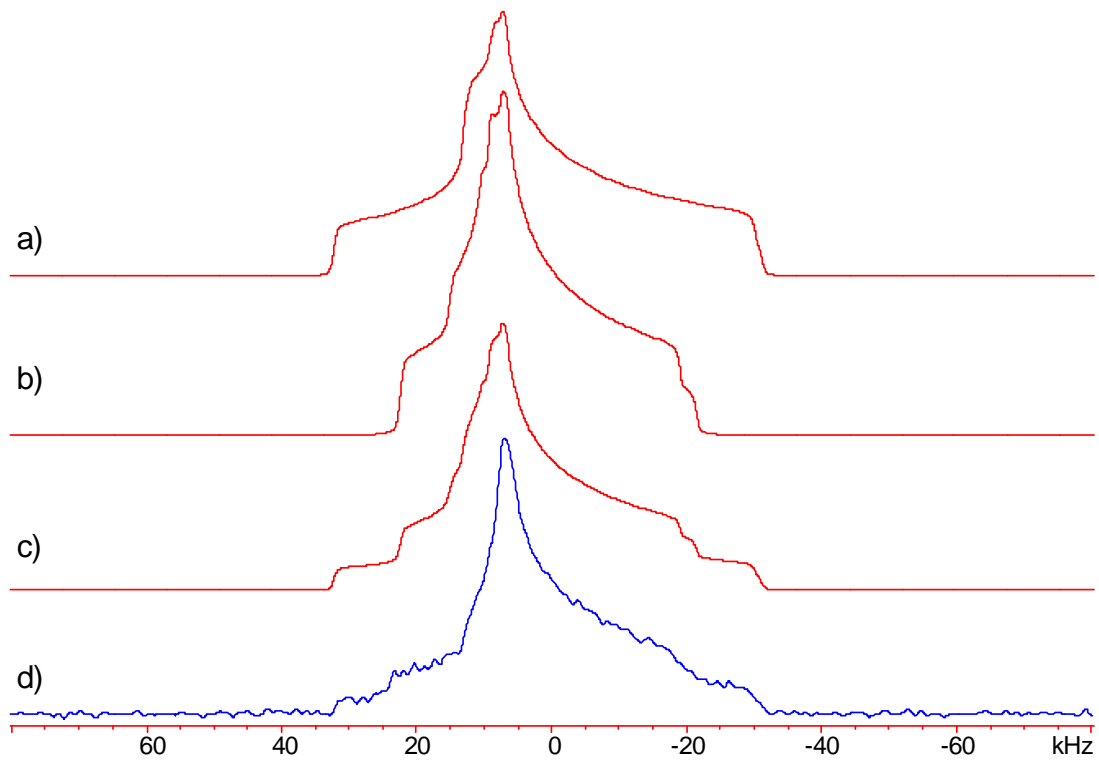


Figure F.8.2. Deconvolution of the NMR patterns of the two different chlorine sites in DI. a) simulated spectrum of site 1, b) simulated spectrum of site 2, c) convolution of the two patterns and d) experimental spectrum.

7. Copyright Release Forms

American Chemical Society's Policy on Theses and Dissertations

If your university requires a signed copy of this letter see contact information below.

Thank you for your request for permission to include **your** paper(s) or portions of text from **your** paper(s) in your thesis. Permission is now automatically granted; please pay special attention to the implications paragraph below. The Copyright Subcommittee of the Joint Board/Council Committees on Publications approved the following:

Copyright permission for published and submitted material from theses and dissertations

ACS extends blanket permission to students to include in their theses and dissertations their own articles, or portions thereof, that have been published in ACS journals or submitted to ACS journals for publication, provided that the ACS copyright credit line is noted on the appropriate page(s).

Publishing implications of electronic publication of theses and dissertation material

Students and their mentors should be aware that posting of theses and dissertation material on the Web prior to submission of material from that thesis or dissertation to an ACS journal may affect publication in that journal. Whether Web posting is considered prior publication may be evaluated on a case-by-case basis by the journal's editor. If an ACS journal editor considers Web posting to be "prior publication", the paper will not be accepted for publication in that journal. If you intend to submit your unpublished paper to ACS for publication, check with the appropriate editor prior to posting your manuscript electronically.

If your paper has **not** yet been published by ACS, we have no objection to your including the text or portions of the text in your thesis/dissertation in **print and microfilm formats**; please note, however, that electronic distribution or Web posting of the unpublished paper as part of your thesis in electronic formats might jeopardize publication of your paper by ACS. Please print the following credit line on the first page of your article: "Reproduced (or 'Reproduced in part') with permission from [JOURNAL NAME], in press (or 'submitted for publication'). Unpublished work copyright [CURRENT YEAR] American Chemical Society." Include appropriate information.

If your paper has already been published by ACS and you want to include the text or portions of the text in your thesis/dissertation in **print or microfilm formats**, please print the ACS copyright credit line on the first page of your article: "Reproduced (or 'Reproduced in part') with permission from [FULL REFERENCE CITATION.] Copyright [YEAR] American Chemical Society." Include appropriate information.

Submission to a Dissertation Distributor: If you plan to submit your thesis to UMI or to another dissertation distributor, you should not include the unpublished ACS paper in your thesis if the thesis will be disseminated electronically, until ACS has published your paper. After publication of the paper by ACS, you may release the entire thesis (**not the individual ACS article by itself**) for electronic dissemination through the distributor; ACS's copyright credit line should be printed on the first page of the ACS paper.

Use on an Intranet: The inclusion of your ACS unpublished or published manuscript is permitted in your thesis in print and microfilm formats. If ACS has published your paper you may include the manuscript in your thesis on an intranet that is not publicly available. Your ACS article cannot be posted electronically on a publicly available medium (i.e. one that is not password protected), such as but not limited to, electronic archives, Internet, library server, etc. The only material from your paper that can be posted on a public electronic medium is the article abstract, figures, and tables, and you may link to the article's DOI or post the article's author-directed URL link provided by ACS. This paragraph does not pertain to the dissertation distributor paragraph above.

Questions? Call +1 202/872-4368/4367. Send e-mail to copyright@acs.org or fax to +1 202-776-8112. 10/10/03, 01/15/04, 06/07/06

Vita Auctoris

Hiyam Hamaed was born in 1979 in Bint Jbeil, South Lebanon. She graduated from Bint Jbeil High School in 1997. She arrived in Windsor, Ontario, Canada in April 1999, where she has lived since then. She has been at the University of Windsor since Winter 2001, obtaining a B.Sc. with Honours chemistry in 2005. She is currently a candidate for the PhD degree in chemistry at the University of Windsor and is planning to graduate in June 2010.